Mechanistic Studies of Proton-Coupled Electron Transfer in Aminotyrosine- and Fluorotyrosine-Substituted Class Ia Ribonucleotide Reductase

by

Ellen Catherine Minnihan

A.B., Chemistry
Johns Hopkins University, 2006

Submitted to the Department of Chemistry
in Partial Fulfillment of the Requirements for the Degree of

Doctor of Philosophy in Biological Chemistry

at the

MASSACHUSETTS INSTITUTE OF TECHNOLOGY

June 2012

Signature of Author: _____
Department of Chemistry
May 18, 2012

Certified by: _____
JoAnne Stubbe
Novartis Professor of Chemistry and Professor of Biology
Thesis Supervisor

Accepted by: _____
Robert W. Field
Haslam and Dewey Professory of Chemistry
Chairman, Departmental Committee on Graduate Studies

This Doctoral Thesis has been examined by a committee of the Departments of Chemistry and Biology as follows:

Daniel G. Nocera
Henry Dreyfus Professor of Energy and Professor of Chemistry
Thesis Chair

JoAnne Stubbe
Novartis Professor of Chemistry and Professor of Biology
Thesis Supervisor

Barbara Imperiali
Class of 1922 Professor of Biology and Professor of Chemistry

Acknowledgments

I would first like to thank my research advisor, JoAnne Stubbe, whose unparalleled passion for science amazed me when I first arrived at MIT and continues to amaze me on a daily basis nearly six years later. Thank you for sharing that enthusiasm with me. I am honored to have been taught by you the skills that are indispensible to a successful career in research science, namely, how to ask smart questions, formulate testable hypotheses, design sophisticated experiments, and critically evaluate data. I would next like to thank my thesis committee for their scientific insight, research advice, and professional guidance during my graduate school career. My Thesis Chairs, Stephen Lippard and Dan Nocera, were eager to engage me in valuable scientific discussion. As pioneers in the fields of bioinorganic chemistry and PCET, respectively, Steve and Dan strongly influenced the way in which I approached my graduate research. I also thank my committee member Barbara Imperiali, whose vast knowledge of the rapidly advancing fields of protein engineering and chemical biology helped inspire much of my early enthusiasm for unnatural amino acid incorporation.

I consider myself fortunate to have had a very collaborative graduate school experience. These collaborators include the Nocera lab at MIT (Dan, Steve, Danny, Rick, Arturo, Pat, Lisa, Bon Jun, Dave), the Drennan lab at MIT (Cathy, Ed, Nozomi, Michael, Christina), the Schultz lab at Scripps (Peter and Doug), the Bennati lab at MPI (Marina and Tomi), the Barry lab at Georgia Tech (Bridgette and Adam), the Britt lab at UC Davis (Dave and Will), and Ulla Uhlin at SLU. Our collaborations have exposed me to a tremendous diversity of techniques, problem-solving skills, and scientific questions. Thank you for sharing your research expertise with me, as I am a more well-rounded and better-equipped scientist as a result of our cooperative endeavors.

The members of the Stubbe lab have made my graduate school experience fantastically memorable. I have been touched by your kindness and helpfulness, and motivated by your intellect and work ethic. Thank you to current members (Mac, Yifeng, Wankyu, Yan, Yimon, Olga, and Alice) and former members (Daniela, Quamrul, Sumit, Ping, Crystal, Luke, Jun, and Xuling). A special thanks to Mo, for passing me the RNR PCET torch and for staying invested in the project's success long after that; to Chia, for being a wise, calming presence in the lab, for fixing what was broken, and for providing an endless supply of tasty snacks; and to Ken, for inspiring hard work, for stimulating scientific discussion, and for training me in advanced experimental techniques. Joey, Rachael, and Mimi: thank you for making grad school history's longest dance party. Whether at the ballet, in cardio class, at the holiday party, on a boat, or at a gala, there are no three people with whom I am more inspired to dance. You have seen me at my worst and yet somehow remain my friends, so let's celebrate by moving in an awkward, pseudo-coordinated, semi-rhythmic fashion! Kanch: a great artist once sang, "before you came into the lab, I missed you so bad." But now you're here as the future of RNR PCET. I'm leaving the lab with the confidence that the project has been passed to very capable hands, and I trust that you're going to make some amazing discoveries. When you do, call me, maybe?

Teaching is something about which I am very passionate. That passion grew from truly rewarding experiences mentoring four fantastic undergraduate researchers in the lab. Thomas, Xin, Heather, and Jonathan: your unadulterated excitement about science could reinvigorate even

a grumpy old graduate student like me. I was inspired by your intelligence and enthusiasm, and was grateful for the positive attitudes and humor you brought to the lab. You each hold tremendous promise as young scientists and future mentors.

A special thanks is extended to friends in the 5:30 club, who celebrated my victories, empathized with my difficulties, solved my problems, and laughed with me always. I'd also like to send love to my friends from home and from college, who have taken the time and energy to maintain meaningful relationships with me despite our hectic, ever-changing lives and the many hundred of miles that physically separate us. I hope our friendships grow richer as we grow older together.

Finally, and most importantly, I would like to thank my family for their unconditional love and support during this journey. Mom, Dad, Steve: I could not have finished this without you. Your belief in me sustained me through the most difficult times at MIT, and I hope to one day return the encouragement, kindness, patience, and guidance that you have so graciously offered me over the last six years. Thank you for sharing with me your love of learning, and for establishing a home environment where intellectual curiosity and academic pursuit is wholeheartedly endorsed. I love you so much.

Mechanistic Studies of Proton-Coupled Electron Transfer in Aminotyrosine- and Fluorotyrosine-Substituted Class Ia Ribonucleotide Reductase

by

Ellen Catherine Minnihan

Submitted to the Department of Chemistry
on May 18, 2012 in Partial Fulfillment of the Requirements
for the Degree of Doctor of Philosophy in Biological Chemistry

ABSTRACT

Ribonucleotide reductase (RNR) catalyzes the conversion of nucleotides to 2′-deoxynucleotides in all organisms. The class Ia RNR from *Escherichia coli* is active as an $\alpha 2\beta 2$ complex and utilizes an unprecedented mechanism of reversible proton-coupled electron transfer (PCET) to propagate a stable tyrosyl radical (Y_{122}•) in β2 over a distance of >35 Å to an active site cysteine (C_{439}) in α2 on each turnover. Generation of the cysteinyl radical (C_{439}•) initiates active site nucleotide reduction. Radical propagation over 35 Å by a pure tunneling mechanism would be too slow to support the observed turnover number. Instead, long-range, reversible PCET is proposed to occur by radical hopping along a specific pathway of redox-active amino acids: Y_{122}• ↔ [W_{48}?] ↔ Y_{356} in β2 to Y_{731} ↔ Y_{730} ↔ C_{439} in α2. The details of this mechanism are kinetically masked in wild-type RNR, and mutation of any of these residues to another native amino acid inactivates the enzyme.

Recent development of technology for the *in vivo*, site-specific incorporation of unnatural amino acids into proteins has provided the opportunity to systematically perturb the native PCET pathway by introduction of tyrosine analogues with modified redox potentials and/or pK_as. This thesis focuses on 3-aminotyrosine (NH_2Y) and fluorotyrosines (F_nYs). NH_2Y has a lower reduction potential than Y and, when incorporated at the three sites of transient Y• formation, generates a thermodynamic minimum and reduces k_{cat} sufficiently to allow characterization of NH_2Y• intermediates. A kinetic model for catalysis by NH_2Y-RNRs has been proposed from the mechanistic studies described herein. Furthermore, the ability to generate NH_2Y• on the pathway has afforded the first characterization of a kinetically stable $\alpha 2\beta 2$ complex. F_nYs span a wide range of solution pK_as and reduction potentials and thus may be used to investigate both PT and ET events. The evolution of an orthogonal, polyspecific tRNA/tRNA synthetase pair for F_nYs is reported. F_nYs at positions 356, 730, and 731 have been used to measure the pH dependence of RNR activity, whereas F_nY•s at position 122 of β2 have been used as radical initiators to begin mapping the relative thermodynamic landscape of the PCET pathway.

Thesis supervisor: JoAnne Stubbe
Title: Novartis Professor of Chemistry and Professor of Biology

Table of Contents

List of Figures

List of Tables

List of Schemes

Abbreviations

α	ribonucleotide reductase large subunit
ADP	adenosine-5′-diphosphate
Amp	ampicillin
ara	arabinose
ATP	adenosine-5′-triphosphate
β	ribonucleotide reductase small subunit
β-ME	β-mercaptoethanol
C•	cysteinyl (thiyl) radical
CAT	chloramphenicol acetyl transferase
CDP	cytidine-5′-diphosphate
Cm	chloramphenicol
CV	column volume
dATP	2′-deoxyadenosine-5′-triphosphate
dC	2′-deoxycytidine
dCDP	2′-deoxycytidine-5′-diphosphate
DCIP	Department of Chemistry Instrumentation Facility
DTT	dithiothreitol
E	effector
EDTA	ethylenediaminetetraacetic acid
EM	electron microscopy
EPR	electron paramagnetic resonance
eq	equivalent(s)
ESI-MS	electrospray ionization mass spectrometry
ET	electron transfer
F_nY	fluorotyrosine (n = 1 – 4)
F_nY•	fluorotyrosyl radical
FPLC	fast protein liquid chromatography
GDP	guanosine-5′-diphosphate
GMML	glycerol minimal medium with leucine

Hepes	4-(2-hydroxyethyl)-1-piperazineethanesulfonic acid
HF	high field
HU	hydroxyurea
Km	kanamycin
IPTG	isopropyl-1-thio-β-galactopyranoside
LB	Luria-Bertani broth
MBI	mechanism-based inhibitor
NADPH	nicotinamide adenine dinucleotide phosphate
NH_2Y	3′-aminotyrosine
NH_2Y•	3′-aminotyrosyl radical
N_3CDP	2′-azido-2′-deoxycytidine-5′-diphosphate
NMR	nuclear magnetic resonance
PCET	proton-coupled electron transfer
PELDOR	pulsed electron-electron double resonance
PLP	pyridoxal-5′-phosphate
PMSF	phenylmethylsulfonyl fluoride
PT	proton transfer
RCQ	rapid chemical quench
rds	rate-determining step
RFQ	rapid freeze quench
RNR	ribonucleotide reductase
RS	tRNA synthetase
RT	room temperature
S	substrate
SAXS	small-angle X-ray scattering
SDS-PAGE	sodium dodecyl sulfate polyacrylamide gele electrophoresis
SF	stopped-flow
Tet	tetracycline
TR	thioredoxin
Tris	tris(hydroxymethyl)-aminoethane
TRR	thioredoxin reductase
TTP	thymidine-5′-triphosphate

W•	tryptophan radical
wt	wild-type
Y•	tyrosyl radical
UAA	unnatural amino acid
UDP	uridine-5′-diphosphate

Chapter 1

An introduction to the class Ia ribonucleotide reductase from *Escherichia coli*

Adapted in part from: Minnihan, E.C., Yokoyama, K., and Stubbe, J. *F1000 Biol. Rep*, **2009**, *1*, 88.

1.1 RIBONUCLEOTIDE REDUCTASES: AN OVERVIEW

1.1.1 Introduction. In all organisms, ribonucleotide reductases (RNRs) catalyze the conversion of nucleotides (NDPs or NTPs) to 2′-deoxynucleotides (dNDPs or dNTPs), the rate limiting reaction in the *de novo* synthesis dNTPs (Figure 1.1).[1-3] As the sole enzyme responsible for reducing all four nucleotide substrates, RNR dictates both the absolute number and relative ratios of dNTPs inside the cell and is one of many factors involved in regulating the fidelity of DNA replication and repair processes. Because of this central metabolic role, RNR has been successfully targeted for anticancer, antibacterial, and antiviral therapies. [4-6]

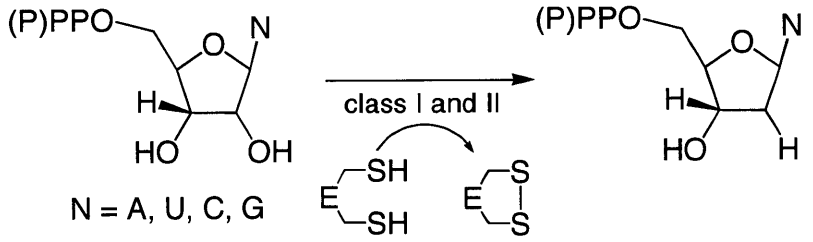

Figure 1.1 Chemical transformation catalyzed by RNR. The site of initial hydrogen atom abstraction is highlighted in red.

1.1.2 Classes of RNRs. The chemical transformation (Figure 1.1) of nucleotide reduction is achieved via a complex mechanism involving protein- and substrate-derived radicals, the details of which will be discussed subsequently.[7] [1,8,9] In the first step of nucleotide reduction, an active-site cysteine is transiently oxidized to a thiyl radical (C•), which then abstracts the 3′-hydrogen from the nucleotide substrate. All RNRs share a common mechanism of nucleotide reduction at the active site of their structurally homologous large subunits (α). However, RNRs differ significantly with respect to the mechanism by which they generate the transient C•; these differences are the basis upon which RNRs are classified (Figure 1.2).[1] The class I RNRs, found in some aerobic bacteria and all eukaryotes, use dimetallocofactors located in a second, smaller subunit (β). The class II RNRs are found in bacteria, archaea, and algae and contain an

adenosylcobalamin cofactor, the Co-C bond of which is cleaved homolytically on each turnover to give a 5′-deoxyadenosyl radical (5′-dA•) that is directly responsible for oxidation of the active site C. The class III enzymes, found in strict and facultative anaerobes, use a glycyl radical (G•) generated by a 4Fe-4S cluster- and *S*-adenosylmethionine (SAM)-containing activating enzyme of the 'radical SAM' superfamily.[10] The class I enzymes are further subdivided on the basis of their dimetallocofactors.[11] The class Ia enzymes are the most extensively characterized, and are known to use a diiron-tyrosyl radical (Y•) cofactor. The identity of the metal in the class Ib cofactor has been a long-standing question in the RNR community, as the enzyme may be reconstituted *in vitro* with either Fe or Mn. Recently, results from our lab have provided convincing evidence that class Ib is active *in vivo* as a dimanganese-Y• cofactor.[12] Finally, Bollinger and co-workers reported the discovery of a novel Fe-Mn cofactor in the class Ic RNR from *Chlamydia trachomatis*.[13] The class Ic enzymes are unique in that they have a F at the site of the conserved Y• in the class Ia and Ib enzymes, both in primary sequence alignments and in their three-dimensional structures. It is hypothesized that that the class Ic can access a high valent Fe^{III}/Mn^{IV} intermediate that acts as the catalytic oxidant, removing the need for a Y• to initiate radical propagation.

A comparison of the architecture of the α subunit, determined by X-ray crystallography for each of the three RNR classes,[10,14,15] reveals that the oxidation of the active-site C by the class II and III RNRs may occur via direct hydrogen atom abstraction (Figure 1.3). In both cases, the carbon-centered radical (5′-dA• or G•, respectively) oxidant is in an identical position in three-dimensional space, juxtaposed adjacent to the active site C on a finger loop in the middle of the 10-stranded α/β barrel. This is particularly interesting as it suggests a common spatial arrangement for C• formation despite the different cofactors used by the two classes and the low

sequence identity between the *Lactobacillus leichmannii* (class II) and bacteriophage T4 (class III) α subunits. Examining the analogous structural space in the class Ia RNR from *Escherichia coli* reveals the presence of two tyrosines, Y_{730} and Y_{731}. This observation raises the question that will be the focus of this thesis: what is the mechanism of C• formation in the class I RNR? We will focus specifically on the mode of oxidation in the prototypical class Ia RNR from *E. coli*, though it is hypothesized that this mechanism is conserved among all class I RNRs.

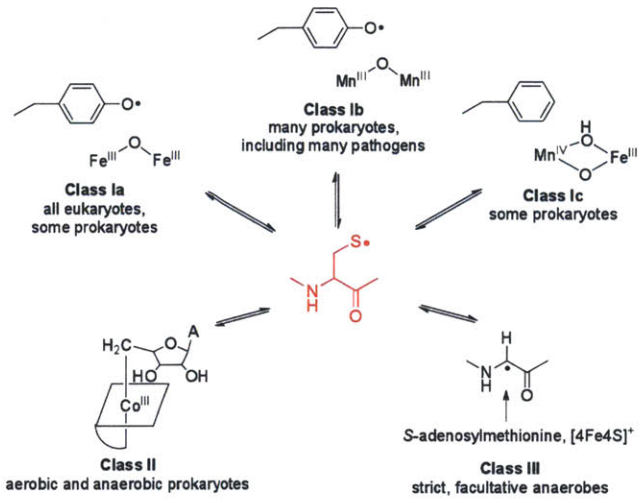

Figure 1.2 RNRs are classified on the basis of the metallocofactor utilitzed to generate a transient active site C•, which then initiates chemistry on the nucleotide. Figure adapted from reference 11.

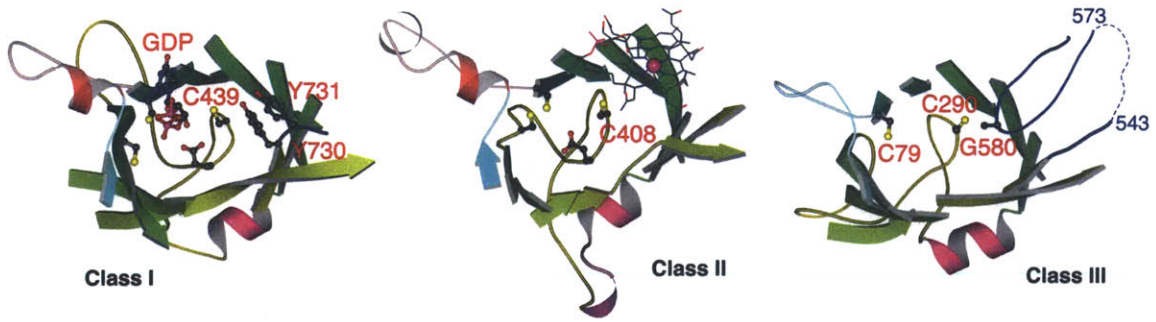

Figure 1.3 A comparison of the active sites of the three classes of RNRs. The active site cysteine for each is shown in sticks, as is the cofactor responsible for its oxidation. Note that these cofactors (Y_{730} and Y_{731} in class I, adenosylcobalamin in class II, and G_{580}• in class III) are all located in the same three-dimensional space within the protein architecture.

1.1.3 Mechanism of nucleotide reduction. Despite pronounced differences in the mechanism of active site C oxidation, all RNRs share a common mechanism of nucleotide reduction in the α subunit, shown in Figure 1.4.[1] In this mechanism, nucleotide chemistry is initiated by abstraction of the 3′-hydrogen atom (H•) from the substrate by the thiyl radical (C_{439}•, *E. coli* class Ia numbering), generating a 3′-nucleotide radical. In the first irreversible step of the reaction, this intermediate rapidly loses water to give a 2′-ketonucleotide radical. A conserved glutamate, E_{441}, facilitates the dehydration step by acting as a proton acceptor. The 2′-ketonucleotide radical is then reduced by H• transfer from one of two additional active site cysteines (C_{462}/C_{225}), yielding a disulfide radical anion and a 3′-keto-2′-deoxynucleotide. The former species is reduced by electron transfer from the disulfide radical anion and proton transfer from E_{441}. In the final step, C_{439} donates H• to reduce the 2′-deoxy-3′-nucleotide radical, yielding the 2′-deoxynucleotide product and regenerating the catalytic C_{439}•. Experimental evidence in support of this mechanism was amassed by Stubbe and co-workers over decades.[1,9] Key experiments included the observation of tritium washout in a reaction conducted on [3′-^{3}H]-NDP[16] and the spectroscopic characterization of the disulfide radical anion intermediate.[17]

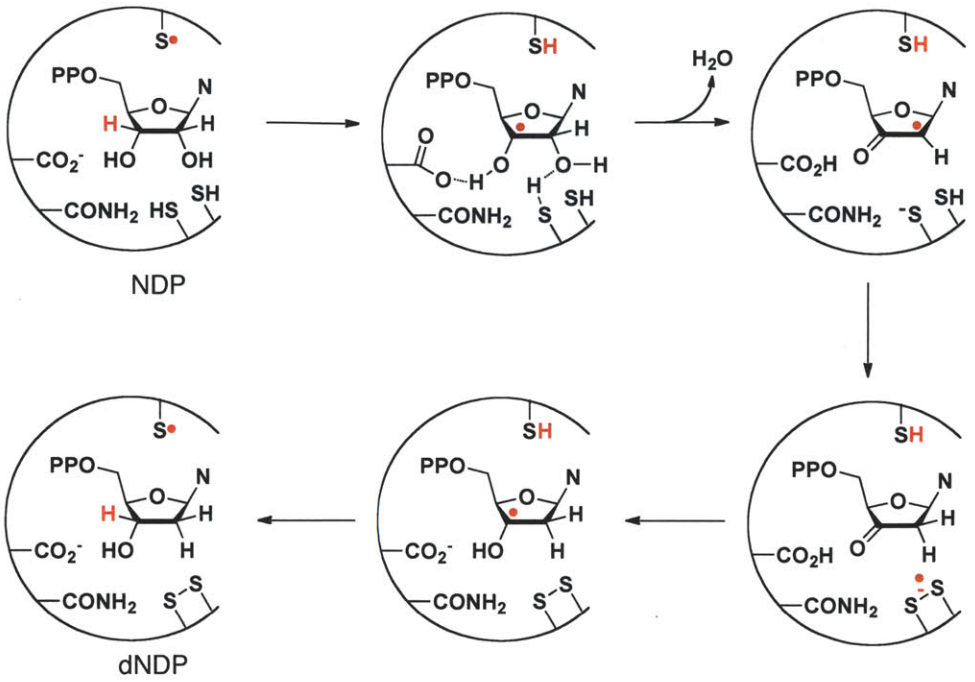

Figure 1.4 The common mechanism for active site nucleotide reduction by RNRs. Details of individual steps are described in the text.

1.1.4 Protein structure and subunit interactions in class Ia RNR. As introduced above, the class Ia RNRs consist of two protein subunits. The larger subunit, α, is a dimer of 172 kDa in the *E. coli* enzyme. It houses the active site where the four substrates (S = CDP, ADP, GDP, UDP) are reduced, and two additional nucleotide binding sites. The specificity site binds allosteric effectors (E = ATP, dGTP, TTP, and dATP) and dictates which of the four substrates is reduced, while the activity site binds ATP/dATP and dictates the overall rate of reduction.[18-22] Saturation of the activity site with ATP stimulates nucleotide reduction, while binding of dATP inhibits it. The first structure of the *E. coli* α2 subunit was reported in 1994 by Uhlin and Eklund and is shown in Figure 1.5, panel A.[14]

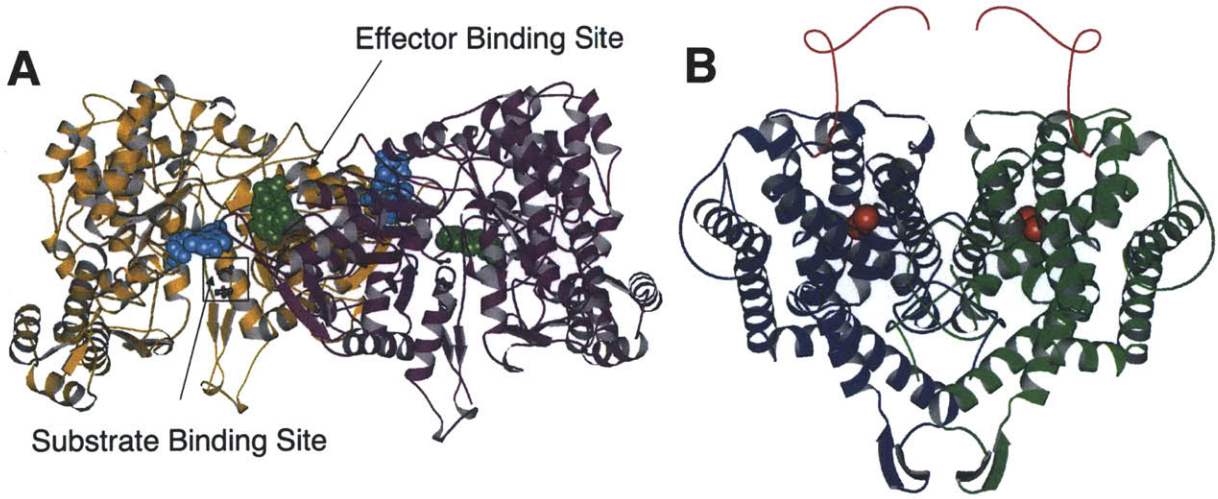

Figure 1.5 Crystal structures of individual *E. coli* class Ia RNR subunits. (A) The α2 subunit, with individual protomers shown in gold and purple. The substrate, GDP, and allosteric effector, TTP, are located at the indicated sites and shown in space-filling model. (B) The β2 subunit, with individual protomers shown in blue and green. Irons (red spheres) indicate the site of the diferric-Y• cofactor. Its thermally labile C-terminal tail (red line, residues 341-375) governs the interaction between subunits and has not been resolved in any crystal structure to date.

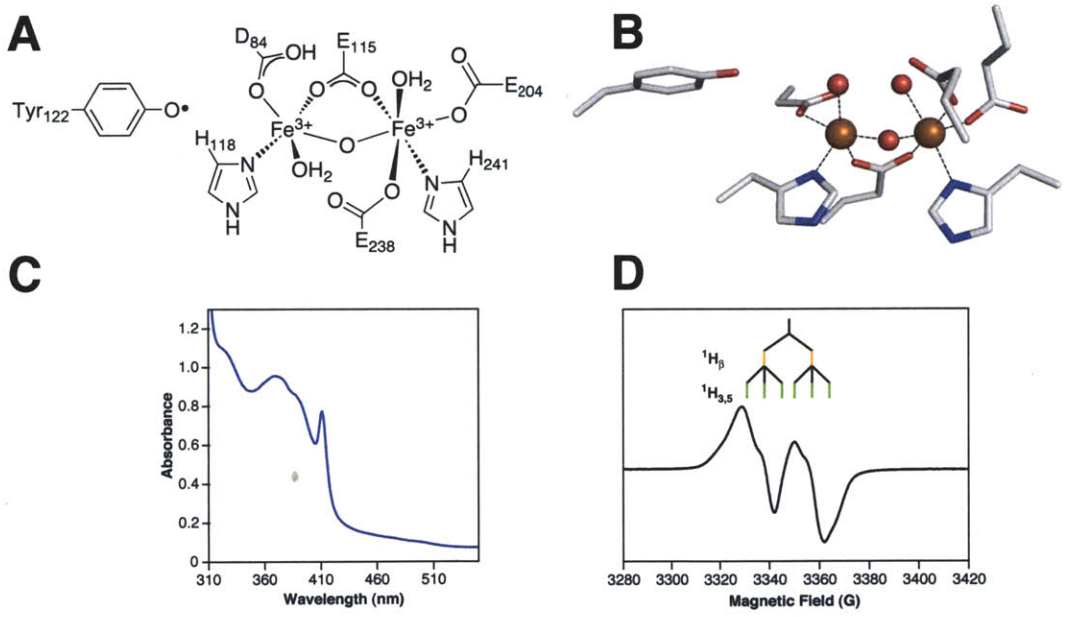

Figure 1.6 Structural and spectroscopic characterization of the diferric-Y_{122}• cofactor from *E. coli* class Ia RNR. (A) Chemical structure of the diferric-Y• cofactor; (B) X-ray crystal structure of the diferric "met" (i.e., tyrosyl radical reduced) form of the enzyme[23]; (C) The UV-vis spectrum of the cofactor, with contributions from the diferric cluster at 325 and 365 nm and a sharp feature at 411 nm for the Y_{122}•. (D) The g ~2 X-band EPR spectrum of Y_{122}•.

The smaller subunit, β, is an obligate dimer (β2) of 87 kDa and contains the diferric-tyrosyl radical cofactor (Y_{122}•) that is essential for catalysis.[24] The structure and key spectroscopic signatures of the diferric-Y_{122}• are shown in Figure 1.6. This unusually stable Y• ($t_{1/2}$ ~4 days at 4 °C) was the first Y• characterized in biology. Since that seminal discovery, the relevance of Y•s to a number of key metabolic transformations has been demonstrated, including O_2 evolution,[25] fatty acid oxidation,[26] peroxide disproportionation,[27] and prostaglandin synthesis.[28] Many crystal structures of the *E. coli* β2 subunit have been reported (Figure 1.5 B), with the first by Nordlund and Eklund in 1990.[23,29,30] Notably, in all structures solved to date, the conformationally flexible C-terminal tail of β2 (residues 340-375) cannot be resolved.

The class Ia RNR from *E. coli* is generally accepted to be active as an α2β2 complex.[31] The affinity between the two individual subunits is weak (K_d = 0.4 μM), but increases two- to eight-fold in the presence of nucleotides (K_d = 50 – 200 nM).[18,32] The interaction between the two subunits is governed by almost exclusively by the C-terminal tails of β2.[32] Recent biophysical data from analytical ultracentrifugation (AUC) and small-angle X-ray scattering (SAXS) techniques support a solution equilibrium of three interconverting states in the *E. coli* enzyme, free α2 and β2, α2β2, and α4β4, the relative populations of which depend on absolute protein concentration and the presence, identity, and concentration of nucleotides in solution.[33] Stopped-flow (SF) fluorescence experiments indicate that the interconversion between free subunits and α2β2 occurs on a time scale that is very fast relative to catalysis.[34]

While a number of the inactive RNR states have been structurally characterized,[33,35,36] a structure of an active class I RNR has yet to be obtained. Nearly two decades ago, upon solving the structure of the *E. coli* α2 subunit, Uhlin and Eklund put forth a docking model for the active *E. coli* α2β2 complex based on shape complementarity between the two subunits (Figure 1.7).[14]

The most provocative feature of this docking model was the >35 Å distance it placed between the diferric-Y_{122}• cofactor in β2 and the active site cysteine, C_{439}, in α2 it was proposed to transiently oxidize. Subsequent experiments utilizing pulsed electron-electron double resonance (PELDOR) spectroscopy, an EPR technique for measuring distances (20-80 Å) between two weakly coupled dipoles, supported this long distance.[37,38]

1.1.5 A model for long-range radical propagation in E. coli *class Ia RNR.* Turnover numbers of class I RNRs vary between 2-10 s^{-1}.[39] ET theory holds that the rate of tunneling, k_{et}, shows exponential dependence on the distance between donor and acceptor (R) and the distance decay constant (β). For a biological system, β has been measured to fall between 1.1-1.4 $Å^{-1}$.[40] Examining k_{ET} as a function of distance, one see that electron transfer over 35 Å by a pure tunneling mechanism would occur at 10^{-5} to 10^{-9} s^{-1} (Figure 1.8). Thus, RNR turnover cannot be supported by a long-distance electron tunneling mechanism between C_{439} and •Y_{122}.

Instead, from the orientation of residues in the docking model and from sequence alignments of class I RNRs, a model was proposed in which a series of absolutely conserved aromatic amino acids generate a hopping pathway for reversible radical migration over 35 Å between the diferric-Y_{122}• of β2 and the active site of α2: Y_{122}• → [W_{48}?] → Y_{356} in β2 to Y_{731} → Y_{730} → C_{439} in α2 (Figure 1.9). Rate acceleration of ET though amino acid hopping has been demonstrated previously in peptides and model proteins.[41,42] Initial site-directed mutagenesis studies of these conserved residues supported their essential role in nucleotide reduction, but provided little insight to the mechanism of radical transport.[43] Study of this phenomenon in *E. coli* class Ia RNR is further complicated by the fact that electron transfer events are masked by a rate-determining conformational change(s) prior to nucleotide reduction. Pre-steady-state kinetic studies of the wt enzyme failed to reveal changes in Y_{122}• due to this masking physical step.[39]

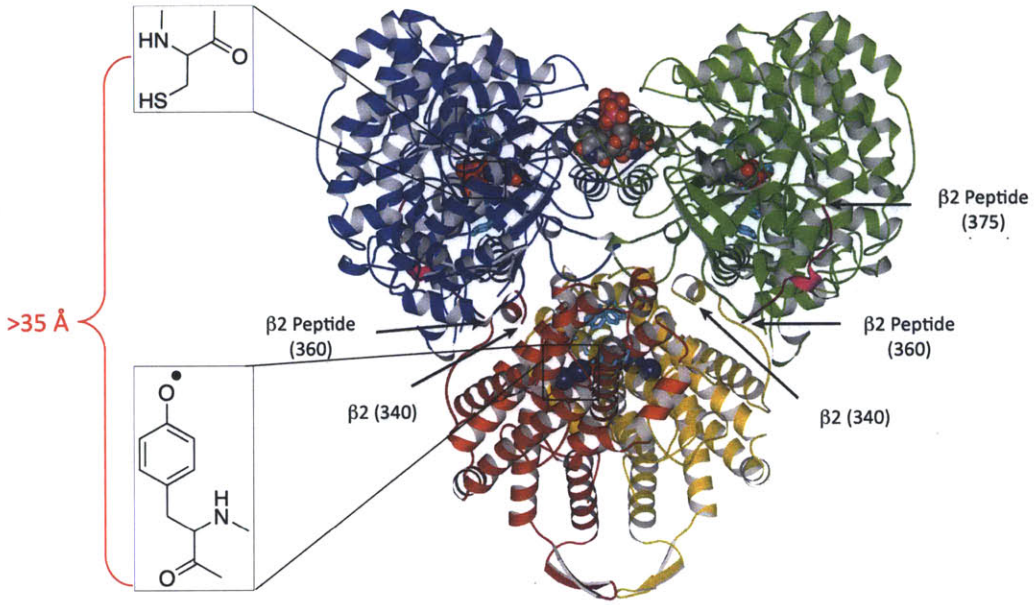

Figure 1.7 Docking model of crystal structures of α2 (blue and green) and β2 subunits (red and gold) of *E. coli* RNR places a distance of >35 Å between Y_{122}• in β2 and C_{439} in α2. A peptide corresponding to the C-terminal tail of β2 (pink) shows part of the binding interaction between subunits. GDP and TTP are shown in space-filling model. Irons are shown as blue spheres.

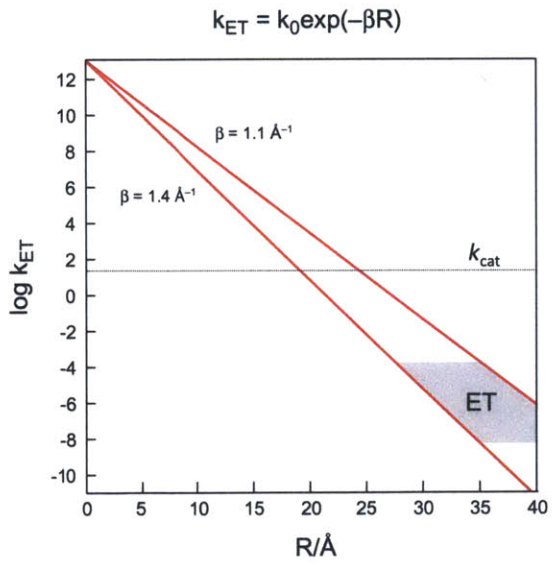

Figure 1.8 The distance dependence of the rate of electron tunneling. Given the exponential dependence of k_{ET} on R, electron transfer over 35 Å by a pure tunneling mechanism would occur at 10^{-5} to 10^{-9} s^{-1}, whereas the steady-state turnover numbers of wt RNR fall between 2-10 s^{-1}. Thus, a long-distance tunneling mechanism cannot support RNR turnover.

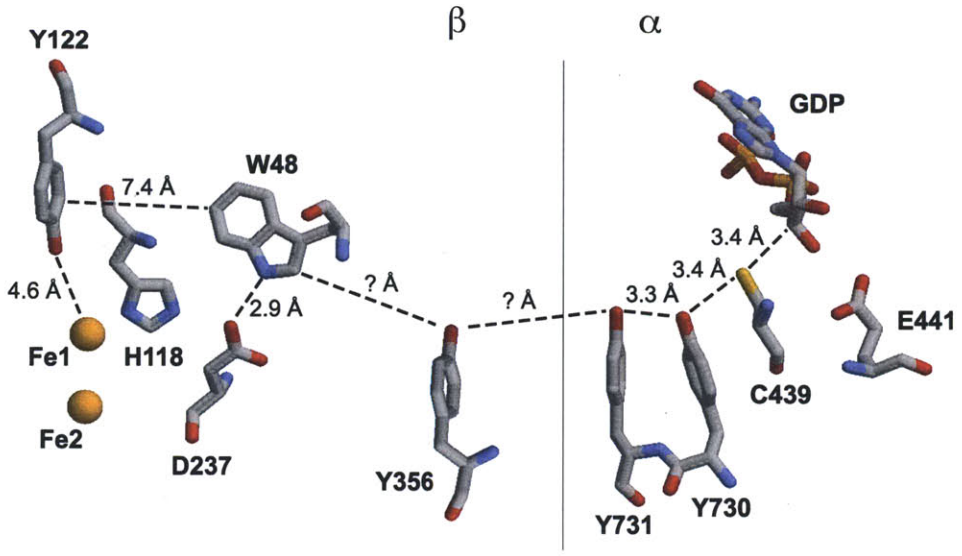

Figure 1.9 Proposed PCET pathway in *E. coli* class Ia RNR. Distances are from independent structures of the α2 and β2 subunits of the *E. coli* enzyme. Y_{356} is disordered in the β2 crystal structure, and therefore its distance relative to other residues is not known.

1.1.6 Mechanistic considerations for long-range PCET. The relay system shown in Figure 1.9 utilizes four Y residues (and possibly one W) to propagate a radical over 35 Å from Y_{122}• to C_{439} in a completely reversible fashion. The thermodynamics of Y oxidation require that proton transfer (PT) accompanies electron transfer (ET) at physiological pH, a process that may occur by either a stepwise or coupled mechanism. When examining a PCET mechanism, one must consider both the sequence of the PT and ET events, as well as the directionality of each. The sequence of events may be explored in the context of a square scheme, as shown in Figure 1.10. According to this scheme, two stepwise pathways are accessible – ET followed by PT, and PT followed by ET. Both of the stepwise pathways generate high energy intermediates that, under many circumstances, would be largely unfavorable in the context of the protein environment.[44] A more thermodynamically accessible alternative is to conduct both transfers in a concerted fashion, which we will call proton-coupled electron transfer (PCET) for the purpose

of this thesis. PCET events occupy the space within the edges of the square scheme (Figure 1.10). Hydrogen-atom transfer (HAT), shown on the diagonal is a very specific subset of general PCET. By thermodynamic arguments, the ET and PT events upon Y oxidation in RNR are assumed to be coupled, and will be referred to as PCET throughout this thesis.

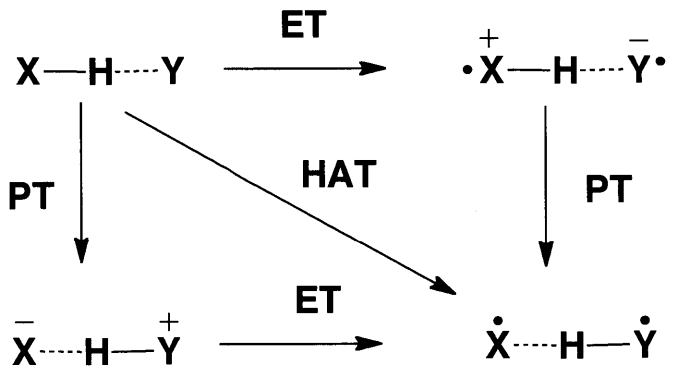

Figure 1.10 A square scheme for PCET. The edges of the figure depict stepwise ET/PT or PT/ET transfers. The space within the square refers to the concerted movement of the two particles, known as PCET. Hydrogen atom transfer (HAT), shown on the diagonal, represents one specific subset of PCET.

A PCET mechanism may be further subdivided into two classes on the basis of the directionality of the movements of the particles. In an orthogonal mechanism, the proton and electron originate from the same donor but move to different acceptors. Such a mechanism could help facilitate long-distance ET by coupling it to short, off-pathway PT. A second mechanism is co-linear PCET, in which the the proton and acceptor move between the same donor/acceptor pair. HAT is, again, a specific subset of co-linear PCET.

Over the past decade, the Stubbe and Nocera labs have collaborated to study the mechanistic underpinnings of radical propagation in the *E. coli* class Ia RNR. From a series of elegant studies employing unnatural amino acids (UAAs), a model emerged for the mechanism of long-range, reversible PCET in RNR (Figure 1.11). The model holds that RNR employs two

different mechanisms of PCET to facilitate long-distance, reversible hole migration, with orthogonal PCET operative in the β2 subunit and co-linear PCET (or, perhaps, HAT) operative in the α2 subunit. The research results that led to this model are described in the following section, and the further experiments intended to explore this model will be the unifying theme of this thesis.

Figure 1.11 The Stubbe/Nocera model for long-range (~35 Å), reversible PCET by a radical hopping mechanism in *E. coli* class Ia RNR. Evidence suggests orthogonal PCET is operative in the β subunit, and co-linear PCET is operative in the α subunit. Residue Y_{356} has not been observed in any crystal structure of β2, and thus its location relative to the other residues is unknown. There is no direct evidence that W_{48} and its putative H^+ acceptor, D_{237}, participate in long-range PCET during turnover.

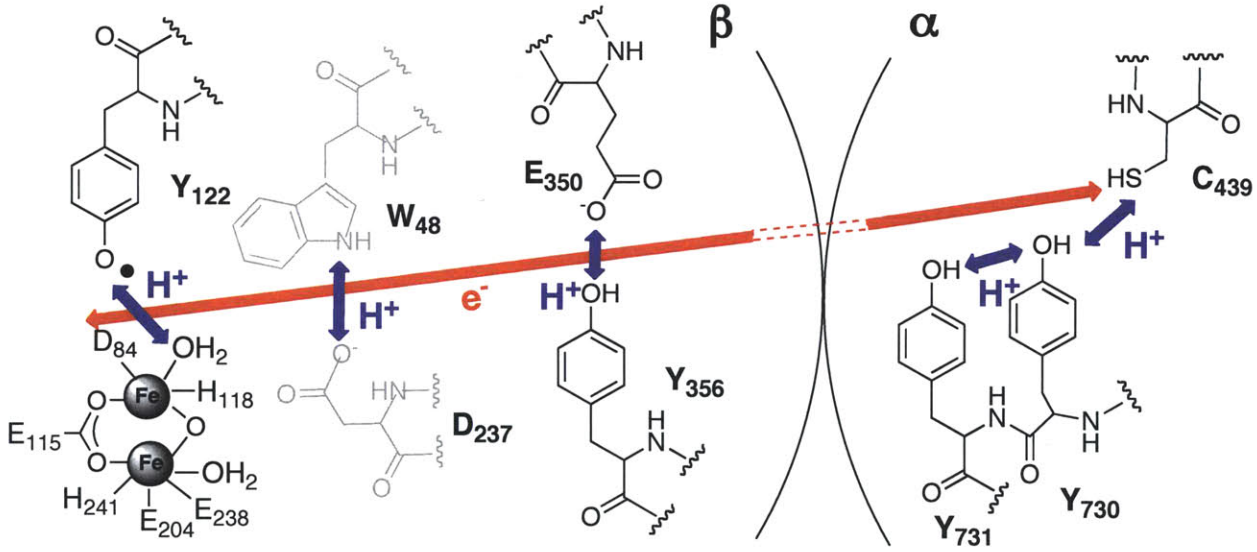

1.2 STRATEGIES FOR MANIUPULATING THE CHEMISTRY OF RNR

The 20 genetically-encoded amino acids do not provide great chemical variety, and thus, the scope of chemical properties that may be introduced into a protein via standard site-directed mutagenesis is severely limited. This point is illustrated by initial mutagenesis studies on RNR, in which each of the pathway tyrosines was individually mutated to phenylalanine, were largely uninformative, as the resulting proteins were completely inactive. Thus, while these studies demonstrated the importance of Y_{356}, Y_{731}, and Y_{730} in catalysis, they provided no mechanistic insight on the role of these residues. A primary goal of this laboratory over the last decade has been to develop means of site-specific, efficient incorporation of unnatural amino acids (UAA) into RNR. In doing so, we hope to perturb the native system in a subtle yet predictable fashion such that the details of radical propagation, invisible in the wt enzyme due to conformational gating, are exposed. Specifically, we emphasize UAAs with altered redox potentials and pK_as relative to the Y, as these are the primary chemical properties that govern ET and PT, respectively.

1.2.1 Methods for unnatural amino acid incorporation. Considerable effort has been dedicated to the development of technology for the site-specific incorporation of UAA into proteins, with expressed protein ligation (EPL) and nonsense codon suppression emerging as two of the most promising methods. Recent advances in these two methods have been reviewed thoroughly by pioneers in the respective fields, Peter Schultz and Tom Muir.[45-48] The foundation of EPL lies in intein-mediated protein self-splicing.[49] Coupling this naturally-occurring phenomenon with the synthetic technique of native chemical ligation[50] has allowed for the semisynthesis of proteins containing UAAs by a combination of molecular biology and solid-phase peptide synthesis (Figure 1.12 A).

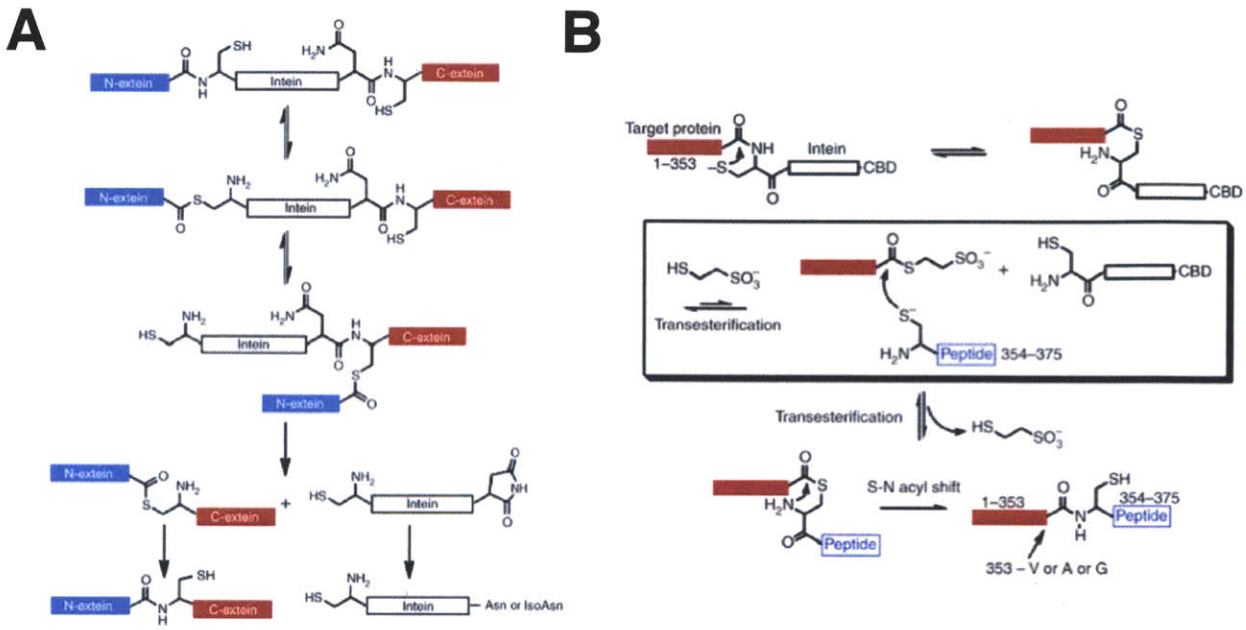

Figure 1.12 (A) Unnatural amino acid incorporation through expressed protein ligation (EPL). The N-terminal peptide of the target protein is expressed *in vivo* as a fusion protein with an intein that has been modified to eliminate the branched ligation. Thiols (R= benzyl, phenyl, alkyl, $CH_2CH_2SO_3Na$) are used to cleave the intein and generate a reactive C-terminal thioester. This construct is then reacted with a peptide generated by solid phase peptide synthesis that contains an N-terminal cysteine and an unnatural amino acid(s) in the position of interest. Reaction between the two constructs results in thiotransesterification, followed by S- to N- acyl shift to regenerate a peptide. There are many variations on this general theme. (B) Strategy for the EPL-mediated semisynthesis of β2.

In the second technique (Figure 1.13 A), a tRNA with a suppressor anticodon is charged with a UAA and incorporates it site-specifically during mRNA translation in response to a nonsense codon (typically the amber stop codon, TAG) placed site-specifically in a gene of interest. Exploitation of Nature's translational machinery, the ribosome, in this way has allowed for incorporation of more than 100 UAAs into a wide variety of proteins in a number of model organisms including *E. coli*, *S. cerevisiae, C. elegans*, and mammalian cells. Incorporation of unnatural amino acids by this method is astonishing, as Nature has evolved many mechanisms to ensure fidelity of the translational process.[51,52] The most efficient means of charging the tRNA

with the UAA is an area of intense research. The method pioneered by Schultz allows for *in vivo* tRNA charging via the evolution of an orthogonal tRNA synthetase (RS)[53] and has proven successful in many proof-of-concept studies.[46] The evolution begins with a library of mutant *Mj*Tyr-RSs, generated by randomization of six to eight residues within 6.5 Å of the amino acid binding pocket. This library is subjected to sequential rounds of positive and negative selection. Positive selection rounds are conducted in the presence of UAA and rely on TAG-suppression in a gene conferring chloramphenicol resistance on the cell; negative selection rounds are conducted in the absence of UAA and rely on the TAG-suppression of the gene encoding for barnase, a toxic ribonuclease. On average, three to six selection rounds are necessary before an RS is found that meets the criteria for orthogonality. *In vitro* attachment of the UAA to the tRNA by chemical or enzymatic synthesis has also proven to be a viable alternative in select systems,[54] though this strategy present limits in scale and yield that prevent it from being widely applicable.

Both EPL and the nonsense codon suppression method have experienced significant technological improvements since their initial application to the study of RNR. For EPL, the development of traceless ligations has eliminated the need for additional point mutations beyond the UAA of interest that were necessary in the original rendition of this method.[55,56] The nonsense codon suppression method would benefit from a more efficient means of evolving orthogonal tRNA/RS pairs for unique UAAs, a process which occurs on the month timescale using *E. coli* as the host. Recently, a single plasmid selection system was reported in which positive and negative selections were conducted via expression of one fusion gene, thus eliminating the need for plasmid isolation and re-transformation in between selection rounds and greatly reducing the time and labor involved in RS evolution.[57]

Improving the suppression efficiency of nonsense codons has been the focus of recent work by the Chin lab. One problem inherent to the *in vivo* nonsense suppression method is the competition between mutant, orthogonal tRNAs and endogenous release factors (RFs) for interaction with the nonsense codon during mRNA translation. This competition often results in high levels of truncated protein expression. Chin and co-worker have reported the evolution of an orthogonal *E. coli* ribosome optimized in the 530 loop of the 16s rRNA for preferential interaction with the orthogonal tRNA over RF-1.[58] The ribosome translates an orthogonal, nonsense codon-containing mRNA, identified by its modified ribosomal binding site,[59] with high specificity and fidelity. These orthogonal ribosome/mRNA pairs serve as a starting point for the engineering of complete orthogonal gene expression systems in *E. coli*.[59,60]

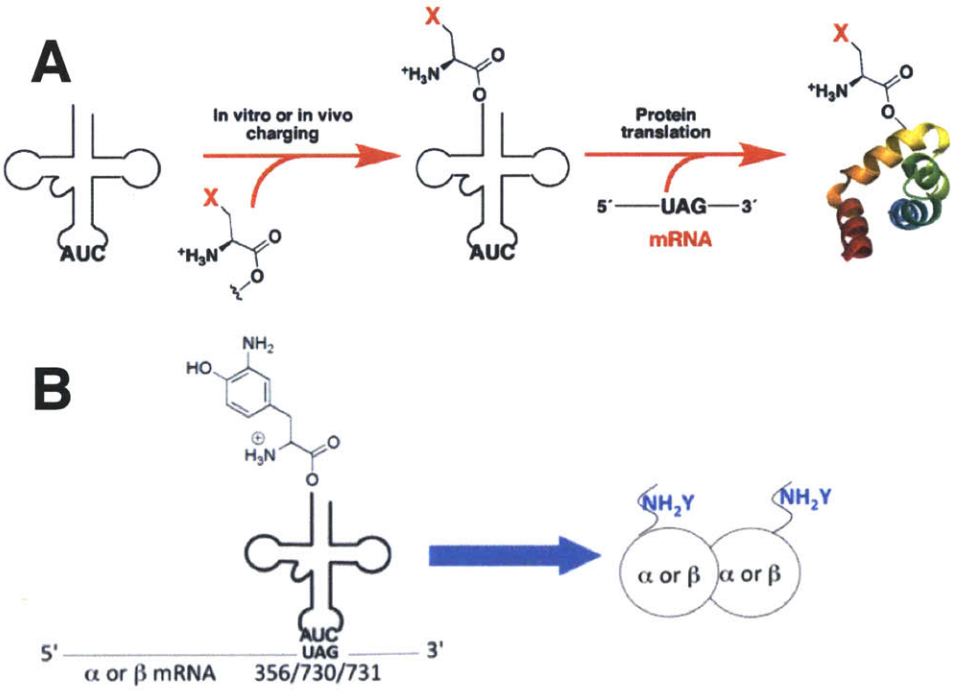

Figure 1.13 (A) Unnatural amino acid incorporation though nonsense codon suppression. An evolved tRNA containing a nonsense anticodon is charged *in vitro* or *in vivo* with an unnatural amino acid. The machinery of the ribosome recognizes a nonsense codon within the mRNA, mutated into the gene of interest, and uses the charged tRNA to site-specifically incorporate the unnatural amino acid into the protein. (B) Site-specific incorporation of NH_2Y into *E. coli* α or β by the *in vivo* nonsense suppression method.

While it is these two well-established methods that have been applied to the incorporation of UAAs into RNR, the field of protein engineering is rapidly growing and there exist many emerging technologies for UAA incorporation. Reconstituted, cell-free translation systems[61] and flexizyme technology[62,63] both show promise for the simultaneous incorporation of multiple different UAAs with high fidelity into peptides, and could show promise as alternative methods for incorporation of UAAs into large proteins such as RNR.

1.2.2 Site-specific incorporation of UAAs at position 356 of β2 by EPL. EPL technology was first applied to the generation of UAA-containing RNRs. Initial studies focused on the determining the role of Y_{356}, located in the conformationally-flexible C-terminal tail of β2 and invisible in all crystal structures of β2 solved to date.[29] Because of its location in the protein (residue 356 of 375 amino acids), this tyrosine was targeted for unnatural amino acid replacement via EPL.[64,65] By this method, residues 1-353 of the subunit were expressed recombinantly as a fusion-construct to an intein domain and chitin binding domain for affinity purification. Following affinity purification and transesterification with an organic thiol, a peptide constituting the C-terminal 22 amino acids of the subunit was ligated to the protein fragment (Figure 1.12 B). The first 19 amino acids of this peptide were generated by solid-phase synthesis, followed by hand-coupling of the final three amino acids, including the unnatural amino acid at position 356. Ligation of the protein and peptide fragments yielded the intact β subunit, with two point mutations – a $S_{354}C$ mutation to mediate the ligation, and a $V_{353}G$ to remove steric bulk at this position and improve ligation yields.

A number of technical difficulties were encountered in generating intact β2s by this method.[64,65] First, the introduction of the two point mutations described above reduced the overall enzyme activity by 75% relative to wt-β2. Second, difficulty was encountered in

obtaining high radical content in early EPL-β2s (0.3-0.4 Y•/β2 compared to 1.2 Y•/β2 in the wt), thereby reducing the enzyme's activity an additional three- to four-fold. The subsequent development of optimized protocol for *in vitro* radical reconstitution in EPL-β2s helped ameliorate this problem in later studies.[66] Finally, under the protein:peptide ligation conditions, hydrolysis outcompetes ligation, thereby generating a substantial amount of 353-truncated protein (β′) and severely compromising protein yield. As the β subunit is an obligate dimer, a statistical mixture of three species, β′2, ββ′, and β2, is generated. The protein of interest, the full-length homodimeric β2, is specifically isolated by anion-exchange chromatography, which separates the three species on account of the highly-charged nature of the β C-terminal tail. After much troubleshooting, a protocol was established that allowed generation of EPL-β2s in >100 mg quantities.

By this method, seven unnatural amino acids with varying reduction potentials and pK_as have been incorporated into the β subunit at position 356 to examine its role in long-range PCET (Figure 1.14, **1-3**, **5-8**). The first of these was 3-nitrotyrosine (Figure 1.14, **1**), a probe of local pK_a environment in the protein. The λ_{max} of the nitrotyrosine phenolate (NO_2Y^-) is at 430 nm, well removed the protein envelope. This spectroscopic handle allowed titration of the pK_a of NO_2Y at position 356 within a protein of 87,000 Da, and demonstrated that it was not perturbed relative to NO_2Y in solution. Furthermore, incorporation of NO_2Y at position 356 rendered the enzyme inactive, indicating that raising the reduction potential at this position by 200 mV shuts down nucleotide reduction.[64] Incorporation of 2,3-difluorotyrosine (2,3-F_2Y, Figure 1.14 **6**) at the same position allowed the first investigation of the proton dependence of ET through position 356.[67] With a solution pK_a of 7.8, 2,3-F_2Y exists in both the phenol and phenolate forms over the pH range RNR is active (6-9). Generation of a pH rate profile of $Y_{356}(2,3)F_2Y$-β2 revealed that

it was active over the entire profile, indicating that ET through this position is not obligately coupled to PT. It further suggested that an intact hydrogen-bonding network is not necessary at that position for radical propagation.

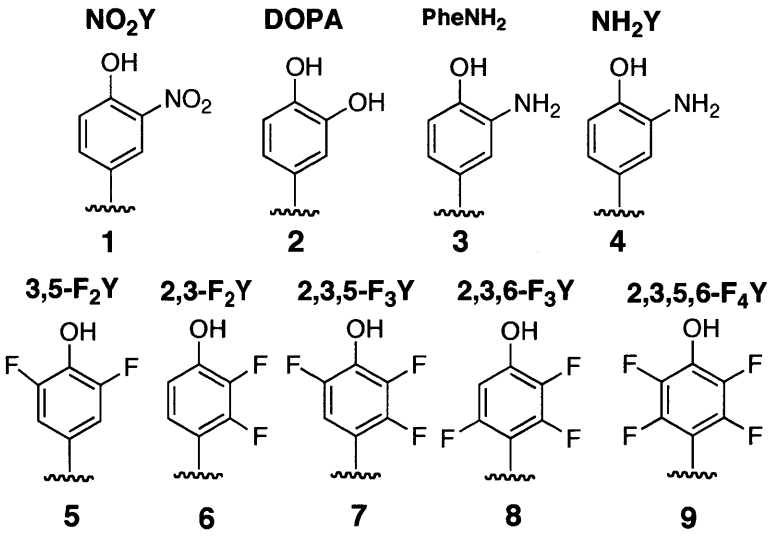

Figure 1.14 Unnatural amino acids that have been incorporated into *E. coli* class Ia RNR. Compounds 1-3 and 5-9 have been incorporated to position 356 of β2 by EPL, while compounds 1 an 4-9 have been incorporated to sites in both α2 and β2 by the *in vivo* nonsense suppressor technique.

Studies were then expanded to include a complete series of fluorinated tyrosines (F_nYs, Figure 1.14, **5-9**) incorporated to position 356. Characterization of the pH dependence of the peak potentials (E_ps) of N-acetyl-fluorotyrosinamides (Ac-F_nY-NH_2s) by differential pulsed voltammetry (DPV) indicated that the mono-, di-, tri-, and tetra-F_nYs have pK_as spanning 4 pH units and E_ps that vary between –50 and +270 mV relative to tyrosine in the pH range where *E. coli* RNR is active.[68] By increasing the number of fluorines on the phenol, both the pK_a and redox potential can be systematically varied; simultaneous manipulation of these two physical properties allow F_nYs to act as indicators of both electron *and* proton movement during radical transfer. pH rate profiles of $Y_{356}F_n$Y-β2s indicate that all mutants are active, and that their

activity falls into three regimes based on the ΔE_p between the $F_nY/F_nY\bullet$ couple and Y/Y• (Figure 1.15). At ΔE_ps <80 mV, $Y_{356}F_nY$-β2s behave identically to wt-β2, whereas at ΔE_ps >200 mV, $Y_{356}F_nY$-β2s cannot catalyze nucleotide reduction, an observation consistent with that made previously with $Y_{356}NO_2Y$-β2. In the intermediate regime, 80 mV < ΔE_ps < 200 mV, it is hypothesized that the rate of radical propagation has slowed to the point that ET through 356, rather than conformational change(s), is rate-limiting. The pH rate profile data indicate that this regime is accessible to $Y_{356}(2,3,5)F_3Y$-β2 at alkaline pH. Thus, this mutant provided a unique opportunity to study the mechanistic underpinnings of radical propagation.

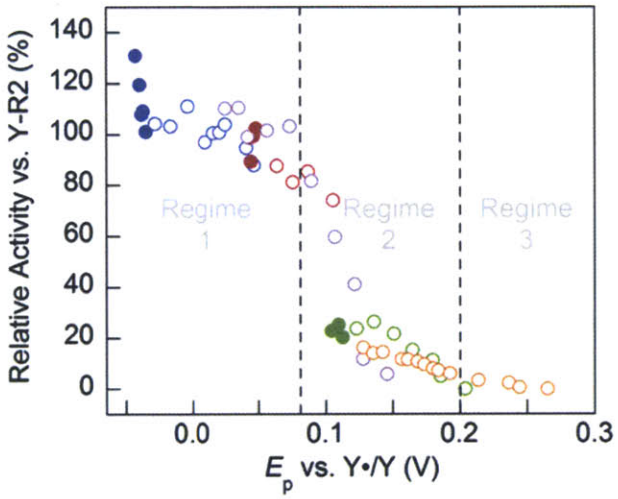

Figure 1.15 Relative activities of EPL-generated $Y_{356}F_nY$-β2s vs wt-β2 plotted as a function of the peak-reduction potential difference between the Ac–F_nY•–NH_2 and Ac–Y•–NH_2. The data fall into three regimes, with the second regime proposed to be the potential range in which radical propagation is rate-limiting. Points are colored as follows: black (wt), blue (3,5-F_2Y), red (2,3-F_2Y), purple (2,3,5-F_3Y), green (2,3,6-F_3Y), and orange (2,3,5,6-F_4Y). Reproduced from [68].

A final UAA incorporated by EPL was 3,4-dihydroxyphenylalanine, or DOPA (Figure 1.14, **2**). With a reduction potential at pH 7 that is 260 mV lower than that of Y, and DOPA acts as a radical sink. Consistent with the collective previous results, this 260 mV perturbation to the thermodynamics of radical propagation makes Y_{356}DOPA-β2 inactive. Reaction of Y_{356}DOPA-

β2 with wt-α2, S, and E resulted in loss of Y_{122}• concomitant with the formation of a new radical, characterized by SF UV-vis and EPR spectroscopy to be $DOPA_{356}$•.[69] Radical formation occurred only in the presence of the second subunit, S, and E. The ability to generate a stable radical at this position allowed measurement of the diagonal distance between Y_{122}• on one α/β pair and $DOPA_{356}$• on the second by PELDOR spectroscopy (Figure 1.16), providing the first structural constraint on the location of residue 356 within the complex.[70] Subsequent studies on the heterodimeric protein Y_{356}DOPA-ββ′ showed that when this protein, lacking the C-terminal 22 amino acids on one protomer, was reacted with wt-α2, CDP, and ATP, it was competent in both forward radical propagation, generating $DOPA_{356}$•, and reverse hole migration, re-oxidizing Y_{122} in concert with loss of $DOPA_{356}$•.[66] This was the first direct observation of the reversibility of the PCET pathway.

Taken together, the results obtained with EPL-β2s containing UAAs at position 356 have provided convincing evidence that Y_{356} is a redox-active participant on the radical propagation pathway in *E. coli* RNR. As described above, this result was particularly valuable as the C-terminal 35 amino acids of β, including Y_{356}, constitute a thermally disordered tail that provides the key recognition features for the α/β interaction but cannot be crystallographically resolved. The docking model predicts a distance of >25 Å between W_{48} in β2 and Y_{731} in α2, and the collective results from these studies support the participation of Y_{356} as a relay between these two residues and across the α/β interface.

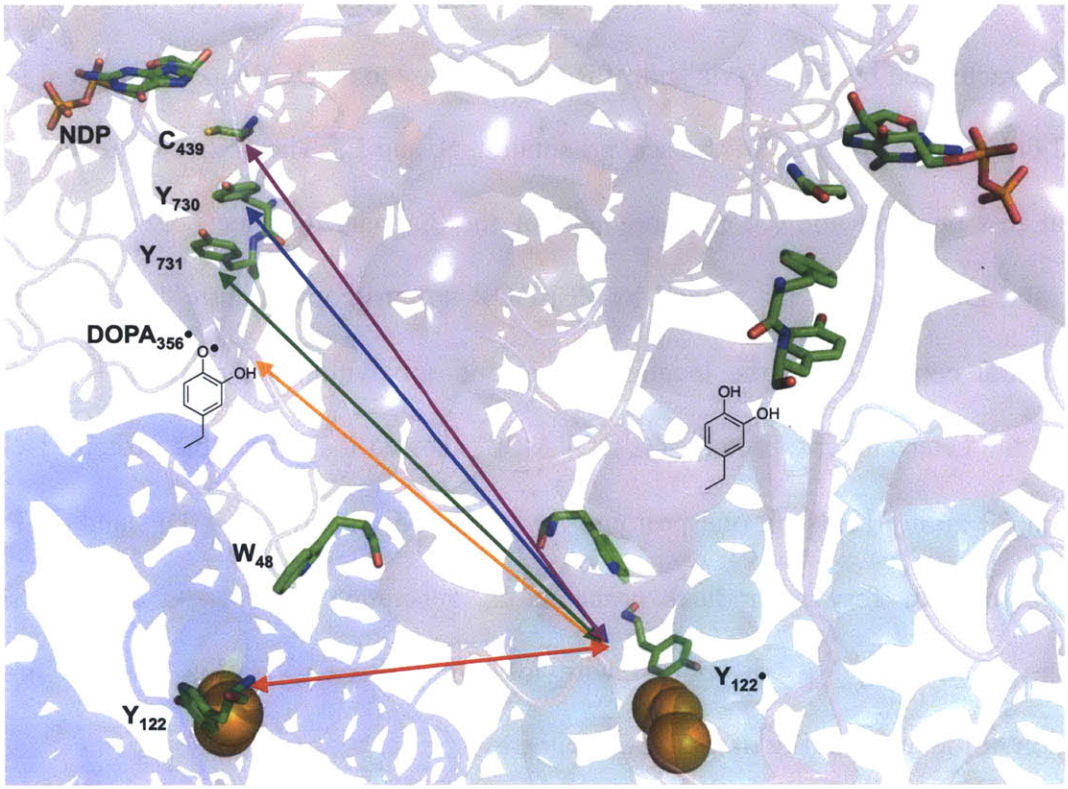

Figure 1.16 Determining the diagonal distance between Y_{122}• on α/β and $DOPA_{356}$• on α′/β′ (orange line) by PELDOR spectroscopy. PELDOR has been similarly applied to measure the Y_{122}•-Y_{122}• distance (red line) and the diagonal distances between Y_{122}• and NH_2Y_{731}• (green line), $NH2Y_{730}$• (blue line) and an active-site N• (purple line). The pathway residues were built in from the docking model of β2 (blue and cyan ribbons) and α2 (purple and red ribbons). Y_{356} is invisible in the crystal structure, and its location within the complex is unknown.

1.2.3 Site-specific incorporation of UAAs at position 730 and 731 of α2 by in vivo nonsense suppression. Having established the participation of Y_{356} in the PCET pathway, attention was turned to the study of radical propagation in α2, namely to address the role of Y_{731} and Y_{730}. Due to the size of the α subunit and the location of these residues within the protein fold, EPL could not be readily applied for site-specific UAA incorporation at these positions. Thus, the *in vivo* nonsense suppression method was explored. This method has a number of pros and cons with respect to EPL. First, it is potentially applicable to the study of all residues of interest in either subunit of RNR. It also greatly minimizes perturbations to the endogenous system relative to other methods of unnatural amino acid incorporation (i.e., no need for

additional point mutations). The technology also allows for large-scale isolation of proteins. Isolated protein yields of 3-30 mg/g cell paste have been obtained in this lab for proteins generated by this method, though yields vary considerably with respect to the amino acid being incorporated, the site of incorporation, and the complexity of the purification process.

Drawbacks to the method with respect to its application to our RNR studies include the fact that a new RS must be evolved for every UAA, which means the UAA choice must be carefully considered at the outset. The UAA must be available in gram quantities, must be nontoxic to the cells, and must be taken up by them through either passive or active transport. Once an RS has been evolved, expression vectors and growth conditions often need to be empirically screened when applying the synthetase to expression of a new protein. One complexity with this method that is of great concern in our studies is the fidelity of the RS. Since the genes coding for the subunits of RNR are essential in *E. coli,* the host organism for protein expression, endogenous levels of the wt subunits are always present at some level in the recombinantly expressed protein. In application of the *in vivo* nonsense codon suppression method, the fidelity of the evolved tRNA/RS pair can introduce an additional mechanism by which wt RNR is produced. The selectivity of the RS for the UAA relative to Y is influenced by both the K_m of the RS for the UAA and the relative abundance and availability of the UAA in the cell. The fidelity of the tRNA/RS is also influenced by the expression system for the protein of interest, the position of UAA incorporation, and the growth medium. Thus, in order to be quantitative about small numbers (e.g., low levels of activity in NH_2Y-RNRs), we require a quantitative way to assess the fidelity of the synthetase in selectively incorporating the UAA over the endogenous Y.

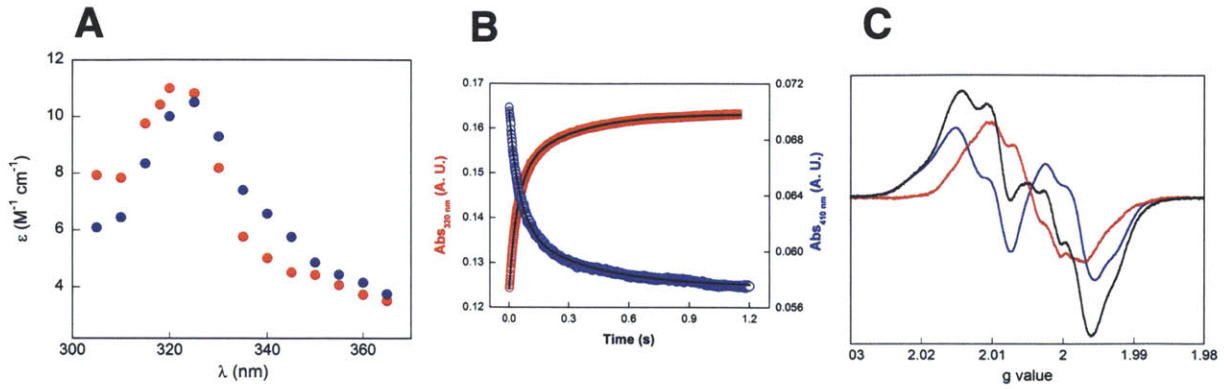

Figure 1.17 Initial spectroscopic characterization of NH_2Y•s. (A) A point-by-point reconstruction of the UV-vis spectra of NH_2Y_{730}• (blue) and NH_2Y_{731}• (red); (B) Averaged SF UV-vis traces for the reaction of $Y_{730}NH_2Y$-α2 with wt-β2, CDP, and ATP. Loss of Y_{122}• (blue, 410 nm) corresponds to the formation of a putative $NH2Y_{730}$• (red, 325 nm); (C) The X-band EPR spectrum of an identical reaction quenched in liquid N_2 after 10 s. The spectrum (black) is a ~1:1 composite of residual Y_{122}• (blue) and NH_2Y_{730}• (red). Adapted from reference 71.

In collaboration with the Schultz lab, an orthogonal RS specific for 3-aminotyrosine (NH_2Y) was evolved and used to incorporate NH_2Y into positions 730 and 731 of α2 subunit (Figure 1.13 B). With a reduction potential 190 mV lower than Y at pH 7, NH_2Y was selected to behave, like DOPA, as a radical sink. Indeed, reaction of $Y_{730}NH_2Y$-α2 (or $Y_{731}NH_2Y$-α2) with wt-β2, S, and E results in the generation of an aminotyrosyl radical, NH_2Y•, coupled to Y_{122}• loss as measured by SF UV-vis and EPR spectroscopy.[71] This novel radical was spectroscopically characterized by UV-vis absorbance and EPR at 9, 94, and 180 GHz (Figure 1.17).[71,72] Like with the DOPA mutant, the ability to trap a stable NH_2Y• at position 730 or 731 allowed for measurement of the diagonal distance between Y_{122}• on one α/β and NH_2Y_{730}• (or NH_2Y_{731}•) on the second by PELDOR spectroscopy (Figure 1.16). The distances measured were in excellent agreement with those predicted by the α2β2 docking model, providing an independent assessment of the validity of this structure. Perhaps the most interesting initial result was that both $Y_{730}NH_2Y$-α2 and $Y_{731}NH_2Y$-α2 appeared active in dNDP formation. The

collected studies on the EPL mutants indicated that RNRs are active when the potential pathway radical is modulated by ±200 mV. The NH_2Y mutation, which placed these proteins on the 200 mV thermodynamic threshold, was insufficient to shut down radical propagation, with $Y_{730}NH_2Y$-α2 and $Y_{731}NH_2Y$-α2 measured to posses 4-7% the wt activity. Mechanstic investigations of catalysis by $Y_{730}NH_2Y$-α2, $Y_{731}NH_2Y$-α2, and the recently reported $Y_{356}NH_2Y$-β2, are the subjects of Chapters 2, 3, 4, and 5 of this thesis and the more detailed analysis of the system, its complexities, and the insights it provides to the mechanism of PCET are presented therein.

Since the initial demonstration of NH_2Y incorporation into α2 by the *in vivo* nonsense method and its extension to incorporation of NH_2Y into β2, additional unnatural amino acids – NO_2Y and F_nYs (Figure 1.14, **1** and **5-9**) – have been incorporated into both the α and β subunits by the nonsense codon suppression method. In a set of experiments paralleling those conducted with the original EPL-generated $Y_{356}NO_2Y$-β2, NO_2Y was substituted at the site of each remaining Y on the pathway and its pK_a determined to look for evidence of position-dependent protein-induced pK_a perturbations. $Y_{730}NO_2Y$-α2 and $Y_{731}NO_2Y$-α2 demonstrated small (0.8 and 1.2 units, respectively) upward shifts in pK_a when titrated in the presence of wt-β2, CDP, and ATP. The pK_as at these sites were minimally perturbed by mutations to adjacent residues that disrupted the hydrogen-bonding network within α2 (e.g. Y to F, Y to A, or S to A). Surprisingly, titrations of both apo and diferric-met $Y_{122}NO_2Y$-β2 revealed an upward pK_a perturbation at that position of >2.5 units. An X-ray crystal structure of the mutant revealed that the diferric cluster of the mutant overlaid with that of the wt enzyme gave an rmsd of 0.3 Å between the two for the primary and secondary coordination sphere, with a reorientation of I_{251} as the only noteworthy change. The observed pK_a perturbation at position 122 reiterated what

has already been hypothesized from structural analysis of the *E. coli* RNR, namely that the highly hydrophobic pocket surrounding the diferric-Y• cofactor is distinct from the protein environments at positions 356 of β2 and 730 and 731 of α2 and helps confer the unique chemical and/or kinetic stability of the Y_{122}•.

In a second set of experiments, the increased reduction potential of NO_2Y relative to Y was exploited to ask what happens when the driving force of radical initiation at position 122 is increased.[73] As introduced previously, NO_2Y (E_p ~1.0 V, pH 7) is 200 mV harder to oxidize than Y at pH 7. This thermodynamic barrier prevents oxidation of NO_2Y at position 356, 731, or 730 by the previous Y• on the PCET pathway, shutting down nucleotide reduction. It was hypothesized that NO_2Y incorporated at position 122 of β2, however, could access unique chemistry that could drive its oxidation. *In vitro* reconstitution of the diferric-Y• in *E. coli* class Ia β2 from ferrous iron and O_2 has been well studied, and has been shown to involve a high-valent Fe^{3+}/Fe^{4+} state (intermediate X). It was hypothesized that intermediate X would possess sufficient oxidizing power to generate a NO_2Y• at position 122. Indeed, when apo-$Y_{122}NO_2Y$-β2 was reacted with Fe(II) and O_2 using rapid-mixing techniques, a NO_2Y_{122}• was generated. Characterization of its formation and decay by RFQ-EPR spectroscopy revealed that NO_2Y_{122}• (1.2 eq/β2) forms within 0.5 s and then decays with a $t_{1/2}$ of 40 s (25 °C). Triple-mixing kinetic experiments in which NO_2Y_{122}• was formed in the first drive, aged, and then mixed with wt-α2, CDP, and ATP, revealed loss of NO_2Y_{122}• concomitant with formation of NO_2Y^- at 100-300 s^{-1}, dCDP at >100 s^{-1}, and accumulation of a new radical with the same rate constant (Scheme 1.1). This radical, later identified as an equilibrium mixture of pathway radicals primarily localized at Y_{356},[74] constituted the first observation of a native Y• intermediate. The ability to observe dCDP production and pathway radical formation with rate constants an order of magnitude higher than

those reporting on the rate-determining conformational change in the wt enzyme (2-10 s^{-1}) was interpreted as an "unmasking" of conformational gating in this mutant. Furthermore, the observation of formation of the nitrotyrosine phenolate (NO_2Y^-) rather than the anticipated phenol (NO_2Y) indicated that proton movement had been decoupled from ET in this system. The loss of this proton coupling is likely intricately linked to the conformational changes that initiate radical propagation in the wt enzyme.

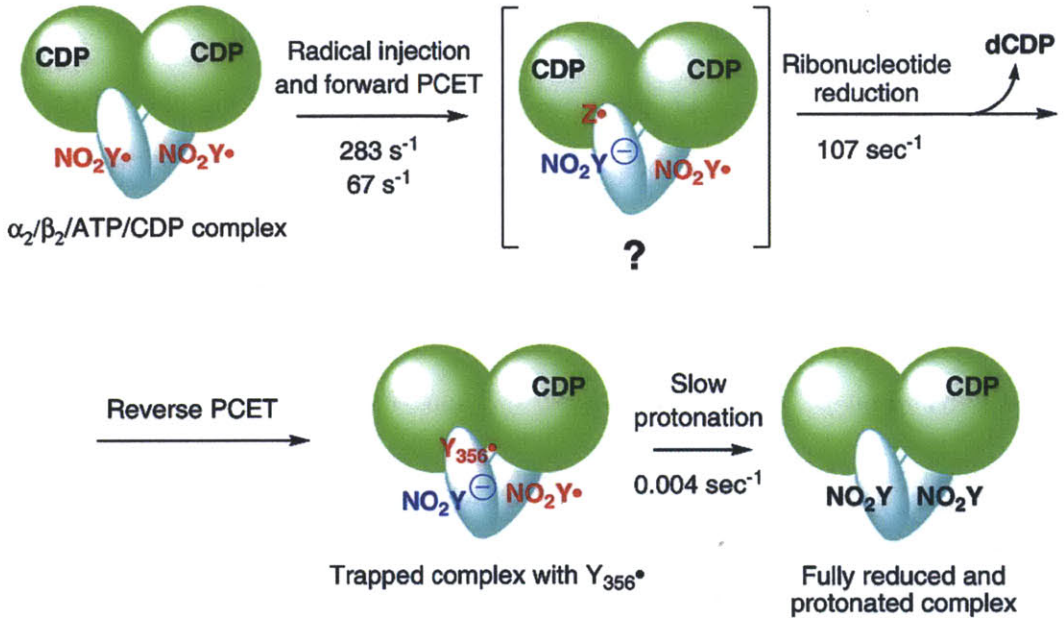

Scheme 1.1 Kinetic model for radical initiation in the reaction of $Y_{122}NO_2Y$-β2 with wt-α2, CDP, and ATP. Details described in text. Figure reproduced from reference 73.

Most recently, the technology for incorporation of F_nYs by the *in vivo* nonsense suppression method has been developed. In a successful collaboration with the Schultz lab, an RS specific for 2,3,5-F_3Y-RS was evolved via the double sieve selection strategy described above. 2,3,5-F_3Y was selected as the target fluorotyrosine for this method for two reasons. Firstly, it may be argued that among the F_nYs, 2,3,5-F_3Y is the most mechanistically informative, as the catalytic activity of EPL-generated Y_{356}(2,3,5)F_3Y-β2 could be titrated with pH within the

reduction potential range in which ET is thought to become rate-limiting (80 mV < ΔE_ps < 200 mV , Figure 1.15) Secondly, it was rationalized that evolution of an orthogonal RS for 2,3,5-F_3Y (pK_a of 6.4) might be more feasible than for other F_nYs, as it is unique among the series in that it exists in the phenolate form at neutral pH. It was thought that this negative charge would offer a unique point of discrimination from tyrosine, which may improve the odds of evolving an orthogonal RS. To our delight, a candidate orthogonal F_3Y-RS emerged after three rounds of selection and was demonstrated to be polyspecific, recognizing the entire series of F_nYs while maintaining good selectivity over Y. This RS was immediately utilized to incorporate four different F_nYs at each of the four positions of conserved Ys along the PCET pathway. Mechanistic studies with these proteins, mimicking the pH rate profiles of EPL-generated $Y_{356}F_n$Y-β2s and the radical initiation experiments with $Y_{122}NO_2$Y-β2, are the subject of Chapter 6 and 7 of this thesis.

1.2.4 C-terminal β2 photopeptides and "photoRNRs." A final application of the site-specific incorporation of UAAs has been for the generation of C-terminal β2 photopeptides and, more recently, intact photoRNRs. The overall goal in these experiments is to employ light to initiate radical propagation in RNR, thereby overcoming the kinetic gating of conformational changes that have complicated study of the wt enzyme and mutants described above. Short lived radical intermediates may then be monitored on the ns timescale by transient absorption (TA) spectroscopy. More specifically, a photooxidant is appended to the N-terminus of a peptide corresponding to the last 19 amino acids in the C-terminus of β2 ([Photo]-Y-β2C19). The choice of oxidant has varied, but benzophenone (BP),[75] anthraquinone (Anq) and Re(bpy)$(CO)_3$CN ([Re])[76,77] have been three of the most successful. The choice of residue at position 356 – whether the native Y or an unnatural F_nY – depends on both the nature of the photooxidant (i.e.,

a H• acceptor like BP or Anq versus an e- acceptor like [Re]) and the desired driving force for radical injection into α2. Upon light excitation, the photooxidant generates a Y_{356}• which may be monitored in the TA spectrum by its 410 nm signature. In the presence of α2, CDP, and ATP, a fraction of the Y_{356}• may oxidize Y_{731}• and initiate hole migration in the α2 subunit, ultimately initiating active site chemistry and generating dCDP (Figure 1.18).[75,76] Introduction of a block in the pathway in the form of F prevents dCDP formation, providing evidence against a superexchange mechanism for ET in α2 and supporting the co-linear transport of a H^+ and e^-.[75] Very recent results from TA experiments studying the reaction of [Re]-2,3,6-F_3Y-β2C19 with various pathway mutants of α2 (C_{439}S-, Y_{730}F-, and Y_{731}F-α2) have indicated that hole migration into α2 may occur in either wt-α2 or C_{439}S-α2. Insertion of the Y_{731}F mutation prevented hole migration, as did a Y_{730}F mutation. The last observation was a surprising one, and led to the proposal that the intact Y_{731}-Y_{730} dyad and its corresponding hydrogen bond network is necessary for radical propagation into α2.[78]

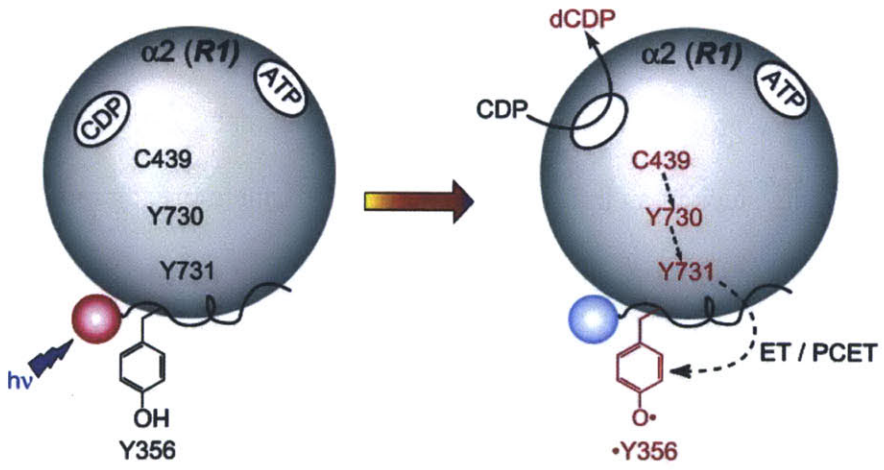

Figure 1.18 Schematic presentation of light-initiated radical propagation in [Photo]-Y-β2C19 peptides. A photooxidant (pink sphere) is appended to the N-terminus of a peptide corresponding to the last 19 amino acids in the C-terminus of β2. The native Y or an unnatural F_nY is incorporated at position 356. α2 is depicted as the gray sphere. Details of the mechanism are described in the text. Reproduced from reference 75.

The study of light-initiated reactions between [Photo]-Y-β2C19 and α2 is very powerful, as this method at present provides the only means of obtaining time-resolved information on the details of radical propagation. However, the utility of this method has been inhibited by the fast conformational dynamics of the [Photo]-Y-β2C19•α2 interaction. Indeed, time-resolved emission and absorption spectroscopic studies of [Re]-Y-β2C19 indicate the presence of multiple populations of the peptide in the presence of α2, with evidence of both protein-bound and solvent-exposed fractions of the peptide's N-terminus,[77] containing both the [Re] photooxidant and Y_{356}. This heterogeneity in peptide conformations is thought to be one of the primary factors for the low accumulation of Y_{356}• and, subsequently, low yields of radical injection to α2.

In an attempt to impose structural constraints on the PCET pathway, recent efforts have focused on appending the photooxidant to the intact β2 subunit at a minimally perturbative position on the C-terminal tail. In the first demonstration of a photoRNR, a cysteine residue installed at position 355 was covalently labeled with [Re]. After establishing that the photochemical properties of the [Re] were not perturbed by conjugation to the protein, the photooxidant was shown to generate a Y_{356}• on the intact protein subunit upon light initiation.[79] This result is a very promising advance towards the eventual goal of kinetic characterization of the radical hopping steps in an intact α2β2 complex. Furthermore, by modifying the site of [Re] attachment and/or installing various pathway blocks into the system, photoRNRs may be used to study the details of both forward and reverse PCET processes.

1.3 CHAPTER PREVIEW

The broad objective of the research efforts described in this thesis is to investigate the detailed mechanism of the proton-coupled electron transfer (PCET) in *Escherichia coli* class Ia RNR via the site-specific incorporation of the tyrosine analogues 3-aminotyrosine (NH_2Y) and fluorotyrosines (F_nY, n = 1-4) into positions of the proposed pathway - 122 and 356 of β2 and 731 and 730 of α2 - by the *in vivo* nonsense codon suppression method. UAAs were selected to alter the redox properties and/or pK_as relative to the native Y, such that details relevant to radical propagation become detectable and measurable. Otherwise, we hoped these UAAs would be minimally perturbative so that observations made with the mutants could be extended to understanding catalysis in the native system. The studies presented herein are intended to help elucidate the kinetics and thermodynamics of long-distance PCET in *E. coli* class Ia RNR and to challenge and refine the working model for radical propagation. The more specific goals of the experiments described in the individual chapters are described below.

The isolation and characterization of $Y_{356}NH_2Y$-β2 by the *in vivo* nonsense suppression method is reported in **Chapter 2**. The ability to incorporate NH_2Y at each of the three positions of transient Y• formation provides a first opportunity to study the mechanistic details at each individual step on the pathway. Steady-state activity assays of the three NH_2Y-RNRs indcate that they are active, with 3-12% the activity of the corresponding wt subunit. Three types of experiments are conducted to rigorously establish that this activity is inherent to NH_2Y-RNRs and not the consequence of contaminating wt protein. Kinetic measurements of NH_2Y• formation in three NH_2Y-RNRs with all S/E pairs indicate that the radical is kinetically competent and generated in two phases. A preliminary kinetic model is generated for catalysis

by NH_2Y-RNRs in which the rate-determining step is oxidation of the next residue on the pathway by NH_2Y•.

In **Chapter 3**, the pathway dependence of NH_2Y• formation and the fidelity of radical propagation through the proposed pathway is tested. We hypothesize that, in the reaction of NH_2Y-RNRs, NH_2Y• formation at position 356, 731, or 730 is the result of these residues participating in the long-distance PCET pathway. However, it can be argued that NH_2Y• formation is the result of introducing a redox-active thermodynamic trap into the protein environment. To provide evidence against the latter argument, two sets of experiments are conducted. The first involves incorporation of a PCET block in the pathway, in the form of a redox-inert F, at a position prior to NH_2Y. The reactions of $Y_{356}F$-β2 with $Y_{731}NH_2Y$-α2 (or $Y_{730}NH_2Y$-α2), S, and E fail to generate NH_2Y•. An identical result is obtained for the reaction of wt-β2 with $Y_{731}F/Y_{730}NH_2Y$-α2. In a second set of experiments, NH_2Y is incorporated at position 413 of α2, located adjacent to the PCET pathway but not proposed to participate in radical propagation. It is demonstrated that this "off-pathway" NH_2Y can be oxidized, but that the rate constants and amplitude of formation of NH_2Y_{413}• are greatly reduced compared to the on-pathway positions. This result is consistent with kinetically-competent NH_2Y• formation relying on a specific, optimized PCET pathway.

In **Chapter 4**, we test and refine the original model for catalysis in NH_2Y-RNRs presented in Chapter 2. Measurement of the pre-steady state kinetics of dCDP formation by rapid chemical quench experiments reveals that product formation is biphasic, with a fast phase similar to the fast phase for NH_2Y• formation and a slow phase on par with the steady-state turnover. Thus, we adjust the original model to account for k_{fast}, and present a revised version in which the slow interconversion between two NH_2Y• populations – one active and one inactive –

is rate-determining in the overall kinetic scheme. The question of whether an on-pathway NH_2Y• can re-initiate radical propagation is also addressed, as is whether RNR may be active when NH_2Y is incorporated at two unique sites on the PCET pathway.

In **Chapter 5**, we demonstrate that the formation of an on-pathway NH_2Y• induces the formation of a kinetically stable α2β2 complex through a series of collaborative biochemical and structural experiments. The original hypothesis is established after observing that the interaction between $Y_{730}NH_2Y$-α2 (or $Y_{731}NH_2Y$-α2) and wt-β2 under turnover conditions is significantly tighter than the corresponding wt-α2 and wt-β2 interaction and is cooperative in nature. Subsequent SF fluorescence experiments establish that k_{off} for the $Y_{730}NH_2Y$-α2•wt-β2 complex in the presence of S/E is $\geq 10^3$-fold slower than the wt-α2•wt-β2 complex. Modified activity assays indicate that the trapped complex is an active form of the enzyme, or can rapidly reorganize to access an active state. Electron microscopy imaging and small-angle X-ray scattering studies of the complex indicate that it is a compact, globular α2β2, and that its structure is consistent with that predicted by the docking model. These studies, combined with previous PELDOR measurements, solidfy the docking model as an accurate representation of the active *E. coli* class Ia RNR. It is proposed trapping an on-pathway radical, either by incorporation of an UAA or use of a mechanism-based inhibitor, is a general mechanism for the stabilization of an α2β2 complex.

The results of a successful collaboration with the Schultz lab to develop an orthogonal RS for the site-specific incorporation of 2,3,5-trifluorotyrosine (F_3Y) into RNR are described in **Chapter 6**. To our delight, the F_3Y-RS demonstrates a relaxed specificity that allows it to recognize the entire series of F_nYs. We report the application of this RS to incorporation of four F_nYs at positions 356 of β2, 731 of α2, and 730 of α2, and isolation of the resulting proteins in

high yields. The pH dependence of nucleotide reductase activity in F_nY-RNRs is also investigated. pH rate profiles are generated for RNRs containing F_nYs at position 356 of β2, 730 of α2, or 731 of α2 and are compared to each other and to the existing data for EPL-generated $Y_{356}F_n$Y-β2s. The activities of F_nY-RNRs fall into a regime in which conformational changes are still rate-limiting. The pH rate profiles are all fit to a two residue ionization model and are interpreted as reporting on the pH dependence of these conformational changes. The observation that radical propagation is rate-limiting in EPL-generated $Y_{356}(2,3,5)F_3$Y-β2, but not in the *in vivo* synthesized mutant, is rationalized in terms of two additional point mutations present in the former protein.

Chapter 7 describes efforts to modulate the driving force of radical initiation by incorporation of F_nYs at position 122 of β2. These experiments were inspired by recent results obtained with the mutant $Y_{122}NO_2$Y-β2, which demonstrated that ET could be decoupled from PT and the rate-limiting conformational change when the potent oxidant NO_2Y_{122}• was used as a radical initiator. A complete series of F_nYs is incorporated to position 122, and the resulting stable F_nY_{122}•s are characterized by UV-vis and X-band EPR spectroscopy. The distinct EPR spectra of these radicals, originating from couplings to the fluorine nuclei, allow for facile deconvolution of complicated reaction spectra containing F_nY_{122}• and another g ~2 radical(s), such as Y•. Product formation is examined for each $Y_{122}F_n$Y-β2 under steady-state and single-turnover conditions. A decrease in overall activity is observed when the potential is raised at position 122 >10 mV relative to Y, though the loss does not strictly correlate with increase in driving force, suggesting that the unique reactivity of $Y_{122}F_n$Y-β2s relative to wt-β2 may stem from differences in conformational dynamics. The reactions of $Y_{122}F_n$Y-β2s with wt-α2 or Y_{731}F-α2 were investigated by hand-quench EPR and stopped-flow UV-vis spectroscopy, and

demonstrate that a new radical, assigned as Y_{356}•, is formed concomitant with F_nY_{122}• loss when the driving force is raised at position 122. The detailed kinetics of Y_{356}• formation and dCDP production were studied by RFQ-EPR and RCQ, respectively, for $Y_{122}(2,3,5)F_3Y$-β2 and indicate that Y_{356}• formation is kinetically competent and faster than dCDP formation. The results of these studies, combined with those from the $Y_{122}NO_2Y$-β2 system, have allowed us to generate a preliminary model of the PCET thermodynamic landscape which may be experimentally tested through additional studies on $Y_{122}F_nY$-β2s. They also allow us to address for the first time the role of W_{48} in long-range PCET.

Chapter 8 is a miscellaneous chapter, summarizing two brief studies. The first describes experiments designed to determine whether E_{350}, a conserved residue located in the conformationally disordered tail of β, is the proton acceptor for orthogonal PCET through Y_{356}. The importance of E_{350} to radical propagation is confirmed by demonstrating that the double mutant $E_{350}A/Y_{356}NH_2Y$-β2 cannot generate NH_2Y• when reacted with wt-β2 CDP, and ATP. To look at E_{350}'s role in more mechanistic detail, the double mutants $E_{350}X/Y_{356}(3,5)F_2Y$-β2 (X = A, D) are prepared and their pH rate profiled determined. Surprisingly, these mutants are inactive across all pH regimes, suggesting that the role of E_{350} is more complicated than originally hypothesized.

The heterodimeric protein $Y_{356}NH_2Y$-ββ′ (where β′ is a truncated protomer of β, lacking the C-terminal 20 residues) is characterized in a second set of experiments. It was thought that the extent of NH_2Y• formation and product formation in this mutant could provide insight to the asymmetry of the α2β2 complex and the half-sites reactivity it induces. While $Y_{356}NH_2Y$-ββ′ was capable of generating a NH_2Y_{356}• (albeit with much slower kinetics compared to $Y_{356}NH_2Y$-β2), the mutant was inactive in nucleotide reduction. We were able to obtain evidence of re-

oxidation of Y_{122} by NH_2Y_{356}• in the reaction of $Y_{356}NH_2Y$-ββ′, wt-α2, CDP, and ATP, akin to what was observed previously in the analogous reaction with Y_{356}DOPA-ββ′. The mechanistic basis for observing reverse ET under these specific conditions are not understood at present.

1.4 REFERENCES

1. Stubbe, J. & van der Donk, W.A. Protein radicals in enzyme catalysis. *Chem. Rev.* **98**, 705-62 (1998).
2. Jordan, A. & Reichard, P. Ribonucleotide reductases. *Annu. Rev. Biochem.* **67**, 71-98 (1998).
3. Nordlund, P. & Reichard, P. Ribonucleotide reductases. *Annu. Rev. Biochem.* **75**, 681-706 (2006).
4. Shao, J., Zhou, B., Chu, B. & Yen, Y. Ribonucleotide reductase inhibitors and future drug design. *Curr. Cancer Drug Targets* **6**, 409-431 (2006).
5. Cerqueira, N., Pereira, S., Fernandes, P.A. & Ramos, M. Overview of ribonucleotide reductase inhibitors: an appeal target in anti-tumor therapy. *J. Curr. Med. Chem* **12**, 1283-94 (2005).
6. Wnuk, S.F. & Robins, M.J. Ribonucleotide reductase inhibitors as anti-herpes agents. *Antiviral Res.* **71**, 122-6 (2006).
7. Reichard, P. & Ehrenberg, A. Ribonucleotide reductase--a radical enzyme. *Science* **221**, 514-9 (1983).
8. Licht, S., Gerfen, G.J. & Stubbe, J. Thiyl radicals in ribonucleotide reductases. *Science* **271**, 477-81 (1996).
9. Licht, S. & Stubbe, J. Mechanistic investigations of ribonucleotide reductases. *Compr. Nat. Prod. Chem.* **5**, 163-203 (1999).
10. Logan, D.T., Andersson, J., Sjöberg, B.M. & Nordlund, P. A glycyl radical site in the crystal structure of a class III ribonucleotide reductase. *Science* **283**, 1499-504 (1999).
11. Cotruvo, J.A. & Stubbe, J. Class I ribonucleotide reductases: metallocofactor assembly and repair in vitro and in vivo. *Annu Rev Biochem* **80**, 733-67 (2011).
12. Cotruvo, J.A. & Stubbe, J. Escherichia coli class Ib ribonucleotide reductase contains a dimanganese(III)-tyrosyl radical cofactor in vivo. *Biochemistry* **50**, 1672-81 (2011).
13. Jiang, W., Yun, D., Saleh, L., Barr, E. W., Xing, G., Hoffart, L. M., Maslak, M. A., Krebs, C. & Bollinger, J. M., Jr. A manganese(IV)/iron(III) cofactor in *Chlamydia trachomatis* ribonucleotide reductase. *Science* **316**, 1188-91 (2007).
14. Uhlin, U. & Eklund, H. Structure of ribonucleotide reductase protein R1. *Nature* **370**, 533-539 (1994).
15. Sintchak, M.D., Arjara, G., Kellogg, B.A., Stubbe, J. & Drennan, C.L. The crystal structure of class II ribonucleotide reductase reveals how an allosterically regulated monomer mimics a dimer. *Nat. Struct. Biol.* **9**, 293-300 (2002).
16. Stubbe, J. & Ackles, D. On the mechanism of ribonucleoside diphosphate reductase from *Escherichia coli*. Evidence for 3'-C--H bond cleavage. *J. Biol. Chem.* **255**, 8027-30 (1980).

17. Lawrence, C.C., Bennati, M., Obias, H. V., Bar, G., Griffin, R. G. & Stubbe, J. High-field EPR detection of a disulfide radical anion in the reduction of cytidine 5'-diphosphate by the E_{441}Q-R1 mutant of *Escherichia coli* ribonucleotide reductase. *Proc Natl Acad Sci U S A* **96**, 8979-8984 (1999).

18. Brown, N.C. & Reichard, P. Ribonucleoside diphosphate reductase: Formation of active and inactive complexes of proteins B1 and B2. *J. Mol. Biol.* **46**, 25-38 (1969).

19. Brown, N.C. & Reichard, P. Role of effector binding in allosteric control of ribonucleoside diphosphate reductase. *J. Mol. Biol.* **46**, 39-55 (1969).

20. Larsson, A. Enzymatic Synthesis of Deoxyribonucleotides. VII. Studies on the Hydrogen Transfer with Tritiated Water. *Biochemistry* **4**, 1984-93 (1965).

21. Larsson, A. & Reichard, P. Enzymatic synthesis of deoxyribonucleotides. X. Reduction of purine ribonucleotides; allosteric behavior and substrate specificity of the enzyme system from *Escherichia coli* B. *J. Biol. Chem.* **241**, 2540-9 (1966).

22. Larsson, K.M., Jordan, A., Eliasson, R., Reichard, P., Logan, D. T. & Nordlund, P. Structural mechanism of allosteric substrate specificity regulation in a ribonucleotide reductase. *Nat. Struct. Mol. Biol.* **11**, 1142-9 (2004).

23. Hogbom, M. et al. Displacement of the tyrosyl radical cofactor in ribonucleotide reductase obtained by single-crystal high-field EPR and 1.4-A x-ray data. *Proc. Natl. Acad. Sci. U S A* **100**, 3209-14 (2003).

24. Sjöberg, B.M., Reichard, P., Gräslund, A. & Ehrenberg, A. Tyrosine free-radical in ribonucleotide reductase from *Escherichia coli*. *J. Biol. Chem.* **253**, 6863-5 (1978).

25. Barry, B.A., el-Deeb, M.K., Sandusky, P.O. & Babcock, G.T. Tyrosine radicals in photosystem II and related model compounds. Characterization by isotopic labeling and EPR spectroscopy. *J. Biol. Chem.* **265**, 20139-43 (1990).

26. Gupta, A., Mukherjee, A., Matsui, K. & Roth, J.P. Evidence for protein radical-mediated nuclear tunneling in fatty acid alpha-oxygenase. *J. Am. Chem. Soc.* **130**, 11274-5 (2008).

27. Zhao, X. et al. A radical on the Met-Tyr-Trp modification required for catalase activity in catalase-peroxidase is established by isotopic labeling and site-directed mutagenesis. *J. Am. Chem. Soc.* **132**, 8268-9 (2010).

28. Tsai, A.L. & Kulmacz, R.J. Prostaglandin H synthase: resolved and unresolved mechanistic issues. *Arch. Biochem. Biophys.* **493**, 103-24 (2010).

29. Nordlund, P., Sjöberg, B.M. & Eklund, H. Three-dimensional structure of the free radical protein of ribonucleotide reductase. *Nature* **345**, 593-8 (1990).

30. Voegtli, W.C. et al. Variable coordination geometries at the diiron(II) active site of ribonucleotide reductase R2. *J. Am. Chem. Soc.* **125**, 15822-30 (2003).

31. Thelander, L. Physicochemical characterization of ribonucleoside diphosphate reductase from *Escherichia coli*. *J. Biol. Chem.* **248**, 4591-4601 (1973).

32. Climent, I., Sjöberg, B.M. & Huang, C.Y. Carboxyl-terminal peptides as probes for *Escherichia coli* ribonucleotide reductase subunit interaction: kinetic analysis of inhibition studies. *Biochemistry* **30**, 5164-71 (1991).

33. Ando, N. et al. Structural interconversions modulate activity of *Escherichia coli* ribonucleotide reductase. *Proc. Natl. Acad. Sci. U S A* **108**, 21046-51 (2011).

34. Hassan, A.Q., Olshansky, L., Yokoyama, K., Lutterman, D. A., Jin, X., Nocera, D. G., & Stubbe, J. *In preparation.*

35. Zimanyi, C.M. et al. *In revision.*

36. Uppsten, M., Farnegardh, M., Jordan, A., Eliasson, R., Eklund, H. & Uhlin, U. Structure of the large subunit of class Ib ribonucleotide reductase from *Salmonella typhimurium* and its complexes with allosteric effectors. *J. Mol. Biol.* **330**, 87-97 (2003).

37. Bennati, M. et al. EPR distance measurements support a model for long-range radical initiation in *E. coli* ribonucleotide reductase. *J. Am. Chem. Soc.* **127**, 15014-5 (2005).

38. Denysenkov, V.P., Prisner, T.F., Stubbe, J. & Bennati, M. High-field pulsed electron-electron double resonance spectroscopy to determine the orientation of the tyrosyl radicals in ribonucleotide reductase. *Proc Natl Acad Sci U S A* **103**, 13386-13390 (2006).

39. Ge, J., Yu, G., Ator, M.A. & Stubbe, J. Pre-steady-state and steady-state kinetic analysis of *E. coli* class I ribonucleotide reductase. *Biochemistry* **42**, 10071-83 (2003).

40. Gray, H.B. & Winkler, J.R. Long-range electron transfer. *Proc Natl Acad Sci U S A* **102**, 3534-3539 (2005).

41. Cordes, M., Kottgen, A., Jasper, C., Jacques, O., Boudebous, H. & Giese, B. Influence of amino acid side chains on long-distance electron transfer in peptides: electron hopping via "stepping stones". *Angew Chem Int Ed Engl* **47**, 3461-3463 (2008).

42. Shih, C., Museth, A. K., Abrahamsson, M., Blanco-Rodriguez, A. M., Di Bilio, A. J., Sudhamsu, J., Crane, B. R., Ronayne, K. L., Towrie, M., Vlcek, A., Jr., Richards, J. H., Winkler, J. R. & Gray, H. B. Tryptophan-accelerated electron flow through proteins. *Science* **320**, 1760-1762 (2008).

43. Climent, I., Sjöberg, B.M. & Huang, C.Y. Site-directed mutagenesis and deletion of the carboxyl terminus of *Escherichia coli* ribonucleotide reductase protein R2 - effects on catalytic activity and subunit interaction. *Biochemistry* **31**, 4801-7 (1992).

44. Mayer, J.M. & Rhile, I.J. Thermodynamics and kinetics of proton-coupled electron transfer: stepwise vs. concerted pathways. *Biochim. Biophys. Acta.* **1655**, 51-8 (2004).

45. Xie, J. & Schultz, P.G. An expanding genetic code. *Methods* **36**, 227-38 (2005).

46. Wang, L., Xie, J. & Schultz, P.G. Expanding the genetic code. *Annu Rev Biophys Biomol Struct* **35**, 225-49 (2006).

47. Muralidharan, V. & Muir, T.W. Protein ligation: an enabling technology for the biophysical analysis of proteins. *Nat Methods* **3**, 429-38 (2006).

48. Flavell, R.R. & Muir, T.W. Expressed protein ligation (EPL) in the study of signal transduction, ion conduction, and chromatin biology. *Acc Chem Res* **42**, 107-16 (2009).

49. Paulus, H. Protein splicing and related forms of protein autoprocessing. *Annu Rev Biochem* **69**, 447-96 (2000).

50. Dawson, P.E., Muir, T.W., Clark-Lewis, I. & Kent, S.B. Synthesis of proteins by native chemical ligation. *Science* **266**, 776-9 (1994).

51. Rodnina, M.V. & Wintermeyer, W. Fidelity of aminoacyl-tRNA selection on the ribosome: kinetic and structural mechanisms. *Annu Rev Biochem* **70**, 415-35 (2001).

52. Zaher, H.S. & Green, R. Quality control by the ribosome following peptide bond formation. *Nature* **457**, 161-6 (2009).

53. Liu, D.R., Magliery, T.J., Pastrnak, M. & Schultz, P.G. Engineering a tRNA and aminoacyl-tRNA synthetase for the site-specific incorporation of unnatural amino acids into proteins in vivo. *Proc Natl Acad Sci U S A* **94**, 10092-7 (1997).

54. Nowak, M.W. et al. In vivo incorporation of unnatural amino acids into ion channels in *Xenopus* oocyte expression system. *Methods Enzymol* **293**, 504-29 (1998).

55. Tam, A., Soellner, M.B. & Raines, R.T. Water-soluble phosphinothiols for traceless staudinger ligation and integration with expressed protein ligation. *J Am Chem Soc* **129**, 11421-30 (2007).

56. Lockless, S.W. & Muir, T.W. Traceless protein splicing utilizing evolved split inteins. *Proc Natl Acad Sci U S A* **106**, 10999-1004 (2009).

57. Melancon, C.E., 3rd & Schultz, P.G. One plasmid selection system for the rapid evolution of aminoacyl-tRNA synthetases. *Bioorg Med Chem Lett* **19**, 3845-7 (2009).

58. Wang, K., Neumann, H., Peak-Chew, S.Y. & Chin, J.W. Evolved orthogonal ribosomes enhance the efficiency of synthetic genetic code expansion. *Nat Biotechnol* **25**, 770-7 (2007).

59. Rackham, O. & Chin, J.W. A network of orthogonal ribosome x mRNA pairs. *Nat Chem Biol* **1**, 159-66 (2005).

60. An, W. & Chin, J.W. Synthesis of orthogonal transcription-translation networks. *Proc Natl Acad Sci U S A* **106**, 8477-82 (2009).

61. Shimizu, Y., Kanamori, T. & Ueda, T. Protein synthesis by pure translation systems. *Methods* **36**, 299-304 (2005).

62. Murakami, H., Ohta, A., Ashigai, H. & Suga, H. A highly flexible tRNA acylation method for non-natural polypeptide synthesis. *Nat Methods* **3**, 357-9 (2006).

63. Ohta, A., Yamagishi, Y. & Suga, H. Synthesis of biopolymers using genetic code reprogramming. *Curr Opin Chem Biol* **12**, 159-67 (2008).

64. Yee, C.S., Seyedsayamdost, M.R., Chang, M.C.Y., Nocera, D.G. & Stubbe, J. Generation of the R2 subunit of ribonucleotide reductase by intein chemistry: insertion of 3-nitrotyrosine at residue 356 as a probe of the radical initiation process. *Biochemistry* **42**, 14541-52 (2003).

65. Seyedsayamdost, M.R., Yee, C.S. & Stubbe, J. Site-specific incorporation of fluorotyrosines into the R2 subunit of *E. coli* ribonucleotide reductase by expressed protein ligation. *Nat. Protoc.* **2**, 1225-35 (2007).

66. Seyedsayamdost, M.R. & Stubbe, J. Forward and reverse electron transfer with the Y356DOPA-β2 heterodimer of *E. coli* ribonucleotide reductase. *J. Am. Chem. Soc.* **129**, 2226-7 (2007).

67. Yee, C.S., Chang, M.C.Y., Ge, J., Nocera, D.G. & Stubbe, J. 2,3-difluorotyrosine at position 356 of ribonucleotide reductase R2: A probe of long-range proton-coupled electron transfer. *J. Am. Chem. Soc.* **125**, 10506-7 (2003).

68. Seyedsayamdost, M.R., Yee, C.S., Reece, S.Y., Nocera, D.G. & Stubbe, J. pH rate profiles of F_nY_{356}-R2s (n = 2, 3, 4) in *Escherichia coli* ribonucleotide reductase: evidence that Y_{356} is a redox-active amino acid along the radical propagation pathway. *J. Am. Chem. Soc.* **128**, 1562-8 (2006).

69. Seyedsayamdost, M.R. & Stubbe, J. Site-specific replacement of Y_{356} with 3,4-dihydroxyphenylalanine in the β2 subunit of *E. coli* ribonucleotide reductase. *J. Am. Chem. Soc.* **128**, 2522-3 (2006).

70. Seyedsayamdost, M.R., Chan, C.T., Mugnaini, V., Stubbe, J. & Bennati, M. PELDOR spectroscopy with DOPA-β2 and NH_2Y-α2s: distance measurements between residues involved in the radical propagation pathway of *E. coli* ribonucleotide reductase. *J. Am. Chem. Soc.* **129**, 15748-9 (2007).

71. Seyedsayamdost, M.R., Xie, J., Chan, C.T., Schultz, P.G. & Stubbe, J. Site-specific insertion of 3-aminotyrosine into subunit α2 of *E. coli* ribonucleotide reductase: direct evidence for involvement of Y730 and Y731 in radical propagation. *J. Am. Chem. Soc.* **129**, 15060-71 (2007).

72. Seyedsayamdost, M.R., Argirevic, T., Minnihan, E.C., Stubbe, J. & Bennati, M. Structural examination of the transient 3-aminotyrosyl radical on the PCET pathway of *E. coli* ribonucleotide reductase by multifrequency EPR spectroscopy. *J. Am. Chem. Soc.* **131**, 15729-38 (2009).

73. Yokoyama, K., Uhlin, U. & Stubbe, J. A hot oxidant, 3-$NO2Y_{122}$ radical, unmasks conformational gating in ribonucleotide reductase. *J. Am. Chem. Soc.* **132**, 15368-79 (2010).

74. Yokoyama, K., Smith, A.A., Corzilius, B., Griffin, R.G. & Stubbe, J. Equilibration of tyrosyl radicals (Y356•, Y731•, Y730•) in the radical propagation pathway of the *Escherichia coli* class Ia ribonucleotide reductase. *J. Am. Chem. Soc.* **133**, 18420-32 (2011).

75. Reece, S.Y., Seyedsayamdost, M.R., Stubbe, J. & Nocera, D.G. Photoactive peptides for light-initiated tyrosyl radical generation and transport into ribonucleotide reductase. *J. Am. Chem. Soc.* **129**, 8500-9 (2007).

76. Reece, S.Y., Seyedsayamdost, M.R., Stubbe, J. & Nocera, D.G. Direct observation of a transient tyrosine radical competent for initiating turnover in a photochemical ribonucleotide reductase. *J. Am. Chem. Soc.* **129**, 13828-30 (2007).

77. Reece, S.Y., Lutterman, D.A., Seyedsayamdost, M.R., Stubbe, J. & Nocera, D.G. Re(bpy)(CO)(3)CN as a probe of conformational flexibility in a photochemical ribonucleotide reductase. *Biochemistry* **48**, 5832-8 (2009).

78. Holder, P.G., Pizano, A.A., Anderson, B.L., Stubbe, J. & Nocera, D.G. Deciphering radical transport in the large subunit of class I ribonucleotide reductase. *J. Am. Chem. Soc.* **134**, 1172-80 (2012).

79. Pizano, A.A. et al. Photo-ribonucleotide reductase beta2 by selective cysteine labeling with a radical phototrigger. *Proc. Natl. Acad. Sci. U S A* **109**, 39-43 (2011).

Chapter 2

Kinetics of radical intermediate formation and deoxynucleotide production in 3-aminotyrosine-substituted *Escherichia coli* ribonucleotide reductases

Adapted in part from: Minnihan, E.C., Seyedsayamdost, M.R., Uhlin, U., and Stubbe, J. *J. Am. Chem. Soc.*, **2011**, *133*, 9430-9440.

2.1 INTRODUCTION

The class Ia ribonucleotide reductase (RNR) from *Escherichia coli* catalyzes the reduction of four nucleoside 5′-diphosphate substrates (S, where S is UDP, CDP, ADP and GDP) to 2′-deoxynucleoside 5′-diphosphates (dNDPs) in a highly orchestrated fashion.[1-3] Allosteric effectors (E, where E is ATP, dGTP, TTP, and dATP) bind to the specificity site (S-site) and ATP/dATP bind to the activity site (A-site), dictating the substrate reduced and the overall enzyme activity, respectively. The active site and both allosteric sites are located in α2, whereas the essential diferric tyrosyl radical (Y_{122}• in *E. coli*) cofactor resides in β2. This stable Y• serves as the radical initiator for the transient oxidation of the active-site cysteine (C_{439}) in α2 which initiates nucleotide reduction.

The active form of the *E. coli* RNR is proposed to be an α2β2 complex.[4] While the individual structures of α2 and β2 have been solved, no structure of the α2β2 complex has been determined to date. Thus, a docking model of the two subunits has been generated based on shape complementarity of the individual subunits, the superposition of their two-fold symmetry axes, and the relative locations of strictly conserved residues.[5] The most provocative feature of the docking model is the 35 Å distance it places between the redox-coupled residues C_{439} in α2 and Y_{122}• in β2.[5] Uhlin and Eklund proposed a mechanism to rationalize this long-range oxidation in which conserved, redox-active aromatic amino acids constitute a specific pathway for radical propagation: Y_{122}• → [W_{48}?] → Y_{356} in β2 to Y_{731} → Y_{730} → C_{439} in α2. Our hypothesis for radical propagation (Figure 2.1) has developed from this original model, and invokes orthogonal proton-coupled electron transfer (PCET) within β2 and co-linear PCET within α2.[6] In the advent of emerging technology for the site-specific incorporation of unnatural

amino acids into proteins, we have begun to provide convincing evidence in support of this hypothesis.

Figure 2.1 The Stubbe/Nocera model for long-range (~35 Å), reversible PCET by a radical hopping mechanism in *E. coli* class Ia RNR. Evidence suggests orthogonal PCET is operative in the β subunit, and co-linear PCET is operative in the α subunit. Residue Y_{356} has not been observed in any crystal structure of β2, and thus its location relative to the other residues is unknown. There is no direct evidence that W_{48} and its putative H^+ acceptor, D_{237}, participate in long-range PCET during turnover.

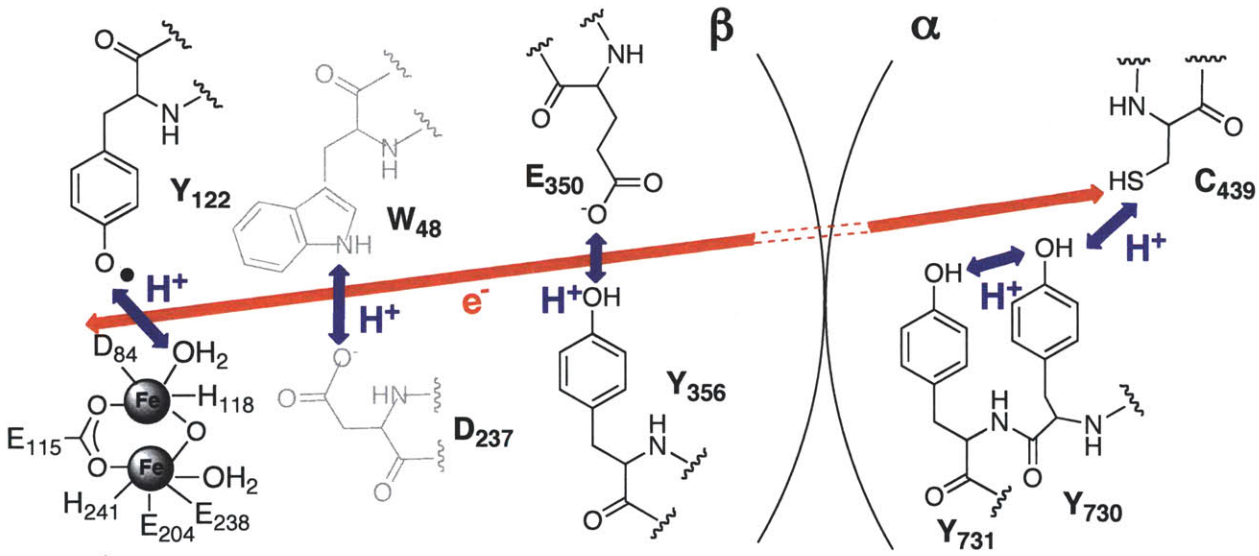

Studies from our laboratory have established that the rate-limiting step in NDP reduction in wt *E. coli* RNR is associated with conformational changes triggered by binding of S and E to α2.[7] These changes occur prior to radical propagation, are intricately linked to its initiation, and mask observation of any radical intermediates generated during long-range propagation.[7] To study the details of this process and to characterize radical intermediates, our laboratory has focused on subtly perturbing the wt enzyme through the site-specific incorporation of tyrosine analogues with different reduction potentials and/or phenolic pK_as in place of the Ys on the pathway. Studies conducted on these mutants have provided evidence for our working model shown in Figure 2.1.

The role of Y_{356} in β2 has been studied most extensively, with more than a half dozen tyrosine analogues substituted at this position using expressed protein ligation (EPL). These include the thermodynamic radical trap 2,3-dihydroxyphenylalanine (DOPA),[8,9] the radical block and pK_a probe 3-nitrotyrosine (NO_2Y),[10,11] and the dual pK_a/reduction potential reporter fluorotyrosines (F_nYs, n = 1-4).[12,13] The data from these studies have provided convincing evidence that Y_{356} is a redox-active participant on the pathway. This result is particularly important as the C-terminal 35 amino acids of β, including Y_{356}, constitute a thermally disordered tail that provides key recognition features for the α2/β2 interaction.[14] The docking model predicts a distance of >25 Å between W_{48} in β2 and Y_{731} in α2, and our collective results support the participation of Y_{356} as a relay between these two residues across the subunit interface.

More recently, Y_{730} and Y_{731} of α2 have been targeted for site-specific replacement using the *in vivo* nonsense codon suppression technology.[15] Employing a specific, orthogonal tRNA/tRNA-synthetase (RS) pair, the radical trap 3-aminotyrosine (NH_2Y, E°′ ~0.64 V, pH 7)[16] was incorporated into each position.[17,18] When combined with β2, CDP, and ATP, $Y_{730}NH_2Y$-α2 (or $Y_{731}NH_2Y$-α2) generated an aminotyrosyl radical (NH_2Y•) in a kinetically-competent fashion. These studies, in conjunction with complementary studies of the "off-pathway" mutant $Y_{413}NH_2Y$-α2 (Chapter 3), provide evidence for a specific radical propagation pathway in α, involving Y_{730} and Y_{731}.[17,19] Initial results also demonstrated that both $Y_{730}NH_2Y$-α2 and $Y_{731}NH_2Y$-α2 were active in dNDP formation and thus indicated that the decrease in reduction potential of NH_2Y relative to Y is insufficient to shut down radical propagation. Using a reduction potential for Y of ~0.83 V (pH 7),[20] the difference between Y and NH_2Y is estimated to be ~190 mV; however, potentials up to 0.93 V have been reported for Y,[16] suggesting the

difference may be greater. The activities of NH_2Y-α2s were surprising, as this observation contrasts with previous studies on Y_{356}DOPA-β2 ($E^{\circ\prime}$ ~0.57 V, pH 7),[21] for which no catalytic activity was detectable (<$1/10^4$ wt).[8] Additionally, previous studies on $Y_{356}NO_2Y$-β2 and $Y_{356}F_nY$-β2s indicated that a 200 mV *increase* in potential relative to Y is sufficient to shut down nucleotide reduction.[10,13]

In this chapter, we report the expression, isolation, and characterization of $Y_{356}NH_2Y$-β2. This is the first mutant at position 356 of β2 generated by the *in vivo* nonsense suppression method. The data obtained with this mutant is free of many of the complexities described previously for the EPL-generated mutant β2s, in which two additional mutations were required to make sufficient protein for biophysical studies.[10] As was previously observed with NH_2Y-α2s, $Y_{356}NH_2Y$-β2 catalyzes dNDP production. Steady-state assays of NH_2Y-RNRs demonstrate they possess 3-12% the activity of the respective wt subunit (k_{obs} ~0.2-0.7 s^{-1}). Three types of experiments have been conducted to establish that the catalytic activity measured is associated with the NH_2Y-RNRs and not with contaminating wt enzyme that co-purifies with each mutant. The X-ray crystal structures of $Y_{730}NH_2Y$-α2 and $Y_{731}NH_2Y$-α2 have been solved and demonstrate that NH_2Y introduces minimal perturbation to the structural integrity of α2 and the conformation of residues involved in radical propagation.

The kinetics of NH_2Y• formation have been examined with each of the three NH_2Y-RNRs in the presence of the physiologically relevant S/E pairs and are all biphasic. The slower phase is invariant with position of NH_2Y in the pathway and with the S/E pair studied, and is proposed to report on the rate-limiting conformational change in the wt enzyme. A comparison of the rate constants for NH_2Y• formation with S or E alone indicates that S is responsible for triggering radical propagation. From these studies, in initial kinetic model is proposed for long

distance radical propagation in NH_2Y-RNRs that may be used to understand mechanistic details of this process relevant to the wt enzyme.

2.2 MATERIALS AND METHODS

2.2.1 Materials. Wt-α2 (2500 nmol/min/mg) and wt-β2 (1.2 Y_{122}•/β2, 7600 nmol/min/mg) were expressed from pTrc-*nrdA* and pTB2-*nrdB*, respectively, and purified following standard protocol.[22,23] $Y_{731}NH_2Y$-α2 and $Y_{730}NH_2Y$-α2 were co-expressed from pTrc-*nrdA*-TAG_{731} or pTrc-*nrdA*-TAG_{730} and pAC-NH_2Y, and purified as described.[17] All α2 proteins were pre-reduced prior to use.[17] *E. coli* thioredoxin (TR, 40 U/mg) and thioredoxin reductase (TRR, 1400 U/mg) were isolated as described.[24,25] 2′-Azido-2′-deoxycytidine 5′-diphosphate (N_3CDP) was synthesized from uridine by known procedures.[26,27] [5-^{3}H]-CDP was purchased from ViTrax (Placentia, CA). Nucleotide primers were purchased from Invitrogen, *Pfu* Ultra II polymerase from Stratagene, and restriction enzymes from New England Biolabs. Assay buffer consists of 50 mM Hepes, 1 mM EDTA, and 15 mM $MgSO_4$, pH 7.6. Protein concentrations were determined by the following extinction coefficients: holo-β2 (ε_{280} = 131,000 M^{-1} cm^{-1}), apo-β2 (ε_{280} = 120,000 M^{-1} cm^{-1}), α2 (ε_{279} = 189,000 M^{-1} cm^{-1}).

2.2.2 Cloning of pTrc-nrdB and generation of pTrc-nrdB(TAG_{356}). The *nrdB* gene was amplified from the plasmid pTB2-*nrdB*[22] using the primers 5′- ATA ATT GGA TCC GAT AAG ACG CGC CAG CGT CGC ATC AGG -3′ and 5′- CTT AAT AAA GAG TAA TGT TAC TGC AGG ATG GCG-3′ with *Pfu* Ultra II polymerase. The fragment was digested with *BamHI* (5′, underlined) and *PstI* (3′, underlined), purified by the PCR Purification Kit (Qiagen), and ligated into pTrc-99A with a 1:4 vector to insert ratio at 25 °C for 30 min using T4 DNA ligase (Promega), yielding pTrc-*nrdB*. pTrc-*nrdB* cloning was conducted by Clement Chan.

The template, pTrc-*nrdB*, was amplified with *Pfu* Ultra II polymerase in the presence of the forward primer (5′- GAA GTG GAA GTC AGT TCT TAG CTG GTC GGG CAG ATT GAC TCG -3′) and its reverse complement to insert an amber stop codon (TAG) at residue 356.

Mutagenesis was then conducted to remove three in-frame ATG codons located 144, 51, and 39 nucleotides upstream of the start of the *nrdB* gene. The forward primer (5'- CAC AGG AAA CAG ACC AAG GAA TTC GAG CTC GGT AC- 3') and its reverse complement were used to remove the first upstream, in-frame ATG. The isolated plasmid from the first reaction was then used as a template for a second mutagenesis reaction, which was amplified in the presence of the forward primer (5'- C AGG CAC AGG AGG CGG CGT AAA AGG CCT TAT CCG GC -3') and its reverse complement to remove the two final in-frame ATG codons. For each reaction, the mutation(s) was confirmed by sequencing at the MIT Biopolymers Laboratory.

2.2.3 Expression and purification of $Y_{356}NH_2Y$-β2. $Y_{356}NH_2Y$-β2 was expressed in a fashion identical to that of NH_2Y-substituted α2s.[17] *E. coli* DH10B cells (Invitrogen) were co-transformed with the plasmids pTrc-*nrdB*-TAG_{356} and pAC-NH_2Y and plated on LB-agar plates supplemented with 100 μg/mL Amp and 25 μg/mL Tet at 37 °C. After 2 days, single colonies were harvested and inoculated into 2xYT (8 mL) with the same antibiotics and grown at 37 °C, 225 rpm until saturation (24 h). A fraction of the saturated starter culture (1 mL) was used to inoculate an intermediate 2xYT culture (200 mL), which was grown in the presence of 100 μg/mL Amp and 25 μg/mL Tet at 37 °C, 200 rpm until saturation. This culture was used to inoculate a fermentor containing 10 L of enriched glycerol minimal media (GMML)[17] with antibiotics, and grown at 37 °C, 500 rpm, and 10 psi air until reaching an OD_{600} ~0.7, at which point NH_2Y and DTT were added to the culture to final concentrations of 1.0 mM and 0.1 mM, respectively. After 15 min, the culture was induced with 1 mM IPTG and the aeration increased. The cells were allowed to grow for an additional 4 h, then harvested by centrifugation (10,000 × *g*, 10 min, 4 °C), flash-frozen in liquid N_2, and stored at -80 °C. Yields of 1.5 g wet cell paste per L of culture were typical.

Purification of the mutant closely mimicked the previously reported protocol for wt and mutant β2s.[11,22] Cells (15 g) were resuspended in buffer B (50 mM Tris, 5% glycerol, pH 7.6) with 1.0 mM PMSF at 5 mL buffer/g of cell paste, homogenized, and lysed via two passes though a French pressure cell at 14,000 psi. To the lysate was added sodium ascorbate (5 mg /g of cell paste) and ferrous ammonium sulfate (5 mg/g of cell paste) with stirring at 4 °C dropwise over 10 min. The resulting solution was allowed to stir for an additional 15 min. Cell debris was cleared by centrifugation (20,000 × *g*, 30 min, 4 °C). To the supernatant was added 0.2 volumes of a 6% w/v streptomycin sulfate solution over 15 minutes with stirring at 4 °C. The resulting solution was allowed to stir for an additional 15 min, then DNA was pelleted by centrifugation (20,000 × *g*, 30 min, 4 °C). To the supernatant was added solid ammonium sulfate (39 g/L) over 20 minutes with stirring at 4 °C. The solution was allowed to stir for an additional 45 minutes, and the protein was pelleted by centrifugation (20,000 × *g*, 30 min, 4 °C). The pellet was resuspended in a minimum volume (~10 mL) of buffer B with PMSF, and desalted on a Sephadex G-25 column (200 mL) equilibrated in the same buffer. Protein-containing fractions were pooled, diluted 2-fold, and loaded directly onto a DEAE Sepharose Fast Flow column (100 mL) equilibrated in buffer B with PMSF. The column was washed with 1 column volume (CV) of 75 mM NaCl, then eluted with a linear gradient (250 mL × 250 mL) of 75 to 450 mM NaCl in Buffer B. Fractions with maximum absorbance at 280 nm and 405 nm were pooled, diluted 2-fold with buffer B, and loaded onto a Q-Sepharose High Performance column (20 mL) equilibrated in buffer B. The column was washed with 10 CVs of 125 mM NaCl, then eluted with a linear gradient (100 mL × 100 mL) of 125 to 450 mM NaCl in buffer B. Fractions with maximum absorbance 280 nm and 405 nm were assessed by SDS-PAGE, which indicated the elution of three relevant proteins with increasing salt concentration: β′2 homodimer (where β′ is

the β subunit truncated at residue 355), $Y_{356}NH_2Y$-ββ′ heterodimer, and $Y_{356}NH_2Y$-β2 homodimer.

Fractions containing primarily full-length $Y_{356}NH_2Y$-β2 were pooled, concentrated using a YM-30 membrane (Amicon), and subjected to FPLC on a Poros HQ/20 column (Applied Biosystems, 1.6 × 10 cm, 20 mL). The column was equilibrated in buffer B and was loaded with $Y_{356}NH_2Y$-β2 (~20 mg). The column was washed with one CV of 150 mM NaCl in buffer B at 1.5 mL/min, then eluted with a gradient of 150 mM to 450 mM NaCl (60 mL × 60 mL) at the same flow rate. This protocol gave $Y_{356}NH_2Y$-β2 of >95% purity, as judged by SDS-PAGE. Protein contained ~0.3 Y_{122}•/β2 as isolated.

2.2.4 ESI-MS characterization of $Y_{356}NH_2Y$-β2. ESI-MS analysis was conducted at the Proteomics Core Facility in the Koch Center for Integrative Cancer Research (MIT). The protein was absorbed on a protein microtrap (Michrom BioResources) and desalted by HPLC (50% water/50% acetonitrile/0.1% formic acid) immediately prior to MS analysis. Molecular weight measurements were made by LC-MS on a QSTAR Elite quadrupole-TOF mass spectrometer, which had been externally calibrated to a resolution of ~50 ppm.

2.2.5 Iron chelation and reconstitution of diiron-Y• cofactor in $Y_{356}NH_2Y$-β2. FPLC-purified $Y_{356}NH_2Y$-β2 (225 μM, 1.0 mL, 0.3 Y•/β2) was placed in a pear-shaped flask fitted with a vacuum adaptor, degassed on a Schlenk line, and brought into an anaerobic chamber at 4 °C. Sodium dithionite and methyl viologen were added to the stirring protein solution to final concentrations of 8 mM and 20 μM, respectively. The resulting pale blue solution was stirred for 1 h at 4 °C. A 50-fold molar excess of ferrozine was added, and the solution was stirred for an additional 15 min. The protein solution was removed from the anaerobic chamber, applied to a G-25 Sephadex column (45 mL), and eluted with reconstitution buffer (50 mM Hepes, 5%

glycerol, pH 7.6). The protein-containing fractions were concentrated to give apo-$Y_{356}NH_2Y$-β2 in >90% yield. The absence of features associated with iron cluster and radical was confirmed by UV-vis spectroscopy. The diiron-Y_{122}• cofactor was then reconstituted as described previously.[28] Briefly, the apo protein was degassed on the Schlenk line and brought into the anaerobic chamber. A solution of ferrous ammonium sulfate was added to the protein in a 5-fold molar excess of Fe^{2+} to β2, and the resulting solution was allowed to stir for 15 minutes at 4 °C. The protein solution was then removed from the anaerobic chamber, and to it was added a 3.5 molar excess of O_2 in the form of O_2-saturated reconstitution buffer. The solution was gently swirled, yielding a pale green-yellow solution indicative of diferric-Y• formation.

2.2.6 Y• and Fe quantitation in $Y_{356}NH_2Y$-β2. The amount of radical in reconstituted $Y_{356}NH_2Y$-β2 was determined by the "dropline" UV-vis absorption method following equation 2.1 and by EPR spectroscopy.

$$[Y_{122}\bullet] = \{ [A_{411nm} - 0.5(A_{406nm} + A_{416nm})] / 1783\ M^{-1}\ cm^{-1} \} \times \text{dilution} \qquad \text{eq. 2.1}$$

EPR spectra were recorded at 77 K on a Bruker EMX X-band spectrometer equipped with a quartz finger dewar containing liquid N_2 in the Department of Chemistry Instrumentation Facility. EPR parameters were as follows: microwave frequency = 9.34 GHz, power = 30 μW, modulation amplitude = 1.5 G, modulation frequency = 100 kHz, time constant = 5.12 ms, scan time = 41.9 s. EPR spin quantitation was carried out in WinEPR (Bruker) by measuring the normalized double integral intensity (DI/N) of the spectrum, correcting it for power, number of scans, and modulation amplitude (equation 2.2), and comparing this $(DI/N)_c$ to that of a Cu^{II} standard or a wt-β2 standard of known $[Y_{122}\bullet]$. Both the dropline and EPR methods indicated that reconstituted $Y_{356}NH_2Y$-β2 contained 0.5 Y_{122}•/β2.

$$(DI/N)_c = DI/N / (\text{power}^{1/2} \times \text{modulation amplitude} \times \text{scan \#}) \qquad \text{eq. 2.2}$$

Iron content of $Y_{356}NH_2Y$-β2 was quantified using the Ferrozine assay,[29] with minor modifications. To a protein solution (50 μL, ~50 μM) was added 100 μL of 2 M HCl, and the resulting solution was incubated at 100 °C for 30 minutes. The sample was then spun on a desktop centrifuge (14,000 × *g*, 4 °C, 30 s) to clear precipitated protein. To the supernatant was added 200 μL of ferrozine (5 mg/mL), 150 μL of saturated ammonium acetate, and 40 μL of sodium ascorbate (15 mg/mL). The solution was vortexed to mix, then spun on a desktop centrifuge (14,000 × *g*, 4 °C, 3 min). The supernatant was transferred to a fresh eppendorf tube, and the absorbance of $(Fz)_3Fe$ was recorded at 562 nm (ε = 27.9 mM^{-1} cm^{-1}). The absorbance was corrected with a blank spectrum containing no protein, and the total [Fe] was determined by comparison to a standard curve of iron concentrations.

2.2.7 Determining the specific activity of $Y_{356}NH_2Y$-β2 by spectrophotometric and radioactive assays. The activity of $Y_{356}NH_2Y$-β2 was determined using the spectrophotometric[7] and radioactive assays[13] according to standard lab protocol. In the former, ribonucleotide reductase activity was monitored through a continuous coupled-enzyme assay in which the consumption of NADPH was determined by monitoring the decrease in absorbance at 340 nm. Wt-α2 (2.5 μM), ATP (3 mM), CDP (1 mM), thioredoxin (TR, 30 μM), and thioredoxin reductase (TRR, 0.5 μM) were mixed in assay buffer in a final volume of 300 μL. The assay was initiated upon addition of $Y_{356}NH_2Y$-β2 (0.5 μM) and NADPH (0.2 mM), and the decrease in A_{340} (ε = 6220 M^{-1} cm^{-1}) was monitored over 1-2 minutes.

For the radioactive assay, wt-α2 (0.5 μM,), [^{3}H]-CDP (1 mM, 5500 cpm/nmol), ATP (3 mM), TR (30 μM), and TRR (0.5 μM) were combined in assay buffer (170 μL total volume) at 25 °C. The assay was initiated by addition of NADPH (1 mM) and $Y_{356}NH_2Y$-β2 (0.1 μM). Aliquots (30 μL) of the reaction mixture were removed at five time points throughout the assay,

and quenched in a boiling water bath. The samples were then subjected to dephosphorylation by mixing sample (30 μL), carrier dC (120 nmol), and calf alkaline phosphatase (14 U, Roche) in dephosphorylation buffer (75 mM Tris, 0.15 mM EDTA, pH 8.5) in a total volume of 500 μL. The samples were incubated at 37 °C for 2 h. Samples were then applied to an AG 1-X8 borate column (Bio-Rad), eluted in a total volume of 8 mL ddH_2O, and subjected to scintillation counting for the quantification of dC by the method of Steeper and Steuart.[30]

2.2.8 Expression, purification, and activity assays of N-Strep-$Y_{356}NH_2Y$-β2. The plasmid pBAD-N-Strep-*nrdB*(TAG_{356}) was generated from the template, pBAD-N-Strep-*nrdB*,[31] by a single mutagenesis reaction, as described for pTrc-*nrdB*(TAG_{356}). pBAD-N-Strep-*nrdB* contains an N-terminal StrepII tag (WSHPQFEK) with a five amino acid linker (SLGGH). The relevant insert, N-Strep-*nrdB*(TAG_{356}), was also cut from pBAD using *NcoI/ZhoI* (20 U each) and ligated into the commercially available plasmid pTrc-HisA digested with the same enzymes at a 5:1 insert-to-backbone ratio using T4 DNA Ligase, giving the new plasmid pTrc-N-Strep-*nrdB*(TAG_{356}). N-Strep-$Y_{356}NH_2Y$-β2 was then expressed from pAC-NH_2Y and pBAD-N-Strep-*nrdB*(TAG_{356}) or pTrc-N-Strep-*nrdB*(TAG_{356}) as described for $Y_{356}NH_2Y$-β2, using either L-ara or IPTG for *nrdB* gene induction.

Purification was conducted as described previously, with minor modification.[31] Cell paste (10 g) was resuspended in 5 mL/g buffer S (100 mM Tris, 150 mM NaCl, 5% glycerol, pH 7.6) with 1 mM PMSF at 4 °C with stirring. The resulting cell suspension was homogenized, and cells were lysed via two passes through the French Press at 14,000 psi. To the cell lysate was added a solution of sodium ascorbate (5 mg/g cell paste) and ferrous ammonium sulfate (5 mg/g cell paste) in buffer S dropwise at 4 °C over 10 minutes. The resulting solution was allowed to stir for an additional 15 minutes. Cell debris was cleared by centrifugation (20,000 x *g*, 4 °C, 30

min). The supernatant (~70 mL) was decanted and loaded onto Streptactin Sepharose resin (~10 mL CV, IBA) equilibrated in buffer S at a flow rate of <1 mL/min. The resin was washed with ~18 CVs of buffer S. The protein was then eluted with a solution of 2.5 mM desthiobiotin in buffer S at a rate of ~2 mL/min. Protein-containing fractions were determined by the Bradford assay, pooled (~25 mL), and concentrated on the desktop centrifuge using an Amicon YM-10 membrane to give 2 mg protein/g cell paste. Purification by this method gave a statistical mixture of β′2, ββ′, and β2′. These three species were separated by anion-exchange FPLC as described in section 2.2.3. Radioactive activity assays were conducted as described in section 2.2.7 and previously.[13]

Table 2.1 Primers used in the construction of N-terminally tagged *nrdA* genes, as described in the Materials and Methods section of this chapter.

Primer	Function	Forward primer nucleotide sequence, 5′ → 3′
1	Insertion of StrepII tag	CCA AAA ACA GGT ACG ACA TAC *ATG GCG TGG AGC CAC CCG CAG TTC GAA AAA* ATG AAT CAG AAT CTG CTG GTG
2	Insertion of 2 AA linker	GC CAC CCG CAG TTC GAA AAA *GGC GCG* ATG AAT CAG AAT CTG CTG GTG
3	Insertion of 5 AA linker	GC CAC CCG CAG TTC GAA AAA *TCT CTG GGC GGC CAT* ATG AAT CAG AATCTG CTG GTG
4	Insertion of 6 AA linker	GC CAC CCG CAG TTC GAA AAA *GGC TCT GGC GGC TCT GGC* ATG AAT CAG AAT CTG CTG GTG
5	TAG_{730}→TAT_{730}	TTC GGG GTC AAA ACA CTG *TAT* TAT CAG AAC ACC CGT GAC GGC GCT
6	Insertion of residues 1-5 of 10 AA linker	GC CAC CCG CAG TTC GAA AAA *AGC AGC GGC CTG GTG* ATG AAT CAG AAT CTG CTG GTG
7	Insertion of residues 6-10 of 10 AA linker	C GAA AAA *AGC AGC GGC CTG GTG CCG CGC GGC AGC CAT* ATG AAT CAG AAT CTG CTG GTG
8	Removal of *nrdA* internal *NdeI*	GGC AAC CGC GTG CGT CAC ATG GAC TAC GGG GTA C
9	Insertion of 5′ *NdeI* site	GGC TAA CAG GAG GAA TTA CAT ATG AAT CAG AAT CTG CTG GTG
10	TAT_{730}→TAG_{730}	TTC GGG GTC AAA ACA CTG *TAG* TAT CAG AAC ACC CGT GAC GGC GCT
11	TAT_{731}→TAG_{731}	TTC GGG GTC AAA ACA CTG TAT *TAG* CAG AAC ACC CGT GAC GGC GCT

2.2.9 Generation of pTrc-N-Strep-X-nrdA and pTrc-N-Strep-X-nrdA-TAG$_{730}$ from pTrc-nrdA (where X = 0, 2, 5, 6, or 10). The Quikchange Kit (Stratagene) was used according to the manufacturer's protocol to insert nucleotides encoding for a StrepII tag (WSHPQFEK) immediately upstream of the *nrdA* gene in the parent construct, pTrc-*nrdA*. To generate pTrc-N-Strep-*nrdA*, the template was amplified in the presence of the forward primer 1 (Table 2.1, StrepII tag in italics, *nrdA* start underlined) and its reverse complement using *Pfu* Ultra II polymerase. To prevent secondary structure formation in the primers, 2% DMSO was added to the reaction mixture. pTrc-N-Strep-*nrdA*-TAG$_{730}$ was generated from pTrc-N-Strep-*nrdA,* primer 10, and its reverse complement via standard site-directed mutagenesis with *Pfu* Ultra II polymerase.

The resulting plasmid, pTrc-N-Strep-*nrdA*-TAG$_{730,}$ was then used as a template for the insertion of 2, 5, 6, or 10 amino acid linkers between the StrepII tag and the start of the *nrdA* gene. Primer 2 (Table 2.1) and its reverse complement were used to insert the 2 amino acid linker, primer 3 and its reverse complement to insert the 5 amino acid linker, and primer 4 and its reverse complement to insert the 6 amino acid linker. All reactions were conducted with *Pfu* Ultra II polymerase following the "touchdown" annealing strategy. Denaturation was conducted at 95 °C for 30 s, followed by annealing at (65 – 2*n*, *n* = 0-5) °C for 30 s and extension at 68 °C for 3 min. Two rounds of extension were performed for each annealing temperature between 65 and 57 °C, and eight rounds were performed for annealing at 55 °C, for a total of 18 extension rounds. To insert a 10 amino acid linker, pTrc-N-Strep-*nrdA*-TAT$_{730}$, was reacted with primer 6 and its reverse complement following the touchdown annealing protocol to insert the first five amino acids of the linker. The resulting product was then used as the template for a mutagenesis reaction to insert the second five amino acids using primer 7 and its reverse complement. The

plasmids pTrc-N-Strep-X-*nrdA*-TAG_{730} (X = 0, 2, 5, 6, 10) were then used as templates for the generation of the corresponding TAT_{730} constructs (amber stop codon → Y mutation) using primer 5.

2.2.10 Expression and purification of N-Strep-X-α2(wt) with 0, 2, 5 or 6 AA linkers. Into *E. coli* DH10B cells (50 μL, Invitrogen) was transformed pTrc-N-Strep-X-*nrdA*-TAG_{730} (X = 0, 2, 5, 6, or 10). The cells were plated on LB/agar with Amp (100 μg/mL) and grown overnight at 37 °C. A single colony from each plate was inoculated into 6 mL LB with Amp and grown at 37 °C and 225 rpm until reaching saturation (~12 hours). Saturated starter cultures were used to inoculate 500 mL LB with Amp (in 2.8 L baffled flask) at a 100-fold dilution. Cells were grown until reaching OD_{600} ~0.7, at which point *nrdA* expression was induced with 1 mM IPTG. Cells were grown an additional 4 hours after induction, then harvested by centrifugation (10,000 × g, 12 min, 4 °C) to give 4-5 g cell paste per L of culture. Induction was assessed by SDS-PAGE (8%).

Cells were resuspended in buffer S with DTT (5 mM) and PMSF (1 mM) at 4 mL/g of cell paste. Cells were lysed via two passes through the French Press at 14,000 psi, and centrifuged (40,000 × *g*, 30 min, 4 °C) to clear cell debris. The soluble fraction was treated with DNase (5 U/mL) and loaded directly onto 1.5 mL of Streptactin Sepharose (1 mL resin/g cells) resin using a pump at a rate of <0.25 mL/min. The column was then washed with 15 CVs of buffer S, and eluted with 2.5 mM desthiobiotin in buffer S.

2.2.11 Expression, purification, and activity assays of N-Strep-$Y_{730}NH_2Y$-α2. N-Strep-$Y_{730}NH_2Y$-α2 was expressed from plasmids pTrc-N-Strep-*nrdA*-TAG_{730} and pAC-NH_2Y as described for $Y_{356}NH_2Y$-β2 in section 2.2.3 with yields of ~2 g cell paste / L culture.

The cell pellet (~5 g) was resuspended in buffer S with 1.0 mM PMSF and 5 mM DTT at 4 mL buffer/g of cell paste. Purification steps were identical to those described for $Y_{356}NH_2Y$-β2 through desalting on G25. Protein-containing fractions were pooled and loaded directly onto a Streptactin Sepharose column (3 mL) equilibrated in buffer S with PMSF and DTT. The column was washed with 20 volumes of buffer S, then eluted with 2.5 mM desthiobiotin in buffer S with 5 mM DTT. The entire elution was concentrated to a minimal volume on an Amicon YM-30 membrane and analyzed by 8% SDS-PAGE.

Activity of the isolated protein was determined by the radioactive assay with β2 (1.0 μM) in 5-fold excess over N-Strep-$Y_{730}NH_2Y$-α2 (0.2 μM). Due to DNA contamination of the protein sample (as judged by the A_{280}/A_{260} ratio), the concentration of the mutant protein was determined by Bradford assay using wt-α2 in the same buffer to generate a standard curve.

2.2.12 Generation of pEVOL-NH_2Y. The parent plasmid pEVOL was obtained as a gift from the Schultz lab (Scripps, La Jolla, CA).[32] pEVOL-NH_2Y contains one copy of the mutant $tRNA_{CUA}$ and two copies of the NH_2Y-RS, one under the control of an *glnS′* promoter and a second under the control of an inducible *ara* promoter. It also contains a gene conferring Cm resistance. It was constructed as described previously for pEVOL-NO_2Y by Dr. Kenichi Yokoyama.[11]

2.2.13 Generation of pET-nrdA(wt) and pET-nrdA(TAG_{730}). The construct pBAD-*nrdA*(wt), which contains *nrdA*(wt) cloned into pBAD-Myc/HisA (Invitrogen) at *NcoI* and *XhoI* restriction sites, was used to isolate the *nrdA* gene. An internal *NdeI* site in the *nrdA* gene was removed by introduction of a silent CAT→CAC mutation by site-directed mutagenesis using *Pfu* Ultra II polymerase and primer 8 (Table 2.1) and its reverse complement. The 5′ restriction site

of the resulting plasmid, pBAD-*nrdA(ΔndeI),* was then converted from *NcoI* (CCATGG) to *NdeI* (CATATG) via mutagenesis using primer 9 and its reverse complement.

The desired *nrdA* insert was obtained by stepwise digestion due to the presence of two *NdeI* sites in the backbone of the parent vector, pBAD-Myc/HisA. Thus, the plasmid (5 μg) was digested with the unique cutters *NsiI* (80 U) and *XhoI* (80 U) at 37 °C for 12 h. The resulting 3.6 kb fragment, containing *nrdA*, was isolated using the Qiagen Gel Extraction kit, and digested with *NdeI* (40 U) at 37 °C for 12 h. The desired *nrdA* fragment (2.3 kb) was isolated by gel extraction and ligated into pET-28a (Novagen) at *NdeI* and *XhoI* sites in a 2:5 vector-to-insert ratio with T4 Ligase at 25 °C for 2 h to yield the final plasmid, pET-*nrdA*(wt). Mutagenesis of this plasmid with the forward primer 10 and its reverse complement yielded the Tyr → TAG mutant, pET-*nrdA*(TAG_{730}). An parallel reaction with primer 11 and its reverse complement gave the plasmid pET-*nrdA*(TAG_{731}).

2.2.14 Expression, purification, and activity assays of (His)$_6$-Y$_{730}$NH$_2$Y-α2. *E. coli* BL21(Star)-DE3 cells (Invitrogen) were co-transformed with pET-*nrdA*(TAG_{730}) and pEVOL-NH_2Y and plated on LB-agar plates with 50 μg/mL Km and 35 μg/mL Cm at 37 °C. Starter (5 mL) and intermediate (100 mL) cultures were grown in 2xYT at 37 °C with Km and Cm. Enriched GMML (500 mL)[17] with the appropriate antibiotics was inoculated with the saturated intermediate culture (1:50 dilution) and grown at 37 °C, 225 rpm until reaching an OD_{600} ~0.6, at which point NH_2Y and DTT were added to the culture to concentrations of 1 mM and 0.1 mM, respectively. After 15 min, the NH_2Y-RS was induced with L-ara to a final concentration of 3.3 mM. After an additional 20 min, *nrdA* expression was induced with 1 mM IPTG. Cells were harvested by centrifugation 3.5 h after induction to give 2 g cell paste/L culture.

The cell pellet was resuspended in buffer B with PMSF (0.5 mM) and β-mercaptoethanol (β-ME, 10 mM) in 5 mL buffer/g cell paste, homogenized, and lysed via two passes though a French pressure cell at 14,000 psi. Cell debris was cleared by centrifugation (40,000 × *g*, 25 min, 4 °C), and DNase (NEB) was added to the supernatant to 10 U/mL. The resulting solution was incubated with rocking for 30 min at 4 °C. The supernatant was added to Ni-NTA agarose (Qiagen, 1 mL/g) and buffer B was adjusted to contain 300 mM NaCl. The resulting slurry was incubated with rocking for 1 h at 4 °C, then loaded into a column, which was washed with 20 CVs of wash buffer (buffer B with 300 mM NaCl and 10 mM imidazole, pH 7.6) with PMSF and β-ME. The protein was eluted with a linear gradient of 10 to 250 mM imidazole in wash buffer. Fractions were pooled, diluted with buffer B with DTT (10 mM), and concentrated using an Amicon YM 30 membrane to give ≥5 mg per g cell paste.

If necessary, the protein was subjected to anion-exchange FPLC to remove any small amount of co-purifying 729-truncated α. A Poros HQ/20 column was equilibrated in assay buffer and was loaded with 10-20 mg of protein. The column was washed with one CV of assay buffer at a flow rate of 4 mL/min, then eluted with a linear gradient of 50 to 450 mM NaCl (60 mL × 60 mL) in the same buffer at the same flow rate. Fractions containing the desired protein, determined by SDS-PAGE, were pooled and concentrated with an Amicon YM-30 membrane. The activity of $(His)_6$-$Y_{730}NH_2Y$-α2 was determined using the spectrophotometric and radioactive assays, as described in section 2.2.7. For the spectrophotometric assay, mutant α2 was 1.0 μM; for the radioactive assay, 0.1 μM. In both cases, wt-β2 was held in a 5-fold excess over α2.

2.2.15 Expression, purification, and activity assays of $(His)_6$-α2(wt). E. coli BL21(Star)-DE3 cells (Invitrogen) were transformed with pET-28a-*nrdA* and plated on LB-agar plates

supplemented with 50 μg/mL Km at 37 °C. After 16 h, single colonies were harvested and inoculated into LB (100 mL) with 50 μg/mL Km and set to grow at 37 °C, 225 rpm. This culture was grown to saturation at 37 °C, 225 rpm and used to inoculate fresh LB (2 × 0.5 L, in baffled flasks) with the appropriate antibiotics at a 1:100 dilution. The culture was grown at 37 °C, 225 rpm until reaching an OD_{600} ~0.6, at which point the culture was induced with 1 mM IPTG. The cells were allowed to grow for an additional 3.5 h (OD_{600}, final >2), then harvested by centrifugation (5,000 × *g*, 10 min, 4 °C). Growth yielded 2.5 g cell paste / L culture. Expression was analyzed by 8% SDS-PAGE.

$(His)_6$-α2(wt) was purified in a single step by Ni-NTA chromatography and assayed as described for $(His)_6$-$Y_{730}NH_2Y$-α2 in the previous section. Yields of 40 mg protein / g of cells were typical. The specific activity of $(His)_6$-α2(wt) was measured between 2200-2500 nmol/min/mg.

2.2.16 Crystal structure determination of $Y_{730}NH_2Y$-α2 and $Y_{731}NH_2Y$-α2. Proteins were crystallized at 4 °C using the hanging drop vapor diffusion method in EasyXtal Tool plates (Qiagen) in the presence of a 20-amino acid peptide corresponding to the C-terminus of the *E. coli* β.[5] Hanging drops consisted of 2 μL of a 1:1 mixture of protein (8-9 mg/mL, final concentration) and peptide (30 mg/mL) solutions in assay buffer and 2 μL of a solution of 25 mM sodium citrate, 1.5 M $LiSO_4$, 2 mM DTT, pH 6 to a final mixture pH of 6.0-6.5. Crystals were grown for one week in a cold room, washed with 1.5 M $LiSO_4$ in 20% ethylene glycol, mounted in fiber loops, and flash-frozen in liquid N_2.

Data sets were collected at 100 K at the European Synchrotron Radiation Facility. A 2.3 Å structure of the *E. coli* wt α2 (PDB-ID 2x0x)[11] was used as the initial model for the refinement of data for the mutant proteins. Processing and scaling were done with the program

MOSFLM/SCALA,[33] refinement with the program Refmac,[34] and model building with the program O.[35] Additional details on data collection and refinement are given in Table 2.5. Structures have been deposited to the PDB with ID codes 2xo4 ($Y_{730}NH_2Y$-α2) and 2xo5 ($Y_{731}NH_2Y$-α2). Crystallization, data collection, and refinement were conducted by Professor Ulla Uhlin (Swedish University of Agricultural Science, Uppsala, Sweden).

2.2.17 Reaction of $Y_{730}NH_2Y$–α2 (or $Y_{731}NH_2Y$–α2 or $(His)_6$-$Y_{730}NH_2Y$-α2) and wt–β2 with various S/E pairs monitored by EPR spectroscopy. Pre-reduced $Y_{730}NH_2Y$-α2 (or $Y_{731}NH_2Y$-α2) and E were mixed rapidly with β2 and S in assay buffer at 25 °C. The reaction was hand-quenched at 20 s in liquid N_2 and its EPR spectrum recorded (see below). Reactions were carried out with 15 μM of each protein subunit and the following S/E pairs: CDP/ATP (1 mM, 3 mM), GDP/TTP (1 mM, 0.2 mM), UDP/ATP (1 mM, 3 mM), and ADP/dGTP/ATP (1 mM, 0.2 mM, 3 mM). The reaction between $(His)_6$-$Y_{730}NH_2Y$-α2 and wt-β2 with CDP/ATP was studied in an identical fashion.

EPR spectra were collected and spin quantitation conducted as described in section 2.2.6. Analysis of the reaction spectra was carried out using an in-house Excel program, as previously described in detail.[17] Briefly, subtraction of the contribution of unreacted Y_{122}• from the composite spectrum yielded a spectrum of NH_2Y•, and relative quantitation of the two spectra was determined by comparison of their double integral peak intensities. Portions of the $Y_{730}NH_2Y$-α2 and $Y_{731}NH_2Y$-α2 data were collected by Dr. Mohammad Seyedsayamdost and reported previously.[36]

2.2.18 Reaction of $Y_{730}NH_2Y$–α2 (or $Y_{731}NH_2Y$–α2 or $(His)_6$-$Y_{730}NH_2Y$-α2) and wt–β2 with S, E, or S/E pairs monitored by stopped-flow (SF) UV-vis spectroscopy. SF kinetics were performed on an Applied Photophysics DX 17MV instrument equipped with the Pro-Data

upgrade. All reactions were carried out in assay buffer at 25 °C. In all cases, pre-reduced $Y_{730}NH_2Y$–α2 (or $Y_{731}NH_2Y$–α2) and E (if present) in one syringe were mixed rapidly with wt-β2 and S (if present) in a second syringe to yield a final concentration of 5 μM NH_2Y-α2/β2. The following S and/or E combinations (final concentrations) were studied: CDP/ATP (1 mM, 3 mM), GDP/TTP (1 mM, 0.2 mM), UDP/ATP (1 or 2 mM, 3 mM), ADP/dGTP (1 mM, 0.2 mM), ADP/dGTP/ATP (1 mM, 0.2 mM, 3 mM), CDP (1 mM), GDP (1 mM), UDP (1 mM), ADP (1 mM), ATP (3 mM), TTP (0.2 mM), and dGTP (0.2 mM). The reactions were monitored at 325 nm for NH_2Y_{730}•, (ε ~10,500 $M^{-1}cm^{-1}$) or 320 nm for NH_2Y_{731}• (ε ~11,000 $M^{-1}cm^{-1}$) using PMT detection. Averaged kinetic traces generated from >5 individual traces were fit iteratively using OriginPro or KaleidaGraph software until residuals were minimized. The reactions between $(His)_6$-$Y_{730}NH_2Y$-α2 and wt-β2 with CDP/ATP or GDP/TTP were examined in an analogous fashion. Portions of the $Y_{730}NH_2Y$-α2 and $Y_{731}NH_2Y$-α2 data were collected by Dr. Mohammad Seyedsayamdost and reported previously.[36]

2.2.19 Reaction of $Y_{356}NH_2Y$-β2 and wt-α2 with various S/E pairs monitored by SF UV-vis and EPR spectroscopy. SF UV-vis experiments were conducted by mixing $Y_{356}NH_2Y$-β2 and pre-reduced wt-α2 in a 1:1 ratio (final concentration of 7.5–10 μM per protein subunit, 3.75–5 μM total Y_{122}•) in the presence of one of the four S/E pairs or CDP alone, as described in section 2.2.18. Reactions were monitored at 324 nm for NH_2Y_{356}• and 410 nm for Y_{122}•. Data analysis was conducted as described above. The reaction of $Y_{356}NH_2Y$-β2 (25 μM) with wt-α2 (25 μM), CDP (1 mM) and ATP (3 mM) at 25 °C was hand-quenched in liquid N_2 at 20 s and analyzed by EPR spectroscopy as described above.

2.2.20 Reaction of $Y_{356}NH_2Y$-β2, wt-α2, N_3CDP, and ATP monitored by EPR spectroscopy. Pre-reduced wt-α2 and ATP were mixed with $Y_{356}NH_2Y$-β2 and N_3CDP in assay

buffer to give final concentrations of 30 μM, 3 mM, 30 μM (15 μM Y•), and 250 μM, respectively, in a reaction volume of 240 μL. The reaction mixture was incubated at 25 °C for 1 min to maximize N• formation, then hand-quenched in liquid N_2. Acquisition of EPR spectra and spin quantitation were conducted as described above. Deconvolution of the three radical species was performed as described previously.[17] The spectral contribution of N• was subtracted first, facilitated by its distinct low-field features. Residual Y_{122}• was subtracted next, yielding the spectrum of the putative NH_2Y_{356}•.

2.2.21 Single-turnover reactions of NH_2Y-α2s with wt-β2, CDP, and ATP. In a total volume of 500 μL was combined wt-β2 (10 μM), [^{3}H]-CDP (0.3-0.5 mM, specific activity of 6,700 or 21,300 cpm/nmol), and ATP (3 mM) in assay buffer at 25 °C. The assay was initiated by addition of pre-reduced α2 (wt, $Y_{730}NH_2Y$-α2, $(His)_6$-$Y_{730}NH_2Y$-α2, or $Y_{731}NH_2Y$-α2, 2.0 μM). The reaction was quenched in a boiling water bath after the time required to consume all the substrate under steady-state conditions. Sample workup and scintillation counting was conducted as described for the standard radioactive assay in section 2.2.7.[13]

2.3 RESULTS

2.3.1 Optimizing the expression and purification of $Y_{356}NH_2Y$-β2. A number of expression systems, growth conditions, and purification techniques were investigated to maximize the production and isolation of full-length $Y_{356}NH_2Y$-β2, generated by the *in vivo* nonsense codon suppression method (Table 2.2). This method results in the expression of a mixture of full-length β (residues 1-375) and truncated β (1-355, designated β′) and, since β is an obligate dimer, a statistical distribution of β2, ββ′, and β′2 is generated. Thus, the relative ratio of full-length to truncated proteins played a large role in selecting an expression system, as did the overall expression of the *nrdB* gene from a given promoter and the compatibility of the *nrdB* promoter with the NH_2Y-RS promoter. Other factors that were considered included ease of protein purification, final purified protein yield, and the possible presence of contaminating endogenous β2 (Table 2.2). $Y_{356}NH_2Y$-β2 was expressed from each of the conditions in Table 2.2, and purified from expresion combinations 1, 2, 3, and 6.

2.3.2 Characterization of $Y_{356}NH_2Y$-β2. Ultimately, $Y_{356}NH_2Y$-β2 isolated from the pTrc-*nrdB*(TAG_{356}) and pAC-NH_2Y[17] expression system was chosen for further study, as it allowed for isolation of $Y_{356}NH_2Y$-β2 on a scale necessary for our biophysical experiments. A purification protocol employing three anion-exchange chromatography steps was required to separate $Y_{356}NH_2Y$-β2 from ββ′ and β′2 and to isolate the desired species in >95% purity (Figure 2.2). ESI-MS analysis of the protein indicated a single major species of 43,402 Da (predicted 43,401 Da, Figure 2.3). Addition of variable amounts of wt-β2 (predicted 43,386 Da) to $Y_{356}NH_2Y$-β2 and analysis by ESI-MS allowed the lower limit of detection of contamination by wt-β2 to be set to <5% the total $Y_{356}NH_2Y$-β2.

The radical content of $Y_{356}NH_2Y$-β2 as isolated was 0.3 Y•/β2. Efforts to increase the amount to levels observed in the wt enzyme (1.2 Y•/β2) via standard reconstitution methods resulted in a maximum of 0.5 Y•/β2. The reduced level of radical is likely associated with perturbation of the cofactor assembly pathway by the introduction of an easily-oxidized Y analogue at position 356. Similar results were observed in previous attempts to increase radical content in Y_{356}DOPA-β2.[8,36]

Table 2.2 Plasmid combinations explored in optimization of $Y_{356}NH_2Y$-β2 expression and purification.

#	*nrdB*(TAG_{356}) plasmid	NH_2Y-RS plasmid	Pro	Con
1	pTrc-*nrdB*	pAC	Decent expression level; full-length:truncated ratio of ~1	Lengthy purification protocol; low isolated protein yield; possible contamination by endogenous β2
2	pBAD-N-Strep-5-*nrdB*	pAC	Ease of isolation; high protein purity; removal of endogenous β2	Poor full-length:truncated ratio; poor binding to Strep resin
3	pTrc-N-Strep-5-*nrdB*	pAC	Ease of isolation; high protein purity; removal of endogenous β2	Poor binding to Strep resin; low isolated protein yield
4	pBAD-N-Strep-5-*nrdB*	pEVOL	Ease of isolation; high protein purity; removal of endogenous β2	Poor full-length:truncated ratio
5	pTrc-N-Strep-5-*nrdB*	pEVOL	Ease of isolation; high protein purity; removal of endogenous β2	Poor overall induction of *nrdB* gene
6	pET-His_6-*nrdB*	pEVOL	Ease of isolation; high protein purity; removal of endogenous β2	Very poor full-length:truncated ratio
7	pBAD-*nrdB*	pEVOL	Potential for higher isolated protein yield	Poor overall induction of *nrdB* gene

Figure 2.2 SDS-PAGE (10%) of the expression and purification of $Y_{356}NH_2Y$-β2. (A) Lane 1, MW marker; lane 2, $Y_{356}NH_2Y$-β2 culture, before *nrdB* induction; lane 3, $Y_{356}NH_2Y$-β2 culture grown with NH_2Y 3.5 h after *nrdB* induction. Top and bottom arrows indicate full-length and truncated proteins, respectively. (B) Lane 1, MW marker; lane 2, purified $Y_{356}NH_2Y$-β2, ~2 μg; lane 3, purified $Y_{356}NH_2Y$-β2, ~1 μg.

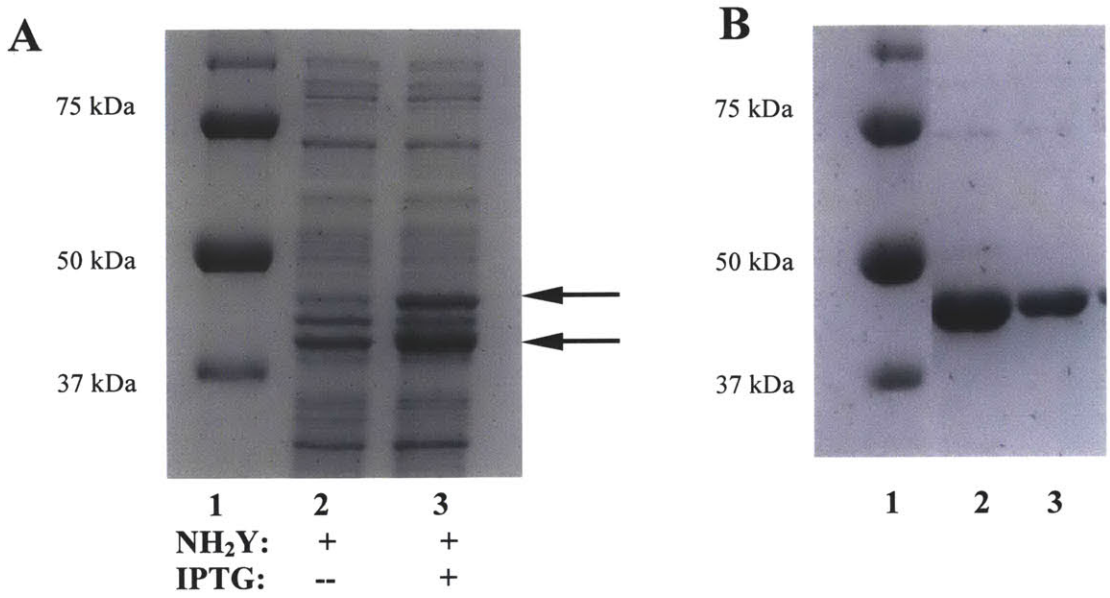

Figure 2.3 ESI-MS analysis of purified $Y_{356}NH_2Y$-β2 indicates the isolation of the desired species (predicted 43,401 Da) and no contamination of wt-β2 (predicted 43,386 Da) within the estimated limit of detection (<5% of $Y_{356}NH_2Y$-β2). An expanded view of the peak of interest is given in the inset.

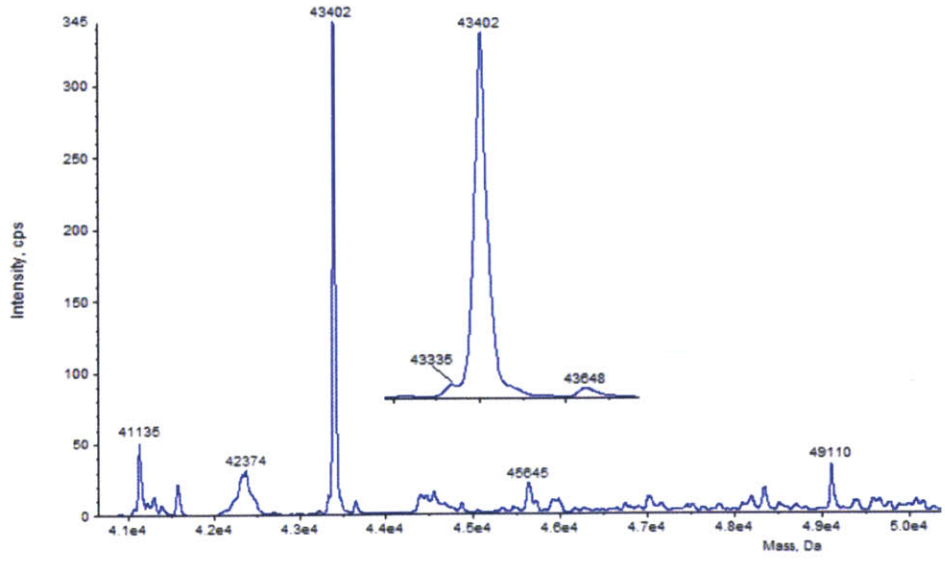

Figure 2.4 Reaction of $Y_{356}NH_2Y$-β2 with wt-α2, CDP, and ATP. (A) EPR spectrum of the reaction mixture hand-quenched after incubation for 20 s at 25 °C. The reaction spectrum (black) is a composite of two species. Subtraction of a spectrum of the Y_{122}• (blue) gives the spectrum of the NH_2Y_{356}• (red). (B) SF UV-vis spectroscopy was used to determine the kinetics of NH_2Y_{356}• formation (324 nm, red) and Y_{122}• loss (410 nm, blue) under single-turnover conditions at 25 °C. Biexponential fits to the data are indicated by black lines.

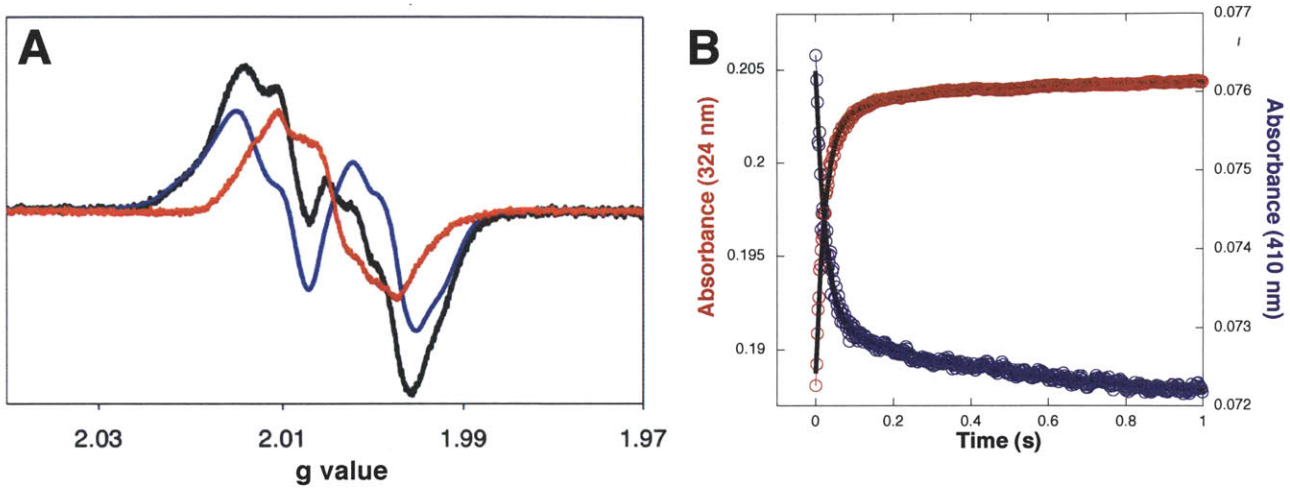

Figure 2.5 Reaction of $Y_{356}NH_2Y$-β2 with wt-α2, N_3CDP, and ATP monitored by EPR spectroscopy. (A) The reaction spectrum (pink) is a composite of three species. Subtraction of the N• component (green) is facilitated by its distinct low-field features. A two-radical composite spectrum (black) remains. (B) Subtraction of a spectrum of Y_{122}• (blue) from the difference spectrum generated in (A) gives the spectrum of the putative NH_2Y_{356}• (red).

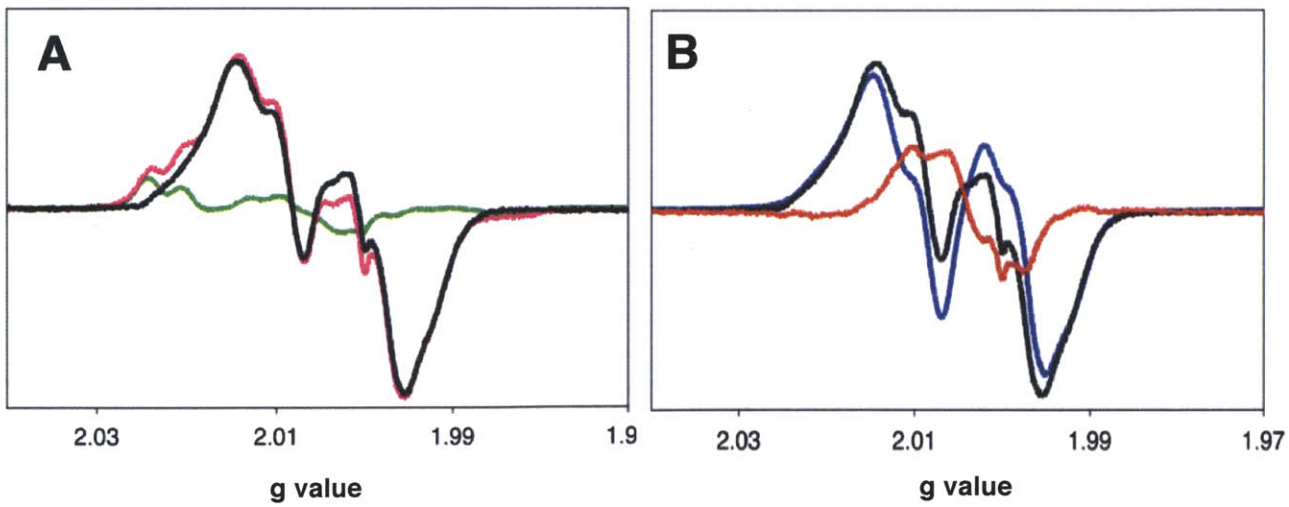

2.3.3 Characterization of NH_2Y• at position 356. $Y_{356}NH_2Y$-β2 was reacted with wt-α2, CDP, and ATP and the reaction quenched at 20 s and examined by EPR spectroscopy (Figure 2.4 A). The reaction spectrum (black) is a composite of two radical species. Subtraction the Y_{122}• spectrum (blue) yields a spectrum suggestive of an NH_2Y• (red),[37] with slight differences in hyperfine features compared to the NH_2Y•s at positions 730 and 731. These differences were examined in greater detailed by high-field EPR characterization, as discussed in Chapter 4 (Argirevic and Bennati, personal communication). Spin quantitation indicates 20% of the total spin is lost during the reaction time with the remaining spin distributed between NH_2Y• (41%) and Y• (59%). Thus, 33% of the total spin at t=0 was trapped as NH_2Y• at t=20 s. For comparison, the reaction with $Y_{731}NH_2Y$-α2 gave 30% spin loss over 20 s, with the remaining radical distributed between NH_2Y• (45%) and Y• (55%).

The kinetics of NH_2Y_{356}• formation and Y_{122}• loss were examined under similar conditions by SF UV-vis spectroscopy (Figure 2.4 B). The data were best fit to two exponentials, giving k_{fast} of 36 s^{-1} and k_{slow} of 2.1 s^{-1}. Twenty-five percent of the starting Y• was converted to NH_2Y• in the fast phase, and an additional 5% in the slow phase. A complete kinetic comparison of NH_2Y• formation in the three NH_2Y-RNRs with all S/E pairs is described in section 2.3.10.

2.3.4 Catalytic activity of $Y_{356}NH_2Y$-β2. Initial experiments indicated that $Y_{730}NH_2Y$-α2 and $Y_{731}NH_2Y$-α2 catalyze dNDP production, despite the introduction of a ~190 mV thermodynamic hole in the PCET pathway.[17] Activity assays revealed that $Y_{356}NH_2Y$-β2 also catalyzes dCDP formation with 4-5% the activity of wt-β2 (Table 2.3). When scaled for radical content ($Y_{356}NH_2Y$-β2 contains 0.5 Y•/β2 versus 1.2 Y•/β2 in wt), the activity is 10-12% that of wt.

The activity of $Y_{356}NH_2Y$-β2 was substantiated by reaction with the mechanism-based inhibitor 2′-azido-CDP (N_3CDP). Studies with wt RNRs have shown that N_3CDP is a stoichiometric inhibitor which requires C_{439}•-mediated 3′-hydrogen atom abstraction from the nucleotide prior to RNR inactivation. A nitrogen-centered nucleotide radical (N•) is formed and covalently bound to the active site.[23,26] Complete enzyme inactivation results after a 50% conversion of Y_{122}• to N•, in agreement with the proposed half-site reactivity of RNR.[7,8] Thus, if the 4-5% activity measured with $Y_{356}NH_2Y$-β2 is associated with contaminating wt-β2, 2-2.5% of the Y• would be converted to N•. Observation of a larger percentage of N• would be indicative of activity inherent to $Y_{356}NH_2Y$-β2. Thus, $Y_{356}NH_2Y$-β2 was reacted with wt-α2, N_3CDP, and ATP, quenched at 1 min, and analyzed by EPR spectroscopy (Figure 2.5). No spin was lost during the reaction, with 56% of the spin associated with Y•, 28% with NH_2Y•, and 16% with N• (Table 2.3). The amount of N• generated is six times higher than predicted on the basis of wt contamination, providing support for $Y_{356}NH_2Y$-β2's inherent activity. This result is consistent with previous inactivation assays of $Y_{730}NH_2Y$-α2 and $Y_{731}NH_2Y$-α2 (Table 2.3).[17]

Table 2.3 Nucleotide reductase activities of NH_2Y-RNRs.

mutant	Y• /β2	Spec Act nmol/min/mg[a]	turnover (s^{-1})	activity (% wt)[b]	% wt (scaled)[c]	N• formed % initial Y•[d]	dCDP /α2[e]
$Y_{730}NH_2Y$- α2[f]	-	156 ± 36	0.3 - 0.6	4 – 8	-	16	0.70
$(His)_6$-$Y_{730}NH_2Y$-α2	-	78 ± 12	0.2 - 0.3	3 – 4	-	14	0.70
$Y_{731}NH_2Y$-α2[f]	-	175 ± 50	0.4 - 0.7	5 – 9	-	15	0.65
$Y_{356}NH_2Y$- β2	0.5	305 ± 38	0.4 - 0.5	4 – 5	10 – 12	16	ND[g]

[a]The average and standard deviation of 3 - 5 assays conducted on 2 or more independent enzyme isolations; [b]2500 nmol/min/mg for wt-α2, 2200 nmol/min/mg for $(His)_6$-α2, 7000 nmol/min/mg for wt-β2; [c]Scaled for radical content (0.5 Y•/ β2 in mutant vs 1.2 Y•/ β2 in wt); [d]N_3ADP was the substrate for $Y_{730}NH_2Y$-α2 and $Y_{731}NH_2Y$-α2, while N_3CDP was the substrate for $(His)_6$-$Y_{730}NH_2Y$-α2 and $Y_{356}NH_2Y$-β2. Error in EPR spin quantitation is ~3% of the initial Y_{122}•; [e] Determined by a hand-quench single turnover assay, as described in the text; [f]Reported previously[17]; [g]Not determined.

2.3.5 Confirming catalysis by NH_2Y-RNRs. Steady-state activity assays revealed that NH_2Y-RNRs possessed between 4-12% the activity of their respective wt subunit, giving turnover numbers of 0.3-0.7 s^{-1}. However, since RNR is essential for *E. coli* viability, expression of NH_2Y-RNRs is always accompanied by endogenous levels of wt-α2 or β2.[38] Additional contamination by wt RNR can arise from the misincorporation of Y in response to the nonsense codon due to the imperfect substrate specificity of the NH_2Y-RS. The results of the reactions of with N_3CDP serve as a first independent test of radical propagation to the enzyme active site in NH_2Y-RNRs. Two additional types of experiments were carried out to further ensure that the reductase activity measured is associated with NH_2Y-RNRs, as described below.

2.3.6 Affinity purification and catalytic activity of N-terminally tagged NH_2Y-RNRs. In an attempt to remove endogenous levels of wt subunit contamination, N-terminally affinity-tagged NH_2Y-RNRs were constructed. Since α is an equilibrium mixture of monomer and dimer in the absence of nucleotides, recombinant, tagged NH_2Y-α2 should be separable from wt-α2 via affinity chromatography (Figure 2.6). A number of StrepII- or $(His)_6$-tagged *nrdA* expression constructs with variable linker regions (0-10 amino acids) were constructed and the encoded proteins expressed and purified (Table 2.4). An N-terminal $(His)_6$ tag and 10 amino acid linker gave the maximum yield, purity, and activity of all the tagged wt-α2s investigated. This construct and the improved pEVOL[32] vector encoding the tRNA/NH_2Y-RS were used to express $(His)_6$-$Y_{730}NH_2Y$-α2, and the resulting protein was purified to homogeneity (Figure 2.7). MALDI-TOF MS of the purified protein gave a major peak corresponding to the full-length protein with a single NH_2Y incorporated (observed, 87,975 Da, predicted + Na^+, 87,976 Da). The only other observable peak corresponded to 729-truncated protein. Further characterization of $(His)_6$-$Y_{730}NH_2Y$-α2 by EPR and SF UV-vis experiments (Figure 2.8 A and B, respectively)

monitoring NH_2Y• formation gave results almost identical to those with the untagged mutant.[17] Thus, this construct was adopted for all future experiments. The affinity tagging strategy was extended to the β2 subunit (Table 2.2), but the yield and/or radical content of the N-terminally StrepII- and $(His)_6$-tagged $Y_{356}NH_2Y$-β2 mutants was low relative to that of untagged $Y_{356}NH_2Y$-β2 and thus study of tagged NH_2Y-β2s was not pursued further.

Tagged NH_2Y-RNRs were assayed for nucleotide reductase activity and were found to be catalytically active, with the results summarized in Table 2.3 and 2.4. $(His)_6$-$Y_{730}NH_2Y$-α2 has ~50% the activity of the untagged mutant and demonstrates a narrower range of activities. Thus, the tagging procedure appears to have been successful in removing varying levels of contaminating wt. Additionally, $(His)_6$-$Y_{730}NH_2Y$-α2 generates seven times more N• in the N_3CDP assay than can be rationalized on the basis of wt contamination (Table 2.3 and Figure 2.9).

Table 2.4 Specific activities of affinity-tagged α2s and $Y_{730}NH_2Y$-α2s.

Construct	Affinity Tag	Linker	Specific Activity (% wt)[a] w/ Y at 730	Specific Activity (% wt)[c] w/ NH_2Y at 730
wt	None	None	100	4-8
1	StrepII	None	86	7
2	StrepII	GA	72	ND[b]
3	StrepII	SLGGH	ND[b]	ND[d]
4	StrepII	GSGGSG	ND[b]	ND[d]
5	StrepII	SSGLVPRGSH	ND[b]	ND[d]
6	$(His)_6$	SSGLVPRGSH	88	3.5

a. Activities reported at a percentage of wild-type (wt) activity (2500 nmol/min/mg) as determined by a radioactive assay for CDP reduction; *b.* Not determined due to either poor protein yield or low protein purity (<50%) after Streptactin purification; *c.* Activities for NH_2Y mutants reported as a percentage of the analogous tagged "wt" protein; *d.* Not determined due to the poor yield or purity of the corresponding protein with Y at position 730.

Figure 2.6 Strategy employed for removal of endogenous levels of wt-α2 and heterodimers of wt α and mutant α from NH_2Y-α2 samples. An N-terminal affinity tag on the mutant protein allows separation of the recombinant α from endogenous α via affinity chromatography under conditions in which the protein exists in an equilibrium between monomer (α) and dimer (α2).

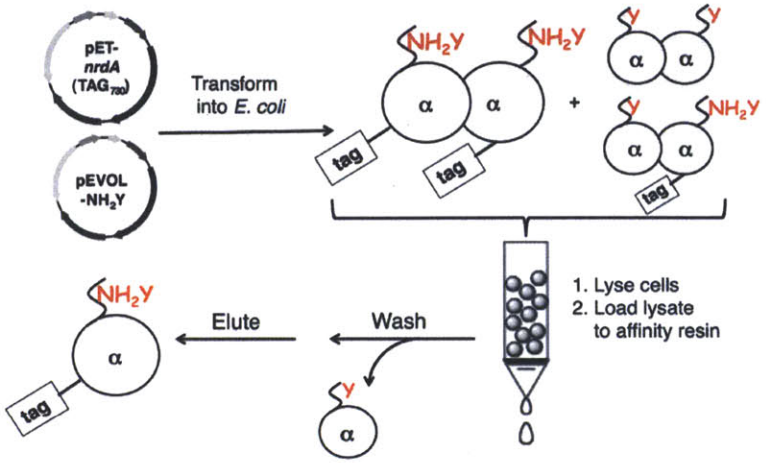

Figure 2.7 SDS-PAGE (8%) of the expression and purification of $(His)_6$-$Y_{730}NH_2Y$-α2. (A) Lane 1, His_6-$Y_{730}NH_2Y$-α2 culture, before *nrdA* induction; lane 2, $(His)_6$-$Y_{730}NH_2Y$-α2 culture grown without NH_2Y, 3 h after induction; lane 3, $(His)_6$-$Y_{730}NH_2Y$-α2 culture grown with NH_2Y (1 mM), 3 h after induction. Top and bottom arrows indicate full-length and truncated proteins, respectively. (B) Lane 1, MW marker; lane 2, $(His)_6$-$Y_{730}NH_2Y$-α (~2 μg) after Ni-NTA chromatography; lane 3, $(His)_6$-$Y_{730}NH_2Y$-α (~2 μg) after anion-exchange FPLC to remove the small fraction of 729-truncated α visible in lane 2.

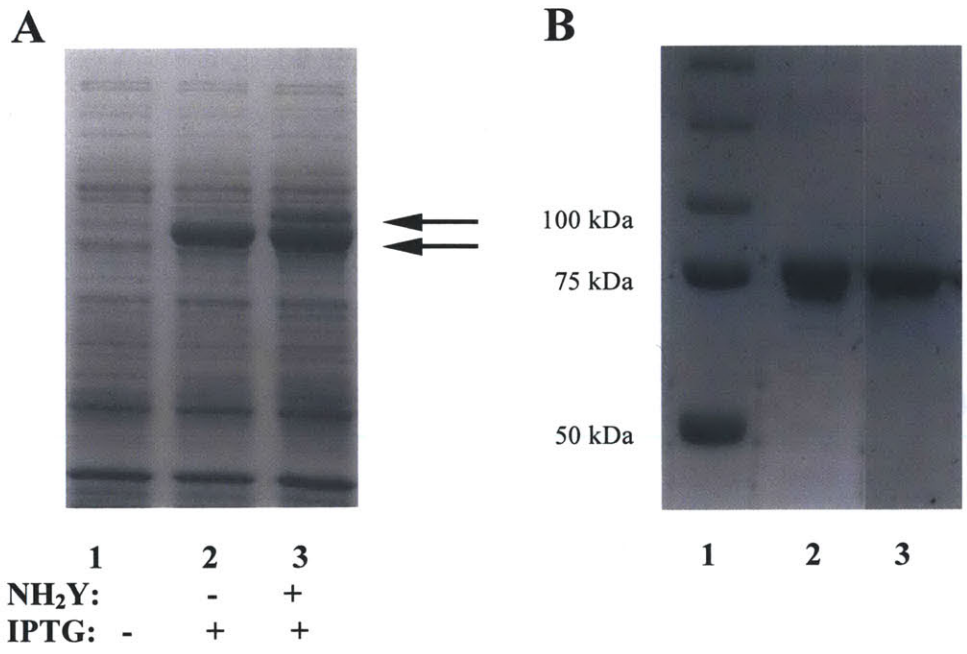

Figure 2.8 Reaction of $(His)_6$-$Y_{730}NH_2Y$-α2 with wt-β2, CDP, and ATP. (A) Reaction monitored by EPR spectroscopy. Subtraction of a spectrum of Y_{122}• (blue) from the composite spectrum (black) yields the spectrum of NH_2Y_{730}• (red). Eight percent of the total initial spin (30 μM) is lost in the 20 s reaction time; of the remaining, 51% is associated with Y• and 49% with NH_2Y_{730}•. This may be compared to the analogous reaction with untagged $Y_{730}NH_2Y$-α2, in which 24% of the spin is lost and the remaining is divided 53% and 47% between Y• and NH_2Y_{730}•, respectively. (B) Reaction monitored by SF UV-vis spectroscopy to determine the kinetics of NH_2Y_{730}• formation (325 nm, red) under single-turnover conditions at 25 °C. Biexponential fit to the data is given by the blue line. *Inset*: An expanded view of the first 0.5 s.

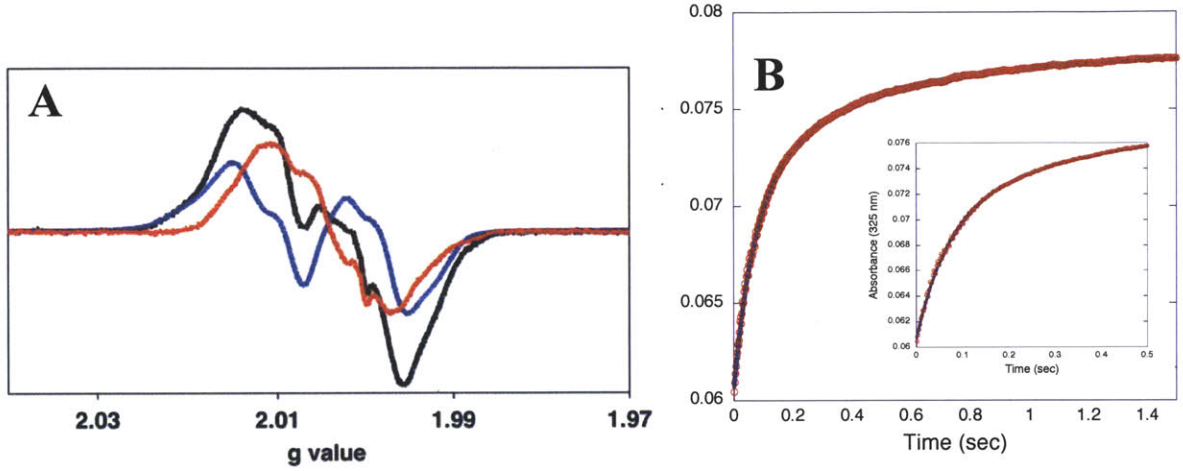

Figure 2.9 Reaction of $(His)_6$-$Y_{730}NH_2Y$-α2 with wt-β2, N_3CDP, and ATP monitored by EPR spectroscopy. (A) The reaction spectrum (pink) is a composite of three species. After subtraction of the N• component (green), a two-radical composite spectrum (black) remains. (B) Subtraction of a spectrum of Y_{122}• (blue) from the difference spectrum generated in (A) gives the spectrum of the putative NH_2Y_{730}• (red). Sixteen percent of the total spin was lost during the 1 min reaction; of the remaining, 48% was associated with Y•, 36% with NH_2Y•, and 16% with N•. The analogous values with untagged $Y_{730}NH_2Y$-α2 were: 18% (spin loss), 43% (Y•), 38% (NH_2Y•), and 19% (N•).

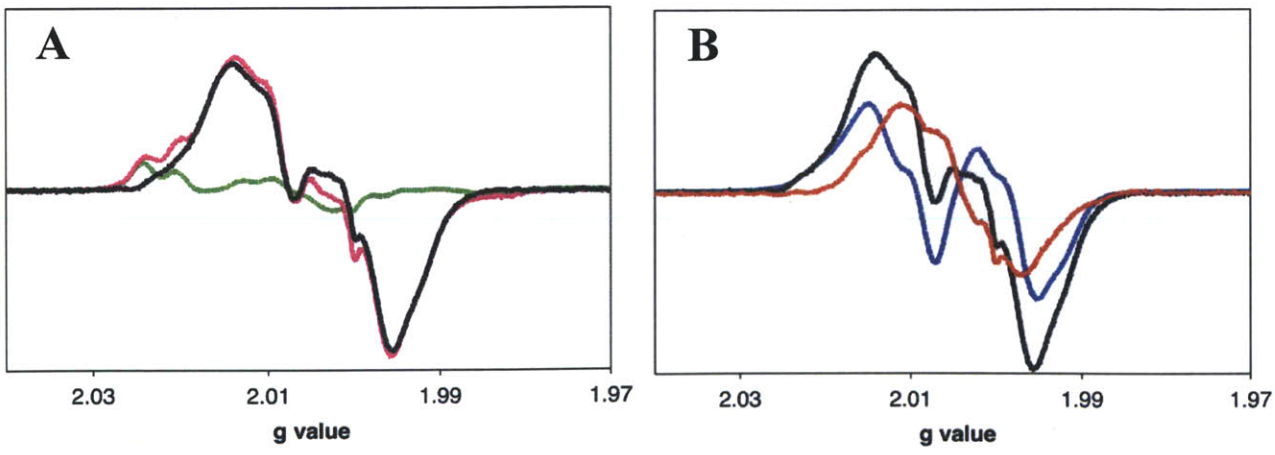

2.3.7 Single turnover assays for dCDP formation. As a final test of catalysis, a hand-quenched single-turnover experiment was conducted using $Y_{730}NH_2Y$-α2 (or $(His)_6$-$Y_{730}NH_2Y$-α2), wt-β2, [5-^{3}H]CDP, and ATP. Under the reaction conditions employed, wt-α2 generates ~3 dCDP/α2.[7] Thus, a sample of $Y_{730}NH_2Y$-α2 with 4% wt activity, in which all of the activity is associated with contaminating wt RNR, should generate 0.12 dCDP/α2. Both $Y_{730}NH_2Y$-α2 and $(His)_6$-$Y_{730}NH_2Y$-α2 generated 0.7 dCDP/α2, or six-fold more product than would be predicted for activity originating solely from contaminating wt (Table 2.3). A similar experiment with $Y_{731}NH_2Y$-α2 yielded 0.65 dCDP/α2, whereas a control experiment using a redox-inactive $Y_{731}F$ mutant generated 0.09 dCDP/α2, consistent with 3% contaminating wt in the latter sample. At present, the basis for sub-stoichiometric formation of dCDP by NH_2Y-RNRs under single-turnover conditions is not understood. However, this observation is consistent with the results of single-turnover N_3CDP assays, in which only ~1/3 of the NH_2Y• formed is converted to N• during a one minute reaction, as described above. Collectively, the steady-state and single-turnover activity assays of both untagged and tagged NH_2Y-RNRs (Table 2.3 and 2.4) and the high accumulation of N• in all mutants (Table 2.3) provide convincing evidence that NH_2Y-RNRs catalyze dNDP formation.

2.3.8 Structural characterization of $Y_{730}NH_2Y$-α2 and $Y_{731}NH_2Y$-α2. To determine whether incorporation of NH_2Y structurally perturbs the PCET pathway, $Y_{730}NH_2Y$-α2 and $Y_{731}NH_2Y$-α2 were crystallized, their structures determined by molecular replacement, and refined to 2.5 and 2.7 Å resolution, respectively (Table 2.5). As the starting model, a 2.3 Å structure of wt-α2 crystallized under similar conditions was used.[11] In all cases, the asymmetric unit contains α2 (molecules A and B), to which is appended a third α (molecule C). This third α also forms a true dimer in the crystal lattice. The major conformation assumed by $Y_{730}NH_2Y$-α2

(Figure 2.10 A) is one in which the NH_2 substitution is oriented to the left when looking toward C_{439} from Y_{731} and the protein surface. Thus, the NH_2 group is situated toward the sterically less-dense side, and its opportunities for intermolecular hydrogen bonding to other residues are minimized. A similar conformation has been reported for the NO_2 group in the crystal structure of $Y_{730}NO_2Y$-α2.[11] Interestingly, additional electron density in the structure of $Y_{730}NH_2Y$-α2 suggests that Y_{731} can undergo a flipping motion away from $Y_{730}NH_2Y$ toward the protein surface, placing a distance of 9.5 Å between the phenolic oxygens of NH_2Y_{730} and Y_{731} (Figure 2.10 B). Concomitant with this flipping are reorientations of N_{733} and R_{411}. This conformational sampling is provocative in that it highlights the dynamic flexibility of residues at the proposed α2/β2 interface and suggests motions that may be possible upon subunit interactions. In the deposited structure, one molecule (C) in the asymmetric unit is built in the flipped conformation. A water molecule, present in the wt structure and hydrogen bonded to Y_{730}, Y_{413} and D_{334}, is also present in this structure, as well as an additional water hydrogen-bonded to Y_{731}.

The major conformation of the residues in the PCET pathway observed in the $Y_{731}NH_2Y$-α2 crystal is shown in Figure 2.10 C. Similar to the 730 mutant, the NH_2 group is oriented to the left and does not interact with any surrounding residues. An analogous conformation has been reported for the NO_2 group of $Y_{731}NO_2Y$-α2.[11] However, in one of the three α monomers (B), the NH_2 substituent is oriented to the right, within hydrogen-bonding distance (2.5 Å) of the adjacent Y_{413}. In molecule C, a water with high occupancy is hydrogen-bonded to the OH groups of residues 730 and 731 as well as to the NH_2 group of NH_2Y_{731}. Higher resolution structures are necessary to determine the role(s) for ordered waters in the PCET pathway.

An overlay of the wt structure with the most common conformations of the $Y_{730}NH_2Y$-α2 and $Y_{731}NH_2Y$-α2 structures is shown in Figure 2.10 D and reveals no significant perturbations

among the three structures in the distance between the phenolic oxygens of the residues at 730 and 731 (3.2-3.4 Å) and the distance between the phenolic oxygen of residue 730 and the sulfur of C_{439} (3.5-3.7Å). In general, the structures reveal no major surprises and suggest that the redox pathway remains intact upon NH_2Y substitution. However, catalysis involving PCET is dependent on 0.1 Å changes and thus functionally-informative structures require the presence of β, S and E, all of which are absent from the structures reported herein.

2.3.9 NH_2Y• formation with S/E pairs monitored by EPR spectroscopy. We have previously reported NH_2Y• formation and its detection by EPR methods in the reaction of $Y_{730}NH_2Y$-α2 or $Y_{731}NH_2Y$-α with wt-β2, CDP and ATP quenched at 10-20 s.[17,37] We now report similar studies on the reaction of $Y_{730}NH_2Y$-α2 and $Y_{731}NH_2Y$-α2 with wt-β2 and the other physiologically relevant S/E pairs (GDP/TTP, ADP/ATP/dGTP, UDP/ATP), with the samples hand-quenched at 20 s. The concentrations of S and E were chosen to saturate the nucleotide binding sites on α2. When examining ADP, both dGTP and ATP effectors were used,[39] as the presence of ATP makes the behavior of ADP/dGTP more closely mimic all other S/E pairs.

The spectra for the reactions with $Y_{730}NH_2Y$-α2 are shown in Figure 2.11 A and are composites of Y_{122}• and NH_2Y_{730}•. Subtraction of the Y_{122}• spectrum yields an NH_2Y• spectrum, with the latter species accounting for 47-53% of the total spin at 20 s. The NH_2Y• spectrum shows very little variation with different S/E pairs. The spectra for the reactions with $Y_{731}NH_2Y$-α2 are similar, with 27-45% of the spin at 20 s associated with NH_2Y• (Figure 2.11 B). In all cases, 20-30% of the total initial spin was lost in the first 20 s, suggesting that rapid freeze-quench (RFQ) techniques are preferable for future EPR analysis of these and similar reactions.

Table 2.5 Crystallographic data collection and refinement statistics for NH_2Y-α2s

	Wt-α2	**$Y_{730}NH_2Y$-α2**	**$Y_{731}NH_2Y$-α2**
PDB-ID	2x0x	2xo4	2xo5
Initial buffer[a]	15 mM $MgSO_4$, 1 mM EDTA	1 mM EDTA, 5 mM DTT, 5% glycerol	15 mM $MgSO_4$, 1 mM EDTA
Data collection, processing and scaling			
Beamline (ESRF)	ID14-2	ID23-2	ID14-1
Cell H32	223.9	224.6	223.2
	336.5	336.7	335.7
Resolution (Å)	2.3	2.5	2.7
Completeness (%)	100/100	100/100	99.9/100
Observed reflections	1069417	501709	493823
Unique reflections	142954	112265	87929
Redundancy	7.5/7.4	4.5/4.5	5.6/5.6
<I/s>	15.8/3.7	10.1/2.2	13.1/3.4
R merge	8.6/54.9	11.3/64.4	11.3/51.1
Refinement			
R fact	18.3	19.8	17.7
R free	22.4	23.3	22.9
Non-hydrogen atoms	17826		
Water molecules	1028	1027	916
R.m.s. deviation			
Bond length (Å)	0.011	0.009	0.014
Bond angles (deg)	1.31	1.164	1.52
B factors			
Averall mch/sch	36/38	38/39	37/38
Chain A	39	41	40
Chain B	39	41	40
Chain C	30	32	31
Waters	40	45	40

a. wt-α2 and $Y_{731}NH_2Y$-α2 are in 50 mM Hepes (pH 7.6), and $Y_{730}NH_2Y$-α2 is in 50 mM Tris (pH 7.6). Additives are specified in the table.

Figure 2.10 Crystal structures of NH_2Y-α2s. Oxygens are colored red, nitrogens, blue, and sulfurs, yellow. (A) The primary conformation assumed by residues of the PCET pathway in $Y_{730}NH_2Y$-α2 (2.5 Å). (B) Electron density suggests a secondary conformation (green) present in the $Y_{730}NH_2Y$-α2 crystal in which the phenol of Y_{731} is oriented away from NH_2Y_{730} and toward the protein surface, placing a distance of 9.5 Å between the phenolic oxygens. This movement is accompanied by changes at R_{411} and N_{733} (shown in sticks), and highlights the dynamic motion possible at the surface believed to participate in α2/β2 subunit interactions. (C) The primary conformation assumed by residues of the PCET pathway in $Y_{731}NH_2Y$-α2 (2.7 Å). A second conformation, in which the NH_2 group is oriented on the right side of the phenol, is observed in one of the three molecules in the asymmetric unit. (D) An overlay of the structures of $Y_{730}NH_2Y$-α2 (cyan) and $Y_{731}NH_2Y$-α2 (magenta) with wt-α2 (yellow, 2.3 Å) solved under the same conditions demonstrates minimal perturbation of the PCET pathway in the predominant conformations assumed by the two mutants. Distances of 3.2-3.4 Å separate the phenolic oxygens of residues 730 and 731, and distances of 3.5-3.7 Å separate the sulfhydryl of 439 and the phenol of 730. Figure generated in PyMol from PDB-IDs 2x0x, 2xo4, and 2xo5.

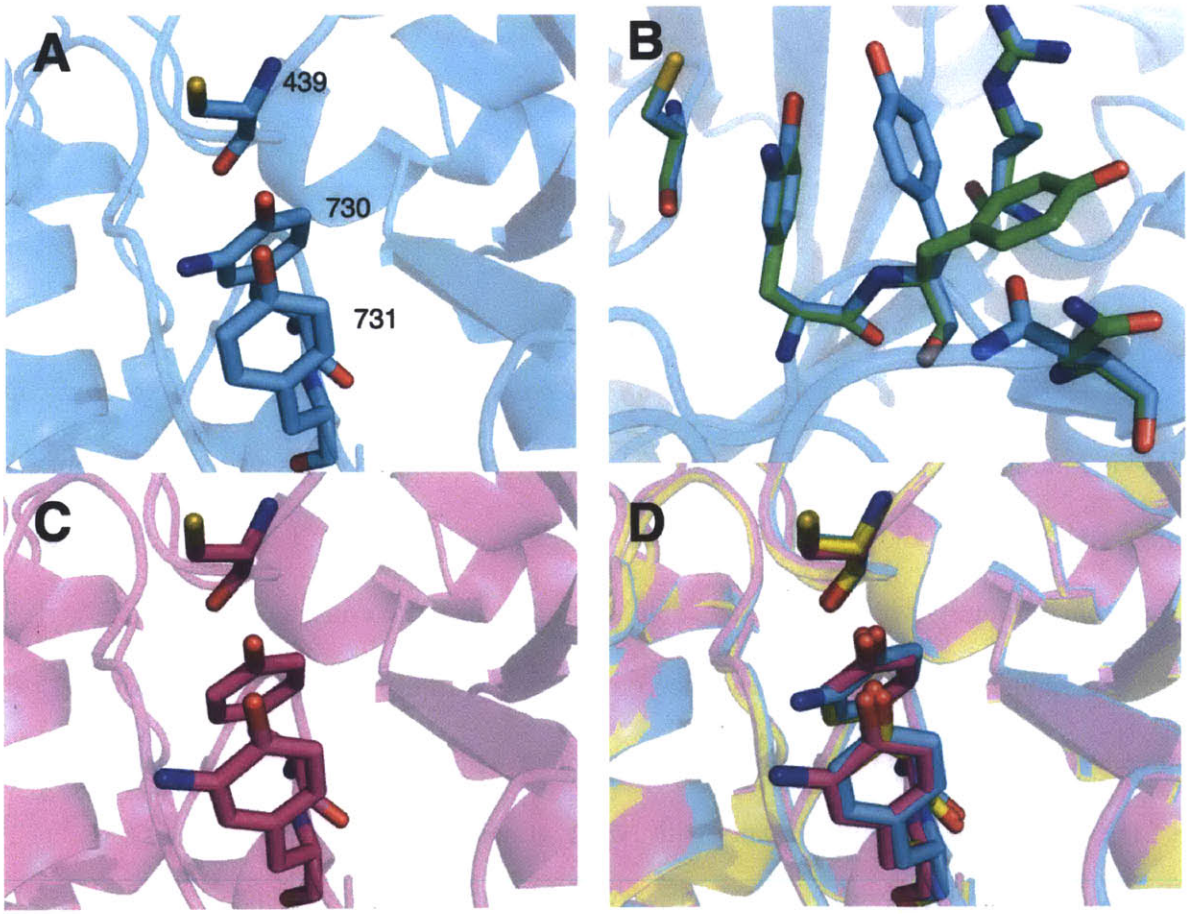

Figure 2.11 EPR spectra of NH_2Y•s formed in the reactions of (A) $Y_{730}NH_2Y$-α2 or (B) $Y_{731}NH_2Y$-α2 and wt-β2 with the S/E pairs CDP/ATP (red), GDP/TTP (green), UDP/ATP (blue), ADP/dGTP/ATP (purple). The spectra below are those generated subsequent to subtraction of Y_{122}• from the composite reaction spectrum. The asterisk (*) indicates an artifact associated with the EPR finger dewar, which is more pronounced in lower concentration samples. A portion of these data were collected by Dr. Mohammad Seyedsayamdost and have been reported previously.[36]

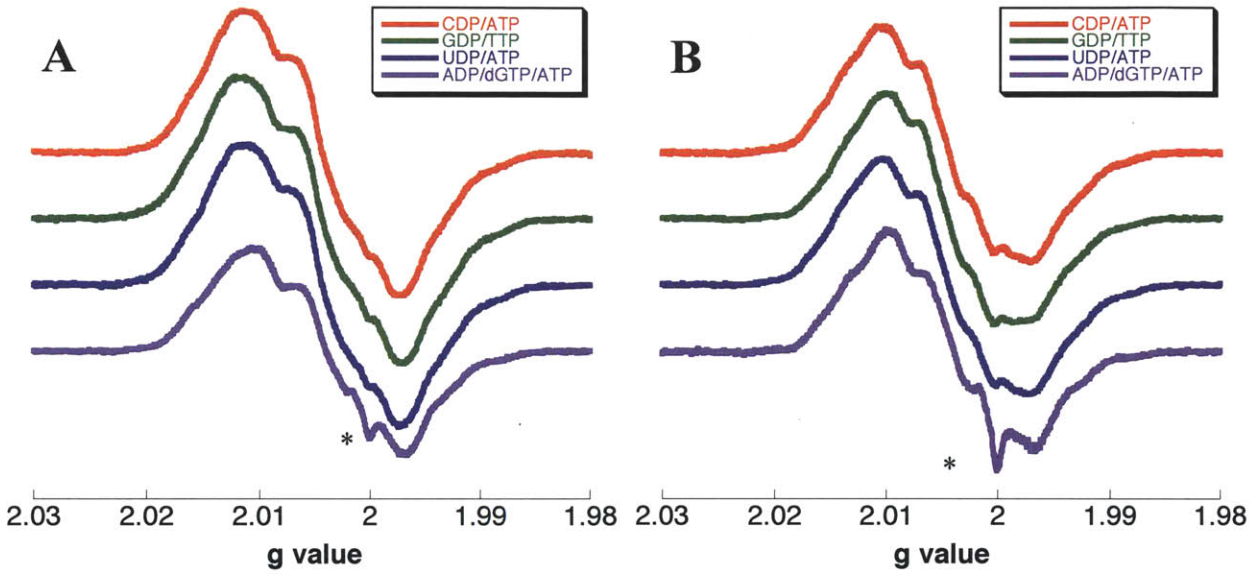

2.3.10 Kinetics of NH_2Y• formation with S/E pairs monitored by SF UV-vis spectroscopy.

SF UV-vis kinetic experiments monitoring NH_2Y• formation and Y• loss were carried out with all three NH_2Y-RNRs and all S/E pairs. In all cases, NH_2Y• formation was biphasic and occurred concomitantly with Y_{122}• loss (Table 2.6). The fast rate constant, k_{fast}, varied from 9 - 45 s^{-1} and demonstrated a small dependence on position within the pathway with both k_{fast} and the conversion amplitude decreasing slightly with increasing distance between NH_2Y from the Y_{122}•. The average k_{fast} for all S/E pairs with NH_2Y at position 356, 731, and 730 is 38 s^{-1} (22% conversion), 19 s^{-1} (20%), and 14 s^{-1} (15%), respectively. k_{fast} also demonstrates a small dependence on the S/E pair, with purines giving rise to faster rate constants than pyrimidines (GDP/TTP ≈ ADP/dGTP/ATP > CDP/ATP > UDP/ATP). In contrast to the fast phase, the slow

phase is nearly invariant with position and S/E pair, with an average k_{slow} of ~ 2.5 s^{-1}. We believe that both rate constants measure protein conformation changes rather than chemical events; our hypothesis is that k_{slow} reports on conformational changes preceding catalysis that are rate-determining in the wt enzyme,[7] as described in the Discussion.

In the SF UV-vis experiments, 30-40% of Y_{122}• is converted to NH_2Y• over the two phases. This conversion is in good agreement with the conversion of total initial Y_{122}• to NH_2Y• (31-41%) in the hand-quench EPR experiments described above, and in a single RFQ EPR experiment with $Y_{731}NH_2Y$-α2, wt-β2, CDP, and ATP.[18] In the case of previous studies with Y_{356}DOPA-β2, a 50% conversion of initial Y_{122}• to DOPA• was reported, which is the maximum conversion one would predict on the basis of the enzyme's proposed half-site reactivity.[8] The difference in accumulation between DOPA• and NH_2Y•s is not understood, but may reflect the difference in reduction potentials between the two amino acids.

Similar SF kinetic experiments were carried out on NH_2Y-RNRs with S or E alone to gain insight about how nucleotide binding conformationally gates PCET. All three NH_2Y-RNRs (Table 2.7) form NH_2Y• with S alone, but both k_{fast} and k_{slow} are reduced relative to those with the corresponding S/E pair. In the absence of E, purine substrates experience an average reduction in rate constants that is two-fold greater than that of pyrimidines. Total amplitudes of NH_2Y• formation are reduced only moderately, with an average of 22% conversion over two phases, compared to a 30% average in the presence of S/E. In presence of E alone (Table 2.7), rate constants and amplitudes of NH_2Y• formation are dramatically decreased, supporting a role for S as the key factor in triggering radical propagation. Recent studies from our laboratory have suggested that the role of E is to maximize the amount of active enzyme complex and enhance k_{cat} by lowering the K_d for subunit interactions in the presence of a properly matched S/E pair

(Hassan, Yokoyama, Olshansky, Nocera, and Stubbe, unpublished results). The nature of the conformational changes induced upon E binding are not known, but it is likely that the NH_2Y probe is sensitive to these changes, resulting in modest enhancements of k_{cat} and conversion amplitude for NH_2Y• formation in the presence of S/E relative to S alone.

Finally, a comparison of the biphasic kinetics of NH_2Y_{356}• formation to the predominantly triphasic kinetics previously reported for $DOPA_{356}$• formation[8] (Table 2.8) supports our hypothesis that the additional mutations required for the ELP method have increased the kinetic complexity of the Y_{356}DOPA-β2 reaction. The striking similarities in the rate constants and amplitudes between the fast phase for NH_2Y• formation and fastest phase for DOPA• formation suggest that this phase reports on a purely conformational event, as an ET event would show correlation between the rate constant for radical formation and the redox potential of the unnatural amino acid at position 356.

Thus, NH_2Y fulfills two roles in studying PCET in *E. coli* RNR. First, its incorporation into three different positions on the pathway has allowed for the kinetic characterization of intermediates formed during long-range radical propagation. Second, NH_2Y acts as a unique conformational probe, providing evidence for the role of S/E in conformational gating that is undetectable in the wt system.

Table 2.6 Kinetics of NH_2Y• formation in β2 and α2 at 25 °C monitored by SF UV-vis kinetics with different S/E pairs.

Substrate/ Effector	NH_2Y_{356}•		NH_2Y_{731}•[b]		NH_2Y_{730}•[b]	
	k (s^{-1})[a]	A (%)	k (s^{-1})	A (%)	k (s^{-1})	A (%)
CDP/ATP						
Fast phase	36 ± 4	25 ± 2	18 ± 2	22 ± 2	12 ± 1	20 ± 2
Slow phase	2.1 ± 0.6	5 ± 1	2.5 ± 0.3	10 ± 1	2.4 ± 0.2	19 ± 2
UDP/ATP						
Fast phase	30 ± 7	11 ± 1	9.3 ± 1.6	15 ± 2	9.3 ± 1.7	8 ± 1
Slow phase	1.5 ± 0.8	2 ± 1	2.0 ± 0.2	22 ± 1	1.7 ± 0.1	20 ± 2
GDP/TTP						
Fast phase	38 ± 6	25 ± 2	28 ± 3	22 ± 2	18 ± 2	15 ± 2
Slow phase	1.8 ± 0.3	7 ± 1	2.3 ± 0.3	9 ± 1	2.3 ± 0.2	16 ± 2
ADP/dGTP/ATP						
Fast phase	46 ± 9	25 ± 2	20 ± 6	19 ± 3	16 ± 2	17 ± 1
Slow phase	3.6 ± 2.0	5 ± 1	5.0 ± 1.8	9 ± 3	2.4 ± 0.2	14 ± 1

a. Errors reported as the standard deviation of >5 SF traces. *b*. A portion of these data were collected by Dr. Mohammad Seyedsayamdost and have been reported previously.[36]

Table 2.7 Kinetics of NH_2Y• formation in β2 and α2 at 25 °C monitored by SF UV-vis with S alone or E alone.

Substrate or effector	NH_2Y_{356}• k (s^{-1})	A (%)	NH_2Y_{731}•[b] k (s^{-1})	A (%)	NH_2Y_{730}•[b] k (s^{-1})	A (%)
CDP						
Fast phase	28 ± 12	18 ± 3	11 ± 1	9 ± 1	5.2 ± 0.5	9 ± 1
Slow phase	2.6 ± 1.3	8 ± 2	1.3 ± 0.1	16 ± 2	0.8 ± 0.1	19 ± 2
UDP[a]						
Fast phase	-	-	4.4 ± 0.2	11 ± 1	1.4 ± 0.2	5 ±1
Slow phase	-	-	0.8 ± 0.1	15 ± 2	0.2 ± 0.1	19 ± 2
GDP						
Fast phase	-	-	7.7 ± 0.8	13 ± 1	2.5 ± 0.1	12 ± 1
Slow phase	-	-	1.4 ± 0.2	10 ± 1	0.3 ± 0.1	16 ± 2
ADP						
Fast phase	-	-	3.0 ± 0.3	2 ± 1	6.5 ± 0.7	2 ± 1
Slow phase	-	-	0.08 ± 0.01	8 ± 1	0.06 ± 0.01	3 ± 1
ATP	-	-				
Fast phase	-	-	0.05 ± 0.01	8 ± 1	27 ± 3	2 ± 1
Slow phase			-	-	-	-
TTP						
Fast phase	-	-	20 ± 1	3 ± 1	1.8 ± 0.2	2 ± 1
Slow phase	-	-	0.07 ± 0.01	8 ± 1	0.06 ± 0.01	10 ± 1
dGTP						
Fast phase	-	-	0.9 ± 0.1	3 ± 1	1.1 ± 0.1	3 ± 1
Slow phase	-	-	0.10 ± 0.01	19 ± 2	0.11 ± 0.01	17 ± 2

a. UDP was 2 mM for experiments with S/E and 1 mM for experiments with S only. This may partially account for the differences in rate constants, as it is now known that 1 mM UDP does not saturate the active site. *b.* Data were collected by Dr. Mohammad Seyedsayamdost and have been reported previously.[36]

Table 2.8 A comparison of the kinetics of radical formation in $Y_{356}NH_2Y$-β2 and Y_{356}DOPA-β2

Substrate or effector	NH_2Y_{356}•		$DOPA_{356}$•[a]	
	k (s^{-1})	A (%)	k (s^{-1})	A (%)
CDP/ATP				
1st phase	36	25	38	21
2nd phase	2.1	5	6.8	17
3rd phase	-	-	0.7	9
UDP/ATP[b]				
1st phase	30	11	16	20
2nd phase	1.5	2	5.0	16
3rd phase	-	-	0.6	9
GDP/TTP				
1st phase	38	25	32	31
2nd phase	1.8	7	1.7	23
3rd phase	-	-	-	-
ADP/dGTP/(ATP)[c]				
1st phase	46	25	46	26
2nd phase	3.6	5	3.8	15
3rd phase	-	-	0.8	10

a. Data were collected by Dr. Mohammad Seyedsayamdost and have been reported previously.[8,36] *b.* UDP was 2 mM for $Y_{356}NH_2Y$-β2 and 1 mM for Y_{356}DOPA-β2. This may account for the differences in rate constants, as it is now known that 1 mM UDP does not saturate the active site. *c.* ATP was present at 3 mM for $Y_{356}NH_2Y$-β2, but was not included in the reaction for Y_{356}DOPA-β2.

2.4 DISCUSSION

2.4.1 NH_2Y-RNRs are catalytically active. When studies on NH_2Y-RNRs were initiated, it was hypothesized that NH_2Y, ~190 mV easier to oxidize than Y at pH 7, would act as a thermodynamic sink, effectively trapping the radical during propagation and shutting down nucleotide reduction. This hypothesis was supported by previous studies on Y_{356}DOPA-β2, in which conversion of DOPA (~260 mV easier to oxidize than Y) to DOPA• rendered the enzyme completely inactive.[8] It was further supported by experiments on $Y_{356}F_nY$-β2s[13] and NO_2Y-RNRs ($Y_{356}NO_2Y$-β2, $Y_{731}NO_2Y$-α2, and $Y_{730}NO_2Y$-α2),[10,11] which indicated that a 200 mV increase in potential relative to Y prevents catalysis.

Thus, it was unexpected when all three NH_2Y-RNRs showed considerable catalytic activity (Table 2.3), as this implies that NH_2Y• is capable of the thermodynamically uphill oxidation of the next residue (Y or C) on the pathway (Figure 2.1). Given the important implications this observation has on the PCET mechanism, we made a considerable effort to establish that the observed activity is inherent to NH_2Y-RNRs and not associated with contaminating wt RNR. Since the genes coding for the subunits of RNR are essential in *E. coli,* the host organism for protein expression, endogenous levels of the wt subunits are always present at some level and thus can co-purify with the recombinantly expressed protein. NH_2Y-RNR expression is sensitive to growth conditions and results in heterogeneity in the quality of NH_2Y-RNR isolated, as manifested by the large standard deviations in NH_2Y-RNR activities (Table 2.3). We hypothesize that the activities at the higher end of these ranges (Table 2.3) are associated with protein isolated from growths with less successful expression, and contains a higher fraction of endogenous RNR. A similar argument has been made with NO_2Y-α2s.[11]

An affinity purification protocol for an optimized tagged-α2, $(His)_6$-$Y_{730}NH_2Y$-α2, was

developed (Figure 2.6) and the isolated protein assayed. This protein gave 50% lower activity and a narrower range of activities relative to untagged $Y_{730}NH_2Y$-α2 (Table 2.3). These results support our proposal that the endogenous wt-α2 that contaminates the latter sample has been largely removed from the former.

In application of the *in vivo* nonsense codon suppression method, the fidelity of the evolved tRNA/RS pair can introduce an additional mechanism by which wt RNR is produced. Both the K_m of the RS for the unnatural amino acid (UAA) and the relative abundance and availability of the UAA in the cell can influence the RS's selectivity for the UAA relative to Y. The fidelity of the tRNA/RS is also influenced by the expression system for the protein of interest, the position of UAA incorporation, and the growth medium. Since this source of contaminating wt protein is not removed by affinity purification, single-turnover experiments utilizing a native substrate (CDP) or a mechanism-based inhibitor (N_3CDP) were conducted on both the tagged and untagged NH_2Y-RNRs. In all cases, at least four-fold more product (dCDP or N•, respectively) was formed than can be rationalized on the basis of contaminating wt (Table 2.3). These single-turnover assays provide the strongest support for the high fidelity of the NH_2Y-RS/tRNA pair and for the catalytic activity of NH_2Y-RNRs.

2.4.2 Initial kinetic model for NH_2Y-RNRs. Our initial model for catalysis by NH_2Y-RNRs is shown in Scheme 2.1. While NH_2Y is drawn at position 730 of α, a similar mechanism incorporating an additional oxidation step(s) may be drawn if NH_2Y is located at position 731 of α or 356 of β. The model indicates that, in the presence of both α2 and β2, the binding of S and E initiates radical propagation, as demonstrated by SF studies described above and previously.[17] NH_2Y• formation occurs by two distinct pathways (steps **1** and **8**) as revealed by its biphasic kinetics (Figure 2.4). We assign the observed k_{fast} to step **8** (green pathway, Scheme 2.1) and

propose that this rate constant reports on PCET between a pathway residue and Y_{122}•, resulting in the formation of an NH_2Y• that is not in an appropriate conformation to oxidize C_{439}. It is likely that this electron excursion or "rattling" occurs in the wt RNR, but that the equilibrium lies strongly in favor of reoxidation of Y_{122}, the proposed thermodynamic minimum on the pathway. While this process is kinetically invisible in the wt enzyme, in the NH_2Y-RNRs, introduction of a new thermodynamic minimum on the pathway results in the rapid formation of a stable NH_2Y• with its rate constant for formation and accumulation dependent on position and S/E pair (Table 2.6). A similar event has been proposed to occur in the adenosylcobalamin-dependent class II RNR. Using a prochirally labeled 5′-deoxyadenosyl moiety of the cofactor, fast stereochemical scrambling of the label occurs, indicating rapid cleavage of the carbon-cobalt bond despite the inability to detect cob(II)alamin by rapid kinetic techniques.[40]

NH_2Y• is also formed by step **1**, with a k_{slow} of ~2.5 s^{-1} that we assign to the slow conformational gating step subsequent to S/E binding in which the protein assumes a conformation optimized for C_{439} oxidation. This assignment is supported by k_{slow} being independent of position and S/E pair (Table 2.6). This number falls within the lower range of values reported for the rate-determining conformational change in wt RNR (2-10 s^{-1}),[7] and may reflect changes induced by the NH_2Y substitution that could slow conformational priming, such as disruption of ordered water molecules or H-bonding networks. It is not yet known whether the two populations of NH_2Y•s formed in steps **1** and **8** interconvert (steps **9** and **-9**), but if they do, the interconversion must be slow (< 2.5 s^{-1}) based on the observation of two distinct kinetic phases. It is possible that these states may interconvert on the time scale of steady-state turnover, and if so, both populations would be relevant to dCDP formation. RFQ methods in conjunction with EPR and ENDOR spectroscopies may be used to probe the existence, and possible

interconversion, of the two $NH_2Y\bullet$ populations. The nature of the conformational changes associated with k_{slow} (**1**) and k_{fast} (**8**) are unknown, but they likely involve subtle reorientations to optimize radical propagation. Temperature dependence[36] and viscogen-dependence (Chapter 4) studies provide further evidence supporting the assignment of these rate constants to conformational changes.[41]

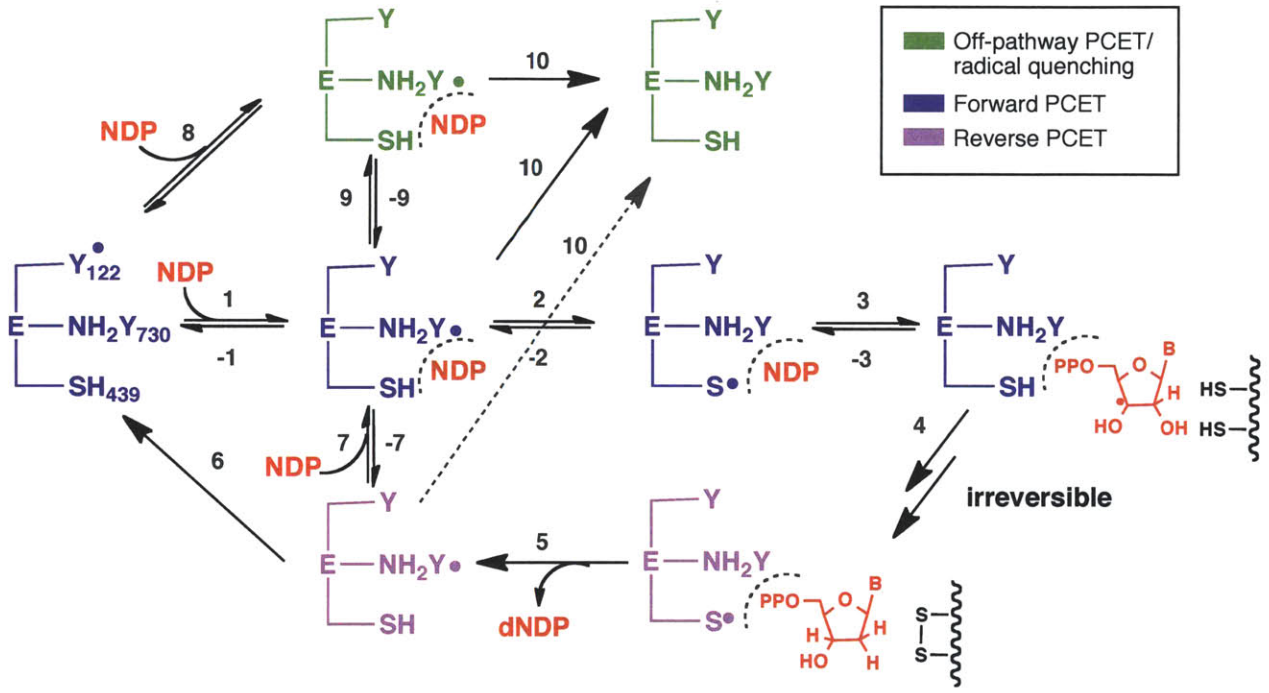

Scheme 2.1. Kinetic model for $NH_2Y\bullet$ formation and nucleotide reduction in NH_2Y-RNRs. The model for $Y_{730}NH_2Y$-α2 is shown, but similar models can be drawn for the 731 and 356 mutants by the addition of one or two Y oxidation steps within step **2**. Enzyme species are colored according to three different pathways – forward PCET (blue), reverse PCET (magenta), and off-pathway PCET and/or radical quenching (green). The rate constants for individual steps, if available, are given in the text. Substrate (NDP) and product (dNDP) are shown in red. Effector is omitted from the scheme for clarity.

We will argue subsequently that the next step, oxidation by NH_2Y• of the subsequent residue in the pathway (step **2**), is the rate-limiting step in the steady state (0.2 to 0.7 s^{-1}). But first let us consider the remaining steps in Scheme 2.1. The chemistry of nucleotide reduction (steps **3** and **4**) occurs rapidly (>100 to 300 s^{-1}) based on kinetic modeling of the wt system[7] and recent experimental evidence using the mutant $Y_{122}NO_2Y$-β2 as a radical initiator.[42] In this mutant, ET is decoupled from both PT and conformational gating, and dCDP is formed at 100-300 s^{-1}. This rate constant is similar to the pre-steady state rate constant for dCTP formation of 55 s^{-1} that has been measured in the *L. leichamannii* RNR.[43] Once dCDP is formed (step **4**), reformation of the NH_2Y• by the reverse PCET should be rapid ($\geq$ 100 s^{-1}, magenta pathway, step **5**). Evidence from single-turnover experiments using $Y_{122}NO_2Y$-β2 also indicate that Y_{356}• is re-formed with a rate constant of at least 100-300 s^{-1} following nucleotide reduction,[42] and kinetic simulations of the wt RNR mechanism require a comparably fast (if not faster) rate constant for reverse PCET.[7]

Our model provides two possible fates for the NH_2Y• generated upon reverse PCET (step **5**). It can either re-initiate the nucleotide reduction process directly (step **7**), or it can regenerate the Y_{122}• through step **6,** or steps **7** and **-1**. The latter two mechanisms would involve one or two transient Y•s, and possibly a W•, as intermediates, depending on the position of NH_2Y on the pathway.[5,6] While steps **-1** and **6** are likely to be endergonic, we have previously demonstrated reverse PCET and slow re-oxidation of Y_{122} by $DOPA_{356}$• and NH_2Y_{356}• only with the heterodimers Y_{356}DOPA-ββ′[9] and $Y_{356}NH_2Y$-ββ′ (Chapter 4) with wt-α2, CDP and ATP. Thus, steps **-1** and/or **6** have thermodynamic precedent. However, re-oxidation of Y_{122}• has never been observed in the relevant homodimers and thus a pathway in which NH_2Y• becomes the radical initiator for all subsequent turnovers (step **7** to step **2**) may also be considered.

We now return to the slow steady-state rate constant for dNDP production by NH_2Y-RNRs (0.2 to 0.7 s^{-1}) and consider two steps to which it may be assigned. It may be associated with reduction of the active-site disulfide (not shown in Scheme 2.1) formed concomitant with dCDP production (step **4**), or with oxidation by NH_2Y• of the subsequent amino acid on the radical propagation pathway (step **2**). Let us consider the first possibility. Under our assay conditions, wt RNR has a turnover number of >2 s^{-1}, more than four times faster than the steady-state rate constant of NH_2Y-RNRs. We think it is unlikely that substitution of NH_2Y for Y would alter the kinetics of disulfide reduction or conformational changes accompanying re-reduction. Disulfide reduction has been proposed to be rate-limiting in *E. coli* wt RNR when assayed at high protein concentration (k_{cat} = 1 s^{-1} at [α2] > 1μM).[7] Thus, steady-state assays were performed on $Y_{730}NH_2Y$-α2 over a 20-fold concentration range, encompassing the regimes in which disulfide reduction is and is not rate limiting for wt-α2. All concentrations yielded identical specific activity measurements for the mutant. Thus, the chemistry of disulfide reduction and the conformational reorganization necessary to prepare RNR for a second turnover seem unlikely to limit k_{cat} in NH_2Y-RNRs.

From the initial experiments presented in this chapter, our favored candidate for the rate-determining step in the overall scheme is step **2**, oxidation of subsequent residues in the pathway by NH_2Y•. One additional consideration with this proposition arises from the three different locations of NH_2Y, and the resulting differences in the amino acid oxidized in step **2**. As drawn in Scheme 2.1, NH_2Y_{730}• oxidizes C_{439}. However, NH_2Y_{356}• and NH_2Y_{731}• will oxidize Y_{731} and Y_{730}, respectively. This mechanistic different raises the important question of the relative reduction potentials of Y_{731}, Y_{730}, and C_{439}. As discussed above, solution reduction (peak) potentials for the Y/Y• couple vary from 0.83-0.93 V at pH 7.[16,20] Meanwhile, the reported

reduction potentials of small molecule thiols vary from 0.92 V[44] to 1.33 V[45] at pH 7. Thus, the thermodynamic barrier to C_{439} oxidation by Y_{730} may range from 0 – 0.5 V. If the oxidation of C_{439} by NH_2Y_{730}• is the most endergonic of the three NH_2Y• oxidations, one might predict that this would be reflected in position-dependent differences in k_{cat}. However, this is not the case (Table 2.3), with the rate constants for $Y_{730}NH_2Y$-α2 and $Y_{731}NH_2Y$-α2 being identical within error. Thus, if step **2** is rate-determining, the similarities in k_{cat} suggest that either the protein environment modulates the relative oxidation potentials of the $Y_{731}/Y_{730}/C_{439}$ triad to be nearly isoenergetic, or that the uphill oxidation of C_{439} is driven by coupling to rapid irreversible chemical step(s) during nucleotide reduction. Very recent experiments using NO_2Y_{122}• as a radical initiator have led to a hypothesis that Y_{356} of β2 is 50-100 mV lower in potential compared to Y_{731} and Y_{730} of α2.[46] Thus, the oxidation of Y_{731} by NH_2Y_{356}• is also a candidate as the most endergonic radical hopping step. However, we observe no considerable reduction in activity of $Y_{356}NH_2Y$-β2 relative to the NH_2Y-α2s (Table 2.3).

Finally, for the sake of completeness, Scheme 2.1 also includes the slow reduction of the NH_2Y• by a number of non-specific pathways (step **10**). This decay process (k_{red} of 0.004 to 0.007 s^{-1})[47] is 100-fold slower than the steady-state turnover number and does not contribute to significant radical loss on the timescale of our experiments.

Our starting model (Scheme 2.1) makes testable predictions about radical formation and dNDP production in NH_2Y-RNRs. For instance, if step **2** is rate limiting, a solvent kinetic isotope effect (KIE) should be apparent when any of the NH_2Y-RNRs is assayed in D_2O. Similarly, the rate constant for dCDP formation in the first turnover, determined by a rapid chemical-quench experiment, should be identical to that in the steady state. Alternatively, if dCDP is formed with a rate constant similar to NH_2Y• formation (~2.5 s^{-1}), a step subsequent to

dCDP formation (step **6** or **7,** or disulfide reduction) must be rate limiting. Finally, the ability to detect a catalytically active NH_2Y• at each position in the pathway is allowing high-field ENDOR spectroscopic experiments to be conducted to elucidate hydrogen-bonding networks relevant to coupling PT and ET events. These and other experiments are described in Chapter 4, which is dedicated to further mechanistic studies intended to challenge and refine the initial kinetic model for NH_2Y-RNR catalysis put forth in Scheme 2.1. As we will see in that chapter, the surprising results of pre-steady state kinetic experiments measuring the rate of dCDP formation in NH_2Y-RNRs will cause us to revise our original model and assign the new rate-determining step to the slow interconversion between two NH_2Y• populations (step **9**), the importance of which was not fully appreciated at the time our original model (Scheme 2.1) was proposed.

2.5 REFERENCES

1. Stubbe, J. & van der Donk, W.A. Protein radicals in enzyme catalysis. *Chem. Rev.* **98**, 705-62 (1998).
2. Jordan, A. & Reichard, P. Ribonucleotide reductases. *Annu. Rev. Biochem.* **67**, 71-98 (1998).
3. Nordlund, P. & Reichard, P. Ribonucleotide reductases. *Annu. Rev. Biochem.* **75**, 681-706 (2006).
4. Thelander, L. Physicochemical characterization of ribonucleoside diphosphate reductase from *Escherichia coli*. *J. Biol. Chem.* **248**, 4591-601 (1973).
5. Uhlin, U. & Eklund, H. Structure of ribonucleotide reductase protein R1. *Nature* **370**, 533-9 (1994).
6. Stubbe, J., Nocera, D.G., Yee, C.S. & Chang, M.C.Y. Radical initiation in the class I ribonucleotide reductase: long-range proton-coupled electron transfer? *Chem. Rev.* **103**, 2167-201 (2003).
7. Ge, J., Yu, G., Ator, M.A. & Stubbe, J. Pre-steady-state and steady-state kinetic analysis of *E. coli* class I ribonucleotide reductase. *Biochemistry* **42**, 10071-10083 (2003).
8. Seyedsayamdost, M.R. & Stubbe, J. Site-specific replacement of Y_{356} with 3,4-dihydroxyphenylalanine in the β2 subunit of *E. coli* ribonucleotide reductase. *J. Am. Chem. Soc.* **128**, 2522-2523 (2006).
9. Seyedsayamdost, M.R. & Stubbe, J. Forward and reverse electron transfer with the Y356DOPA-β2 heterodimer of *E. coli* ribonucleotide reductase. *J. Am. Chem. Soc.* **129**, 2226-7 (2007).
10. Yee, C.S., Seyedsayamdost, M.R., Chang, M.C.Y., Nocera, D.G. & Stubbe, J. Generation of the R2 subunit of ribonucleotide reductase by intein chemistry: insertion of 3-nitrotyrosine at residue 356 as a probe of the radical initiation process. *Biochemistry* **42**, 14541-52 (2003).
11. Yokoyama, K., Uhlin, U. & Stubbe, J. Site-specific incorporation of 3-nitrotyrosine as a probe of p*K*a perturbation of redox-active tyrosines in ribonucleotide reductase. *J. Am. Chem. Soc.* **132**, 8385-97 (2010).
12. Yee, C.S., Chang, M.C.Y., Ge, J., Nocera, D.G. & Stubbe, J. 2,3-difluorotyrosine at position 356 of ribonucleotide reductase R2: A probe of long-range proton-coupled electron transfer. *J. Am. Chem. Soc.* **125**, 10506-7 (2003).
13. Seyedsayamdost, M.R., Yee, C.S., Reece, S.Y., Nocera, D.G. & Stubbe, J. pH rate profiles of F_nY_{356}-R2s (n = 2, 3, 4) in *Escherichia coli* ribonucleotide reductase: evidence that Y_{356} is a redox-active amino acid along the radical propagation pathway. *J. Am. Chem. Soc.* **128**, 1562-8 (2006).
14. Nordlund, P., Sjöberg, B.M. & Eklund, H. Three-dimensional structure of the free radical protein of ribonucleotide reductase. *Nature* **345**, 593-8 (1990).
15. Xie, J. & Schultz, P.G. An expanding genetic code. *Methods* **36**, 227-38 (2005).

16. DeFelippis, M.R. et al. Electrochemical properties of tyrosine phenoxy and tryptophan in indolyl radicals in peptides and amino acid analogs. *J. Phys. Chem.* **95**, 3416-9 (1991).

17. Seyedsayamdost, M.R., Xie, J., Chan, C.T., Schultz, P.G. & Stubbe, J. Site-specific insertion of 3-aminotyrosine into subunit α2 of *E. coli* ribonucleotide reductase: direct evidence for involvement of Y730 and Y731 in radical propagation. *J. Am. Chem. Soc.* **129**, 15060-71 (2007).

18. Seyedsayamdost, M.R. & Stubbe, J. Replacement of Y_{730} and Y_{731} in the α2 subunit of *Escherichia coli* ribonucleotide reductase with 3-aminotyrosine using an evolved suppressor tRNA/tRNA-synthetase pair. *Methods Enzymol.* **462**, 45-76 (2009).

19. Minnihan, E.C., Seyedsayamdost, M.R. & Stubbe, J. Use of 3-aminotyrosine to examine the pathway dependence of radical propagation in *Escherichia coli* ribonucleotide reductase. *Biochemistry* **48**, 12125-32 (2009).

20. Tommos, C., Skalicky, J.J., Pilloud, D.L., Wand, A.J. & Dutton, P.L. De novo proteins as models of radical enzymes. *Biochemistry* **38**, 9495-507 (1999).

21. Jovanovic, S.V., Steenken, S., Tosic, M., Marjanovic, B. & Simic, M.G. Flavonoids as antioxidants. *J. Am. Chem. Soc.* **116**, 4846-51 (1994).

22. Salowe, S.P. & Stubbe, J. Cloning, overproduction, and purification of the B2 subunit of ribonucleoside-diphosphate reductase. *J. Bacteriol.* **165**, 363-6 (1986).

23. Salowe, S.P., Ator, M.A. & Stubbe, J. Products of the inactivation of ribonucleoside diphosphate reductase from *Escherichia coli* with 2'-azido-2'-deoxyuridine 5'-diphosphate. *Biochemistry* **26**, 3408-16 (1987).

24. Chivers, P.T. et al. Microscopic pK_a values of *Escherichia coli* thioredoxin. *Biochemistry* **36**, 14985-91 (1997).

25. Russel, M. & Model, P. Direct cloning of the *trxB* gene that encodes thioredoxin reductase. *J. Bacteriol.* **163**, 238-42 (1985).

26. Salowe, S. et al. Alternative model for mechanism-based inhibition of *Escherichia coli* ribonucleotide reductase by 2'-azido-2'-deoxyuridine 5'-diphosphate. *Biochemistry* **32**, 12749-60 (1993).

27. Artin, E. et al. Insight into the mechanism of inactivation of ribonucleotide reductase by gemcitabine 5'-diphosphate in the presence or absence of reductant. *Biochemistry* **48**, 11622-9 (2009).

28. Bollinger, J.M., Jr. et al. Use of rapid kinetics methods to study the assembly of the diferric-tyrosyl radical cofactor of *E. coli* ribonucleotide reductase. *Methods Enzymol.* **258**, 278-303 (1995).

29. Fish, W.W. Rapid colorimetric micromethod for the quantitation of complexed iron in biological samples. *Methods Enzymol.* **158**, 357-64 (1988).

30. Steeper, J.R. & Steuart, C.D. A rapid assay for CDP reductase activity in mammalian cell extracts. *Anal. Biochem.* **34**, 123-30 (1970).

31. Hristova, D., Wu, C.H., Jiang, W., Krebs, C. & Stubbe, J. Importance of the maintenance pathway in the regulation of the activity of *Escherichia coli* ribonucleotide reductase. *Biochemistry* **47**, 3989-99 (2008).

32. Young, T.S., Ahmad, I., Yin, J.A. & Schultz, P.G. An enhanced system for unnatural amino acid mutagenesis in *E. coli*. *J. Mol. Biol.* **395**, 361-74 (2010).

33. Leslie, A.G.W. *Joint CCP4 and ESF-EACBM Newsletter* **26** (1992).

34. Collaborative Computational Project, N. The CCP4 suite: programs for protein crystallography. *Acta Crystallogr. D: Biol. Crystallogr.* **50**, 760-3 (1994).

35. Jones, T.A., Zou, J.Y., Cowan, S.W. & Kjeldgaard, M. Improved methods for building protein models in electron density maps and the location of errors in these models. *Acta Crystallogr. A* **47**, 110-9 (1991).

36. Seyedsayamdost, M.R. Massachusetts Institute of Technology (2007).

37. Seyedsayamdost, M.R., Argirevic, T., Minnihan, E.C., Stubbe, J. & Bennati, M. Structural examination of the transient 3-aminotyrosyl radical on the PCET pathway of *E. coli* ribonucleotide reductase by multifrequency EPR spectroscopy. *J. Am. Chem. Soc.* **131**, 15729-38 (2009).

38. Aberg, A. et al. Evidence for two different classes of redox-active cysteines in ribonucleotide reductase of *Escherichia coli*. *J. Biol. Chem.* **264**, 12249-52 (1989).

39. Larsson, A. & Reichard, P. Enzymatic synthesis of deoxyribonucleotides. X. Reduction of purine ribonucleotides; allosteric behavior and substrate specificity of the enzyme system from *Escherichia coli* B. *J. Biol. Chem.* **241**, 2540-9 (1966).

40. Licht, S.S., Booker, S. & Stubbe, J. Studies on the catalysis of carbon-cobalt bond homolysis by ribonucleoside triphosphate reductase: evidence for concerted carbon-cobalt bond homolysis and thiyl radical formation. *Biochemistry* **38**, 1221-33 (1999).

41. Patel, A.D., Nocek, J.M. & Hoffman, B.M. Kinetic-dynamic model for conformational control of an electron transfer photocycle: mixed-metal hemoglobin hybrids. *J .Phys. Chem. B* **112**, 11827-37 (2008).

42. Yokoyama, K., Uhlin, U. & Stubbe, J. A hot oxidant, 3-NO2Y_{122} radical, unmasks conformational gating in ribonucleotide reductase. *J. Am. Chem. Soc.* **132**, 15368-79 (2010).

43. Licht, S.S., Lawrence, C.C. & Stubbe, J. Class II ribonucleotide reductases catalyze carbon-cobalt bond reformation on every turnover. *J. Am. Chem. Soc.* **121**, 7463-8 (1999).

44. Madej, E. & Wardman, P. The oxidizing power of the glutathione thiyl radical as measured by its electrode potential at physiological pH. *Arch. Biochem. Biophys.* **462**, 94-102 (2007).

45. Licht, S. & Stubbe, J. Mechanistic investigations of ribonucleotide reductases. *Compr. Nat. Prod. Chem.* **5**, 163-203 (1999).

46. Yokoyama, K., Smith, A.A., Corzilius, B., Griffin, R.G. & Stubbe, J. Equilibration of tyrosyl radicals (Y356•, Y731•, Y730•) in the radical propagation pathway of the

Escherichia coli class Ia ribonucleotide reductase. *J. Am. Chem. Soc.* **133**, 18420-32 (2011).

47. Seyedsayamdost, M.R., Yee, C.S. & Stubbe, J. Use of 2,3,5-F_3Y-β2 and 3-NH_2Y-α2 to study proton-coupled electron transfer in *Escherichia coli* ribonucleotide reductase. *Biochemistry* **50**, 1403-11 (2011).

Chapter 3

Use of 3-aminotyrosine to examine pathway dependence of radical propagation in *Escherichia coli* ribonucleotide reductase

Adapted in part from: Minnihan, E.C., Seyedsayamdost, M.R., and Stubbe, J. *Biochemistry*, **2009**, *48*, 12125-12132.

3.1 INTRODUCTION

As introduced in Chapters 1 and 2, the class I ribonucleotide reductases are the only known enzymes whose physiological function requires long-range radical propagation, with the tyrosyl radical (Y_{122}•) in the β2 subunit mediating the oxidation of a cysteine (C_{439}) in the α2 subunit 35 Å removed in the *E. coli* class Ia RNR.[1,2] Upon binding of substrate (S) and allosteric effector (E), the rapid, reversible oxidation is thought to occur in a pathway-dependent fashion through a series of aromatic amino acids (Figure 3.1). This provocative mechanism was first proposed by Uhlin and Eklund on the basis of a docking model of the α2β2 complex and on the strict conservation of the residues in primary sequence alignments.[1] Mutagenesis studies in which each of the residues was replaced individually by F demonstrated their importance in catalysis, structure, or both.[3-6] However, despite the appeal of a conserved PCET pathway, evidence in support of transient radical intermediates in RNR has been challenging to obtain because the reaction in the wt enzyme is rate-limited by conformational changes associated with the generation of the active α2β2/S/E quaternary complex.[7]

Only with the advent of technology for the site-specific incorporation of unnatural amino acids into β2 and α2 has the involvement of the three tyrosines (356 in β2, 731 and 730 in α2, Figure 3.1) been implicated, the distance of the individual oxidation "steps" measured, and the mechanistic underpinnings of long-range PCET examined.[8-12] From these collective studies, we have proposed that radical propagation occurs via orthogonal PCET in the β2 subunit, with the proton transferring off-pathway to an amino acid acceptor or to solvent, and via co-linear PCET in the α2 subunit, with both proton and electron transferring between the same donor/acceptor pair.[2,8]

In Chapter 2, we demonstrated the site-specific incorporation of 3-aminotyrosine (NH_2Y) into the α2 and β2 subunits at the site of each conserved pathway Y. SF UV-vis and EPR studies revealed that NH_2Y• is generated in a nucleotide-dependent manner with multiphasic kinetics, and that the rates of formation are maximized when substrate and effectors are bound.[8,13] In addition, the studies described in Chapter 2 indicated that NH_2Y-RNRs are capable of supporting nucleotide reduction, suggesting that the observed NH_2Y• at each position is an intermediate on the proposed reaction pathway.

On the basis of differential pulsed voltammetry measurements on *o*-aminophenol,[14] we estimate that NH_2Y ($E^{\circ\prime}$ ~0.64 V, pH 7) is easier to oxidize than Y by at least 190 mV at pH 7 in aqueous solution, though differences in the literature values for the peak potential of Y (0.83-0.93 V, pH 7) suggest that the ΔE may be even greater.[13-15] From a thermodynamic perspective, the detection of NH_2Y• in NH_2Y-RNRs may not be entirely surprising. Thus, it was necessary to establish the pathway dependence of NH_2Y• formation in NH_2Y-RNRs (Figure 3.1). To provide further support for a defined pathway, F has been incorporated in place of each Y in the pathway to function as a block of NH_2Y• formation. Incubation of Y_{356}F-β2:$Y_{731}NH_2Y$-α2, Y_{356}F-β2:$Y_{730}NH_2Y$-α2, or wt-β2:Y_{731}F/$Y_{730}NH_2Y$-α2 with CDP/ATP completely blocks NH_2Y oxidation, supporting the importance of a specific pathway. As a further test of the pathway dependence, the residue Y_{413} was selected for site-specific "off-pathway" NH_2Y incorporation due to its proximity to Y_{731} and Y_{730} in α2. Analogous studies were conducted with wt-β2:$Y_{413}NH_2Y$-α2, wt-β2:Y_{731}F/$Y_{413}NH_2Y$-α2, and Y_{356}F-β2:$Y_{413}NH_2Y$-α2 in which evidence for NH_2Y• formation was sought by SF UV-vis and EPR spectroscopies. The results of these experiments establish that functional long-range PCET in RNR occurs via an optimized pathway of amino acids spanning >35 Å across the α:β interface.

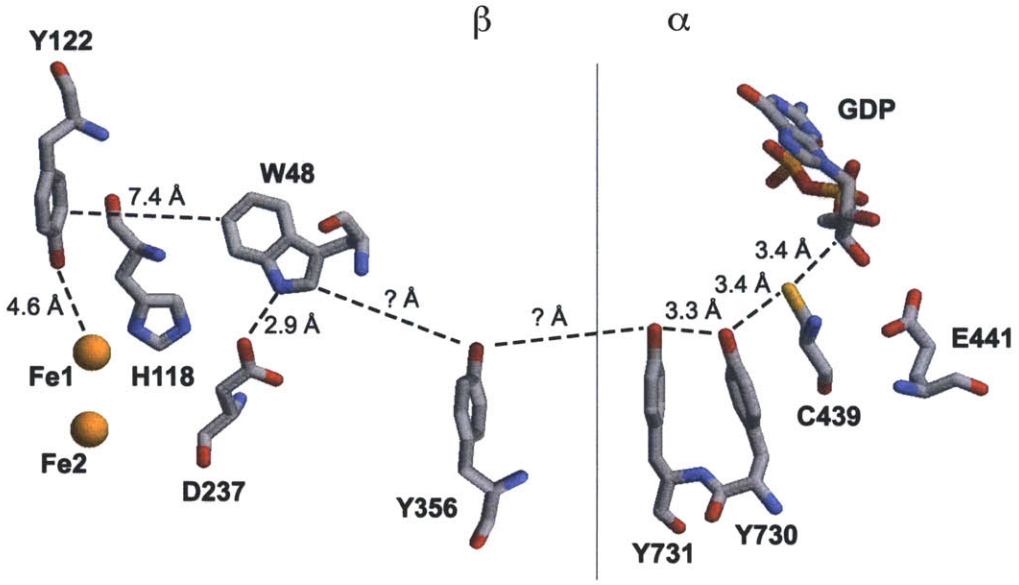

Figure 3.1 The proposed radical propagation pathway within an α:β pair of *E. coli* RNR. Y_{356}, Y_{731}, and Y_{730} have been shown to be redox-active during radical transfer and their positions within the complex have been determined structurally[1] and/or experimentally.[12] Y_{356} is located in the structurally disordered C-terminal tail of β,[16] and thus its location in the complex is not known.

3.2 MATERIALS AND METHODS

3.2.1 Materials. The expression and purification of wt-α2 (2500 nmol/min/mg), wt-β2 (1.2 Y_{122}•/dimer, 7600 nmol/min/mg), $Y_{731}NH_2Y$-α2 (150 nmol/min/mg), $Y_{730}NH_2Y$-α2 (110 nmol/min/mg), His-Y_{356}F-β2 (1.0-1.2 Y_{122}•/dimer, <1 nmol/min/mg), and Y_{730}F-α2 (<25 nmol/min/mg) were conducted as previously described.[8,17] His-Y_{356}F-β2 will be referred to as "Y_{356}F-β2" henceforth. *E. coli* thioredoxin (TR, 40 units/mg) and thioredoxin reductase (TRR, 1400 units/mg) were isolated as previously described.[17] [5-^{3}H]-CDP (15 Ci/mmol) was purchased from ViTrax (Placentia, CA). Assay buffer is 50 mM Hepes, 15 mM $MgSO_4$, 1 mM EDTA, pH 7.6.

3.2.2 Generation of pTrc-nrdA-$TAG_{730}TTT_{731}$, pTrc-nrdA-TAG_{413} and pTrc-nrdA-$TAG_{413}TTT_{731}$. The Quikchange Kit (Stratagene) was used according to manufacturer's instructions to generate pTrc-*nrdA*-$TAG_{730}TTT_{731}$, pTrc-*nrdA*-TAG_{413} and pTrc-*nrdA*-$TAG_{413}TTT_{731}$. To generate pTrc-*nrdA*-$TAG_{730}TTT_{731}$, the template, pTrc-*nrdA*-TAG_{730},[8] was amplified in the presence of the forward primer 5'-TTC GGG GTC AAA ACA CTG TAG TTT CAG AAC ACC CGT GAC GGC GCT-3') and its reverse complement to insert a TTT codon (F) at residue 731. To generate pTrc-*nrdA*-TAG_{413}, the template, pTrc-*nrdA*-wt, was amplified in the presence of forward primer 5'-GCG TCT ACC GGT CGT ATC TAG ATT CAG AAC GTT GAC CAC TGC-3') and its reverse complement to insert the amber stop codon (TAG) at residue 413. pTrc-*nrdA*-$TAG_{413}TTT_{731}$ was then generated from pTrc-*nrdA*-TAG_{413}, with forward primer 5'-C GGG GTC AAA ACA CTG TAT TTT CAG AAC ACC CGT GAC G-3') and its reverse complement to insert a TTT codon (F) at residue 731. For each plasmid, the mutation(s) was confirmed by sequencing the entire gene at the MIT Biopolymers Laboratory.

3.2.3 Expression, purification, and activity determination of $Y_{731}F/Y_{730}NH_2Y$-α2. $Y_{731}F/Y_{730}NH_2Y$-α2 was expressed, purified, and pre-reduced as described for $Y_{730}NH_2Y$-α2 and $Y_{731}NH_2Y$-α2.[8] *E. coli* DH10B cells (Invitrogen) were co-transformed with pTrc-*nrdA*-$TAG_{730}TTT_{731}$ and pAC-NH_2Y and plated on LB-agar plates supplemented with 100 μg/mL Amp and 25 μg/mL Tet at 37 °C. After 2 days, single colonies were harvested and inoculated into 8 mL of 2xYT rich medium with 100 μg/mL Amp, 25 μg/mL Tet and set to grow at 37 °C, 225 rpm. After reaching saturation (~24 h), the saturated small culture (~5 mL) was inoculated into a fresh 2xYT (300 mL) with the same antibiotic. This culture was grown at 37 °C, 225 rpm until reaching saturation (~24 h). Enriched GMML[8] (10L, in fermentor) with the appropriate antibiotics was inoculated with 250 mL of saturated 2xYT culture (1:40 dilution). The culture was grown at 37 °C, 225 rpm with 10 psi air until reaching an OD_{600} ~0.7, at which point NH_2Y (Sigma) and DTT (Promega) were added to the culture to final concentrations of 1 mM and 0.1 mM, respectively. After 15 min, the culture was induced with 1 mM IPTG. The cells were allowed to grow for an additional 5 h (OD_{600}, final ~1.3), then harvested by centrifugation (10,000 × *g*, 10 min, 4 °C) to give 2 g cell paste / L culture.

Cells were resuspended in buffer A (50 mM Tris, 1 mM EDTA, 5% glycerol, pH 7.6) with 1.0 mM PMSF and 5 mM DTT at 5 mL buffer/g of cell paste, homogenized, and lysed via passage though a French pressure cell at 14,000 psi. Cell debris was cleared by centrifugation (15,000 × *g*, 40 min, 4 °C), and the resulting pellet discarded. To the supernatant was added 0.2 volumes of an 8% w/v streptomycin sulfate solution over 15 min with stirring at 4 °C. The resulting solution was allowed to stir for an additional 15 min, then precipitated DNA was cleared by centrifugation (15,000 × *g*, 35 min, 4 °C). To the supernatant was added solid ammonium sulfate to 66% saturation (39 g/L) over 20 min with stirring at 4 °C. The solution

was allowed to stir for an additional 30 min, and the protein was pelleted by centrifugation (15,000 × *g*, 40 min, 4 °C). The pellet was resuspended in a minimum volume of buffer A with PMSF and DTT, and desalted on a Sephadex G-25 column (1 L) equilibrated in the same buffer. Protein-containing fractions were pooled and loaded directly onto a dATP affinity column (100 mL) at a rate of 1.5 mL/min. The column was washed until no further protein was eluting (as judged by Bradford assay), then the desired protein was eluted with a solution of 10 mM ATP in buffer A with 10 mM DTT. Protein-containing fractions were determined by Bradford assay, and concentrated with an Amicon Ultrafiltration device with a YM-30 cellulose membrane. The protein was desalted on a Sephadex G-25 column (1 L) equilibrated in buffer A with 10 mM DTT. The resulting protein was concentrated, flash-frozen in liquid N_2, and stored at -80 °C. By this method, 3 mg of $Y_{731}F/Y_{730}NH_2Y$-α2 /g cell paste was obtained.

The protein was then subjected to HU treatment and pre-reduction following standard lab protocol.[8] To the protein was added DTT in buffer A to a final concentration of 35 mM. The resulting mixture was incubated at room temperature (RT) with gentle agitation for 40 min. HU and additional DTT were added to final concentrations of 15 mM, and the protein solution was incubated at RT with gentle agitation for an additional 20 min. The protein was desalted on G-25 Sephadex (250 mL) equilibrated in assay buffer. The protein-containing fractions were pooled and concentrated on the desktop centrifuge (5,000 × *g*, 4 °C) with a YM-30 cellulose membrane (Amicon) to give the desired protein in 80% recovery.

Specific activity was determined by the radioactive RNR assay as described in Chapter 2 and elsewhere.[9] Assays were conducted with mutant α2 and wt β2 at concentrations of 0.5 μM and 2.5 μM, respectively, in assay buffer at 25 °C. [5-^{3}H]-CDP had a specific activity of 1450

cpm/nmol. The reaction product was dephosphorylated by treatment with alkaline phosphatase and the resulting dC was quantitated by the method of Steeper and Steuart.[18]

3.2.4 Expression, purification, and activity determination of $Y_{413}NH_2Y$-α2 and $Y_{731}F/Y_{413}NH_2Y$-α2. $Y_{413}NH_2Y$-α2 and $Y_{731}F/Y_{413}NH_2Y$-α2 were expressed and purified as described for $Y_{730}NH_2Y$-α2 and $Y_{731}NH_2Y$-α2[8] and $Y_{731}F/Y_{730}NH_2Y$-α2 (section 3.2.3). However, an additional step using a Poros HQ/20 FPLC anion exchange column (Applied Biosystems, 1.6 × 10 cm, 20 mL) was required to obtain protein of >95% purity as judged by SDS-PAGE. The column was equilibrated in 50 mM Tris, 1 mM EDTA, and 5 mM DTT, pH 7.6 and was loaded with 15-20 mg of $Y_{413}NH_2Y$-α2 or $Y_{731}F/Y_{413}NH_2Y$-α2. The column was washed with one column volume (CV) of equilibration buffer at a flow rate of 4 mL/min, then eluted with a linear gradient of 100 to 500 mM NaCl (60 mL × 60 mL) in the same buffer at the same flow rate. In the case of $Y_{731}F/Y_{413}NH_2Y$-α2, the protein was chromatographed twice. Subsequent to the FPLC purification step, the protein was pre-reduced according to the standard procedure.[8]

The activities of $Y_{413}NH_2Y$-α2 and $Y_{731}F/Y_{413}NH_2Y$-α2 were determined using the spectrophotometric[17] and/or radioactive assays[9] as described in section 2.2.7 with minor modifications. Mutant α2s (0.1 or 0.2 μM) were assayed in the presence of a 5-fold excess of β2 (0.5 μM or 1.0 μM) in assay buffer at 25 °C. [5-^{3}H]-CDP had activity between 2700 and 4800 cpm/nmol.

3.2.5 Determination of the K_d for $Y_{413}NH_2Y$-α2 and β2 interaction. The K_d between $Y_{413}NH_2Y$-α2 and wt β2 was determined using $Y_{730}F$-α2 as a competitive inhibitor of nucleotide reduction.[11,19] $Y_{413}NH_2Y$-α2 (0.7 μM) and β2 (0.35 μM) were incubated with CDP (1 mM), ATP (1.6 mM), TR (50 μM), TRR (1 μM), and NADPH (0.2 mM) in assay buffer. Inhibition of

RNR activity (as measured by decrease in NADPH consumption) was determined in the presence of increasing $Y_{730}F$-α2 (0.1 μM to 3 μM). The data analysis for this procedure typically relies on the mutant α2 of unknown K_d acting as the inhibitor of nucleotide reduction, as described previously[11] and in section 5.2.2 The analysis was modified, as the K_d of the active $Y_{413}NH_2Y$-α2 is not known, whereas the K_d of the inhibitor ($Y_{730}F$-α2, 0.075 μM) for wt-β2 had been previously determined under conditions in which the K_i and K_d of the inhibitor are equivalent.[4] The K_d for the $Y_{413}NH_2Y$-α2:wt-β2 complex was approximated and the experimentally determined relative activities were then used to extrapolate the K_d for the $Y_{730}F$-α2:wt-β2 complex. The K_d for $Y_{413}NH_2Y$-α2 was refined by iterative fitting of the experimental data until the fit yielded a K_d for $Y_{730}F$-α2 that was in good agreement with the literature value.

3.2.6 Reaction of NH_2Y-α2s with $Y_{356}F$-β2 monitored by EPR spectroscopy. EPR (9 GHz) analysis of the reaction between pre-reduced $Y_{730}NH_2Y$-α2 (or $Y_{731}NH_2Y$-α2) and $Y_{356}F$-β2, CDP, and ATP in assay buffer at 25 °C was conducted by Dr. Mohammad Seyedsayamdost as previously described.[20]

3.2.7 Reaction of $Y_{356}F$-β2 with $Y_{730}NH_2Y$-α2 (or $Y_{731}NH_2Y$-α2) monitored by SF UV-vis spectroscopy. SF kinetics were performed on an Applied Photophysics DX 17MV instrument equipped with the Pro-Data upgrade. Pre-reduced $Y_{730}NH_2Y$-α2 (or $Y_{731}NH_2Y$-α2) and ATP were mixed with $Y_{356}F$-β2 and CDP to yield final concentrations of 8 μM, 3 mM, 8 μM and 1 mM, respectively, in assay buffer at 25 °C. The concentrations of Y_{122}•, NH_2Y_{731}• and NH_2Y_{730}• were monitored at 410 nm (ε = 3,700 M^{-1} cm^{-1}), 320 nm (ε = 11,000 $M^{-1}cm^{-1}$) and 325 nm (ε = 10,500 M^{-1} cm^{-1}), respectively, using PMT detection. In each experiment, 5–7 traces were averaged and kinetic parameters obtained by curve fitting using OriginPro or Kaleidagraph software. Iterative rounds of fitting were carried out until both the residual plot and the r^2

correlation value were optimized. The SF UV-vis experiments between $Y_{356}F$-β2 and $Y_{730}NH_2Y$-α2 (or $Y_{731}NH_2Y$-α2) were conducted by Dr. Mohammad Seyedsayamdost.

3.2.8 Reaction of $Y_{731}F/Y_{730}NH_2Y$-α2, $Y_{413}NH_2Y$-α2, and $Y_{731}F/Y_{413}NH_2Y$-α2 with wt-β2 monitored by EPR and SF UV-vis spectroscopies. For EPR analysis, pre-reduced $Y_{731}F/Y_{730}NH_2Y$-α2, $Y_{413}NH_2Y$-α2, or $Y_{731}F/Y_{413}NH_2Y$-α2 (50 μM, final concentration) was mixed with wt-β2 (50 μM, 1.2 Y•/β2), CDP (1 mM), and ATP (3 mM) in assay buffer at 25 °C. The reactions were quenched at 40 s by hand in liquid N_2. EPR spectra were recorded at 77 K on a Bruker EMX X-band spectrometer equipped with a quartz finger dewar containing liquid N_2 in the Department of Chemistry Instrumentation Facility. EPR parameters were as follows: microwave frequency = 9.34 GHz, power = 32 μW, modulation amplitude = 1.5 G, modulation frequency = 100 kHz, time constant = 5.12 ms, scan time = 41.9 s. EPR spin quantitation was carried out in WinEPR (Bruker) using Cu^{II} as a standard.[21] EPR subtractions were conducted with an in-house, Excel-based program using the spectrum of Y_{122}• from either wt β2 or a wt-β2:mutant-α2 complex as a reference.

For SF UV-vis analysis, pre-reduced $Y_{731}F/Y_{730}NH_2Y$-α2, $Y_{413}NH_2Y$-α2, or $Y_{731}F/Y_{413}NH_2Y$-α2 (5 μM, final concentration) was reacted with wt β2 (5 μM) in the presence of CDP (1 mM) and ATP (3 mM) at 25 °C as described in section 3.2.7.

3.3 RESULTS

3.3.1 Reaction of $Y_{730}NH_2Y$-α2 (or $Y_{731}NH_2Y$–α2) with $Y_{356}F$-β2 monitored by EPR and SF spectroscopies. It was previously demonstrated that reaction of either $Y_{730}NH_2Y$-α2 or $Y_{731}NH_2Y$-α2 with wt-β2, CDP, and ATP resulted in the loss of Y_{122}• (λ_{max} = 410 nm, g_{av} of 2.0047) concomitant with formation of a new radical species, assigned as NH_2Y• on the basis of its absorbance and EPR spectroscopic features (λ_{max} = 320-325 nm, g_{av} of 2.0043).[8] As described in the previous chapter, an analogous result was obtained in the reaction of $Y_{356}NH_2Y$-β2 with wt-α2, CDP, and ATP.[13] In this chapter, experiments in which the radical propagation pathway is disrupted with a Y to F mutation are described. The results of these experiments establish that trapping of NH_2Y• at residues 730 and 731 is the result of the participation of these residues in radical transfer, rather than the consequence of introducing a pathway-independent thermodynamic trap into α2.

First, the reaction of $Y_{730}NH_2Y$-α2 (or $Y_{731}NH_2Y$-α2) with $Y_{356}F$-β2 was examined. If formation of NH_2Y_{730}• (or NH_2Y_{731}•) requires a redox-active Y_{356} residue, then no NH_2Y• should be observed. The reactions of $Y_{356}F$-β2, $Y_{730}NH_2Y$-α2 (or $Y_{731}NH_2Y$-α2), CDP, and ATP, quenched at 77 K after 20 s and 2 min and monitored by EPR spectroscopy, have been reported previously.[20] Analysis of the EPR spectra, subsequent to subtraction of the spectrum of the resting Y_{122}• at time zero, gave no evidence of NH_2Y• at either time point for reactions with $Y_{730}NH_2Y$-α2 or with $Y_{731}NH_2Y$-α2 (Figure 3.2, A and B). In addition, spin quantitation of the signal at t = 0 in comparison to t = 20 s and 2 min revealed no significant loss of spin. A control with non-tagged $Y_{356}F$-β2 gave the same result as that observed with His-$Y_{356}F$-β2, demonstrating that the His-tag does not interfere with radical formation.

To determine if NH_2Y• was formed transiently, the reactions of NH_2Y-α2s with $Y_{356}F$-β2, CDP, and ATP were monitored by SF UV-vis spectroscopy at 325 nm (λ_{max} of NH_2Y_{730}•) or 320 nm (λ_{max} of NH_2Y_{731}•) and at 410 nm (λ_{max} of Y_{122}•). The results for $Y_{730}NH_2Y$-α2 and $Y_{731}NH_2Y$-α2 with $Y_{356}F$-β2 are shown in Figure 3.3, A and B. A small increase at 325 (320 nm) corresponding to ~2 % of total initial Y_{122}• was observed. However, these spectral changes were not correlated with the expected decrease in absorbance at 410 nm due to loss of the Y•. In fact, a small increase in this wavelength was observed (Figure 3.3, blue insets). The lack of correspondence between the spectral changes at 325 (or 320) nm and 410 nm indicates these features are not related to NH_2Y• formation. The nature of these changes is not understood at present, but similar changes have been observed previously under different reaction conditions[20] and may be related to minor structural changes of the Y_{122}• diferric cluster upon α2β2 complex formation. The SF UV-vis and EPR spectroscopic data together indicate that no NH_2Y• is formed at residues 730 or 731 with $Y_{356}F$-β2, with our lower limit of detection approximated as less than 2% (by SF UV-vis) and less than 3% (by EPR) of the total initial Y_{122}•. These data support the conclusion that a redox-active residue at 356 is essential for radical transfer into α2.

3.3.2 Reaction of $Y_{731}F/Y_{730}NH_2Y$-α2 with wt-β2 monitored by EPR and SF spectroscopies. To assess the role of residue Y_{731} in the radical transfer chain, the double mutant $Y_{731}F/Y_{730}NH_2Y$-α2 was isolated, characterized, and examined for NH_2Y• formation. The protein was purified to homogeneity and its specific activity measured to be 36 nmol/min/mg. This low activity, approximately 1.4% that of the wild-type enzyme, is likely associated with co-purifying endogenous α2, rather than activity inherent to the mutant protein. This result is in agreement with the activity of $Y_{731}F$-α2 (26 nmol/min/mg) and contrasts to activities measured in $Y_{730}NH_2Y$-α2 or $Y_{731}NH_2Y$-α2 (155-175 nmol/min/mg).[13,20]

$Y_{731}F/Y_{730}NH_2Y$-α2 and ATP were mixed with wt-β2 and CDP and the reaction examined by EPR and SF UV-vis spectroscopy. With EPR, the reactions were quenched at 40 s or 2 min and analyzed as described above. No NH_2Y• formation was detected in either case and the total spin relative to starting Y_{122}• remained unchanged (Figure 3.2 C). The SF UV-vis experiments gave results similar to those observed with $Y_{356}F$-β2 at both 325 nm and 410 nm (Figure 3.3 C). Thus, formation of NH_2Y_{730}• also requires a redox-active Y_{731} for radical propagation.

Figure 3.2 Reaction of $Y_{730}NH_2Y$-α2 and $Y_{356}F$-β2 (A), $Y_{731}NH_2Y$-α2 and $Y_{356}F$-β2 (B), or $Y_{731}F/Y_{730}NH_2Y$-α2 and wt-β2 (C) with CDP and ATP hand quenched at 77 K at 20-40 s and monitored by EPR spectroscopy. The residual Y_{122}• signal (blue) was subtracted from the composite reaction spectrum (black) to give a difference spectrum (red). The inset gives an expanded view of the difference spectrum. No NH_2Y• is observed in any case. Reactions (A) and (B) were conducted by Dr. Mohammad Seyedsayamdost and reported previously.[20]

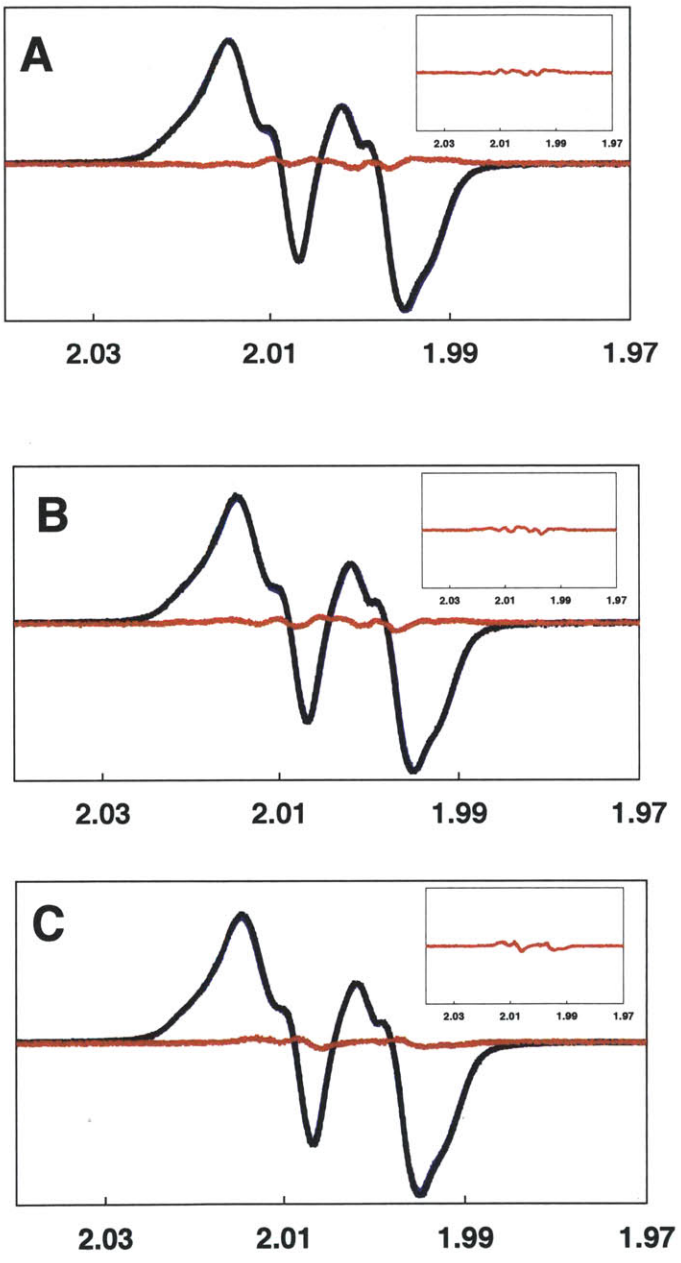

Figure 3.3 Reaction of $Y_{730}NH_2Y$-α2 and $Y_{356}F$-β2 (A), $Y_{731}NH_2Y$-α2 and $Y_{356}F$-β2 (B), or $Y_{731}F/Y_{730}NH_2Y$-α2 and wt-β2 (C) monitored by SF UV-vis spectroscopy at 25 °C. Each reaction was monitored at 325 or 320 nm (red trace, λ_{max} of NH_2Y_{730}• and NH_2Y_{731}•, respectively) and at 410 nm (blue trace, λ_{max} of Y_{122}•). Insets show magnified views of the initial 0.5 s of each trace. Reactions (A) and (B) were conducted by Dr. Mohammad Seyedsayamdost.

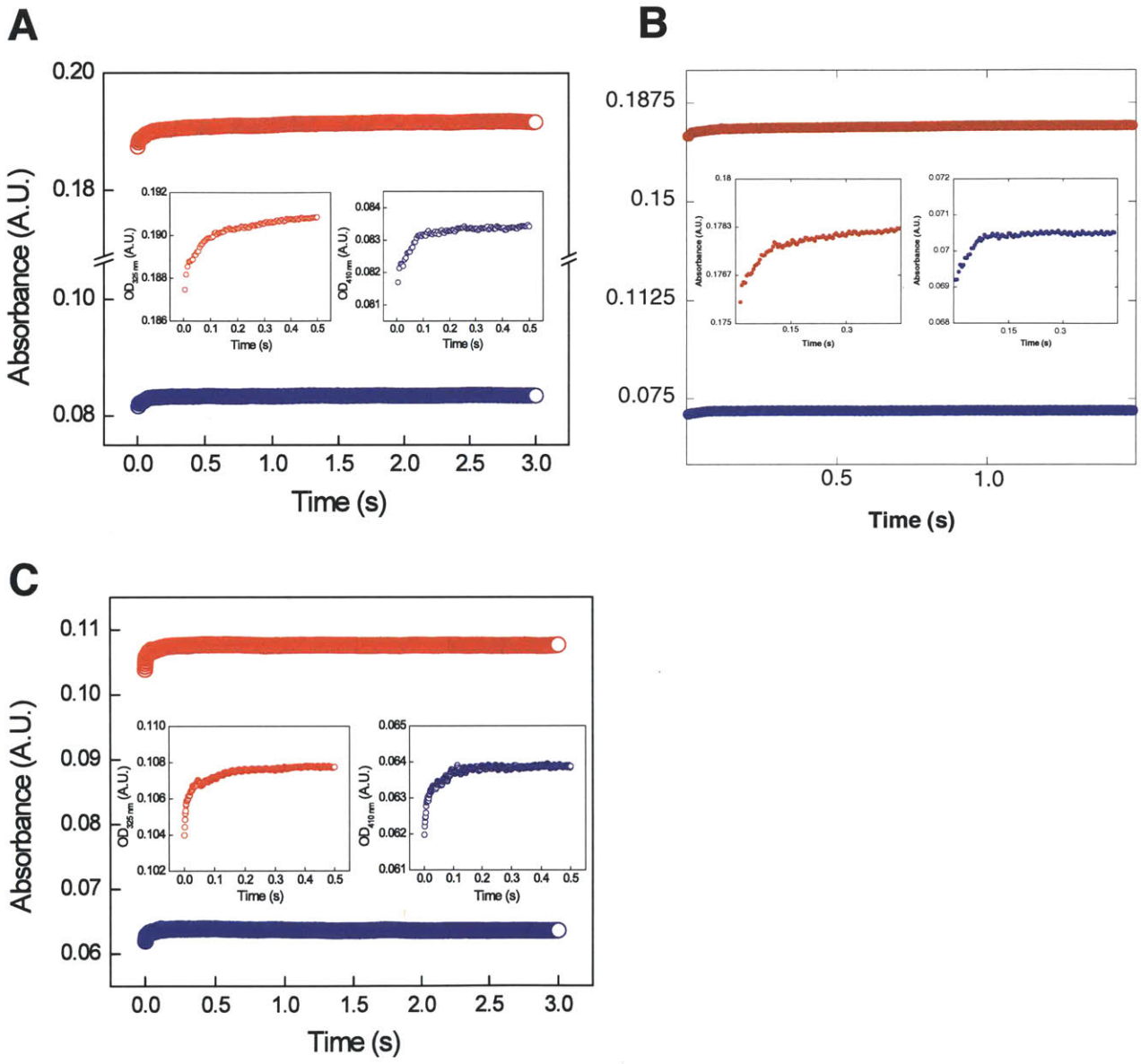

3.3.3 Expression, purification, and characterization of $Y_{413}NH_2Y$-α2 and $Y_{731}F/Y_{413}NH_2Y$-α2. As an additional test of the pathway dependence of NH_2Y• formation at Y_{730} and Y_{731}, NH_2Y was site-specifically incorporated at a Y in α2 that is not thought to participate in the radical transfer pathway (Figure 3.1). Residue Y_{413} was selected, as the X-ray structure of *E. coli* α2[1] reveals distances of 5.0 Å or 5.2 Å between the phenolic oxygen of Y_{413} and that of Y_{730} or Y_{731}, respectively (Figure 3.4). Thus, Y_{413} is a distance from Y_{730} and Y_{731} that is reasonable for ET between these residues. Y_{731} and Y_{730} are separated by 3.3 Å in the same structure. Alignment of 142 primary sequences of class Ia/b α subunits reveals that while 413 is not conserved, it is always an aromatic amino acid. Y, F, and W occupy this position 65%, 21%, and 14% of the time, respectively. Thus, the proteins $Y_{413}NH_2Y$-α2 and $Y_{731}F/Y_{413}NH_2Y$-α2 were studied to look for evidence of off-pathway NH_2Y• formation.

$Y_{413}NH_2Y$-α2 and $Y_{731}F/Y_{413}NH_2Y$-α2 were expressed in a fashion analogous to other NH_2Y-RNRs (Figure 3.5 A, lanes 2 and 3). Their purification, however, proved more difficult than for previous NH_2Y-sustituted α2s. In both cases, a significant lower molecular weight contaminant co-purified with the desired protein after dATP affinity chromatography (Figure 3.5 A, lane 5). Analysis of this co-purifying protein by MALDI-MS gave a molecular weight of 52 kDa, thereby eliminating the most obvious candidates for this species, including 412-truncated α (47 kDa) or co-purifying endogenous β (43.5 kDa). Protein of high purity (>90%, as judged by SDS-PAGE, Figure 3.5 A, lanes 6-8) was eventually isolated via anion-exchange FPLC with an optimized salt gradient, but at the expense of overall protein yield (Figure 3.5 B). In the case of $Y_{731}F/Y_{413}NH_2Y$-α2, two sequential FPLC injections were necessary to provide protein of suitable purity.

Figure 3.4 Location of Y_{413} (magenta) in relation to Y_{731} (blue), Y_{730} (blue), and C_{439} (yellow) of the radical propagation pathway within the α subunit. Y_{413} is located 5.0 and 5.2 Å from Y_{730} and Y_{731}, respectively, with distances measured between phenolic oxygens (red). The figure was generated as a PyMol (www.pymol.org) rendition of PDB ID: 1RLR.[1]

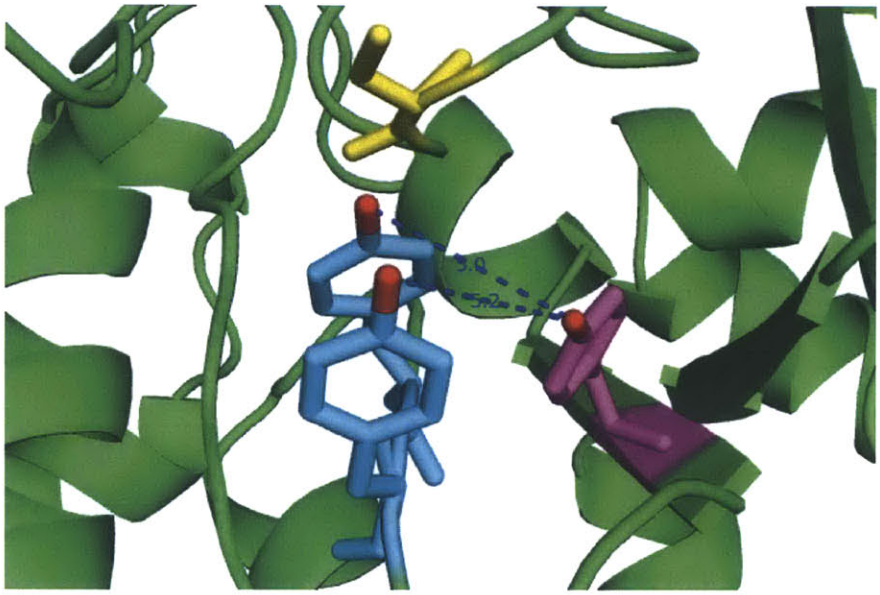

Figure 3.5 Purification of $Y_{413}NH_2Y$-α2. (A) SDS-PAGE (8%) analysis of $Y_{413}NH_2Y$-α2 purification steps. Lanes are as follows: (1) MW marker, (2) pre-induction sample, (3) post induction sample, (4) purified wt α (~0.5 μg), (5) protein after dATP affinity column, (6-8) purified $Y_{413}NH_2Y$-α, ~1, ~2, and ~5 μg, respectively; (B) Protein elution profile during final FPLC chromatography step. The sharp peak at t =19 min was the protein of interest. Linear salt gradient is indicated by the black line.

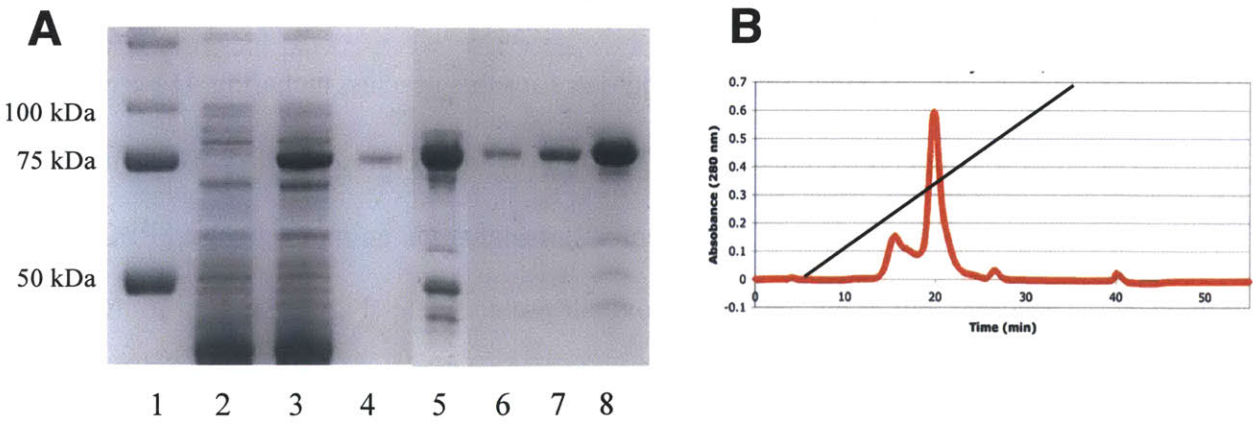

The activities of the purified mutants were determined by the spectrophotometric and/or radioactive RNR assays. The specific activity of $Y_{413}NH_2Y$-α2 was 46% of wt α2 (~1200 nmol/min/mg), while that of $Y_{731}F/Y_{413}NH_2Y$-α2 was 1.9% of wt α2 (~48 nmol/min/mg). The activity of $Y_{731}F/Y_{413}NH_2Y$-α2 is similar to that of $Y_{731}F/Y_{730}NH_2Y$-α2, and is likely associated with endogenous *E. coli* α2 that co-purified with the recombinantly expressed mutant protein.

The reduction in activity of $Y_{413}NH_2Y$-α2 relative to wt α2, the proximity of Y_{413} to the putative α2:β2 interface, and the difficulty encountered in purification of the related mutants provided the impetus to determine the K_d for the interaction between this mutant and β2 using a modified version of the competitive inhibition assay developed by Climent et al.[19] Data analysis was modified relative to the previously published method[11] to accommodate for the condition that the active species, rather than the inhibitor, was also the species of unknown K_d (Figure 3.6). Analysis by this method afforded a K_d of 0.05 μM, similar to the value of 0.06 μM for wt-α2:β2 in the presence of CDP and ATP (Hassan and Stubbe, unpublished results). This finding, in conjunction with the activity of $Y_{413}NH_2Y$-α2, suggests that $Y_{413}NH_2Y$-α2 is folded and that binding between subunits is minimally perturbed. However, attempts to crystallize $Y_{413}NH_2Y$-α2 under conditions optimized for wt-α2 and successfully used to crystallize other NH_2Y-α2 mutants failed to provide crystals of $Y_{413}NH_2Y$-α2, suggesting that mutation of Y_{413} produces some effect on protein stability or solubility. Instead, a small amount of wt-α2 that co-purified with the mutant protein (<2% contamination) was selectively crystallized under these conditions (Ulla Uhlin, personal communication). Indeed, there is structural evidence for Y_{413} participating in an extended hydrogen-bonding network with Y_{730} via an intervening ordered water.[1,13] More recently, high-field ENDOR of NH_2Y_{730}• in $Y_{730}NH_2Y$-α2 has provided spectroscopic evidence for the relevance of this hydrogen-bonding network during long-range radical propagation.[22]

Figure 3.6 The K_d of the wt-β2:$Y_{413}NH_2Y$-α2 complex was determined using $Y_{730}F$-α2 as a competitive inhibitor of nucleotide reduction. The previously-determined K_d for wt-β2:$Y_{730}F$-α2 was used as a measure of the validity of the approximated K_d for wt-β2:$Y_{413}NH_2Y$-α2. The K_d for $Y_{413}NH_2Y$-α2 was refined by iterative fitting of the experimental data until a plot of $Y_{730}F$-$\alpha2_{bound}$ vs $Y_{730}F$-$\alpha2_{free}$ (below) yielded a K_d of $Y_{730}F$-α2 that was in good agreement with the literature value.

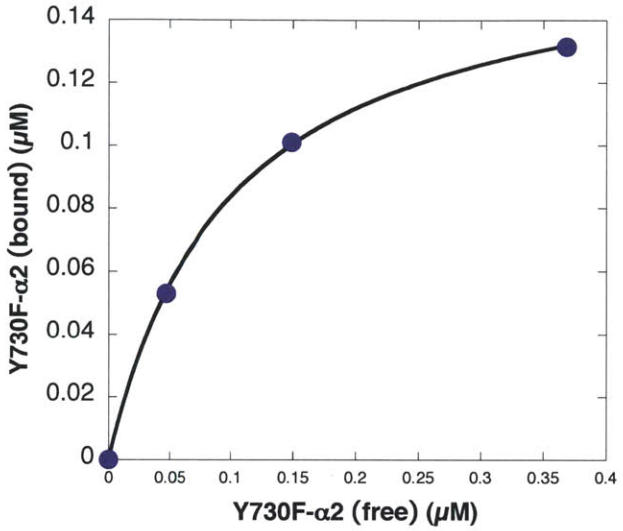

3.3.4 Reaction of $Y_{413}NH_2Y$-α2 or $Y_{731}F/Y_{413}NH_2Y$-α2 with wt-β2, and $Y_{413}NH_2Y$-α2 with $Y_{356}F$-β2 monitored by EPR spectroscopy. EPR experiments were carried out as described above by mixing $Y_{413}NH_2Y$-α2 (or $Y_{731}F/Y_{413}NH_2Y$-α2) with CDP, ATP and wt-β2, or $Y_{413}NH_2Y$-α2 with CDP, ATP, and $Y_{356}F$-β2. Each reaction was quenched at 40 s. The resulting spectra, subsequent to subtraction of the resting Y_{122}• in the mutant-α2:β2 complex, are shown in Figure 3.7, and the spin quantitation of the resulting NH_2Y• is given in Table 3.1. In the reactions of $Y_{413}NH_2Y$-α2 and $Y_{731}F/Y_{413}NH_2Y$-α2 with wt-β2 (Figure 3.7, A and B, respectively), the difference EPR spectrum reveals features characteristic of an NH_2Y•. For the reaction with $Y_{413}NH_2Y$-α2, the signal attributed to NH_2Y• accounts for 12% of the total spin. Differences in the spectral features relative to those previously reported NH_2Y_{730}• and NH_2Y_{731}• cannot be assigned at this stage, but likely report on differences in the dihedral angles of the C_β-protons on

NH_2Y at position 413 versus those at positions 730 and 731. For the reaction with $Y_{731}F/Y_{413}NH_2Y$-α2, the signal attributed to NH_2Y• accounts for 7% of the total spin. The magnitude of the signal in both cases is substantially lower than the "on pathway" radicals, which have been shown by EPR to constitute 53% and 45% of the total spin at the same time point when NH_2Y is incorporated at 730 or 731, respectively.[8] The difference EPR spectrum from the reaction of $Y_{413}NH_2Y$-α2 with $Y_{356}F$-β2 with CDP/ATP quenched at 40 s reveals no detectable NH_2Y• (Figure 3.7, C).

3.3.5 Reaction of $Y_{413}NH_2Y$-α2 or $Y_{731}F/Y_{413}NH_2Y$-α2 with wt-β2 monitored by SF UV-vis spectroscopy. Given the results of the EPR experiments above, the kinetics of formation of the NH_2Y_{413}• were assessed for both $Y_{413}NH_2Y$-α2 and $Y_{731}F/Y_{413}NH_2Y$-α2 using SF UV-vis spectroscopy. The results with $Y_{413}NH_2Y$-α2 and $Y_{731}F/Y_{413}NH_2Y$-α2 are shown in Figure 3.8 A and B, respectively, and are summarized in Table 3.1. For the reaction with $Y_{413}NH_2Y$-α2 monitored at 325 nm, the observed absorbance increase may be fit to biphasic kinetics with rate constants of 26.4 s^{-1} and 4.2 s^{-1}. These phases correspond to 30% and 70%, respectively, of the total absorbance increase observed at 325 nm over the reaction course. The faster phase is not correlated, however, with a decrease at 410 nm, and thus is not associated with NH_2Y• formation.

The $A_{410\ nm}$ decrease can be fit to biphasic kinetics with rate constants of 5.3 s^{-1} and 0.5 s^{-1}, corresponding to 47% and 53% of the total absorbance change at 410 nm during the reaction. The rate constant of 5.3 s^{-1} agrees well with the rate constant of 4.2 s^{-1} at 325 nm, and together suggest the formation of NH_2Y_{413}•. Using the extinction coefficients of NH_2Y• and Y•, the extent of formation of NH_2Y_{413}• was determined to be 8% of the starting Y_{122}•. This is substantially lower than the amount of NH_2Y• observed in SF UV-vis studies with NH_2Y at 730

(39%) and 731 (35%) under analogous reaction conditions.[8] While a rate constant of 4-5 s^{-1} is fast enough to be involved in nucleotide reduction,[7,13] the collective data on the three Y_{413} mutant complexes suggest NH_2Y_{413}• formation is off-pathway and we propose that it is not functionally relevant to catalysis.

For the reaction of $Y_{731}F/Y_{413}NH_2Y$-α2, a slow increase in absorbance at 325 nm was observed concomitant with a loss of absorbance at 410 nm (Figure 3.8 B). The first 30 s of data collected at both wavelengths were fit to a monoexponential function with a rate constant of 0.04 s^{-1}. No fast burst phase was detected at earlier time points. The SF data suggest that 12% of the starting Y_{122}• is converted to NH_2Y_{413}• over the course of 30 s. The slow rate of radical formation, 320 to 475-fold slower than NH_2Y• formation at 730 (13 s^{-1}) or 731 (19 s^{-1}), suggest off-pathway oxidation.

Figure 3.7 Formation of NH_2Y_{413}• monitored by EPR spectroscopy. In each case, CDP and ATP were mixed at 25 °C with (A) wt β2 and $Y_{413}NH_2Y$-α2, (B) wt β2 and $Y_{731}F/Y_{413}NH_2Y$-α2, and (C) $Y_{356}F$-β2 and $Y_{413}NH_2Y$-α2 and quenched at 77 K after 40 s. For each reaction, the residual Y_{122}• signal (blue) was subtracted from the composite reaction spectrum (black) to give a putative NH_2Y_{413}• (red). The inset gives an expanded view of the difference spectrum, which in the case of (A) and (B) corresponds to the putative NH_2Y_{413}•.

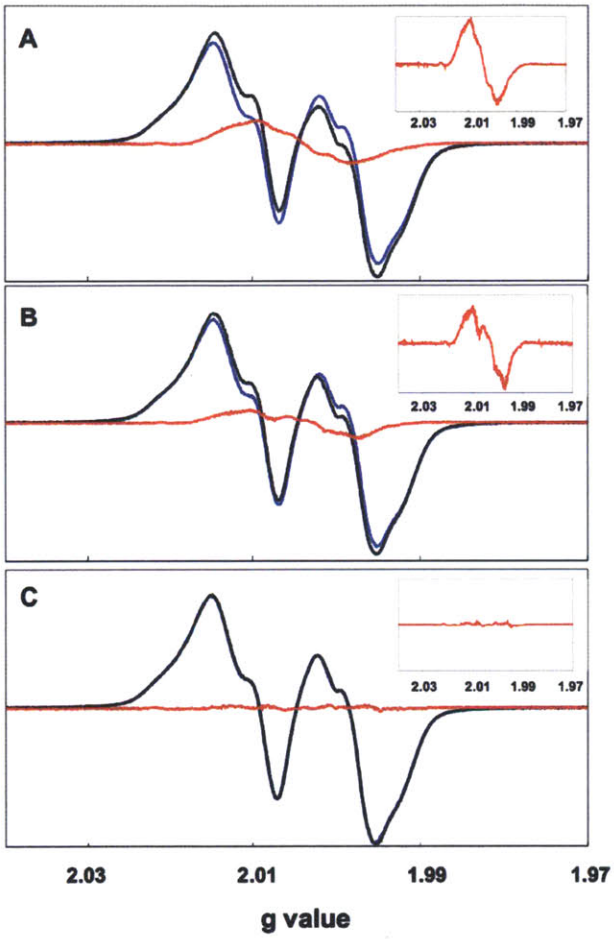

Figure 3.8 Reaction of wt β2, CDP, ATP and (A) $Y_{413}NH_2Y$-α2 or (B) $Y_{731}F/Y_{413}NH_2Y$-α2 monitored by SF UV-vis spectroscopy. The reaction was monitored for an increase at 325 nm (λ_{max} of NH_2Y_{413}•) and a decrease at 410 nm (λ_{max} of Y_{122}•). The reaction with $Y_{413}NH_2Y$-α2 (A) was complete within 2 seconds. The reaction with $Y_{731}F/Y_{413}NH_2Y$-α2 was monitored over 200 s (B), with the first 30 s expanded in the inset. Exponential fits to the data are indicated by solid black lines.

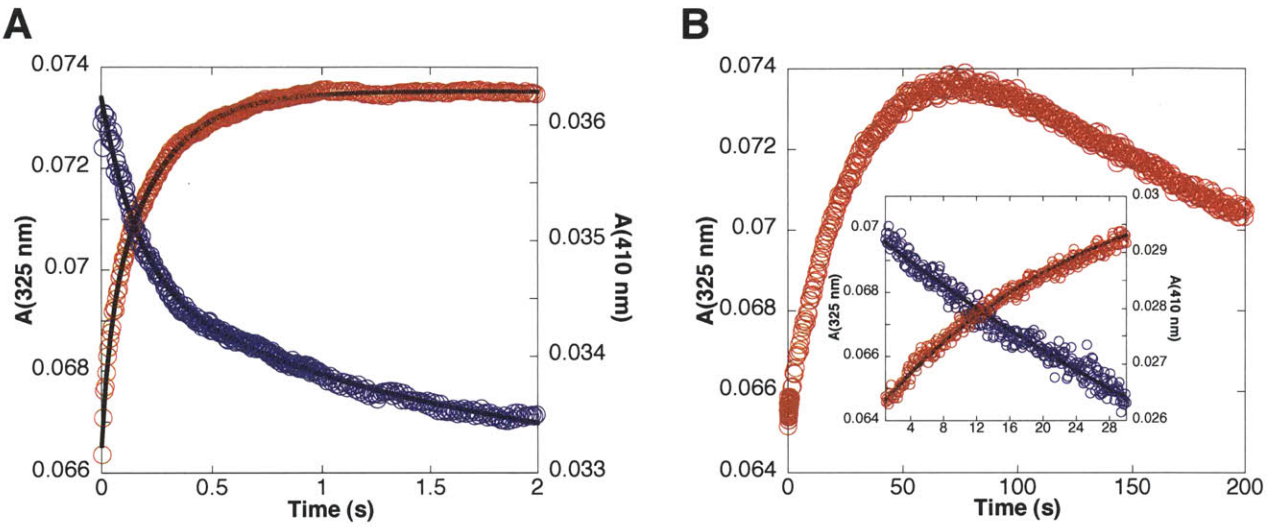

Table 3.1 Characterization of NH_2Y• formation in α:β complexes with various on- and off-pathway mutations

β:α complex	% NH_2Y• (EPR)[a]	% NH_2Y• (SF UV-vis)[a]	first phase k_{obs} (s^{-1})	second phase k_{obs} (s^{-1})
wt-β2:$Y_{730}NH_2Y$-α2[b]	53	39	12.8	2.5
wt-β2:$Y_{731}NH_2Y$-α2[b]	45	35	19.2	2.7
$Y_{356}F$-β2:$Y_{730}NH_2Y$-α2	<3%[c]	<2%[c]	--[c]	--[c]
$Y_{356}F$-β2:$Y_{731}NH_2Y$-α2	<3%	<2%	--[c]	--[c]
wt-β2:$Y_{731}F/Y_{730}NH_2Y$-α2	<3%	<2%	--[c]	--[c]
wt-β2:$Y_{413}NH_2Y$-α2	12	8	4.8[d]	0.5
wt-β2:$Y_{731}F/Y_{413}NH_2Y$-α2	7	12	0.04	--
$Y_{356}F$-β2:$Y_{413}NH_2Y$-α2	<3%	ND[e]	--	--

a. Y_{122}• converted to NH_2Y•, as a percent of the total spin in the reaction at the time of quench. *b.* Reported previously.[8] *c.* No conversion detected; our lower limit of detection is approximated to be 3% of the total initial Y_{122}• by EPR and 2% by SF UV-vis spectroscopy. *d.* Taken as the average of k_{obs} measured at 325 nm and 410 nm. *e.* Not determined.

3.4 DISCUSSION

3.4.1 Testing pathway dependence by insertion of the non-oxidizable "block," phenylalanine. The rate and extent of NH_2Y• formation in the presence of the second subunit, CDP, and ATP (when NH_2Y has been site-specifically incorporated into α2 at residue 730, 731, or 413 or into β2 at position 356) may be used as indicators of the participation of a specific residue in a defined pathway for C_{439} oxidation in RNR (Figure 3.1). We have previously established that formation of NH_2Y• is biphasic, giving rise to rate constants and amplitudes (as a percent of initial Y_{122}•) for NH_2Y• formation of 19 s^{-1} (24%) and 2.7 s^{-1} (11%) at 731, and 13 s^{-1} (20%) and 2.5 s^{-1} (19%) at 730.[8] As described in Chapter 2, we have analyzed the kinetics of NH_2Y• formation with all S/E pairs and argue that both rate constants are kinetically competent for deoxynucleotide formation.[13] An unexpected observation of our initial studies with the 730-, 731-, and 356-substituted proteins was the ability of these NH_2Y-RNRs to catalyze deoxynucleotide formation, suggesting that the NH_2Y• observed at each of three positions is a radical intermediate relevant to catalysis.

In our current studies, replacement of Y with a non-oxidizable F in the pathway at positions 356 in β or in 731 in α, and incorporation of NH_2Y within the pathway after the block, resulted in no detectable NH_2Y• by EPR analysis at 20 s or 2 min (Table 3.1). Since the EPR signal is always a composite of Y• and NH_2Y•, subtraction of the Y• signal is required for spin quantitation of the two species. The width of the Y• signal relative to the NH_2Y• makes this subtraction straightforward, with the lower limit of detection of an NH_2Y• estimated to be 3% of the total spin. It should be noted that cleaner subtractions are achieved when Y_{122}• in an α:β complex is used as the reference, as the hyperfine interactions of Y_{122}• in β2 appear to be subtly affected by complex formation with α2.

To establish that NH_2Y• is not generated transiently in the presence of a Y to F mutation, SF UV-vis was conducted and the reaction was monitored at 325 (320) nm and 410 nm. An increase in the former absorption is associated with NH_2Y• formation at 730 (731) and a decrease of the latter with Y• loss. Monitoring a reaction at 325 nm is complicated by contributions from the diferric cluster, which also absorbs in this region. Thus, we have assumed transient features observed by SF are related to NH_2Y• formation only if the rate constant and amplitude increase of the 325 nm feature parallels the rate constant and amplitude decrease of the 410 nm feature. As indicated in Figure 3.3, in all experiments described herein in which the pathway has been "blocked," a small rise phase (approximately 2% of the Y•) has been observed at 325 nm. This rise is rapid (corresponding to a rate constant >20 s^{-1}), has no corresponding decrease at 410 nm, and is attributed to a small change associated with the diferric Y• cofactor. In the current analysis, this feature is not considered further. Thus, the SF data are in agreement with the EPR results, indicating that a redox-active Y at 356 and 731 is a prerequisite for NH_2Y• formation.

3.4.2 Testing pathway dependence by incorporation of an "off-pathway" radical trap, NH_2Y_{413}. As noted above, at pH 7.0 NH_2Y is easier to oxidize than Y by 190 mV and thus could be oxidized in an off-pathway process. To test this proposal, studies were conducted in which NH_2Y was incorporated in place of a residue proximal to the proposed pathway. Y_{413} (Figure 3.4) is located within ~5 Å of both Y_{731} and Y_{730}, a distance feasible for a single oxidation "hop," and thus became the target of our off-pathway studies. Three experiments were carried out using mutants in which NH_2Y was site-specifically incorporated at position 413.

In the first, NH_2Y was incorporated at residue 413 while keeping all other on-pathway residues intact. In two additional experiments, a pathway block was introduced in the form of a

Y to F mutation at either 356 or 731. When the single mutant, $Y_{413}NH_2Y$-α2, was reacted with wt-β2, CDP, and ATP, SF experiments revealed formation of NH_2Y_{413}• with a rate constant of 4-5 s^{-1}, corresponding to an 8% conversion of the initial Y_{122}• to NH_2Y_{413}• (Table 3.1). EPR analysis of the same reaction after 40 s was in agreement with the SF results, indicating the formation of a NH_2Y• species accounting for 12% of the total spin (Figure 3.7 A). The differences in the percent conversion of Y_{122}• to NH_2Y_{413}• as measured by SF and EPR may be indicative of the error inherent to the two methods in quantitation of low levels of radical species. Alternately, the differences may arise from the 10-fold difference in protein concentration used in the two experiments.[7] As argued above, the rate constant and accumulation of NH_2Y• is indicative of the relevance of that specific residue to catalysis in RNR. The rate constant of 4.2 s^{-1} for NH_2Y_{413}• formation is slower by a factor of 4 and the amplitude is reduced by 75% relative to NH_2Y• formation at 731. This result suggests that NH_2Y at position 413 can be oxidized in an off-pathway fashion by either Y_{731} or by Y_{356}. With F incorporated at 731 and NH_2Y at 413, NH_2Y• is still observed. However, a fit of the SF data for the first 30 s gave a rate constant of 0.04 s^{-1} and an amplitude of 12%. EPR spin quantitation of the same reaction after 40 s indicated 7% of the total spin was associated with the putative NH_2Y• (Figure 3.7 B). Finally, with F at 356 and NH_2Y at 413, no NH_2Y• was detected (Figure 3.7 C). Thus the oxidation at 413 appears to occur predominantly through Y_{356}. The very slow rate constant for NH_2Y_{413}• formation with F at 731 (~0.2% that of NH_2Y• formation at 731, and ~2% of the steady-state rate constant for dCDP formation) and the complete absence of NH_2Y_{413}• with F at 356 suggest that radical formation at 413 in the NH_2Y-mutants results from off-pathway ET.

It is experimentally challenging to determine directly whether NH_2Y_{413}• can participate as a chemically- and kinetically-competent intermediate in C_{439} oxidation. However, strong

evidence that ET through 413 does *not* constitute a viable alternate radical pathway comes from the observation that no NH_2Y• is generated in the reaction with $Y_{731}F/Y_{730}NH_2Y$-α2. Y_{413} cannot serve as a bypass to a block at 731, and thus cannot support the oxidation of Y at 730 required for C_{439}• formation and subsequent nucleotide reduction. The NH_2Y_{413}• observed in experiments with $Y_{413}NH_2Y$-α2 or $Y_{731}F/Y_{413}NH_2Y$-α2 thus results from an off-pathway oxidation and is nonfunctional.

Many examples of off-pathway oxidation exist in the literature for heme- and non-heme iron-dependent systems. Likewise, evidence for off-pathway oxidation has been reported previously in the class I *E. coli* RNR.[17,23] The phenotypes are usually slow rate constants for radical formation and low amplitudes of new radical species. Thus the experiments presented herein using F and NH_2Y as an oxidation block and trap, respectively, support the original proposal of Uhlin and Eklund for long-range oxidation of C_{439} in α via a conserved pathway of defined aromatic amino acids.

3.5 REFERENCES

1. Uhlin, U. & Eklund, H. Structure of ribonucleotide reductase protein R1. *Nature* **370**, 533-9 (1994).
2. Stubbe, J., Nocera, D.G., Yee, C.S. & Chang, M.C.Y. Radical initiation in the class I ribonucleotide reductase: long-range proton-coupled electron transfer? *Chem. Rev.* **103**, 2167-201 (2003).
3. Climent, I., Sjöberg, B.M. & Huang, C.Y. Site-directed mutagenesis and deletion of the carboxyl terminus of *Escherichia coli* ribonucleotide reductase protein R2. Effects on catalytic activity and subunit interaction. *Biochemistry* **31**, 4801-7 (1992).
4. Ekberg, M., Sahlin, M., Eriksson, M. & Sjöberg, B.-M. Two conserved tyrosine residues in protein R1 participate in an intermolecular electron transfer in ribonucleotide reductase. *J. Biol. Chem.* **271**, 20655-9 (1996).
5. Rova, U. et al. Evidence by site-directed mutagenesis supports long-range electron transfer in mouse ribonucleotide reductase. *Biochemistry* **34**, 4267-75 (1995).
6. Rova, U., Adrait, A., Pötsch, S., Gräslund, A. & Thelander, L. Evidence by mutagenesis that Tyr(370) of the mouse ribonucleotide reductase R2 protein is the connecting link in the intersubunit radical transfer pathway. *J. Biol. Chem.* **274**, 23746-51 (1999).
7. Ge, J., Yu, G., Ator, M.A. & Stubbe, J. Pre-steady-state and steady-state kinetic analysis of *E. coli* class I ribonucleotide reductase. *Biochemistry* **42**, 10071-83 (2003).
8. Seyedsayamdost, M.R., Xie, J., Chan, C.T., Schultz, P.G. & Stubbe, J. Site-specific insertion of 3-aminotyrosine into subunit α2 of *E. coli* ribonucleotide reductase: direct evidence for involvement of Y730 and Y731 in radical propagation. *J. Am. Chem. Soc.* **129**, 15060-71 (2007).
9. Seyedsayamdost, M.R., Yee, C.S., Reece, S.Y., Nocera, D.G. & Stubbe, J. pH rate profiles of F_nY_{356}-R2s (n = 2, 3, 4) in *Escherichia coli* ribonucleotide reductase: evidence that Y_{356} is a redox-active amino acid along the radical propagation pathway. *J. Am. Chem. Soc.* **128**, 1562-8 (2006).
10. Seyedsayamdost, M.R. & Stubbe, J. Site-specific replacement of Y_{356} with 3,4-dihydroxyphenylalanine in the β2 subunit of *E. coli* ribonucleotide reductase. *J. Am. Chem. Soc.* **128**, 2522-3 (2006).
11. Seyedsayamdost, M.R. & Stubbe, J. Forward and reverse electron transfer with the Y356DOPA-β2 heterodimer of *E. coli* ribonucleotide reductase. *J. Am. Chem. Soc.* **129**, 2226-7 (2007).
12. Seyedsayamdost, M.R., Chan, C.T., Mugnaini, V., Stubbe, J. & Bennati, M. PELDOR spectroscopy with DOPA-β2 and NH2Y-α2s: distance measurements between residues involved in the radical propagation pathway of *E. coli* ribonucleotide reductase. *J. Am. Chem. Soc.* **129**, 15748-9 (2007).

13. Minnihan, E.C., Seyedsayamdost, M.R., Uhlin, U. & Stubbe, J. Kinetics of radical intermediate formation and deoxynucleotide production in 3-aminotyrosine-substituted *Escherichia coli* ribonucleotide reductases. *J. Am. Chem. Soc.* **133**, 9430-40 (2011).

14. DeFelippis, M.R. et al. Electrochemical properties of tyrosine phenoxy and tryptophan in indolyl radicals in peptides and amino acid analogs. *J. Phys. Chem.* **95**, 3416-9 (1991).

15. Tommos, C., Skalicky, J.J., Pilloud, D.L., Wand, A.J. & Dutton, P.L. De novo proteins as models of radical enzymes. *Biochemistry* **38**, 9495-507 (1999).

16. Nordlund, P., Sjöberg, B.M. & Eklund, H. Three-dimensional structure of the free radical protein of ribonucleotide reductase. *Nature* **345**, 593-8 (1990).

17. Yee, C.S., Seyedsayamdost, M.R., Chang, M.C.Y., Nocera, D.G. & Stubbe, J. Generation of the R2 subunit of ribonucleotide reductase by intein chemistry: insertion of 3-nitrotyrosine at residue 356 as a probe of the radical initiation process. *Biochemistry* **42**, 14541-52 (2003).

18. Steeper, J.R. & Steuart, C.D. A rapid assay for CDP reductase activity in mammalian cell extracts. *Anal. Biochem.* **34**, 123-30 (1970).

19. Climent, I., Sjöberg, B.M. & Huang, C.Y. Carboxyl-terminal peptides as probes for *Escherichia coli* ribonucleotide reductase subunit interaction: kinetic analysis of inhibition studies. *Biochemistry* **30**, 5164-71. (1991).

20. Seyedsayamdost, M.R. Massachusetts Institute of Technology (2007).

21. Palmer, G. Electron paramagnetic resonance. *Methods Enymol.* **10**, 595-610 (1967).

22. Argirević, T., Riplinger, C., Stubbe, J., Neese, F. & Bennati, M. High-frequency ENDOR combined with DFT cluster model calculations provide evidence for the hydrogen bond network involved in the PCET of the α-subunit of *E. coli* ribonucleotide reductase. *Submitted.*

23. Sahlin, M. et al. Tryptophan radicals formed by iron/oxygen reaction with *Escherichia coli* ribonucleotide reductase protein R2 mutant Y122F. *J. Biol. Chem.* **269**, 11699-702 (1994).

Chapter 4

A detailed investigation of the mechanism of nucleotide reduction by NH_2Y-RNRs

4.1 INTRODUCTION

In Chapter 2, three NH_2Y-RNRs – $Y_{731}NH_2Y$-α2, $Y_{730}NH_2Y$-α2, and $Y_{356}NH_2Y$-β2 – were shown to be catalytically active in dNDP production when combined with the second subunit, substrate (S), and allosteric effector (E), with turnover numbers of 0.2-0.7 s^{-1}. A number of strategies were employed to convincingly demonstrate that the catalytic activity is inherent to NH_2Y-RNRs and not the result of co-purifying wt enzyme. These included quantitation of product formation in single-turnover assays with both the native substrate and a mechanism-based inhibitor and activity assays of N-terminally tagged NH_2Y-RNRs isolated by affinity chromatography. The kinetics of formation of 3-aminotyrosyl radical (NH_2Y•s) at position 356, 731, and 730 were characterized with the four S/E pairs and were found in all cases to be biphasic (k_{fast} of 9-46 s^{-1} and k_{slow} of 1.5-5.0 s^{-1}) and kinetically-competent towards nucleotide reduction. From the existing body of data, a model for catalysis by NH_2Y-RNRs was proposed (Scheme 4.1). Its most salient features are summarized below.

In the original model, NH_2Y• formation occurs by two distinct pathways (steps **1** and **8**) as revealed by its biphasic kinetics. The observed k_{fast} was assigned to the formation of a NH_2Y• population (step **8**, green pathway) that is "off-pathway" or in an inactive conformation that is not relevant to catalysis. A second, catalytically relevant NH_2Y• population is formed in step **1**. Its rate constant for formation, k_{slow} of ~2.5 s^{-1}, reports on the conformational changes that gate radical propagation in the wt enzyme (2-10 s^{-1}) and is 2.5- to 5-fold slower than the steady-state k_{cat} for the NH_2Y-RNRs. The two populations of NH_2Y•s formed in steps **1** and **8** interconvert (steps **9** and **-9**) slowly (<2.5 s^{-1}), if at all. The chemistry of nucleotide reduction (steps **3** and **4**) occurs rapidly (>100-300 s^{-1}), as does reformation of the NH_2Y• by the reverse PCET (≥ 100 s^{-1}, magenta pathway, step **5**). These proposals are experimentally substantiated by the results of

single-turnover experiments in which $Y_{122}NO_2Y$-β2, reacted with wt-α2, CDP, and ATP, produces dCDP and traps a Y_{356}• on reverse hole migration with rate constant of at least 100-300 s^{-1}.[1] The NH_2Y• generated upon reverse radical migration (step **5**) has two conceivable pathways of reinitiation: either directly (step **7** to step **2**), or through re-oxidation of Y_{122}• (via step **6,** or steps **7** and **-1**) by a pathway involving an additional zero to three amino acid intermediates, depending on the location of NH_2Y•. Perhaps the most important aspect of the kinetic scheme is the assignment of the slow (0.2 to 0.7 s^{-1}) steady-state rate constant for dNDP production by NH_2Y-RNRs. By process of elimination, step **2**, the oxidation of subsequent residue on the pathway by NH_2Y•, emerged as the candidate for the rate-determining step in the overall kinetic scheme.

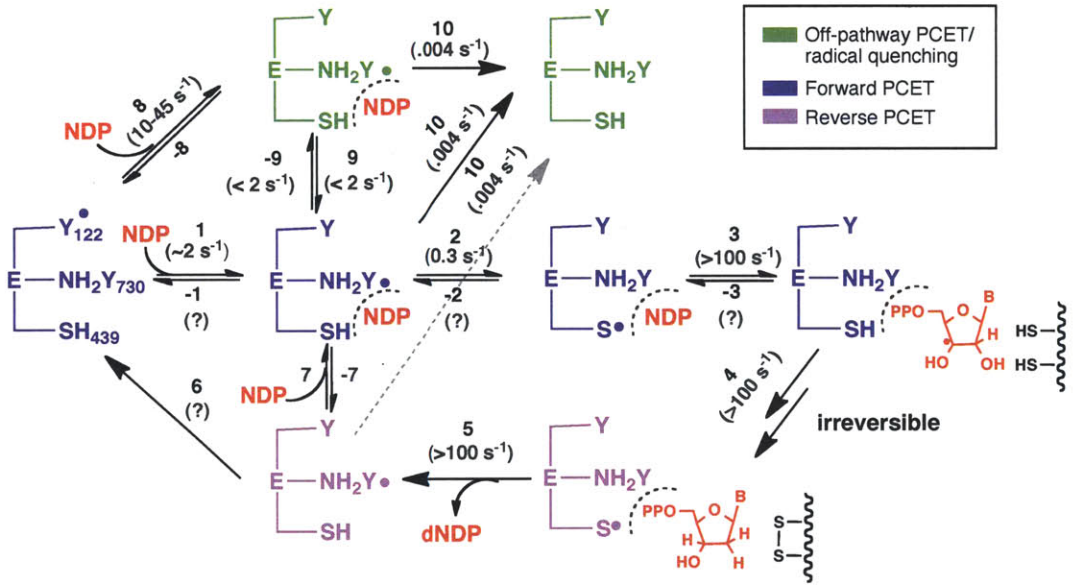

Scheme 4.1. Original kinetic model for NH_2Y• formation and nucleotide reduction in NH_2Y-RNRs. The model for $Y_{730}NH_2Y$-α2 is shown, but similar models can be drawn for the 731 and 356 mutants by the addition of one or two Y oxidation steps within step **2** above. Enzyme species are colored according to three different pathways – forward PCET (blue), reverse PCET (magenta), and off-pathway PCET and/or radical quenching (green). The proposed rate constants assigned to individual steps, if available, are indicated above the arrows. Substrate (NDP) and product (dNDP) are shown in red. Effector is omitted from the scheme for clarity.

Experiments to test and refine this model are presented in Chapter 4. Experiments conducted in D_2O or with 3-[^{2}H]-CDP were carried out to determine the solvent isotope effect (IE) on NH_2Y• formation (step **1** and **8**) and dCDP production, and the kinetic IE on 3′-H• abstraction from 3-[^{2}H]-CDP (step **3**) respectively. Studies of the kinetics of NH_2Y• formation in the presence of various viscogen concentrations were conducted to test the prediction that the observed rate constants report on protein conformational changes that gate catalysis. In perhaps the most important experiments of the chapter, we directly investigate whether step **2** is rate limiting in the overall kinetic scheme, as was proposed in Chapter 2, by determining the rate constant for dCDP formation in the first turnover in a rapid chemical quench (RCQ) experiment, and comparing it to the steady-state k_{cat}. We also examine the mechanism of PCET reinitiation to ask whether radical recycling through NH_2Y• (step **7** then step **2**) is possible, and investigate whether an RNR containing two NH_2Y substitutions in place of pathway residues is active towards nucleotide reduction. The results of these mechanistic studies have allowed us to generate a revised model (Scheme 4.2), the details of which are described in the Discussion.

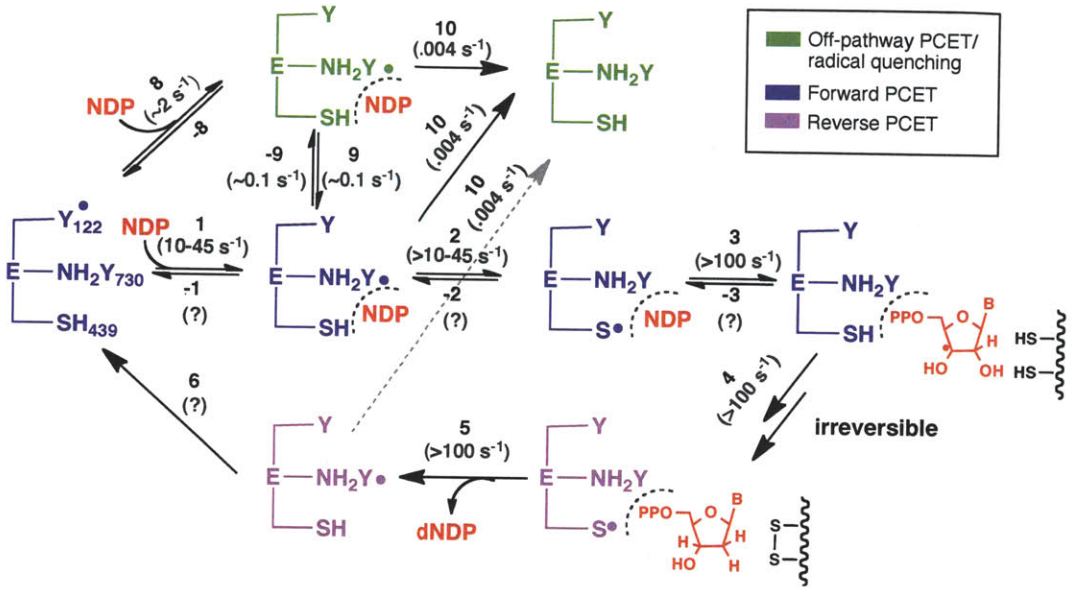

Scheme 4.2 Revised kinetic model for $NH_2Y\bullet$ formation and nucleotide reduction in NH_2Y-RNRs. Numbering of the individual steps and coloring of the three pathways is the same as in Scheme 4.1. The rate constants assigned to individual steps, if available, are indicated above the arrows. Those rate constants that are new or have been reassigned relative to the original model (Scheme 4.1) are described in the Discussion.

4.2 MATERIALS AND METHODS

4.2.1 Materials. Wt-α2 (2500 nmol/min/mg) and wt-β2 (1.2 Y_{122}•/β2, 7600 nmol/min/mg) were expressed from pTrc-*nrdA* and pTB2-*nrdB*, respectively, and purified as previously described. $Y_{731}NH_2Y$-α2 and $Y_{730}NH_2Y$-α2 were co-expressed from pTrc-*nrdA*(TAG_{731}) or pTrc-*nrdA*(TAG_{730}) and pAC-NH_2Y, and purified as described.[2] His_6-$Y_{730}NH_2Y$-α2 was co-expressed from pET-*nrdA*(TAG_{730}) and pEVOL-NH_2Y, and purified as described previously[3] and in section 2.2.14. All α2 proteins (mutant and wt) were pre-reduced prior to use according to standard protocol.[2] $Y_{356}NH_2Y$-β2 was expressed from pTrc-*nrdB*(TAG_{356}) and pAC-NH_2Y and purified as described previously[3] and in section 2.2.3. *E. coli* thioredoxin (TR, 40 units/mg) and thioredoxin reductase (TRR, 1400 units/mg) were isolated as previously described.[4,5] [5-^{3}H]-CDP was purchased from ViTrax (Placentia, CA). Assay buffer is 50 mM Hepes, 15 mM $MgSO_4$, 1 mM EDTA, pH 7.6. 3′-[^{2}H]-cytidine-5′-diphosphate was obtained as a frozen stock solution previously prepared by Dr. Brenda Kellogg (Stubbe lab) and was characterized by UV-vis, ^{1}H NMR, and ^{31}P NMR prior to use.

4.2.2 Reaction of $Y_{356}NH_2Y$–β2 and wt-a2, CDP, an ATP in D_2O buffer monitored by EPR spectroscopy. The reaction of $Y_{356}NH_2Y$-β2 (25 μM) with wt-α2 (25 μM), CDP (1 mM) and ATP (3 mM) in D_2O assay buffer at 25 °C was hand-quenched at 20 s in liquid N_2. Final reaction solution was >99% deuterium. An EPR spectrum of the reaction mixture was recorded at 77 K on a Bruker EMX X-band spectrometer equipped with a quartz finger dewar containing liquid N_2 in the Department of Chemistry Instrumentation Facility. EPR parameters were as follows: microwave frequency = 9.34 GHz, power = 30 μW, modulation amplitude = 1.5 G, modulation frequency = 100 kHz, time constant = 5.12 ms, scan time = 41.9 s. Spin quantitation and analysis of composite reaction spectra were carried out as described previously.[2]

4.2.3 Preparation of high-field EPR samples of NH_2Y_{356}•. Protein samples of $Y_{356}NH_2Y$-β2 and wt-α2 were prepared in H_2O and D_2O for high-field EPR analysis of NH_2Y_{356}• by Tomislav Argirevic (Bennati lab, Max Planck Institute, Göttingen, Germany). $Y_{356}NH_2Y$-β2 and wt-α2, each in their respective storage buffer, were combined in a 1:1 ratio and diluted 10-fold into assay buffer. The α/β protein complex solution was concentrated on a YM-30 amicon and then a YM-10 microcon centrifugation filter to give a final complex concentration of 130 μM (65 μM Y•), as determined by ε_{280} = 320 mM^{-1} cm^{-1}. A sample in D_2O assay buffer was prepared analogously, with buffer exchange by dilution/concentration until the solution was >99% deuterated. The deuterated α/β complex was concentrated to 120 μM (60 μM Y•). An aliquot (100 μL) of each sample was flash frozen in liquid N_2, packed on dry ice, and shipped to the Bennati lab.

Upon receipt, the protein samples were thawed and the reaction sample was prepared as described previously.[6] High field (94 GHz) EPR data collection and analysis was performed by Tomislav Argirevic as described previously.[6]

4.2.4 PELDOR measurement of the distance between Y_{122}• in α/β and NH_2Y_{356}• in α′/β′. A solution of $Y_{356}NH_2Y$-β2 (90 μM, final concentration, 0.5 Y•/β2) and CDP (2 mM) in assay buffer with 5% glycerol was mixed in a 1:1 ratio with a solution of pre-reduced wt-α2 (90 μM) and ATP (6 mM) in a total volume of 240 μL. The reaction was hand-quenched in liquid N_2 after 30 seconds and analyzed by 9 GHz CW EPR as described above and previously[3] to determine the distribution of Y_{122}• and NH_2Y_{356}• in the sample. The reaction sample was then subjected to PELDOR analysis on a Bruker E580 Pulsed EPR spectrometer in the Francis Bitter Magnet Lab (MIT). Optimized PELDOR parameters were determined from initial echo-detected field swept EPR, inversion recovery (T1 measurement), and echo decay (T2 measurement)

experiments. Data were collected for 10 h at 15 K using the following parameters: p0 = 16 ns, p1 = 32 ns, p3 = 32 ns, d1 = 128 ns, d2 = 2000 ns, d3 = 40 ns, d30 = 16 ns, d0 = 354 ns, pg = 64, ELDOR = 9.7628 GHz, srt = 4.2 μs, h = 100, n = 1000. The data was transformed and analyzed using the software DeerAnalysis 2009 (ETH, Zurich).[7] The experimental oscillation curve was analyzed using the Tikhonov regularization procedure.[8]

4.2.5 Determining the identity of the product(s) formed by $Y_{730}NH_2Y$-α2. The nature of the product(s) formed by $Y_{730}NH_2Y$-α2 in both single-turnover and in steady-state assays was assessed by HPLC analysis. In the former case, wt-β2 (10 μM) was combined with [^{3}H]-CDP (0.3 mM, 20,000 cpm/nmol), and ATP (3 mM) in assay buffer in a total volume of 600 μL at 25 °C. The assay was initiated by addition of His_6-$Y_{730}NH_2Y$-α2 (2 μM). Aliquots (250 μL) were removed at 1 min and 10 min and quenched in a boiling water bath. An aliquot of each sample was dephosphorylated in the presence of carrier dC and analyzed following the method of Steeper and Steuart.[9] A reaction with His_6-α2(wt) was performed in parallel as a positive control.

Samples were adjusted to contain equimolar carrier cytosine and deoxycytidine (dC) prior to lyophilization. A portion of the eluate (7 mL) from the borate column was lyophilized to dryness, then redissolved in ddH_2O (400 μL). An aliquot (50 μL) was counted directly to calculate the total recovery of radioactivity off the HPLC. A second aliquot (200 μL) was loaded to an Econosil C18 (10 um) column (250 mm x 4.6 mm) equilibrated in 20 mM KPi, pH 6.7 and eluted isocratically at 1 mL/min. Under these conditions, cytosine has retention time of 4.5 min and dC, 10.0 min. Elution profiles were monitored at 271 nm by photodiode array, and fractions (0.7 mL/fraction) were collected and analyzed by scintillation counting. [^{3}H]-CDP contains a radiochemical impurity that constitutes 0.4% its total radioactivity and elutes in the void volume of the column. Its contribution was subtracted in all samples prior to analysis.

To determine the identity of the product(s) formed in the steady-state, the radioactive assays was performed on $Y_{730}NH_2Y$-α2 (0.7 μM, final concentration) and a five-fold excess of wt-β2 as described previously.[10] Aliquots (30 μL) were taken at 30 s and 4 min and quenched, dephosphorylated, and worked up as described for the single-turnover experiments. The eluate (7 mL) from the borate column was lyophilized to dryness, and resuspended in ddH_2O (300 μL). Carrier cytosine and dC (95 nmol each) were added prior to lyophilization. The sample was redissolved in water, chromatographed, and analyzed as described above for the single-turnover assays.

4.2.6 Measuring steady state turnover with 3′-[^{2}H]-CDP. The spectrophotometric assay was conducted according to the standard lab protocol,[11] with protein concentrations increased to account for the low activity of His_6-$Y_{730}NH_2Y$–α2. Ribonucleotide reductase activity was monitored through a continuous coupled-enzyme assay in which the consumption of NADPH was determined by monitoring the decrease in absorbance at 340 nm. Wt-β2 (7.5 μM), ATP (3 mM), CDP or 3′-[^{2}H]-CDP (250 μM), TR (30 μM), and TRR (0.5 μM) were mixed in assay buffer in a final volume of 300 μL. The assay was initiated upon addition of His_6-$Y_{730}NH_2Y$–α2 (2.5 μM) or wt-α2 (2.5 μM) and NADPH (0.2 mM), and the linear decrease in A_{340} was monitored over 2 min.

4.2.7 Steady-state activity assays of His_6-$Y_{730}NH_2Y$-α2 in D_2O. Deuterated assay buffer (50 mM Hepes, 1 mM EDTA, 15 mM $MgSO_4$) was prepared in from a fresh bottle of D_2O (99%, Cambridge Isotope Labs), and the pD was adjusted to 7.6 using a solution of NaOD. Equation 4.1 was used to correct for the meter's lower sensitivity to deuterons:

$$pD = (\text{pH meter reading}) + 0.4 \qquad \text{(eq. 4.1)}$$

The deuterated buffer was stored in an airtight vessel with solid desiccant under vacuum for future use. Fresh solutions of ^{3}H-CDP, ATP, and NADPH were prepared in deuterated buffer. TR, TRR, wt β2 and His_6-$Y_{730}NH_2Y$-α2 were exchanged into deuterated buffer via dilution and reconcentration until the total proton concentration was calculated to be 1%. The activity of His_6-$Y_{730}NH_2Y$-α2 was then measured by the radioactive assay following the previously reported protocol.[10]

4.2.8 SF UV-vis spectrophotometric analysis of NH_2Y• formation in D_2O. SF kinetics were performed on an Applied Photophysics DX 17MV instrument equipped with the Pro-Data upgrade. Reactions were carried out in deuterated assay buffer described above and the temperature maintained at 25 °C by a Lauda circulating water bath. In all cases, pre-reduced His_6-$Y_{730}NH_2Y$–α2 and ATP in one syringe were rapidly combined with wt-β2 and CDP from a second syringe to yield a final concentration of 5 μM for each protein subunit, 1 mM CDP and 3 mM ATP, respectively. The final solution was >90% deuterated. The reactions were monitored at 325 nm for NH_2Y_{730}•, (ε ~10,500 $M^{-1}cm^{-1}$) and 410 nm for Y_{122}• (ε ~3,700 $M^{-1}cm^{-1}$) using PMT detection.[2] In each experiment, >5 of the most reproducible traces were averaged and kinetic parameters obtained by curve fitting using KaleidaGraph.

4.2.9 SF UV-vis spectrophotometric analysis of viscosity effects on NH_2Y• formation. SF UV-vis experiments were conducted as described above, except that the assay buffer was supplemented with varying concentrations of glycerol such that the final reaction solution contained 0 – 40% w/v glycerol.

4.2.10 Testing the effect of protein concentration, subunit ratio, and reductant on steady-state assays of NH_2Y-RNRs. To test the effect of protein concentration and subunit ratio on specific activity, radioactive assays using [^{3}H-CDP] (7100 cpm/nmol) were conducted at 25 °C

as described previously[10] and monitored over 12 min. All NH_2Y-RNRs used were untagged. Protein concentrations (of limiting subunit, if applicable) ranged from 0.1 – 2.0 μM, and proteins were assayed in either a 1:1 or 1:5 subunit ratio.

Subsequently, spectrophotometric assays were conducted on His_6-$Y_{730}NH_2Y$-α2 (10 μM) in the presence of 1.5 eq wt-β2 (15 μM) to determine the specific activity under conditions identical to those employed for RCQ experiments (*vide infra*).

The effect of substituting DTT for TR/TRR/NADPH was investigated by the radioactive assay. A stock assay mixture of [^{3}H]-CDP (1 mM), ATP (3 mM), and DTT (15 mM) was prepared fresh in assay buffer. 15 mM DTT was selected on the basis of previous studies in which DTT in the range of 10 mM – 20 mM gave maximum activity for wt-α2.[12] $Y_{730}NH_2Y$-α2 and wt-β2 were maintained at either a 1:1 or 1:5 ratio, using 1 μM $Y_{730}NH_2Y$-α2 in all cases.

4.2.11 Kinetics of dCDP formation with NH_2Y-RNRs under single-turnover conditions monitored by RCQ. RCQ experiments were conducted on a KinTek Model RQF-3 Chemical Quench Flow instrument. Pre-reduced His_6-$Y_{730}NH_2Y$-α2 and ATP were mixed rapidly with wt-β2 (1.2 Y•/β2) and [^{3}H]-CDP (20,000 cpm/nmol) in assay buffer at 25 °C to final concentrations of 10 μM α2, 15 μM β2, 0.5 mM CDP, and 3 mM ATP. For each time-point, 25 μL from each syringe was rapidly mixed then quenched with perchloric acid (2%) at defined times. The sample was immediately centrifuged, neutralized with 0.5 M KOH, and placed on ice. A total of 20 time points were collected between 5 ms and 100 s, with each point collected in duplicate. After removal of the precipitated $KClO_4$, reaction mixtures were dephosphorylated in the presence of carrier dC and analyzed by the method of Steeper and Steuart.[9] A zero time point was collected by mixing the wt-β2/[^{3}H]-CDP mixture with an equal volume of assay buffer on the RCQ instrument. Hand quench reactions were conducted before and after the time course to

assess the extent of α2 oxidation over the time it took to conduct the experiment (~2 h). An identical experiment was conducted with His_6-α2(wt) to determine whether the presence of the affinity tag affects the kinetics of dCDP formation compared to wt-α2.

An analogous RCQ experiments was conducted for the reaction between $Y_{356}NH_2Y$-β2 and His-α2(wt) (12.5 μM each, 6.25 μM Y•, final concentration).

4.2.12 Kinetics of dCDP formation with NH_2Y-RNRs under multiple-turnover conditions monitored by RCQ. The experiment described in the previous section was modified to include TR, TRR, and NADPH in the reaction mixture. A syringe containing His_6-$Y_{730}NH_2Y$-α2 (20 μM, all concentrations indicated are in the syringe), ATP (6 mM), TR (80 μM), and TRR (1.6 μM) in assay buffer was mixed rapidly in a 1:1 ratio with a second syringe containing wt-β2 (30 μM), [^{3}H]-CDP (1 mM, 20,000 cpm/nmol), and NADPH (2 mM) in assay buffer. Time points (5 ms - 100 s) were collected and analyzed in a fashion identical to that described in the previous section.

4.2.13 Determining whether radical reinitiation during multiple turnovers occurs through Y_{122}• or NH_2Y_{730}•. This question was addressed by two modified versions of the standard radioactive assay. In the first, either met-β2 or Y_{356}F-β2 was used as an inactive form of β2. In a final volume of 170 μL was combined wt-β2 (1.0 μM), [^{3}H]-CDP (1 mM), ATP (3 mM), thioredoxin (TR, 30 μM), and thioredoxin reductase (TRR, 0.5 μM) in assay buffer at 25 °C. The assay was initiated by addition of NADPH (1 mM) and $Y_{730}NH_2Y$-α2 (1.0 μM). Thus, α2 and β2 were in a 1:1 mixture at initiation. After 30 s, either met-β2 or Y_{356}F-β2 was added to this reaction mixture to a final concentration of 10 μM. Aliquots (30 μL) were removed at 1 min intervals after the addition of the inactive β2 and quenched in a boiling water bath. Aliquots

were dephosphorylated in the presence of carrier dC and analyzed by the method of Steeper and Steuart.[9]

In the second assay, $Y_{122}NO_2Y$-β2 was used as a radical initiator[1] for the reaction with $Y_{730}NH_2Y$-α2, CDP, and ATP. Apo-$Y_{122}NO_2Y$-β2 in 50 mM Hepes, pH 7.6 was degassed on a Schlenk line and brought into an anaerobic chamber maintained at 4 °C. To the solution was added 5 eq of Fe^{2+} and the resulting solution allowed to stir for 10 min. The solution was transferred to a sealed eppendorf tube and removed from the anaerobic box. To it was added 3.5 eq O_2 in the form of O_2-saturated reconstitution buffer (50 mM Hepes, 5% glycerol, pH 7.6). The solution was aged for ~5 s, then quickly diluted to a final concentration of 20 μM in a solution containing wt-α2 or $Y_{730}NH_2Y$-α2 (20 μM), [^{3}H]-CDP (0.5 mM, 20,000 cpm/nmol), ATP (3 mM), thioredoxin (TR, 30 μM), thioredoxin reductase (TRR, 0.5 μM), and NADPH (1 mM) in assay buffer at 25 °C. Aliquots (60 μL) were removed in 20 s increments and quenched with 2% perchloric acid. The samples were neutralized with KOH, chilled on ice, centrifuged to remove the resulting salt, dephosphorylated and analyzed as described above.

4.2.14 Activity assays of $Y_{730}NH_2Y$-α2 (or $Y_{731}NH_2Y$-α2) with $Y_{356}NH_2Y$-β2. Radioactive assays were conducted following the literature procedure[10] with $Y_{730}NH_2Y$-α2 (or $Y_{731}NH_2Y$-α2) at a concentration of 0.5-1.0 μM and $Y_{356}NH_2Y$-β2 (0.5 Y•/β2) in a five-fold excess over α2. [^{3}H]-CDP had a specific activity of 7130 cpm/nmol.

4.3 RESULTS

4.3.1 A more detailed characterization of NH_2Y_{356}• by EPR spectroscopy. Previously, detailed electronic structural information for NH_2Y_{730}• was obtained by EPR experiments at 9 GHz and 94 GHz using H_2O or D_2O solvent, and ^{14}N and ^{15}N-labeled NH_2Y.[6] This characterization yielded the *g* tensors of the radical, the hyperfine coupling constants and geometry of the amino group, and the orientation of the NH_2 protons with respect to the phenol ring. Thus, it provided subtle details of the electronic structure of a radical intermediate and provided information about the local environment at position 730. We aimed to characterize the NH_2Y_{356}• in a similar fashion to deduce information about any similarities or differences among the NH_2Y•s at the three different positions with respect to their overall electronic structures, protein environments, and hydrogen bonding interactions.[6,13]

To help understand the origin of the various hyperfine features in the NH_2Y_{356}• X-band EPR spectrum, we first examined the radical formed when $Y_{356}NH_2Y$-β2 was reacted with wt-α2, CDP, and ATP in D_2O buffer. When the amino protons are exchanged with deuterons, the spectrum is simplified and the remaining major hyperfine couplings arise from coupling to the β-methylene proton(s). These hyperfine couplings, in turn, provide detailed structural information about the orientation of these protons with respect to the phenol ring and give some insight to the local protein environment.[14] Characterization of the reaction of $Y_{356}NH_2Y$-β2 with wt-α2, CDP, and ATP in H_2O buffer by EPR spectroscopy was described in section 2.3.3. In a reaction hand-quenched at 20 s, 20% total initial spin is lost and the remaining spin distributed between NH_2Y• (41%) and Y• (59%).

To obtain the spectrum of deuterated NH_2Y_{356}• (ND_2Y_{356}•), the reaction was conducted as described above, except that all reagents were prepared in D_2O assay buffer (99% deuterium).

The reaction was hand quenched in liquid N_2 at 20 s and the spectrum analyzed by X-band EPR (Figure 4.1, A). Subtraction of the remaining Y_{122}• (60% the total spin) gave a spectrum of ND_2Y_{356}• (Figure 4.1 A and B, red) that is a ~1:2:2:1 quartet arising from couplings to one β-methylene proton and the ^{14}N nucleus. A simulated fit to the experimental data (Figure 4.1 B, blue) gave hyperfine coupling constants (A_z) of 26 MHz and 30 MHz for the ^{1}H and ^{14}N nuclei, respectively. The experimental and simulated spectra bear strong resemblance to the previously-reported spectrum and simulation of ND_2Y_{730}• (Figure 3.5, C, red and blue).[6]

From the X-band EPR studies in H_2O and D_2O, we know that the NH_2Y• formed at position 356 of β2 is similar with respect to its hyperfine coupling constants to NH_2Y•s formed at positions 730 and 731 of α2. To determine the detailed electronic structure of NH_2Y_{356}• and to deduce some information about the local protein environment of the radical, we sought to characterize the radical by 94 GHz (W band) EPR spectroscopy. Concentrated aliquots of $Y_{356}NH_2Y$-β2•wt-α2 in both H_2O and D_2O were prepared and shipped to Tomi Argirevic (Bennati lab), who rapidly mixed each aliquot with buffer containing CDP and ATP in an EPR tube and froze the sample after 30 s. The W band spectra of ND_2Y_{356}• and NH_2Y_{356}•, obtained after subtraction of the remaining Y_{122}•, are shown in Figure 4.2, red, panels A and B, respectively). The spectra were successfully simulated (Figure 4.2, blue, panels A and B) using the parameters for NH_2Y_{730}• as starting values.[6] A comparison of the spectra of ND_2Y•s at positions 356, 731, and 730 is shown in Figure 4.2 C, and the calculated hyperfine coupling constants and *g* tensors are given in Table 4.1.[15] The values indicate that the electronic structure of NH_2Y•s are strikingly similar at all three positions. The only major difference between the three radicals are the hyperfine couplings associated with the β-methylene protons, which suggests that the conformational orientation of each radical within the protein is slightly

different. Interestingly, the g_x values are almost identical among the three radicals, indicating that all exist in similar hydrogen bonding environments. The hydrogen bonding network of NH_2Y_{730}• has been characterized in detail recently by a combination of ENDOR spectroscopy and DFT calculations. These methods reveal two strong hydrogen bond interactions in addition to the hydrogen bond between the NH_2 and phenol.[13] In addition, a much weaker hydrogen bond to a water, also observed in the crystal structure, is observed. Given the similarities between g values for NH_2Ys at the three positions, it is interesting to speculate that they may share similar hydrogen bonding networks to mediate long-range radical propagation.

Figure 4.1 Reaction of $Y_{356}NH_2Y$-β2 with wt-α2, CDP, and ATP in deuterated assay buffer. (A) X-band EPR spectrum of the reaction mixture hand-quenched after incubation for 20 s at 25 °C. The reaction spectrum (blue) is a composite of two species. Subtraction of a spectrum of the Y_{122}• (green) gives the spectrum of the NH_2Y_{356}• (red). An expanded view of the experimental (red) and simulated (blue) NH_2Y_{356}• in D_2O (B) may be compared to the experimental and simulated spectrum of NH_2Y_{730}• in the same buffer (C, red and blue, respectively). The spectra in (C) have been reported previously.[6]

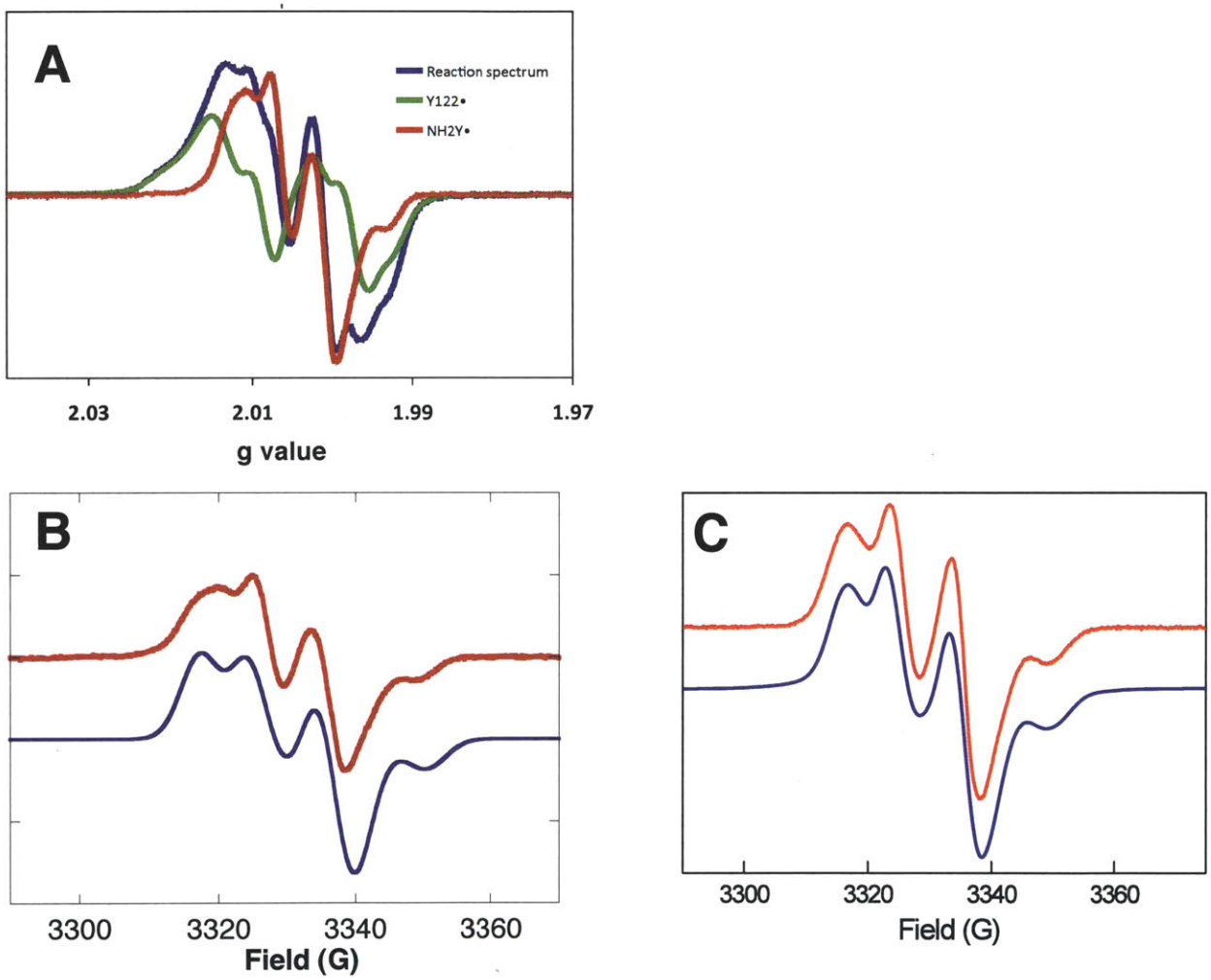

Figure 4.2 High field (94 GHz) EPR spectra of NH_2Y_{356}•. The radical spectrum in D_2O buffer (A) and H_2O buffer (B). Experimental data are shown in red, and corresponding simulations shown in blue. A comparison of the spectra of ND_2Y• at positions 356 (red), 731 (green), and 730 (blue) is shown in panel (C). The spectrum for ND_2Y• at position 731 is thought to contain a second, minor species, which gives rise to its unique spectral features. All spectra were collected and analyzed by Tomi Argirevic (Bennati lab).[15]

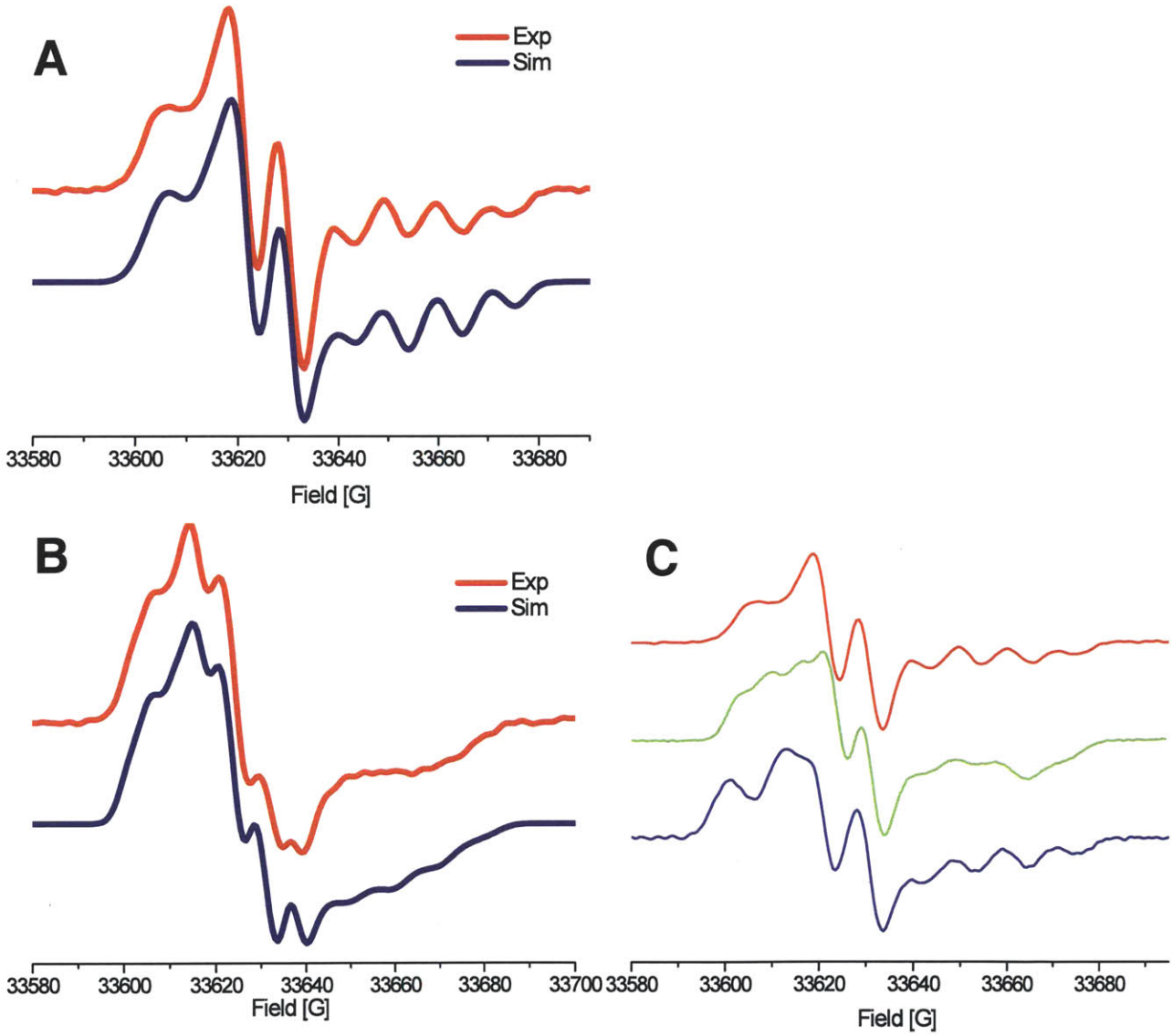

Table 4.1 EPR parameters for $NH_2Y\bullet$ generated at positions 730, 731, and 356 in H_2O and D_2O. (A) Hyperfine coupling constants (MHz) for the various nuclei in $NH_2Y\bullet$ and $ND_2Y\bullet$; (B) *g* values obtained from W-band EPR analysis of the radicals. Parameters determined by Tomi Argirevic (Bennati lab).[15]

A

	$NH_2Y_{730}\bullet$ ($ND_2Y_{730}\bullet$)			$NH_2Y_{731}\bullet$ ($ND_2Y_{731}\bullet$)			$NH_2Y_{356}\bullet$ ($ND_2Y_{356}\bullet$)		
Nucleus/[MHz]	A_{xx}	A_{yy}	A_{zz}	A_{xx}	A_{yy}	A_{zz}	A_{xx}	A_{yy}	A_{zz}
C_β-H_1	30.8	28.0	30.5	23	22	21	29	24.5	27
C_β-H_2	-	-	-	13	8	7	-	-	-
^{14}N	2.4	1.6	30.5	2.4	1.6	30.5	2.4	1.6	30.7
NH_2(H2)	13	4.4	27.6	18.2	4.4	25.7	13	4.4	27.6
NH_2(H1)	6.7	8.0	18.0	6.7	8.0	21.8	4.8	15	16

B

$NH_2Y_{730}\bullet$			$NH_2Y_{731}\bullet$			$NH_2Y_{356}\bullet$		
g_x	g_y	g_z	g_x	g_y	g_z	g_x	g_y	g_z
2.0052	2.0042	2.0022	2.0052	2.0042	2.0022	2.0050	2.0041	2.0021

4.3.2 Determining the $Y_{122}\bullet$-$NH_2Y_{356}\bullet$ distance by PELDOR spectroscopy. In recent years, the validity of the docking model and the long distance it places between $Y_{122}\bullet$ and C_{439} has been tested using an advanced EPR technique, pulsed electron-electron double resonance (PELDOR) spectroscopy. By this method, the distance between two weakly coupled spins separated by 20-80 Å may be accurately determined. The distance between $Y_{122}\bullet$s of the two β protomers has been measured and is in agreement with the distance measured in the X-ray structure of β2 alone.[16] In addition, diagonal distances between the two α/β pairs have been determined for $Y_{122}\bullet$ and the active site, and $Y_{122}\bullet$ and unnatural amino acid radicals at each of the three pathway positions ($DOPA_{356}\bullet$, $NH_2Y_{731}\bullet$, and $NH_2Y_{730}\bullet$).[17,18] All measurements are in excellent agreement with the distances predicted by the docking model. Once the details of

NH_2Y_{356}• formation had been extensively characterized, we sought to measure the diagonal distance between NH_2Y_{356}• and Y_{122}• by PELDOR spectroscopy and predicted that it would be in agreement with that which has been previously measured for $DOPA_{356}$• and Y_{122}• (30.6 Å),[18] and more recently between NO_2Y_{122}• and Y_{356}•.[19]

A sample of the reaction between $Y_{356}NH_2Y$-β2, wt-α2, CDP, and ATP was prepared as described above, and was determined to contain 15 μM (43%) NH_2Y_{356}• and 20 μM (57%) Y_{122}• by standard analysis of the CW X-band spectrum. The same sample was then analyzed at 15 K on a pulsed EPR X-band spectrometer. An inversion recovery experiment was conducted to determine T1; it was measured to be biphasic with τ values of 3.3 ms and 200 μs. An echo decay experiment was then conducted to determine T2; T2 at 15 K was also biphasic, with τ values of 1.3 μs and 200 ns. Finally, a field swept echo-detected spectrum was collected, and on the basis of this spectrum, the pump and detection frequencies for the PELDOR experiment were selected (Figure 4.3, A). From these values, an optimized PELDOR pulse sequence was designed. A two-step phase cycle was applied, and data was collected for 10 h at 15 K. After that time, clear modulation was visible in the raw data (Figure 4.3, B). The normalized experimental data were analyzed using DeerAnalysis2009 software and fit by the Tikhonov regularization procedure to give distances of 30.2 (+/- 1.6) Å and 32.6 (+/- 0.5) Å (Figure 4.3 C and D). These are in good agreement with the two expected distances in this sample: 30.6 Å (Y_{122}•-NH_2Y_{356}•), and 33 Å (remaining Y_{122}•-Y_{122}•). The large distribution on the measured Y_{122}•-NH_2Y_{356}• distance may arise from a number of factors. First, it may reflect poor quality in the experimental data and/or fit, leading to a large error in this measurement. At the time these data were collected, we had little experience in conducting PELDOR experiments at MIT, and the acquisition parameters used to collect these data (Figure 4.3 B) could likely benefit from further optimization.

Alternatively, it may be reflective of Y_{356}• sampling a series of conformations within the protein. A similar hypothesis has been proposed for the large distance distributions measured for Y_{122}•-NH_2Y_{730}• and Y_{122}•-NH_2Y_{731}•.[18] Given our inexperience with the technique at the time of data collection, we find the first explanation more likely.

Figure 4.3 PELDOR analysis of the Y_{122}•-NH_2Y_{356}• distance. (A) Echo-detected X-band EPR spectrum of the reaction of $Y_{356}NH_2Y$-β2 with wt-α2, CDP, and ATP hand quenched at 20 s. Pump and detect frequencies for the PELDOR experiment are indicated by arrows; (B) Raw data from PELDOR pulse sequence after 10 h collection at 15 K demonstrate clear oscillations; (C) Fit (red) to the experimental data obtained using the software DEERAnalysis 2009; (D) Distribution of distances extracted from the fit shown in (C).

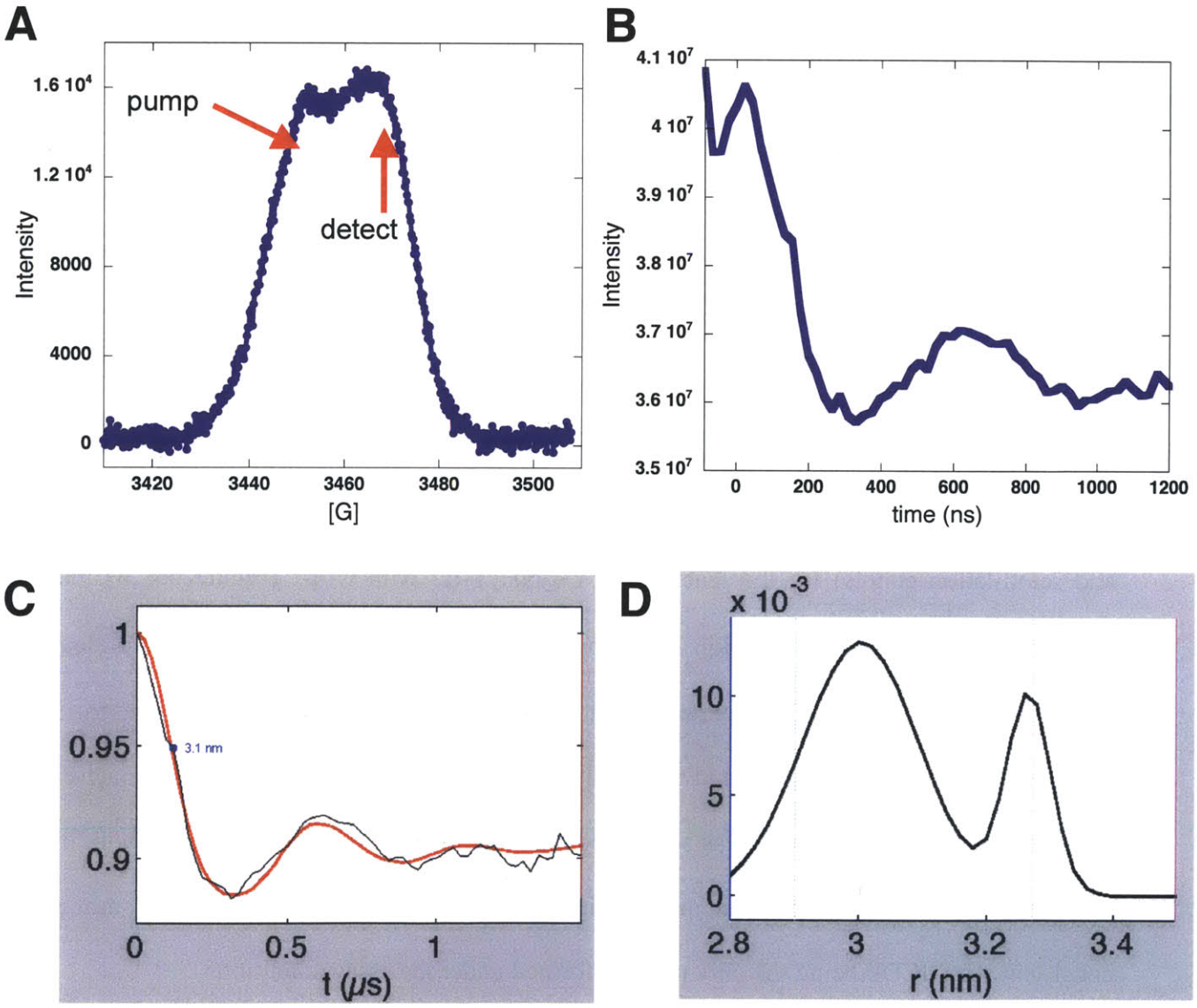

4.3.3 Determining the identity of product(s) formed in the reaction of $Y_{730}NH_2Y$-α2 with wt-β2 under steady-state and single-turnover conditions. The observation of cytosine release in the single-turnover assays of certain $Y_{122}F_nY$-β2s with wt-α2, CDP, and ATP (Chapter 7) prompted us to more closely analyze the product formed in the reaction of $Y_{730}NH_2Y$-α2 and wt-β2. Slow base release has been a well-documented phenomenon in reactions with either mechanism-based inhibitors or active-site mutants of α2.[20-23] The method of Steeper and Steuart employed in the standard radioactive assay protocol relies on the chromatographic separation of deoxycytidine (dC) from cytidine.[9] Cytosine and dC, however, cannot be differentiated by this method when the radiolabel of the substrate is located on the base. Thus, we opted to analyze the product formed in the reaction of $Y_{730}NH_2Y$-α2, wt-β2, CDP and ATP by HPLC.

First, the product formed under steady-state assay conditions was first analyzed. Two timepoints (t = 30 s and 4 min) from the discontinuous steady-state assay were dephosphorylated, applied to a borate column, and eluted following the standard protocol. [9] The eluate was lyophilized in the presence of carrier cytosine and dC, redissolved, and injected on a C-18 HPLC column. Authentic standards of cytosine and dC were shown to elute from the column with retention times of 4.5 and 9.7 min, respectively. The elution profile (absorbance and scintillation counts) for the reaction of $Y_{730}NH_2Y$-α2 with wt-β2 (Figure 4.4 B) may be compared to the analogous reaction between wt-α2 and wt-β2 (Figure 4.4 A). A radioactive impurity from the [^{3}H]-CDP preparation that elutes just after the void volume is present in all samples (indicated by an asterisk in Figure 4.4 B). It constitutes 0.4% of the total radioactivity in the assay reaction mixture, and was subtracted from all samples during analysis. In both the wt and the mutant, a time-dependent increase in radioactivity is observed for the 9.7 min peak, consistent with dCDP being the only product formed under the assay conditions.

Product formation was then examined for the single-turnover reaction of $Y_{730}NH_2Y$-α2, wt-β2, CDP, and ATP. Aliquots removed from the assay mixture and quenched at t = 1 and 10 minutes were analyzed by the HPLC method. Since this was a single turnover experiment, we anticipated all dCDP would be formed within 12 s, given an anticipated rate constant for product formation of $\geq 0.3\ s^{-1}$. However, we opted to monitor to longer times as base release usually occurs on a slower time scale. The chromatogram of the reactions between wt-α2 and wt-β2 (Figure 4.4 C) and $Y_{730}NH_2Y$-α2 and wt-β2 (Figure 4.4 D) reveal the exclusive formation of dC. The amount of dC does not increase with time, as expected. There was no evidence of cytosine formation in either reaction after subtracting the radiochemical impurity at 4.5 min. Thus, we conclude from these experiments that $Y_{730}NH_2Y$-α2 produces dCDP as its only product under single- and multiple-turnover conditions. Additionally, it is worth noting that the total radioactivity associated with the dC peak formed under single-turnover conditions with 2 μM $Y_{730}NH_2Y$-α2 is nearly equivalent to that associated with the radiochemical impurity (Figure 4.4 D). The presence of this impurity has introduced difficulty in product quantitation in RCQ experiments given the low stoichiometry of product formation in this (0.7 dCDP/α2) and other NH_2Y-RNRs, particularly at early time points (<100 ms), as presented later in this chapter.

Figure 4.4 HPLC analysis of product formation in the reaction of $Y_{730}NH_2Y$-α2 (or wt-α2) with wt-β2, CDP, and ATP. Product formed in the steady-state assay of wt-β2 with (A) wt-α2 or (B) $Y_{730}NH_2Y$-α2. Blue/cyan and red/orange traces are t =30 s and t = 4 min timepoints, respectively, in the discontinuous assay. Absorbance profiles (solid red or blue lines) arise from the addition of equimolar carrier cytosine and dC into all samples prior to lyophilization. Radioactivity associated with each fraction is shown in cyan or orange dots. Note the different scales of the right *y*-axis among the panels. Asterisk (*) indicates a radioactive impurity that is present in all samples in a constant amount.

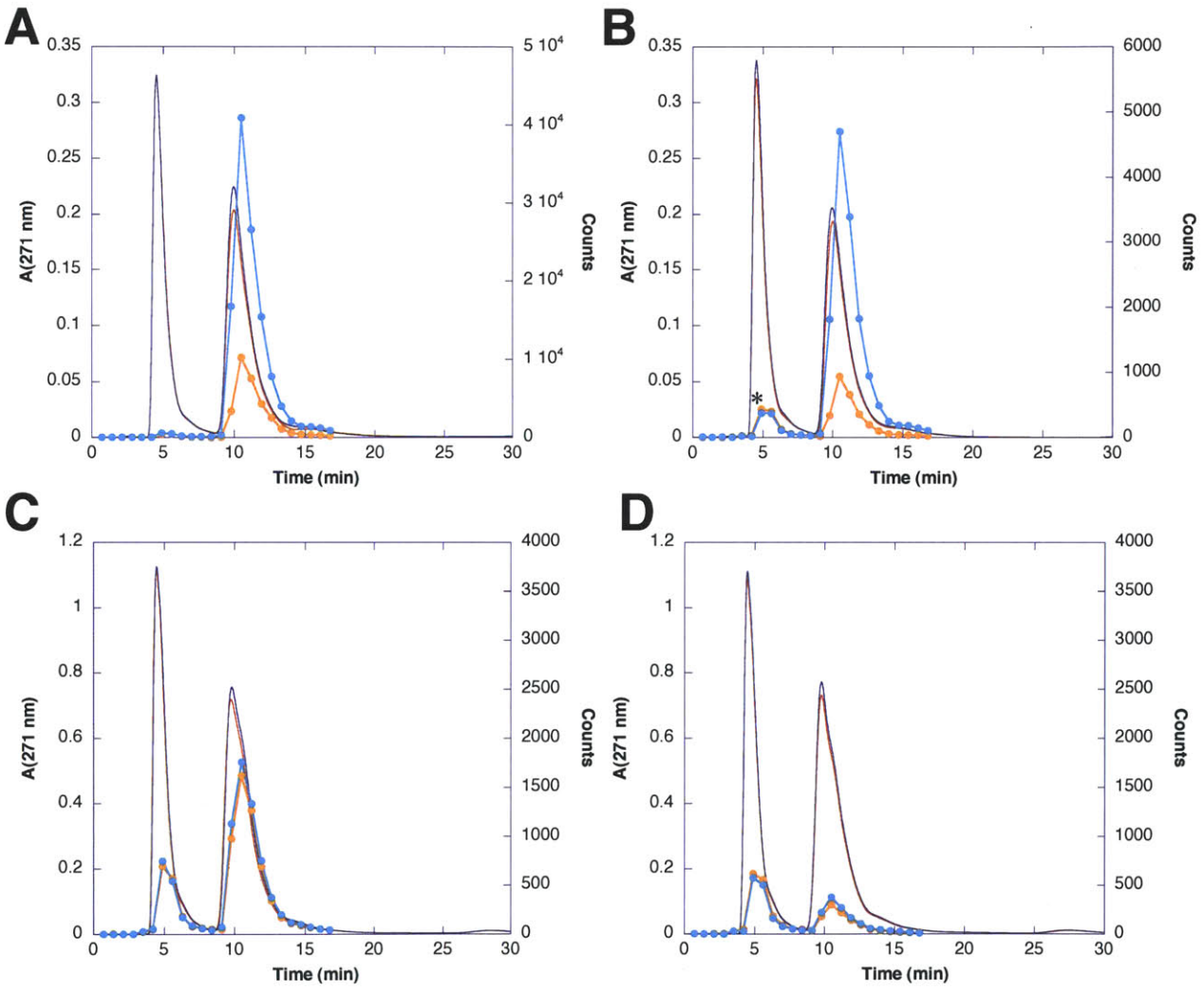

4.3.4 Measuring the substrate $^{D}(V_{max})$ IE for nucleotide reduction by His_6-$Y_{730}NH_2Y$-α2.

NH_2Y-RNRs present us with a unique opportunity to study the details of the PCET and nucleotide reduction mechanisms, as they are catalytically active but the thermodynamics are perturbed to the extent that phenomena that are kinetically masked in the wild-type system can be monitored in NH_2Y-RNRs. Our working model for catalysis in NH_2Y-RNRs was first presented in Chapter 2 and summarized in Scheme 4.1. To further refine this model, we sought to gain information about the rate-limiting step in the overall kinetic scheme by looking for solvent and substrate isotope effects (IEs). As a first experiment, the turnover of the labeled substrate 3′-[^{2}H]-cytidine-5′-diphosphate (3′-[^{2}H]-CDP) by His_6-$Y_{730}NH_2Y$-α2 was determined under saturating conditions. Our model predicts that the chemistry of nucleotide reduction is fast (>100 s^{-1}) and that the rate-determining step precedes the C_{439}•-mediated 3′-H• abstraction from the substrate (step **3**, Scheme 4.1). Thus, no KIE should be observed under these conditions. The observation of a KIE would indicate that nucleotide reduction has become partially rate-limiting in the mutant system. 3′-[^{2}H]-CDP[24] had been prepared previously (Kellogg and Stubbe) and was characterized by UV-vis and NMR to confirm its identity and its chemical purity. It was then used as a substrate at saturating concentrations (250 μM – 1mM) in the standard spectrophotometric assay. Both His_6-α2(wt) and His_6-$Y_{730}NH_2Y$-α2 were assayed, and the specific activities measured with labeled and unlabeled substrates compared.

The results are summarized in Table 4.2 and indicate that there is a $^{D}(V_{max})$ for CDP reduction of 1.3-1.4 for both wt-α2 and $Y_{730}NH_2Y$-α2. The observed KIE was highly reproducible across many assays using two separate chemical preparations of the labeled substrate. The observation of a measurable KIE for wt-α2 was somewhat surprising, given previous reports of the absence of a $^{D}(V_{max})$ KIE for UDP and ADP. Nonetheless, the observed

KIE is very small and is also observed in a control with wt-α2, suggests that 3′-H• abstraction is not rate-limiting for $Y_{730}NH_2Y$-α2.

Table 4.2 $^{D}(V_{max})$ for CDP reduction by His_6-α2(wt) and His_6-$Y_{730}NH_2Y$-α2

Protein (His tagged)	**Substrate**	**[α]** (μM)	**Average SA** (nmol/min•mg)	**Std Dev** (nmol/min•mg)	**% wt**	**H/D**
wt-α2	3′-^{2}H	0.1	1546	29		
	3′-^{1}H	0.1	2089	27		1.4
$Y_{730}NH_2Y$-α2	3′-^{2}H	2.0	83	3	5.4	
	3′-^{1}H	2.0	111	5	5.3	1.3

4.3.5 Measuring the solvent deuterium isotope effect for nucleotide reduction by His_6-$Y_{730}NH_2Y$-α2. Next, the steady state turnover rate of His_6-$Y_{730}NH_2Y$-α2 was examined in D_2O to look for a solvent IE on nucleotide reduction. If the rate-determining step of the reaction was oxidation of C_{439} by NH_2Y_{730}• (step **2** in Scheme 4.1) by hydrogen atom transfer, then one would expect to see an IE when this reaction is conducted in D_2O as the thiol proton of C_{439} is readily exhangeable with solvent.

Assay reagents were prepared in deuterated buffer, and the pD was adjusted using a solution of NaOD. Enzymes were exchanged into deuterated buffer by concentration and dilution cycles until the total proton concentration was calculated to be 1%. The result of assays of both His_6-α2(wt) and His_6-$Y_{730}NH_2Y$-α2 are reported in Table 4.3. On the basis of solvent IEs measured on PCET model systems, we were expecting to observe small effects (1.5-3.0),[25,26] and thus were quite surprised to measure solvent IEs of 4.5 and 6.0 for the wt-α2 and $Y_{730}NH_2Y$-α2 reactions. Note that the activity measurements do not take into account the difference in viscosity between H_2O and D_2O, and thus the KIEs are inflated by ~20%. Measurements in H_2O buffer will need to be repeated in the presence of an appropriate viscogen (e.g., 8% glycerol).

The only previous reports of solvent IEs measured on RNRs come from the 1960s, when Blakley et al. reported an IE of ~4 on the reduction of NTPs in ^3H_2O by RTPR[27] and Larsson et al. measured an IE of ~3.5 on the *E. coli* RDPR reaction.[28] However, much has changed with respect to the preparation and quality of the enzyme, so it is hard to make a useful comparison with the results of these much earlier works.

Table 4.3 Deuterium solvent KIEs on steady-state nucleotide reductase activity

Protein	Solvent	Spec Act (nmol/min/mg)	H/D
His-α2(wt)	H_2O	1900	-
His-α2(wt)	D_2O	420	4.5
His-$Y_{730}NH_2Y$-α2	H_2O	60	-
His-$Y_{730}NH_2Y$-α2	D_2O	10	6.0

4.3.6 Measuring the solvent deuterium isotope effect for NH_2Y• formation in His_6-$Y_{730}NH_2Y$-α2. In the previous section, large deuterium solvent IEs on steady-state rate of dNDP formation were reported. The IE observed for $Y_{730}NH_2Y$-α2 is unexpectedly large on the basis of what has been observed for model systems, and is likely a combination of IEs on several distinct mechanistic steps. To begin to take this steady-state IE and deconvolute its component parts, the solvent IE on one step, the formation of NH_2Y• (step **1** and **8** of Scheme 4.1), was investigated.

The reaction between His_6-$Y_{730}NH_2Y$-α2, wt-β2, CDP, and ATP was monitored at 25 °C in either H_2O or D_2O buffer. Average kinetic traces showing NH_2Y• formation in H_2O and D_2O, monitored at 325 nm, are given in Figure 4.5 A and B, respectively. As reported previously,[2] NH_2Y• formation in H_2O buffer occurs with rate constants of 13 s^{-1} (16% initial Y_{122}•) and 2.3 s^{-1} (15%), whereas formation in D_2O occurs significantly more slowly, with rate constants of 6.2 s^{-1} (15%) and 1.2 s^{-1} (15%).

Figure 4.5 NH_2Y_{730}• formation in the reaction of His-$Y_{730}NH_2Y$-α2 with wt-β2, CDP, and ATP at 25 °C in (A) H_2O buffer and (B) D_2O buffer. Biexponential fits to the data are shown in blue and red, respectively. Rate constants and amplitudes are given in the main text.

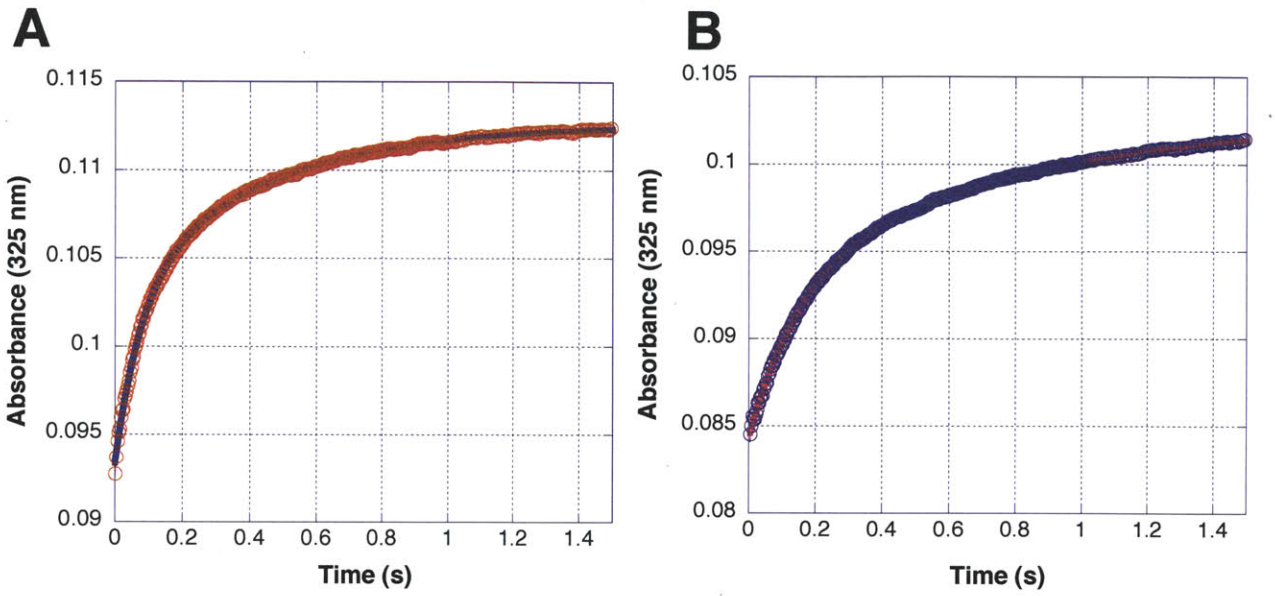

When taking into account the difference in viscosity between the two solutions, a solvent IE of ~1.7 is observed on both of the rate constants for NH_2Y• formation. Thus, we may assume that this solvent IE contributes to the solvent IE for steady-state nucleotide reduction reported in the previous section. These results highlight the complexity in extracting mechanistically informative information from solvent IEs, as they frequently reflect a number of different chemical processes, and the extent to which each contributes to the overall IE is difficult to discern.

4.3.7 Determining the effect of viscosity on NH_2Y• formation in His_6-$Y_{730}NH_2Y$-α2. The rate constants for NH_2Y• formation have been characterized at three positions for all S/E pairs (Chapter 2). A primary goal is to determine the underlying phenomena on which these rate constants and amplitudes report. Previous studies on the temperature dependence of NH_2Y• formation are consistent with the phases reporting on two conformational changes.[29] This

hypothesis was corroborated by comparing the rate constants and amplitudes between the fast phase for NH_2Y_{356}• formation and fastest phase for $DOPA_{356}$• formation (Table 2.8). The striking similarity between the numbers suggest that this phase reports on conformational changes rather than radical propagation, as the latter would be expected to show dependence on the redox potential of the unnatural amino acid at position 356. To test this hypothesis, the effect of viscosity on the rate constants for NH_2Y• formation was investigated. If one or more kinetic phases are reporting on protein conformational dynamics, then one would predict that k_{obs} should be dependent on the solution viscosity (η),[30] and should adhere roughly to the relation shown in eq 4.2:

$$k_{obs} \propto \eta^{-1} \qquad \text{(eq. 4-2)}$$

However, it is possible (though unlikely) that these phases could report on a large protein motion/rearrangement, concomitant with the significant redistribution of waters. In such a case, one would expect a dependence on osmolarity according the relation in eq 4.3:

$$k_{obs} \propto \exp-(\Delta\eta/55.6)m \qquad \text{(eq. 4-3)}$$

Finally, if one was monitoring a pure ET event through a protein, then no change in k_{obs} should be observed with increasing viscosity, assuming the relative hydrophobicity of the protein interior is not perturbed. To test whether the kinetic phases observed during NH_2Y• formation are related to protein conformational dynamics, SF UV-vis spectroscopy was conducted on the reaction of $Y_{730}NH_2Y$-α2 with wt-β2, CDP, and ATP in glycerol concentrations between 0-40% w/v, and the magnitude of glycerol effect was assessed.[30] The results of these experiments are summarized in Table 4.4. Indeed, a pronounced effect of viscosity on the rate constants of NH_2Y• formation is observed. This effect is more noticeable in the fast phase. No change in the amplitude of the phase is observed, suggesting that the same process is being observed at all

viscosities tested. A plot of η^{-1} versus k_{obs} (average of the rate constants measured at 325 and 410 nm) for the fast phase is roughly linear, with a slope of ~14 Pa (Figure 4.6). This linear relationship is consistent with the fast phase reporting on protein conformational changes, as we had previously predicted.

Table 4.4 Effect of viscosity on the kinetics of NH_2Y_{730}• formation.

Glycerol (% w/v)	η (Pa•s)	λ (nm)	Fast phase		Slow phase	
			k (s^{-1})	A (%)	k (s^{-1})	A (%)
0	1	325	13.3	18.1	2.5	14.3
		410	10.0	17.8	1.7	12.4
10	1.291	325	10.6	17.4	2.1	12.2
		410	10.6	14.8	2.2	12.7
25	2.061	325	8.8	11.1	2.0	15.9
		410	5.2	16.3	0.5	16.4
40	3.653	325	1.6	18	0.04	4.5
		410	1.4	18	--	--

Figure 4.6 Plot of η^{-1} vs k_{obs} (average at 325 and 410 nm) for the fast phase of NH_2Y_{730}• formation

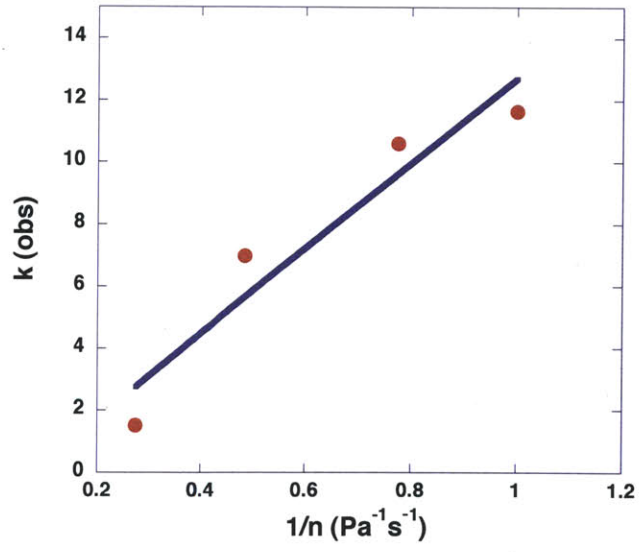

4.3.8 Determining the effect of enzyme concentration, subunit ratio, and reductant on NH_2Y-RNR activities. Over the past several years, the activities of the three NH_2Y-RNRs have been determined from proteins expressed and isolated under a wide variety of conditions, and containing a number of different affinity tags/linkers (Chapter 2). Activities have been measured by two different assays (radioactive and spectrophotometric). The sensitivity of the former implies that it requires much lower protein concentrations, even for mutants with low activity. Spectrophotometric assays are typically run at 3- to 10-fold higher protein concentrations. In almost all cases, steady-state activities were measured using a 1:5 subunit ratio, where the reported specific activity is based on the limiting subunit. From these studies, the range of activities measured for each mutant has been determined (Table 2.3).

The goal of these assays was to systematically address the effect of protein concentration on k_{cat} and to determine if the calculated specific activities of NH_2Y-RNRs changed significantly if assayed in an equimolar subunit ratio. It has been demonstrated that at high protein concentrations (>0.4 μM), both wt subunits display a decrease in specific activity relative to that observed for when the limiting subunit is held between 0.1-0.4 μM.[31] It is not known whether this relates to rate-limiting TR re-reduction of active site cysteines, or to changes in quaternary structure. Thus, we assayed NH_2Y-RNRs at a range of protein concentrations (0.1 μM – 10 μM) and 1:1 and 1:5 subunit ratios.

The results of these assays suggest that the activity of both $Y_{730}NH_2Y$-α2 (Table 4.5, entry 1 and 2) and $Y_{356}NH_2Y$-β2 (Table 4.5, entry 4 and 7) are consistent over a 20-fold change in protein concentration (0.1-2.0 μM). In contrast to the wt subunits, no inhibition is observed at higher protein concentrations (0.4-2.0 μM), suggestion that NH_2Y-RNR activities are not limited by TR-mediated cysteine re-reduction. Furthermore, the results with $Y_{356}NH_2Y$-β2 indicate that

the activity is indistinguishable whether assayed in a 1:5 or 1:1 ratio (entry 4 and 7 versus 5 and 6) over this protein concentration range. A >3-fold reduction in activity is measured, however, at 10 μM protein concentration (entry 3). This observation is noteworthy, as the conditions in entry 3 were those used to examine the kinetics of dCDP formation by NH_2Y-RNRs (*vide infra*). For comparison, SF-UV vis and EPR spectroscopy experiments examining $NH_2Y\bullet$ formation have been carried out in the ranges of 5-15 μM and 15-30 μM, respectively. The implications of this reduction in activity at high protein concentrations will be discussed subsequently.

Table 4.5 NH_2Y-RNR assays measuring the effect of protein concentration and subunit ratio.

Entry	Mutant	[Mutant] (μM)	[wt subunit] (μM)	Spec Act (nmol/min/mg)	SA (% wt)[a]	Scaled[b]
1	$Y_{730}NH_2Y$-α2	0.1	0.5	140	5.6	-
2	$Y_{730}NH_2Y$-α2	2.0	10	152	6.1	-
3	His_6-$Y_{730}NH_2Y$-α2[c]	10.0	15.0	40	1.8[c]	-
4	$Y_{356}NH_2Y$-β2	0.1	0.5	259	3.7	9
5	$Y_{356}NH_2Y$-β2	0.4	0.4	233	3.3	8
6	$Y_{356}NH_2Y$-β2	2.0	2.0	315	4.5	11
7	$Y_{356}NH_2Y$-β2	2.0	10	317	4.5	11

a. Wt activities are 2500 (wt-α2), 2200 (His_6-α2(wt)), and 7000 (wt-β2) nmol/min/mg; *b.* Scaled for radical content (for $Y_{356}NH_2Y$-β2 assays); *c.* Protein concentrations and subunit ratios employed for RCQ experiments. Spectrophotometric assay became non-linear after 30 s; activity measured from the initial linear region.

A second approach to addressing the question of whether NH_2Y-RNR activities are limited by disulfide re-reduction is to compare the results of $Y_{730}NH_2Y$-α2 activity assays using DTT versus TR/TRR/NADPH as the reducing system. Previous studies indicated that DTT concentrations of 10-20 mM gave the highest specific activities, while DTT >20 mM resulted in inhibition of wt and mutant α2s.[12] Assays were conducted at 1:1 and 1:5 subunit ratios. The results are summarized in Table 4.6 and indicate that substituting DTT for TR/TRR/NADPH reduces the observed specific activity of $Y_{730}NH_2Y$-α2 by at least an order of magnitude. The

activity is reduced even further (and becomes non-linear over the assay timecourse) when the subunits are equimolar. One hypothesis to rationalize this loss of activity would be susceptibility of the NH_2Y• to reduction by DTT. In the presence of high [DTT], some of the NH_2Y• may be reduced by a pathway that would result in irreversible loss of the catalytic radical. The increased activity of the 1:5 subunit ratio relative to the 1:1 subunit ratio is also consistent with this hypothesis, as there is a five-fold excess of Y_{122}• in the former that can help recover activity lost through NH_2Y• quenching. However, this hypothesis has not been tested experimentally and is one of many possible explanations for the loss of activity with DTT compared to TR/TRR/NADPH. From the DTT assay results, we conclude that TR/TRR/NADPH should be used as the reducing system in all assays despite complexities that may arise from protein interactions upon disulfide reduction.

Table 4.6 Activity of $Y_{730}NH_2Y$-α2 as a function of reductant (DTT vs TR/TRR/NADPH)

Mutant	Reductant	[α] (μM)	[β] (μM)	Complex (%)	Spec Act (nmol/min/mg)	SA (% wt)
$Y_{730}NH_2Y$-α2	TR/TRR/NADPH	0.1	0.5	80%	140	5.6
$Y_{730}NH_2Y$-α2	DTT	1	5	99	13	0.5
$Y_{730}NH_2Y$-α2	DTT	1	1	73	[a]	-

a. Slope was non-linear over the time of the assay. A fit of the data to the earliest region gave a specific activity of 5 nmol/min/mg.

4.3.9 Pre-steady state kinetics of dCDP formation in NH_2Y-RNRs measured by RCQ. In our original kinetic model (Scheme 4.1), we argued that step **2**, oxidation of the subsequent amino acid on the pathway by NH_2Y•, is rate-limiting. If this is true, the rate constant for dCDP formation in the first turnover, determined by a rapid chemical-quench (RCQ) experiment should be identical to that in the steady-state (k_{cat}). Alternatively, if dCDP is formed with a rate constant similar to NH_2Y• formation (~2.5 s^{-1}), a step subsequent to dCDP formation must be rate-

limiting. We sought to address this question by examining the pre-steady state kinetics of dCDP formation in NH_2Y-RNRs, starting with the tagged protein His_6-$Y_{730}NH_2Y$-α2, which we hypothesize to be free from contaminating wt-α2 (Chapter 2).[3]

Pre-steady state experiments of dCDP formation in wt RNR indicate that a total of ~3 dCDP are generated per α2 in the absence of reductant, and that the first ~1.8 dCDP are formed in a burst phase with a rate constant of 2-10 s^{-1}.[31] Before exploring the kinetics of dCDP formation in His_6-$Y_{730}NH_2Y$-α2, it was necessary to examine the kinetics of product formation in His_6-α2(wt). In all respects examined thus far (steady-state activity, K_d for β2, etc.), His-α2(wt) behaves identically to wt-α2. This similarity also holds true with respect to the kinetics of product formation (Figure 4.7 A). The reaction of His_6-α2(wt), wt-β2, CDP, and ATP generates 1.2 dCDP/α2 with a fast rate constant of 2.6 s^{-1}, and an additional 1.2 dCDP with a slow rate constant of 0.2 s^{-1}. Thus, a slight perturbation is observed with tagged α2, as the rate constant and amplitude of the fast phase are both reduced slightly relative to untagged α2.

The reaction of His-$Y_{730}NH_2Y$-α2 was examined in an analogous fashion and the results shown in Figure 4.7 B. Formation of dCDP is biphasic, with a fast phase of 14 s^{-1} (0.3 dCDP/α2) and a slow phase of 0.06 s^{-1} (0.22 dCDP/α2). For comparison, the reaction of His_6-$Y_{730}NH_2Y$-α2, wt-β2, CDP, and ATP monitored by SF UV-vis spectroscopy generates NH_2Y_{730}• at 13 s^{-1} (16% initial Y_{122}• converted) and 2.3 s^{-1} (15%) (Table 4.7).[3] Interestingly, the fast phase has a rate constant on par with k_{fast} for NH_2Y• formation. At the time these data were collected, the steady state activities of His-$Y_{730}NH_2Y$-α2 had been measured at final protein concentrations between 0.1 and 2.0 μM, and a k_{cat} of 0.2-0.3 s^{-1} had been routinely measured under those conditions. Thus, the slow phase (0.06 s^{-1}) in the His-$Y_{730}NH_2Y$-α2 reaction was interpreted as consistent with what has been reported previously for the second phase for wt-α2 (~0.1 s^{-1}) in the

absence of reductant. In the wt system, this phase is associated with the very slow reduction of the 3rd and 4th equivalent of dCDP/α2 in the absence of reductant (i.e., after disulfide exchange of the active site disulfide with the C-terminal reduced cysteines).[31] Finally, it worth noting that only 0.55 dCDP/α2 were formed in the RCQ experiment, compared to the 0.7 dCDPs that were obtained in a hand-quench experiment immediately prior to RCQ experiment. This lower stoichiometry is likely related to loss of enzyme activity (~20%) at 25 °C over the length of the RCQ experiment, as was determined by comparing hand-quench single turnover assays at the start and finish of the RCQ timecourse.

With our initial interpretation of the data in mind, the kinetics of dCDP formation by His-$Y_{730}NH_2Y$-α2 were measured by RCQ in the presence of the TR/TRR/NADPH to determine the effect of reductant on the slow phase. We hypothesized that k_{slow} might increase to the slow rate constant for NH_2Y_{730}• formation (2.5 s^{-1}, Table 4.7), or to k_{cat} (0.2-0.3 s^{-1}). The results of the RCQ timecourse in the presence of reductant are shown in Figure 4.7 C and D and summarized in Table 4.7. The data may be fit to a single exponential "burst" phase corresponding to the first turnover, followed by a linear phase for subsequent turnovers. A fast rate constant of 7 s^{-1} was measured, which we assume is on par with k_{fast} from the single-turnover experiment given the error in the quantitation when such little product is formed. Surprisingly, k_{slow} (0.07 s^{-1}) was indistinguishable from that determined in the single-turnover experiment. The observation that the linear phase was 3- to 4-fold reduced than our previously determined k_{cat} prompted reexamination of the steady-state activity of His-$Y_{730}NH_2Y$-α2 at higher protein concentration. Indeed, when a steady state assay was conducted under conditions identical to the RCQ experiment (10 μM $Y_{730}NH_2Y$-α2 and 15 μM wt-β2), k_{cat} was reduced to 0.1 s^{-1}, consistent with

what was observed in the RCQ experiment (Table 4.7). Furthermore, the assay became nonlinear after 30 s, suggesting some extent of decoupling or inhibition.

Figure 4.7 Kinetics of dCDP formation in the reaction between wt-β2, CDP, ATP and (A) His-α2(wt) or (B) His-$Y_{730}NH_2Y$-α2 under single turnover conditions at 25 °C monitored by RCQ. Final protein concentrations were 10 and 15 μM. A biexponential fit to the data is indicated by the black line. Kinetic constants are described in the text. (C) Kinetics of dCDP formation for His-$Y_{730}NH_2Y$-α2 in the presence of TR/TRR/NADPH (multiple turnovers) at the same temperature/protein concentrations. (D) An expanded view of the early time points from panel C. Error bars are the standard deviation between two trials. Multiple turnover data were fit (black line) to a monoexponential burst phase + linear phase.

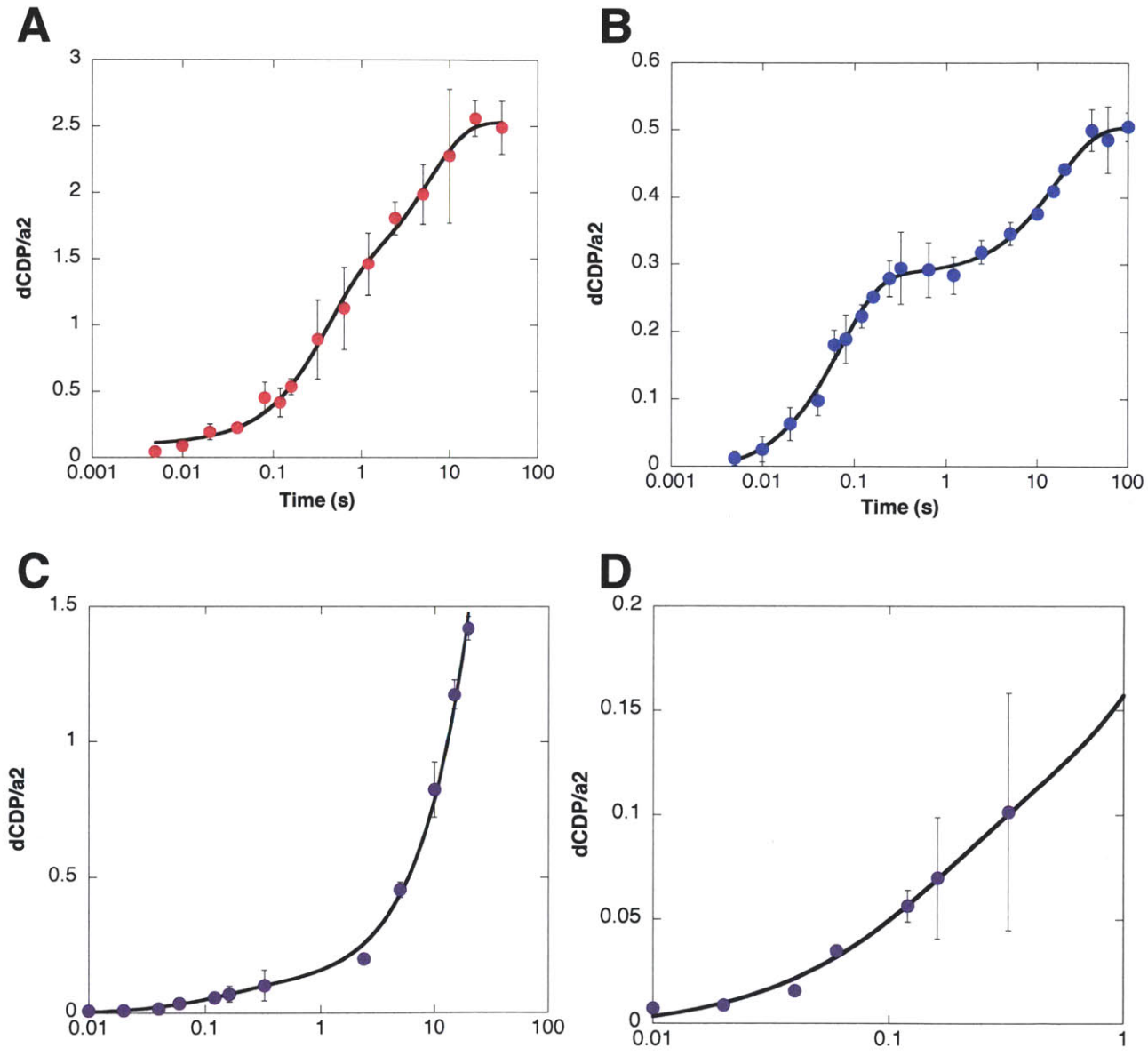

Figure 4.8 Kinetics of dCDP formation in the reaction between His-α2(wt), CDP, ATP and $Y_{356}NH_2Y$-β2 under single turnover conditions at 25 °C monitored by RCQ. Final protein concentrations were 12.5 each μM (6.25 μM Y•). Error bars are the standard deviation between two trials. A biexponential fit to the data is indicated by the black line. Kinetic constants are described in the text.

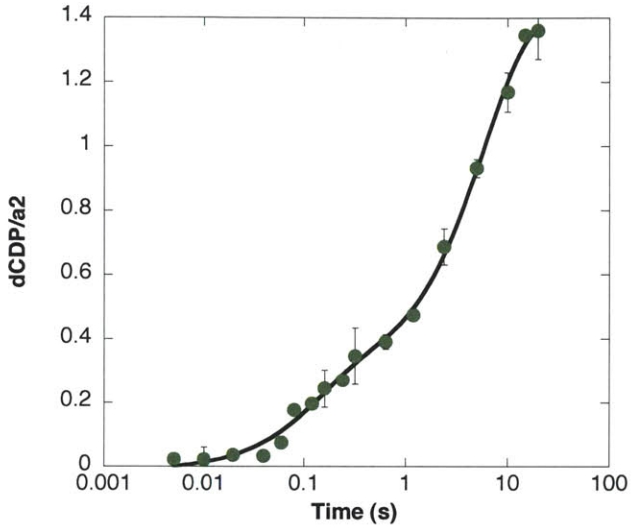

Table 4.7 Rate constants for NH_2Y• formation, pre-steady state dCDP production, and steady state dCDP formation in NH_2Y-RNRs.

	NH_2Y• formation[a]		dCDP formation, one turnover		dCDP formation, multiple turnover		k_{cat} (s^{-1})[a]	
	k_{fast} (s^{-1})	k_{slow} (s^{-1})	k_{fast} (s^{-1})	k_{slow} (s^{-1})	k_{fast} (s^{-1})	k_{slow} (s^{-1})	≤ 2 μM	10 μM
730[b]	13	2.3	14	0.06	7	0.07	0.2-0.3	0.1[d]
731	18	2.5	-[c]	-	-	-	0.4-0.7	-
356	36	2.1	7.5	0.17	-	-	0.4-0.5	-

a. As originally reported in reference [3]; *b*. Rate constants reported for position 730 are for His-$Y_{730}NH_2Y$-α2. Rate constants for position 731 and 356 are for the untagged protein. His-$Y_{730}NH_2Y$-α2 and $Y_{730}NH_2Y$-α2 behave identically within error in NH_2Y• formation as determined by SF UV-vis and EPR spectroscopy; *c*. Not determined; *d*. Assay becomes nonlinear after 30 s.

We next investigated whether the kinetics of dCDP formation varied with the site of NH_2Y incorporation by conducting a single-turnover RCQ experiment on the reaction of $Y_{356}NH_2Y$-β2 with wt-α2, CDP, and ATP. In previous SF UV-vis studies of NH_2Y• formation at three positions, we noted that k_{fast} appears to increase with position on the order of 356 (36 s^{-1}) > 731 (18 s^{-1}) > 730 (12 s^{-1}). The slow rate constant was invariant with position and S/E pair. Given the similarity between k_{fast} for NH_2Y• formation and k_{fast} for dCDP formation in His-$Y_{730}NH_2Y$-α2, we anticipated that trend would extend to the reactions of $Y_{356}NH_2Y$-α2. Thus, the reaction of $Y_{356}NH_2Y$-β2 (12.5 μM, 6.25 μM Y•) with wt-α2 (12.5 μM), CDP, and ATP was studied by RCQ. Previous hand-quench experiments indicated that the stoichiometry of dCDP formed per α2 did not depend on the [Y•]:[α2] ratio, and thus we opted to conduct the assay at a 1:1 $Y_{356}NH_2Y$-β2:wt-α2 ratio (0.5:1 Y•:wt-α2). This observation is consistent with a catalytic role for β2, that is, that one β2 is in an equilibrium with many α2s on the timescale of turnover, providing a catalytic oxidant (Y_{122}•) to each. This hypothesis is explored in more detail in Chapter 7.

The results of the single-turnover RCQ experiment with $Y_{356}NH_2Y$-β2 are shown in Figure 4.8. A biexponential fit to the data give rate constants of 7.5 s^{-1} (0.3 dCDP/α2) and 0.16 s^{-1} (1.1 dCDP/α2). The fast rate constant is 5-fold slower than we anticipated on the basis of the k_{fast} for NH_2Y• formation, but is 3-fold faster than k_{slow} for NH_2Y• formation and 15-fold faster than steady-state k_{cat} (determined at 2 μM protein). Thus, we tentatively propose that k_{fast} for NH_2Y• formation and k_{fast} for dCDP formation are in rough agreement with one another given the error in the latter number due to experimental scatter and the low stoichiometry of product formation (0.3 dCDP/α2). The slow rate constant for dCDP formation, 0.16 s^{-1}, is on par with that measured for the reaction with $Y_{730}NH_2Y$-α2 under single turnover conditions. The various

rate constants for dCDP formation are assigned to individual steps in a revised kinetic model in the Discussion.

4.3.10 Determining whether NH_2Y_{730}• can re-initiate dCDP formation. A key question raised in the original model (Scheme 4.1) is the mechanism of radical re-initiation. The model indicates that it may happen in one of two ways: via steps **6** and **1** (regeneration of Y_{122}•), or via **7** and **2** (re-initiation through NH_2Y•). To address this question, two different types of assays were conducted. In the first, a standard steady-state assay was initiated with a 1:1 ratio of wt-β2 and $Y_{730}NH_2Y$-α2. After a short time (30 s), a 10-fold excess of an inactive β2 (met-β2 or $Y_{356}F$-β2) was added to the assay mixture, with the intention of out-competing the existing wt-β2 and binding the majority of $Y_{730}NH_2Y$-α2 to either met-β2 or $Y_{356}F$-β2. The rate of steady-state dCDP formation by $Y_{730}NH_2Y$-α2 was measured over several minutes after the addition of the inactive β2. As a positive control, an assay was conducted in which a 10-fold excess of wt-β2 was added at 30 s. If the protein continued to show activity with met-β2, than either pathway could be active (**6** + **1** or **7** + **2**); if the protein continued to show activity with $Y_{356}F$-β2, then this would provide strong evidence for re-initiation through NH_2Y_{730}•. As a control, a 10-fold addition of wt-β2 at 30 s was also conducted. The results are shown in Table 4.8 and indicate that the measured activity is reduced at least 20-fold when an excess of inactive β2 was added at 30 s, suggesting that re-initiation through NH_2Y_{730}• cannot account for the activity measured in $Y_{730}NH_2Y$-α2.

Table 4.8 Assays testing re-initiation by NH_2Y_{730}• with $Y_{356}F$-β2 and met-β2.

β2 (10 eq)	**SA** (nmol/min/mg)	**% wt**
wt	128	5.1
$Y_{356}F$	4	0.16
met	6	0.25

The next experiment to test the pathway of re-initiation utilized NO_2Y_{122}• as a radical initiator. A total of 0.6 dCDP/α2 has been reported for the reaction of $Y_{122}NO_2Y$-β2 with wt-α2, CDP, and ATP under single turnover conditions (i.e., no reductant). This low stoichiometry of product formation is associated either with the inability to re-oxidize NO_2Y^- during reverse radical propagation, or the uncoupling of PT and ET that occurs in this system. If the analogous reaction were conducted with $Y_{730}NH_2Y$-α2, a re-initiation model through a pathway radical would suggest that more dCDPs should be observed per α2. Thus, a reaction was conducted in which NO_2Y_{122}• was generated on a rapid time scale (<10 s) by hand-mixing Fe(II)-loaded $Y_{122}NO_2Y$-β2 with O_2, then diluted to a final concentration of 20 μM into a mixture of all other assay components (CDP, ATP, TR, TRR, NADPH) and either wt-α2 or $Y_{730}NH_2Y$-α2 (20 μM). The results of these assays are shown in Table 4.9 and indicate that $Y_{730}NH_2Y$-α2 generates ~0.1 dCDP/α2 under these conditions, and that there is no obvious time dependence for product formation. This is consistent with the results of the previous experiments, suggest that radical propagation cannot re-initiate though NH_2Y_{730}•. The NO_2Y experiment also suggests that only a small fraction of the NH_2Y• formed is active (at least in an initial the fast phase), as the reaction with $Y_{730}NH_2Y$-α2 generates only 20% of the product made in the reaction with wt-α2.

Table 4.9 Assays testing re-initiation by NH_2Y_{730}• with $Y_{122}NO_2Y$-β2.

α2	Time	dCDP/α2[a]
wt	20	0.44
	40	0.51
	60	0.59[b]
$Y_{730}NH_2Y$	20	0.101
	40	0.090
	60	0.074

a. The results are the average of two experiments. In all cases, the error between each experiment for each time point was <10%; *b.* The slope observed for the reaction with wt-α2 is consistent with <0.05% contaminating wt-β2 in the $Y_{122}NO_2Y$-β2 sample. [1]

4.3.11 Analyzing the catalytic activity of $Y_{730}NH_2Y$-α2 (or $Y_{731}NH_2Y$-α2) with $Y_{356}NH_2Y$-β2. Through many different methods, the catalytic activity of RNRs in which a single NH_2Y has been substituted at position 356, 730 or 731 has been established. Given these results, it was interesting to ask whether RNRs containing multiple NH_2Ys on the pathway could generate dCDP. Thus, $Y_{730}NH_2Y$-α2 (or $Y_{731}NH_2Y$-α2) was assayed for activity with $Y_{356}NH_2Y$-β2. The concentration of the NH_2Y-α2 was varied between 0.5 and 1.0 μM, and $Y_{356}NH_2Y$-β2 was held in a five-fold molar excess. In all cases, no catalytic activity was observed. Under the conditions employed, activities of ~0.5% wt should be discernable over background.

4.4 DISCUSSION

The experiments described in this chapter were intended to directly test our model for catalysis in NH_2Y-RNRs (Scheme 4.1). Many of the results of these studies are consistent with the originally proposed model. A solvent IE was observed for steady-state catalysis by His-$Y_{730}NH_2Y$-α2, as would be expected if the oxidation of C_{439} by NH_2Y_{730}• occurred by a concerted, co-linear PCET mechanism. While the magnitude of this IE cannot be predicted, it was indeed much larger than anticipated. Further studies suggested that a solvent IE on both phases of NH_2Y• formation (step **1** and **8**) contributes to this overall steady-state effect. Furthermore, no significant KIE was observed using 3′-[^{2}H]-CDP as a substrate, suggesting that 3′-H• abstraction (step **3**) is not rate-limiting in the overall kinetic scheme. This is consistent with our recent studies on the reaction of $Y_{122}NO_2Y$-β2 with wt-α2, CDP, and ATP that indicated that dCDP is formed with rates >100 s^{-1}.[1] Studies on the effect of viscosity on NH_2Y• formation are consistent with previous experiments investigating the temperature dependence of its formation[29] and with the hypothesis that the rate constants and amplitudes report on conformational changes that accompany radical initiation. Thus, NH_2Y serves a dual role as a reporter on radical propagation events and conformational changes that cannot be detected in the wt RNR.

As summarized in the introduction and described in detail in Chapter 2, our original model (Scheme 4.1) showed two initial pathways of NH_2Y• formation, consistent with the biphasic kinetics observed for its generation by SF UV-vis spectroscopy. The faster phase was assigned to step **8** and was said to report on a conformation of NH_2Y• that is not immediately active towards catalysis. The slower phase (2.5 s^{-1}) was assigned to step **1** and hypothesized to report on a conformational change analogous to that which is rate-limiting in the wt system. It

was posited that the NH_2Y• formed in the slow phase (step **1**) propagates to the enzyme active site, with the rate-determining step (rds, k_{cat} of 0.2-0.7 s^{-1}) in the overall kinetic scheme being the oxidation of the next residue on the pathway by NH_2Y• (step **2**).

The results of pre-steady state experiments on dCDP formation in NH_2Y-RNRs presented in this chapter require that we modify the model from its original form. In the reaction of $Y_{730}NH_2Y$-α2 with wt-β2, CDP, and ATP monitored by RCQ, dCDP was made in a fast phase at 14 s^{-1} (0.3 dCDP/α2) and a slow phase at 0.06 s^{-1} (0.22 dCDP/α2). The observation of pre-steady state dCDP formation with a rate constant that is 50-fold faster than the steady-state k_{cat} discounts our hypothesis that step **2** is rate-limiting in the overall catalytic scheme, and thus we will adapt our model accordingly. The excellent agreement between k_{fast} for dCDP formation and k_{fast} for NH_2Y• formation suggests that the NH_2Y• population formed in k_{fast} is active towards nucleotide reduction, and that formation of NH_2Y• and dCDP in this phase are gated by the same conformational change(s). A rate constant on par with k_{slow} for NH_2Y• formation is not observed in the kinetics of dCDP formation, indicating that this population, if active, encounters a subsequent slow step on the pathway prior to nucleotide formation. In light of these observations, our revised model has reversed the assignments of k_{fast} and k_{slow} for NH_2Y• formation (Scheme 4.2). The fast rate constant is now assigned to step **1**, and the slow to step **8** (step numbering is the same as in Scheme 4.1). This reassignment is supported by RCQ analysis of the reaction with $Y_{356}NH_2Y$-β2, wt-α2, CDP, and ATP, which generates dCDP with with a rate constant 3-fold higher than the k_{slow} for NH_2Y_{356}• formation. The discrepancy between k_{fast} for dCDP formation and k_{fast} for NH_2Y• formation in the 356 data is attributed to error associated with kinetic characterization by RCQ in the presence of low levels of product and significant radiochemical background.

We now consider the k_{slow} for dCDP formation which, in the case of both the $Y_{730}NH_2Y$-$\alpha 2$ and $Y_{356}NH_2Y$-$\beta 2$ reactions, is 2.5- to 4-fold slower than anticipated on the basis of the previously-determined turnover numbers for the mutants (Table 7.4). Subsequent measurement of the activity of $Y_{730}NH_2Y$-$\alpha 2$ at the elevated protein concentrations used for RCQ (10-12.5 μM in these studies) gave a turnover number of 0.1 s^{-1}, indicating a decrease in k_{cat} with increasing protein concentration. Indeed, when the reaction of $Y_{730}NH_2Y$-$\alpha 2$ in the presence of TR/TRR/NADPH was examined by RCQ at 10 μM protein, a linear phase of 0.07 s^{-1} was observed, consistent with the new k_{cat} measurement. A similar observation has been characterized previously for wt *E. coli* class Ia RNR.[31] That k_{slow} for dCDP formation in the single-turnover experiment is identical to k_{cat} indicates that the rds occurs at a step up to and/or including nucleotide reduction. Thus, we may reexamine our kinetic model and look for a candidate rds on the forward PCET pathway. By the logic described above, steps **1** (10-45 s^{-1}), **8** (2.5 s^{-1}), **2** (10-45 s^{-1}) and **3** (>100 s^{-1}) have all been assigned rate constants much faster than k_{cat}. By process of elimination, we must consider step **9** as a possible candidate for the overall slow step on the NH_2Y-RNR catalytic scheme. Step **9** reports on the interconversion between the two distinct NH_2Y• populations that have been observed to form at each of the three pathway positions and with all of the matched S/E pairs. We propose a model in which two initial NH_2Y• populations are formed, with that formed in step **1** (k_{fast}) immediately assuming a conformation that allows oxidation of the subsequent amino acid on the pathway (step **2**, $k \geq$10-45 s^{-1}) and radical propagation to the enzyme active site. This population is responsible for generating ~50% of the total dCDP formed in a single turnover. After this initial product formation, some subtle rearrangement occurs that provokes the conversion of the inactive NH_2Y• population (formed in step **8**) to an active conformation (step **9**), that then may propagate to the active site

and initiate chemistry. We propose that this interconversion (step **9**) occurs at 0.06-0.1 s^{-1} and is the overall rds in the revised kinetic scheme (Scheme 4.2). In the case of the reaction of $Y_{730}NH_2Y$-α2, the stoichiometry of dCDP formation between the two phases is consistent with the relative amplitudes of the two phases of NH_2Y• formation observed by SF UV-vis, and thus is consistent with both populations being active, albeit on very different time scales.

The distinguishing features between the two NH_2Y• populations are unknown, but we propose that they are divided on the basis of a subtle structural difference, as larger residue rearrangements or rotations would be highly unfavorable for a residue in a fairly rigid, hydrogen-bonded local environment, as exists at position 730 of α2 (though positions 731 of α2 and 356 of β2, located at the subunit interface, may access more conformational freedom).[3] Examination of kinetics of NH_2Y_{730}• formation in the reaction of $Y_{730}NH_2Y$-α2 with wt-β2, CDP, and ATP studied by rapid freeze-quench (RFQ) EPR spectroscopy failed to give any spectral evidence of two radical populations,[32] though many of the fine electronic details of the radical structure are not visible at this low field. Thus, we propose high-field (HF) EPR analysis of NH_2Y• samples formed at early time points. Comparison of HF spectra (and the hyperfine coupling constants and *g* values extracted from them) of radicals trapped at early time points by RFQ may be compared to those already characterized from an analogous t = 30 s hand-quench reaction[6,15] to look for evidence of structural differences between the two. In a final modification to our original model, we have been prompted to remove steps **7** and **-7** due to the inability to detect radical re-initiation through a pathway NH_2Y• in two different experiments.

The argument that only a fraction of the NH_2Y• population is in an active conformer at a given time may help rationalize the lack of activity observed in the reaction of $Y_{356}NH_2Y$-β2 with $Y_{731}NH_2Y$-α2 (or $Y_{730}NH_2Y$-α2). If the effect of multiple populations is multiplicative,

that is if only a small fraction (~20% of the total initial Y_{122}•) of the NH_2Y_{356}• is able to oxidize NH_2Y_{731}, and then only a fraction of the NH_2Y_{731}• (or NH_2Y_{730}•, ~20% of the total NH_2Y_{356}•) is able to oxidize the next pathway residue, then the amount of active NH_2Y-RNR could easily be reduced such that it is undetectable in the RNR assay at 1 μM protein concentration, as was used in the experiment described in section 4.3.11.

In the following chapter, we provide biochemical and structural evidence that the generation of NH_2Y_{730}• in the reaction of $Y_{730}NH_2Y$-α2, wt-β2, CDP, and ATP results in the formation of a kinetically stable α2β2 complex. One of the primary questions associated with this observation is the origin of the complex's unusual stability, as the wt-α2β2 complex has a dissociation constant on the order of 100 s^{-1}.[33] We hypothesize that stability is protective in nature, that is, that the protein subunits associate more tightly when a radical is on pathway to prevent quenching of the catalytic oxidant. The revised model presented herein helps explain why the reaction of $Y_{730}NH_2Y$-α2, wt-β2, CDP, and ATP can be catalytically active while maintaining a persistent NH_2Y_{730}• and hence, a stable a2β2 complex.

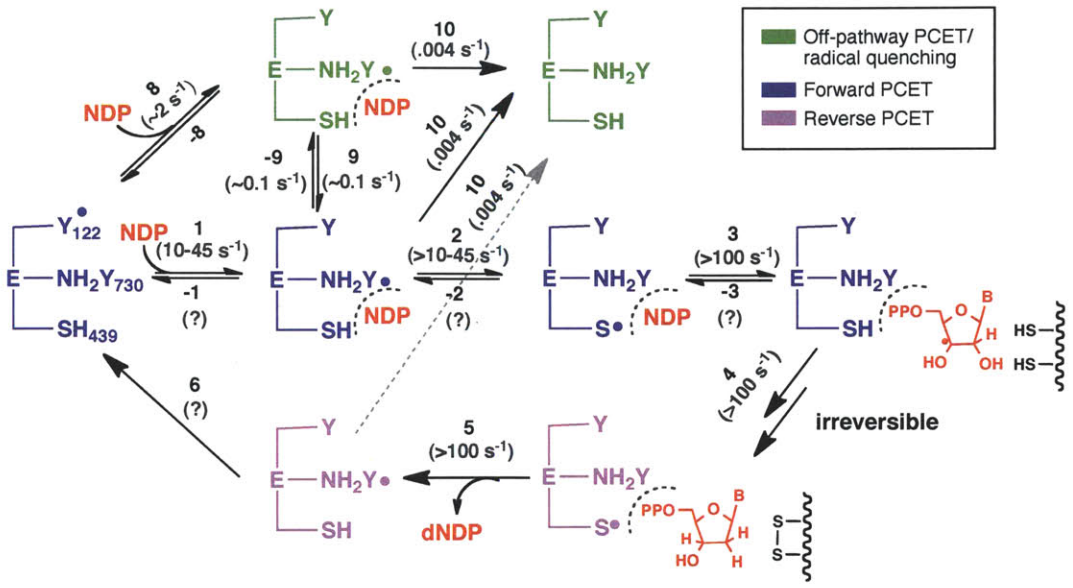

Scheme 4.2 Revised kinetic model for $NH_2Y\bullet$ formation and nucleotide reduction in NH_2Y-RNRs. Numbering of the individual steps and coloring of the three pathways is assumed to be the same as in Scheme 4.1. The rate constants assigned to individual steps, if available, are indicated above the arrows. Those rate constants that are new or have been reassigned relative to the original model (Scheme 4.1) are described in this section.

4.5 REFERENCES

1. Yokoyama, K., Uhlin, U. & Stubbe, J. A hot oxidant, 3-NO2Y_{122} radical, unmasks conformational gating in ribonucleotide reductase. *J. Am. Chem. Soc.* **132**, 15368-79 (2010).
2. Seyedsayamdost, M.R., Xie, J., Chan, C.T., Schultz, P.G. & Stubbe, J. Site-specific insertion of 3-aminotyrosine into subunit α2 of *E. coli* ribonucleotide reductase: direct evidence for involvement of Y730 and Y731 in radical propagation. *J. Am. Chem. Soc.* **129**, 15060-71 (2007).
3. Minnihan, E.C., Seyedsayamdost, M.R., Uhlin, U. & Stubbe, J. Kinetics of radical intermediate formation and deoxynucleotide production in 3-aminotyrosine-substituted *Escherichia coli* ribonucleotide reductases. *J. Am. Chem. Soc.* **133**, 9430-40 (2011).
4. Chivers, P.T. et al. Microscopic pK_a values of *Escherichia coli* thioredoxin. *Biochemistry* **36**, 14985-91 (1997).
5. Russel, M. & Model, P. Direct cloning of the *trxB* gene that encodes thioredoxin reductase. *J. Bacteriol.* **163**, 238-42 (1985).
6. Seyedsayamdost, M.R., Argirevic, T., Minnihan, E.C., Stubbe, J. & Bennati, M. Structural examination of the transient 3-aminotyrosyl radical on the PCET pathway of *E. coli* ribonucleotide reductase by multifrequency EPR spectroscopy. *J. Am. Chem. Soc.* **131**, 15729-38 (2009).
7. Jeschke, G. et al. *Appl. Magn. Reson.* **2006**, 473-498 (2006).
8. Chiang, Y.W., Borbat, P.P. & Freed, J.H. The determination of pair distance distributions by pulsed ESR using Tikhonov regularization. *J. Magn. Reson.* **172**, 279-95 (2005).
9. Steeper, J.R. & Steuart, C.D. A rapid assay for CDP reductase activity in mammalian cell extracts. *Anal. Biochem.* **34**, 123-30 (1970).
10. Seyedsayamdost, M.R., Yee, C.S., Reece, S.Y., Nocera, D.G. & Stubbe, J. pH rate profiles of F_nY_{356}-R2s (n = 2, 3, 4) in *Escherichia coli* ribonucleotide reductase: evidence that Y_{356} is a redox-active amino acid along the radical propagation pathway. *J. Am. Chem. Soc.* **128**, 1562-8 (2006).
11. Yee, C.S., Seyedsayamdost, M.R., Chang, M.C.Y., Nocera, D.G. & Stubbe, J. Generation of the R2 subunit of ribonucleotide reductase by intein chemistry: insertion of 3-nitrotyrosine at residue 356 as a probe of the radical initiation process. *Biochemistry* **42**, 14541-52 (2003).
12. Mao, S.S. et al. A model for the role of multiple cysteine residues involved in ribonucleotide reduction: amazing and still confusing. *Biochemistry* **31**, 9733-43 (1992).
13. Argirević, T., Riplinger, C., Stubbe, J., Neese, F. & Bennati, M. High-frequency ENDOR combined with DFT cluster model calculations provide evidence for the hydrogen bond network involved in the PCET of the α-subunit of *E. coli* ribonucleotide reductase. *Submitted.*

14. Svistunenko, D.A. & Cooper, C.E. A new method of identifying the site of tyrosyl radicals in proteins. *Biophys. J.* **87**, 582-95 (2004).

15. Argirevic, T. Ph.D. Thesis. (2011).

16. Denysenkov, V.P., Prisner, T.F., Stubbe, J. & Bennati, M. High-field pulsed electron-electron double resonance spectroscopy to determine the orientation of the tyrosyl radicals in ribonucleotide reductase. *Proc Natl Acad Sci U S A* **103**, 13386-13390 (2006).

17. Bennati, M. et al. EPR distance measurements support a model for long-range radical initiation in *E. coli* ribonucleotide reductase. *J. Am. Chem. Soc.* **127**, 15014-5 (2005).

18. Seyedsayamdost, M.R., Chan, C.T., Mugnaini, V., Stubbe, J. & Bennati, M. PELDOR spectroscopy with DOPA-β2 and NH_2Y-α2s: distance measurements between residues involved in the radical propagation pathway of *E. coli* ribonucleotide reductase. *J. Am. Chem. Soc.* **129**, 15748-9 (2007).

19. Yokoyama, K., Smith, A.A., Corzilius, B., Griffin, R.G. & Stubbe, J. Equilibration of tyrosyl radicals (Y356•, Y731•, Y730•) in the radical propagation pathway of the *Escherichia coli* class Ia ribonucleotide reductase. *J. Am. Chem. Soc.* **133**, 18420-32 (2011).

20. Ator, M.A. & Stubbe, J. Mechanism of inactivation of *Escherichia coli* ribonucleotide reductase by 2'-chloro-2'-deoxyuridine 5'-diphosphate: evidence for generation of a 2'-deoxy-3'-ketonucleotide via a net 1,2 hydrogen shift. *Biochemistry* **24**, 7214-21 (1985).

21. Mao, S.S. et al. Interaction of C225SR1 mutant subunit of ribonucleotide reductase with R2 and nucleoside diphosphates: tales of a suicidal enzyme. *Biochemistry* **31**, 9744-51 (1992).

22. van der Donk, W.A., Yu, G. X., Perez, L., Sanchez, R. J., Stubbe, J., Samano, V. & Robins, M. J. Detection of a new substrate-derived radical during inactivation of ribonucleotide reductase from *Escherichia coli* by gemcitabine 5'-diphosphate. *Biochemistry* **37**, 6419-26 (1998).

23. Artin, E. et al. Insight into the mechanism of inactivation of ribonucleotide reductase by gemcitabine 5'-diphosphate in the presence or absence of reductant. *Biochemistry* **48**, 11622-9 (2009).

24. Stubbe, J. & Ackles, D. On the mechanism of ribonucleoside diphosphate reductase from *Escherichia coli*. Evidence for 3'-C--H bond cleavage. *J. Biol. Chem.* **255**, 8027-30 (1980).

25. Markle, T.F., Rhile, I.J., Dipasquale, A.G. & Mayer, J.M. Probing concerted proton-electron transfer in phenol-imidazoles. *Proc. Natl. Acad. Sci. U S A* **105**, 8185-90 (2008).

26. Irebo, T., Johansson, O. & Hammarstrom, L. The rate ladder of proton-coupled tyrosine oxidation in water: a systematic dependence on hydrogen bonds and protonation state. *J. Am. Chem. Soc.* **130**, 9194-5 (2008).

27. Blakley, R.L., Ghambeer, R.K., Batterham, T.J. & Brownson, C. Studies with hydrogen isotopes on the mechanism of action of cobamide-dependent ribonucleotide reductase. *Biochem. Biophys. Res. Commun.* **24**, 418-26 (1966).

28. Larsson, A. Enzymatic Synthesis of Deoxyribonucleotides. VII. Studies on the Hydrogen Transfer with Tritiated Water. *Biochemistry* **4**, 1984-93 (1965).

29. Seyedsayamdost, M.R. Massachusetts Institute of Technology (2007).

30. Danyal, K., Mayweather, D., Dean, D.R., Seefeldt, L.C. & Hoffman, B.M. Conformational gating of electron transfer from the nitrogenase Fe protein to MoFe protein. *J. Am. Chem. Soc.* **132**, 6894-5 (2010).

31. Ge, J., Yu, G., Ator, M.A. & Stubbe, J. Pre-steady-state and steady-state kinetic analysis of *E. coli* class I ribonucleotide reductase. *Biochemistry* **42**, 10071-83 (2003).

32. Seyedsayamdost, M.R. & Stubbe, J. Replacement of Y_{730} and Y_{731} in the α2 subunit of *Escherichia coli* ribonucleotide reductase with 3-aminotyrosine using an evolved suppressor tRNA/tRNA-synthetase pair. *Methods Enzymol.* **462**, 45-76 (2009).

33. Hassan, A.Q., Olshansky, L., Yokoyama, K., Lutterman, D. A., Jin, X., Nocera, D. G., & Stubbe, J. *In preparation.*

Chapter 5

Biophysical characterization of a stable aminotyrosyl radical-induced $\alpha 2\beta 2$ complex of *E. coli* class Ia RNR

In collaboration with (alphabetical): Nozomi Ando, Edward Brignole, Catherine L. Drennan*, Daniel G. Nocera*, and Lisa Olshansky

5.1 INTRODUCTION

Ribonucleotide reductase is the sole enzyme responsible for the conversion of nucleotides to 2′-deoxynucleotides, providing the cell with the monomeric precursors necessary for DNA replication and repair processes.[1,2] RNR activity is intricately linked to the fidelity of the DNA replication process, as normal RNR activity maintains both the correct absolute cellular concentration of deoxynucleotides, as well as the appropriate relative ratios among the four products.[3] The class Ia RNRs are found in many aerobic bacteria and all eukaryotes and consist of two protein subunits. The larger subunit, α, houses the active site where the four nucleoside diphosphate substrates (S = CDP, ADP, GDP, UDP) are reduced, and two additional nucleotide binding sites. The specificity site binds allosteric effectors (E = ATP, dGTP, TTP, and dATP) and dictates which of the four substrates is reduced, while the activity site binds ATP/dATP and dictates the overall rate of reduction.[4-8] Saturation of the activity site with ATP stimulates nucleotide reduction, while binding of dATP to the site inhibits it. A third allosteric site that binds ATP has been proposed for the mouse RNR.[9] The smaller subunit, β, is an obligate dimer (β2) and contains a diferric-tyrosyl radical cofactor (Y•) that is essential for catalysis.[10] This unusually stable Y• is responsible for the generation of a transient active site cysteine radical (C•) via a mechanism of long-distance reversible proton-coupled electron transfer (PCET) prior to nucleotide reduction.[11,12]

RNR regulation is complicated and layered, with enzyme quaternary structure functioning as one regulatory mode. The most extensively studied class Ia RNR, that from the model bacterium *Escherichia coli*, is generally accepted to be active as an α2β2 complex.[13] The affinity between the two individual subunits is weak (K_d = 0.4 μM), but increases two- to eight-fold in the presence of nucleotides (K_d = 50 – 200 nM).[4,14] The individual *E. coli* class Ia α2 and

β2 subunits are isolated individually and mixtures of the two subunits are readily separable by anion-exchange chromatography and size-exclusion chromatography, even in the presence of nucleotides.[15] Similar observations have been made with human RNR. X-ray crystal structures of the individual *E. coli* α2 and β2 subunits have been solved, but no structure of the putative active complex exists.[11,16] Recent biophysical data from analytical ultracentrifugation (AUC) and small-angle X-ray scattering (SAXS) techniques support a solution equilibrium of three interconverting states in the *E. coli* enzyme, the relative populations of which depend on absolute protein concentration and the presence, identity, and concentration of nucleotides in solution: α2 + β2 ↔ α2β2 ↔ α4β4.[17] Stopped-flow (SF) fluorescence experiments indicate that the α2 + β2 ↔ α2β2 interconversion occurs on a time scale that is very fast relative to catalysis;[18] the kinetics of the α2β2 ↔ α4β4 transition have not yet been explored. The active forms of the mammalian RNRs from mouse and human are still a question of significant debate, but are likely of the form $(\alpha 2)_n(\beta 2)_m$ (n, m = 1 or 3).[9,19]

For both the *E. coli* and mammalian RNRs, higher order oligomers that represent enzyme inactive states have been characterized.[4,20] Data from a number of methods indicate that dATP-induced inactivation of the *E. coli* enzyme occurs via the formation of an α4β4 ring,[17,20] while dATP inactivation in the mammalian RNR has been shown to occur via formation of α6 hexamers.[19,21] Furthermore, it is now recognized that at least two clinically used drugs inactivate RNR concomitant with changes in oligomeric state. The di- and triphosphates of the drug clofarabine (ClF), an adenosine analogue used in the treatment of acute pediatric leukemias, have been demonstrated to reversibly inhibit human α through the generation of a stable hexamer.[22] The 2′,2′-difluoro-2′-deoxycytosine analogue gemcitabine (F_2C) is used in the treatment of non-small cell lung carcinomas and advanced pancreatic cancer. Its diphosphate (F_2CDP) has also

been implicated in the induction of higher order oligomers of RNR.[15] An altered conformation of α, which migrates more slowly on SDS-PAGE, has been observed in the *E. coli*, human, and *L. leichmannii* RNRs. This species has been proposed to be α2β2 in the *E. coli* enzyme and α6β6 in the human,[15,23] though additional experiments are necessary to corroborate this preliminary claim.

Despite the extensive low-resolution (>4 Å) structural and biophysical characterization of a number of the inactive RNR states, a structure of an active class I RNR remains elusive. Nearly two decades ago, upon solving the structure of the *E. coli* α2 subunit, Uhlin and Eklund put forth a docking model for the active *E. coli* α2β2 complex based on shape complementarity between the two subunits.[11] The most provocative feature of this docking model was the 35 Å distance it placed between the diferric-Y_{122}• cofactor in β2 and the active site cysteine, C_{439}, it was proposed to transiently oxidize. Subsequent experiments utilizing pulsed electron-electron double resonance (PELDOR) spectroscopy, a technique for measuring distances (20-80 Å) between two weakly coupled dipoles, supported this long distance.[24,25] From the docking model and from sequence alignments of class I RNRs, a model was proposed in which a series of absolutely conserved aromatic amino acids generates a hopping pathway for radical migration between Y_{122}• and C_{439}. Initial site-directed mutagenesis studies of these conserved residues supported their essential role in nucleotide reduction, but provided little insight to the mechanism of radical transport.[26] Study of this phenomenon in *E. coli* class Ia RNR is further complicated by the fact that electron transfer events are masked by a rate-determining conformational change(s) prior to nucleotide reduction. Pre-steady-state kinetic studies of the wild-type enzyme failed to reveal changes in Y_{122}• due to this masking physical step.[27]

With recent advances in unnatural amino acid incorporation and protein engineering technology, our laboratory has been able to partially sidestep these limitations and has begun to provide some of the first concrete evidence in support of the proposed radical propagation pathway. Collective studies with the radical trap 3,4-dihydroxyphenylalanine (DOPA),[28] the pK_a reporter and high potential radical initiator 3-nitrotyrosine (NO_2Y),[29-31] and the dual pK_a/redox potential reporters fluorotyrosines (F_nYs)[32-34] have allowed us to expand Uhlin and Eklund's original hypothesis to the proposed mechanism for long-range, reversible PCET shown in Figure 5.1. Orthogonal PCET, in which the electron and proton transfer to different acceptors, is proposed to be operative in the β2 subunit, while co-linear PCET, in which the proton and electron move between the same donor/acceptor pair, is proposed for transfer within α2.[12,35]

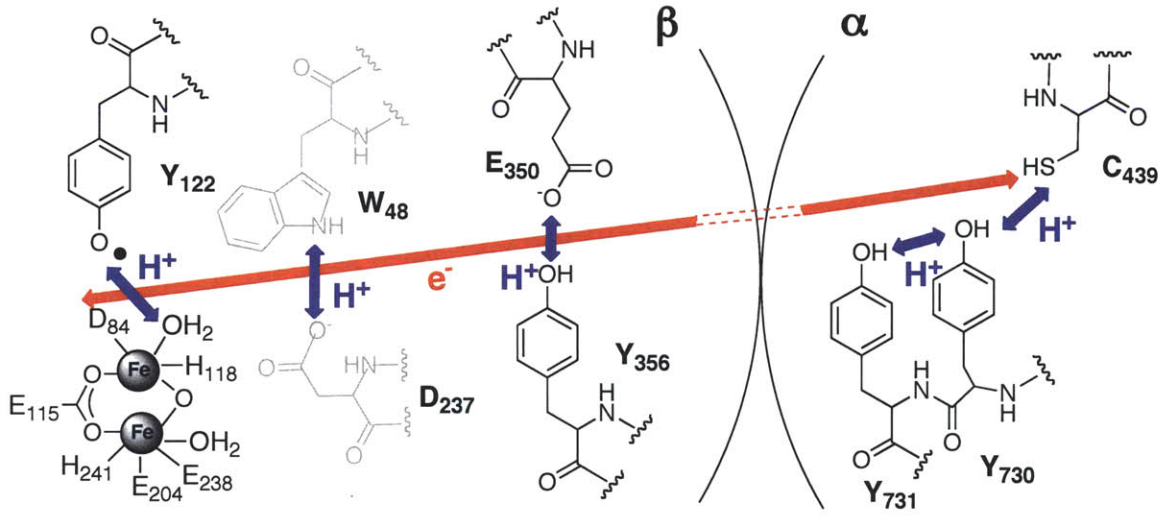

Figure 5.1 The Stubbe/Nocera model for long-range (~35 Å), reversible PCET by a radical hopping mechanism in *E. coli* class Ia RNR. Residue Y_{356} has not been observed in any crystal structure of β2, and thus its location relative to the other residues is unknown. Though W_{48} has long been implicated in radical propagation, there is no direct evidence that W_{48} and its putative H^+ acceptor, D_{237}, participate in long-range PCET during turnover and thus are shown in gray.

The incorporation of 3-aminotyrosine (NH_2Y) to the site of the three transiently oxidized Ys in the PCET pathway has proven particularly mechanistically informative (Chapters 2, 3 and

4). With a reduction potential 190 mV lower than Y at pH 7,[36] NH_2Y incorporation at position 356 of β2, 731 of α2, or 730 of α2 introduces a new local energetic minimum on the pathway. This thermodynamic perturbation is sufficiently large to allow for kinetic detection of NH_2Y• intermediates, but not so large as to shut down the radical propagation pathway. Indeed, NH_2Y-RNRs have been demonstrated to possess 3-12% the activity of their corresponding wt subunit (Chapter 2).[37,38] Formation of NH_2Y• occurs with biphasic kinetics (Chapter 2) in a pathway-dependent fashion (Chapter 3),[39] with the slow conversion of an inactive NH_2Y• population to an active one representing the rate-determining step in catalysis (Chapter 4). The ability to generate a stable NH_2Y• at each of the pathway positions has also allowed for three additional PELDOR distance measurements between Y_{122}• and each NH_2Y•.[25] Each of these measurements is consistent with the distance predicted by the docking model.

In this chapter, we present strong evidence that generation of a NH_2Y• on the PCET pathway induces the formation of a kinetically stable α2β2 complex of *E. coli* class Ia RNR. Compared to the complex of wt-α2 and wt-β2, $Y_{730}NH_2Y$-α2 (or $Y_{731}NH_2Y$-α2) and wt-β2 exhibit a significantly tighter dissociation constant (7-17 nM) and a cooperative binding phenotype as demonstrated by competitive inhibition spectrophotometic assays and Ni-NTA pull-down assays. SF fluorescence experiments indicate that the k_{off} for the $Y_{730}NH_2Y$-α2•wt-β2 complex is reduced by at least two orders of magnitude relative to wt-α2•wt-β2, and activity assays indicate that the complex is either an active enzyme form or exists in rapid equilibrium with one. A first image of the complex, generated from the alignment and classification of ~20,000 electron microscopy (EM) particles, is that of a compact, globular α2β2 that resembles the docking model proposed nearly two decades ago. This conclusion is further supported by the results of preliminary SAXS experiments. Furthermore, SAXS experiments demonstrate that the

mutant complex is unique from the wt complex with respect to its resistance of dATP-induced heterotetramerization. We propose that those mutant RNRs in which introduction of an unnatural amino acid on the PCET pathway allows for trapping a stable radical on pathway during catalysis (eg. $Y_{122}NO_2Y$-β2 or $Y_{122}F_nY$-β2) likely also generate stabilized α2β2 complexes. Finally, the data presented in this chapter help define a new strategy for stabilizing an active conformer of the enzyme for the purpose of crystallography.

5.2 MATERIALS AND METHODS

5.2.1 Materials. Wt-α2 (2500 nmol/min/mg), His_6-α2(wt) (2300 nmol/min/mg), and wt-β2 (1.2 Y_{122}•/β2, 7600 nmol/min/mg) were expressed from pTrc-*nrdA*, pET-*nrdA*, and pTB2-*nrdB*, respectively, and purified as previously described.[29,38] Met-β2 was generated by treatment of wt-β2 with HU, as described previously.[40] $Y_{731}NH_2Y$-α2 and $Y_{730}NH_2Y$-α2 were co-expressed from pTrc-*nrdA*(TAG_{731}) or pTrc-*nrdA*(TAG_{730}) and pAC-NH_2Y, and purified as described previously.[37] $Y_{731}F/Y_{730}NH_2Y$-α2 was expressed and purified as described in section 3.2.3. His_6-$Y_{730}NH_2Y$-α2 was co-expressed from pET-*nrdA*(TAG_{730}) and pEVOL-NH_2Y, and purified as described previously[38] and in section 2.2.14. All α2 proteins (mutant and wt) were treated with HU and incubated with DTT ("pre-reduced") prior to use according to standard protocol.[37] $Y_{356}NH_2Y$-β2 was expressed from pTrc-*nrdB*(TAG_{356}) and pAC-NH_2Y and purified as described previously[38] and in section 2.2.2. *E. coli* thioredoxin[41] (TR, 40 units/mg) and thioredoxin reductase[42] (TRR, 1400 units/mg) were isolated as previously described. Assay buffer is 50 mM Hepes, 15 mM $MgSO_4$, 1 mM EDTA, pH 7.6.

5.2.2 Determination of the K_d between NH_2Y-α2s and wt-β2 by competitive inhibition spectrophotometric assays. The dissociation constant (K_d) for the interaction between $Y_{730}NH_2Y$-α2 (or $Y_{731}NH_2Y$-α2, $Y_{731}F/Y_{730}NH_2Y$-α2, or His_6-$Y_{730}NH_2Y$-α2) and wt-β2 was determined by the competitive inhibition spectrophotometric assay, as previously described.[14] Ribonucleotide reductase activity was monitored through a continuous coupled-enzyme assay in which the consumption of NADPH was determined by monitoring the decrease in A_{340} (ε = 6220 M^{-1} cm^{-1}). β2 (0.15 μM), ATP (1.6 mM), CDP (1 mM), TR (50 μM), and TRR (1 μM) were mixed in assay buffer in a final volume of 300 μL. The mutant NH_2Y-α2 was added as a competitive inhibitor of wild-type α2 to final concentrations ranging from 25 nM to 10 μM. The

assay was initiated upon addition of wt α2 (0.3 μM) and NADPH (0.2 mM), and the decrease in A_{340} was monitored over two min. Assays were run in duplicate for the various inhibitor concentrations, with good reproducibility observed between runs. The relative activities in the presence of increasing inhibitor were then used to extrapolate a K_d. For those mutants that demonstrated non-cooperative binding (i.e., a hyperbolic saturation curve), the K_d between the NH_2Y-α2 and wt-β2 was determined by equation 5.1:

$$[I\bullet\beta2]_{bound} = [I]_{free} / (K_d + [I]_{free}) \qquad \text{(eq. 5.1)}$$

where $[I]_{free}$ is the concentration of unbound inhibitor (i.e., NH_2Y-α2) and $[I\bullet\beta2]_{bound}$ is the concentration of inhibitor in complex with wt-β2. These variables are defined as described in eqs. 5.2 – 5.4. In eq 5.2, the assumption is made that the amount of wt-α2•β2 complex in solution in the presence of varying concentrations of inhibitor ($[wt\text{-}\alpha2\bullet wt\text{-}\beta2]_X$) scales with the relative activity of wt-α2 as determined by the spectrophotometric assay. The concentration of wt-α2•β2 complex in the absence of inhibitor ($[wt\text{-}\alpha2\bullet wt\text{-}\beta2]_0$) is calculated from the respective concentrations of the individual subunits and the K_d for the wt-α2•β2 complex (0.18 μM) determined by the same method.[14] The total amount of β2 bound to inhibitor ($[I\bullet\beta2]_{bound}$) represents the difference between the concentration of wt-α2•β2 at a given inhibitor concentration (X) and I = [0] (eq. 5.3). Knowledge of the total inhibitor in solution and the amount in complex with β2 allows calculation of $[I]_{free}$ (eq. 5.4), and a plot of $[I\bullet\beta2]_{bound}$ vs. $[I]_{free}$ allows for the straightforward calculation of K_d by eq 5.1.

$$[wt\text{-}\alpha2\bullet wt\text{-}\beta2]_X = [wt\text{-}\alpha2\bullet wt\text{-}\beta2]_0 \times \text{relative activity} \qquad \text{(eq. 5.2)}$$

$$[I\bullet\beta2]_{bound} = [wt\text{-}\alpha2\bullet wt\text{-}\beta2]_0 - [wt\text{-}\alpha2\bullet wt\text{-}\beta2]_X \qquad \text{(eq. 5.3)}$$

$$[I]_{free} = [I]_{total} - [I\bullet\beta2]_{bound} \qquad \text{(eq. 5.4)}$$

For those mutants that demonstrated cooperative binding, the Hill equation (eq. 5.5) was applied, where Θ represents the fraction of occupied ligand-binding sites, [I] the concentration of mutant α2 in an assay mixture, *n* is the Hill coefficient, an indicator of the degree of positive or negative cooperativity, and c is a constant:

$$\Theta = [I]^n / (K_d + [I]^n) \times c \qquad \text{(eq. 5.5)}$$

5.2.3 Determining the dissociation constant for $Y_{356}NH_2Y$-β2 and wt-α2. The dissociation constant (K_d) between untagged $Y_{356}NH_2Y$-β2 and wt-α2 was determined using the competitive inhibition spectrophotometric assay as described in section 5.2.2 with minor modification. Wt-α2 was 0.15 μM and wt-β2 was 0.3 μM. $Y_{356}NH_2Y$-β2 was added as a competitive inhibitor of wt-β2 at concentrations between 50 nM and 2 μM, and the resulting decrease in RNR activity as a function of inhibitor concentration determined. Data collection and analysis was conducted as described above for the NH_2Y-α2s.

5.2.4 His_6-$Y_{730}NH_2Y$-α2 pull-down assays. A mixture (300 μL) was generated of untagged wt-β2 (10 μM, final concentration), CDP (1 mM), and ATP (3 mM) in EDTA-free assay buffer (50 mM Hepes, 15 mM $MgSO_4$, pH 7.6) at 25 °C. To it was added either His_6-α2(wt) or His_6-$Y_{730}NH_2Y$-α2 (5-10 μM) to initiate radical propagation. The reaction mixture was immediately combined with a small amount of Ni-NTA resin (Qiagen, ~150 μL) suspended in the same buffer and incubated on ice for 30 s. The sample was then centrifuged (30 s, 1000 × *g*, 4 °C) and the supernatant removed. The resin "pellet" was rapidly resuspended in a volume (600 μL) of wash buffer (EDTA-free assay buffer with 300 mM NaCl and 15 mM imidazole, pH 7.6), centrifuged (30 s, 1000 × *g*, 4 °C), and the supernatant removed. The wash step was repeated a second time. Resin-bound protein was then eluted by resuspending the resin in elution buffer (EDTA-free assay buffer with 250 mM imidazole, pH 7.6), centrifuging (30 s,

1000 × *g*, 4 °C), and removing the supernatant. The entire process took ~200 s from reaction initiation to protein elution. The contents of each fraction (flow through, washes, elution) for the His_6-$Y_{730}NH_2Y$-α2 reaction were assessed by SDS-PAGE (8%) and compared to the fractions obtained in the parallel reaction with His_6-α2(wt).

5.2.5 Kinetics of dissociation of the NH_2Y-α2/β2 complex. The kinetics of dissociation (k_{off}) of the $Y_{730}NH_2Y$-α2•wt-β2 complex were determined by a competitive SF fluorescence experiment using β2 labeled with the environmentally-sensitive fluorophore 2-dimethylamino-naphthalene (DAN). A mutant β2 containing a single Cys, His_6-β2(C268S/C305S/V365C), was expressed and purified in its apo form according to literature protocol,[43] and its diferric-Y• cofactor reconstituted to give 1.1 Y•/β2 as determined by the dropline UV-vis method.[44] The mutant β2 was site-specifically labeled at C365 with 6-bromoacetyl-2-dimethylaminonaphthalene (BADAN, 3 eq/β2) for 2 h at ambient temperature; these modified conditions are optimized relative to the previously reported protocol.[43] A comparison of the protein free thiol content before and after labeling, determined by the 5,5'-dithiobis-2-nitrobenzoic acid (DTNB) assay, revealed a total of 2.0 BADAN/β2. The protein was rendered met by treatment with HU following the literature procedure.[40] The resulting protein is henceforth referred to as DAN-β2(V365C). Expression, purification, and preparation of DAN-β2(V365C) was conducted by Lisa Olshansky (Nocera lab, MIT).

SF fluorescence experiments were performed on an Applied Photophysics DX 17MV instrument equipped with the Pro-Data upgrade and a 150 W Xe arc lamp. Reactions were carried out in assay buffer at 25 °C, maintained by a Lauda circulating water bath. Fluorescence excitation was at 390 nm, and DAN emission observed at wavelengths >420 nm using a long pass filter and a PMT detector. Monochromator slit widths were set to 8.0 mm.

In all cases, syringe A contained α2 (wt or $Y_{730}NH_2Y$, 0.16 μM), β2 (wt or met, 0.5 μM), CDP (1 mM) and ATP (3 mM) in assay buffer (concentrations given are in the syringe). Syringe B contained BADAN-β2 (17.5 μM) in assay buffer. The contents of syringe A and B were mixed rapidly in a 1:1 ratio and the fluorescence change monitored over either 250 ms or 2 s. Given the known half-life of the NH_2Y_{730}• (~2.7 min), effort was made to begin collecting data as soon as possible after mixing the syringe A components. In all cases, data collection was intiated within 1 min of mixing and was finished by 6 min (~2 half lives). The dead time of the instrument was determined to be <2 ms. The most reproducible kinetic traces (10-20 traces per reaction) were averaged and fit iteratively to eq 5.6 using KaleidaGraph software until residuals were minimized:

$$y = Ae^{(-kt)} + c \qquad \text{(eq 5.6)}$$

where y is the fluorescence signal, A is the amplitude of the fluorescence change, k is the rate constant for complex dissociation, t is time and c is a constant. Fitting the data to a biexponential function was also investigated, but did not give a significant improvement in the residuals compared to the monoexponential fit. SF fluorescence experiments were conducted in collaboration with Lisa Olshansky.

5.2.6 Demonstrating the NH_2Y-α2•wt-β2 complex retains nucleotide reductase activity. His_6-$Y_{730}NH_2Y$-α2 (5 μM), wt-β2 (10 μM), ^{3}H-CDP (1 mM, 20,000 cpm/nmol), and ATP (3 mM) in a total volume of 25 μL were mixed in assay buffer at 25 °C and the resulting solution aged for 30 s. A fraction of this mixture (20 μL) was then diluted into a standard steady-state "assay mix" containing additional ^{3}H-CDP (1 mM), ATP (3 mM), TR (30 μM), TRR (0.5 μM) and NADPH (1 mM) in assay buffer in a total volume of 200 μL. The assay mix contained either no additional wt-β2 or an additional 5 eq. of wt-β2. Aliquots were removed at fixed

timepoints between 30 s and 4 min, quenched, dephosphorylated, and analyzed by the method of Steeper and Steuart[45] following the standard radioactive protocol as described previously[33] and in section 2.2.7.

5.2.7 Examining the $Y_{730}NH_2Y$-α2•wt-β2 complex by EM. Electron microscopy (EM) data collection and analysis were conducted by Dr. Edward Brignole (Drennan lab, MIT, and Asturias lab, Scripps). $Y_{730}NH_2Y$-α2 (1.5 μM) with ATP (3 mM) and wt-β2 (3.0 μM) with CDP (1 mM) and assay buffer were mixed in a total volume of 20 μL at ambient temperature. 8 μL of the reaction mixture was withdrawn into a plastic pipette tip that was preloaded with 50 μL stain solution (2% uranyl acetate, 0.2% trehalose) above 10 μL assay buffer supplemented with 3 mM ATP and 1 mM CDP. 10 μL assay buffer with ATP and CDP was taken into the tip below the reaction mixture. The solutions in the pipette tip were separated by 20 μL of air. The buffer, reaction mixture, buffer, and stain were applied in rapid succession from the pipette tip to a carbon film supported on a 300 mesh Cu/Rh EM grid (Ted Pella) that was rendered briefly hydrophilic by glow discharge immediately prior to use.[46] A similar quick rinse procedure was described to capture transient complexes of actin and myosin filaments.[47] The grid was blotted from its edge and washed 2-3 times with 5 μL of stain solution. 10 grids were prepared by this method and one with suitable stain and particle distribution was imaged at 120 kV on a Tecnai F20 electron microscope (FEI) equipped with an UltraScan 4000 CCD camera (Gatan) using Leginon [48] operated in manual mode at a dose of ~22 e-/Å^2. A total of 48 pairs of images of the untilted and -55° tilted specimen were collected at a magnification of 50,000× with a pixel size of 2.18 Å at the specimen level.

Particles were selected from untilted images using e2boxer.py[49] and were matched with their tilted partners using a modified version of TiltPicker.[50] An initial dataset of 26,845 particle

pairs was windowed from the images using SPIDER.[51,52] Particles were density normalized and band-pass filtered between 270 and 30 Å prior to initial reference-free alignment and rotationally invariant K-means clustering followed by an iterative routine consisting of multi-reference alignment/clustering and reference-free alignment in each class.[53] This approach has been used successfully to examine a number of conformationally heterogeneous complexes by single-particle EM.[17,54-56] Stability of the clustering was measured by the number of particles that "jump" between classes in each iteration. By this criterion and by visual assessment of the class averages, the clustering improved dramatically by filtering the high-resolution features below 30 Å and by using full-sized particles rather than down-sampled images. A total of 18,811 particles were divided into 10 stable classes using this procedure.

5.2.8 Examining the $Y_{730}NH_2Y$-α2•wt-β2 complex by SAXS. Small-angle X-ray scattering (SAXS) experiments were conducted in collaboration with Dr. Nozomi Ando (Drennan lab, MIT) at the Cornell High Energy Synchrotron Source G1 station (Ithaca, NY) using a 10.05 keV 100 μm square X-ray beam with a flux of several 10^{12} photons/s. Data were collected at room temperature on a Pilatus 100K detector at a sample-to-detector distance of 1.2 m; the transmission intensity was measured with a PIN diode beamstop. To minimize radiation damage, samples (final volumes of 30 μL) were oscillated with respect to the X-ray beam in an *in vacuo* 2-mm pathlength quartz capillary flow cell described previously.[57]

Protein solution scattering was measured from fresh samples of RNR in modified assay buffer (50 mM Hepes, 15 mM $MgCl_2$, 1 mM EDTA, pH 7.6). Nucleotides were added at the following final concentrations: CDP (1 mM), GDP (1 mM), TTP (100 μM), and dATP (175 μM). Background scattering was measured with matching buffer solutions. Twenty to forty exposures of 5 s each were collected per sample. For protein samples, exposures were separated

with 10 s pauses to minimize accumulation of radiation damage in the flow cell. Detailed data acquisition and reduction procedures were conducted as described previously.[58] Briefly, scattering images were integrated about the beam center and normalized by the recorded transmission intensity prior to background subtraction to yield the scattering profiles, i.e. scattering intensity (I) vs. momentum transfer (q). Here, $q=4\pi/\lambda\sin\theta$, where λ is the X-ray wavelength and 2θ is the scattering angle with respect to the X-ray beam. For each sample, exposures that did not exhibit radiation damage were averaged. Data analysis was conducted by Dr. Nozomi Ando.

By this protocol, the following reaction mixtures were examined: (1) wt-α2, wt-β2, GDP, TTP, (2) wt-α2, met-β2, GDP, TTP, (3) $Y_{730}NH_2Y$-α2, wt-β2, GDP, TTP, (4) $Y_{730}NH_2Y$-α2, met-β2, GDP, TTP, and (5) $Y_{730}NH_2Y$-α2, wt-β2, and TTP only. In all cases, final concentrations of α2 and β2 were 30 μM each. Finally, an experiment was conducted to determine whether dATP destabilizes the NH_2Y•-induced $Y_{730}NH_2Y$-α2•wt-β2 complex. The following mixtures were examined: (1) wt-α2, wt-β2, CDP, dATP, (2) wt-α2, met-β2, CDP, dATP, and (3) $Y_{730}NH_2Y$-α2, wt-β2, CDP, dATP. For all reaction, α2, β2, and CDP were preincubated on ice (~1 min) and dATP added immediately before data acquisition. The kinetics of dissocation of the $Y_{730}NH_2Y$-α2•β2•CDP ternary complex in the presence of dATP were examined by collecting a single exposure every 2 minutes over 22 min.

5.3 RESULTS

5.3.1 Determination of the K_d between NH_2Y-α2s and wt-β2 or wt-α2 and NH_2Y-β2. We initially sought to determine the extent to which incorporation of NH_2Y at position 356 of β2 or 731 or 730 of α2 disrupted the protein interface. Structural characterization of $Y_{730}NH_2Y$-α2 and $Y_{731}NH_2Y$-α2 by X-ray crystallography (section 2.3.8) indicated that the major conformers of each mutant were minimally perturbed relative to the wt structure, and that the residues in the PCET pathway were superimposable among the three structures.[38] However, minor conformers were also characterized for each of the mutants. In the structure of $Y_{730}NH_2Y$-α2, electron density was observed that suggested an altered conformation for Y_{731} in which the phenol side chain "flipped" away from NH_2Y_{730} and towards the protein surface (and presumed interface for α/β interaction), with accompanying rearrangement of the nearby, surface-exposed R_{411} (Figure 2.10). In the structure of $Y_{731}NH_2Y$-α2, two protomers in the asymmetric unit have the NH_2 group oriented to the sterically less-dense side of the protein, while a third has the opposite orientation. In this minor conformation, it is possible that the NH_2 group could disrupt ordered waters or H-bonding networks relevant to subunit affinity and/or catalysis.

Thus, we sought to assess the integrity of the subunit interface upon incorporation of an NH_2Y by determining the dissociation constant (K_d) for $Y_{730}NH_2Y$ (or $Y_{731}NH_2Y$-α2) with wt-β2, and $Y_{356}NH_2Y$-β2 with wt-α2. Adapted from the method originally reported by Climent et al.,[14] a spectrophotometric competitive inhibition assay for RNR activity has been used routinely to determine the K_d between wt-α2 and either mutant β2s or peptides corresponding to the C-terminal tail of β2.[59,60] In this assay, wt-α2•β2 complex of known initial concentration is disrupted by titrating into the assay mixture increasing concentrations of an inhibitor (in this case, an NH_2Y-RNR mutant). The corresponding decrease in RNR activity is representative of

the amount of inhibitor in complex, and is used to extrapolate a K_d for the inhibitor-subunit•wt-subunit interaction. Thus, the assay relies on the inhibitor being an inactive RNR mutant. While we have demonstrated that NH_2Y-RNRs possess 3-9% the activity of their corresponding wt subunit, their contribution to RNR activity was indistinguishable from background in the spectrophotometric assay over the concentration ranges studied. Thus, for the purpose of the competitive inhibition assays, NH_2Y-RNRs were inactive.

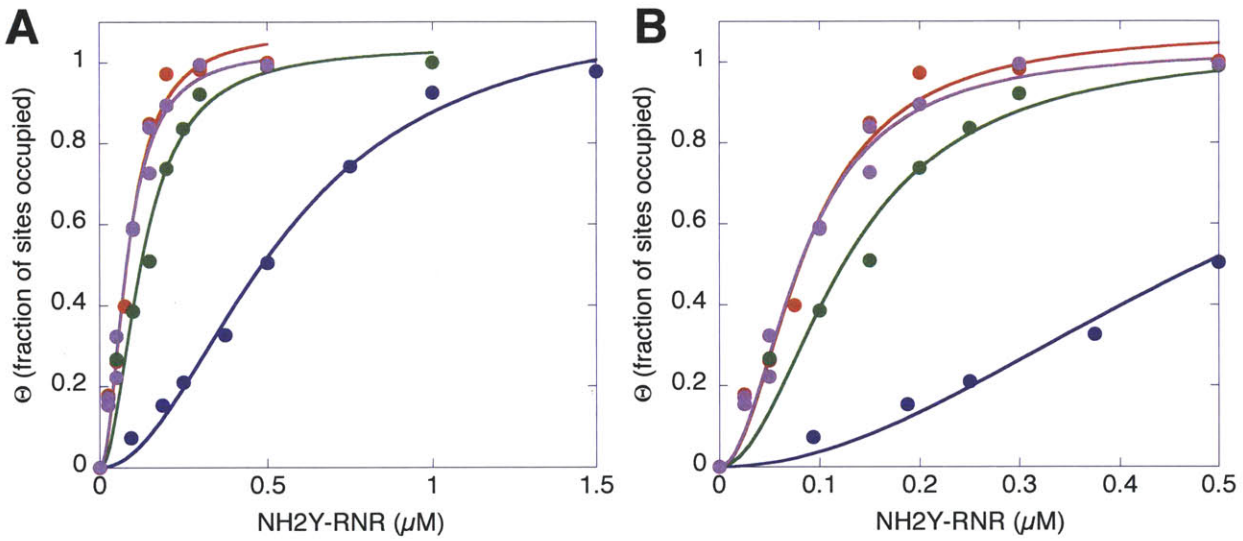

Figure 5.2 Cooperative binding of NH_2Y-RNRs to a second, wt subunit as determined by the spectrophotometric competitive inhibition assay. (A) The following α2•β2 pairs were explored: $Y_{730}NH_2Y$-α2 and wt-β2 (red), $Y_{731}NH_2Y$-α2 and wt-β2 (green), His_6-$Y_{730}NH_2Y$-α2 and wt-β2 (purple), and $Y_{356}NH_2Y$-β2 and wt-α2 (blue). In all cases, the data were fit to eq 5.5; (B) An expanded view of the data in panel A highlights the cooperative nature of the NH_2Y-α2•β2 interaction. The data shown are the average of 2-3 replicates, with error between measurements <10%.

The K_ds of $Y_{730}NH_2Y$-α2 and $Y_{731}NH_2Y$-α2 were explored first, and the results from these experiments shown in Figure 5.2. We were surprised to discover that application of eq. 5.1 failed to give a satisfactory fit to the experimental data. Indeed, a plot of $[I]_{bound}$ versus $[I]_{free}$ appeared significantly more sigmoidal than hyperbolic in shape. Thus, the Hill equation (eq. 5.5) for cooperative ligand-receptor binding was applied and a Hill coefficient (n) of 2 gave a

reasonable fit to the data (Figure 5.2, solid lines) and a K_d of 17 nM for the $Y_{731}NH_2Y$-α2:wt-β2 interaction (Figure 5.2, green and Table 5.1) and of 7 nM for the $Y_{730}NH_2Y$-α2•wt-β2 interaction (Figure 5.2, red). These binding constants are 10- and 26-fold tighter, respectively, than the wt-α2•wt-β2 (0.18 μM) interaction in the presence of CDP/ATP measured by the same method. Furthermore, they are 3.5- and 8.5-fold lower than the tightest reported K_d for the wt subunits in the presence of CDP/ATP (60 nM), determined by steady-state fluorescence titrations using a site-specifically labeled DAN-β2.[18] Examination of the binding between His-$Y_{730}NH_2Y$-α2•wt-β2 by this assay also indicated that the interaction was cooperative (Figure 5.2, purple) with a K_d of 7 nM, identical to that determined for the untagged $Y_{730}NH_2Y$-α2•wt-β2 interaction.

The interaction between $Y_{356}NH_2Y$-β2 and wt-α2 was examined in an identical fashion. While the binding showed cooperative behavior similar to that observed in NH_2Y-α2s, the strength of subunit interaction was not enhanced to the same extent (Figure 5.2, blue). A K_d of 0.30 μM was determined for $Y_{356}NH_2Y$-β2•wt-α2, two-fold weaker than the wt-α2•wt-β2 interaction and very similar to the K_d of 0.34 μM reported for Y_{356}DOPA-β2•wt-α2.[59]

The results presented above raised the question: what is the source of the cooperative behavior and, in the case of NH_2Y-α2s, the enhanced subunit affinity? We hypothesized these behaviors arose not from properties associated with the ground state structure of the mutants, but with the conformational changes associated with formation of a stable NH_2Y• on the pathway. To test this hypothesis, we measured the K_d for the interaction between $Y_{731}F/Y_{730}NH_2Y$-α2•wt-β2 by the same method. This mutant was prepared previously for the purpose of investigating the pathway dependence of NH_2Y• formation (Chapter 3), as it contains NH_2Y at a position 730 but cannot generate NH_2Y• due to the presence of the redox inert F at position 731.[39] If the tight, cooperative behavior observed in the other NH_2Y-α2s is associated with incorporation of NH_2Y

to the ground state enzyme, one would predict that the K_d of the $Y_{731}F/Y_{730}NH_2Y$-α2 should resemble that of $Y_{730}NH_2Y$-α2. However, if it is associated with $NH_2Y\bullet$ formation, the K_d for the double mutant should resemble that of $Y_{731}F$-α2 (0.24 μM).[61]

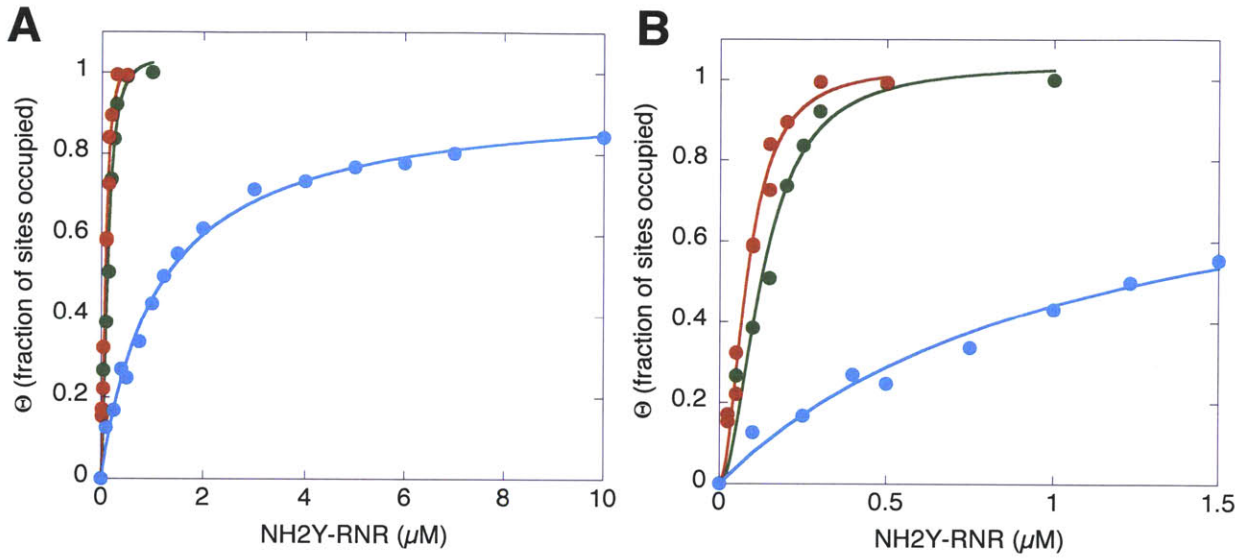

Figure 5.3 Comparing the K_ds of various NH_2Y-α2s to wt-β2. (A) The tight, cooperative binding between $Y_{730}NH_2Y$-α2 and wt-β2 (red) or $Y_{731}NH_2Y$-α2 and wt-β2 (green) may be compared to the weaker, non-cooperative binding between $Y_{731}F/Y_{730}NH_2Y$-α2 and wt-β2 (cyan); (B) An expanded view of the data in panel A emphasizes the differences in NH_2Y-α2:wt-β2 interactions.

Table 5.1 Dissociation constants (K_ds) for NH_2Y-RNRs determined in this chapter.

Protein	K_d (nM)[a]
$Y_{730}NH_2Y$-α2	7 ± 1
His_6-$Y_{730}NH_2Y$-α2	7 ± 1
$Y_{731}NH_2Y$-α2	17 ± 3
Y_{356} NH_2Y-β2	300 ± 33
$Y_{731}F/Y_{730}NH_2Y$-α2	1140 ± 70

a. Errors are reported as the errors to fits to eq. 5.1 or 5.5, as described in the text.

The data for the double mutant fit very well to the traditional K_d model (eq. 5.1), and showed no evidence of the cooperativity observed for the NH_2Y-RNR single mutants (Figure 5.3, cyan and Table 5.1). A K_d of 1.14 μM is observed, 65-fold weaker than the wt-α2•β2 interaction and >160-fold weaker than the $Y_{730}NH_2Y$-α2•wt-β2 interaction. This K_d is 4-fold higher than the reported value for $Y_{731}F$-α2•wt-β2, and is in agreement with the K_d recently reported for the double mutant $Y_{731}F/Y_{730}NO_2Y$-α2•wt-β2 (1.45 μM).[30] Thus, this result supports a model in which formation of an on-pathway NH_2Y• stabilizes α2β2 interactions.

The cooperative binding model is interesting in light of the model for half-sites reactivity in class Ia RNRs.[27] This hypothesis holds that radical propagation is initiated on a single α/β pair of the α2β2 complex, and that radical propagation occurs on the second pair only after dCDP production, or a conformational change accompanying product formation, occurs on the first. The NH_2Y-RNR binding studies suggest that turnover in one α/β pair induces a tight association in the second α/β pair, perhaps bringing an intermediate quaternary structure into a compact α2β2 consistent with the PELDOR data[24,25] and proposed docking model.[11]

5.3.2 Wt-β2 "pull-down" with His_6-$Y_{730}NH_2Y$-α2. We sought additional biochemical evidence for an enhanced subunit interaction between NH_2Y-α2s•wt-β2. The half-life of NH_2Y_{730}• determined by EPR spectroscopy has been reported as ~2.7 min at 25 °C,[62] and it is known that His_6-tagged α2s bind to Ni-NTA agarose with high affinity.[38] An experiment was thus designed in which His_6-$Y_{730}NH_2Y$-α2, wt-β2 (untagged), CDP and ATP were reacted under single-turnover conditions (i.e., no reductant) to generate NH_2Y_{730}• on the His-tagged protein, the reaction mixture incubated briefly with Ni-NTA, the resin quickly washed with low [imidazole], and the protein eluted with high [imidazole] to determine whether wt-β2 co-elutes with His-$Y_{730}NH_2Y$-α2 under these conditions. The entire process, from reaction initiation to

protein elution, took ~3.3 min or 1.25 half-lives of the NH_2Y_{730}• in complex. An identical control reaction was also examined with His_6-α2(wt) in place of His_6-$Y_{730}NH_2Y$-α2 to compare the relative amounts of wt-β2 "trapped" under these conditions.

The results of the experiments with His-α2(wt) and His_6-$Y_{730}NH_2Y$-α2 at a 1:2 molar ratio of α2:β2 are show in Figure 5.4. This subunit ratio was initially selected to maximize the ratio of bound-to-free His_6-$Y_{730}NH_2Y$-α2. Analysis of the individual steps (flow-through, washes, elution, Figure 5.4 A) indicate that the majority of α2 and β2 are lost in the flow-through, likely due to the brief (~30 s) incubation time with the resin before initial centrifugation step. However, analysis of a concentrated fraction of the elution (Figure 5.4 B) indicates the pull-down of untagged β2 for both His_6-α2(wt) and His_6-$Y_{730}NH_2Y$-α2, with the mutant α2 pulling down 2-fold more β2 than the wt as determined by densitometry analysis. At this point, it was unknown whether His_6-α2(wt) pulled down wt-β2 as a result of insufficient washing, or the 2-fold excess of β2 in the reaction, or because of some relevant interaction between the two subunits. Thus, the reaction was repeated a second time with a 1:1 α2:β2 ratio (Figure 5.5) and increased wash volumes. A reduction is observed in the co-elution of wt-β2 with His_6-α2(wt) with increased washing, with no observable effect on co-elution of wt-β2 with His_6-$Y_{730}NH_2Y$-α2. The effect of nucleotides in the buffer was also examined by repeating the experiment with CDP and ATP in all wash steps. This did not make an appreciable difference in the pull-down results (data not shown).

The results of these experiments are consistent with our hypothesis for a long-lived $Y_{730}NH_2Y$-α2•wt-β2 complex. In order to determine the exact subunit stoichiometry between $Y_{730}NH_2Y$-α2 and wt-β2, this experiment may be repeated in the presence of α2 and β2 gel standards of known concentration. Densitometry measurments of the elution fractions compared

to the respective subunit standard curves should allow for accurate quantitation of the subunits' absolute and relative concentrations. This pull-down assay has additional usefulness, as it allows for rapid screening of a solution conditions that maximize formation of the complex. These conditions may then be applied for other more time- and labor-intensive biophysical methods, such as EM.

Figure 5.4 Pull-down assay of wt-β2 by His_6-α2(wt) or His_6-$Y_{730}NH_2Y$-α2 analyzed by SDS-PAGE. Subunits were assayed in a 1:2 α2:β2 ratio. (A) Individual steps are as indicated: flow through (FT), first wash (W1), second wash (W2), and elution (E) for His_6-α2 (left) and His_6-$Y_{730}NH_2Y$-α2 (right); (B) Elution fractions from panel A concentrated 5-fold and loaded in different amounts (5, 10, and 20 μL, as indicated).

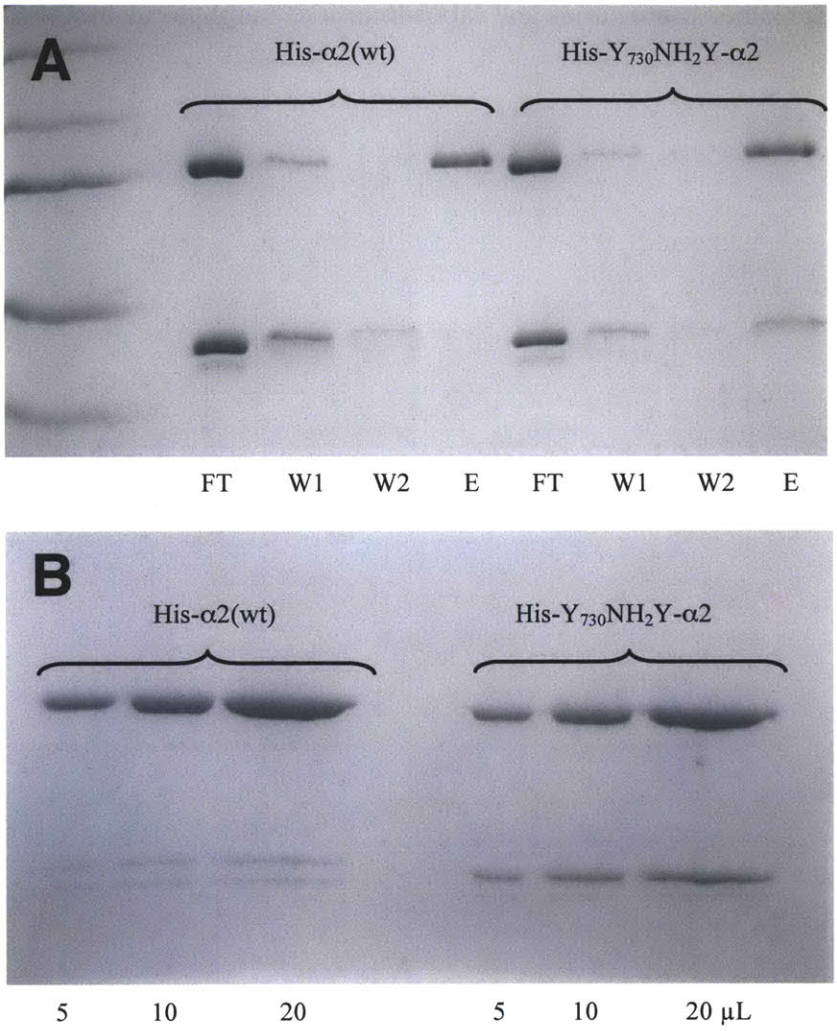

Figure 5.5 Pull-down assay of wt-β2 by His_6-α2(wt) or His_6-$Y_{730}NH_2Y$-α2 analyzed by SDS-PAGE. Subunits were assayed in a 1:1 α2:β2 ratio. (A) Individual steps are as indicated: flow through (FT), first wash (W1), second wash (W2), and elution (E) for His_6-α2 (left) and His_6-$Y_{730}NH_2Y$-α2 (right); (B) Elution fractions from panel A concentrated 5-fold and loaded in different amounts (5, 10, and 20 μL, as indicated).

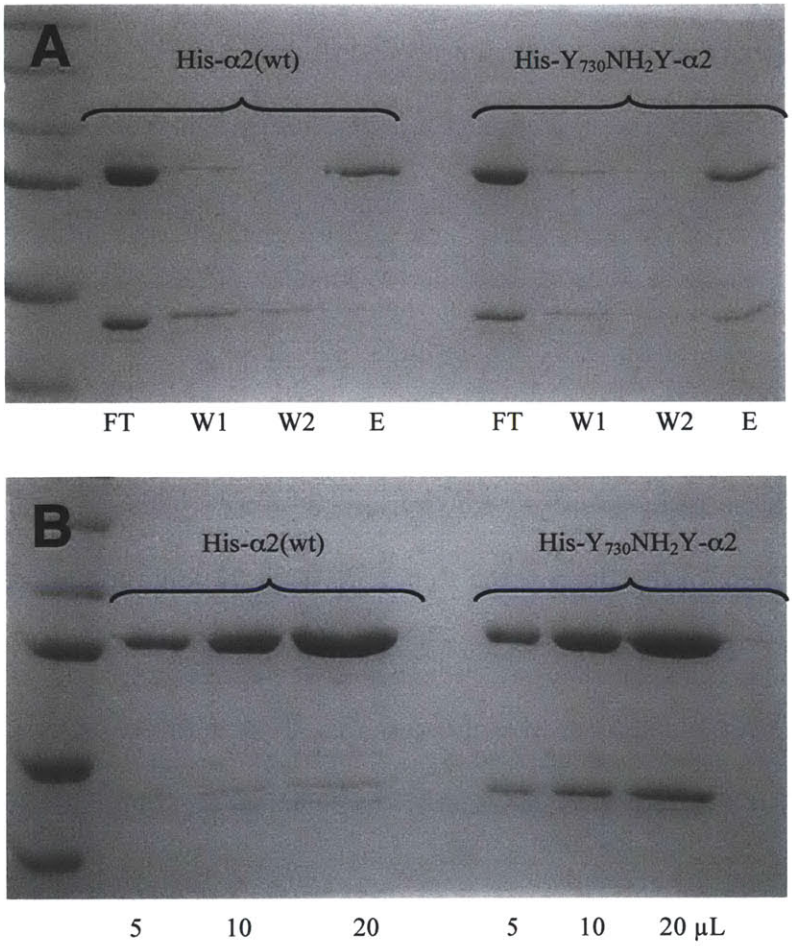

5.3.3 Kinetics of dissociation of the NH_2Y-α2•β2 complex. We next sought to kinetically characterize the lifetime of the NH_2Y•-induced $Y_{730}NH_2Y$-α2•wt-β2 complex. A steady state fluorescence method for measuring the dissociation constant (K_d) for subunit interactions has been developed recently in which β2 is site-specifically labeled at a single cysteine residue with the environmentally-sensitive fluorophore dansyl (DAN), introduced at a minimally disruptive position within the C-terminal tail. Through trial and error, it was determined that a β2 labeled at position 365, DAN-β2(V365C), was the best mutant for this approach.[43] This fluorescence technique was subsequently adapted for SF studies to examine the kinetics of association and dissociation (k_{on} and k_{off}) between *E. coli* α2 and β2 (or C-terminal β2 peptides). To measure k_{off}, an initial complex of wt-α2, met-β2, CDP, and ATP is rapidly mixed with a large excess of DAN-β2 and the corresponding increase in fluorescence emission monitored.[60] This emission increase is associated with the movement of the fluorophore from a more hydrophilic to a more hydrophobic environment, as is predicted to occur upon association of the DAN-β2 tail with α2. The SF fluorescence method was first demonstrated on C-terminal 20mer to which was appended a rhenium photooxidant.[60] It has been extended recently to the intact β2 subunit using DAN-β2(V365C).[18]

In this experiment, we utilized DAN-β2(V365C) as a competitive inhibitor of β2 to compare k_{off}s of four α:β complexes in the presence of CDP and ATP: (1) met-β2 and wt-α2, (2) wt-β2 and wt-α2, (3) $Y_{730}NH_2Y$-α2 and met-β2, and (4) $Y_{730}NH_2Y$-α2 and wt-β2. In all cases, the unlabeled α2 and β2 subunits and nucleotides were combined in one syringe and rapidly mixed with a second syringe containing DAN-β2(V365C) to give DAN-β2 in a 35-fold excess over unlabeled β2. The averaged kinetic traces for the dissociation of met-β2•wt-α2 and wt-β2•wt-α2 in the presence of CDP/ATP are shown in Figure 5.6 A and B, respectively.

Monoexponential fits to the data (1.5 – 150 ms) gave k_{off} values of 63 s^{-1} and 74 s^{-1}, respectively. The results indicate that neither the presence of Y_{122}• nor of the α2 active site disulfide formed upon dCDP formation has a discernable impact on the dissociation constant for α2β2. Furthermore, the amplitude of the fluorescence change was identical in both experiments (~0.063 V). Thus, the ability to initiate radical propagation/generate dCDP has no noticeable effect on the affinity of the wt subunits for one another. The averaged kinetic trace for dissocation of the $Y_{730}NH_2Y$-α2•met-β2 complex with CDP/ATP (Figure 5.6 C) also fits best to a monoexponential with a k_{off} of 38 s^{-1}. Thus, the rate constant for subunit dissociation of $Y_{730}NH_2Y$-α2 from β2 is ~2 fold slower than the wt-α2•β2 interaction, even under conditions in which NH_2Y_{730}• cannot be formed. The amplitude of fluorescence change (0.076 V) is similar to that observed in the wt-α2 reactions.

Finally, the dissociation constant of interest – that for $Y_{730}NH_2Y$-α2 and wt-β2 in the presence of CDP and ATP – was investigated. In sharp contrast to the other three experiments, the averaged kinetic trace over the first 150 ms showed no pronounced increase in fluorescence (Figure 5.6 D, inset). Indeed, the reaction monitored over a total of 2 s showed a total fluorescence change of 0.01 V, or ~15% of the ΔV_{avg} over 150 ms for the previous three experiments. A monoexponential fit to this change (Figure 5.6 D) gives a k_{off} of 3 s^{-1}. We hypothesize that this small amplitude change corresponds to the interaction of DAN-β2(V365C) with free $Y_{730}NH_2Y$-α2 in solution, as a small fraction (<5%) of the total initial protein would be unbound in the initial solution given the K_d reported in section 5.3.1. Thus, k_{off} for the $Y_{730}NH_2Y$-α2•wt-β2 complex is too slow to be measurable with the data from this initial SF fluorescence experiment. It is more appropriate to measure the dissociation constant of this

complex by steady-state fluorescence emission spectroscopy; these experiments are ongoing (Olshansky, Minnihan, Nocera, and Stubbe).

The SF fluorescence experiments establish that that the $Y_{730}NH_2Y$-α2•wt-β2 complex is a kinetically stable species. One of the most interesting remaining questions is whether the lifetime of the complex is identical to that of the NH_2Y_{730}• - previously determined to decay at 0.26 min^{-1} – or whether the complex is longer-lived. If the latter is true, this opens up exciting possibilities with respect to stabilizing a complex suitable for protein crystallization. This value will be obtained in the near future from the steady-state fluorescence experiments proposed above.

5.3.4 Determining whether the NH_2Y-α2•wt-β2 complex is an active conformer. With highly suggestive biochemical evidence for the formation of a kinetically stable $Y_{730}NH_2Y$-α2•wt-β2 complex available, we wanted to determine whether the complex was representative of an active state of the enzyme or trapped in some inactive form. To address this question, a modified RNR activity assay was conducted in which His_6-$Y_{730}NH_2Y$-α2 (5 μM) was incubated with wt-β2 (2 eq), CDP, and ATP in the absence of reductant – conditions under which it is known that a long-lived NH_2Y_{730}• is formed. The resulting NH_2Y-α2•wt-β2 complex was then assayed for nucleotide reductase activity using the standard radioactive assay (Figure 5.7). The first reaction was initiated by addition of His_6-$Y_{730}NH_2Y$-α2 to a mixture of wt-β2, [^{3}H]-CDP, and ATP. The reaction was aged for 30 s on ice, then diluted into a fresh solution containing all the components necessary for a steady-state radioactive RNR assay (additional ^{3}H-CDP, ATP, TR, TRR, and NADPH). The nucleotide reductase activity of His_6-$Y_{730}NH_2Y$-α2 was measured by removing aliquots between 30 s and 3 min and analyzing them for product by the standard method (Figure 5.7). By this method, the activity of His_6-$Y_{730}NH_2Y$-α2 was measured as 70

(±4) nmol/min/mg. As a positive control for His_6-$Y_{730}NH_2Y$-α2 activity, an experiment was conducted in which wt-β2 was omitted from the initial reaction mixture, but included in the subsequent steady-state assay mixture. This positive control gave a specific activity of 88 (±1) nmol/min/mg. While the activity of the "complexed" His_6-$Y_{730}NH_2Y$-α2 is only 80% that of the positive control, this decrease can be readily accounted for by the loss of total spin observed for the same reaction quenched at 30 s and analyzed by EPR spectroscopy.[37,38] To confirm this hypothesis, the experiment was modified to include additional wt-β2 (5 eq) in the steady-state assay mixture (path A in Figure 5.7). The specific activity of "complexed" His_6-$Y_{730}NH_2Y$-α2 under these conditions was measured as 86 (±10) nmol/min/mg, consistent with the positive control for His_6-$Y_{730}NH_2Y$-α2 activity. Thus these experiments indicate that the stable $Y_{730}NH_2Y$-α2•wt-β2 complex is not trapped in a kinetically inactive state. Instead, these experiments indicate that either the complex induced upon NH_2Y_{730}• formation is active, or that it is in rapid equilibrium with the active structure.

The results from the SF fluorescence experiments described above indicate that k_{off} for the complex will be slow on the time scale of the steady-state assay. This observation might support the conclusion that it is the stable $Y_{730}NH_2Y$-α2•wt-β2 complex itself that is active in nucleotide reduction. However, it is important to note that we do not yet have any information about how the stability of the $Y_{730}NH_2Y$-α2•wt-β2 complex is affected in the presence of reductant (TR/TRR/NADPH or DTT), and thus cannot speculate at this time on the timescale of k_{off} under steady-state assay conditions. This is another kinetic constant that will be interesting to investigate by the steady-state fluorescence titrations proposed in the previous section.

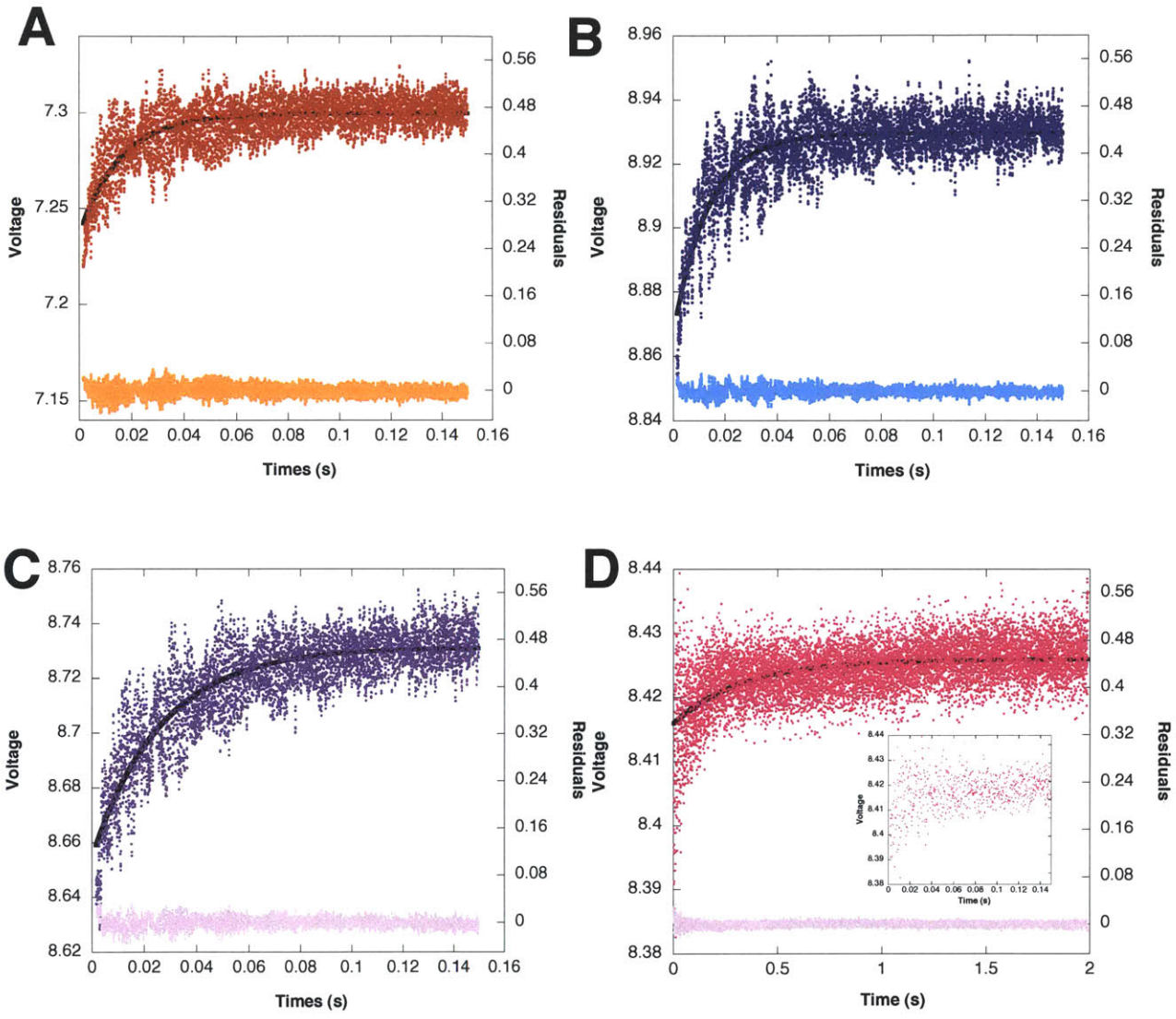

Figure 5.6 SF fluorescence measurements of k_{off}s for various α•β complexes. The average of 10-20 individual kinetic traces are shown for met-β2 and wt-α2 (panel A, red), wt-β2 and wt-α2 (panel B, blue), $Y_{730}NH_2Y$-α2 and met-β2 (panel C, purple), and $Y_{730}NH_2Y$-α2 and wt-β2 (panel D, magenta) all in the presence of CDP/ATP. Monoexponential fits to the data are indicated by solid black lines. Residuals to the fits are shown in orange (A), cyan (B), and pink (C and D). Note the difference in timescale in panel D relative to panels A, B, and C. An expanded view of the first 150 ms of the $Y_{730}NH_2Y$-α2:wt-β2 trace is also given (D, inset).

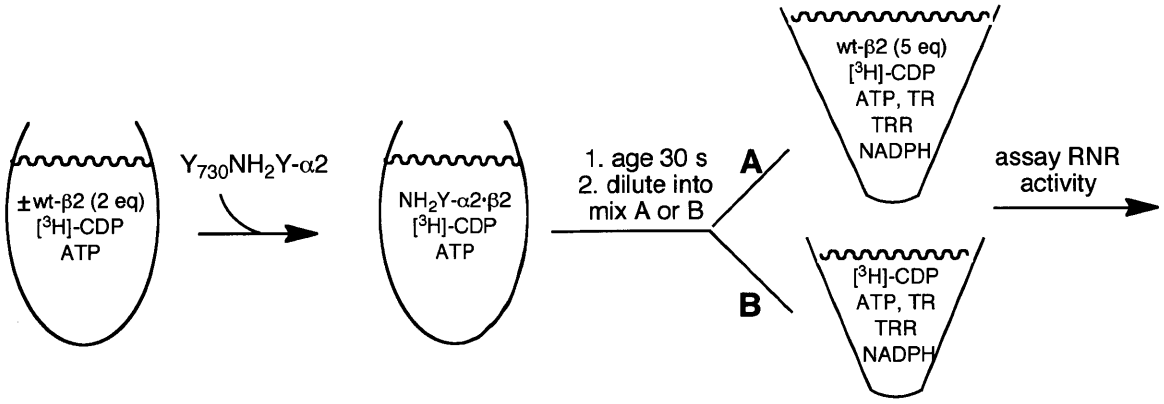

Figure 5.7 Assaying the NH_2Y-α2•wt-β2 complex for RNR activity. His_6-$Y_{730}NH_2Y$-α2 was added to a mixture of wt-β2, [^{3}H]-CDP, and ATP to generate NH_2Y_{730}• and the putative NH_2Y-α2•wt-β2 complex. After aging the mixture for 30 s, it was diluted into a mixture containing the components necessary for a steady-state RNR assay with either (A) 5 additional eq. of wt-β2 or (B) no additional β2. Timepoints were then removed and analyzed as usual for the radioactive assay.

5.3.5 Examining the structure and oligomeric state of the $Y_{730}NH_2Y$-α2•wt-β2 complex by EM. In the previous sections, it has been assumed that the stabilized $Y_{730}NH_2Y$-α2•wt-β2 complex is an α2β2 heterodimer. This is believed to be the active oligomeric state of the wt *E. coli* RNR proposed by the docking model[11] and is supported by recent biophysical studies.[17] In an effort to experimentally determine the oligomeric state and investigate the overall structure of the complex, we have attempted to obtain to images the $Y_{730}NH_2Y$-α2•wt-β2 complex by negative-stain electron microscopy (EM) in collaboration with the Drennan lab (MIT) and Asturias lab (Scripps).

The EM experiments were designed with two primary considerations in mind. First, the concentrations were chosen to optimize the amount of $Y_{730}NH_2Y$-α2 in complex. For the experiments described herein, $Y_{730}NH_2Y$-α2 (1.5 μM) was reacted with two equivalents of wt-β2 in the presence of CDP, and ATP. As β2 is a small particle with respect to the detection

limits of EM, we hypothesized that having an excess of β2 would not complicate particle picking and averaging, provided it did not induce crowding or aggregation on the carbon grid. Using the K_d reported in section 5.3.1, we estimate that >99% of the $Y_{730}NH_2Y$-α2 should be bound at this concentration and subunit stoichiometry. However, EPR and SF UV-vis studies on NH_2Y_{730}• formation indicate that only 40% of Y_{122}• is converted to NH_2Y_{730}•, out of a theoretical maximum of 50% (due to half-sites reactivity, sections 2.3.9 and 2.3.10). Thus, assuming an even distribution of initial Y_{122}• across the two β monomers, we calculate that only 80% of the total $Y_{730}NH_2Y$-α2 generates a stable NH_2Y_{730}• and thus exists in a long-lived complex. A second consideration was the time it takes to prepare an EM sample (from reaction initiation to staining) relative to the lifetime of the putative complex. This was addressed by modifying the standard sample preparation protocol. A "quick rinse" procedure was employed similar to that which has been previously reported for the trapping of transient protein complexes for EM.[46] Following this method, layered solutions of assay buffer, reaction mixture, buffer, and stain were taken up in a single pipette tip, with each solution separated by an intervening distance of air. The solutions were discharged onto the carbon grid in quick succession, ensuring that the samples were adsorbed onto the grid, washed, and stained within one NH_2Y_{730}• half-life.

From grids prepared in this fashion, a total of 48 untilted images and their -55° tilted partners were collected. In total, 26,845 particles were picked manually from the untilted images and matched with their partner particle in the corresponding tilted image. The untilted particles were reduced in size by a factor of two to speed processing and aligned and classified iteratively. After each round of classification, the resulting classes were visually inspected. Particles too small to be α2 were removed from the data set manually, as were particles that were consistently found in unstable classes (i.e., classes in which a high percentage of the total particles "jump"

between classes in each iteration). Class stability was found to substantially improve by using the full-size particles, and thus those were used for the final classification rounds. Ultimately, 18,811 full-sized particles were filtered to 30 Å to reduce the contribution of spatial frequencies with poor signal to noise and distributed among 10 classes. The average aligned particle for each of these classes is shown in Figure 5.8, panel A, and the number of particles in each class indicated. The classes were qualitatively assesed by examining their relative stabilities. Classes C, E, and H were the least stable, with 13%, 19%, and 11% of the particles jumping, respectively. The remaining classes had between 3.7 – 7.4% of their particles jump per round.

Inspection of the 2D aligned particles reveals the presence of several classes readily recognizable as unbound α2 (Figure 5.8, panel A, classes D, E, and F). To our excitement, several other classes are highly suggestive of a compact α2β2 complex akin to that proposed in the docking model (Figure 5.8, panel A, classes A, G, and H). To substantiate this observation, structural projections in 15° increments of α2 alone and α2β2 were rendered from the crystal structure of wt-α2 and the docking model, respectively, and were matched to the averaged experimental particle classes. The best projection to each class is shown in Figure 5.8 B, and the 3D structure that would give rise to such a projection is shown in Figure 5.8 C. Indeed, classes A, G, and H match well to structural projections rendered from the docking model. Unfortunately, due to the small size of the α2β2 complex (~260 kDa) and to the heterogeneity of the particles on the grid (as evidenced by the number of free α2 particles and the significant fraction of particles filtered out during alignment and classification), many of the classes are low-resolution averages for which a protein structure cannot be readily assigned (Figure 5.8, panel A, classes B, C, I, and J). It is unclear why so many free α2 molecules are observed, as we had predicted that a sample would be >80% $Y_{730}NH_2Y$-α2•wt-β2. Clearly, the number of

particles in the various classes and the inability to generate well-resolved averages indicate that the actual protein populations on the grid are significantly more heterogenous than anticipated. The origin of this heterogeneity is not known, and may reflect conformational distortions or subunit dissociation that occurs upon adsorption of the protein to the grid and staining. Alternatively, it may reflect a significant degree of protein flexibility within the proposed complex.

Due the complexities articulated above, we may make limited conclusions from the data presented in Figure 5.8. We conclude that some fraction of protein in the reaction mixture exists in a compact, globular form that is strongly reminiscent of the $\alpha 2\beta 2$ docking model with respect to its gross structural architecture. Unfortunately, given the difficulty in generating stable classes and in assigning conformations to each of those classes, we cannot accurately quantitate the fraction of particles existing in this docking model-like structure. Additionally, there is no evidence either from the raw images or class averages of a particle class representing a higher-order oligomer (e.g., $\alpha 4\beta 4$), as has been observed by a number of biophysical methods in the wt enzyme at micromolar protein concentrations, with the exact concentration depending on the specific nucleotides present in solution (~5-10 μM for CDP/ATP).[17]

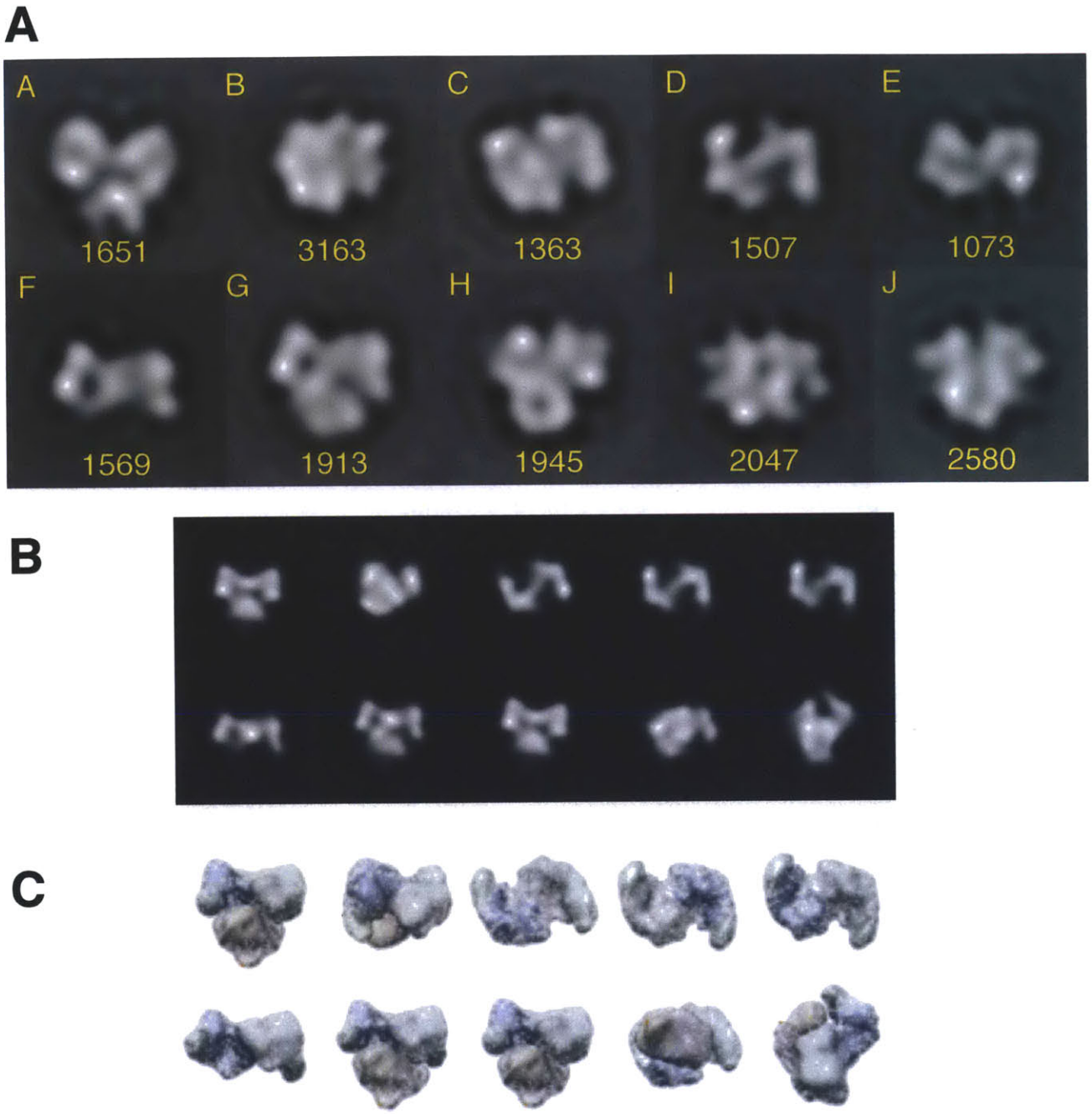

Figure 5.8 (A) Final standard 2D alignment and classification of 18,811 full-sized EM particles filtered to 30 Å. The total number of particles in each class is indicated under the aligned particle. (B) Atomic models of α2 (PDB: 4r1r)[63] and the docking model of α2β2[11] were filtered to 25 Å, projected in 15° increments, and projections were matched with class averages using a multi-reference alignment routine implemented in SPIDER. The 2D projections that best correlate with each class average are shown. (C) Crystal structures of α2 (in blue and light blue with cone domain in green) and the docking model (β2 in red and orange) are viewed according to the 2D projection angle that matches each class average. Grey density maps were simulated at 15 Å from the atomic coordinates using Chimera. Figure generated by Dr. Ed Brignole.

5.3.6 Examining the structure and oligomeric state of the $Y_{730}NH_2Y$-α2•wt-β2 complex by SAXS. The results of EM studies presented above are cautiously promising, as they indicate that a fraction of the $Y_{730}NH_2Y$-α2•wt-β2 mixture exists as a compact α2β2 complex similar to that proposed in the docking model and that reconstructed from recent biophysical experiments on RNR in the absence of dATP.[17] However, given that we observed a much more heterogeneous population of species by EM than predicted on the basis of our earlier solution biochemical experiments, we sought to complement the EM experiments by extending our collaboration with the Drennan lab to characterize the $Y_{730}NH_2Y$-α2•wt-β2 complex by small-angle X-ray scattering (SAXS). The strengths of SAXS lie in the ability to use this biophysical technique to examine the molecular weight and approximate shape of proteins in solution in real-time under non-perturbative conditions.[64,65] Samples analyzed by SAXS may be a single homogeneous protein solution or may be equilibrium mixtures of protein oligomers,[17] and may also be examined over a wide, micromolar concentration range.

Thus, we sought to characterize the structure(s)/equilibria formed in solution for the reaction of $Y_{730}NH_2Y$-α2, wt-β2, S, and E, and compare these results to structure(s)/equilibria observed by SAXS for the analogous reaction with wt-α2 and to those structures obtained for the $Y_{730}NH_2Y$-α2 reaction by EM (Figure 5.8). Previous AUC results on the reaction of wt-α2, met-β2, S, and E displayed an increase in the apparent sedimentation coefficient with increasing protein concentration, indicating that multiple protein species are rapidly interconverting on the timescale of sedimentation.[17] Together with these AUC results, SAXS experiments conducted in the presence of variable [dATP] led to the a model for *E. coli* RNR in which free α2, free β2, α2β2, and α4β4 are in equilibrium at micromolar protein concentrations (Figure 5.9 A).[17] Additional SAXS experiments conducted on wt-α2 and met-β2 indicate that this 3-state model

(Figure 5.9 A) holds in the presence of other E/S pairs (Ando and Drennan, personal communication). By this model, the α2β2 complex is an intermediate between the dissociated state and an inhibited α4β4 complex. Thus, at increasing protein concentrations, the α4β4 species is increasingly favored over α2β2. Given our results from the previous biochemical studies, we anticipated that of the distribution of oligomer species formed by $Y_{730}NH_2Y$-α2, wt-β2, S and E would be quite distinct from that of wt RNR. Specifically, we anticipated that the reaction of $Y_{730}NH_2Y$-α2 and wt-β2 would preferentially stabilize a globular α2β2 structure relative to the equilibrium of free subunits, α2β2, and α4β4 observed for the reaction of wt-α2 and wt-β2. In addition, we hypothesized that inhibiting radical transfer to $Y_{730}NH_2Y$-α2 (i.e. by use of met-β2 or omission of substrate) would reduce the stability of α2β2 and thus lead to greater accumulation of α4β4 at high protein concentrations.

To test our hypothesis, we examined reactions of RNR at 30 μM protein and a 1:1 subunit ratio. Previous SAXS data indicates that the reaction of wt-α2 with met-β2, GDP, and TTP at the same concentration gave a mixture of α2β2 and α4β4 (Ando and Drennan, personal communication). Various combinations of reaction mixtures for α2 (wt or $Y_{730}NH_2Y$) and β2 (wt or met) were examined with GDP/TTP or just TTP (no substrate). In all cases, the reaction (30 μL total volume) was initiated by addition of α2 to a mixture of β2, GDP, and TTP in assay buffer at ambient temperature. The sample was loaded into a flow cell, centered about the X-ray beam, and gently oscillated to minimize radiation damage. A total of 20 to 40 exposures were collected with a 5 second rest between each acquisition. The total reaction time, from initiation to the completion of data collection, took <6 minutes. The resulting images were integrated, normalized for beam intensity, corrected for background scattering, assessed for radiation damage, and averaged.[58] Scattering profiles, or plots of scattering intensity (*I*) vs. momentum

transfer (q), were generated from the averaged data, and then used to generate a Kratky plot (Iq^2 vs. q) for each reaction mixture. The Kratky representation of SAXS data emphasizes the rate of intensity falloff with q. Scattering from folded, globular species decays as q^{-4}, which gives rise to a pronounced peak when plotted as Iq^2 vs. q (Figure 5.9 B). By comparison, multimodal peaks are indicative of distinct, folded domains in a non-globular arrangement (Figure 5.9 C). The compact α2β2 complex proposed by the docking model[11] has a pronounced monomodal Kratky plot with a peak at q ~0.04 Å^{-1} (Figure 5.9 B, dotted) while the multimodal Kratky plot with peaks at q ~0.024 Å^{-1} and ~0.06 Å^{-1} (Figure 5.9 C, dotted) is considered the hallmark of an α4β4 ring.[17] Mixtures of α2β2 and a α4β4 lead to an apparent smearing of the peaks. Qualitatively, greater definition of multimodal peaks indicates higher levels of α4β4, while sharpening of the Kratky curve to a single peak at q ~0.025 Å^{-1} indicates higher levels of α2β2.

The Kratky plot of wt-α2, met-β2, GDP, and TTP is multimodal with poorly defined peaks, indicative of a mixture of species (Figure 5.10 A, green trace). A solution of wt-α2, wt-β2, GDP, and TTP is similarly multimodal (Figure 5.10 B, green trace). These results are in agreement with an equilibrium between free α2 and β2, α2β2, and α4β4 at 30 μM protein, as has been observed by SAXS previously (Ando and Drennan, personal communication). Meanwhile, a solution mixture of $Y_{730}NH_2Y$-α2, wt-β2, GDP and TTP at identical protein concentration reveals a unimodal peak at q ~0.04 Å^{-1} consistent with stabilization of a globular α2β2 complex under these conditions (Figure 5.10 C and D, green trace). Omitting GDP from the mixture gives rise to a less pronounced peak and a shift in peak position to lower q (Figure 5.10 D, dark blue trace), indicative of the loss of globularity, consistent with the formation of NH_2Y_{730}• as the driving force behind complex stabilization. The incomplete shift to the multimodal peak observed in the wt reactions is consistent with SF UV-vis evidence that

$Y_{730}NH_2Y$-α2, wt-β2, and TTP alone generates a small amount of NH_2Y_{730}• (Chapter 2),[38] suggesting a fraction of stable complex can form even in the absence of substrate. Thus, the distribution of complexes in $Y_{730}NH_2Y$-α2, met-β2, GDP, and TTP was also examined. The Kratky plot for that reaction mixture (Figure 5.10 D, light blue) looks quite similar to that of wt-α2, met-β2, GDP, and TTP (Figure 5.10 A, green), thereby solidifying our hypothesis about the role of NH_2Y_{730}• in complex formation. Thus, we conclude from the collective results of SAXS experiments with the GDP/TTP pair that formation of NH_2Y_{730}• stabilizes a single globular, well-folded species, distinct from the equilibrium of species observed in the wt enzyme under the same condition.

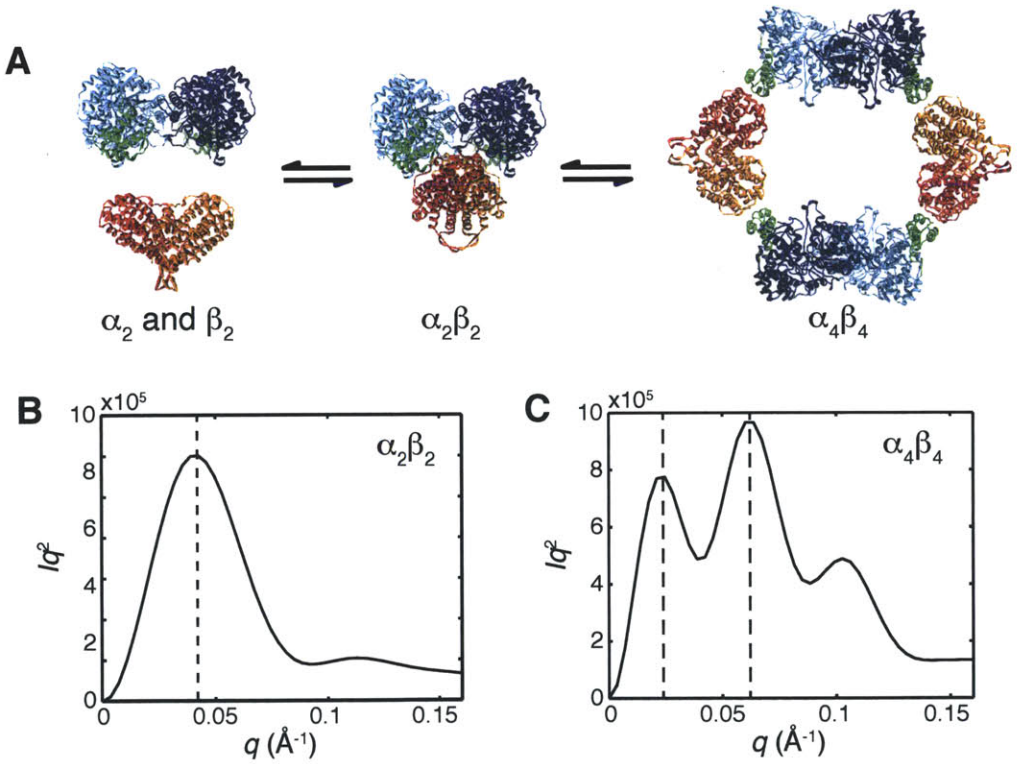

Figure 5.9 (A) A three-state model for *E. coli* class Ia solution equilibrium and theoretical Kratky plots for (B) the α2β2 docking model and (C) the α4β4 crystal structure (PDB 3UUS) calculated with CRYSOL. Figure generated by Dr. Nozomi Ando.

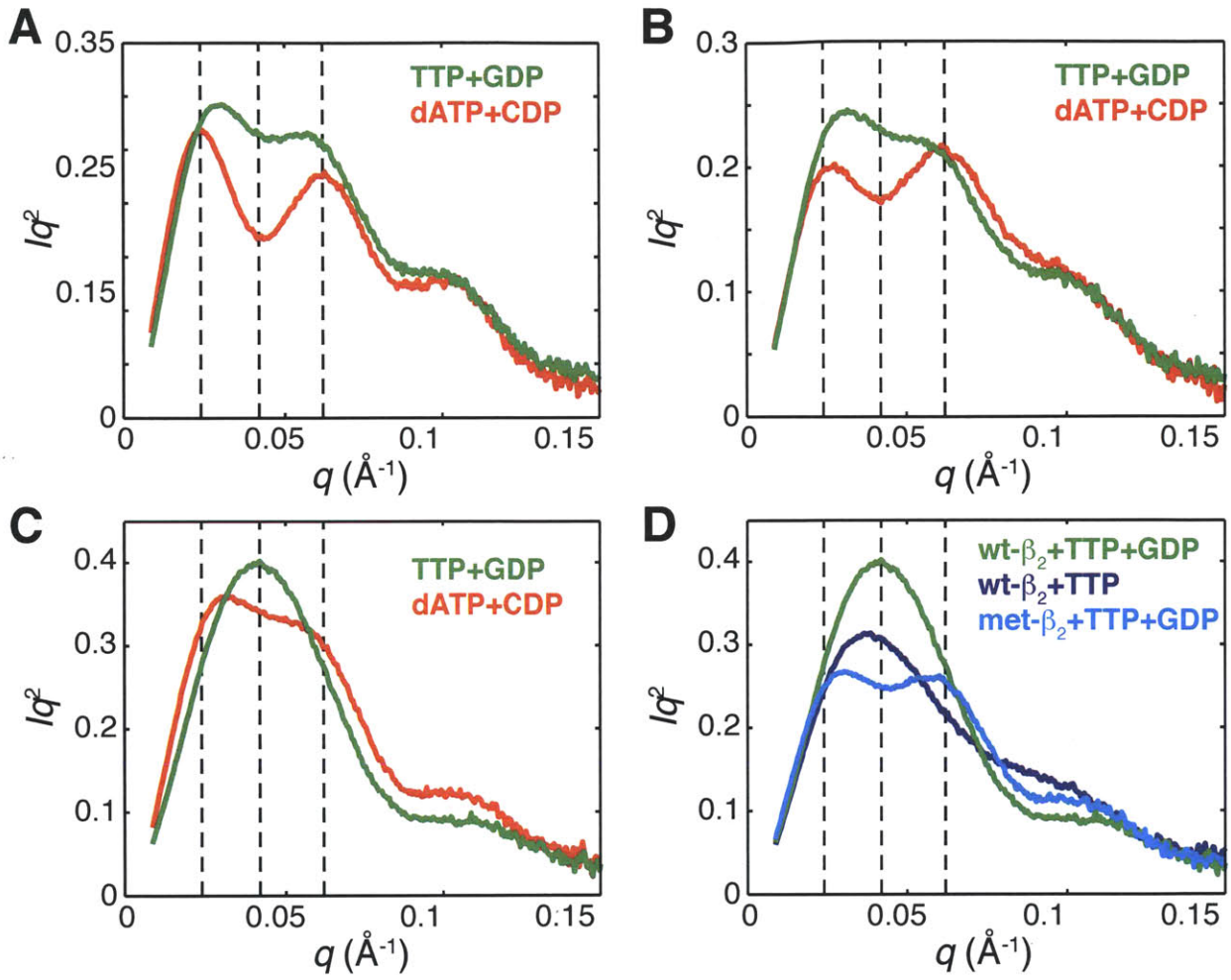

Figure 5.10 Kratky plots of the SAXS profiles of the reactions with wt-α2 or $Y_{730}NH_2Y$-α2 with wt-β2 or met-β2, GDP, and TTP. Dotted lines indicate q~ 0.024, 0.04, 0.06 Å^{-1} positions. Final protein concentration was 30 μM in all samples. Solutions containing GDP/TTP are shown in green, CDP/dATP in red, and TTP only in dark blue. Protein contents for each experiment are: (A) wt-α2 and met-β2, (B) wt-α2 and wt-β2, (C and D) $Y_{730}NH_2Y$-α2 and wt-β2. A unimodal profile (e.g. C, green) is indicative of a single well-folded, globular species, whereas a multimodal profile with distinct peaks and a q ~0.06 Å^{-1} feature is considered the hallmark of an α4β4 ring (e.g. A, red). Figure generated by Dr. Nozomi Ando.

We next investigated the effects of CDP and dATP on the $Y_{730}NH_2Y$-α2•wt-β2 complex. Previous SAXS studies of wt-α2 and met-β2 in the presence of CDP and the dATP indicated that the solution equilibrium shifts completely towards α4β4 by 1-2 μM protein, and that the formation of the α4β4 rings is the primary mode of dATP-based inhibition.[17] We sought to determine whether dATP at saturating concentrations (175 μM) shifts the equilibrium to of the mutant enzyme in a similar fashion, from $Y_{730}NH_2Y$-α2•wt-β2 to $Y_{730}NH_2Y$-α4•wt-β4. A sample of wt-α2 (30 μM), met-β2 (30 μM), CDP (1 mM), and dATP (175 μM) was prepared and analyzed as described above for the GDP/TTP reactions. The Kratky representation of the scattering plot (Figure 5.10 A, red trace) bears a very close resemblance to that which has been reported previously, showing a well-defined multimodal curve with a pronounced q ~0.06 $Å^{-1}$ signature (Figure 5.9 C).[17] A similar shift to a more well-defined multimodal curve was observed for wt-α2, wt-β2, CDP, and dATP (Figure 5.10 B, red trace) when compared to the same proteins with GDP and TTP (Figure 5.10 B, green). The effect of dATP on the $Y_{730}NH_2Y$-α2•wt-β2 complex was examined next. $Y_{730}NH_2Y$-α2, wt-β2, and CDP were incubated briefly (30 s, rt) to generate the complex, after which dATP was added to the mixture and the SAXS data collected. The results (Figure 5.10 C, red) indicate a more complicated equilibrium of species when compared to the GDP/TTP data, but demonstrate a significantly less pronounced shift towards α4β4 when compared to the wt subunit. Thus, these data suggest that once the initial $Y_{730}NH_2Y$-α2•wt-β2 complex is formed, it is more resistant to dATP-mediated inactivation than the wt complex. Finally, we asked whether the $Y_{730}NH_2Y$-α2•wt-β2 complex formed in the presence of CDP and then incubated with dATP demonstrated a time-dependent shift towards α4β4. A mixture was prepared and the reaction initiated as described for the previous experiment, except that exposures were taken once every two minutes over the course

of 22 min (Figure 5.11 A). Over this timecourse, minimal changes in the solution species were observed, indicating that the $Y_{730}NH_2Y$-α2•wt-β2 complex is a kinetically stable species even in the presence of dATP. Singular value decomposition analysis of the data indicates a two-state transition over this time. Thus, linear combinations of the theoretical scattering of α2β2 docking model and experimental scattering of α4β4 was fit to the data as done previously.[17] By this analysis, α2β2 is slowly converted to the α4β4 ring (Fig. 5.11 B). However, the plot of this conversion is non-saturating, indicating that the complete transition from α2β2 to α4β4 is not complete within the 22 min the reaction was monitored. Thus, the k_{off} for complex dissociation appears to be quite slow in both the presence of the native CDP/ATP pair (section 5.3.3) and in the presence of inhibitory concentrations of dATP (Figure 5.11 A).

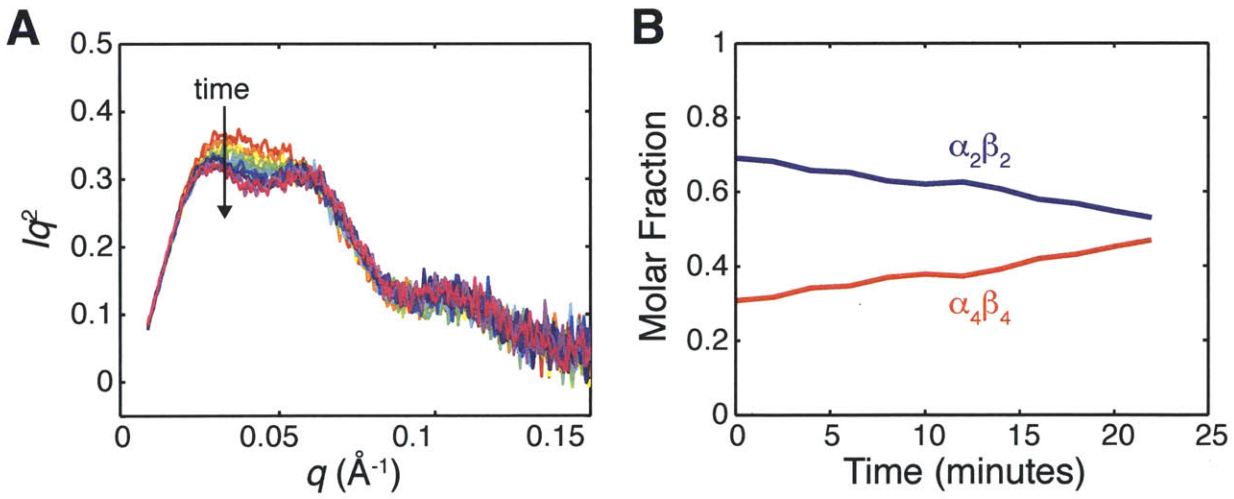

Figure 5.11 Kinetic stability of the $Y_{730}NH_2Y$-α2:wt-β2 complex in the presence of CDP (1 mM) and dATP (175 μM). The concentration of each protein subunit was 30 μM. (A) A Kratky plot of the SAXS profile of a mixture of $Y_{730}NH_2Y$-α2, wt-β2, CDP, and dATP indicates no major shift in solution species over 22 min. (B) Fitting the data with linear combinations of the theoretical scattering from the α2β2 docking model and experimental scattering of a4b4 yields molar fraction of each species. Figure generated by Dr. Nozomi Ando.

5.4 DISCUSSION

With a strategy employing multiple biochemical approaches, significant evidence supports the conclusion that the reaction of $Y_{730}NH_2Y$-α2, wt-β2, S, and E generates a kinetically stable complex, and that the origin of the stability lies in the ability to generate a long-lived NH_2Y_{730}•. Though all the work presented in this chapter focused on a specific mutant, $Y_{730}NH_2Y$-α2, we have preliminary evidence from other unnatural amino acid-containing systems that suggests a possible common mechanism of α2β2 stabilization. We hypothesize that formation of a stable α2β2 complex is a phenomenon common to any conditions under which an intermediate radical is trapped along the PCET pathway (Figure 5.1). For instance, we have recently reported the accumulation of a Y_{356}• intermediate under turnover conditions when a high-potential unnatural Y• (NO_2Y_{122}• or F_nY_{122}•) is used to initiate radical propagation at site 122.[31,34] The lifetime of this Y_{356}• depends on the identity of the Y analogue at position 122, but in all cases the 356 radical persists on the second-to-minute timescale. Interestingly, the Y_{356}• generated upon reaction of $Y_{122}F_nY$-β2, wt-α2, CDP, and ATP is formed rapidly (>20 s^{-1}), accumulates to 50% the total initial Y_{122}•, and then, in the absence of reductant, demonstrates slow (0.02 – 0.002 s^{-1}) but complete conversion of Y_{356}• to F_nY_{122}• (Chapter 7). The persistence of this radical at position 356 and its ability to undergo slow reverse radical propagation is strongly suggestive of complexation between α2 and β2, as a Y_{356}• on the structurally-disordered C-terminal tail of free β2 would be completely solvent exposed and likely quenched on the order of microseconds.[66]

The reactions of $Y_{122}NO_2Y$-β2 or $Y_{122}F_nY$-β2 with wt-α2, or $Y_{730}NH_2Y$-α2 with wt-β2 are all capable of generating dCDP, albeit to different extents and with different kinetics. $Y_{122}NO_2Y$-β2 reacts with wt-α2 to generate 0.6 dCDP/α2 in a single turnover; it cannot perform

a subsequent one.[31] $Y_{730}NH_2Y$-α2 generates 0.7 dCDP/α2 in a single turnover and is active in the steady-state with 3-4% the wt activity (Chapter 2). Finally, $Y_{122}F_nY$-β2s are active with 10-27% wt activity and generated the predicted 2-3 dCDP/α2 (Chapter 7). This observation supports a mechanism in which performing successful active site chemistry in one α/β pair while maintaining a stable population of pathway radical, accumulated either during forward or reverse radical propagation, strengthens the subunit interaction. It is interesting to question whether the enhancement in subunit affinity would be observed under conditions in which a pathway radical is formed but dCDP is not. To test this, one could examine the stability of the complex formed in the reaction of $Y_{356}NH_2Y$-β2 with $Y_{731}F$-α2, CDP, and ATP, or the reaction of wt-β2 with $Y_{731}NH_2Y/Y_{730}F$-α2. (As an aside, the ability to generate NH_2Y_{731}• in the reaction of wt-β2 with $Y_{731}NH_2Y/Y_{730}F$-α2, a prerequisite for the experiment just proposed, would also be interesting to investigate given recent results obtained with photo-RNRs suggesting that an intact Y at position 730 is necessary for radical propagation from Y_{356}• to Y_{731}).[66] Alternatively, one could examine the reaction of Y_{356}DOPA-β2 with wt-α2, CDP, and ATP. In this reaction, a long-lived $DOPA_{356}$• is formed by nucleotide reduction is completely shut down (<0.1% wt activity), indicating that the radical is trapped entirely at position 356 during forward PCET.

Similarly, we would like to ask whether a stable α2β2 complex is formed when a mechanism-based inhibitor (MBI) that disrupts dCDP formation is used as the substrate. Over the past several decades, the basis of inhibition by a number of 2′-substituted-2′-deoxynucleotides (including 2′-chloro-, 2′-fluoro-, and 2′-azido-NDPs) has been studied. A common mechanism has emerged for their inhibition, which involves loss of the 2′-substitutent and generation of a 3′-keto-2′-deoxynucleotide radical, which then is reduced by an active site thiol by one of two pathways.[2,67] Most MBIs of this type use some combination of the two

pathways, which leads to the generation of various metastable radicals in enzyme active site depending on the specific inhibitor used. Recently, SEC and SDS-PAGE results for studies examining the inactivation of *E. coli* class Ia RNR by F_2C implicated the formation of a long-lived $\alpha2\beta2$ complex as one of drug's modes of inhibition,[15] suggesting that dCDP formation and/or release is not a prerequisite for stable complex formation. In light of the results presented herein and previously with F_2C, it would be interesting to reexamine the reaction of wt-$\alpha2$ and wt-$\beta2$ with N_3CDP and ATP. In this reaction, the nucleotide covalently modifies the enzyme active site and 50% of the initial Y_{122}• is converted to a long-lived nitrogen-based radical (N•) in the active site.[68,69] Though only a 50% loss of Y_{122}• is observed under these conditions, the enzyme loses >90% of its activity at early time points, suggesting a method of sequestering the remaining, radical-loaded $\beta2$. Determining whether formation of N• enhances subunit interaction would help elucidate which radical and chemical steps must be successfully completed to stabilize the $\alpha2\beta2$ complex.

As noted in the introduction, PELDOR spectroscopy has been used to measure diagonal distances between Y_{122}• in one α/β pair and unnatural amino acid radicals at position 356 of β, 731 of α, 730 of α in the second α/β pair. These experiments required very high protein concentrations (50-300 μM), conditions which we now know drive the wt complex to form $\alpha4\beta4$ rings.[17,70] The distances measured by this technique, however, are all in excellent agreement with the $\alpha2\beta2$ docking model. In retrospect, this observation is also consistent with the formation of a tight $\alpha2\beta2$ complex upon radical trapping.

In conclusion, the results presented herein provide a snapshot of the active *E. coli* class Ia RNR. These experiments, in combination with the previously-reported PELDOR distances,[24,25] help to solidify the docking model as an accurate representation of the active structure.

Experiments are underway to exploit the kinetic stability of the $Y_{730}NH_2Y$-α2•wt-β2 complex for the purpose of protein crystallography, as the benefits of an atomic resolution structure of the active RNR complex cannot be overstated.

5.5 REFERENCES

1. Jordan, A. & Reichard, P. Ribonucleotide reductases. *Annu. Rev. Biochem.* **67**, 71-98 (1998).
2. Stubbe, J. & van der Donk, W.A. Protein radicals in enzyme catalysis. *Chem. Rev.* **98**, 705-62 (1998).
3. Hakansson, P., Hofer, A. & Thelander, L. Regulation of mammalian ribonucleotide reduction and dNTP pools after DNA damage and in resting cells. *J. Biol. Chem.* **281**, 7834-41 (2006).
4. Brown, N.C. & Reichard, P. Ribonucleoside diphosphate reductase: Formation of active and inactive complexes of proteins B1 and B2. *J. Mol. Biol.* **46**, 25-38 (1969).
5. Brown, N.C. & Reichard, P. Role of effector binding in allosteric control of ribonucleoside diphosphate reductase. *J. Mol. Biol.* **46**, 39-55 (1969).
6. Larsson, A. Enzymatic Synthesis of Deoxyribonucleotides. VII. Studies on the Hydrogen Transfer with Tritiated Water. *Biochemistry* **4**, 1984-93 (1965).
7. Larsson, A. & Reichard, P. Enzymatic synthesis of deoxyribonucleotides. X. Reduction of purine ribonucleotides; allosteric behavior and substrate specificity of the enzyme system from *Escherichia coli* B. *J. Biol. Chem.* **241**, 2540-9 (1966).
8. Larsson, K.M., Jordan, A., Eliasson, R., Reichard, P., Logan, D. T. & Nordlund, P. Structural mechanism of allosteric substrate specificity regulation in a ribonucleotide reductase. *Nat. Struct. Mol. Biol.* **11**, 1142-9 (2004).
9. Kashlan, O.B. & Cooperman, B.S. Comprehensive model for allosteric regulation of mammalian ribonucleotide reductase: refinements and consequences. *Biochemistry* **42**, 1696-1706 (2003).
10. Sjöberg, B.M., Reichard, P., Gräslund, A. & Ehrenberg, A. Tyrosine free-radical in ribonucleotide reductase from *Escherichia coli*. *J Biol Chem* **253**, 6863-6865 (1978).
11. Uhlin, U. & Eklund, H. Structure of ribonucleotide reductase protein R1. *Nature* **370**, 533-539 (1994).
12. Stubbe, J., Nocera, D.G., Yee, C.S. & Chang, M.C.Y. Radical initiation in the class I ribonucleotide reductase: long-range proton-coupled electron transfer? *Chem. Rev.* **103**, 2167-201 (2003).
13. Thelander, L. Physicochemical characterization of ribonucleoside diphosphate reductase from *Escherichia coli*. *J. Biol. Chem.* **248**, 4591-4601 (1973).
14. Climent, I., Sjöberg, B.M. & Huang, C.Y. Carboxyl-terminal peptides as probes for *Escherichia coli* ribonucleotide reductase subunit interaction: kinetic analysis of inhibition studies. *Biochemistry* **30**, 5164-71 (1991).
15. Wang, J., Lohman, G.J. & Stubbe, J. Enhanced subunit interactions with gemcitabine-5'-diphosphate inhibit ribonucleotide reductases. *Proc. Natl. Acad. Sci. U S A* **104**, 14324-9 (2007).

16. Nordlund, P., Sjöberg, B.M. & Eklund, H. Three-dimensional structure of the free radical protein of ribonucleotide reductase. *Nature* **345**, 593-8 (1990).

17. Ando, N. et al. Structural interconversions modulate activity of *Escherichia coli* ribonucleotide reductase. *Proc. Natl. Acad. Sci. U S A* **108**, 21046-51 (2011).

18. Hassan, A.Q., Olshansky, L., Yokoyama, K., Lutterman, D. A., Jin, X., Nocera, D. G., & Stubbe, J. *In preparation.*

19. Rofougaran, R., Vodnala, M. & Hofer, A. Enzymatically active mammalian ribonucleotide reductase exists primarily as an α6β2 octamer. *J. Biol. Chem.* **281**, 27705-11 (2006).

20. Rofougaran, R., Crona, M., Vodnala, M., Sjöberg, B.M. & Hofer, A. Oligomerization status directs overall activity regulation of the *Escherichia coli* class Ia ribonucleotide reductase. *J. Biol. Chem.* **283**, 35310-8 (2008).

21. Fairman, J.W. et al. Structural basis for allosteric regulation of human ribonucleotide reductase by nucleotide-induced oligomerization. *Nat. Struct. Mol. Biol.* **18**, 316-22 (2011).

22. Aye, Y. & Stubbe, J. Clofarabine 5'-di and -triphosphates inhibit human ribonucleotide reductase by altering the quaternary structure of its large subunit. *Proc. Natl. Acad. Sci. U S A* **108**, 9815-20 (2011).

23. Wang, J., Lohman, G.J. & Stubbe, J. Mechanism of inactivation of human ribonucleotide reductase with p53R2 by gemcitabine 5′-diphosphate. *Biochemistry* **48**, 11612-21 (2009).

24. Bennati, M. et al. EPR distance measurements support a model for long-range radical initiation in *E. coli* ribonucleotide reductase. *J. Am. Chem. Soc.* **127**, 15014-5 (2005).

25. Seyedsayamdost, M.R., Chan, C.T., Mugnaini, V., Stubbe, J. & Bennati, M. PELDOR spectroscopy with DOPA-β2 and NH_2Y-α2s: distance measurements between residues involved in the radical propagation pathway of *E. coli* ribonucleotide reductase. *J. Am. Chem. Soc.* **129**, 15748-9 (2007).

26. Climent, I., Sjöberg, B.M. & Huang, C.Y. Site-directed mutagenesis and deletion of the carboxyl terminus of *Escherichia coli* ribonucleotide reductase protein R2 - effects on catalytic activity and subunit interaction. *Biochemistry* **31**, 4801-7 (1992).

27. Ge, J., Yu, G., Ator, M.A. & Stubbe, J. Pre-steady-state and steady-state kinetic analysis of *E. coli* class I ribonucleotide reductase. *Biochemistry* **42**, 10071-83 (2003).

28. Seyedsayamdost, M.R. & Stubbe, J. Site-specific replacement of Y_{356} with 3,4-dihydroxyphenylalanine in the β2 subunit of *E. coli* ribonucleotide reductase. *J. Am. Chem. Soc.* **128**, 2522-3 (2006).

29. Yee, C.S., Seyedsayamdost, M.R., Chang, M.C.Y., Nocera, D.G. & Stubbe, J. Generation of the R2 subunit of ribonucleotide reductase by intein chemistry: insertion of 3-nitrotyrosine at residue 356 as a probe of the radical initiation process. *Biochemistry* **42**, 14541-52 (2003).

30. Yokoyama, K., Uhlin, U. & Stubbe, J. Site-specific incorporation of 3-nitrotyrosine as a probe of p*K*a perturbation of redox-active tyrosines in ribonucleotide reductase. *J. Am. Chem. Soc.* **132**, 8385-97 (2010).

31. Yokoyama, K., Uhlin, U. & Stubbe, J. A hot oxidant, 3-NO2Y_{122} radical, unmasks conformational gating in ribonucleotide reductase. *J. Am. Chem. Soc.* **132**, 15368-79 (2010).

32. Yee, C.S., Chang, M.C.Y., Ge, J., Nocera, D.G. & Stubbe, J. 2,3-difluorotyrosine at position 356 of ribonucleotide reductase R2: A probe of long-range proton-coupled electron transfer. *J. Am. Chem. Soc.* **125**, 10506-7 (2003).

33. Seyedsayamdost, M.R., Yee, C.S., Reece, S.Y., Nocera, D.G. & Stubbe, J. pH rate profiles of F_nY_{356}-R2s (n = 2, 3, 4) in *Escherichia coli* ribonucleotide reductase: evidence that Y_{356} is a redox-active amino acid along the radical propagation pathway. *J. Am. Chem. Soc.* **128**, 1562-8 (2006).

34. Minnihan, E.C., Young, D.D., Schultz, P.G. & Stubbe, J. Incorporation of fluorotyrosines into ribonucleotide reductase using an evolved, polyspecific aminoacyl-tRNA synthetase. *J. Am. Chem. Soc.* **133**, 15942-5 (2011).

35. Reece, S.Y., Hodgkiss, J.M., Stubbe, J. & Nocera, D.G. Proton-coupled electron transfer: the mechanistic underpinning for radical transport and catalysis in biology. *Philos. Trans. R. Soc. Lond. B Biol. Sci.* **361**, 1351-64 (2006).

36. DeFelippis, M.R. et al. Electrochemical properties of tyrosine phenoxy and tryptophan in indolyl radicals in peptides and amino acid analogs. *J. Phys. Chem.* **95**, 3416-3419 (1991).

37. Seyedsayamdost, M.R., Xie, J., Chan, C.T., Schultz, P.G. & Stubbe, J. Site-specific insertion of 3-aminotyrosine into subunit α2 of *E. coli* ribonucleotide reductase: direct evidence for involvement of Y730 and Y731 in radical propagation. *J. Am. Chem. Soc.* **129**, 15060-71 (2007).

38. Minnihan, E.C., Seyedsayamdost, M.R., Uhlin, U. & Stubbe, J. Kinetics of radical intermediate formation and deoxynucleotide production in 3-aminotyrosine-substituted *Escherichia coli* ribonucleotide reductases. *J. Am. Chem. Soc.* **133**, 9430-40 (2011).

39. Minnihan, E.C., Seyedsayamdost, M.R. & Stubbe, J. Use of 3-aminotyrosine to examine the pathway dependence of radical propagation in *Escherichia coli* ribonucleotide reductase. *Biochemistry* **48**, 12125-32 (2009).

40. Wu, C.H., Jiang, W., Krebs, C. & Stubbe, J. YfaE, a ferredoxin involved in diferric-tyrosyl radical maintenance in *Escherichia coli* ribonucleotide reductase. *Biochemistry* **46**, 11577-88 (2007).

41. Chivers, P.T. et al. Microscopic pK_a values of *Escherichia coli* thioredoxin. *Biochemistry* **36**, 14985-91 (1997).

42. Russel, M. & Model, P. Direct cloning of the *trxB* gene that encodes thioredoxin reductase. *J. Bacteriol.* **163**, 238-42 (1985).

43. Hassan, A.Q., Wang, Y., Plate, L. & Stubbe, J. Methodology to probe subunit interactions in ribonucleotide reductases. *Biochemistry* **47**, 13046-13055 (2008).

44. Bollinger, J.M., Jr. et al. Use of rapid kinetics methods to study the assembly of the diferric-tyrosyl radical cofactor of *E. coli* ribonucleotide reductase. *Methods Enzymol.* **258**, 278-303 (1995).

45. Steeper, J.R. & Steuart, C.D. A rapid assay for CDP reductase activity in mammalian cell extracts. *Anal. Biochem.* **34**, 123-30 (1970).

46. Aebi, U. & Pollard, T.D. A glow discharge unit to render electron microscope grids and other surfaces hydrophilic. *J. Electron. Microsc. Tech.* **7**, 29-33 (1987).

47. Zhao, F.Q. & Craig, R. Capturing time-resolved changes in molecular structure by negative staining. *J. Struct. Biol.* **141**, 43-52 (2003).

48. Suloway, C. et al. Automated molecular microscopy: the new Leginon system. *J. Struct. Biol.* **151**, 41-60 (2005).

49. Tang, G. et al. EMAN2: an extensible image processing suite for electron microscopy. *J. Struct. Biol.* **157**, 38-46 (2007).

50. Voss, N.R., Yoshioka, C.K., Radermacher, M., Potter, C.S. & Carragher, B. DoG Picker and TiltPicker: software tools to facilitate particle selection in single particle electron microscopy. *J. Struct. Biol.* **166**, 205-13 (2009).

51. Frank, J. et al. SPIDER and WEB: processing and visualization of images in 3D electron microscopy and related fields. *J. Struct. Biol.* **116**, 190-9 (1996).

52. Shaikh, T.R. et al. SPIDER image processing for single-particle reconstruction of biological macromolecules from electron micrographs. *Nat. Protoc.* **3**, 1941-74 (2008).

53. Brignole, E.J. & Asturias, F. Single-particle electron microscopy of animal fatty acid synthase describing macromolecular rearrangements that enable catalysis. *Methods Enzymol.* **483**, 179-202 (2010).

54. Brignole, E.J., Smith, S. & Asturias, F.J. Conformational flexibility of metazoan fatty acid synthase enables catalysis. *Nat. Struct. Mol. Biol.* **16**, 190-7 (2009).

55. Gibbons, B.J. et al. Subunit architecture of general transcription factor TFIIH. *Proc. Natl. Acad. Sci. U S A* **109**, 1949-54 (2011).

56. Mulder, A.M. et al. Visualizing ribosome biogenesis: parallel assembly pathways for the 30S subunit. *Science* **330**, 673-7 (2010).

57. Nielsen, S.S., Moller, M. & Gillilan, R.E. High-throughput biological small-angle X-ray scattering with a robotically loaded capillary cell. *J. Appl. Crystallogr.* **45**, 213-23 (2012).

58. Ando, N., Chenevier, P., Novak, M., Tate, M.W. & Gruner, S.M. High hydrostatic pressure small-angle X-ray scattering cell for protein solution studies featuring diamond windows and disposable sample cells. *J. Appl. Crystallogr.* **41**, 167-75 (2008).

59. Seyedsayamdost, M.R. & Stubbe, J. Forward and reverse electron transfer with the Y356DOPA-β2 heterodimer of *E. coli* ribonucleotide reductase. *J. Am. Chem. Soc.* **129**, 2226-7 (2007).

60. Reece, S.Y., Lutterman, D.A., Seyedsayamdost, M.R., Stubbe, J. & Nocera, D.G. Re(bpy)(CO)(3)CN as a probe of conformational flexibility in a photochemical ribonucleotide reductase. *Biochemistry* **48**, 5832-8 (2009).

61. Ekberg, M., Sahlin, M., Eriksson, M. & Sjöberg, B.M. Two conserved tyrosine residues in protein R1 participate in an intermolecular electron transfer in ribonucleotide reductase. *J. Biol. Chem.* **271**, 20655-9 (1996).

62. Seyedsayamdost, M.R. Massachusetts Institute of Technology (2007).

63. Eriksson, M. et al. Binding of allosteric effectors to ribonucleotide reductase protein R1: reduction of active-site cysteines promotes substrate binding. *Structure* **5**, 1077-92 (1997).

64. Putnam, C.D., Hammel, M., Hura, G.L. & Tainer, J.A. X-ray solution scattering (SAXS) combined with crystallography and computation: defining accurate macromolecular structures, conformations and assemblies in solution. *Q. Rev. Biophys.* **40**, 191-285 (2007).

65. Jacques, D.A. & Trewhella, J. Small-angle scattering for structural biology--expanding the frontier while avoiding the pitfalls. *Protein Sci.* **19**, 642-57 (2010).

66. Holder, P.G., Pizano, A.A., Anderson, B.L., Stubbe, J. & Nocera, D.G. Deciphering radical transport in the large subunit of class I ribonucleotide reductase. *J. Am. Chem. Soc.* **134**, 1172-80 (2012).

67. Licht, S. & Stubbe, J. Mechanistic investigations of ribonucleotide reductases. *Compr. Nat. Prod. Chem.* **5**, 163-203 (1999).

68. Salowe, S. et al. Alternative model for mechanism-based inhibition of *Escherichia coli* ribonucleotide reductase by 2'-azido-2'-deoxyuridine 5'-diphosphate. *Biochemistry* **32**, 12749-60 (1993).

69. Fritscher, J. et al. Structure of the nitrogen-centered radical formed during inactivation of *E. coli* ribonucleotide reductase by 2'-azido-2'-deoxyuridine-5'-diphosphate: trapping of the 3'-ketonucleotide. *J. Am. Chem. Soc.* **127**, 7729-38 (2005).

70. Zimanyi, C.M. et al. *In revision.*

Chapter 6

Incorporation of fluorotyrosines into ribonucleotide reductase using an evolved, polyspecific aminoacyl-tRNA synthetase and pH rate profiles of the resulting F_nY-RNRs

Adapted in part from: Minnihan, E.C., Young, D.D., Schultz, P.G. and Stubbe, J. *J. Am. Chem. Soc.*, **2011**, *133*, 15942-15945.

6.1 INTRODUCTION

Examples of amino acid radicals participating in charge transfer reactions are prevalent in nature.[1] Of these, tyrosyl radicals (Y•s) have been shown to mediate a number of key metabolic transformations, including O_2 evolution, fatty acid oxidation, peroxide disproportionation, and prostaglandin synthesis.[2-5] The thermodynamics of Y oxidation require that proton transfer (PT) accompanies electron transfer (ET) at physiological pH, a process that may occur by either a stepwise or coupled (PCET) mechanism. To investigate the mechanism of Y• formation and Y•-mediated catalysis in metalloenzymes, a method by which the native Y• may be subtly perturbed is necessary. A series of N-acetyl-fluorotyrosinamides (N-Ac-F_nY-NH_2s, n=1-4) have been characterized in solution and found to have phenolic pK_as from 5.6-8.4 and peak potentials ranging from 705-968 mV (Figure 6.1).[6,7] Thus, this series of Y analogues provides a means of systematically modulating the chemical properties governing both the PT and ET events.

Ribonucleotide reductase (RNR) catalyzes the formation of all four 2′-deoxynucleotides from the corresponding nucleoside diphosphates (NDPs) by a mechanism involving protein and nucleotide radicals.[1] In the class Ia RNRs, a stable diferric-Y• cofactor in the β2 subunit initiates catalysis by transiently oxidizing a cysteine at the active site in the α2 subunit. The mechanism of radical initiation has been best studied in the *E. coli* RNR, and is believed to involve an unprecedented mechanism of reversible long-range (>35 Å) PCET along a pathway of absolutely conserved redox active amino acids: Y_{122}• ↔ [W_{48}?] ↔ Y_{356} in β2 to Y_{731}↔Y_{730}↔ C_{439} in α2.[8,9] This hypothesis has been tested by the site-specific incorporation of more than a half-dozen unnatural amino acids (UAAs) into positions along the pathway, using both expressed protein ligation (EPL)[10] and *in vivo* nonsense suppression[11,12] techniques. Previously, a series of F_nYs were site-specifically incorporated at position 356 of β by expressed protein ligation (EPL).

Substitution of 2,3,5-F_3Y into this position did not shut down nucleotide reduction, but slowed radical transport to the point that electron transfer, rather than conformational change(s), became rate-limiting.[13,14] Thus, this mutant protein provided a unique opportunity to begin characterization of individual steps relating to proton and electron transfer. Additionally, the activity showed no correlation with the protonation state of the phenol, indicating proton and electron movement is orthogonal at this position (Figure 6.2) and that an ordered hydrogen bonding network involving the Y_{356} phenol is not necessary for catalysis.[13,15]

F_nYs incorporated in place of other conserved Ys along the pathway would be comparably informative. However, the EPL technology used to generate $Y_{356}F_n$Y-β2s is inherently complicated and low yielding[10,16] and cannot be readily extended to positions in the interior of β2 (43 kDa/monomer) or α2 (86 kDa/monomer). While other strategies for incorporation of F_nYs exist, namely global incorporation[7,17] or site-specific insertion of photocaged F_nYs,[18] these techniques are applicable to mono- and di-F_nYs only and are minimally useful in the RNR system due to lack of specificity and complications arising from photolysis, respectively.

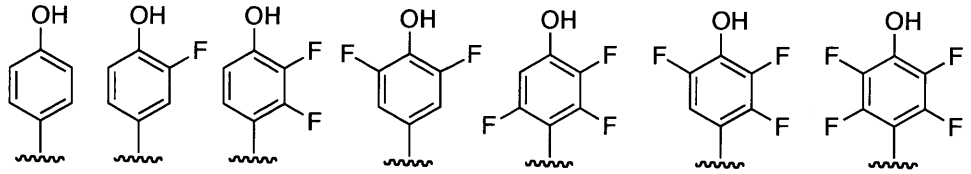

	Y	3-FY	2,3-F_2Y	3,5-F_2Y	2,3,6-F_3Y	2,3,5-F_3Y	2,3,5,6-F_4Y
pK_a:	10	8.4	7.8	7.2	7.0	6.4	5.6
E_p(mV):	642	705	810	755	911	853	968

Figure 6.1 Structures, pK_as and peak potentials of F_nYs relative to Y.

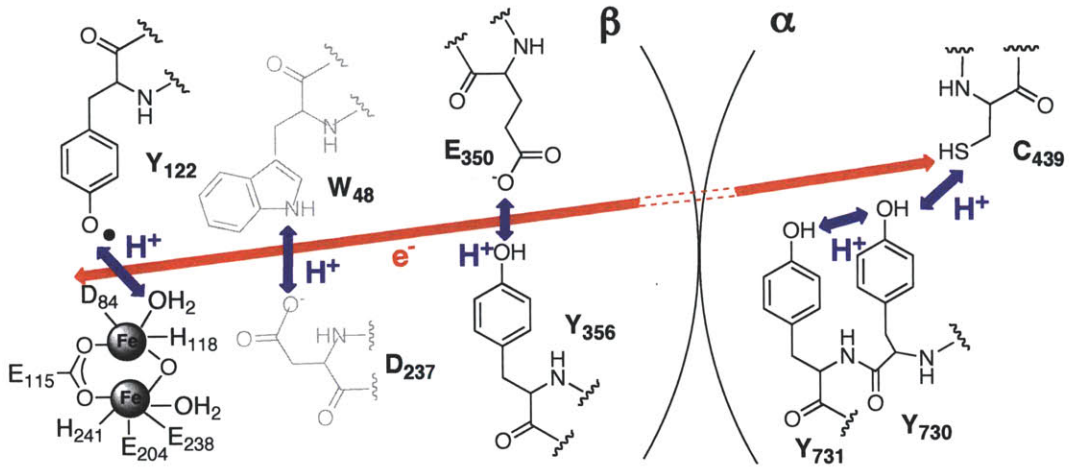

Figure 6.2 Working mechanism for long-range PCET pathway in *E. coli* class Ia RNR. The current hypothesis holds that protons (blue arrows) move orthogonally to the electron (red arrow) in β2 and co-linearly with the electron in α2. The mechanism across the α/β interface is unknown. W_{48} and its putative proton acceptor, D_{237}, are shown in gray, as there is no direct experimental evidence that these residues participate in long-range PCET during turnover.

Instead, we sought to incorporate F_nYs using the *in vivo* translational amber stop codon suppression method. This method relies on the evolution of a unique, orthogonal tRNA/tRNA synthetase (RS) pair that exclusively recognizes an unnatural amino acid and inserts it site-specifically during protein translation in response to an amber stop codon mutated into the gene of interest (Figure 6.3).[19] In this chapter, we report the results of a fruitful collaboration with the Schultz lab (Scripps), from which two RSs were prepared by directed evolution. Each RS is capable of charging an orthogonal tRNA with an entire series of F_nYs, while maintaining high specificity over endogenous Y.[20]

The F_nY-RS has been successfully applied to the incorporation of four different F_nYs to the four sites of conserved Ys on the PCET pathway (Figure 6.2).[20] We initiated study of these mutants by conducting experiments modeled after those previously conducted on EPL-generated $Y_{356}F_nY$-β2s,[13] namely to construct pH rate profiles for each of $Y_{356}F_nY$-β2, $Y_{731}F_nY$-β2, and $Y_{730}F_nY$-β2. It was our hope that these pH rate profiles would provide a method of directly

testing our current hypothesis for radical propagation in *E. coli* RNR, which posits that different mechanisms of PCET are operative in the two subunits.[9] Orthogonal PCET is proposed to be functional in β, and co-linear PCET is functional in α (Figure 6.2). If correct, we predicted that the pH rate profile at position 730 would be quite distinct from that observed at 356 in that it would display a strong correlation between enzymatic activity and the protonation state of the F_nY. Additionally, we have no knowledge about proton transfer across the β/α interface, so pH rate profiles at position 731 could prove informative in formulating a hypothesis regarding PCET between position 731 of α2 and (presumably) 356 of β2.

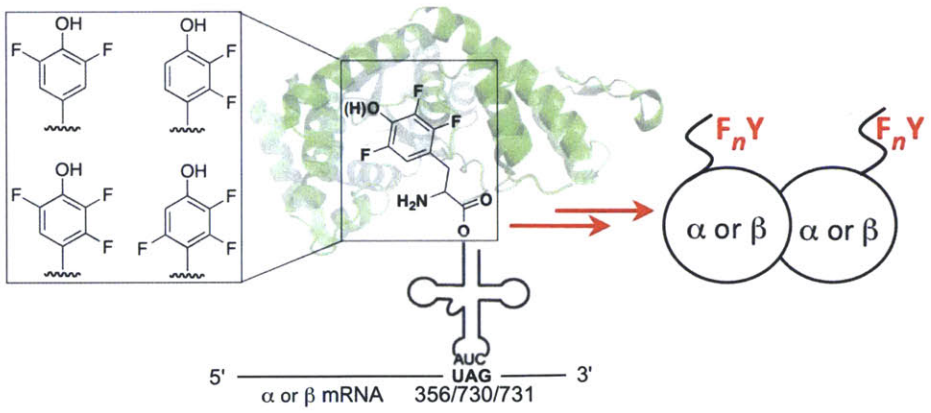

Figure 6.3 Translational incorporation of F_nYs into positions of the *E. coli* RNR PCET pathway via the *in vivo* nonsense codon suppression method. The evolved F_nY-RS has been demonstrated to be polyspecific for a complete series of F_nYs, while remaining highly discriminating against endogenous Y.

The pH rate profiles of $Y_{356}F_nY$-β2, $Y_{731}F_nY$-α2, and $Y_{730}F_nY$-α2 are presented in Chapter 6. In all cases, the pH rate profiles of the various mutants may be fit to a two proton ionization model. Furthermore, we see noticeable trends in overall activity as a function of the F_nY incorporated, and observe subtle differences with respect to position in the protein (356 of

β2 versus 731 of α2 and 730 of α2). Unfortunately, however, we do not observe the same phenotype as in the EPL-generated $Y_{356}(2,3,5)F_3Y$-β2; that is, we have no evidence for a change in the rate-determining step from a conformational change(s) to radical chemistry in any of the F_nY-RNRs described herein. Thus, the pH rate profiles we have generated are not mechanistically informative with respect to radical propagation, and instead likely reflect the complicated pH dependence of the subtle structural rearrangements that gate the process. Given this predicament, a possible strategy for slowing radical propagation in F_nY-RNRs in proposed.

6.2 MATERIALS AND METHODS

6.2.1 Materials. The generation of plasmids pET-*nrdA*(TAG_{730}), pET-*nrdA*(TAG_{731}), pBAD-*nrdB*(TAG_{356}) was described in Chapter 2.[21] Wt-α2 (2500 nmol/min/mg), His-α2(wt) (2200 nmol/min/mg), and wt-β2 (1.2 Y_{122}•/β2, 7600 nmol/min/mg) were expressed and purified as previously described.[21] *E. coli* thioredoxin (TR, 40 U/mg) and thioredoxin reductase (TRR, 1400 U/mg) were isolated as described.[22,23] [5-^{3}H]-CDP was purchased from ViTrax (Placentia, CA). Assay buffers for pH titrations consist of 50 mM Good's buffer (MES for pH 6.0-6.8, Hepes for pH 7.0-8.0, and TAPS for pH 8.2-9.0), 1 mM EDTA, and 15 mM $MgSO_4$.

6.2.2 Purification of tyrosine phenol lyase. E. coli strain SVS370 was obtained as a gift from Dr. Robert Phillips (University of Georgia) and was grown on a 7.5 L scale using standard culture techniques and maintaining 100 μg/mL Amp in all cultures. This strain harbors the plasmid pTZTPL, which encodes for tyrosine phenol lyase (TPL) under the control of a constitutive promoter.[24] This growth yielded 5 g/L.

TPL was purified from a fraction of the cell pellet (25 g), adapting the previously described protocol.[24] Briefly, the cells were resuspended at 5 mL/g in buffer T (100 mM KPi, 1 mM ETDA, 0.1 mM pyridoxal phosphate (PLP), and 5 mM β-mercaptoethanol (β-ME), pH 7.0), homogenized, and lysed via passage through the French Press at 14,000 psi. The lysate was centrifuged to clear the cell debris (30,000 × *g*, 25 min, 4 °C) and the DNA precipitated by the dropwise addition of 0.12 vol of protamine sulfate (2% w/v solution) to the stirring supernatant over 10 min at room temperature. The DNA was cleared by centrifugation (30,000 × *g*, 25 min, 4 °C). To the supernatant was added solid ammonium sulfate to 60% saturation over 20 min at 4 °C, and the resulting solution allowed to stir for an additional 15 min. The solution was centrifuged (30,000 × *g*, 25 min, 4 °C), the protein pellet resuspended in buffer T, and the

resulting solution dialyzed in a YM 10 cassette against a solution of 25% saturated $(NH_4)_2SO_4$ in buffer T (2 × 4 L, 14 h total). The protein solution was then diluted 3-fold with the dialysis buffer, loaded to an octyl Sepharose column (200 mL column volume, CV) equilibrated in the same buffer, and eluted with a 25% to 0% gradient of saturated $(NH_4)_2SO_4$ in buffer T. The elution fractions were assayed using a coupled spectrophotometric assay as described below. Those fractions containing considerable activity were pooled, concentrated, flash-frozen and stored at -80 °C. One unit (U) of activity is defined as 1 μmol product/min. A total of 1340 U of enzyme was isolated, or 56 U/g cell paste, in good agreement with the previously-reported yield.[24]

Enzyme activity was determined by a specrtrophotometric assay employing lactate dehydrogenase and monitoring NADH consumption. In a total volume of 300 μL was combined tyrosine (2 mM), PLP (50 μM), β-ME (5 mM), lactate dehydrogenase (0.3 mg/mL, Sigma, from *L. leichmannii*), and NADH (0.2 mM) in 50 mM KP_i, pH 8.0. The reaction was initiated upon addition of a small volume of TPL (~5 μL) and the reaction monitored at 320 nm.

6.2.3 Fluorotyrosine (F_nY) synthesis. Fluorotyrosines were synthesized following a previously-reported protocol.[7,24] Fluorophenol (15 mmol), sodium pyruvate (90 mmol), and β-mercaptoethanol (7.5 mmol) were dissolved in 1 L of 30 mM NH_4OAc and the pH of the solution was adjusted to 8.0 with NaOH. PLP (60 μmol) and TPL (45 U) were added last. The solution was allowed to stir in the dark at ambient temperature for 48 h. After 48 h, an additional 10 U of TPL and 40 μmol of PLP were added. The reaction was stirred in the dark for another 24 h. The reaction mixture was acidified to pH 3 with concentrated HCl and vacuum filtered through 3 cm of Celite layered onto a Büchner funnel with a coarse frit. The solution was then extracted with 0.5 volumes of EtOAc, and the aqueous phase loaded onto an AG50W-X8 cation

exchange column (H^+ state, 260 mL CV). The column was washed with 10 CVs of ddH_2O, then eluted with 1L of a 10% NH_4OH solution. Fractions (20 mL) were collected and checked for product by UV-vis and nihydrin staining. Product-containing fractions were pooled, concentrated to dryness under vacuum, redissolved in a minimal volume of ddH_2O, and lyophilized to dryness to give the desired product in 50-90% yield. Product was characterized by UV-vis, ^1H, and ^{19}F NMR spectroscopy, as described previously.[7]

6.2.4 Evolution of orthogonal synthetase specific for F_3Y (F_3Y-RS). Evolution of a F_3Y-RS was conducted by Dr. Douglas Young (Schultz lab, Scripps). Evolution was conducted on four synthetase libraries following the traditional chloramphenicol acetyl transferase/barnase double-sieve selection method.[11,19] Synthetases contained mutations at eight positions surrounding the amino acid binding pocket. After three rounds of selection, the most promising synthetases were those that grew on 150 μg/mL Cm in the presence of 2,3,5-F_3Y and died at 20 μg/mL Cm in the absence of 2,3,5-F_3Y. These synthetases were PCR-amplified from pBK, and cloned into two positions in the previously described pEVOL[25] plasmid via stepwise digestion and ligation using the appropriate sticky ends (*NdeI/PstI* or *BglII/SalI*). Constructs containing the two most promising F_3Y-RSs were named pEVOL-F_3Y-RS-E3 and pEVOL-F_3Y-RS-E11, indicating the library name and colony number.

The substrate specificities of pEVOL-F_3Y-RS-E3 and pEVOL-F_3Y-RS-E11 were assessed by a high-throughput GFP expression assay in which read-through of an amber stop codon at position 151 results in full-length protein and maturation of the fluorophore. pEVOL-F_3Y-RS-E3 or pEVOL-F_3Y-RS-E11 was co-transformed with pET-GFP_{Y151X}[25] into BL21(DE3) cells and grown in the presence of Amp (100 μg/mL) and Cm (50 μg/mL). Colonies were selected and grown to saturation overnight at 37 °C, then used to inoculate 2xYT media (10 mL)

at OD_{600} 0.2. The culture was grown to OD_{600} 0.8 and induced with 0.02% w/v ara and IPTG (1 mM), then aliquoted (100 μL/well) into a 96 well plate containing 80 different UAAs (1 mM).[26] An initial fluorescence measurement was taken using a Spectramax Gemini EM (Ex/Em= 395/509 nm; Molecular Probes) to normalize for background fluorescence. The plate was incubated at 30 °C for 16 h, followed by a second fluorescence measurement. Controls included three wells of 2,3,5-F_3Y, three wells containing no UAA, three wells of uninduced culture, and three wells containing a bacterial culture with no GFP plasmid. The relative fluorescence of each well was then plotted to determine potential polyspecificity of the F_3Y-RSs.

Protein expression was repeated as described above on a small (10 mL) scale for those UAAs that showed considerable incorporation by the GFP assay. Cells were harvested by centrifugation and lysed using Bug Buster (Novagen) and the protein was purified on Ni-NTA spin columns (Qiagen) according to the manufacturer's protocol. Purified GFP was then analyzed by LC/MS on an Agilent 1100 Series LC/MSD. The chromatographic peak corresponding to GFP (between 6.3 min and 7.1 min) was charge deconvoluted using Agilent LC/MSD ChemStation software (revision B.03.02). Deconvolution parameters were set to higher than M_r = 20,000 and lower than M_r = 30,000, maximum charge = 50, and minimum peaks in set = 3–8. Error in measurements was ± 0.02%, as determined from external control samples. Polyspecificity assays and GFP isolation/characterization were conducted by Dr. Douglas Young.

6.2.5 Expression and purification of His-$Y_{730}F_nY$-α2s and His-$Y_{731}F_nY$-α2s. A generalized protocol was established for the expression of all F_nY-containing α2s.[20] *E. coli* BL21-DE3 cells (Invitrogen) were co-transformed with pET-*nrdA*(TAG_{730}) (or pET-*nrdA*(TAG_{731})), encoding for α with an N-terminal His_6 tag and a stop codon at the site of one of

the two conserved Ys,[21] and pEVOL-F_3Y-RS-E3. Cells were plated on LB-agar plates supplemented with 50 μg/mL Km and 35 μg/mL Cm at 37 °C. After 14 h, single colonies were harvested and inoculated into 8 mL of 2xYT with antibiotics and grown at 37 °C, 225 rpm. After ~12 h, the small culture was inoculated into fresh 2xYT (100 mL, pH 7.0) with the same antibiotics at a 1:100 dilution. The culture was grown at 37 °C, 225 rpm until reaching an OD_{600} ~0.3, at which point F_nY (500 mM stock solution in water, NaOH solubilized) was added to the culture to a final concentrations of 0.7-2 mM. After 5 min, the F_3Y-RS was induced with L-ara (0.05% w/v). At OD_{600} ~0.6, *nrdA* expression was induced with 1 mM IPTG. The cells were allowed to grow for an additional 4 h (final OD_{600} >3), then harvested by centrifugation (3,000 × *g*, 10 min, 4 °C). No toxicity from F_nYs (up to 2 mM) was observed as determined by comparison to the OD_{600} of a flask without F_nY. Yields of 0.5-0.6 g cell paste/100 mL culture were obtained. Success of expression was assessed by 8% SDS-PAGE.

The cell pellet (1.0 – 5.0 g) was resuspended in lysis buffer (50 mM Hepes, 5% glycerol, pH 7.6) with 1.0 mM PMSF and 10 mM β-ME at 5 mL buffer/g of cell paste, homogenized, and lysed via two passes though a French pressure cell at 14,000 psi. Cell debris was cleared by centrifugation (30,000 × *g*, 25 min, 4 °C), and the resulting pellet discarded. To the supernatant was added DNase (NEB) to 10 U/mL. The resulting solution was incubated with rocking for 30 min at 4 °C. To the supernatant was added Ni-NTA agarose (Qiagen, 1.0 mL), and the buffer adjusted to contain 300 mM NaCl. The resulting slurry was incubated with rocking for 1 h at 4 °C. The slurry was loaded into a column and allowed to gravity pack, and the column was washed with 30 CVs of wash buffer (lysis buffer + 300 mM NaCl + 10 mM imidazole) with 1.0 mM PMSF and 10 mM β-ME. The protein was eluted with a linear gradient of 10 to 250 mM imidazole in wash buffer. Protein-containing fractions were pooled, diluted >5-fold with lysis

buffer with 10 mM DTT and concentrated on an Amicon YM 30 membrane to give ~10 mg protein/g of cell paste. The purified protein contained a mixture of full-length and 729- (or 730-)truncated α, with the ratio of the two species varying according to the suppression efficiency achieved with the respective F_nY. This efficiency varied as follows: 2,3,5-$F_3Y \approx$ 3,5-$F_2Y >$ 2,3,6-$F_3Y \approx$ 2,3-$F_2Y >$ 2,3,5,6-F_4Y.

When necessary, separation of the truncated protein from the desired F_nY-α2 was achieved by FPLC. The affinity-purified protein (10-20 mg) was injected onto a POROS HQ/20 column (16 mm × 100 mm, 20 mL CV). The column was washed with 50 mM NaCl in lysis buffer with 10 mM DTT for 1 CV at a rate of 2 mL/min. The protein was then eluted with a gradient of 75 mM to 500 mM NaCl in lysis buffer with DTT over 3 CVs at a rate of 2 mL/min. Protein-containing fractions were assessed by 8% SDS-PAGE, and full-length fractions were diluted 5-fold into lysis buffer with DTT and concentrated on an Amicon YM-30 membrane.

6.2.6 Expression and purification of $Y_{356}F_nY$-β2s. *E. coli* TOP10 cells were co-transformed with pBAD-*nrdB*(TAG_{356})[12] and pEVOL-F_nYRS-E3[20] and plated on LB-agar plates supplemented with 100 μg/ml Amp and 35 μg/ml Cm at 37 °C. A 2xYT culture (5 mL) with the same antibiotics was grown to saturation and was used to inoculate 5 × 500 mL of 2xYT at a 100-fold dilution. The cells were grown until reaching an OD_{600} of 0.3, at which point F_nY was added to the media to a final concentration of 0.5-2.0 mM. At an OD_{600} of 0.5, the F_nY-RS and *nrdB* gene were induced with L-ara (0.05% w/v). The cells were grown for an additional 4-5 h to a final OD_{600} of ~1.5, then harvested by centrifugation (3,000 × *g*, 10 min, 4 °C). Yields of 2 g/L were obtained. Success of expression was assessed by 10% SDS-PAGE.

$Y_{356}F_nY$-β2s were purified by anion-exchange chromatography following the protocol described for $Y_{356}NH_2Y$-β2 (section 2.2.3) and reported previously.[27] Unlike for $Y_{356}NH_2Y$-β2,

the homodimer (β2) and heterodimer (ββ′) fractions of $Y_{356}F_nY$-β2s were separable with only two columns (DEAE + Q-sepharose), and thus the final anion-exchange FPLC step was not necessary. Typical yields of full-length $Y_{356}F_nY$-β2 were 4-25 mg of protein per g of cell paste. A comparable amount of heterodimer, $Y_{356}F_nY$-ββ′, was also isolated as a side product.

6.2.7 pH rate profiles of F_nY-RNRs. pH rate profiles of His_6-F_nY-α2s were determined by the radioactive assay as described previously.[13] In a total volume of 200 μL was combined wt-β2 (1.5 μM), [^{3}H]-CDP (1 mM, SA: 6,000-20,000 cpm/nmol), ATP (3 mM), thioredoxin (TR, 30 μM), and thioredoxin reductase (TRR, 0.5 μM) in assay buffer (pH 6.0-9.0, in 0.2 unit increments) at 25 °C. The assay was initiated by addition of NADPH (1 mM) and His_6-$Y_{730}F_nY$-α2 (or His_6-$Y_{731}F_nY$-α2) to a final concentration of 0.3 μM. Aliquots (40 μL) of the reaction mixture were removed at 1 min increments throughout the assay and quenched in perchloric acid (2% v/v, 25 μL). The solution was neutralized by the addition of KOH (0.5 M, 20 μL) and incubated on ice to facilitate the precipitation of $KClO_4$. The resulting salt was removed by centrifugation (10 min, 20,000 × *g*, 4 °C). The supernatant was then subjected to dephosphorylation by mixing sample (80 μL), carrier dC (6 μL, 120 nmol), and calf alkaline phosphatase (14 U, 0.7 μL, Roche) in dephosphorylation buffer (75 mM Tris, 0.15 mM EDTA, pH 8.5) in a total volume of 500 μL. The samples were incubated at 37 °C for 2 h. Samples were then applied to an AG 1-X8 borate column (Bio-Rad), eluted with ddH_2O in a total volume of 8 mL, and subjected to scintillation counting for the quantification of dC (i.e., the method of Steeper and Steuart).[28]

pH rate profiles of $Y_{356}F_nY$-β2s were determined by the spectrophotometric assay. Ribonucleotide reductase activity was monitored through a continuous coupled-enzyme assay in which the consumption of NADPH was determined by monitoring the decrease in $A_{340\ nm}$.[10] Wt-

α2 (1-3 μM), ATP (3 mM), CDP (1 mM), TR (30 μM), and TRR (0.5 μM) were mixed in assay buffer buffer in a final volume of 300 μL. The assay was initiated upon addition of $Y_{356}F_nY$-β2 (0.2-0.6 μM) and NADPH (0.2 mM), and the decrease in A_{340} was monitored over 1-2.5 min. pHs between 6.0 and 9.0 were assessed in 0.2 pH unit increments. Assays were conducted in at least duplicate, with deviation <<10% between runs.

Data obtained for F_nY-RNRs by both methods were fit to the standard equation for a two proton ionization model (eq. 6-1):

$$k_{obs} = \frac{k_{max}}{1 + 10^{(pKa - pH)} + 10^{(pH - pKa')}} \qquad \text{(eq. 6-1)}$$

6.3 RESULTS

6.3.1 Evolution of orthogonal synthetase specific for F_3Y (F_3Y-RS). A collaboration with the Schultz lab (Scripps) was established with the expressed purposed of evolving a mutant, orthogonal aminoacyl-tRNA synthetase (aaRS) specific for the incorporation of the UAA 2,3,5-trifluorotyrosine (2,3,5-F_3Y) into RNR. Originally, we sought to evolve an aaRS for this particular F_nY, as previous data suggested that the redox potential of 2,3,5-F_3Y is sufficiently increased relative to Y at alkaline pH such that its incorporation at position 356 of β2 changes the rate-determining step in RNR from a conformational change[29] to PCET.[13] Its three fluorine substituents together and low phenolic pK_a (6.4, Figure 6.1) were expected to facilitate evolution of an RS selective for the phenolate of 2,3,5-F_3Y over the phenol of Y.

To selectively incorporate 2,3,5-F_3Y into proteins, an orthogonal *Methanococcus jannaschii* aaRS-tRNA pair that suppresses the amber stop codon (TAG) was evolved to uniquely encode this amino acid by a double sieve selection process based on cellular viability.[19] A library of TyrRS mutants was generated by randomizing eight positions near the RS active site (Figure 6.4 A), based on the known structure of Tyr-bound *Mj*TyrRS,[30] including those residues closest to the aromatic ring (Y32, L65, and H70) and those involved in H-bonding to the Y phenol (Y32 and D158). The library was subjected to three positive and negative selection cycles, after which individual candidates were isolated and assessed for viability in the presence and absence of 2,3,5-F_3Y at different Cm concentrations. The selection resulted in two primary clones, E3 (Y32L, L65G, H70N, F108F, Q109Q, D158S, I159Y, L162H) and E11 (Y32H, L65Y, H70G, F108Y, Q109A, D158N, I159I, L162R), that conferred Cm resistance (>150 μg/mL) only in the presence of 2,3,5-F_3Y (Figure 6.4 B). Given the mutations and the structure,[30] we tried to understand the basis for recognition of 2,3,5-F_3Y by the aaRSs. As

mentioned above, we had predicted that the negative charge on the phenolate of 2,3,5-F_3Y would be the basis for discrimination against Y, and anticipated the introduction of positively charged side chains in the mutants. E3 contains a L162H mutation, but the protonation state of this residue is unknown. E11 contains a single basic side chain (L162R); however, a crystal structure of the *p*-acetylphenylalanine RS containing the same mutation revealed that the R side chain was directed away from the active site.[31] Y32 and/or D158 are mutated in both 2,3,5-F_3Y-RSs to residues that could conceivably behave as H-bond donors to the phenolate of 2,3,5-F_3Y. The substitution of G at either position 65 (E3) or 70 (E11) may enlarge the substrate binding pocket. Thus, there exists minimal evidence indicating that the observed discrimination occurs on the basis of the phenolate. Instead, it appears that the fluorine substitutents provide the key recognition elements. The introduction and retention of many polar side chains provide opportunities for the three F atoms to participate in multipolar interactions of the nature C-F···H-N/O or C-F···C=O.[32] Given the sensitivity of these interactions to distance and geometry, it is impossible to speculate on the specific atoms involved without a high resolution structure. Crystallization attempts are underway to better understand the basis of F-protein interactions in the 2,3,5-F_3Y-RSs. The nature of these interactions is of general interest, given the large number of fluorinated pharmaceuticals.[32]

Figure 6.4 A) Structure of substrate-bound wt *Mj*TyrRS and locations of mutated residues. The active site of the wt *Mj*TyrRS/tRNA/Tyr ternary complex (PDB 1J1U) is shown.[30] Residues that are mutated in the TyrRS libraries are drawn in sticks, and the Tyr substrate is shown in space-filling model; B) Mutations of E3 and E11 RSs relative to the native *Mj*TyrRS.[20]

A

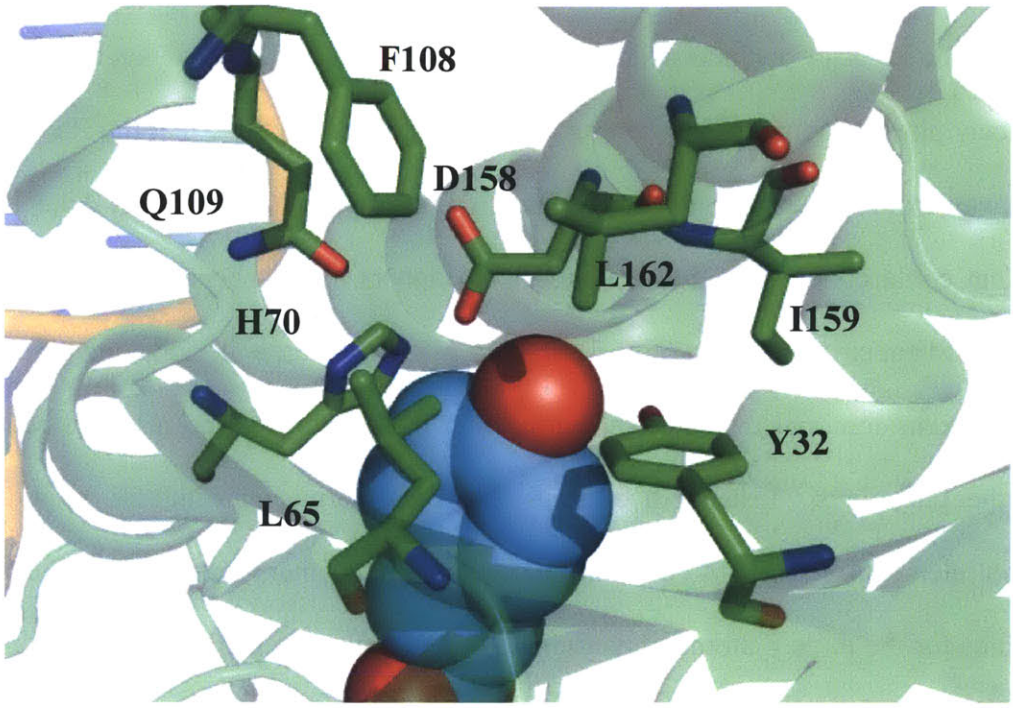

B

Clone	32	65	70	108	109	158	159	162
WT	Y	L	H	F	Q	D	I	L
E3	L	G	N	F	Q	S	Y	H
E11	H	Y	G	Y	A	N	I	R

The two aaRSs were cloned into the previously described pEVOL system[25] for enhanced expression of proteins containing 2,3,5-F_3Y. We confirmed the selective incorporation of 2,3,5-F_3Y into proteins by aaRSs E3 and E11 using pET-$GFP_{Y151TAG}$, a plasmid that encodes a C-terminally His_6 tagged GFP.[25] Full-length, fluorescent protein is observed only when the TAG codon is suppressed by an amino-acylated tRNA. E3 afforded 10 mg/L of purified GFP, while E11 yielded 4 mg/L. Both aaRSs incorporated a single 2,3,5-F_3Y into GFP, with an observed mass of 27,759 Da (expected: 27,758 Da) determined by LC-MS analysis of the Ni-NTA purified protein. In the absence of 2,3,5-F_3Y, low levels of phenylalanine incorporation could be detected for E3; however, this background incorporation is not detected in the presence of 2,3,5-F_3Y (a property observed with several previously evolved aaRSs).[26] No background incorporation was detected for E11 in the absence of 2,3,5-F_3Y.

6.3.2 Initial expressions of His_6-Y_{730}(2,3,5)F_3Y-α2. As described in Chapter 2, the mutant RNR His_6-$Y_{730}NH_2$Y-α2 was highly overexpressed from the vectors pET-*nrdA*(TAG_{730}) (encoding for His_6-tagged α2 with a 10 amino acid linker) and pEVOL-NH_2Y-RS, and rapidly purified in good yield by Ni-NTA chromatography. It is hypothesized that the success of His_6-$Y_{730}NH_2$Y-α2 expression is due to the well-paired promoter strength of the pET (T7) and pEVOL (*ara*) vectors. Thus, initial attempts at expressing 2,3,5-F_3Y-containing RNRs were made with the analogous vector pair, pET-*nrdA*(TAG_{730}) and pEVOL-F_3YRS-E3 (or -E11). These were conducted in rich (2xYT) medium to allow for higher levels of protein expression and to determine whether any significant misincorporation of Y occurred in the absence of F_3Y. Growths were conducted in a fashion analogous to that described previously for His_6-$Y_{730}NH_2$Y-α2.[21] Briefly, F_3Y was added to the growth media at early log phase to a final concentration of 1 or 2 mM, followed by arabinose induction of the F_3Y-RS five minutes later. After one doubling

time, IPTG was added to induce the *nrdA* gene. The cells were allowed to grow an additional 3-5 hours post-induction.

By this protocol, both pEVOL-F_3Y-RS-E3 (Figure 6.5 A) and pEVOL-F_3Y-RS-E11 (Figure 6.5 B) were successful in generating full-length α as judged by SDS-PAGE analysis. Full-length protein was observed in the presence of both 1 and 2 mM F_3Y, whereas only truncated protein was expressed in the absence of F_3Y. Expression using F_3Y-RS-E3 yielded a significantly better full-length to truncated ratio compared to F_3Y-RS-E11 (~1:1 to ~1:2), and thus the former was used for all further expressions described in this chapter. The specific incorporation of F_3Y over Y was more rigorously tested by repeating the expression in a minimal medium (GMML). Indeed, full-length protein was observed in the presence of F_3Y only (data not shown). Since the F_3Y-RS showed no observable background incorporation of Y in either medium (by SDS-PAGE analysis), all future growths were conducted in 2xYT because the richer medium offered significantly enhanced protein expression, higher cell yields, and minimized cellular toxicity at high F_3Y concentrations.

Figure 6.5 Expression of His_6-Y_{730}(2,3,5)F_3Y-α2 using the E3 (panel A) and E11 (panel B) F_nY-RSs analyzed by SDS-PAGE (8%) of whole cells four hours after IPTG-induction of the *nrdA* gene. Lanes are as follows: (1) His_6-α standard, (2) no F_3Y in medium (3) 1 mM F_3Y in medium, (4) 2 mM F_3Y in medium, and (5) His_6-α standard.

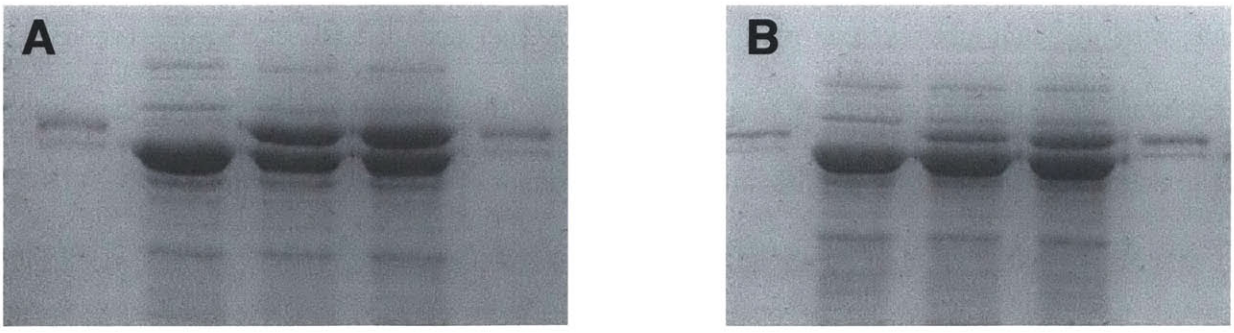

6.3.3 Examining the polyspecificity of F_3Y-RS: incorporation of different F_nYs with a single RS. Given the robust expression of full-length α in the presence of F_3Y and F_3Y-RS-E3, it was interesting to address whether F_3Y-RS-E3 would be able to receive other F_nYs as substrates while maintaining good selectivity over Y. Recent experiments have shown that some aaRSs exhibit a degree of polyspecificity.[26] This feature arises from the lack of other UAAs in the selection medium to eliminate synthetases that can recognize them. To determine if the E3 and E11 2,3,5-F_3Y aaRSs were polyspecific, expressions identical to those described in the previous section were conducted in an attempt to incorporate 3,5-F_2Y, 2,3-F_2Y, and 2,3,6-F_3Y site-specifically into α2. All three F_nYs were incorporated into positions 730 and 731 of α2 with varying degrees of success. The optimization of these expressions is described subsequently (section 6.3.5).

6.3.4 Examining the polyspecificity of F_3Y-RS: determining substrate diversity. The chemical diversity of substrates accepted by the F_3Y-RSs was assessed by screening against a library of UAAs using a GFP fluorescence assay.[26] Of the ~80 UAAs in the library, both aaRSs were capable of aminoacylating 3-fluorotyrosine and 3-chlorotyrosine (Figure 6.6, molecules 2 and 8). The results of this first screen indicated the aaRSs exhibit some polyspecificity for other halogenated Ys, prompting a second GFP screen on Ys with a narrower range of substitutions. Consistent with the results obtained in the α2 test expressions described above, the evolved aaRSs were capable of incorporating all members of the F_nY series (3-FY, 2,3-F_2Y, 3,5-F_2Y, 2,3,6-F_3Y, and 2,3,5,6-F_4Y) into GFP, as well as several other halogenated analogues (Figure 6.6). The incorporation of each UAA was confirmed by LC/MS analysis of the mutant GFPs. Interestingly, several of the analogues (Figure 6.6, compounds 2-5) were incorporated into GFP at higher levels than 2,3,5-F_3Y, and thus the evolved aaRSs are henceforth called "F_nY-RSs."

6.3.5 Optimizing expression and purification of His_6-$Y_{730}F_nY$-α2s and His_6-$Y_{731}F_nY$-α2s. Initial attempts at F_nY (n = 2, 3) incorporation to positions 730 and 731 of α2 were generally successful, as described in section 6.3.3. In the interest of improving full-length protein expression levels and minimizing waste of F_nYs, energy was invested in developing an optimized expression protocol for F_nY-α2s. Variables examined included the pH of the growth medium, the final F_nY concentration in the medium, the time of addition of F_nY to the medium, and the F_nY-RS sequence used (E3 or E11).

The first variable, pH of the growth medium, was examined because it was not known whether cellular uptake of the F_nY would vary with the protonation state of the phenol. However, the results of various trials indicate that there is little dependence on growth medium pH. In this case, three different conditions were tested – the unadjusted pH of the 2xYT medium (~7.0), 0.5 pH units above the F_nY pK_a, and 0.5 units below the F_nY pK_a. No significant difference in protein expression was observable by whole-cell SDS-PAGE analysis, so 2xYT was used without pH adjustment for all future growths. Next, the timing of addition of F_nY to the medium was investigated. The expression of full-length protein was compared when F_nY was added from the start of the growth versus from mid-log phase, with a slight improvement observed with its earlier addition. Thus, the optimized protocol now calls for addition of F_nY at early log phase (OD_{600} = 0.25-0.3), followed by induction of the F_nY-RS with L-ara at OD_{600} = 0.3-0.5, and IPTG induction of *nrdA* approximately one doubling time after F_nY addition (OD_{600} = 0.5-0.6).

The optimal concentration of amino acid in the medium (0.5-2.0 mM) showed a strong dependence on the F_nY, with the incorporation efficiency varying as follows: 2,3,5-F_3Y ≈ 3,5-F_2Y > 2,3,6-F_3Y ≈ 2,3-F_2Y > 2,3,5,6-F_4Y. Finally, the sequence dependence of the F_nY-RS was

explored. Recall that the directed evolution of an RS for 2,3,5-F_3Y resulted in two candidates with very different sequences (Figure 6.4 B). The results of the polyspecificity assay revealed that in almost all cases, E3 was the more efficient RS in F_nY incorporation to GFP (Figure 6.6 B).[20] The same observation was made for F_nY incorporation to α2. The results of the polyspecificity assay indicate that the E11 RS may be slightly more efficient at 2,3-F_2Y incorporation to GFP, as well as being better for some of the bulky mono- and dihalogenated Ys analogues. A direct comparison of His_6-Y_{730}(2,3)F_2Y-α2 expression using pEVOL-F_nY-RS-E3 and pEVOL-F_nY-RS-E11 indicated no discernable difference between the two RSs. Thus, the F_nY-RS-E3 was used for all subsequent expression of F_nY-RNRs.

A protocol for F_nY-α2 purification was developed next, based on that optimized previously for the isolation of His_6-$Y_{730}NH_2$Y-α2.[21] A gel demonstrating the total protein fraction at each step from lysis through Ni-NTA elution during the purification of His_6-Y_{730}(2,3,5)F_3Y-α2 is given as Figure 6.7. As is evident from the gel, the majority of the full-length protein is soluble upon cell lysis, whereas the majority of truncated protein is insoluble and remains in the cell debris pellet upon centrifugation. This difference in solubility makes for the relatively facile separation of full-length and truncated protein, both of which possess an N-terminal His_6 tag and bind to Ni-NTA resin with similar affinity. Indeed, the elution fractions from the Ni column show that His_6-Y_{730}(2,3,5)F_3Y-α2 as isolated contains a minimal (~10%) contaminant from the truncated protein. To remove the truncated protein, F_nY-α2s were subjected to a second purification step utilizing anion-exchange FPLC. This step also serves to remove any remaining, contaminating DNA from the protein fraction. Following this two-step purification protocol, the various $Y_{730}F_n$Y-α2s and $Y_{731}F_n$Y-α2s (n = 2,3) have been isolated in 2.5-10 mg/g final yields (Table 6.1)

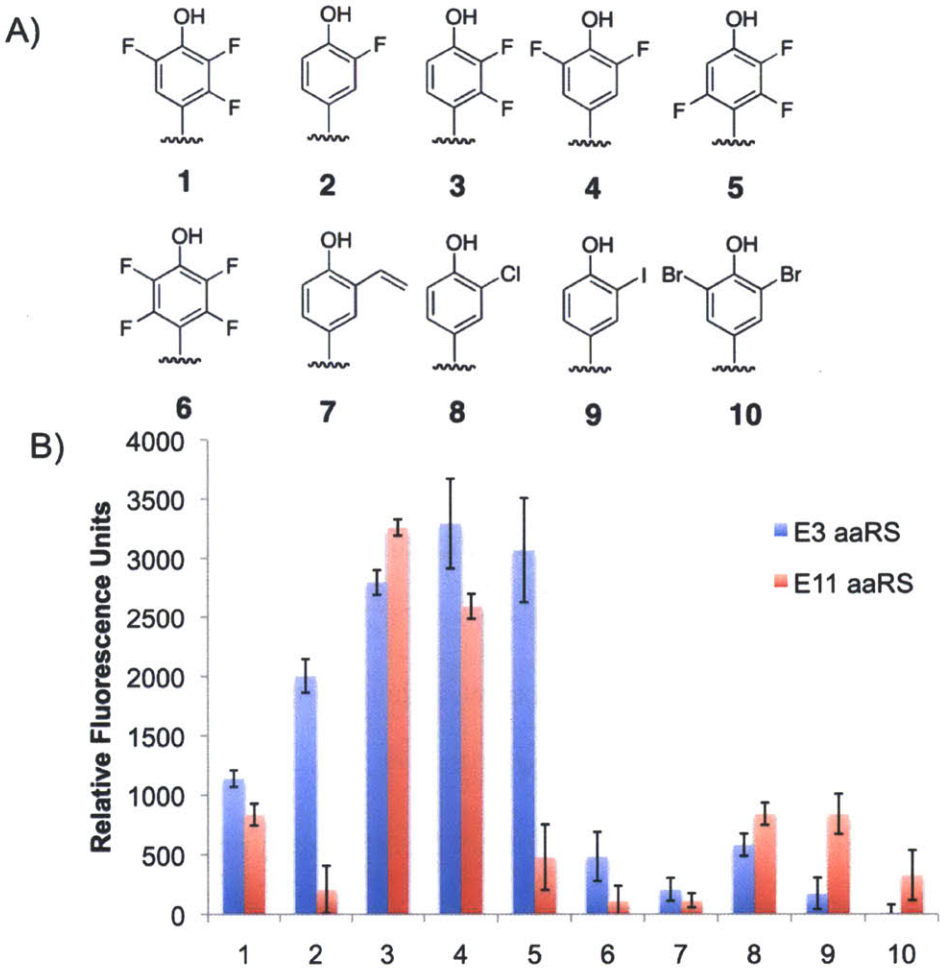

Figure 6.6 Polyspecificity of F_nY-RSs. A) Y analogues that screened positive for GFP incorporation. B) GFP fluorescence assay of the two evolved aaRSs (blue = E3; red = E11) based on suppression of $GFP_{Y151TAG}$ in the presence of 1 mM UAA. Data collected and chart generated by Dr. Douglas Young.[20]

Figure 6.7 Purification of His-Y_{730}(2,3,5)F_3Y-α2. Lanes (from left to right) contain the following: (1) His-α(wt) standard; (2) soluble fraction after lysis; (3) insoluble fraction after lysis; (4) flow-through upon column loading; elution fractions from Ni column with increasing [imidazole].

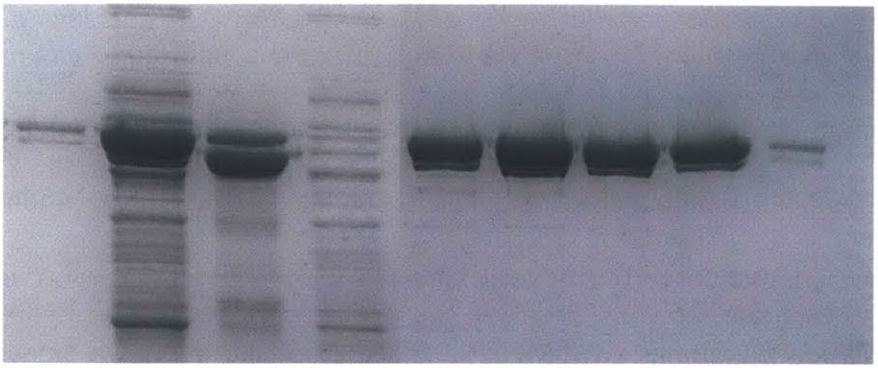

1 2 3 4 ---------- elution fractions ----------

Table 6.1 Isolated yields of F_nY-RNRs.

F_nY	**2,3-F_2Y**	**3,5-F_2Y**	**2,3,6-F_3Y**	**2,3,5-F_3Y**	**2,3,5,6-F_4Y**
Yield at 730-α2[a,b]	3	3	3	10[c]	<0.3
Yield at 356-β2[c]	4	22	3[d]	24	-
Yield at 122-β2[e]	8	30	12[f]	35	-

a. Yield of purified F_nY-RNRs reported in mg of protein/g of cell paste. [UAA] in the growth medium varied from 0.5 – 2 mM depending on the F_nY. *b*. Similar yields were obtained at position 731 of α2. *c*. Yield shown here is for full-length homodimer, $Y_{356}F_n$Y-β2. An equivalent amount of heterodimer, $Y_{356}F_n$Y-ββ′ was also isolated as a side product. *d*. Isolated by Alice Choi (Stubbe lab). *e*. Described in detail in Chapter 7 of this thesis. *f*. Isolated by Kanchana Ravichandran (Stubbe lab).

6.3.6 Troubleshooting incorporation of 2,3,5,6-F_4Y into RNRs. The results of the polyspecificity assay indicated that of the F_nYs, 2,3,5,6-F_4Y was least successfully incorporated to GFP by the F_nY-RSs (Figure 6.6). A similar observation was made upon attempts to incorporate F_4Y into position 730 of RNR. Growths were conducted to examine the effect of F_4Y concentration (1, 1.5, and 2 mM) and the time of addition to the medium (from the start versus at mid-log phase), but no conditions resulted in the definitive observation of full-length α by SDS-PAGE. An attempt to purify any expressed full-length His_6-$Y_{730}F_4Y$-α2 from the best of these expression conditions (2 mM F_4Y, added from the start) was made following the optimized protocol described above. SDS-PAGE analysis of elution fractions after FPLC anion-exchange chromatography indicated a ~1:1 mixture of proteins proposed to be full-length His-$Y_{730}F_4Y$-α2 and 729-truncated protein. The negative ionization mode MALDI-MS spectrum of the elution fraction indicates two peaks in the MW range of interest. The peak at 84,545 Da most likely corresponds to 729-truncated α (predicted: 84,478 Da, 0.07% error), while the peak at 88,039 Da most likely corresponds to His_6-$Y_{730}F_4Y$-α (predicted: 88,011 Da, 0.03% error). However, the MALDI-MS analysis is not completely conclusive, given the low resolution of the instrument on a protein this size and the frequent difficulty encountered in finding conditions conducive to α ionization. However, the result is suggestive of the full-length protein His_6-$Y_{730}F_4Y$-α2 being present in very low amounts.

Subsequent LC/MS analysis[25] of the lysate of *E. coli* cells grown in the presence 2,3,5,6-F_4Y indicated that reduced cellular uptake is a primary reason for the inefficient incorporation of F_4Y relative to the other F_nYs, rather than poor recognition of the F_4Y by the RS.[20] This is perhaps the better of the two possibilities, as uptake issues may be overcome by the construction of dipeptides, which can be actively transported into the cell via peptide permeases.[33,34]

Synthesis of F_nY-containing dipeptides and studies of their uptake by *E. coli* are underway (D. Young, personal communication).

6.3.7 Optimizing expression and purification of $Y_{356}F_nY$-β2s. Because β2 is purified as an obligate dimer and both full-length monomers (β) and truncated monomers (β′) are expressed and soluble in the growth conditions, a statistical distribution of the possible dimers (β2, ββ′, and β′2) is generated. Thus, the ratio of full-length to truncated proteins is of great concern, in addition to the overall expression levels of *nrdB*. This ratio is dependent on both the unnatural amino acid of interest and the expression vectors for *nrdB* and the aaRS. When we initiated incorporation of F_nYs at position 356 of β2, time was taken to explore the possible combinations of *nrdB* and F_nY-RS expression vectors to determine which resulted in the highest isolated yield of $Y_{356}F_n$Y-β2s. Three combinations were explored: pEVOL-F_nY-RS with (1) pTrc-*nrdB*(TAG_{356}), (2) pET-*nrdB*(TAG_{356}), or (3) pBAD-*nrdB*(TAG_{356}). Of these, the pEVOL/pBAD combination gave both the best overall expression of *nrdB* and the best full-length to truncated ratio of the three combinations. Furthermore, we were pleasantly surprised to discover that the heterodimer (ββ′) could be easily resolved from the full-length homodimer (β2) by only two chromatographic steps (gravity-flow DEAE and Q-sepharose), thereby eliminating the need for the third FPLC-based anion exchange step. Using this expression and purification strategy, $Y_{356}F_n$Y-β2 homodimers were readily isolated in yields of 3-24 mg/g (Table 6.1).

6.3.8 Rationale and design of pH rate profiles of F_nY-RNRs. We initiated our studies of the pH dependence of F_nY-RNRs with two goals in mind. The first was to investigate our hypothesis for different mechanisms of PCET operative in the two subunits of RNR. As depicted in Figure 6.2 and introduced above, the Stubbe/Nocera model for PCET[35] holds that orthogonal PCET is operative in the β2 subunit, that is, that the proton and electron move to

different acceptors upon Y_{356} oxidation. This claim was supported by results with EPL-generated $Y_{356}F_nY$-β2s, which showed no correlation between activity and phenolic protonation state. The model also proposes that co-linear PCET is operative in the α2 subunit, with the proton and electron moving between the same donor/acceptor pair. Upon oxidation of Y_{730} by Y_{731}•, both the H^+ and the e^- of Y_{730} would move in a concerted fashion to reduce Y_{731}•. A similar transfer would occur between Y_{730}• and C_{439}. This proposal was based on a thermodynamic argument that the oxidation of the oxidation of C by Y would be less uphill if it proceeded via a hydrogen atom transfer (HAT) mechanism, rather than via orthogonal PCET.[11] (Interestingly, recent measurements of the solution reduction potential of glutathione at neutral pH suggest that potentials of Y and C may be much more closely matched than previously predicted.)[36] The relatively short distances separating Y_{731}, Y_{730}, and C_{439} (3.5-3.7 Å) in the ground state crystal structure of $\alpha2^8$ also made a co-linear mechanism physically accessible, assuming some minimal conformational rearrangement(s) upon α2β2, substrate, and effector complex formation and radical initiation. Furthermore, sequence alignments of class Ia αs and analysis of *E. coli* α2 structures fail to reveal an obvious conserved residue that could serve as a proton acceptor. Finally, the results of transient absorption (TA) studies of light-initiated hole migration from a photooxidant-labeled C-terminal β peptide into α2 have demonstrated the importance of an extended hydrogen bonding network in α2 and have suggested the unidirectional movement of a proton and electron.[37,38] However, no strong experimental data exist in support of the claim that co-linear PCET is operative in α2, and we hypothesized that the pH rate profiles of $Y_{730}F_nY$-α2s could provide the first evidence for reasons described below.

Differential pulsed voltammetry (DPV) studies of N-Ac-F_nY-NH_2s[7] have been conducted previously to determine the pH dependence of F_nY/F_nY• peak potentials (Figure 6.8) and to

confirm their solution pK_as, reported previously.[6] We may combine these solution pK_as with knowledge of the protein-induced local pK_a perturbation experienced at each position on the pathway, determined by pH titrations of $Y_{730}NO_2Y$-α2, $Y_{731}NO_2Y$-α2, or $Y_{356}NO_2Y$-β2 in complex with the second subunit, CDP, and ATP, to extrapolate the effective pK_a for each F_nY at each of three positions: 730 or 731 of α2, or 356 of β2 (Table 6.2). Examination of the effective pK_a of 3,5-F_2Y, 2,3,6-F_3Y and 2,3,5-F_3Y at position 730 reveals that these $Y_{730}F_nY$-α2s should exist in both their protonated (fluorophenol) and deprotonated (fluorophenolate) states over the pH range in which RNR is active (pH 6-9). Accessibility to both the phenol/phenolate forms of these amino acids might allow us to test whether co-linear PCET is the operative mechanism at position 730, as one would predict that $Y_{730}F_nY$-α2s should display a pronounced decrease in activity that correlates with F_nY_{730} deprotonation.

Our second goal in studying the pH dependence of F_nY-RNRs was to determine whether we could access conditions with one or more of the mutants in which radical propagation was rate limiting. Indeed, previous studies indicated that Y_{356}(2,3,5)F_3Y-β2 generated by EPL could access this regime uniquely among the $Y_{356}F_nY$-β2s, and under conditions in which the difference in peak potential between F_3Y and Y varied from +80-200 mV. However, studies with EPL-generated $Y_{356}F_nY$-β2s were complicated for a number of reasons, namely the presence of two additional mutations ($V_{353}G$ and $S_{354}C$) necessary for efficient peptide ligation and the low radical content in the isolated mutants (0.3-0.4 Y•/β2). The combined effects resulted in an EPL-generated "wt"-β2 that had only 7% the activity of wt-β2. Thus, we sought to determine whether radical propagation was rate-limiting in Y_{356}(2,3,5)F_3Y-β2 generated by the *in vivo* suppression method. We also hoped to elucidate conditions for $Y_{731}F_nY$-α2 and $Y_{730}F_nY$-α2s in which radical propagation becomes rate limiting through each of these positions.

Figure 6.8 Solution reduction potential (vs NHE) as a function of pH for N-Ac-F_nY-NH_2s, as determined by DPV (*left*). Coloring is as indicated in the figure legend. An expanded view of the DPV data from pH 6-9, the range over which F_nY-RNR activities were tested, is also given (*right*). Figure adapted from references 10, 13, and 39.

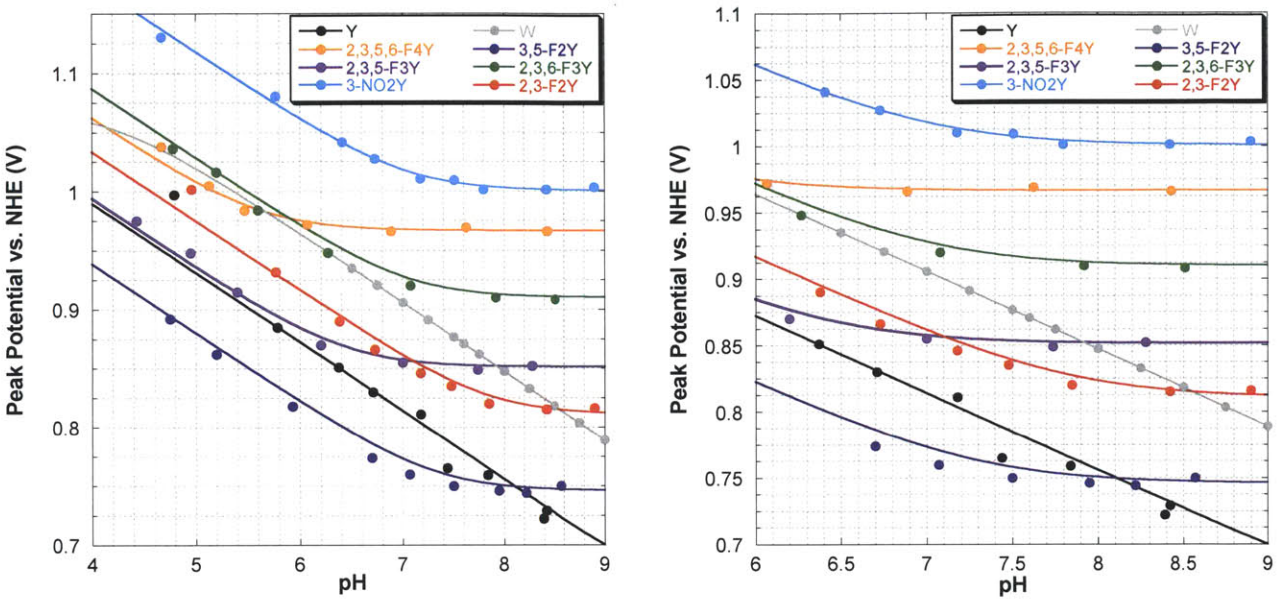

Table 6.2 Predicted pK_as of Y and F_nYs in different solution and protein environments. The solution pK_as were determined from DPV, as shown in Figure 6.8. The pK_as at the various positions within RNR (730 and 731 of α2, 356 of β2) are predicted based on the protein-induced pK_a perturbations at each site determined by titration of $Y_{730}NO_2Y$-α2, $Y_{731}NO_2Y$-α2, or $Y_{356}NO_2Y$-β2 in complex with the second subunit, CDP, and ATP.[10,12]

	ΔpK_a[a]	Y	2,3-F_2Y	3,5-F_2Y	2,3,6-F_3Y	2,3,5-F_3Y
pK_a, solution		10.0	7.8	7.2	7.0	6.4
pK_a at 730-α2	+1.2	11.2	9.0	8.4	8.2	7.6
pK_a at 731-α2	+0.9	10.9	8.7	8.1	7.9	7.3
pK_a at 356-β2	+0.4	10.4	8.2	7.6	7.4	6.8

a. Change in effective pK_a induced by the local protein environment.

6.3.9 Testing whether TR/TRR coupling reaction is affected at pH extremes. A few controls were necessary before undertaking a detailed analysis of nucleotide reductase activity of F_nY-RNRs as a function of pH. One such control was to determine the extent to which the TR/TRR coupling reaction is affected at pH extremes so changes in their concentrations can be made if necessary to ensure that the coupling enzymes are not rate-limiting in the assay. To examine the pH dependence of the coupling reaction, radioactive activity assays were performed on His-α2(wt) at pH 6.0, 7.6, and 9.0 using different absolute concentrations of TR and TRR, and different relative ratios between the two coupling enzymes (Table 6.3 A). The results of assays under these four conditions in three different pH regimes (Table 6.3 B) indicate the standard assay conditions should faithfully report on dCDP formation from pH 6.0 to 9.0. In all cases, the standard deviation for the four activities measured is <3% the total activity. Thus, we conclude that the TR/TRR coupling reaction behaves indistinguishably over the pH range examined in rate profiles.

Table 6.3 (A) Different TR/TRR concentrations and ratios examined at pH 6.0, 7.6, and 9.0; (B) Activity of His-α2(wt) as a function of pH and TR/TRR concentration/ratio. The rightmost column gives the average specific activity over the four conditions examined. The small standard deviation among measurements is taken to be indicative of no perturbation to the TR/TRR coupling.

A

Condition	TR	TRR	Ratio of TR:TRR compared to standard assay conditions
1	30 μM	0.5 μM	1:1
2	60 μM	1.0 μM	2:2
3	60 μM	0.5 μM	2:1
4	30 μM	1.0 μM	1:2

B

Condition	pH	SA (nmol/min/mg)	Avg SA (±SD)
1		119	
2	6.0	116	115 (± 3)
3		112	
4		111	
1		1597	
2	7.6	1712	1651 (± 38)
3		1638	
4		1656	
1		1300	
2	9.0	1311	1332 (± 39)
3		1388	
4		1328	

6.3.10 Testing the effect of protein concentration and subunit ratio on pH rate profiles.

For the pH rate profiles reported herein, assays were conducted in a 1:5 subunit ratio, with final protein concentrations of 0.2-0.6 μM and 1.0-3.0 μM for the limiting and excess subunits, respectively. However, previous pH rate profile assays performed on EPL-generated 356 mutants utilized 1:1 subunit ratios, with 3 μM of each subunit. In order to compare the results between the *in vivo* suppression- and EPL-generated proteins, it was necessary to address whether the pH rate profiles were significantly altered by protein concentration or subunit ratio.

This control was intended to assess how enzyme activity would be affected by the potentially complicated equilibria of α/β quaternary structures that may exist in the low micromolar range. Thus, pH rate profiles for $Y_{730}(2,3,5)F_3Y$-α2 and $Y_{730}(3,5)F_2Y$-α2 were conducted at a 1:1 subunit ratio (1 μM in each) and compared to assays conducted in a 1:5 subunit ratio (0.3 μM:1.5 μM). The results are shown in Figure 6.9 A-D in terms of overall activity, and as a percent maximum activity.

A slight (16-22%) overall decrease in activity is observed with the 1:1 subunit ratio (Figure 6.9, A and C). The activity trend, as demonstrated by the percent maximum activity curves, appears to be nearly identical (Figure 6.9, B and D). The reduction in overall activity is likely due to the percent of α2 in complex, which is calculated to be 79% in the 1:1 conditions and 95% in the 1:5 conditions based on a K_d of 0.06 μM, as was recently measured in our lab for the wt complex in the presence of CDP and ATP.[40] Thus, we conclude that the nature of the pH rate profile does not change considerably with protein concentration in this range or with subunit stoichiometry.

Figure 6.9 The effect of protein concentration and subunit ratio on pH rate profiles. (A) The specific activity as a function of pH of His_6-$Y_{730}(2,3,5)F_3Y$-α2 at a 1:5 ratio (0.3 μM:1.5 μM, red) and 1:1 ratio (1 μM:1 μM, blue); (B) The percent maximum activity as a function of pH for His_6-$Y_{730}(2,3,5)F_3Y$-α2, with the same color scheme. (C) and (D) are the analogous pH rate profiles for the protein His_6-$Y_{730}(3,5)F_2Y$-α2.

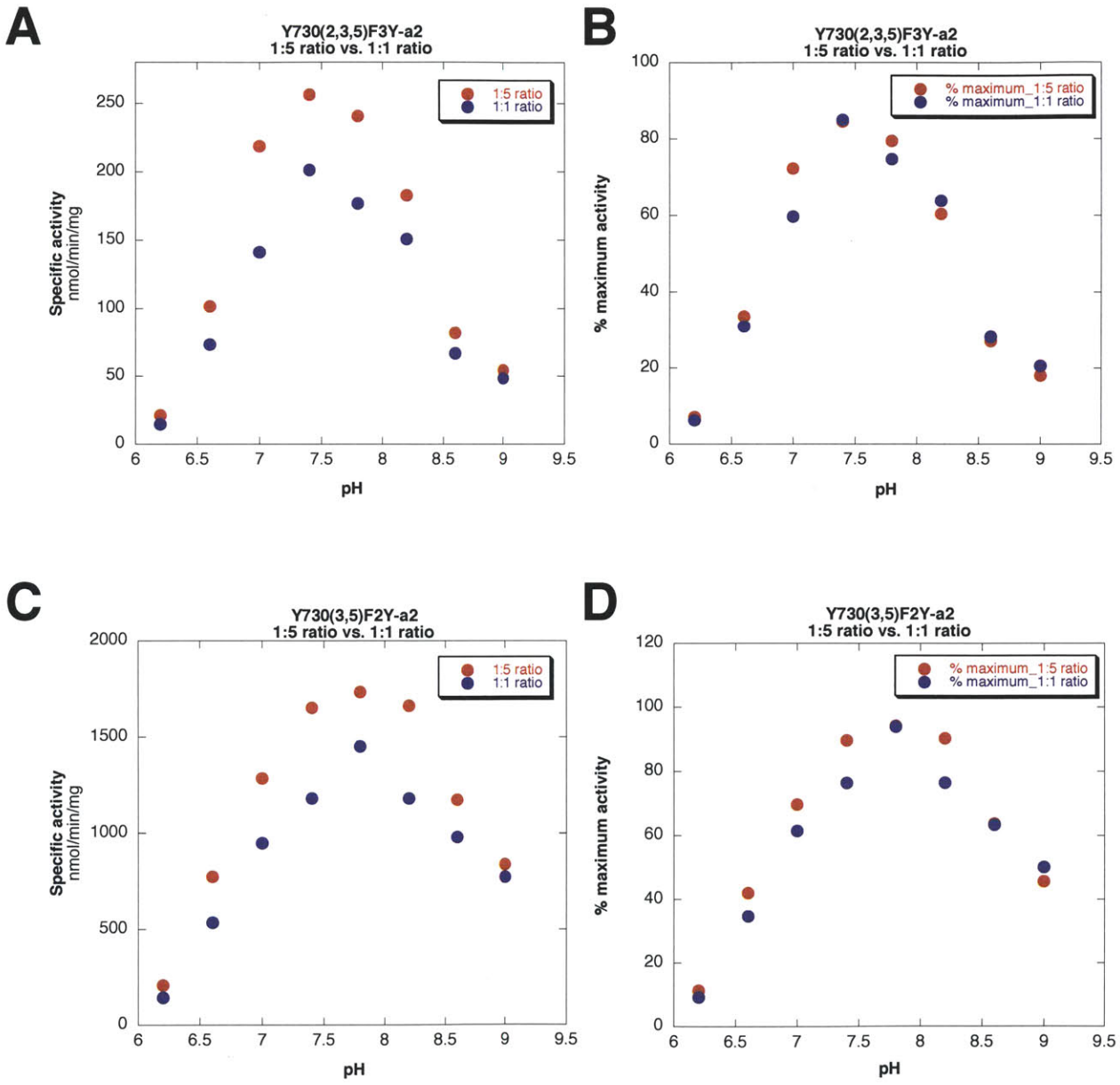

6.3.11 pH rate profiles of F_nY-RNRs. To initiate the study, the pH rate profile of wt-β2 was determined and compared to that of His-α2(wt). While the pH rate profile of EPL-generated "wt"-β2 has been reported, a profile for the wt enzyme has not. Thus, activity measurements for wt β2 were made in the pH 6.0-8.8 range by the spectrophotometric assay and compared to the analogous results for His_6-α2(wt) measured by the radioactive assay. Assays conducted at pH ≥9.0 were frequently nonlinear and thus were excluded during data analysis. For these and many of the pH rate profiles described herein, the activity at each pH will be presented as the percent of the maximum observed activity over the entire pH range. This presentation is intended to facilitate extrapolation of activity trends despite considerable differences in absolute activities among the different mutants and the different subunits. For instance, wt-β2 has a max activity of ~7000 nmol/min/mg, His_6-α2(wt) of ~2200 nmol/min/mg, and EPL "wt"-β2 of ~450 nmol/min/mg.

Returning to the pH rate profiles of wt-β2 and His_6-α2(wt), we see that despite the different assay techniques and the presence of a tag on α2, the two pH rate profiles are superimposable (Figure 6.10, A). A comparison of the profile of wt-β2 to that of the EPL-generated subunit (Figure 6.10, B) reveals that the latter demonstrates a slight alkaline shift, and has a more rapid loss of activity at high pH. Recall that the EPL-generated "wt"-β2 has a maximum activity of 6% that of wt-β2, which highlights the extent to which the two additional point mutations disrupt overall enzyme activity. The pH rate profiles of the wt subunits demonstrate the bell shape that is characteristic of ionization of two groups. Fitting the pH rate profile of His_6-α2(wt) and wt-β2 (Figure 6.10 C and D, respectively) to this model (eq. 6-1) gives pK_as of 6.8 and 9.0 (Table 6.4).

Figure 6.10 (A) A comparison of the pH rate profiles of His_6-α2(wt) (red) and wt-β2 (blue) indicates that the two are superimposable. (B) An overlay of these data with the pH rate profile of EPL generated "wt"-β2 shows some slight differences. Fits of the pH rate profiles of (C) His-α2(wt) and (D) wt-β2 to a two independent ionization events are shown as black lines.

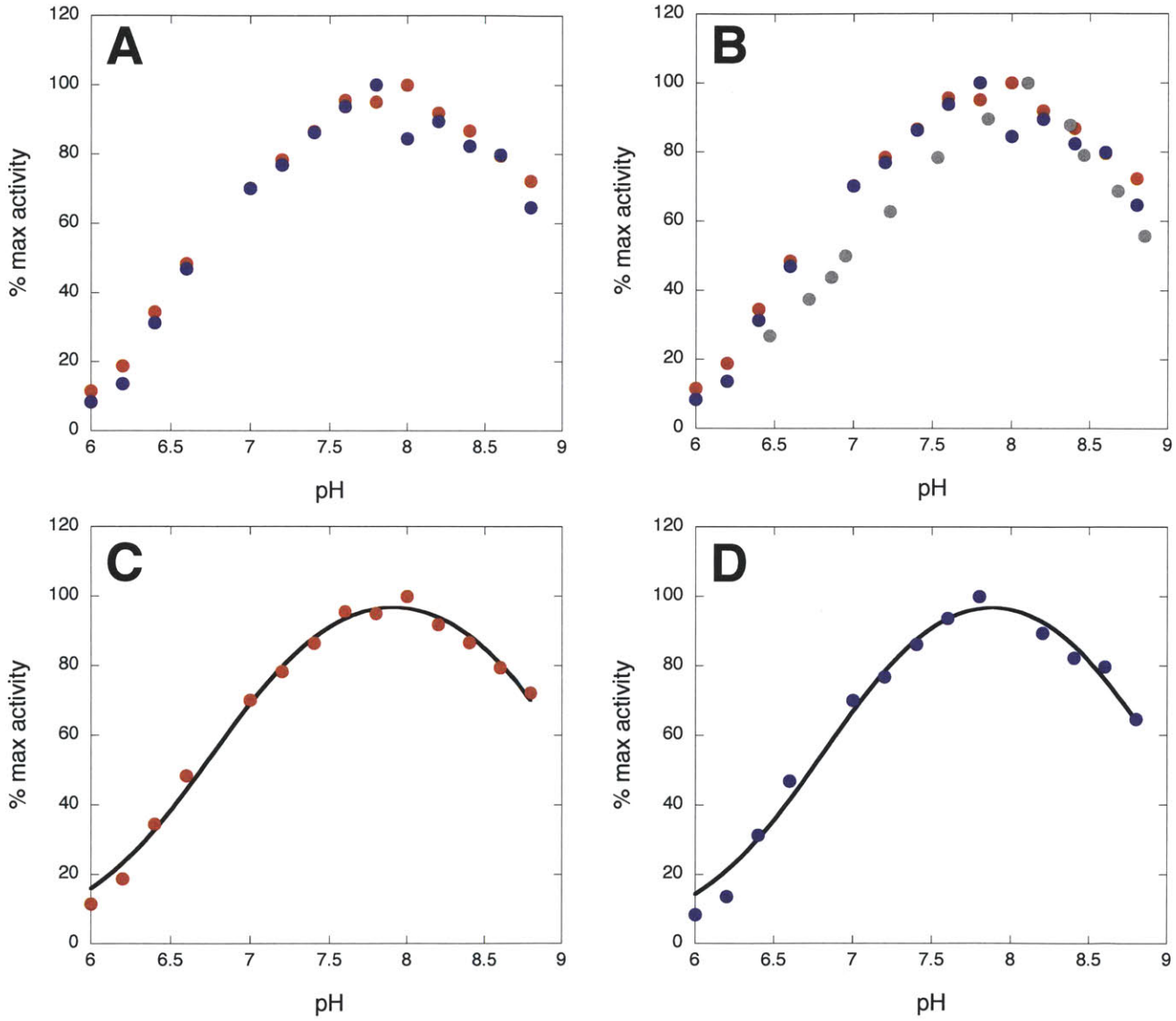

Table 6.4 pK_as obtained by fitting experimental pH rate profile data to a two proton ionization model (eq. 6-1).

	Y			**3,5-F_2Y**			**2,3-F_2Y**			**2,3,6-F_3Y**			**2,3,5-F_3Y**		
	pK_1	pK_2	pK_a[a]	pK_1	pK_2	pK_a	pK_1	pK_2	pK_a	pK_1	pK_2	pK_a	pK_1	pK_2	pK_a
730	6.8	9.0	11.2	7.0	8.5	8.4	7.2	8.7	9.0	7.6	7.9	8.2	7.3	7.8	7.6
731	6.8	9.0	10.9	7.1	8.1	8.1	7.2	8.1	8.7	-[b]	-	7.9	7.0	7.6	7.3
356	6.8	9.0	10.4	7.0	8.0	7.6	7.0	8.6	8.2	-	-	7.4	7.0	7.5	6.8
EPL[c]	7.1	8.8	10.4	7.1	8.7	7.6	7.0	8.7	8.2	7.5	8.7	7.4	7.1	8.7	6.8

a. Predicted effective pK_a for each F_nY at each position, as described in Table 6.2; *b.* Not determined; *c.* The analogous $Y_{356}F_n$Y-β2 generated by EPL. Data reported previously.[13]

We then investigated the pH dependence of the activity of four different $Y_{730}NH_2$Y-α2s. The pH rate profiles, showing absolute specific activity as a function of pH, for the resulting mutants are shown in Figure 6.11, A and B. The scaled specific activities (i.e., percent maximum activity) are overlaid in Figure 6.11. C and the fit of each titration to eq. 6-1 is shown as a solid line. The pK_as determined from the fit are summarized in Table 6.4 and will be discussed subsequently. First, we can examine whether activity is correlated with the protonation state of the phenol. In the case of $Y_{356}F_n$Y-β2s, activity is observed even at pHs where the F_nY should be deprotonated, indicating that neither proton transfer nor an intact hydrogen bonding network is a requirement for electron transfer through position 356. pH titrations of the mutant $Y_{730}NO_2$Y-α2 suggest that the pK_a at positions 730 is perturbed up to ~1.2 pH units relative to the free amino acid in solution, and we assume that the solution phenolic pK_as of F_nYs are similarly perturbed by the protein environment (Table 6.2 and 6.4). If a mechanism of co-linear PCET is operative through position 730, one would predict a minimum of a 75% loss of activity at 0.6 pH units greater than the pK_a However, for all mutants for which we were able to measure activity at a pH 0.6 units greater than the effective pK_a (Y_{730}(3,5)F_2Y-α2, Y_{730}(2,3,6)F_3Y-α2, and Y_{730}(2,3,5)F_3Y-α2), a significantly higher percent of total activity

was retained (40-70% the maximum activity). This observation may be rationalized in a number of ways. One interpretation would be that our hypothesis of co-linear PCET through position 730 of α2 is incorrect. Alternatively, a different mechanism for radical propagation could become operative at high pH that salvages a higher fraction of protein activity. For instance, the mechanism of radical propagation could change dramatically if C_{439} is deprotonated, as this would both eliminate the need for a proton acceptor and would significantly lower cysteine's reduction potential. Finally, the pH rate profiles could be reporting on the conformational changes that gate radical propagation, rather than on the actual chemistry of PCET, as is the case for the wt RNR. As described in the subsequent paragraphs, F_nY-RNRs generated by the *in vivo* suppression method possess between 12-100% the activity of wt RNR. These activity reductions are not terribly dramatic, particularly when compared with those characterized in the analogous EPL-generated mutants, and can be readily accounted for by changes to the rate of the conformational changes that occur upon binding of the two subunits with substrate and effector. Thus, we favor an explanation in which the pH rate profiles we have characterized report on the complexities of protein conformational dynamics, rather than on the chemistry of radical propagation.

We can next consider the overall activity of each mutant when incorporated at position 730 of α2. Figure 6.11, A and B, reveals that the overall activities of $Y_{730}F_n$Y-α2s are quite distinct and that their activities correlate roughly with the peak potentials for the corresponding N-Ac-F_nY-NH_2s. This behavior is distinct from what has been previously reported for EPL-generated $Y_{356}F_n$Ys-β2s, for which the activities of the 2,3-F_2Y, 3,5-F_2Y, and 2,3,5-F_3Y mutants were identical to that of wt-β2 in the pH 6.0-7.5 regime. For $Y_{730}F_n$Y-α2s, the maximum activities of the 3,5-F_2Y and 2,3-F_2Y mutants are ~88% and ~30%, respectively, that of wt-α2.

The 2,3,5-F_3Y and 2,3,6-F_3Y mutants show the most pronounced reductions, displaying maximum activities that are ~12-15% that of wt. Importantly, we do not observe any behavior reminiscent of that observed for EPL-generated Y_{356}(2,3,5)F_3Y-β2 (Figure 6.12 A and B). We neither observe a mutant that displays near wt activity on the low pH side and a dramatic loss of activity on the alkaline side, nor do we observe the ability to turn the enzyme "on" and "off" when ΔE_p increases from +80 to +200 mV (Figure 6.11 D). This suggests we that we do not access a regime in which radical propagation is rate limiting with any of the $Y_{730}F_n$Y-α2s (Figure 6.12 B), and is consistent with our hypothesis that the pH rate profiles of $Y_{730}F_n$Y-α2s report on protein conformational changes that gate radical propagation, rather than the chemistry itself.

Figure 6.11 (A) Specific activity as a function of pH for all $Y_{730}F_nY$-α2s. Points are colored as follows: red (wt), blue (3,5-F_2Y), purple (2,3-F_2Y), pink (2,3,6-F_3Y), and gray (2,3,5-F_3Y). (B) An expanded view of the less active mutants. Error bars, where shown, are the average of 2-3 independent trials. (C) Relative activity as a function of pH for all $Y_{730}F_nY$-α2s . In this graph, all specific activities have been replotted as the percent maximum activity observed for each respective $Y_{730}F_nY$-α2. Fits to a two proton model are shown in solid lines. (D) Relative activities of $Y_{730}F_nY$-α2s (as a percent that of His-α2(wt) at the same pH) determined from the data in (A), and plotted as a function of the peak-reduction potential difference between the Ac−F_nY•−NH_2 and Ac−Y•−NH_2.

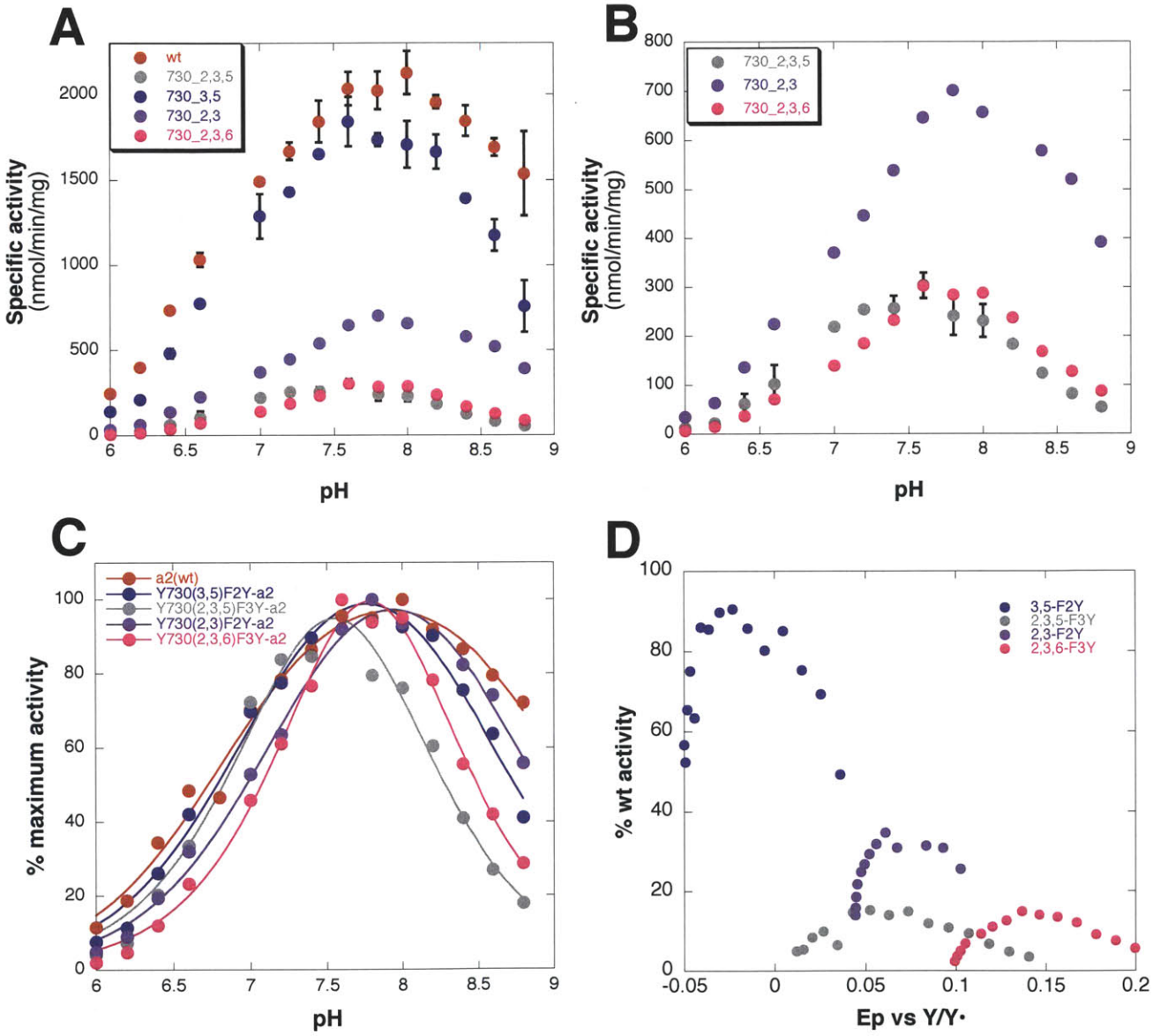

Figure 6.12 (A) Specific activity as a function of pH for all EPL-generated $Y_{356}F_nY$-β2s . Points are colored as follows: black (wt), blue (3,5-F_2Y), red (2,3-F_2Y), purple (2,3,5-F_3Y), green (2,3,6-F_3Y), and orange (2,3,5,6-F_4Y). (B) Relative activities of $Y_{356}F_nY$-β2s vs "wt"-β2 determined from the data in (A) plotted as a function of the peak-reduction potential difference between the Ac–F_nY•–NH_2 and Ac–Y•–NH_2. The data fall into three regimes, with the second regime proposed to be the potential range in which radical propagation is rate-limiting. Figures reproduced from reference 13.

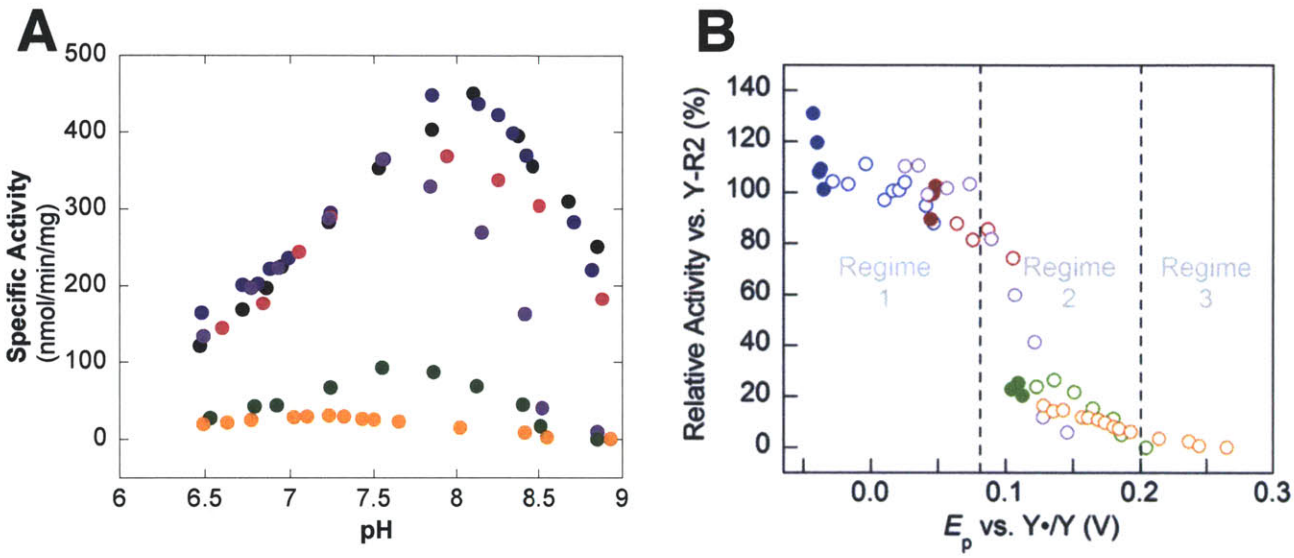

The ability to incorporate F_nYs at positions within both α2 and β2 in high yield affords us the opportunity to now examine pH rate profiles as a function of position within the PCET pathway. Our original model predicted that the pH rate profile at position 356 should be quite distinct from that at 730. However, as detailed above, the pH rate profiles of $Y_{730}F_nY$-α2s do not behave as anticipated, likely because we are measuring conformational changes that precede radical initiation. Looking at the position dependence of the pH rate profiles may provide some insight to radical propagation across the interface, as the mechanism of PCET between 356 of β2 and 731 of α2 is currently a "black box" due to a lack of molecular detail about the protein interface (Figure 6.2). Thus, we have examined the pH rate profiles of two F_nY-RNRs, 3,5-F_2Y and 2,3,5-F_3Y, at positions 730, 731, and 356 to determine how the profiles vary as a function of position in the pathway.

The pH rate profiles of RNRs containing 3,5-F_2Y have been characterized and compared at each of three positions – 356 of β2, 731 of α2, and 730 of α2. The pH rate profile of Y_{356}(3,5)F_2Y-β2 was first compared to that of wt-β2, His-α2(wt), and Y_{731}(3,5)F_2Y-α2 (Figure 6.13, A), and finally to Y_{730}(3,5)F_2Y-α2 (Figure 6.13, B). Visual inspection indicates that all the proteins – both wt and mutants – behave very similarly in the acidic range (pH 6.0-7.6). This similarity is reflected in the first pK_1 obtained by fitting the data to eq. 6-1 (Table 6.4). Interestingly, the pH rate profiles of Y_{356}(3,5)F_2Y-β2 and Y_{731}(3,5)F_2Y-α2 are identical over the entire pH regime, giving rise to identical pK_2s and suggesting that these two positions may share some molecular similarity. The sensitivity of Y_{730}(3,5)F_2Y-α2 activity to alkaline pH is distinct, falling between that of the wt subunits and Y_{356}(3,5)F_2Y-β2 /Y_{731}(3,5)F_2Y-α2. While the data in Figure 6.13 are given as percents of maximal activities, it is worth noting that all three 3,5-F_2Y-RNRs have between 82-90% of the maximal activity of their corresponding wt subunit, suggesting the specific activity does not change as a function of position, i.e., the reduction in overall activity as a function of incorporating 3,5-F_2Y is consistent among all three positions.

The pH rate profiles of RNRs containing 2,3,5-F_3Y at each of three positions were analyzed in a similar fashion. As was observed with 3,5-F_2Y, the pH rate profiles of Y_{356}(2,3,5)F_3Y-β2 and Y_{731}(2,3,5)F_3Y-α2 are very similar (Figure 6.13 C and Table 6.4), and distinct from Y_{730}(2,3,5)F_3Y-α2 (Figure 6.13 D). The maximum activity of 2,3,5-F_3Y mutants at each of the three positions is only 15% that of the corresponding wt subunit. This position-independent activity is consistent with what was observed for the 3,5-F_2Y mutants and indicates the overall reductions in activity, first shown in Figure 6.11 A, are specific to the F_nY rather than to the location within the pathway.

Figure 6.13 A comparison of the pH rate profiles of 3,5-F_2Y-RNRs and 2,3,5-F_3Y-RNRs at three different positions. (A) A comparison of $Y_{356}(3,5)F_2Y$-β2 (gray) and $Y_{731}(3,5)F_2Y$-α2 (cyan) reveals that the two are nearly identical, and are distinct from His-α2(wt) (red) and wt-β2 (blue). Fits to eq. 6-1 are shown as solid lines. (B) $Y_{730}(3,5)F_2Y$-α2 (purple), however, behaves uniquely from both the wt subunits and the 356 and 731 mutants. (C) A comparison of $Y_{356}(2,3,5)F_3Y$-β2 (gray) and $Y_{731}(2,3,5)F_3Y$-α2 (cyan) reveals that the two are nearly identical, and are distinct from His-α2(wt) (red) and wt-β2 (blue). (D) $Y_{730}(2,3,5)F_3Y$-α2 (purple) behaves uniquely from both the wt subunits and the 356 and 731 mutants.

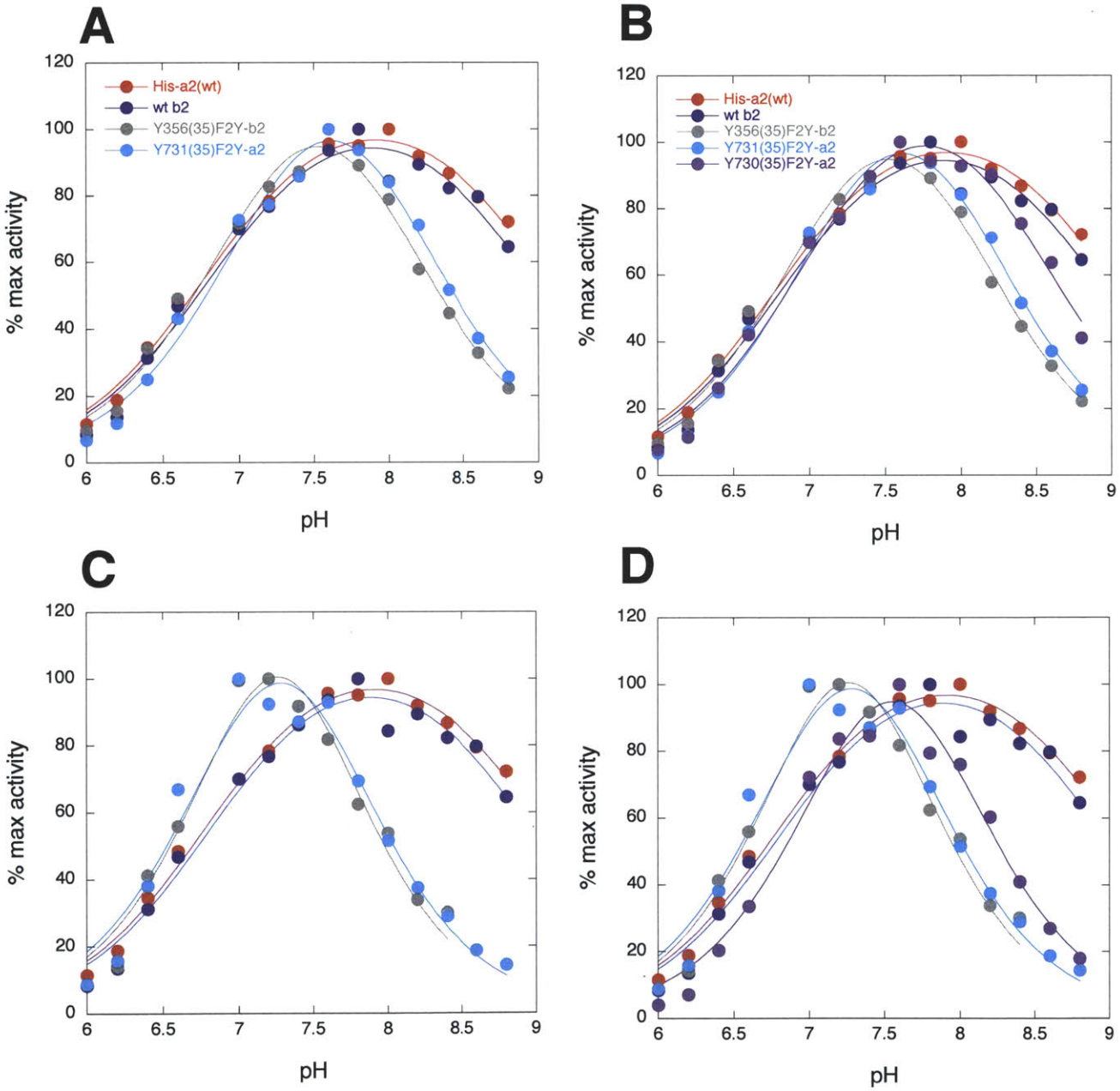

6.3.12 pH rate profiles of EPL-generated $Y_{356}F_nY$-β2s are different from those of $Y_{356}F_nY$-β2s prepared by the in vivo suppression method. In the previous section, we proposed that the pH rate profiles of F_nY-RNRs prepared by the *in vivo* suppression method report on conformational changes that gate the chemistry of radical initiation. The observed effect of F_nY substitution on overall activity (Figure 6.11 A) appears consistent among the three positions and is quite distinct from that observed in EPL-generated $Y_{356}F_nY$-β2s (Figure 6.12 A). Furthermore, we fail to observe a scenario in which electron transfer is rate limiting, as was hypothesized to occur for EPL-generated $Y_{356}(2,3,5)F_3Y$-β2 at alkaline pH. These results suggest that the pH rate profiles of the EPL-generated proteins are inherently different from those generated by the *in vivo* method. Overlays of wt-β2, $Y_{356}(3,5)F_2Y$-β2, and $Y_{356}(2,3,5)F_3Y$-β2 generated by the two methods (Figure 6.14 A, B, and C, respectively) qualitatively demonstrate these differences.

Perhaps the most interesting difference between proteins generated by the two methods is the pK_2 determined by fitting the data for EPL $Y_{356}F_nY$-β2s (Table 6.4). Regardless of the F_nY substitution, the experimental data are fit to a pK_2 of 8.7. This likely implicates a role for the C_{354} mutation in mediating loss of activity at high pH. This S-to-C mutation was introduced as the site of ligation of the C-terminal peptide during the protein semi-synthesis, and has been implicated as the reason for the slow uncoupling observed in steady-state assays of EPL-generated RNRs.[10] Thus, there is precedent for this mutation interfering with radical propagation even at pH 7.6. Given this observation, it is possible that re-introduction of the $S_{354}C$ mutation to the *in vivo* generated $Y_{356}(2,3,5)F_3Y$-β2 may slow down the kinetics of radical propagation to a sufficient degree such that conformational dynamics are no longer rate limiting. If so, study of this mutant using rapid kinetic techniques in conjunction with UV-vis and magnetic

spectroscopies would provide an opportunity to examine the mechanistic underpinnings of radical propagation. The ability to generate this mutant by the *in vivo* nonsense suppression method will allow for its facile isolation on the >100 mg scale, providing the large quantities of protein necessary for these biophysical techniques.

Figure 6.14 A comparison of the pH rate profiles of *in vivo* generated β2s vs the analogous mutants generated by EPL: (A) wt-β2 (red) vs EPL (blue), (B) $Y_{356}(3,5)F_2Y$-β2 (pink) vs EPL (cyan), (C) $Y_{356}(2,3,5)F_3Y$-β2 (violet) vs EPL (light blue). Fits to eq. 6-1 are shown in solid lines.

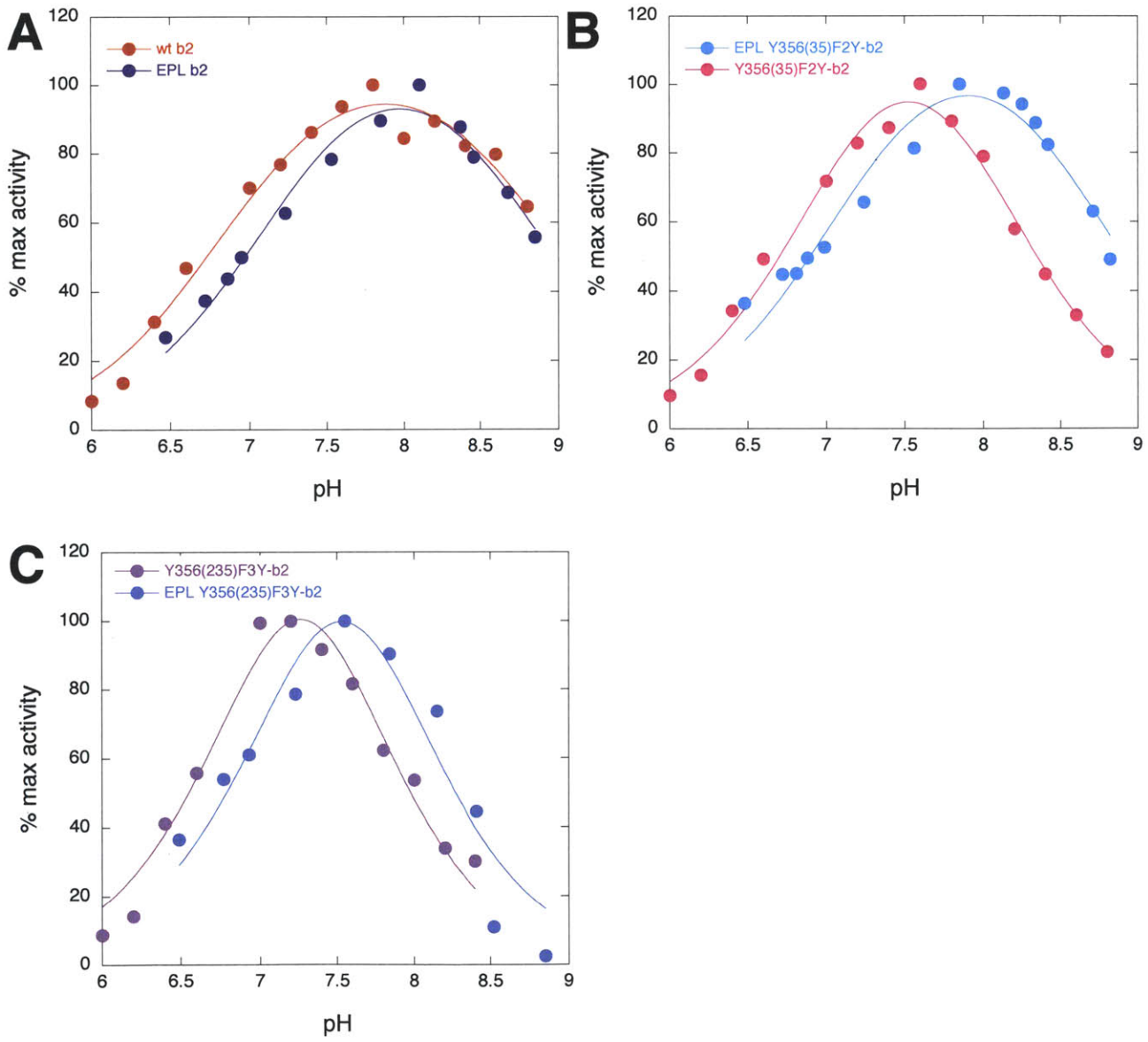

6.4 DISCUSSION

A long-standing goal of this lab has been to site-specifically incorporate F_nYs into RNRs using the *in vivo* nonsense codon suppression method. This method relies on the evolution of a unique, orthogonal tRNA/tRNA synthetase (RS) pair that exclusively recognizes an unnatural amino acid and inserts it site-specifically during protein translation in response to an amber stop codon mutated into the gene of interest.[19] Through a fruitful collaboration with Dr. Douglas Young (Schultz lab, Scripps), two RSs were prepared by directed evolution. Each is capable of charging an orthogonal tRNA with an entire series of F_nYs, while maintaining high specificity over endogenous Y.[20]

Using these polyspecific F_nY-RSs, F_nYs were incorporated into the three sites of transient Y• formation (356 of β2, 730 and 731 of α2) and into position 122 of β2, the site of the stable diferric-Y• cofactor in the wt enzyme (Chapter 7).[20] The expression and purification of the F_nY-RNRs were optimized, allowing for rapid purification of large quantities (3-25 mg/g) of recombinant proteins. With these proteins available, we have conducted experiments modeled after those previously conducted on EPL-generated $Y_{356}F_n$Y-β2s,[13] namely to construct pH rate profiles for each of the $Y_{356}F_n$Y-β2s, $Y_{731}F_n$Y-α2s, and $Y_{730}F_n$Y-α2s.

The pH rate profiles of F_nY-RNRs have been surprising in many respects. First, the results presented above indicate that the profiles of EPL-generated $Y_{356}F_n$Y-β2s vary significantly from the pH rate profiles of the analogous proteins prepared by the *in vivo* nonsense suppression method. This discrepancy most likely arises from the two additional point mutations at positions 353 and 354 that were introduced to the former to achieve efficient peptide ligation by the EPL method. These changes reduce the activity of EPL-generated "wt"-β2 protein to 7% that of the native wt subunit. The hypothesis that pK_2 for the EPL-generated mutants

corresponds to deprotonation of C_{354} could be tested by inserting one or both of the EPL mutations into the *in vivo* generated protein and testing whether the original EPL results can be recapitulated. If so, this could provide an exciting opportunity to explore the details of PCET by accessing a regime in which radical propagation, rather than conformational change, is rate-determining.

Another surprising observation that emerged from these studies is the similarity between the pH rate profiles of 356 and 731 mutants. Though we cannot mechanistically interpret their individual pH rate profiles, these results suggest some similarities with respect to the environment of the PCET interface. A final observation concerns the overall activity of the F_nY-RNRs as a function of the peak potential of the specific F_nY incorporated. Namely, the maximum activities of F_nY-RNRs vary from 12-90% that of their respective wt subunit. These activities are consistent with previous observations that RNRs are functional when the driving force of radical propagation is modulated by up to +/- 200 mV relative to Y.[21,27,41]

We have interpreted the pH rate profiles for $Y_{730}F_n$Y-α2s, $Y_{731}F_n$Y-α2s, and $Y_{356}F_n$Y-β2s described herein as reporting on the proton dependence of rate-determining conformational changes. In all cases, the experimental data may be fit to a model invoking two independent ionization events, with pK_1 varying from 6.8-7.3 and pK_2 from 7.5-9.0 depending on the position and the F_nY substitution. Given the size of the protein, the subtleties of the conformational changes that govern catalysis, and the extent to which the protein environment can perturb pK_as, we cannot at present assign pK_1 and pK_2 to the deprotonation and protonation of two specific amino acids. However, inspection of the sequence alignments of class Ia RNRs combined with analysis of *E. coli* α2 X-ray structures could be informative in determining whether any candidate residues emerge. Those of interest would be residues that are conserved among α2

primary sequences and that structurally communicate to the PCET pathway via a hydrogen bonding network. Ultimately, as we were unable to find conditions during these initial experiments that indicated we were monitoring the details of radical propagation, we have not yet resolved the key mechanistic question concerning the nature of PCET that is operative at each position in $\alpha 2$.

6.5 REFERENCES

1. Stubbe, J. & van der Donk, W.A. Protein radicals in enzyme catalysis. *Chem. Rev.* **98**, 705-762 (1998).
2. Barry, B.A., el-Deeb, M.K., Sandusky, P.O. & Babcock, G.T. Tyrosine radicals in photosystem II and related model compounds. Characterization by isotopic labeling and EPR spectroscopy. *J. Biol. Chem.* **265**, 20139-43 (1990).
3. Gupta, A., Mukherjee, A., Matsui, K. & Roth, J.P. Evidence for protein radical-mediated nuclear tunneling in fatty acid alpha-oxygenase. *J. Am. Chem. Soc.* **130**, 11274-5 (2008).
4. Zhao, X. et al. A radical on the Met-Tyr-Trp modification required for catalase activity in catalase-peroxidase is established by isotopic labeling and site-directed mutagenesis. *J. Am. Chem. Soc.* **132**, 8268-9 (2010).
5. Tsai, A.L. & Kulmacz, R.J. Prostaglandin H synthase: resolved and unresolved mechanistic issues. *Arch. Biochem. Biophys.* **493**, 103-24 (2010).
6. Kim, K. & Cole, P.A. Kinetic analysis of a protein tyrosine kinase reaction transition state in the forward and reverse directions. *J. Am. Chem. Soc.* **120**, 6851-6858 (1998).
7. Seyedsayamdost, M.R., Reece, S.Y., Nocera, D.G. & Stubbe, J. Mono-, di-, tri-, and tetra-substituted fluorotyrosines: new probes for enzymes that use tyrosyl radicals in catalysis. *J. Am. Chem. Soc.* **128**, 1569-79 (2006).
8. Uhlin, U. & Eklund, H. Structure of ribonucleotide reductase protein R1. *Nature* **370**, 533-539 (1994).
9. Stubbe, J., Nocera, D.G., Yee, C.S. & Chang, M.C.Y. Radical initiation in the class I ribonucleotide reductase: long-range proton-coupled electron transfer? *Chem. Rev.* **103**, 2167-201 (2003).
10. Yee, C.S., Seyedsayamdost, M.R., Chang, M.C.Y., Nocera, D.G. & Stubbe, J. Generation of the R2 subunit of ribonucleotide reductase by intein chemistry: insertion of 3-nitrotyrosine at residue 356 as a probe of the radical initiation process. *Biochemistry* **42**, 14541-52 (2003).
11. Seyedsayamdost, M.R., Xie, J., Chan, C.T., Schultz, P.G. & Stubbe, J. Site-specific insertion of 3-aminotyrosine into subunit α2 of *E. coli* ribonucleotide reductase: direct evidence for involvement of Y730 and Y731 in radical propagation. *J. Am. Chem. Soc.* **129**, 15060-71 (2007).
12. Yokoyama, K., Uhlin, U. & Stubbe, J. Site-specific incorporation of 3-nitrotyrosine as a probe of p*K*a perturbation of redox-active tyrosines in ribonucleotide reductase. *J. Am. Chem. Soc.* **132**, 8385-97 (2010).
13. Seyedsayamdost, M.R., Yee, C.S., Reece, S.Y., Nocera, D.G. & Stubbe, J. pH rate profiles of F_nY_{356}-R2s (n = 2, 3, 4) in *Escherichia coli* ribonucleotide reductase: evidence that Y_{356} is a redox-active amino acid along the radical propagation pathway. *J. Am. Chem. Soc.* **128**, 1562-8 (2006).

14. Seyedsayamdost, M.R., Yee, C.S. & Stubbe, J. Use of 2,3,5-F_3Y-β2 and 3-NH_2Y-α2 to study proton-coupled electron transfer in *Escherichia coli* ribonucleotide reductase. *Biochemistry* **50**, 1403-11 (2011).

15. Yee, C.S., Chang, M.C.Y., Ge, J., Nocera, D.G. & Stubbe, J. 2,3-difluorotyrosine at position 356 of ribonucleotide reductase R2: A probe of long-range proton-coupled electron transfer. *J. Am. Chem. Soc.* **125**, 10506-7 (2003).

16. Seyedsayamdost, M.R., Yee, C.S. & Stubbe, J. Site-specific incorporation of fluorotyrosines into the R2 subunit of *E. coli* ribonucleotide reductase by expressed protein ligation. *Nat. Protoc.* **2**, 1225-35 (2007).

17. Rappaport, F. et al. Probing the coupling between proton and electron transfer in photosystem II core complexes containing a 3-fluorotyrosine. *J. Am. Chem. Soc.* **131**, 4425-33 (2009).

18. Wilkins, B.J. et al. Site-specific incorporation of fluorotyrosines into proteins in *Escherichia coli* by photochemical disguise. *Biochemistry* **49**, 1557-9 (2010).

19. Xie, J. & Schultz, P.G. An expanding genetic code. *Methods* **36**, 227-38 (2005).

20. Minnihan, E.C., Young, D.D., Schultz, P.G. & Stubbe, J. Incorporation of fluorotyrosines into ribonucleotide reductase using an evolved, polyspecific aminoacyl-tRNA synthetase. *J. Am. Chem. Soc.* **133**, 15942-5 (2011).

21. Minnihan, E.C., Seyedsayamdost, M.R., Uhlin, U. & Stubbe, J. Kinetics of radical intermediate formation and deoxynucleotide production in 3-aminotyrosine-substituted *Escherichia coli* ribonucleotide reductases. *J. Am. Chem. Soc.* **133**, 9430-40 (2011).

22. Chivers, P.T. et al. Microscopic pK_a values of *Escherichia coli* thioredoxin. *Biochemistry* **36**, 14985-91 (1997).

23. Russel, M. & Model, P. Direct cloning of the *trxB* gene that encodes thioredoxin reductase. *J. Bacteriol.* **163**, 238-42 (1985).

24. Chen, H., Gollnick, P. & Phillips, R.S. Site-directed mutagenesis of His343-->Ala in Citrobacter freundii tyrosine phenol-lyase. Effects on the kinetic mechanism and rate-determining step. *Eur. J. Biochem.* **229**, 540-9 (1995).

25. Young, T.S., Ahmad, I., Yin, J.A. & Schultz, P.G. An enhanced system for unnatural amino acid mutagenesis in *E. coli*. *J. Mol. Biol.* **395**, 361-74 (2010).

26. Young, D.D. et al. An evolved aminoacyl-tRNA synthetase with atypical polysubstrate specificity. *Biochemistry* **50**, 1894-900 (2011).

27. Yokoyama, K., Uhlin, U. & Stubbe, J. A hot oxidant, 3-NO2Y_{122} radical, unmasks conformational gating in ribonucleotide reductase. *J. Am. Chem. Soc.* **132**, 15368-79 (2010).

28. Steeper, J.R. & Steuart, C.D. A rapid assay for CDP reductase activity in mammalian cell extracts. *Anal. Biochem.* **34**, 123-30 (1970).

29. Ge, J., Yu, G., Ator, M.A. & Stubbe, J. Pre-steady-state and steady-state kinetic analysis of *E. coli* class I ribonucleotide reductase. *Biochemistry* **42**, 10071-83 (2003).

30. Kobayashi, T. et al. Structural basis for orthogonal tRNA specificities of tyrosyl-tRNA synthetases for genetic code expansion. *Nat. Struct. Biol.* **10**, 425-32 (2003).

31. Turner, J.M., Graziano, J., Spraggon, G. & Schultz, P.G. Structural characterization of a p-acetylphenylalanyl aminoacyl-tRNA synthetase. *J. Am. Chem. Soc.* **127**, 14976-7 (2005).

32. Muller, K., Faeh, C. & Diederich, F. Fluorine in pharmaceuticals: looking beyond intuition. *Science* **317**, 1881-6 (2007).

33. Dunten, P. & Mowbray, S.L. Crystal structure of the dipeptide binding protein from Escherichia coli involved in active transport and chemotaxis. *Protein Sci.* **4**, 2327-34 (1995).

34. Liu, C.C. & Schultz, P.G. Adding new chemistries to the genetic code. *Annu. Rev. Biochem.* **79**, 413-44 (2010).

35. Reece, S.Y., Hodgkiss, J.M., Stubbe, J. & Nocera, D.G. Proton-coupled electron transfer: the mechanistic underpinning for radical transport and catalysis in biology. *Philos. Trans. R. Soc. Lond. B Biol. Sci.* **361**, 1351-64 (2006).

36. Madej, E. & Wardman, P. The oxidizing power of the glutathione thiyl radical as measured by its electrode potential at physiological pH. *Arch. Biochem. Biophys.* **462**, 94-102 (2007).

37. Reece, S.Y., Seyedsayamdost, M.R., Stubbe, J. & Nocera, D.G. Photoactive peptides for light-initiated tyrosyl radical generation and transport into ribonucleotide reductase. *J. Am. Chem. Soc.* **129**, 8500-9 (2007).

38. Holder, P.G., Pizano, A.A., Anderson, B.L., Stubbe, J. & Nocera, D.G. Deciphering radical transport in the large subunit of class I ribonucleotide reductase. *J. Am. Chem. Soc.* **134**, 1172-80 (2012).

39. Tommos, C., Skalicky, J.J., Pilloud, D.L., Wand, A.J. & Dutton, P.L. De novo proteins as models of radical enzymes. *Biochemistry* **38**, 9495-507 (1999).

40. Hassan, A.Q., Olshansky, L., Yokoyama, K., Lutterman, D. A., Jin, X., Nocera, D. G., & Stubbe, J. *In preparation.*

41. Seyedsayamdost, M.R. & Stubbe, J. Site-specific replacement of Y_{356} with 3,4-dihydroxyphenylalanine in the β2 subunit of *E. coli* ribonucleotide reductase. *J. Am. Chem. Soc.* **128**, 2522-3 (2006).

Chapter 7

Mapping the thermodynamic landscape of the PCET pathway: Use of F_nY_{122}•s as radical initiators

Adapted in part from: Minnihan, E.C., Young, D.D., Schultz, P.G. and Stubbe, J. *J. Am. Chem. Soc.*, **2011**, *133*, 15942-15945.

7.1 INTRODUCTION

The site-specific incorporation of a series of fluorotyrosines (F_nYs) into *E. coli* RNR using a polyspecific tRNA synthetase (F_nY-RS) has been demonstrated previously at the three sites of transient Y• formation: 356 of β2, 731 of α2, and 730 of α2 (Chapter 6). In this chapter, we describe the incorporation of F_nYs at position 122 of β2, the site of the stable Y• ($t_{1/2} \sim 4$ days, 4 °C) in the wt enzyme. The model for long-range (>35 Å), reversible PCET holds that the reduction of Y_{122}• occurs concomitant with oxidation of C_{439} in α2 along a pathway of absolutely conserved redox active amino acids: Y_{122}• ↔ [W_{48}?] ↔ Y_{356} in β2 to Y_{731}↔Y_{730}↔ C_{439} in α2. The intermediates of radical propagation in the wt enzyme are kinetically masked by rate-limiting conformational changes.[1] Thus, changes to Y_{122}• or any of the pathway residues are undetectable by rapid biophysical techniques.

Recently, we have provided evidence for the first catalytically-relevant radical intermediates on the PCET pathway through the site-specific replacement of conserved Ys with unnatural Y analogues. Incorporation of a thermodynamic minimum on the pathway in the form of 3-aminotyrosine (NH_2Y) at position 356 of β2, Y_{731} of α2, or Y_{730} of α2 has been one successful strategy for visualizing radical intermediates. Reaction of a NH_2Y-RNR with the second subunit, substrate, and allosteric effector results in the formation of an NH_2Y• intermediate that is detectable spectroscopically and is capable of C_{439} oxidation (Chapters 2, 3, and 4). A second successful strategy has been to raise the oxidizing power of radical initiation by the site-specific insertion of 3-nitrotyrosine (NO_2Y) at position 122 of β2. Reaction of apo-$Y_{122}NO_2Y$-β2 with Fe^{2+} and O_2 affords assembly of a novel diferric-NO_2Y_{122}• cofactor.[2] Surprisingly, use of the potent oxidant NO_2Y_{122}• as a radical initiator decoupled ET from PT, lifting the conformational gating that is rate-limiting in the wt enzyme and allowing the first

detection of a transient Y• on the pathway. Through a combination of techniques including isotopic labeling, site-specific F_nY incorporation, and PELDOR spectroscopy, it was determined that that the Y• was distributed among three positions on the pathway (356, 731, and 730), with the equilibrium lying strongly in favor of radical localization to 356 of β2.[2,3] This led to the model shown in Figure 7.1. However, the high redox potential of NO_2Y relative to Y (ΔE_p ~200 mV, pH 7) introduced complications to the system, namely the short half-life of NO_2Y_{122}• ($t_{1/2}$ ~ 40 s at 25 °C) and the inability of the enzyme to perform multiple turnovers. Indeed, when NO_2Y_{122}•-β2 is rapidly mixed with wt-α2, CDP, and ATP, 0.6 dCDP/α2 are formed; no additional dCDP is formed in the presence of the TR/TRR/NADPH reducing system. These observations suggest that chemistry occurs on one α/β pair and, upon reverse hole migration, inability to reoxidize $NO_2Y_{122}^-$ to NO_2Y_{122}• results in accumulation of Y_{356}•.

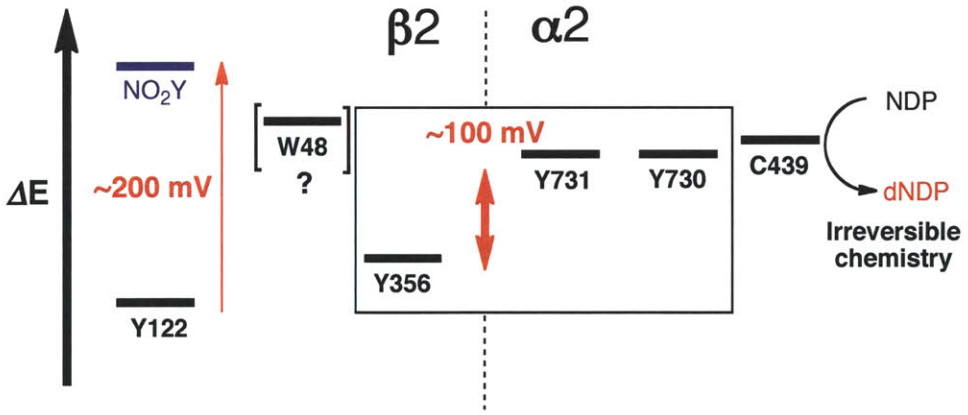

Figure 7.1 Model derived from studies using NO_2Y_{122}• as a radical initiator for the relative redox potentials of residues in the PCET pathway of *E. coli* RNR. Adapted from reference 3.

Given the results obtained with NO_2Y_{122}•, we sought to modulate the properties of position 122 more subtly by the site-specific replacement of Y_{122} with F_nYs. Previous titrations of $Y_{122}NO_2Y$-β2 revealed a significant (>2.5 pH units) perturbation of the phenolic hydroxyl pK_a at this position.[4] Under the assumption that $Y_{122}F_nY$-β2s experience a similar perturbation, all

F_nYs should be protonated at physiological pH and should vary from 100 mV harder to 50 mV easier to oxidize than Y.[5] As a result, incorporation of F_nYs at this position allows us to explore the reactivity of a wide range of oxidants at position 122. By "titrating" the oxidizing power at this position, we hope to further refine the thermodynamic hypothesis presented in Figure 7.1.

A second complexity in using NO_2Y_{122}• as a radical initiator arises with respect to deconvolution and interpretation of new pathway radical(s). X-band EPR analysis of reaction spectra is inherently complicated due to extensive spectral overlap and similarity between NO_2Y_{122}• and the newly formed Y•(s). Thus, deconvolution of the species formed in NO_2Y_{122}• reactions required a sophisticated combination of isotopic labeling, iterative subtraction methods, spectral simulations, and highfield (HF) EPR analysis.[3] In this respect, use of F_nY_{122}•s as radical initiators has proven beneficial. F_nY_{122}• were predicted to have very unique EPR spectra, arising from the very large hyperfine couplings of the unpaired electron to the fluorine nuclei.[5] Indeed, the width of the F_nY_{122}• X-band EPR spectra and the presence of distinct fluorine hyperfine couplings have served as unique spectroscopic handles to allow accurate subtraction of F_nY•s from other g ~2 radicals (e.g. Y•, [β-$^2H_2$]Y•, NH_2Y•, NO_2Y•).[2,6]

Chapter 7 discusses our recent success in the application of F_nY_{122}•s as unnatural radical initiators of long-range PCET in class Ia RNR. The isolation of $Y_{122}F_n$Y-β2s, the spectral and biochemical characterization of their F_nY_{122}•s, and their nucleotide reductase activities will be presented. Evidence will be provided for the kinetically-competent trapping of a Y_{356}• intermediate that participates in multiple-turnover catalysis. The ability to detect and characterize the oxidation of Y_{356} by F_nY_{122}• facilitates the design of experiments to address a long-standing mechanistic question, namely, does W_{48} participate in long-range radical propagation, and if so, what is its specific role? It has been demonstrated previously that this

residue plays a key role in the *in vitro* diferric-Y_{122}• cluster assembly, but the inability to mutate this residue while maintaining activity has limited our investigation of its role in reversible PCET over 35 Å.[7] Thus, though W48 has long been proposed to participate in long-range PCET relevant to dCDP formation,[8,9] there is no experimental evidence to substantiate this claim. Reaction of the double mutant $Y_{122}NO_2Y/Y_{356}F$-β2 with wt-α2, CDP, and ATP results in the formation of several W•+s located at different positions (including W_{48}) throughout β2, thereby suggesting that this "hot" oxidant will perform off-pathway oxidation when the native pathway has been blocked (Yokoyama and Stubbe, unpublished results). Similar studies with double mutants $Y_{122}F_nY/Y_{356}F$-β2 provide no evidence for the discrete formation of a W_{48}•/W_{48}•+, suggesting that the proposed role of this residue in long-range radical propagation should be reevaluated. Finally, we use the collective data obtained using F_nY_{122}•s as radical initiators to expand and refine the pathway thermodynamic model presented in Figure 7.1. This revised model makes a number of testable predictions that will be the focus of future experiments, the results from which may allow for a quantitative interpretation of the thermodynamics of long-range, reversible PCET in *E. coli* class Ia RNR.

7.2 MATERIALS AND METHODS

7.2.1 Materials. Fluorotyrosines (F_nYs, n=2-4) were synthesized enzymatically from pyruvate, ammonia, and the appropriate fluorinated phenol, with tyrosine phenol lyase (TPL) as the catalyst as described previously[5,10] and in section 6.2.3. The desired products were isolated in 60-85% yield and characterized by ^{1}H NMR, ^{19}F NMR, and UV-vis absorption spectroscopy. TPL was expressed, purified, and assayed following a modification of the literature protocol,[10] as described in section 6.2.2. The generation of plasmids pBAD-*nrdB*(TAG_{122}), pBAD-*nrdB*($TAG_{122}TTT_{356}$), and pEVOL-F_nYRS-E3 have been described previously.[4,11] Wt-α2 (2500 nmol/min/mg), $Y_{731}F$-α2 (<25 nmol/min/mg), and wt-β2 (1.2 Y_{122}•/β2, 7600 nmol/min/mg) were expressed and purified as previously described. His_6-α2(wt) (2200 nmol/min/mg) was expressed and purified as previously described.[12] All α2 proteins were pre-reduced prior to use. *E. coli* thioredoxin (TR, 40 U/mg) and thioredoxin reductase (TRR, 1400 U/mg) were isolated as described.[13,14] [5-^{3}H]-CDP was purchased from ViTrax (Placentia, CA). Assay buffer consists of 50 mM Hepes, 1 mM EDTA, and 15 mM $MgSO_4$, pH 7.6.

7.2.2 Expression and purification of $Y_{122}F_nY$-β2s. $Y_{122}F_nY$-β2s were expressed from pBAD-*nrdB*(TAG_{122})[4] and pEVOL-F_nYRS-E3[11] in *E. coli* TOP10 cells as described for $Y_{356}F_nY$-β2s (section 6.2.6). Yields of 2 g/L were obtained. Success of expression was assessed by 10% SDS-PAGE.

$Y_{122}F_nY$-β2s were purified from 8-10 g cells following the protocol described previously for $Y_{122}NO_2Y$-β2, $Y_{356}NH_2Y$-β2 (section 2.2.3), and $Y_{356}F_nY$-β2s (section 6.2.6). Unlike for the 356-substituted β2s, the 121-truncated protein is likely degraded by the cell during protein expression and thus separation of truncated protein from the desired full-length protein is not a concern in the isolation of these mutations. Purified protein yields varied with F_nY from 7.5-35

mg of protein per g of cell paste. The double mutants, $Y_{122}F_nY/Y_{356}F$-β2s were expressed from the plasmids pBAD-*nrdB*($TAG_{122}TTT_{356}$) and pEVOL-F_nYRS-E3 and purified in an identical fashion. $Y_{122}(2,3,6)F_3Y$-β2 and $Y_{122}(2,3,6)F_3Y/Y_{356}F$-β2 were expressed, purified, and studied in detail by Kanchana Ravichandran (Stubbe lab).

7.2.3 Characterization of F_nY_{122}•s by 9 GHz EPR spectroscopy. EPR spectra were recorded under conditions identical to those described in section 2.2.6. EPR spin quantitation was carried out using Cu(II)[15] and wt-β2 standards. Power saturation behavior of each radical was determined by collecting spectra at various microwave powers from 20 μW to 4 mW and plotting the double integral intensity (DI/N) of the signal as a function of the power (P) according to eq. 7.1, where *K* is a scaling constant and *b* is a parameter that reflects spectral homogeneity:

$$\text{amplitude} = K(P^{0.5})/[1+(P/P_{1/2})]^{0.5b} \qquad \text{(eq. 7.1)}$$

EPR spectra were simulated with the EasyFit function of EasySpin (version 3.1.7).[16] The experimental spectrum, microwave frequency, and sweep width were submitted to the program, as were the *g* values previously determined by HF EPR for Y_{122}•. The experimental data were subjected to iterative least-squares fitting by systematically varying the hyperfine coupling constants (A_x, A_y, and A_z) by ± 30 MHz for one β-methylene proton (C_β-H1) and for the nuclei (F or H) at the 3 and 5 positions on the phenol ring, using the simulation parameters of Y_{122}• and 3-FY_{122}•[5] as starting points. The nuclei at the 2 and 6 ring positions were added to the simulation if they were fluorine in a given F_nY. Otherwise, the coupling constants for nuclei at these positions and for the second β-methylene proton were taken to be smaller than the intrinsic spectral line width and were ignored in the simulation.

7.2.4 In vitro reconstitution of diferric-F_nY_{122}•s. The iron contained in as-isolated $Y_{122}F_nY$-β2s was reduced and removed under anaerobic conditions using dithionite, methyl viologen, and ferrozine following the protocol described in section 2.2.5 and elsewhere.[12] By this method, "apo"-$Y_{122}F_nY$-β2 was recovered in >90% yield. Quotation marks are used for "apo," as this method failed to remove all the iron from as-isolated $Y_{122}F_nY$-β2s, as described in section 7.3.2. "Apo" protein routinely contained a residual 0.3-1.0 Fe/β2. This protein (~1 mM) was degassed and brought into an anaerobic chamber at 4 °C. To it was added 5 equivalents (eq) of Fe(II) and the resulting solution was stirred for 15 min. The solution was removed from the anaerobic box and 3.5 eq of O_2 was added to it in the form of oxygen-saturated reconstitution buffer (50 mM Hepes, 5% glycerol, pH 7.6). An aliquot was removed immediately, transferred to an EPR tube, and frozen within 30 s in a dry ice/acetone bath. The extent of radical formation in the reconstituted sample was quantitated by EPR by comparison to Cu(II) and wt-β2 standards.

7.2.5 Stability of F_nY_{122}•s. The stability of F_nY_{122}•s was assessed by either EPR or UV-vis spectroscopy. For the former experiment, Fe(II)-loaded $Y_{122}F_nY$-β2 was rapidly mixed with O_2-saturated buffer, then incubated on ice. Samples were removed from the protein solution at specific time points after reconstitution (1-10 min), loaded into an EPR tube, and frozen in a dry ice/acetone bath. The total radical content of each sample was determined by EPR spectroscopy. For the latter, a protein sample (~30 μM) was placed in a cuvette in the Cary 3 UV-vis spectrometer, and a spectrum was collected from 240 – 700 nm every 2-5 min over 30-90 min at room temperature. After subtraction of a blank spectrum of sample buffer, the protein spectra were examined for changes associated with the Fe cluster (~325 and 365 nm) and F_nY_{122}• (396-

420 nm, depending on the F_nY_{122}•). No changes were observed at these wavelengths over the time monitored

7.2.6 Steady-state activity assays of $Y_{122}F_nY$-β2s. The activities of $Y_{122}F_nY$-β2s were examined by the spectrophotometric and radioactive assay for nucleotide reduction, as described in section 2.2.7.[17,18] $Y_{122}F_nY$-β2 was assayed at final concentrations of 0.5 μM-1.0 μM; wt-α2 was used in a five-fold excess relative to β2.

7.2.7 Kinetics of dCDP formation with $Y_{122}(2,3,5)F_3Y$-β2 monitored by RCQ. Rapid chemical quench (RCQ) experiments were conducted on a KinTek Model RQF-3 Chemical Quench Flow instrument. Pre-reduced His-α2(wt) and ATP were mixed rapidly with $Y_{122}(2,3,5)F_3Y$-β2 (0.4 F_3Y•/β2) and [^{3}H]-CDP (20,000 cpm/nmol) in assay buffer at 25 °C to final concentrations of 10 μM α2, 30 μM β2, 0.5 mM CDP, and 3 mM ATP. In this experiment, a three-fold excess of β2 was used relative to α2 to account for the fact that the β2 contained only 0.4 2,3,5-F_3Y•/β2 (compared to 1.2 Y•/β2 in the wt). Time points (5 ms – 100 s) were collected and analyzed as described in section 4.2.11. Hand quenched reactions were collected at the beginning and end of the RCQ experiment as positive controls. The stability of the diferric-2,3,5-F_3Y_{122}• cofactor was also monitored by measuring the UV-vis spectrum of a protein sample maintained at 25 °C over the time of sample collection (~2 h). The UV-vis spectrum of the diferric-2,3,5-F_3Y_{122}• showed minimal change over this time.

7.2.8 Hand-quench single-turnover reactions of $Y_{122}F_nY$-β2s with wt-α2, CDP, and ATP. In a total volume of 500 μL was combined His_6-α2 (2.0 μM), [^{3}H]-CDP (0.5 mM, 20,000 cpm/nmol)), and ATP (3 mM) in assay buffer at 25 °C. The assay was initiated by addition of $Y_{122}F_nY$-β2 to either 2.0 μM in protein or F_nY• concentration. Aliquots (200 μL) were removed

at 30 s and 5 min and quenched in a boiling water bath. 95% of each sample was analyzed by dephosphorylation and the method of Steeper and Steuart.[19]

7.2.9 Determining the identity of the product(s) formed by $Y_{122}F_nY$-β2s. The nature of the product formed in both steady-state and single-turnover assays was assessed by HPLC analysis. A fraction (2 mL) of the eluate from borate columns of two assay time points (t = 30 s and 2 min for steady-state assays, 30 s and 5 min for single turnovers) from each of the reactions described above was adjusted to contain 95 nmol of each carrier cytosine and deoxycytidine (dC), then lyophilized to dryness and redissolved in 300 μL ddH_2O. An aliquot (50 μL) of the solution was counted directly and used to calculate the total recovery of radioactivity off the HPLC column. A second aliquot (200 μL) was loaded to an Econosil C18 (10 um) column (250 mm × 4.6 mm) equilibrated in 20 mM KPi, pH 6.7 and eluted isocratically at 1 mL/min. The absorbance profile of the eluate was monitored at 271 nm by photodiode array, and fractions (0.5 – 0.75 min/fraction) were collected and the radioactivity of each fraction was determined by scintillation counting.

7.2.10 Reaction of $Y_{122}F_nY$-β2s (or $Y_{122}F_nY/Y_{356}F$-β2s) with wt-α2 (or $Y_{731}F$-α2), CDP, and ATP monitored by EPR. Pre-reduced wt-α2 (or $Y_{731}F$-α2) and ATP were mixed rapidly with $Y_{122}F_nY$-β2 (0.2-0.6 $F_nY\bullet$/β2) and CDP in assay buffer on ice to give final reagent concentrations of 20-40 μM, 3 mM, 20-40 μM, and 1 mM, respectively. The reaction mixture was hand-quenched at 25 s in an acetone/dry ice bath or an isopentane/liquid N_2 bath and its EPR spectrum was recorded using the acquisition parameters described in section 2.2.6 and previously.[6] The reactions of $Y_{122}F_nY/Y_{356}F$-β2s with wt-α2, CDP, and ATP were conducted and analyzed in an identical fashion. Analysis of the reaction spectra was carried out using an in-house Excel program, as described in section 2.2.17. Subtraction of the $F_nY_{122}\bullet$ contribution

from the composite spectrum was conducted using the distinct low- and high-field fluorine couplings as indicators of the quantity of F_nY_{122}• to subtract. This subtraction yielded a spectrum of the putative Y_{356}•, and the relative quantitation of the two species was determined by comparison of their double integral peak intensities.

7.2.11 Reaction of $Y_{122}F_nY$-β2s (or $Y_{122}F_nY/Y_{356}F$-β2s) with wt-α2 (or $Y_{731}F$-α2), CDP, and ATP monitored by SF UV-vis spectroscopy. SF kinetics were performed on an Applied Photophysics DX 17.MV instrument equipped with the Pro-Data upgrade. All reactions were carried out in assay buffer at 25 °C. Pre-reduced His_6-α2(wt) (or $Y_{731}F$-α2) and ATP in one syringe were mixed rapidly with $Y_{122}F_nY$-β2 and CDP in a second syringe to yield a final concentration of 20-25 μM protein, 1 mM CDP and 3 mM ATP. The reactions were monitored at 400-410 nm for F_nY_{122}•, 510 nm for W• (ε ~2,200 $M^{-1}cm^{-1}$), and 560 nm for $W•^+$ (ε ~3,000 $M^{-1}cm^{-1}$) using PMT detection. Individual traces (6-10) were averaged and analyzed using KaleidaGraph software.

7.2.12 Reaction of $Y_{122}(2,3,5)F_3Y$-β2, wt-α2, CDP, and ATP monitored by RFQ-EPR spectroscopy. Rapid freeze quench (RFQ) experiments were carried out on an Update Instruments 1019 syringe ram unit and a model 715 Syringe Ram controller. Operation of the instrument has been described in detail previously.[20] An isopentane bath (~7 L) was maintained at -143 ± 4 °C by gradual cooling using an outer jacket of liq N_2. Bath temperature measurements were made with a Fluke 52 dual-input thermometer supplemented with an Anritsu Cu thermocouple probe. For all experiments, a ram drive velocity of 1.25 cm/s was used and the ram displacement adjusted to expel a sample volume of 400 μL per reaction.

One syringe contained $Y_{122}(2,3,5)F_3Y$-β2 (80 μM, 0.4 $F_3Y•$/β2) and CDP (2 mM) in assay buffer. A second syringe contained wt-α2 (80 μM) and ATP (6 mM) in assay buffer. The

contents of the two syringes were mixed rapidly in a 1:1 ratio and the mixture aged for a time period dictated by the length of a calibrated reaction loop (16 ms – 2 s). The sample was sprayed over a short distance (~1 cm) into a custom made glass funnel filled with cold isopentane, to which was attached a pre-calibrated, thin-walled EPR tube (Wilmad) by a short rubber fitting, and packed with a chilled stainless steel rod. Excess isopentane was removed from the packed sample, which was then transferred to a liq N_2 bath until EPR analysis. A packing factor of 0.60 ± 0.03 was determined from three independent test reactions with wt-β2. EPR spectra of the reaction mixtures were collected and analyzed as described for the hand-quench reactions.

7.2.13 Reaction of $Y_{356}(3,5)F_2Y$-β2 (0.7 Y•/β2) with wt-α2 (or $Y_{731}F$-α2), CDP, and ATP monitored by EPR and SF-UV vis spectroscopy. The reaction of $Y_{356}(3,5)F_2Y$-β2 with wt-α2 (or $Y_{731}F$-α2), CDP, and ATP was monitored by EPR and SF UV-vis spectroscopy as described in sections 7.2.10 and 7.2.11 for $Y_{122}F_nY$-β2s. Final protein concentrations were 35 μM for EPR experiments and 15 μM for SF UV-vis experiments.

7.3 RESULTS

7.3.1 Isolation of $Y_{122}F_nY$-β2s. The proteins $Y_{122}F_nY$-β2 (F_nY = 3,5-F_2Y, 2,3-F_2Y, 2,3,5-F_3Y, and 2,3,6-F_3Y) were expressed from the plasmids pEVOL-F_nY-RS and pBAD-*nrdB*(TAG_{122}) in 2xYT media. The effect of media pH, [F_nY], and induction time were all examined. Minimal effect on protein expression was observed as a function of pH of the culture medium. The minimal [F_nY] necessary to obtain good protein expression was determined for each F_nY and varied between 0.5-1.5 mM. No toxicity was observed as a result of addition of F_nY to the media. Induction times between 4-5 hours were determined to be optimal; no cell death nor improved cell yield was achieved with longer induction. Figure 7.2 shows a typical gel for the expressions of Y_{122}(3,5)F_2Y-β2 and Y_{122}(2,3,5)F_3Y-β2 as a function of induction time. The expression levels of full-length Y_{122}(2,3)F_2Y-β2 and Y_{122}(2,3,6)F_3Y-β2 were reduced relative to the 3,5-F_2Y- and 2,3,5-F_3Y-containing mutants, consistent with what has been observed previously for the relative incorporation of these amino acids into positions 356 of β2 and 730 and 731 of α2 (Chapter 6).

Protein was isolated following the procedure developed for untagged wt-β2, which utilizes two anion exchange columns. $Y_{122}F_nY$-β2 were isolated in similar final purity as wt-β2, with the only significant impurity being proteolyzed β2 (<10%, Figure 7.3). This proteolysis did not seem to be affected significantly by the concentration of protease inhibitor used, nor the nature of the protease inhibitor (i.e., PMSF versus Roche protease cocktail). The double mutants Y_{122}(2,3,5)F_3Y/Y_{356}F-β2, Y_{122}(2,3)F_2Y/Y_{356}F-β2, and Y_{122}(2,3,6)F_3Y/Y_{356}F-β2 were purified in an identical fashion. The protein yields for $Y_{122}F_nY$-β2s are reported in Table 7.1.

Figure 7.2 Whole cell SDS-PAGE (10%) showing the expression of $Y_{122}(3,5)F_2Y$-β2 (left) and $Y_{122}(2,3,5)F_3Y$-β2 (right) as a function of induction time. [F_nY] was 1.0 mM in this expression, but was subsequently lowered to 0.5 mM with minimal effect on protein expression levels. Lanes labeled "pre" are pre-induction samples, lanes to the right of these are samples at the indicated time after *nrdB* induction. The leftmost lane is a MW ladder, and "std" indicates a wt-β2 standard.

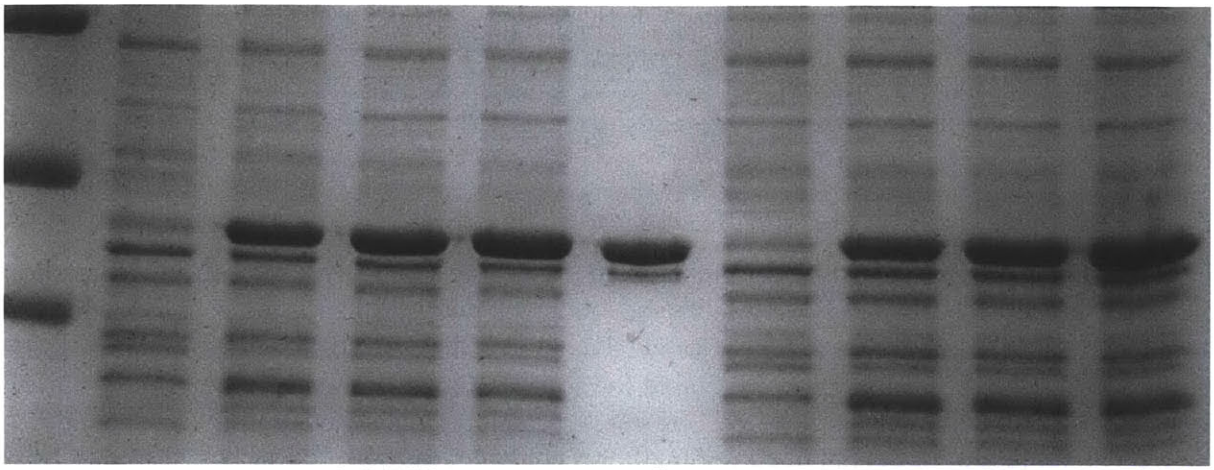

Figure 7.3 Gel of increasing amounts of purified $Y_{122}(3,5)F_2Y$-β2, compared to wt-β2 isolated by the same procedure.

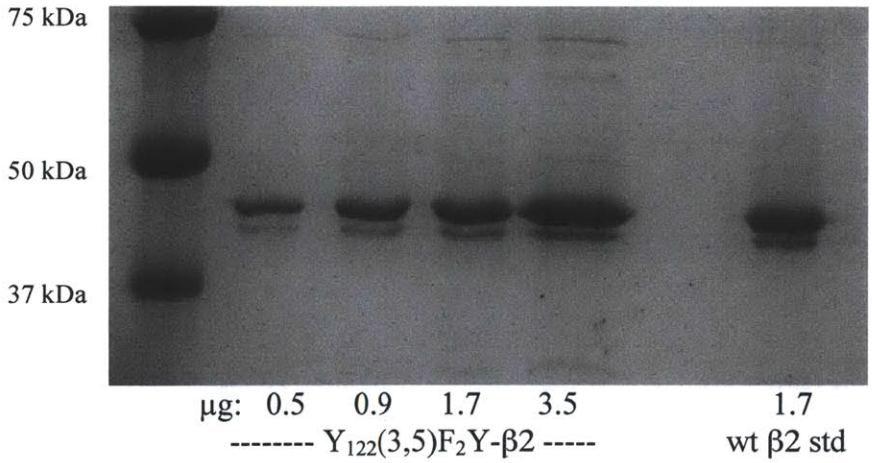

Table 7.1 Purified protein yields for $Y_{122}F_nY$-β2s, as-isolated radical content, and reconstituted radical content.

Protein	Yield (mg protein/g cells)	F_nY•/β2 (as-isolated)	F_nY•/β2 (reconstituted)	λ_{max}, nm (F_nY•)
$Y_{122}(3,5)F_2Y$-β2	30	0.2	0.4	396
$Y_{122}(2,3,5)F_3Y$-β2	36	<0.02	0.4	404
$Y_{122}(2,3,5)F_3Y/Y_{356}F$-β2	31	0.03	0.9	404
$Y_{122}(2,3)F_2Y$-β2	8	0.05	0.55	410
$Y_{122}(2,3)F_2Y/Y_{356}F$-β2	5	<0.05	0.55	410
$Y_{122}(2,3,6)F_3Y$-β2[a]	11	-[b]	0.7[c]	420
$Y_{122}(2,3,6)F_3Y/Y_{356}F$-β2[a]	9	-[b]	0.7[c]	420

a. Expressed, purified, reconstituted, and studied by Kanchana Ravichandran. *b.* No radical detected by EPR. *c.* 1.0 2,3,6-F_3Y•/β2 can be obtained within 300 ms of reconstitution (as determined by RFQ-EPR). There appear to be two F_3Y•s, one of which is less stable (decays within 3 min) while the second radical is stable for at least 30 min. Radical content (both radicals present) of 0.7 is obtained when the reconstituted protein is quenched within 30 seconds. A stable radical content of 0.5 is obtained 3 min after reconstitution.

7.3.2 Reconstitution of the diferric-F_nY_{122}• cofactors. X-band EPR analysis of the purified $Y_{122}F_nY$-β2s at 77 K confirmed that the as-isolated proteins contained 0.02-0.2 F_nY_{122}•/β2 (Table 7.1), compared to 1.2 Y_{122}•/β2 in the wt protein. These results suggest that the F_nY_{122}•s are inherently less stable that the native Y_{122}•, or that the mechanism of cluster is impaired by the F_nY mutation. In an attempt to obtain higher radical content, the as-isolated, partially-loaded protein was subjected to anaerobic iron reduction and chelation using a protocol employing methyl viologen, dithionite, and ferrozine.[21,22] While this protocol has been applied successfully to wt *E. coli* β2, it was less successful in removing existing ferric iron from $Y_{122}F_nY$-β2s. $Y_{122}F_nY$-β2s routinely contained 0.3-1.0 Fe/β2 *after* this treatment. Nevertheless, subsequent *in vitro* reconstitution of the cofactor in this "apo" protein gave higher radical content (0.4-0.9 F_nY_{122}•/β2, Table 7.1). A single attempt was made to remove the iron from $Y_{122}F_nY$-β2s by chelation with 8-hydroxyquinoline-6-sulfonate following the method of Atkin et al.[23] While this procedure was more successful in removal of the iron, significant protein precipitation

occurred under the published conditions and the recovery of apo protein was only ~20% the starting material (Ravichandran and Stubbe, unpublished results). At present, it is unclear why the as-isolated F_nY_{122}• loading is so much lower for $Y_{122}F_nY$-β2s than for wt-β2 (1.2 Y•/β2), but it may be the result of instability of the radical due to either structure or redox properties. We attribute the low radical loading in reconstituted $Y_{122}F_nY$-β2s at least in part to the inability to effectively remove the iron from the as-isolated protein. A recommended future strategy for obtaining higher radical loading is to express the protein in the presence of an iron chelator and isolate it in its apo form. Reconstitution of the apo protein with ferrous iron and oxygen may yield increased radical. Indeed, when Y_{122}(2,3,6)F_3Y-β2 was expressed and purified in its apo form and its cofactor assembly studied by RFQ-EPR, a total of 1.0 2,3,6-F_3Y_{122}•/β2 was obtained. However, due to low radical stability, the total radical dropped to 0.7 F_3Y_{122}•/β2 within 30 s after reconstitution (Table 7.1, Ravichandran and Stubbe, unpublished results). These early studies with 2,3,6-F_3Y_{122}• also highlight the fact that mixtures of F_nY_{122}•s may form (i.e., different conformers, rotamers, etc.), particularly in those F_nYs with asymmetrical fluorine substitution, and that each radical population may have a different stability. Thus, if low radical content continues to be measured in standard, hand-mixing reconstitutions, it may be necessary to study the assembly of the individual F_nY_{122}•s by rapid kinetic methods to determine whether a certain population of each F_nY_{122}• decays immediately after assembly on the fast (ms-s) timescale.

7.3.3 Characterization of F_nY_{122}•s by 9 GHz EPR spectroscopy. The reconstituted $Y_{122}F_nY$-β2s were next characterized by EPR spectroscopy. The X-band (9 GHz) EPR spectra of the F_nY_{122}•s at position 122 of β2 (Figure 7.4) are quite distinct from the previously-reported EPR spectra of F_nY•s generated on the corresponding free amino acids using UV-photolysis.[5]

The spectra of the latter are relatively featureless, with spectral line broadening arising from a large distribution of dihedral angles for the β-methylene protons. In contrast, structural constraints imposed by the protein give rise to F_nY_{122}• spectra with well-defined couplings to the fluorine nuclei (150-180 MHz) and one of the β-methylene protons (36-52 MHz).

The F_nY_{122}•s were also quite distinct from Y_{122}• with respect to their microwave relaxation properties. Typically, radicals coupled to the class Ia differic cluster have been determined to saturate at microwave powers at least an order of magnitude higher than radicals distant from the metal center. Measurement of the microwave power at half saturation ($P_{1/2}$) revealed that F_nY_{122}•s have values that are 20- to 75-fold lower than that of Y_{122}• (0.37-0.68 mW for F_nY_{122}•s compared to 28 mW for Y_{122}•, Table 7.2). Previous studies on NO_2Y_{122}• indicate that this mutation caused a mere 2-fold reduction in $P_{1/2}$ (11.4 mW).[2] In fact, the saturation properties of F_nY_{122}•s much more closely resemble those of the more distal pathway radicals, $DOPA_{356}$• and NH_2Y_{730}• (Table 7.2), than they do the native Y_{122}•.[6,24] This suggests a distinct electronic environment between the native cofactor and the F_nY_{122}•s. Efforts are underway to crystallize the $Y_{122}F_nY$-β2s in an attempt to better understand the subtle electronic and structural differences between these mutants and the wt-β2 (Dr. Nozomi Ando and Michael Funk, Drennan lab, MIT).

We next sought to recreate the experimental F_nY_{122}• EPR spectra via simulation. After providing the software an experimental spectrum and its acquisition parameters, the EasyFit function of the EasySpin software was used to generate a simulation. The relevant nuclei were added to the simulation (one β-methylene proton, nuclei at the 3 and 5 ring positions, fluorines at the 2 and/or 6 ring positions, as necessary) and their hyperfine coupling constants determined by iterative least-squares fitting to the experimental spectra, (Figure 7.4, red lines) using the

previously calculated parameters for Y_{122}• and 3-FY_{122}• as starting references.[5] The derived coupling constants are given in Table 7.3. While the simulations obtained by this method provide reasonable initial fits to the data, there are some features in the experimental spectra that cannot be accurately recreated in the simulations. These features may reflect a number of things, such as unusual spatial orientations (Euler angles) of the various nuclei, or the possibility that the sample contains a heterogeneous mixture of radicals. Indeed, in the case of 2,3,6-F_3Y_{122}•, a mixture of 2,3,6-F_3Y_{122}• populations has been experimentally demonstrated (Ravichandran and Stubbe, unpublished results). Subtleties such as these are difficult to discern by X-band EPR, and thus a collaboration has been initiated with the Britt lab (University of California, Davis) to conduct HF EPR and ENDOR analyses of the F_nY_{122}•s. Data collection and spectral analysis of samples of 3,5-F_2Y_{122}• and 2,3,5-F_3Y_{122}• are ongoing (Dr. William Myers, Britt lab) to more accurately determine the molecular and electronic structure of these radicals. Furthermore, these studies should complement the protein structural information we hope to obtain by X-ray crystallography.

Figure 7.4 X-band EPR spectra for *E. coli* wt-β2 (Y_{122}•, black), $Y_{122}(3,5)F_2Y$-β2 (3,5-F_2Y_{122}•, dark blue), $Y_{122}(2,3,5)F_3Y$-β2 (2,3,5-F_3Y•, cyan), $Y_{122}(2,3)F_2Y$-β2 (2,3-F_2Y•, green), and $Y_{122}(2,3,6)F_3Y$-β2 (2,3,6-F_3Y•, purple). Spectra were recorded at 77 K and 32 μW power and normalized for radical concentration. Simulations (red) were performed in EasySpin. The 2,3,6-F_3Y• sample was prepared and analyzed by Kanchana Ravichandran, and is believed to be a mixture of different radical species.

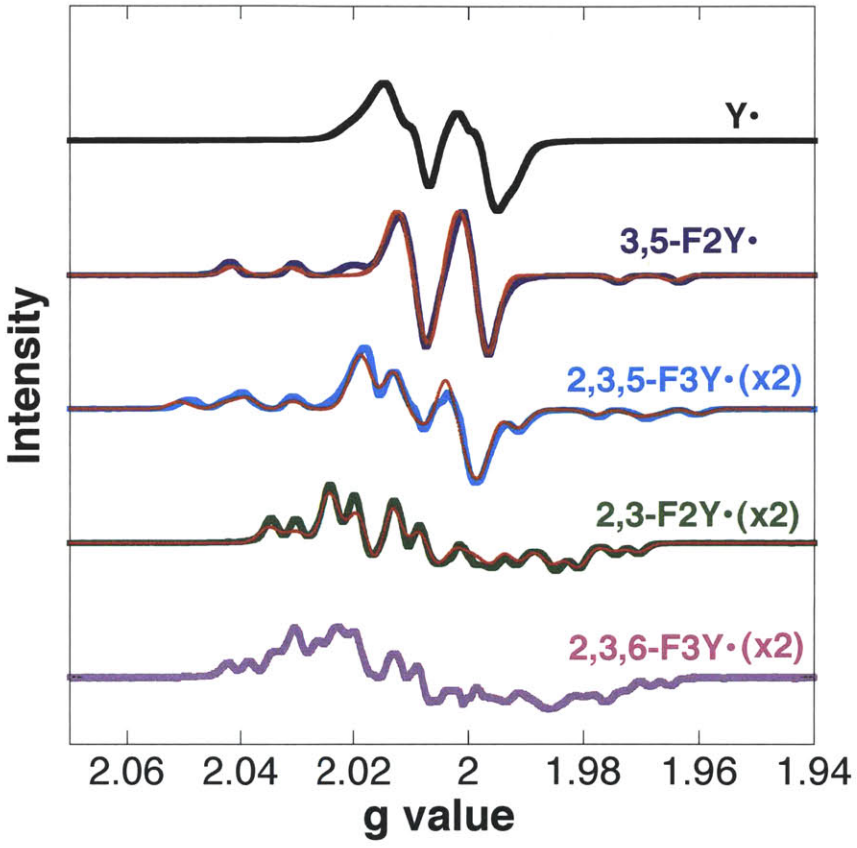

Table 7.2 Microwave power at half saturation ($P_{1/2}$) for F_nY_{122}•s compared to other known natural and unnatural Y•s on the PCET pathway. Data for 2,3,6-F_3Y_{122}• was collected by Kanchana Ravichandran. *b* is a constant that reflects the degree of spectral line homogeneity.

Mutant	$P_{1/2}$ (mW)	*b*
2,3,5-F_3Y_{122}•	0.59	0.7
2,3,6-F_3Y_{122}•	0.68	0.68
2,3-F_2Y_{122}•	0.63	0.66
3,5-F_2Y_{122}•	0.37	0.8
Y_{122}•	28.0	1.2
NO_2Y_{122}•	11.4	1.2
$DOPA_{356}$•	0.80	-
NH_2Y_{730}•	0.42	1.2

Table 7.3 EPR simulation parameters for (A) 3,5-F_2Y_{122}•, (B) 2,3,5-F_3Y_{122}•, and (C) 2,3-F_2Y_{122}•. Simulations were conducted with the EasyFit function in EasySpin[16] using the parameters for 3-FY_{122}• as a starting point.[18]

(A) 3,5-F_2Y_{122}•

Nucleus	A_x (MHz)	A_y (MHz)	A_z (MHz)
^{19}F	-21	-10	160
^{19}F	1	13	-154
^{1}H- Cβ^a	49	52	46

(B) 2,3,5-F_3Y_{122}•

Nucleus	A_x (MHz)	A_y (MHz)	A_z (MHz)
^{19}F	15	3	53
^{19}F	-15	-3	183
^{19}F	18	3	-152
^{1}H- Cβ^a	52	46	36

(C) 2,3-F_2Y_{122}•

Nucleus	A_x (MHz)	A_y (MHz)	A_z (MHz)
^{19}F –C2	6	0	50
^{19}F – C3	14	12	179
^{1}H - Cβ^a	51	53	52
^{1}H – C5	-19	-37	-21

7.3.4 Assessing the stability of F_nY_{122}•s. On the basis of the as-isolated and reconstituted F_nY_{122}• yields (Table 7.1), we hypothesized that F_nY_{122}•s are less stable than the native wt Y_{122}•, due to differences in either structure or reduction potential. A very pronounced difference in stability was observed for the NO_2Y_{122}• ($t_{1/2}$ ~40 s, 25 °C)[2] relative to the wt Y_{122}• ($t_{1/2}$ ~4 days, 4 °C). Similarly, mutations of residues in the hydrophobic pocket surrounding Y_{122}• in the wt protein have been shown to cause a 10-fold decrease in radical stability.[25] Thus, it was necessary to assess whether F_nY_{122}•s decay on the timeframe of our planned biophysical studies. To test the stability of the initial radical formed upon reconstitution, a sample was frozen immediately (t <30 s) after O_2 addition to the Fe(II)-loaded protein and a second sample was frozen 2-10 minutes later. Both samples were analyzed by EPR spectroscopy, and spin quantitation revealed no loss of total spin in the later time point. EPR samples were then thawed, and the radical stability was measured spectrophotometrically for an additional 30 to 90 minutes at room temperature. UV-vis spectra were collected of the buffered protein solution at regular intervals, and changes to the iron cluster and F_nY_{122}• were assessed by monitoring their characteristic absorbance features. $Y_{122}(3,5)F_2Y$-β2, $Y_{122}(2,3,5)F_3Y$-α2, and $Y_{122}(2,3)F_2Y$-β2 have absorbance features for their corresponding F_nY_{122}•s at 396 nm, 404 nm, and 410 nm, respectively (Table 7.1), slightly blue shifted from the λ_{max} values determined for 3,5-F_2Y• (395 nm), 2,3,5-F_3Y• (400 nm), and 2,3-F_2Y• (408 nm) generated by transient absorption spectroscopy on benzophenone(BPA)-F_nY-OMe dipeptides.[5] No changes were observed over this time, indicating that the diferric clusters and F_nY_{122}•s of $Y_{122}F_n$Y-β2s were stable for more than >60 min at 25 °C. Furthermore, no loss in radical content was observed during long-term protein storage (-80 °C) or when the protein was subjected to five freeze/thaw cycles.

7.3.5 Activity assays of $Y_{122}F_nY$-β2s. We next sought to examine the nucleotide reductase activities of the various $Y_{122}F_nY$-β2s. Previous studies have indicated that the potent oxidant NO_2Y_{122}•, formed upon rapid cofactor assembly in the protein $Y_{122}NO_2Y$-β2 (1.2 NO_2Y•/β2), conducts a single turnover in which it generates 0.6 dCDP/α2 with a rate constant of >100 s^{-1}.[2] At present the stoichiometry of product formation is not entirely understood, but is consistent with the previously observed half-site reactivity of the enzyme, as 50% of the total NO_2Y_{122}• formed (1.2 NO_2Y•/β2) is converted to dCDP. Similarly, it is not known whether the enzyme can only catalyze a single turnover as a result of either the inability to re-oxidize NO_2Y^- at position 122 because of the difference in reduction potential between Y and NO_2Y^- or because of the loss of proton-coupling to ET.

Given the unexpected results with $Y_{122}NO_2Y$-β2, we sought to determine the activity of $Y_{122}F_nY$-β2s and compare the reactivity of the potent NO_2Y_{122}• oxidant to the intermediate potential oxidants, F_nY_{122}•s. The activities of $Y_{122}F_nY$-β2s were measured in the steady state by both the spectrophotometric and radioactive assays. In all cases, the assays were linear over 2 minutes, indicating that all mutants were capable of conducting multiple turnovers. The averaged results of these two methods are given in Table 7.4.

Table 7.4 Specific activities of $Y_{122}F_nY$-β2s as determined by the spectrophotometric and radioactive assays for nucleotide reduction.

Sample	Y•/β2	Spec Act (nmol/min/mg)	k_{cat} (s^{-1})	Spec Act (scaled)[a]	% wt
wt	1.2	6500	9.4	n/a	100
3,5-F_2Y	0.2	1100	1.6	6600	100
2,3,5-F_3Y	0.4	580	0.8	1740	27
2,3-F_2Y	0.5	280	0.4	672	10
2,3,6-F_3Y[b]	0.4	250	0.4	750	11

a. The "scaled" column indicates the activity after accounting for different radical content between wt-β2 and the $Y_{122}F_nY$-β2s; *b.* Data collected by K. Ravichandran. Assay becomes nonlinear within 30 s of initiation. Activity reported is that measured in the linear region.

To account for the different radical content among the mutants and between the mutants and wt-β2, a scaling term was applied to extrapolate the activity of each mutant to a hypothetical radical content of 1.2 F_nY_{122}•/β2, as 1.2 Y_{122}•/β2 is the radical stoichiometry routinely observed in recombinantly expressed wt-β2. It is widely accepted that the activity of wt-β2 scales with its radical content up to at least 1.2 Y•/β2, though the ability to scale above this (i.e., to a hypothetical maximum of 2.0 Y•/β2) remains in question.[26,27] To test whether this was true for $Y_{122}F_nY$-β2s, activity assays were conducted on two different preparations of the enzyme containing different radical content (0.2 vs. 0.4 3,5-F_2Y_{122}•/β2). As predicted, the measured specific activity of the latter sample was twice as high as the former (Ravichandran and Stubbe, unpublished results). Thus, the assumption that $Y_{122}F_nY$-β2 activity scales linearly with radical (up to 1.2 Y•/β2) appears to be valid under conditions in which β2 is the limiting subunit.

The data in Table 7.4 indicate clear differences in activities among the three mutants. Thus, we questioned whether these differences relate to the redox properties of the various F_nYs. pH titrations of the mutant $Y_{122}NO_2Y$-β2 indicated that its phenolic pK_a at position 122 is perturbed by >2.5 units.[4] This perturbation is likely due to the highly hydrophobic environment surrounding the radical, and may be thermodynamic or kinetic in nature. For this discussion and the remainder of the chapter, we will assume that F_nYs incorporated at position 122 experience a comparable pK_a shift. However, we note that the nature of fluorine bonding is unique in the protein environment and poorly understood,[28] and the chemical and pharmacological changes induced upon addition of fluorine to small molecules have been well-documented, especially among organofluorine pharmaceuticals.[29] Thus, the assumption that NO_2Y and F_nYs experience identical pK_a perturbations may be a flawed one. Unfortunately, the λ_{max} of both F_nY and F_nY^- (260-280 nm) overlap with the normal protein absorbance envelope, making pH titrations like

those conducted on NO_2Y-containing RNRs impossible. The peak potentials (E_ps) of Y, W, NO_2Y and F_nYs as a function of pH have been examined previously by solution differential pulsed voltammetry (DPV) of N- and C-terminally protected amino acids.[5,30] At a solution pH of 7.6, where RNR assays are typically conducted, we see a mixture of protonated and deprotonated phenols, and a trend in E_p of NO_2Y>F_4Y>2,3,6-F_3Y>W>2,3,5-F_3Y>2,3-F_2Y>Y>3,5-F_2Y (Figure 7.5, dashed gray line). However, if position 122 experiences a >2.5 unit pK_a perturbation, we must examine the protonation states and E_ps at a solution pH of ~5 on Figure 7.5 (dotted line). If a pH 7.6 reaction has an effective pH of 5 at position 122, we can assume that all F_nYs are protonated and can examine the relative, pH-independent redox potentials of F_nYs relative to Y, W, and NO_2Y. Under this assumption, we calculate the redox potentials of F_nYs vary from that of Y by the values given in Table 7.5. By examining activity as a function of reduction potential perturbation, we see that lowering the potential at 122 by a small amount by the 3,5-F_2Y_{122} mutation does not interfere with the steady-state rate of deoxynucleotide formation. There is a noticeable trend towards decreasing specific activity with increasing potential at 122 to the point that the assay rapidly becomes nonlinear with Y_{122}(2,3,6)F_3Y-β2 and that the enzyme can perform only a single turnover with $Y_{122}NO_2$Y-β2 (Table 7.5). However, the change in specific activity compared to the change in E_p among the mutants does not demonstrate Nerstian behavior, indicating that differences in steady-state k_{cat} do not directly report on differences in driving force at 122. The fact that the specific activities of Y_{122}(2,3,5)F_3Y-β2 and Y_{122}(2,3)F_2Y-β2 are reduced, but that the enzymes are still active for multiple turnovers is interesting, as it suggests that the kinetics of radical propagation and deoxynucleotide formation could perhaps be perturbed in a mechanistically informative way. Thus, we sought to explore these reactions further by examining the kinetics of dCDP formation by rapid chemical quench (RCQ) studies.

Figure 7.5 Solution reduction potential (vs NHE) as a function of pH for N-Ac-F_nY-NH_2s, as determined by DPV (*left*). The dashed line indicates a solution pH of 7.6 which is routinely used for RNR assays. The dotted line indicates a pH of 5, which is the effective pH at position 122 under normal assay conditions given the known pK_a perturbation at this site (>2.5 units). An expanded view of the DPV data from pH 4-9 (*right*). Adapted from references 5, 17, and 30.

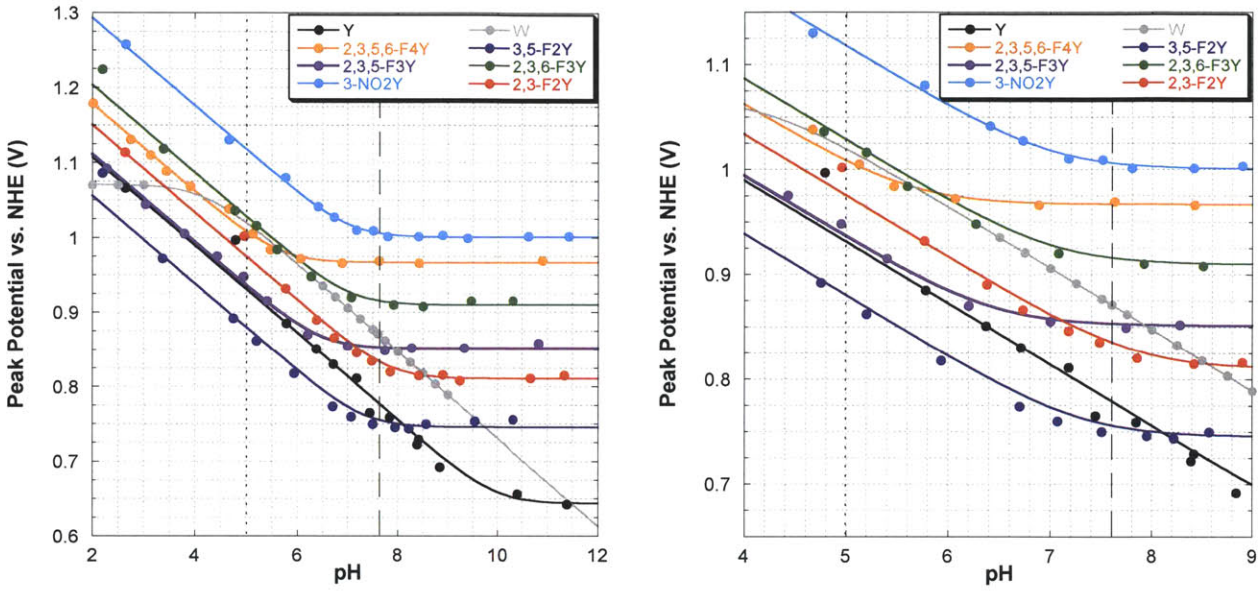

Table 7.5 Peak potentials of F_nYs and NO_2Y relative to Y and specific activities of $Y_{122}F_n$Y-β2s.

	ΔE_p (mV) (vs. Y•/Y)[a]	Specific activity (% wt β2)[b]
Y	-	100
3,5-F_2Y	-50	100
2,3,5-F_3Y	+10	25
2,3-F_2Y	+45	10
2,3,6-F_3Y	+100	11[c]
NO_2Y	+190	-[d]

a. Proposed difference at position 122, measured from the pH-independent region of Figure 7.5; *b.* Specific activity as a percent wild-type activity, after scaling for differences in radical content; *c.* The steady-state assay of this mutant becomes nonlinear after 30 s. *d.* Not capable of multiple turnovers.

7.3.6 Kinetics of dCDP formation in $Y_{122}(2,3,5)F_3Y$-β2 monitored by RCQ and identification of a second product formed in the reaction . Previously, rapid chemical quench (RCQ) experiments were conducted on wt RNR to determine the kinetics of dCDP formation under single turnover conditions. These experiments indicated a burst phase in which 1.7 dCDP/α2 were formed with a rate constant of 2-10 s^{-1}. This rate constant was determined to report on a rate-determining conformational change that masked the kinetic details of radical propagation and nucleotide reduction chemistry. The results of analogous RCQ experiments for the reaction of $Y_{122}NO_2Y$-β2, wt-α2, CDP, and ATP were very exciting, as they indicated rate constants of dCDP formation of >100 s^{-1}. The uncoupling of PT from ET in this mutant apparently freed the system from the conformational gating that is rate-limiting in the wt, and allowed the first kinetic measurements of a intermediate radical formation on a native pathway residue (Y_{356}•). However, several lines of evidence support the conclusion that the rate constant of 100 s^{-1} is still reporting on a conformational change (Yokoyama and Stubbe, unpublished results). Measuring of the kinetics of Y_{356}• formation in the reaction of $Y_{122}NO_2Y$-β2, wt-α2, CDP, and ATP in the presence of various glycerol concentrations shows a dependence on viscogen that is consistent with a conformational change.[31] Furthermore, the reaction of $Y_{122}NO_2Y$-β2 with $Y_{731}NH_2Y$-α2, CDP, and ATP monitored by RFQ-EPR indicated the formation of NH_2Y_{731}• at ~100 s^{-1}, suggesting that this rate constant was not associated with pure ET or with the chemistry of nucleotide reduction.

Like NO_2Y, the site-specific insertion of 2,3,5-F_3Y at position 122 raises the driving force of radical initiation, but the extent of perturbation is much smaller (10 mV versus 190 mV). $Y_{122}(2,3,5)F_3Y$-β2 displays a steady-state activity that is reduced relative to wt-β2, yet unlike $Y_{122}NO_2Y$-β2 it is capable of doing many turnovers. Thus, it was interesting to examine the

kinetics of dCDP formation in this mutant to determine whether the chemistry is conformationally gated as in the wt (2-10 s^{-1}) or as in the proton-decoupled $Y_{122}NO_2Y$-β2 (>100 s^{-1})?[1,2] Or is it possible that, by changing the thermodynamics of radical initiation, we observe a distinct rate constant that reports on the details of radical propagation? To address these questions, we examined dCDP formation in the reaction of $Y_{122}(2,3,5)F_3Y$-β2, wt-α2, CDP, and ATP under single turnover conditions using the RCQ method.

A complexity in this experiment arises from the substoichiometric radical content in $Y_{122}(2,3,5)F_3Y$-β2 (0.4 $F_3Y\bullet$/β2). The experiment could be designed such that there is a 1:1 stoichiometry between the subunits or between α2 and $F_3Y\bullet$ (i.e., 1:3 α2 to β2). In this case, we chose the latter. The effect of the F_nY-to-α2 ratio is explored in more detail in section 7.3.7. The averaged results of two kinetic traces from 5 ms to 40 s are shown in Figure 7.6. The most striking feature of the data is the stoichiometry of dCDP formation. At 40 s, the reaction has generated 3.2 dCDP/α2, on par with what is routinely observed in the analogous RCQ reaction between wt-α2 and wt-β2 (~3.5 dCDP/α2).[1] However, the predicted plateau in product formation that one would expect for a single-turnover experiment is not observed, as the data indicate that product is continuing to increase beyond the 40 s reaction course. Indeed, a 100 s hand-quenched reaction performed in parallel with this RCQ experiment indicated a total of 5.6 "dCDP"/α2! A stoichiometry of 4 dCDP/α2 is the theoretical limit of product formed under single turnover conditions, as the four C-terminal cysteine residues of each α monomer provide the reducing equivalents for two CDP reductions per active site (though in practice a stoichiometry of ~3-3.5 dCDP/α2 is more routinely observed, likely due to some irreversible protein oxidation during isolation). Thus, a product stoichiometry of >4 "dCDP" per α2 is not possible, and implies that an alternative product is being generated. While this result was

surprising, it is not unprecedented. Similar behavior has been observed previously in studies of the mechanism of RNR inactivation by the mechanism-based inhibitor (MBI) 2′-chloro-2′-deoxyuridine and in the C_{225}S-α2 mutant.[32,33] In these systems, the substrate was observed to slowly decompose to release base, inorganic phosphate, and 2-methylene-3(2H)-furanone as shown in eq. 7.2 (where X = Cl for wt RNR or OH for C_{225}S-α2). As described in the subsequent section, dC and cytosine are not readily distinguishable in our assay given the location of the radiolabel on the CDP substrate and the chromatographic method routinely used to separate product (dCDP) from unreacted CDP. Thus, we hypothesized the second product to be cytosine, and subsequently confirmed this suspicion as described in section 7.3.7.

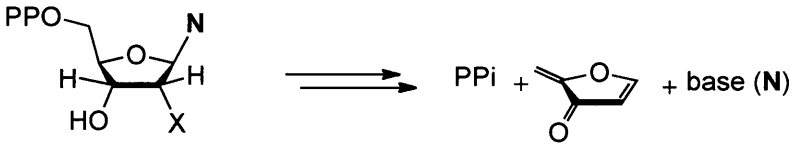

eq. 7.2

Returning to the RCQ kinetic trace (Figure 7.6), we observe that product is formed with biphasic kinetics. In the fast phase, 1.8 eq of product per α2 are formed with a rate constant of 2.4 s^{-1}. This phase is identical in amplitude to what has been reported previously for the wt enzyme, and is on the slower end of the range of rate constants reported for the conformational change.[1] Thus, the first phase of product formation in the mutant looks to behave as wt-β2, suggesting that the product formed in this phase is dCDP and that that the chemistry of nucleotide reduction is gated by conformational change(s) similar to that(those) that kinetically gate the wt enzyme.

In the second, slower phase, an additional 2.2 eq of product are formed per α2 are with a rate constant of 0.025 s^{-1}. While this slow phase is slower than the steady-state turnover number of Y_{122}(2,3,5)F_3Y-β2 (0.8 s^{-1}) and thus likely not mechanistically informative to catalysis, it is

necessary to identify this additional product and incorporate its formation into any complete mechanistic model for radical initiation by F_nY_{122}•s.

7.3.7 Determining the stoichiometry and identity of product(s) formed in $Y_{122}F_nY$-β2s under steady-state and single-turnover conditions. The observation that $Y_{122}(2,3,5)F_3Y$-β2 forms more than the theoretical maximum of dCDP/α2 necessitated the chemical identification of the product formed. The radioactive assay sample workup relies on the use of borate anion-exchange chromatography to separate 2′-deoxycytidine (dC, dephosphorylated product) from cytidine (dephosphorylated substrate). The latter chelates the borate-charged resin through its vicinal diol, while the former is collected in the column flow through and is quantitated by scintillation counting. When the enzyme is operating "normally," dC is the only radiolabeled compound in the column flow through. However, as noted above, there is precedent for base release accompanying enzyme inactivation in the presence of either mechanism-based inhibitors or active-site mutants of α2 (eq. 7.2).[32-35] Cytosine would thus co-elute with dC under normal radioactive assay workup,[19] and given that the radiolabel is located at the 5 position of the base, the both molecules will contribute during scintillation counting. In order to distinguish the two products, subsequent HPLC analysis of the borate column eluate was necessary.

The product formed under steady-state assay conditions was first analyzed by this method. Product formation is linear in these assays over the course of two minutes, suggesting that no significant inactivation occurs in the present of the TR/TRR/NADPH reducing system. Samples from the discontinuous steady-state assay were taken at t = 30 s and t = 2 min, dephosphorylated and chromatographed as usual, lyophilized in the presence of carrier cytosine and dC, redissolved, and injected on a C-18 HPLC column. Prior analysis of molecular standards indicated that cytosine and dC elute with retention times of 3.6 and 8.5 min,

respectively. The results obtained with wt-β2 and a representative mutant, $Y_{122}(2,3,5)F_3Y$-β2, are shown in Figure 7.7. The other $Y_{122}F_nY$-β2s behave similarly to $Y_{122}(2,3,5)F_3Y$-β2. In all samples for both the wt and mutants, a radioactive component is present that elutes just after the void volume. The amount of this sample is constant among all mutants and all time points, suggesting that it is associated with a radiochemical impurity in the [^{3}H]-CDP used, rather than cytosine release. This contaminant constitutes 0.4% of the total radioactivity in the assay reaction mixture, and once quantitated, was ignored in further analysis. In both the wt and the mutant, a linear increase in dC formation with time is observed. Indeed, when one calculates the number of moles of dC corresponding to each of the t = 8.5 min peaks, specific activities are extrapolated that are identical to those reported in Table 7.4. Thus, product analysis supports the conclusion that $Y_{122}F_nY$-β2s form dCDP as their sole product under multiple-turnover conditions (i.e. in the presence of the native protein reducing system).

The observation that product formation in steady-state activity assays of the $Y_{122}(2,3,6)F_3Y$-β2 mutant becomes nonlinear within 30 s (Table 7.4, Ravichandran and Stubbe, unpublished work) prompted us to examine the steady-state activities of $Y_{122}F_nY$-β2s over longer times, as this result suggests some fraction of enzyme inactivation. The concentration of enzyme in the assay was lowered and the concentration of CDP increased so that <50% of the product would be consumed over 15 min assuming 100% wt-β2 activity. The results of assays conducted over 15 min are shown in Figure 7.8. Product formation is linear over that time for both wt β2 and $Y_{122}(3,5)F_2Y$-β2 (Figure 7.8 A). However, consistent with the observation with $Y_{122}(2,3,6)F_3Y$-β2, a loss of linearity is observed for $Y_{122}(2,3,5)F_3Y$-β2 and $Y_{122}(2,3)F_2Y$-β2 after several minutes (Figure 7.8 B). Product analysis of the t = 15 min time point by the HPLC method described above indicates that dC is formed as the exclusive product under multiple-

turnover conditions, even in the non-linear region. Thus, $Y_{122}F_n$Y-β2s continue to generate dCDP with high fidelity under multiple turnover conditions despite some amount of slow uncoupling. These results are summarized in Table 7.6.

Figure 7.6 Kinetics of dCDP formation in the reaction between $Y_{122}(2,3,5)F_3Y$-β2, wt-α2, CDP, and ATP under single turnover conditions at 25 °C monitored by RCQ. Error bars indicate the standard deviation between two experiments. Rate constants and amplitudes are described in the text. The data are plotted in (A) linear (*inset*: expanded view of first 6 s) and (B) log scales.

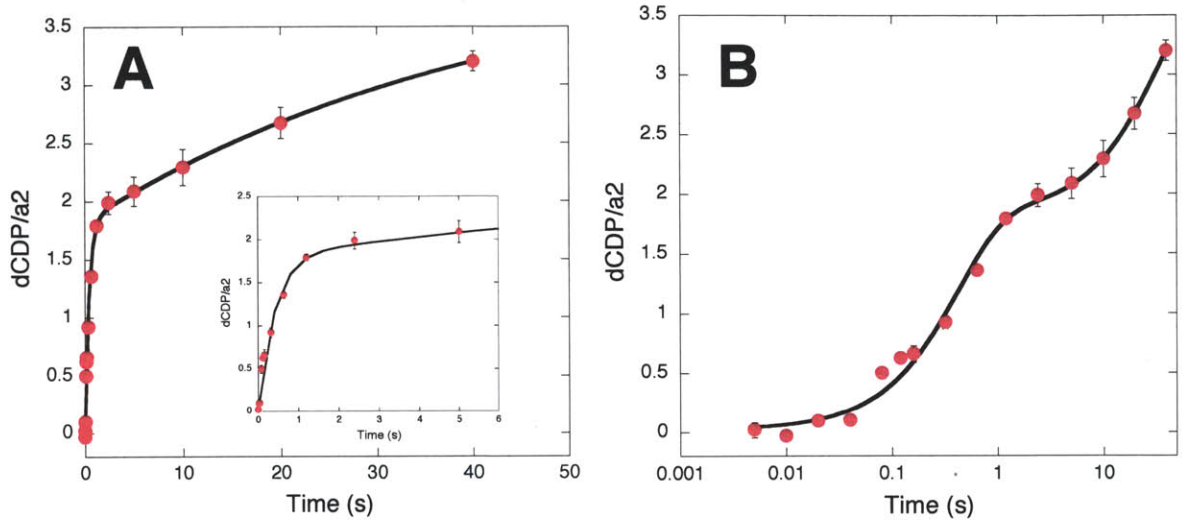

Figure 7.7 HPLC analysis of product formation in the steady-state reaction of wt-α2 with (A) wt-β2 and (B) $Y_{122}(2,3,5)F_3Y$-β2. Blue/cyan and red/orange traces are t =30 s and t = 2 min timepoints, respectively, in the discontinuous assay. Absorbance profiles (solid red and blue lines) arise from the addition of equimolar carrier cytosine and dC into all samples prior to lyophilization. Radioactivity associated with each fraction shown in cyan and orange dots. A small radiochemical impurity elutes with cytosine near the void volume, as described in the text.

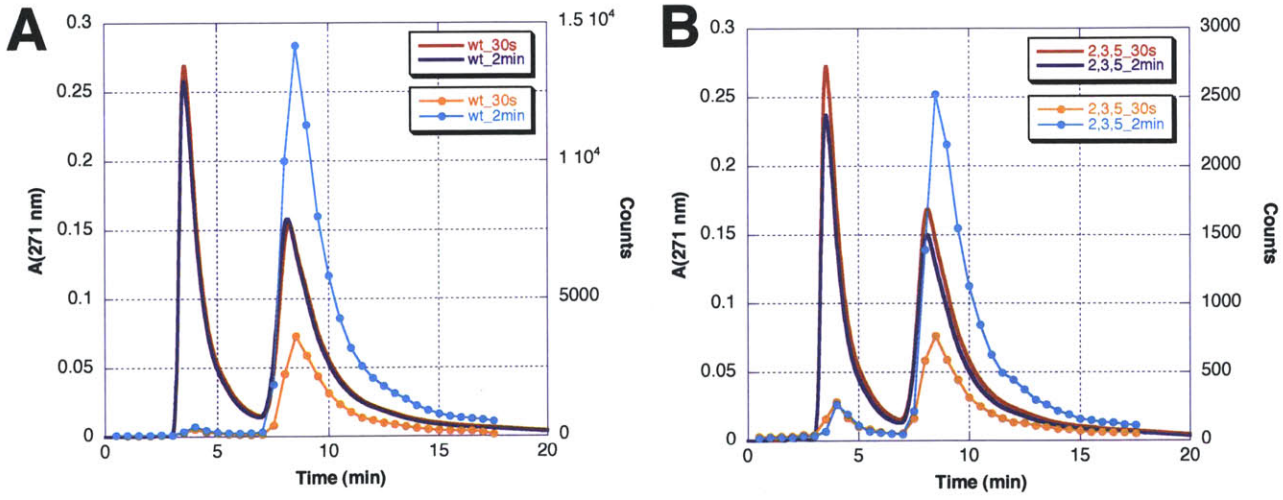

Figure 7.8 Product formation over long times in steady-state assays of wt-β2 and $Y_{122}F_nY$-β2s. (A) Product formation for wt-β2 (red dots) and $Y_{122}(3,5)F_2Y$-β2 (blue) are linear (black line) over 15 min; (B) An expanded view of the Y-axis (raw scintillation counts) highlights the loss of linearity at long times in $Y_{122}(2,3,5)F_3Y$-β2 (purple) and $Y_{122}(2,3)F_2Y$-β2 (green).

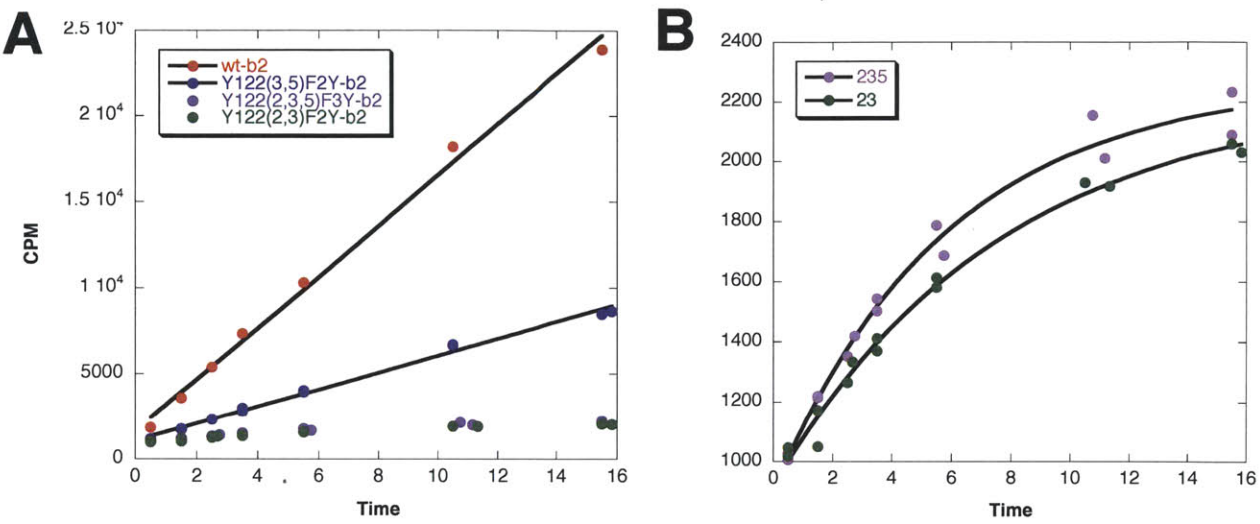

Table 7.6 Analysis of product formation in $Y_{122}F_nY$-β2s under single- and multiple-turnover conditions.

	$F_nY\bullet$ $t_{1/2}$ (4 °C)	SS activity (<2 min)	SS activity (2-15 min)	Product under multiple turnover conditions	Product under single turnover conditions
Y	>days	L	L	dCDP only	2-2.9 dCDP/α2
3,5-F_2Y	>h	L	L	dCDP only	2-2.8 dCDP/α2[c]
2,3,5-F_3Y	>h	L	NL	dCDP only[b]	2 dCDP/α2[c,d] 0.5-5.0 cytosine/α2[e]
2,3-F_2Y	>h	L	NL	dCDP only[b]	2 dCDP/α2[b] 0.5-5.0 cytosine/α2[e]
2,3,6-F_3Y	>1/2 h[f]	NL	NL	dCDP only[b]	2.5-3 dCDPs/α2[g]

a. "L" indicates linear, "NL" indicates non-linear; *b.* dCDP was the only product in all cases, even in the non-linear region of the steady-state assay; *c.* The quantitation of dCDP/α2 was the same regardless of whether α2 was stoichiometric to β2 or $F_nY_{122}\bullet$; *d.* 2 dCDP/α2 are formed with a rate constant of 2.4 s^{-1}, as determined by RCQ; *e.* Cytosine increases with respect to time and $F_nY\bullet$ content (0.5-5.0 eq/α2). It is likely that additional eq of this product would be formed if the reaction were allowed to progress for >5 min; *f.* The first radical decays within 3 minutes, while the second radical is stable for at least 30 min; *g.* The same number of dCDPs are seen in the presence and absence of the first radical.

We next examined the reaction of $Y_{122}F_nY$-β2s with wt-α2, CDP, and ATP under single turnover conditions. The RCQ results with $Y_{122}(2,3,5)F_3Y$-β2 presented above already suggested that the enzyme was demonstrating unusual behavior in the absence of reductant. Thus, we sought to analyze all $Y_{122}F_nY$-β2s under single-turnover conditions by hand-quench assays. Two variables were explored in the hand-quench assays: the length of the reaction (30 s or 5 min) and the effect of $Y_{122}F_nY$-β2 concentration. The former was investigated as RCQ results indicate that the product formed in the slow phase is generated with a rate constant of 0.025 s^{-1}, and thus very long time points needed to be examined. The latter was investigated to address the question of substoichiometric radical content in $Y_{122}F_nY$-β2s, i.e., to determine whether an effect was observable when the assay was conducted with 1:1 α2:β2 or 1:1 α2:F_nY_{122}•. The results are given in Table 7.6 and indicate that $Y_{122}(3,5)F_2Y$-β2 behaves identically to wt-β2 at long and short times, and that 2.0-2.8 dCDP/α2 are formed regardless of radical concentration. This is an important observation, as the fact that substoichiometric radical can generate maximum product indicates that the radical is catalytic in turnover in this mutant, and that α2/β2 association/dissociation constants and radical propagation are fast relative to the rate-determining step. In other words, one β2 may rapidly associate and dissociate with several different α2 subunits and provide a catalytic oxidant, F_nY_{122}•, to each to initiate nucleotide reduction.

$Y_{122}(2,3,5)F_3Y$-β2 and $Y_{122}(2,3)F_2Y$-β2, however, behave quite distinctly from wt-β2 and the 3,5-F_2Y mutants (Table 7.6 and Table 7.7). For these mutants, an increase in product formation is observed with both time and with increasing [F_nY_{122}•]. The increase with time is consistent with what has been observed previously by RCQ (Figure 7.6). Importantly, these assays are support a conclusion in which more product molecules are being generated than the

theoretical maximum of dCDP/α2 allowed in the absence of reductant. Thus, we investigated the identity of the product formed under each condition by HPLC assays. Again, all samples demonstrated an identical radiochemical impurity eluting at 4.5 min as determined by HPLC product analysis of a blank sample in which β2 was omitted from the reaction mix (Figure 7.9 A). This impurity co-elutes with cytosine, and thus was subtracted from all subsequent cytosine quantitation. The elution profile of products formed from the reaction with $Y_{122}(3,5)F_2Y$-β2 (Figure 7.9 B) is super-imposable at t=30 s and t=5 min, and is nearly identical to that of wt-β2 at the same times (data not shown), confirming that this mutant, like wt-β2, generates dCDP exclusively (Table 7.6 and 7.7). This is in contrast to what was observed with $Y_{122}(2,3)F_2Y$-β2 and $Y_{122}(2,3,5)F_3Y$-β2. In these mutants, 2 dCDP/α2 are formed within 30 s and no additional dC is formed over the 5 minute time course (Figure 7.9 C and Table 7.7). Additionally, anywhere from 0.5-5 additional eq of cytosine are formed per α2, with the number of equivalents increasing with the time of the reaction and the concentration of F_nY_{122}• (Table 7.7). We assign this product as cytosine based on the co-elution of radioactivity with the carrier cytosine, and on the knowledge that base release is a common feature in the mechanism of RNR inactivation (eq. 7.2).[35,36] However, given that this product elutes so close to the column void volume, it should be characterized it further by UV-vis spectroscopy, MS, and TLC analysis to confirm its identity.

One possible mechanism to account for the stoichiometry of product formation and the observation of cytosine release in $Y_{122}(2,3,5)F_3Y$-β2 and $Y_{122}(2,3)F_2Y$-β2 is presented in the Discussion. This hypothesis takes into account both precedence from studies of MBIs, and recent measurements of the rate of re-oxidation of F_nY_{122}•s by Y_{356}• (*vide infra*, section 7.3.9). Importantly, we conclude that dC is the only product formed by $Y_{122}F_nY$-β2s in the presence of reductant (Table 7.6), suggesting that the mutants catalyze nucleotide reduction in a similar

fashion to wt-β2 under multiple-turnover conditions and that these mutants may be used as only mild to moderate perturbants of the native system.

Table 7.7 Relative ratio of two products formed by $Y_{122}F_nY$-β2s under single turnover conditions as determined by HPLC analysis.

Sample	[α2] (μM)	[F_nY_{122}•] (uM)	Time (s)	dC/ α2	cytosine/ α2
wt	2	2.4	300	1.8	0.0
3,5	2	0.4	30	1.8	0.0
	2	0.4	300	1.8	0.0
	2	2	30	1.7	0.1
	2	2	300	1.7	0.0
2,3,5	2	0.8	30	1.9	0.5
	2	0.8	300	2.1	2.3
	2	2.4	30	1.9	1.2
	2	2.4	300	2.1	4.7
2,3	2	1	30	1.9	0.8
	2	1	300	2.0	3.0
	2	2	30	1.9	1.3
	2	2	300	2.1	5.0

Figure 7.9 HPLC analysis of product formation under single turnover conditions of wt-α2 with (A) no β2 (i.e., assay blank), (B) $Y_{122}(3,5)F_3Y$-β2, or (C) $Y_{122}(2,3)F_2Y$-β2. Panel A highlights the radiochemical impurity that elutes at 4.5 min that contaminants all samples. Assays shown in panel B and C contain equimolar α2 and F_nY_{122}•. Red/orange and blue/cyan and traces are 30 s and 5 min timepoints, respectively. Absorbance profiles (solid red or blue lines) arise from the addition of carrier cytosine and dC into all samples prior to lyophilization. Radioactivity associated with each fraction shown in orange or cyan dots. In reaction (B), all radioactivity at 4.5 min (~600 counts) is accounted for by the impurity. In reaction (C), a fraction of each 4.5 min peak (~600 counts) is impurity, while the remainder of the radioactivity is associated with cytosine release. Note that the right *y*-axis (counts) is different among the three panels

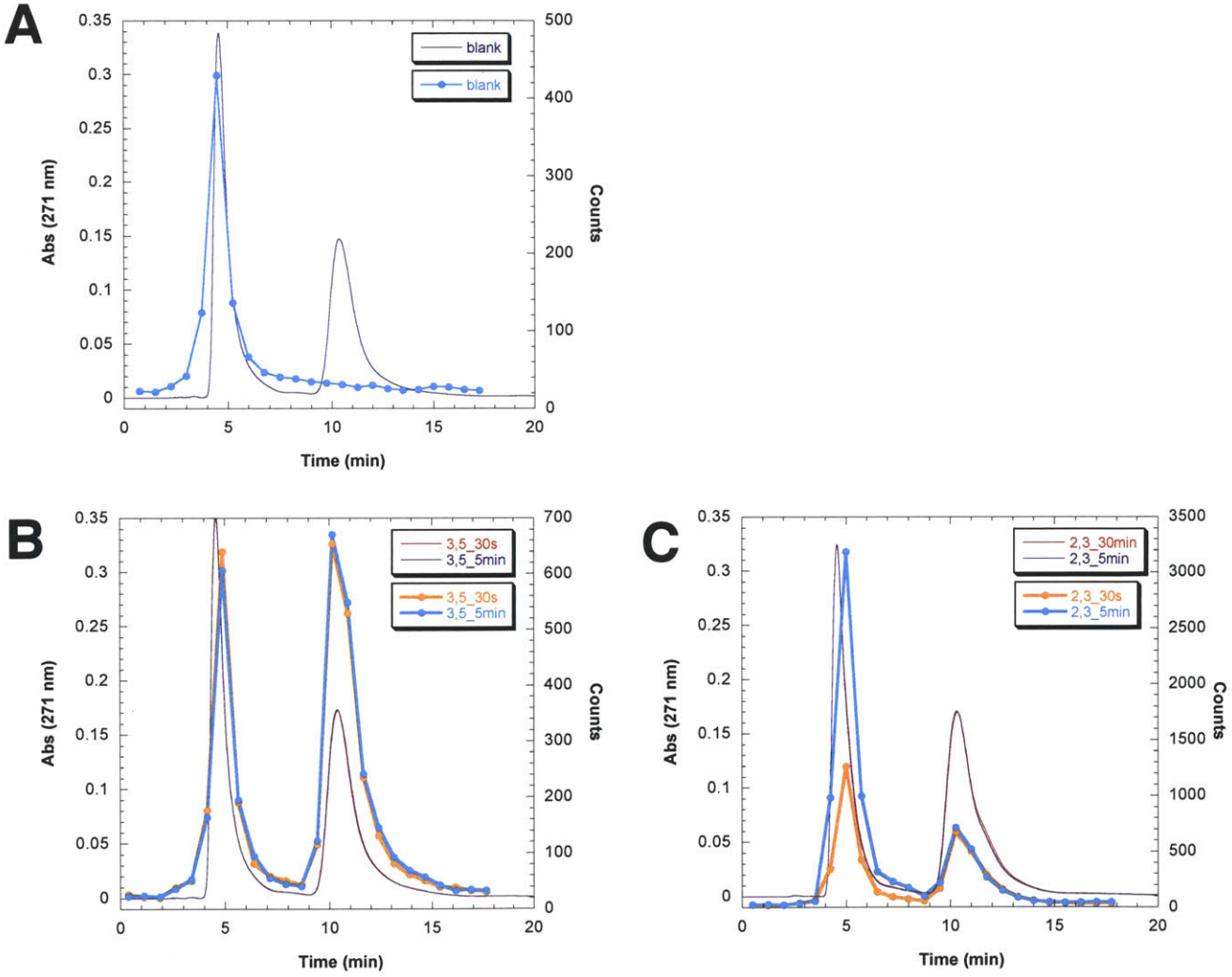

7.3.8 Using $Y_{122}F_nY$-β2s as radical initiators: looking for evidence of pathway radical intermediates by hand-quench EPR and SF UV-vis spectroscopies. As described in the introduction to this chapter, use of NO_2Y_{122}• as a highly oxidizing radical initiator results in the conversion of 50% of the initial NO_2Y_{122}• to a new "pathway radical," consistent with half-sites reactivity of RNR. This pathway radical accumulates either because of the inability of Y• to re-oxidize NO_2Y^- to NO_2Y• due to differences in redox potentials, or because of the proton-decoupling that results in the formation of a stable NO_2Y^- at position 122.[2] Extensive evidence suggests that the new radical in the NO_2Y mutant is primarily located at Y_{356} (Figure 7.1).[3]

We sought to identify whether the use of F_nY_{122}•s as radical initiators would result in pathway radical accumulation. Nucleotide reductase activity assays of $Y_{122}(3,5)F_2Y$-β2 indicated that the mutant had an activity identical to wt-β2, when scaled for differences in radical content (Table 7.4), suggesting that this mutation does not affect catalysis to an observable extent. Indeed, when $Y_{122}(3,5)F_2Y$-β2 was reacted with wt-α2, CDP, and ATP for 25 s, quenched in a dry ice/acetone bath, and examined by EPR spectroscopy, there was neither evidence of formation of a new radical, nor evidence of any spin loss over the reaction course (Table 7.8 and Figure 7.10). This is not surprising, given that incorporation of 3,5-F_2Y at position 122 is expected to lower the potential by ~50 mV at that position (assuming a 2.5 unit pK_a perturbation, Figure 7.5). However, $Y_{122}(2,3,5)F_3Y$-β2 and $Y_{122}(2,3)F_2Y$-β2 possess only 30% and 10%, respectively, the wt RNR activity (scaled for radical). This result is noteworthy, as it indicates that introduction of 2,3,5-F_3Y or 2,3-F_2Y at position 122 slightly perturbs radical propagation energetics or, more likely, the conformational changes that gate it, but not to the extent that it prevents multiple catalytic turnovers. The reactivities of these mutants were further investigated by EPR spectroscopy. A solution of $Y_{122}(2,3,5)F_3Y$-β2 was rapidly mixed with wt-

α2, CDP and ATP under single-turnover conditions (i.e., no reductant) in an EPR tube and quenched in a dry ice/acetone bath at 25 sec. The spectrum of the reaction mixture (Figure 7.11 A, blue) is a composite of two species: 2,3,5-F_3Y_{122}• (green) and a new radical (red). The new radical constitutes 25% of the total spin at t = 25 s and is assigned as Y_{356}•. (Table 7.8). This assignment was reached after conducting additional EPR experiments in which specific positions of the pathway were blocked by replacement of Y with a redox-inert F. When $Y_{122}(2,3,5)F_3Y$-β2 was reacted with $Y_{731}F$-α2, CDP, and ATP, a very similar new radical was formed in identical yield to the reaction with wt-α2 (Figure 7.11 B). Conducting the reaction with the double mutant $Y_{122}(2,3,5)F_3Y/Y_{356}F$-β2 and wt-α2 failed to yield evidence of a new radical (Figure 7.11 C). The assignment of this radical as Y_{356}• is further substantiated by its striking similarity to the X-band EPR spectrum of the radical observed when NO_2Y_{122}• is used as a radical initiator (Figure 7.12). Given that the hyperfine features of a Y• directly report on the orientation of one (or both) of its β-methylene proton(s),[37,38] the fact that the two pathway radicals are superimposable is highly suggestive of similar radical structures/environments. In the case of initiation by NO_2Y_{122}•, the identity of this radical has been convincingly assigned as Y_{356}• by PELDOR diagonal distance measurements between the new radical and Y_{122}•.[3] These measurements are consistent with those reported previously for the diagonal distance between Y_{122}• and $DOPA_{356}$•[39] and NH_2Y_{356}• (Chapter 4).

An identical radical was observed in the reaction of $Y_{122}(2,3)F_2Y$-β2 with wt-α2, CDP and ATP, and constitutes 40% of the total spin at 25 s (Table 7.8 and Figure 7.13 A). Reaction of $Y_{122}(2,3)F_2Y$-β2 with $Y_{731}F$-α2 gives 32% conversion to new radical, and reaction of the double mutant $Y_{122}(2,3)F_2Y/Y_{731}F$-β2 with wt-α2 gives no evidence of new radical (Figure 7.13 B and C, respectively).

Table 7.8 Pathway radical formation at t = 25 s in hand-quenched reactions of $Y_{122}F_nY$-β2s with α2 (wt or $Y_{731}F$-α2), CDP, and ATP

β2	α2	ΔE (mV) (vs. Y•/Y)	Y_{356}• by EPR (% initial radical)[a]	Spin loss (% initial radical)
$Y_{122}(3,5)F_2Y$	wt	-50	0[b]	0
$Y_{122}(2,3,5)F_3Y$	wt	+10	25	0
$Y_{122}(2,3,5)F_3Y$	$Y_{731}F$	+10	25	0
$Y_{122}(2,3,5)F_3Y/Y_{356}F$	wt	+10	0	0
$Y_{122}(2,3)F_2Y$	wt	+45	40	<10
$Y_{122}(2,3)F_2Y$	$Y_{731}F$	+45	32	<10
$Y_{122}(2,3)F_2Y/Y_{356}F$	wt	+45	0	0
$Y_{122}(2,3,6)F_3Y$[c]	wt	+100	50	0
$Y_{122}(2,3,6)F_3Y$[c]	$Y_{731}F$	+100	43	0
$Y_{122}(2,3,6)F_3Y/Y_{356}F$[c]	wt	+100	0	13

a. Pathway radical obtained by hand-quenching at 25 s in either dry ice/acetone or liq N_2 at 25 s. Final protein concentrations were 20-40 μM. *b.* "0" indicates that no pathway radical was observed within the lower limit of detection of the instrument (<0.5 μM for reactions with F_nY_{122}•s); *c.* Characterization of $Y_{122}(2,3,6)F_3Y$-β2 was performed by K. Ravichandran.

Figure 7.10 EPR spectrum of the reaction of $Y_{122}(3,5)F_2Y$-β2, wt-α2, CDP, and ATP hand-quenched after 25 s incubation. Subtraction of a spectrum of the 3,5-F_2Y_{122}• (red) from the reaction spectrum (blue) gives a difference spectrum (green) that is only spectral noise.

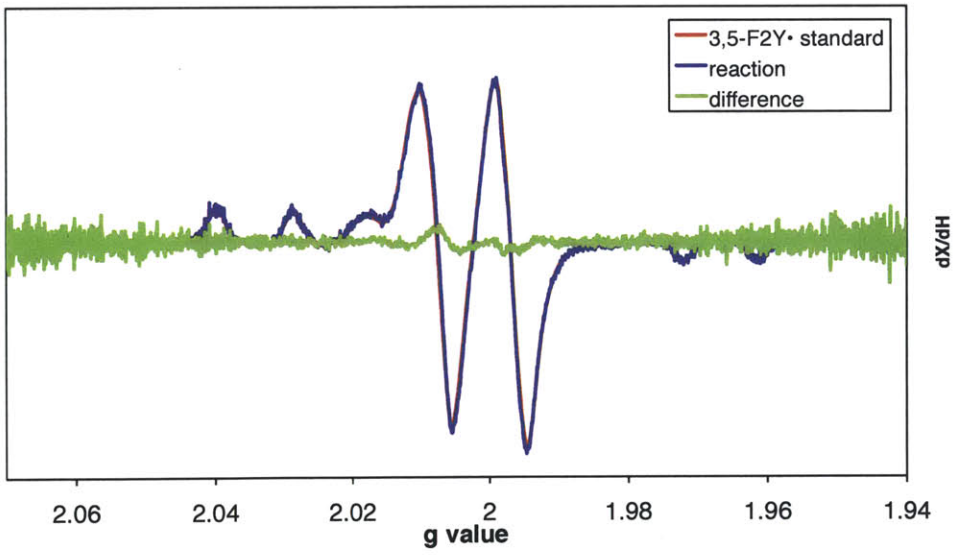

Figure 7.11 EPR spectrum of the reaction of (A) $Y_{122}(2,3,5)F_3Y$-β2, wt-α2, CDP, and ATP hand-quenched after 25 s incubation. The reaction spectrum (blue) is a composite of two species. Subtraction of a spectrum of the 2,3,5-F_3Y_{122}• (green) gives the spectrum of a new radical (red); (B) The analogous reaction between $Y_{122}(2,3,5)F_3Y$-β2 and $Y_{731}F$-α2; (C) The analogous reaction between $Y_{122}(2,3,5)F_3Y/Y_{356}F$-β2 and wt-α2. *The sharp g ~2 feature is associated with an imperfection in the N_2 finger dewar used to collect data at 77 K.

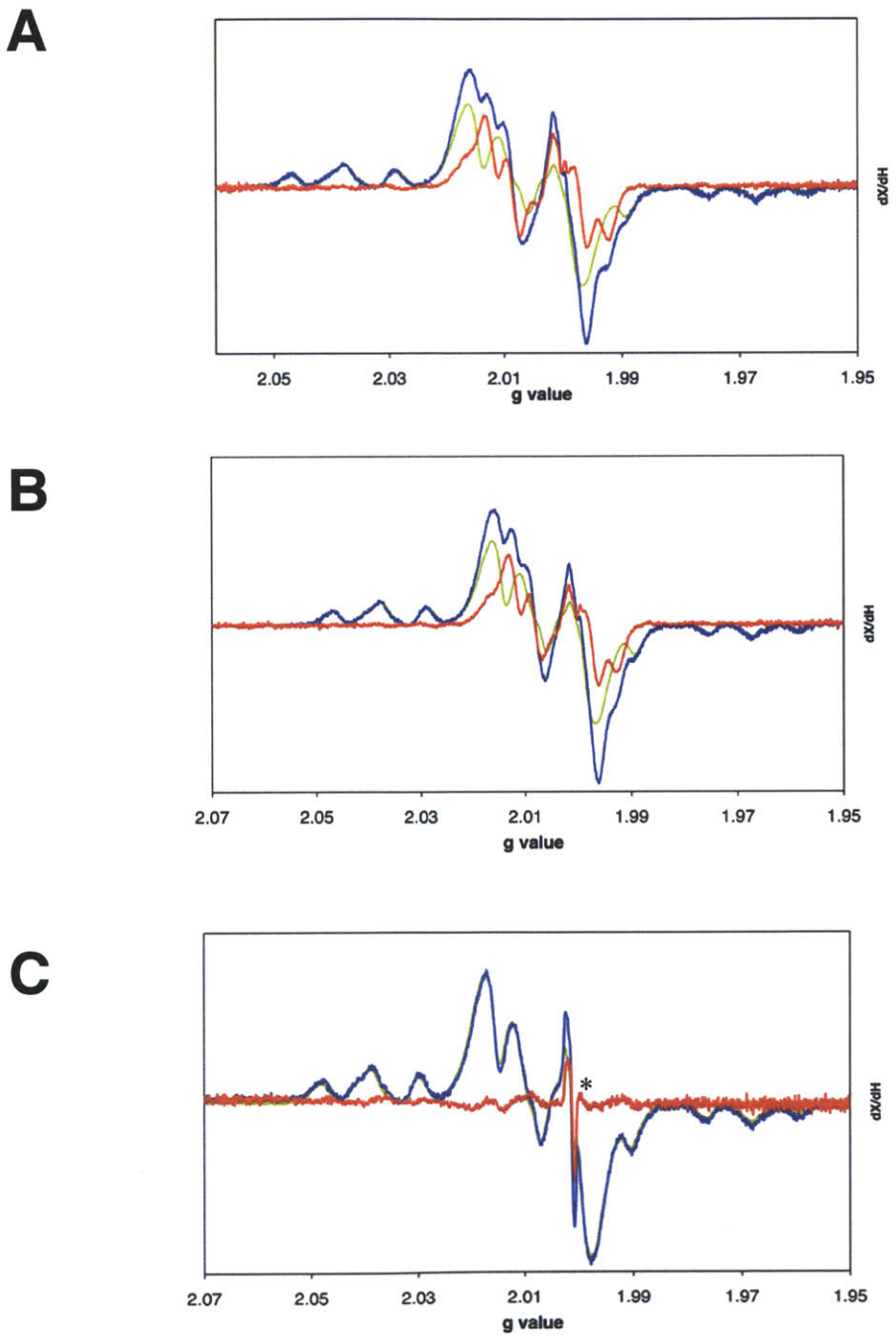

Figure 7.12 A comparison of the spectrum of the new radical formed by $Y_{122}(2,3,5)F_3Y$-β2 (blue) with the spectrum of Y_{356}• formed by $Y_{122}NO_2Y$-β2 (red) indicates significant similarity between the two species.

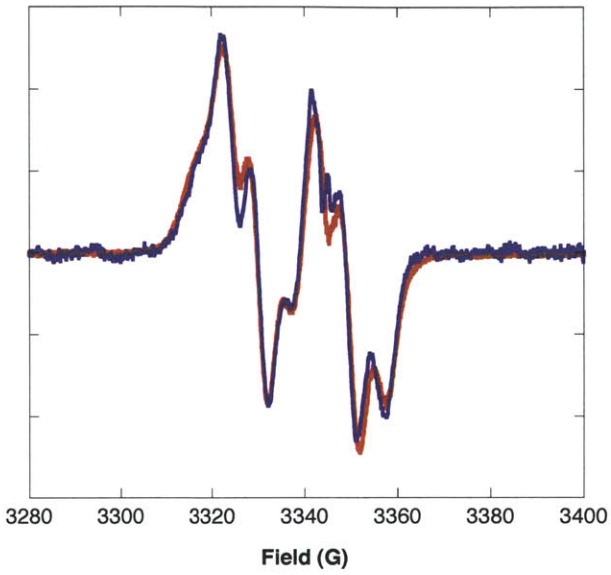

Figure 7.13 EPR spectrum of the reaction of (A) $Y_{122}(2,3)F_2Y$-β2, wt-α2, CDP, and ATP hand-quenched after 25 s incubation. The reaction spectrum (blue) is a composite of two species. Subtraction of a spectrum of the 2,3-F_2Y_{122}• (green) gives the spectrum of a new radical (red); (B) The analogous reaction between $Y_{122}(2,3)F_2Y$-β2 and $Y_{731}F$-α2; (C) The analogous reaction between $Y_{122}(2,3)F_2Y/Y_{356}F$-β2 and wt-α2. *The sharp g ~2 feature is associated with an imperfection in the N_2 finger dewar used to collect data at 77 K.

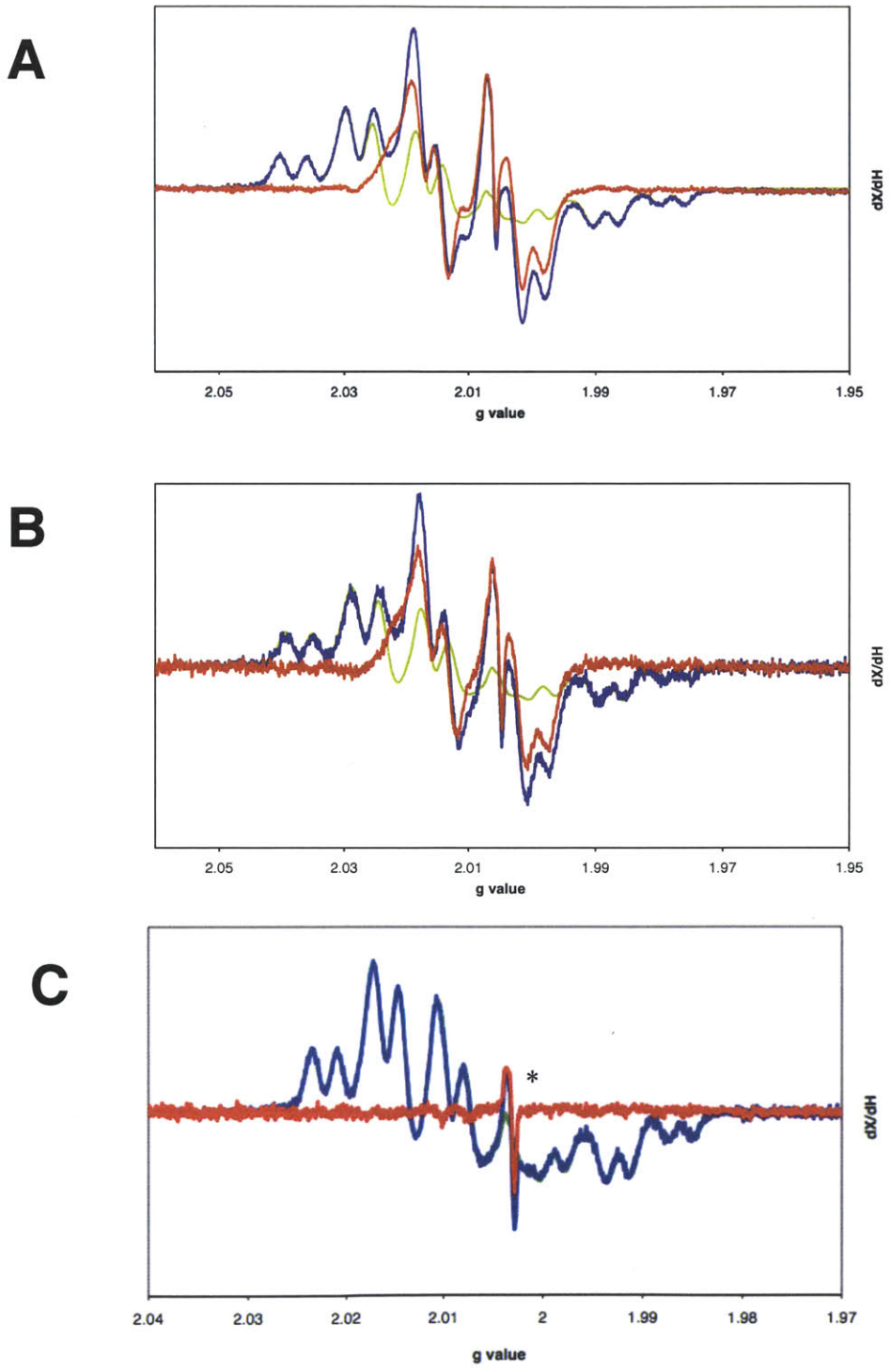

The reactivity of $Y_{122}(2,3,6)F_3Y$-β2 was investigated in parallel by Kanchana Ravichandran. When used as a radical initiator, this mutants generates 50% Y_{356}• in the reaction with wt-α2 and 43% Y_{356}• in the reaction with $Y_{731}F$-α2 (Table 7.8). The differences in Y_{356}• accumulation as a function of F_nY_{122}• initiator is discussed subsequently (section 7.3.9).

An additional important result from these EPR experiments was the inability to detect a W•/W•+ when the $Y_{356}F$ mutation was incorporated to $Y_{122}F_nY$-β2s. This observation (or lack thereof) provides us with important information about the relative thermodynamic properties of Y_{122} and W_{48} and hints at whether W_{48} should be included in the mechanism for long-range radical propagation. In order to make a stronger statement about its role, we examined the identical reactions by SF UV-vis to determine whether any kinetic information could be gathered about the generation of pathway radicals, namely W_{48}•/W_{48}•+ or Y_{356}•.

The reaction of $Y_{122}(2,3,5)F_3Y$-β2 with wt-α2, CDP, and ATP was examined first to look for evidence of pathway radicals. For all reactions with F_nY_{122}•s, differentiation between the loss of F_nY_{122}• (λ_{max} of 396-420 nm) and the formation of a new pathway Y_{356}• by UV-vis techniques was anticipated to be challenging, as both species are predicted to have low extinction coefficients (~2000-3000 M^{-1} cm^{-1}) and have considerable spectral overlap. Furthermore, the F_nY_{122}•s do not exhibit the sharpness that is characteristic of Y_{122}• in the wt enzyme (λ_{max} of 411 nm); a pathway Y_{356}• may be similarly broadened. With this caveat in mind, the reaction with $Y_{122}(2,3,5)F_3Y$-β2 with wt-α2, CDP, and ATP was conducted at 25 °C and monitored at the λ_{max} of the 2,3,5-F_3Y_{122}• (404 nm, Table 7.1), as well as the predicted λ_{max}s for W• (510 nm) and W•+ (560 nm) to look for any correlated kinetic changes. No significant changes were observed at any of these wavelengths for the reaction with wt-α2 (Figure 7.14 A), or with $Y_{731}F$-α2 (Figure

7.14 B). The reaction between $Y_{122}(2,3,5)F_3Y/Y_{356}F$-β2 and wt-α2 also failed to give any evidence of 2,3,5-F_3Y_{122}• loss or W•/W•+ formation (Figure 7.14 C).

The results of the SF reaction of $Y_{122}(2,3)F_2Y$-β2 with $Y_{731}F$-α2 were slightly different. In this case, a decay in 2,3-F_2Y_{122}• at 410 nm is observed with a corresponding increase of a feature at 400 nm (Figure 7.15 A). These features were not observed in a control experiment in which substrate (CDP) was omitted. The rate constant for loss at 410 (0.3 s^{-1}) corresponds to that of formation of the new feature. While this rate constant is very slow, it is similar to the k_{cat} measured from the steady state activity assay (~0.4 s^{-1}). It is hard to accurately quantitate this change, since neither the exact extinction coefficient of 2,3-F_2Y• at 122, nor that of the species forming at 400 nm, is known. However, if we assume an ε of 2000-3000 M^{-1} cm^{-1} for F_nY_{122}•, then the observed change would correspond to a loss of ~10% the initial 2,3-F_2Y_{122}•. No changes were observed at 510 nm or 560 nm over the same time frame (Figure 7.15 B). The reaction between $Y_{122}(2,3)F_2Y/Y_{356}F$-β2 and wt-α2 was also examined by SF UV-vis, but showed no spectral changes (data not shown). It is unclear at this point whether the changes observed at 400/410 nm in the reaction between $Y_{122}(2,3)F_2Y$-β2 and $Y_{731}F$-α2 are interesting, given that they are slow and correspond to only ~10% change in the total radical content.

As discussed above, the fact that a kinetically competent conversion of F_nY_{122}• to Y_{356}• is not observed by SF UV-vis is not entirely surprising, as the anticipated overlap between the two species would make spectral deconvolution very challenging. A similar problem has been encountered in trying to examine oxidation of Y_{731} by 2,3,6-F_3Y_{356}• in light-initiated radical propagation in photo-RNRs.[40] Perhaps the most interesting result of the SF experiments is the failure to detect any evidence of a W•/W•+ intermediate, even in those mutants containing the $Y_{356}F$ mutation.

Figure 7.14 SF UV-vis spectroscopy of the reaction of (A) $Y_{122}(2,3,5)F_3Y$-β2, wt-α2, CDP, and ATP at 25 °C monitored at 404 nm ($2,3,5\text{-}F_3Y_{122}$•, green), 510 nm (W_{48}•, blue), and 560 nm (W_{48}•+, red); (B) The analogous reaction between $Y_{122}(2,3,5)F_3Y$-β2 and $Y_{731}F$-α2; (C) The analogous reaction between $Y_{122}(2,3,5)F_3Y/Y_{356}F$-β2 and wt-α2. The traces shown are the average of 6-10 individual shots.

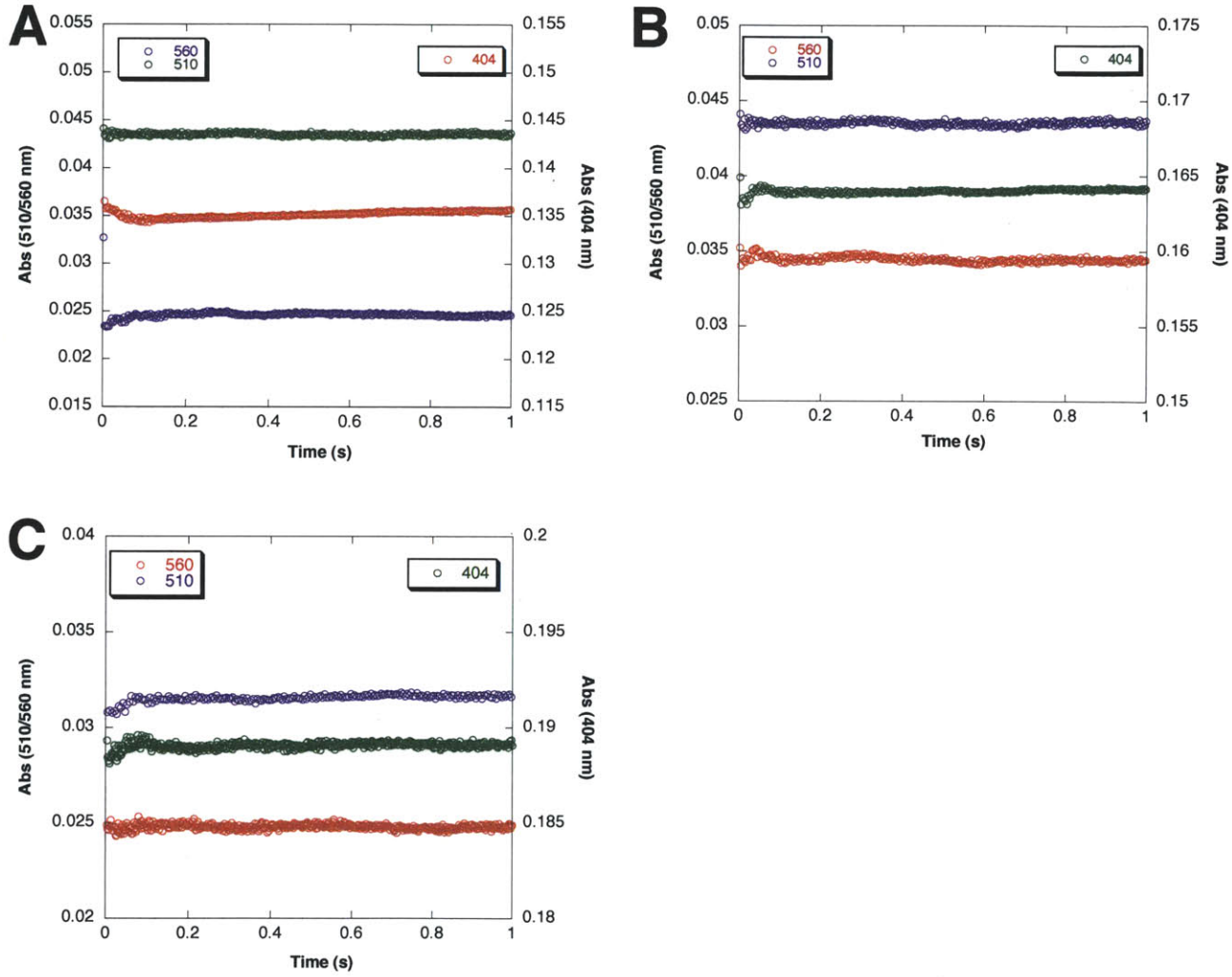

Figure 7.15 SF UV-vis spectroscopy of the reaction of $Y_{122}(2,3)F_2Y$-β2, $Y_{731}F$-α2, CDP, and ATP at 25 °C monitored at (A) 400 nm (2,3,5-F_3Y_{122}•, red) and 410 nm (possible Y_{356}•, blue) and (B) 560 nm (W_{48}•+, pink) or 510 nm (W_{48}•, cyan). The traces shown are the average of 6-10 individual shots. Fits to the averaged traces in (A) are shown in solid black lines.

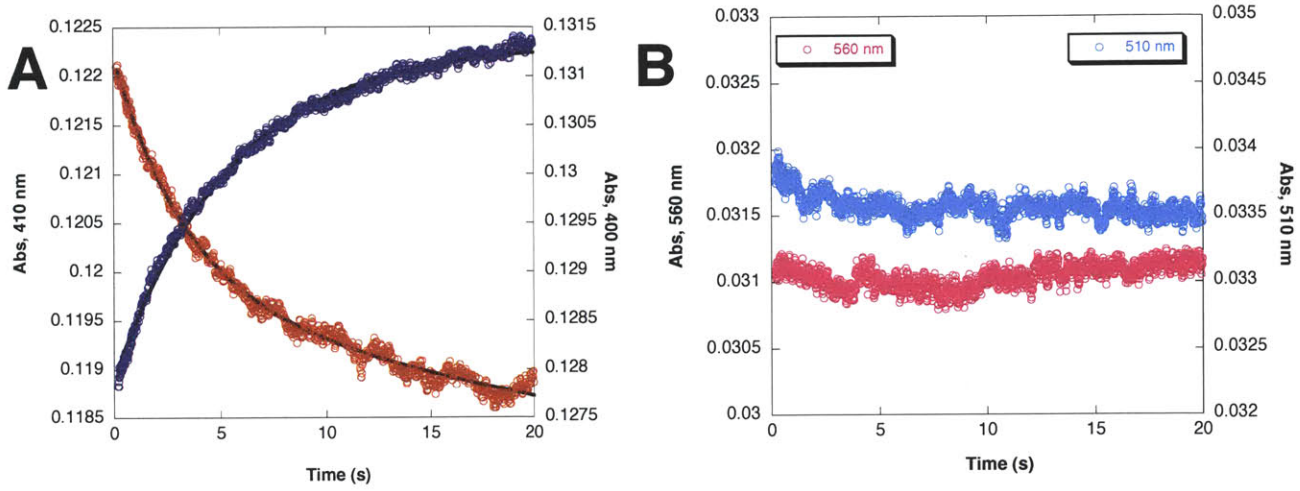

7.3.9 Using $Y_{122}F_nY$-β2s as radical initiators: looking for evidence of pathway radical intermediates by rapid freeze quench (RFQ) EPR spectroscopy. Given the inability to detect any F_nY_{122}• to Y_{356}• conversion by SF UV-vis, RFQ EPR experiments were necessary to determine the kinetic competence of Y_{356}• formation when F_nY_{122}•s are used as radical initiators. A timecourse (23 ms – 2 s) for pathway radical formation in the reaction of $Y_{122}(2,3,5)F_3Y$-β2, wt-α2, CDP, and ATP was generated. To our surprise, analysis of the reaction mixture at the earliest timepoint (Figure 7.16 A) indicated conversion of 30% 2,3,5-F_3Y_{122}• to Y_{356}•, a higher amplitude of conversion than was observed in the 25 s hand-quench experiment (Table 7.8). Following the reaction to longer times indicated a maximum of 50% pathway radical formation by 308 ms, with no apparent loss of total radical in that time within the error of spin quantitation. A monoexponential fit to the experimental data gave a rate constant for Y_{356}• formation of 20 s^{-1} (Figure 7.16 B). However, given that 60% of the total radical is formed within the first

timepoint, it is necessary to repeat this experiment collecting samples at earlier quench times to determine whether a second, faster phase for radical formation is being overlooked in the current analysis.

Figure 7.16 The reaction of $Y_{122}(2,3,5)F_3Y$-β2, wt-α2, CDP, and ATP monitored by RFQ-EPR spectroscopy. (A) Subtraction of the 2,3,5-F_3Y_{122}• contribution (black) from the 23 ms reaction spectrum (blue) indicates the formation of significant Y_{356}• (red); (B) Fitting (black) the experimental RFQ-EPR data (pink dots) gives a rate constant for Y_{356}• formation of 20 s^{-1}

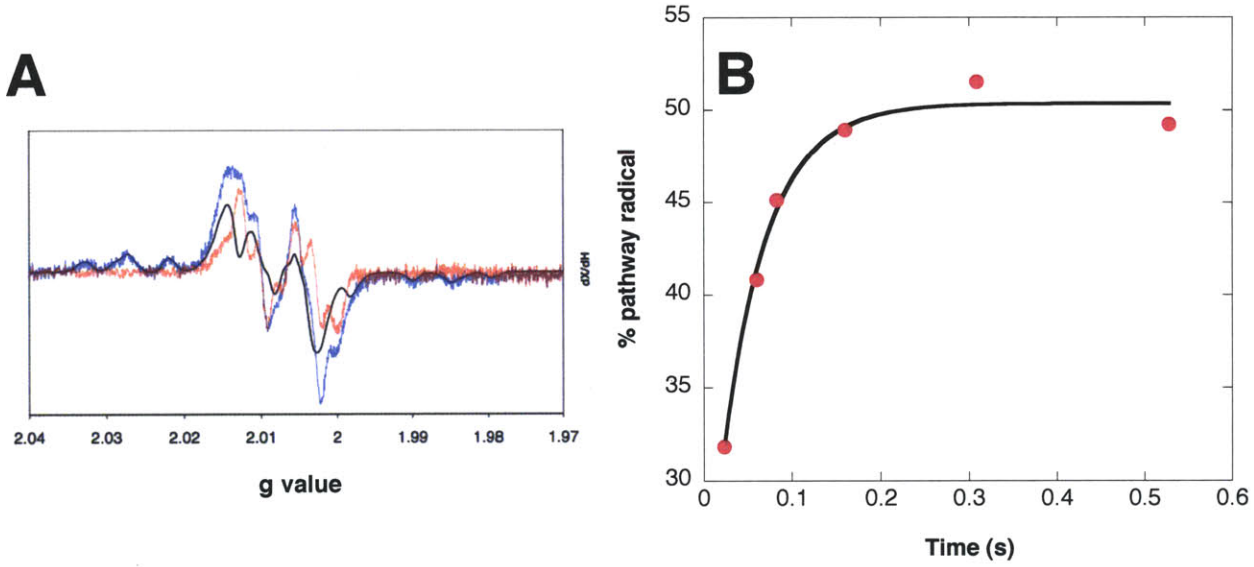

A second surprise result from the RFQ-EPR experiment was the apparent loss of Y_{356}• at time points longer than 500 ms. At 2 s, the spectrum of the reaction contained a total of 41% pathway radical (data not shown). At first, we could not rationalize the observation that Y_{356}• was lost without loss of total spin. A subsequent experiment was conducted to determine the stability of the Y_{356}•s formed by F_nY_{122}•s (Ravichandran and Stubbe, unpublished results). In this experiment, $Y_{122}F_nY$-β2, wt-α2, CDP, and ATP were mixed by hand and frozen in isopentane (-140 °C) at 25 s. EPR analysis indicated that the reaction mixtures had F_nY_{122}•/Y_{356}• distributions in close agreement with those previously observed and reported in Table 7.8. Next, the EPR reaction samples were rapidly thawed in a water bath, aged for a known amount of time,

and refrozen. EPR analysis indicated that for all reactions, Y_{356}• loss was observed between freeze/thaw cycles. Unexpectedly, no total spin was lost from the reaction mixture; instead, loss of Y_{356}• was correlated with F_nY_{122}• reformation. All reaction samples demonstrated the complete conversion of Y_{356}• to F_nY_{122}•, indicating an equilibrium between the two species. This result is very exciting, as it is the first documentation of reverse radical propagation in an active RNR and sets important thermodynamic precedent for the system. Recall that the Y_{356}• formed when NO_2Y_{122}• was used as a radical initiator was not capable of NO_2Y^- re-oxidation.[2] The only other observations of Y_{122} re-oxidation have been in the reactions of the inactive mutants Y_{356}DOPA-ββ′[22] or $Y_{356}NH_2Y$-ββ′ (Chapter 8) with wt-α2, CDP, and ATP. The rate of F_nY_{122}• re-oxidation differed for each reaction, with the rate constant for re-oxidation varying according to 2,3,5-F_3Y (fastest) > 2,3-F_2Y > 2,3,6-F_3Y. For 2,3,5-F_3Y_{122}•, re-oxidation occurred at 0.02 s^{-1}. Thus, we rationalize that the loss of Y_{356}• in RFQ EPR timepoints >500 ms is associated with the re-oxidation of 2,3,5-F_3Y_{122} by Y_{356}•. The observation of reverse radical propagation also explains why the amount of pathway radical generated in a Y_{122}(2,3,5)F_3Y-β2 reaction is sensitive to the freezing technique, as our experimental observations are consistent with higher levels of Y_{356}• accumulating when faster quenching techniques are used (e.g., -140 °C isopentane versus dry/ice acetone). It is important to note that the temperature at which the F_nY_{122}• re-oxidation rate constant was measured cannot be accurately determined; due to the nature of the freeze/thaw experiment, the average temperature fell somewhere between 4 and 25 °C. Thus, under single-turnover conditions (i.e., no reductant), the re-oxidation rate is roughly an order of magnitude slower than the steady-state rate constant measured for this enzyme at 25 °C, and demonstrates thermodynamic but not kinetic competence for F_nY_{122} reoxidation by Y_{356}•.

7.3.10 Using $Y_{356}(3,5)F_2Y$-β2 as a radical sink: looking for evidence of pathway radical intermediates. Our combined results using either NO_2Y_{122}• or F_nY_{122}• as radical initiators have indicated that the potential of Y_{356} in β2 is lower than that of Y_{731} and Y_{730} in α2. Thus, the question arose as to whether lowering the potential at position 356 slightly by incorporating 3,5-F_2Y at this position would allow for trapping a F_2Y_{356}• using the native Y_{122}• as a radical initiator. This "pathway radical" should be detectable by EPR, even if present in very small amounts, given the wide fluorine couplings of the F_2Y•. Indeed, the unique spectra features of this radical have allowed the presence of small amounts (<3% the total radical) of 3,5-F_2Y_{730}• and 3,5-F_2Y_{731}• to be detected and roughly quantitated when NO_2Y_{122}• was used as a radical initiator.[3]

In some ways, this experiment mimics earlier experiments in which DOPA or NH_2Y was incorporated at position 356, and formation of the resulting $DOPA_{356}$• or NH_2Y_{356}• was kinetically characterized.[24] However, the primary difference with this experiment is that the redox potential perturbation is ~10-fold lower for 3,5-F_2Y (~20 mV easier to oxidize than Y at pH 7.6, assuming no pK_a perturbation at position 356[17]) than for NH_2Y or DOPA (~190 and 260 mV easier to oxidize, respectively, at pH 7). Such a modest perturbation in redox potential does not significantly influence the activity of the $Y_{356}(3,5)F_2Y$-β2 relative to wt-β2, as indicated by the similarity of their maximal activities and pH rate profiles (section 6.3.11).

$Y_{356}(3,5)F_2Y$-β2 was reacted with wt-α2, CDP, and ATP at pH 7.6, hand quenched at 25 s, and analyzed by EPR spectroscopy to look for 3,5-F_2Y_{356}•. Analysis of the reaction spectrum indicated no evidence of pathway radical within our limits of detection (<3% total spin), nor did it indicate any total spin loss over the reaction course (Figure 7.17, red). Thus, under these

conditions, it does not appear that 3,5-F_2Y_{356}• may be trapped. The same experiment was conducted using Y_{731}F-α2, and showed no evidence of pathway radical (Figure 7.17, blue).

The reaction of Y_{356}(3,5)F_2Y-β2 with wt-α2 (or Y_{731}F-α2), CDP, and ATP was also investigated by SF UV-vis spectroscopy to determine if any small, rapid changes were missed in the hand-quench EPR reaction. The reaction was monitored at 410 nm to look for loss of Y_{122}• and at 396 nm to look for formation of 3,5-F_2Y_{356}•. The latter wavelength was selected as 396 nm is consistent with the λ_{max} of both 3,5-F_2Y• formed by solution photolysis and at position 122 of β2 (Table 7.1). No changes were visible at either wavelength using wt-α2 nor Y_{731}F-α2 (Figure 7.18 A and B, respectively). These results are in agreement with the EPR experiments, and indicate that one cannot trap 3,5-F_2Y_{356}• when using Y_{122}• as the radical initiator.

Figure 7.17 EPR spectra of the reactions of $Y_{356}(3,5)F_2Y$-β2 with wt-α2 (red) or $Y_{731}F$-α2 (blue), CDP, and ATP quenched after 25 s at 25 °C. *Inset*: An expanded view of the fluorine "wing" region shows smooth baseline and no evidence of $3,5\text{-}F_2Y_{356}$• formation.

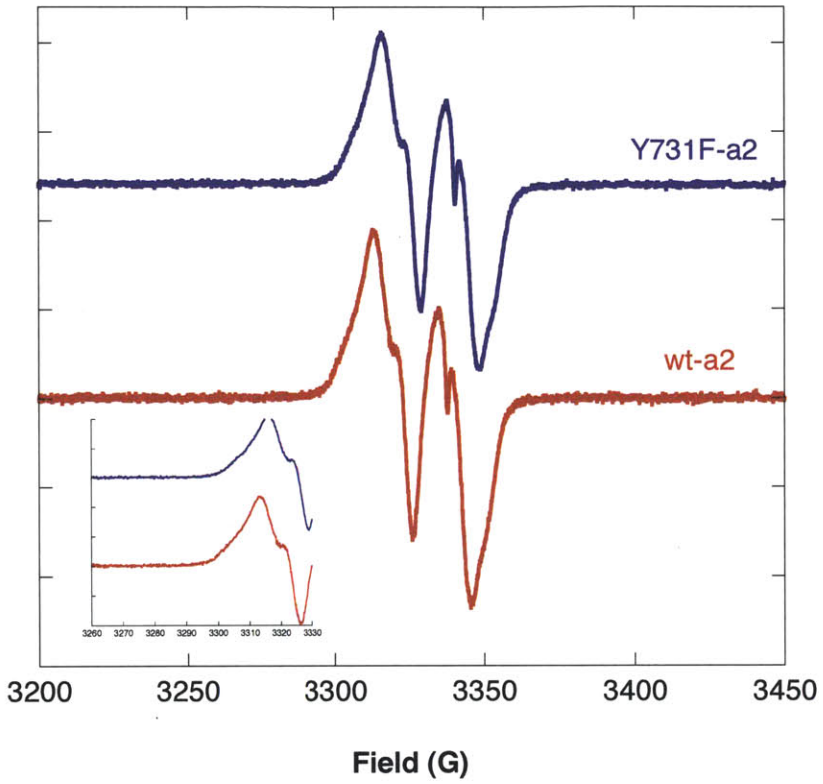

Figure 7.18 SF UV-vis spectroscopy of the reaction of $Y_{356}(3,5)F_2Y$-β2 with wt-α2 (A) or $Y_{731}F$-α2 (B), CDP, and ATP under single-turnover conditions at 25 °C. The kinetics were followed at 396 nm (cyan/blue) to look for F_2Y_{356}• formation and 410 nm (pink/red) to look for Y_{122}• loss. Traces shown below are the average of 8-10 individual shots.

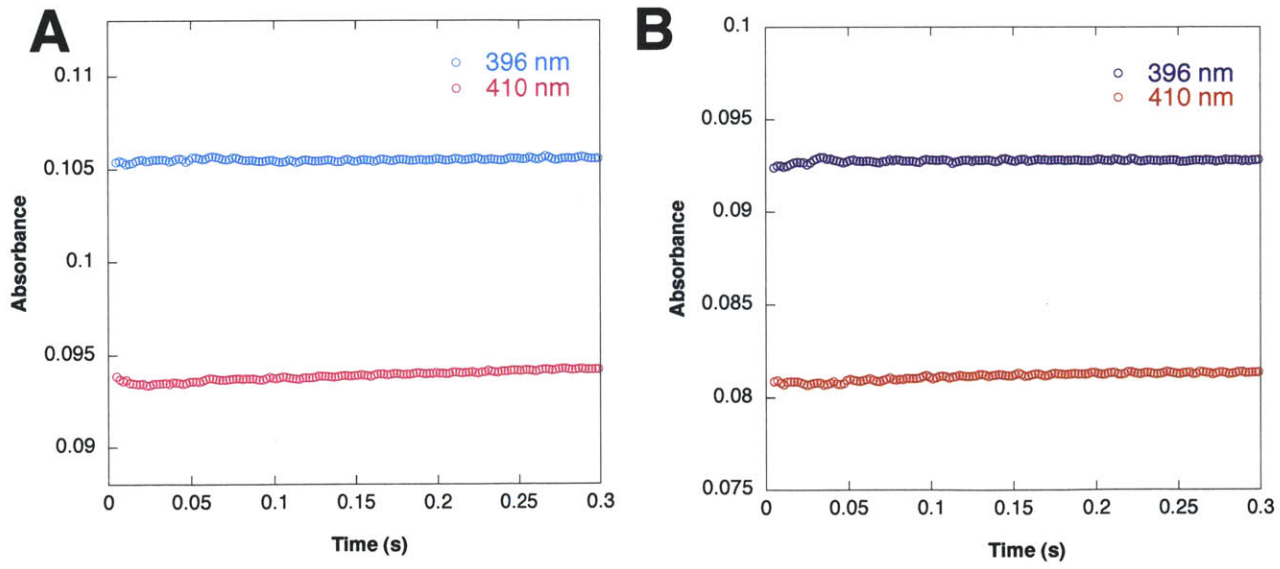

7.4 DISCUSSION

7.4.1 Revised model for the thermodynamic landscape of radical propagation: experimental observations and predictions. In the introduction to this chapter, recent results using NO_2Y_{122}• as a radical initiator were summarized. When this potent oxidant is used to initiate radical propagation, ET is decoupled from PT and from the conformational change(s) that is(are) rate-limiting in the wt enzyme. This decoupling allowed the first detection of a transient Y• on the pathway, hypothesized to be formed during reverse radical propagation and demonstrated to be localized primarily at position 356 of β2.[2] The relative distribution of this radical across the three pathway Ys at 356, 731, and 730 led to the thermodynamic model for the PCET pathway shown in Figure 7.1.[3] The primary goal in this chapter was to incorporate F_nYs to position 122 to modulate the driving force at this position in a more subtle fashion, thereby exploring reactivity in the 200 mV reduction potential regime separating NO_2Y and the native Y. Studies of these intermediate potential oxidants allow us to propose a more detailed model for the thermodynamic landscape between Y_{122}• and Y_{356}, which may be further refined by rapid kinetic studies on Y_{356}• and dCDP formation in $Y_{122}(2,3)F_2Y$-β2 and $Y_{122}(2,3,6)F_3Y$-β2 modeled from the initial experiments on $Y_{122}(2,3,5)F_3Y$-β2 described herein.

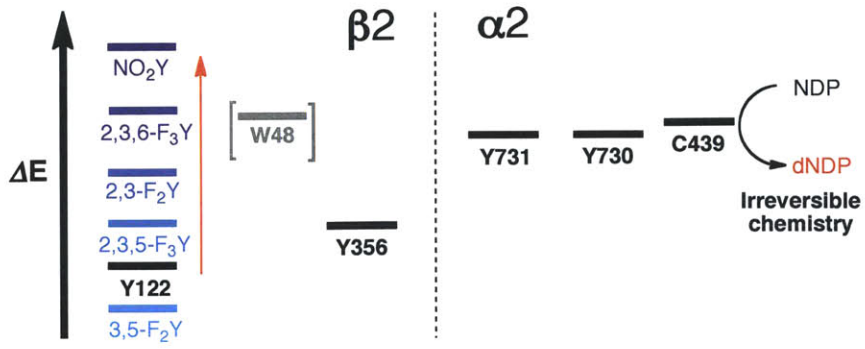

Figure 7.19 Revised model, derived from studies using NO_2Y_{122}• and F_nY_{122}• as a radical initiators, for the relative redox potentials of residues participating in the PCET pathway of *E. coli* RNR.

This model places F_nYs, Y, and NO_2Y at relative redox potentials identical to those in the pH-independent region as determined by solution DPV on N- and C-terminally protected amino acids (Figure 7.5). We assume the pH-independent region is most appropriate here, since pH titrations of $Y_{122}NO_2Y$-β2 indicated a phenolic pK_a perturbation at position 122 of >2.5 units. However, as noted in the Results section, the unique chemical properties of fluorine may further perturb this pK_a in a fashion that we cannot readily predict. Thus, we make the cautious initial assumption that that all F_nY_{122}s are in the protonated (phenol) state at a solution pH of 7.6. We also assume that, while the absolute peak potentials of F_nYs determined by DPV may be slightly different than the solution reversible redox potentials, the relative redox potentials (ΔE) determined by this method are roughly accurate. The model places the three transiently oxidized Ys in a position identical to that given in Figure 7.1. All three have increased reduction potentials with respect to Y_{122}, and Y_{731} and Y_{730} are further elevated by 50-100 mV compared to Y_{356} and roughly isoenergetic with one another.[3] Finally, C_{439} is placed at a reduction potential quite similar to or slightly elevated above the 730/731 dyad on the basis of recent measurements of the solution reduction potential of glutathione radical.[41]

Under the assumptions outlined above, 3,5-F_2Y is easier to oxidize than Y by ~50 mV and we would predict that no radical intermediates would accumulate when using this mutant as a radical initiator. Indeed, the 3,5-F_2Y_{122}• appears to be quite stable (0.2 3,5-F_2Y_{122}•/β2 present after a ~36 h purification protocol), behaves as the wt RNR in steady-state assays, and fails to give any evidence of pathway radical(s) when reacted with wt-α2 or Y_{731}F-α2. On the other hand, 2,3,5-F_3Y and 2,3-F_2Y are ~10 mV and ~45 mV, respectively, harder to oxidize than Y. These mutants both show reduced steady-state activity and demonstrate accumulation of a new Y• when reacted with wt-α2 or Y_{731}F-α2. The similarity of this radical to that which is formed

by NO_2Y_{122}•, and the failure to observe this radical in the $Y_{122}F_nY/Y_{356}F$-β2 double mutant support the conclusion that this radical is localized at 356. PELDOR experiments measuring the F_nY_{122}• to pathway Y• distance would further solidify this conclusion. Thus, these results are consistent with 356 having a lower potential relative to Y_{731} and Y_{730}. The highest potential F_nY, 2,3,6-F_3Y, is ~100 mV harder to oxidize than Y and has been incorporated at position 122 and studied in detail by Kanchana Ravichandran. The radical formed upon cluster assembly in this mutant appears to be a mixture of species, most likely different conformations of the 2,3,6-F_3Y_{122}• arising in part form the residue's asymmetry, and each of these species appears to have its own unique stability. Upon initial analysis, this mutant shows the lowest steady-state activity in nucleotide reduction.

Pre-steady state measurements of the kinetics of Y_{356}• formation and dCDP production in the reaction of $Y_{122}(2,3,5)F_3Y$-β2 with wt-α2, CDP, and ATP were also presented in this chapter. RFQ-EPR and RCQ experiments reveal that Y_{356}• forms at 20 s^{-1} and dCDP at 2.5 s^{-1}, respectively. These observations are unique from both the wt system,[1] in which conformational gating at 2-10 s^{-1} masks observation of changes in Y_{122}•, and the $Y_{122}NO_2Y$-β2 mutant, in which Y_{356}• and dCDP both form at >100 s^{-1}.[2] This latter result was interpreted as an "unmasking" of the rate-limiting conformational change, though the rate constants measured for Y_{356}• and dCDP formation are believed to also report on protein conformational dynamics, rather than directly on radical propagation. From the results presented herein, we propose a kinetic model for catalysis by $Y_{122}(2,3,5)F_3Y$-β2 (Figure 7.20). Upon association of $Y_{122}(2,3,5)F_3Y$-β2, wt-α2, CDP, and ATP, Y_{356}• is formed with a rate constant of 20 s^{-1} (step **A**). Y_{356}• is then propagated to the enzyme active site, where fast nucleotide reduction and reverse PCET occurs at a rate >100 s^{-1}, as demonstrated in the $Y_{122}NO_2Y$-β2 mutant (step **C**). These steps, however, are masked by a

slow conformational change (step **B**) of 2.5 s^{-1}. Steps **A-C** are then repeated to generate dCDP on the second α/β pair (step **D**). A steady-state turnover number of 0.8 s^{-1} was measured for this mutant (Table 7.4), and is assigned to re-oxidation of Y_{122} by Y_{356}• in the presence of reductant (step **E**). (We will argue subsequently that the rate of this reverse PCET is sensitive to the presence of reductant in the system.) Loss of linearity in the steady-state assay over long times (Figure 7.8) may be the consequence of some slow uncoupling during reserve PCET that results in loss of total spin from the system. The subunits may then dissociate, bind new substrate, re-associate, and perform another turnover (steps **F** and **G**).

The model implies that the Y_{356}• observed is formed during forward PCET, as step **B** is slower than step **A**. This makes the Y_{356}• detected in this system unique from that observed with the $Y_{122}NO_2Y$-β2 mutant, which is hypothesized to accumulate during reverse PCET. While the two radicals look quite similar by X-band EPR (Figure 7.12), a comparison of the forward- and reverse-PCET Y_{356}• radicals by HF EPR could provide insight to subtle electronic structural differences between the two and afford us the first opportunity to address the importance of conformational differences in forward and reverse PCET. That is, is the pathway identical with respect to its structural and thermodynamic properties in both directions, or can it be modulated to induce directionality?

The model for catalysis by $Y_{122}(2,3,5)F_3Y$-β2 is one of many possible interpretations of the existing data. To test its validity, pre-steady state kinetic analysis will need to be performed on $Y_{122}(2,3)F_2Y$-β2 and $Y_{122}(2,3,6)F_3Y$-β2. Initially, differences in the steady-state activities, extent of Y_{356}• formation in hand-quench EPR experiments (Table 7.8), and rates of Y_{122} re-oxidation among these three mutants were interpreted as reflective of the differences in driving force among the respective F_nY_{122}•s. However, the fact that the differences in the various rates

do not display Nerstian behavior (i.e., a 10-fold decrease in activity with every 59 mV increase in potential) suggested alternative explanations are required for our observations. Furthermore, a subsequent RFQ-EPR experiment between $Y_{122}(2,3,5)F_3Y$-β2 and wt-α2 indicated that a maximum of 50% 2,3,5-F_3Y_{122}• was converted to Y_{356}• within 250 ms, and that the reduced accumulation of Y_{356}• observed in the hand-quench experiment (25%, Table 7.8) was likely due to loss of radical via specific reoxidation of Y_{122}, or due a temperature-dependent equilibrium between the two radical sites. Thus, experimental evidence indicates that raising the potential at position 122 anywhere between 10 and 200 mV allows for trapping of 50% of the total radical content as Y_{356}•. These observations led us to interpret the observed rate constants as reporting on protein conformational changes, as was concluded for the rate constants of formation of Y_{356}• in $Y_{122}NO_2Y$-β2 and NH_2Y•s in NH_2Y-RNRs (Chapter 2). It is interesting to note that these conformational changes, while not strictly related to reduction potential, do appear to display some sensitivity to the oxidizing power of the radical initiator (2-10 s^{-1} for Y_{122}•, 20 s^{-1} for 2,3,5-F_3Y•, >100 s^{-1} for NO_2Y_{122}•), and thus we may anticipate that the rate constants for Y_{356}• formation monitored by RFQ will increase according to the trend: 2,3,6-F_3Y• > 2,3-F_2Y• > 2,3,5-F_3Y• > Y•.

Finally, we note that all the experiments described in this chapter are complicated by the fact that the as-isolated and reconstituted proteins have substoichiometric radical content (i.e., <1.0 F_nY•/β2, Table 7.1). For the steady-state activities reported in Table 7.4, we have opted to scale the measured activities so that all the values are normalized with respect to wt-β2 (1.2 Y•/β2). Activity measurements on samples of wt-β2 and $Y_{122}(3,5)F_2Y$-β2 of different radical content seem to suggest this is a valid extrapolation. To avoid this complexity, future efforts should focus on obtaining 1.0 F_nY•/β2. The best strategy to do so is likely to overexpress the

protein in its apo (Fe-free) form, and reconstitute the cofactor *in vitro* with Fe^{2+} and O_2. As alluded to in the Results section, it may be necessary to explore this assembly by rapid chemical techniques (SF UV-vis and RFQ-EPR), as it is possible that multiple radical populations are generated and that each has its own distinct stability. This has already been demonstrated for Y_{122}(2,3,6)F_3Y-β2 (Table 7.1), in which 1.0 2,3,6-F_3Y_{122}•/β2 was generated by RFQ assembly, 0.7 2,3,6-F_3Y_{122}•/β2 was assembled by hand-mixing and quenching within 30s, and 0.5 2,3,6-F_3Y_{122}•/β2 was stable for times >3 min (Ravichandran and Stubbe, unpublished results). Thus, a more systematic exploration of radical assembly and stability of F_nY_{122}•s is necessary prior to further studies on the chemistry of $Y_{122}F_nY$-β2s.

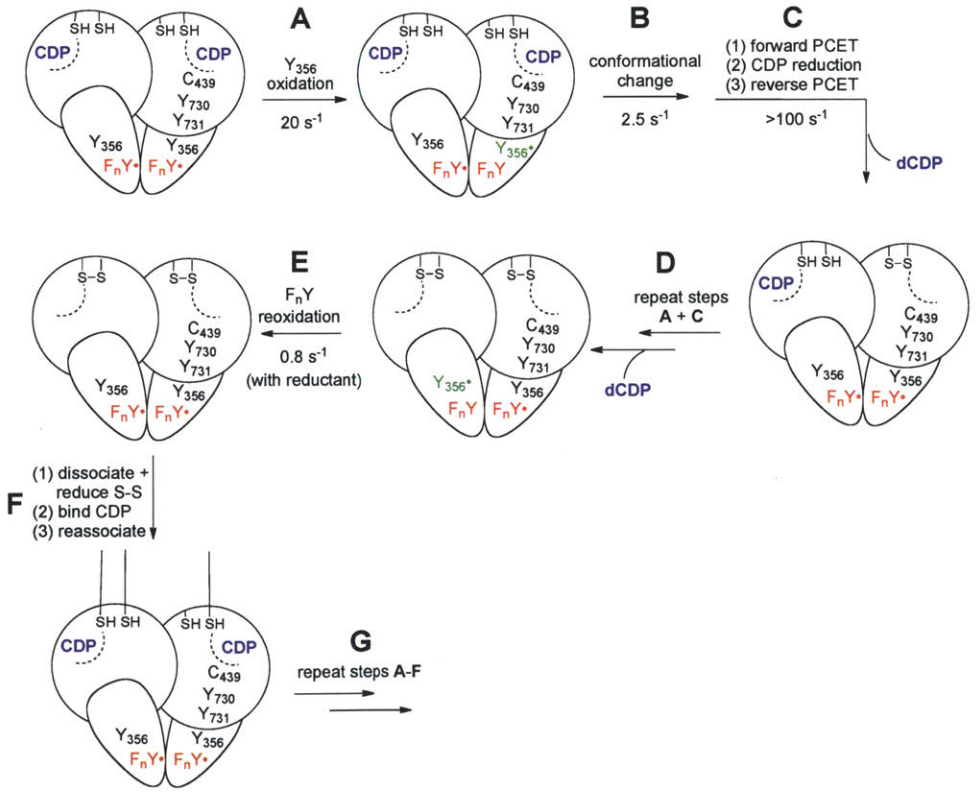

Figure 7.20 Kinetic model for dCDP formation in the reaction of Y_{122}(2,3,5)F_3Y-β2 with wt-α2, CDP, and ATP under steady-state conditions

7.4.2 What is the role of W_{48} in long-range radical propagation? A long-standing question is whether W_{48} participates in long-range radical propagation. It has been demonstrated previously that this residue plays a key role in *in vitro* diferric-Y•cluster assembly, but inability to mutate this residue while maintaining activity has limited our investigation of its role in reversible PCET over 35 Å. Reaction of the double mutant $Y_{122}NO_2Y/Y_{356}F$-β2 with wt-α2 results in the formation of a number W•+s located at positions (including W_{48}) throughout β2, thereby suggesting that this "hot" oxidant performs off-pathway oxidation when the native pathway has been blocked. Interestingly, none of the $Y_{122}F_nY/Y_{356}F$-β2 double mutants described in this chapter gave indication of W_{48}•/W_{48}•+ formation by either hand-quench EPR or SF UV-vis spectroscopy; neither did analogous reactions with $Y_{122}(2,3,6)F_3Y$-β2 (Ravichandran and Stubbe, unpublished results) despite the fact that 2,3,6-F_3Y is predicted to have a slightly higher redox potential than W given the local pK_a perturbation at position 122 (Figure 7.19). A single RFQ-EPR experiment examining Y_{356}• formation in the reaction with $Y_{122}(2,3,5)F_3Y$-β2 also gave no evidence for a W•/W•+. We estimate our lower limit of radical detection to be 3% of the total radical by EPR and 10% by SF UV-vis at the protein concentrations routinely employed for each respective method. Thus, the results of the experiments in Chapter 7 do not support the participation of W_{48} as a discrete radical intermediate in long-range radical propagation. However, we cannot rule out the likely possibility that W_{48} plays a more subtle role in proton coupling and/or conformational gating/dynamics.

7.4.3 A possible mechanism for cytosine release in the single-turnover reactions of $Y_{122}F_nY$-β2 and wt-α2. One of the more surprising results presented in this chapter was the observation that the single-turnover reaction of $Y_{122}(2,3,5)F_3Y$-β2 (or $Y_{122}(2,3)F_2Y$-β2)) with wt-α2, CDP, and ATP formed two eq. of dCDP in a burst phase at 2.5 s^{-1}, followed by cytosine

release with a rate constant of 0.025 s^{-1}. This result is interesting as it is the first example of a mutation in β2, at the radical initiator site >35 Å removed from the active site, disrupting the mechanism of nucleotide reduction such that chemistry on the native substrate mimics that typically observed for a MBI. This observation provides yet another example of the incredible delicacy and sensitivity with which nature tunes RNR reactivity.

While this result was unexpected, a mechanistic model for the observation may be formulated based on extensive studies of the mode of inactivation by MBIs and active-site mutants from Stubbe lab studies conducted over several decades.[42] In this model (Figure 7.21), the two eq. dCDP are formed first as in the multiple turnover conditions (Figure 7.20), that is that Y_{356}• is generated at 20 s^{-1}, followed by dCDP formation on one α/β pair (Figure 7.21, steps **A-C**) and then on the second (step **D**). The chemistry of dCDP formation is gated by a conformational change at 2.5 s^{-1}. Noting that the rate of cytosine release in the reaction of $Y_{122}(2,3,5)F_3Y$-α2 (0.025 s^{-1}) is indistinguishable from that of Y_{122} re-oxidation in the same enzyme (0.02 s^{-1}, step **E**), we propose that the generation of cytosine is rate-limited by reverse ET from Y_{356}• to Y_{122} on the second α/β pair in the absence of reductant. The subunits then dissociate, bind additional substrate, and reassociate. Radical propagation is re-initated by F_nY_{122}•, and the active site disulfide produced during the first turnover is unable to reduce the 3′-keto-2′-radical nucleotide intermediate formed in the normal catalytic cycle. Instead, this radical is reduced by C_{439}, regenerating C_{439}• and allowing reverse PCET. The resulting 2′-deoxy-3′-ketonucleotide slowly decomposes to give cytosine, inorganic phosphate, and 2-methylene-3(2H)-furanone (eq. 7.2), a process that has been well-documented.[32,33,35] This proposal assumes that the C-terminal cyteines, which can slowly (~0.1 s^{-1}) re-reduce the active-site disulfide in the wt enzyme in the absence of reductant,[1] cannot do so in this mutant system at a rate that is

competitive with the collective steps (step **G**) that give rise to cytosine release on the oxidized enzyme. This may be related to the changes in conformational dynamics that result in unmasking of pathway radical formation. This model also predicts that cytosine release should occur in $Y_{122}(2,3)F_2Y$-β2 and $Y_{122}(2,3,6)F_3Y$-β2 at rate constants identical to those for Y_{122} reoxidation. The very slow rate of reoxidation in $Y_{122}(2,3,6)F_3Y$-β2 (0.002 s^{-1}) may account for why cytosine release was not observed in single-turnover assays of this mutant: the reaction was not monitored long enough to observe cytosine accumulation. One would predict that if you let this reaction go for a sufficiently long time, cytosine release should be detected.

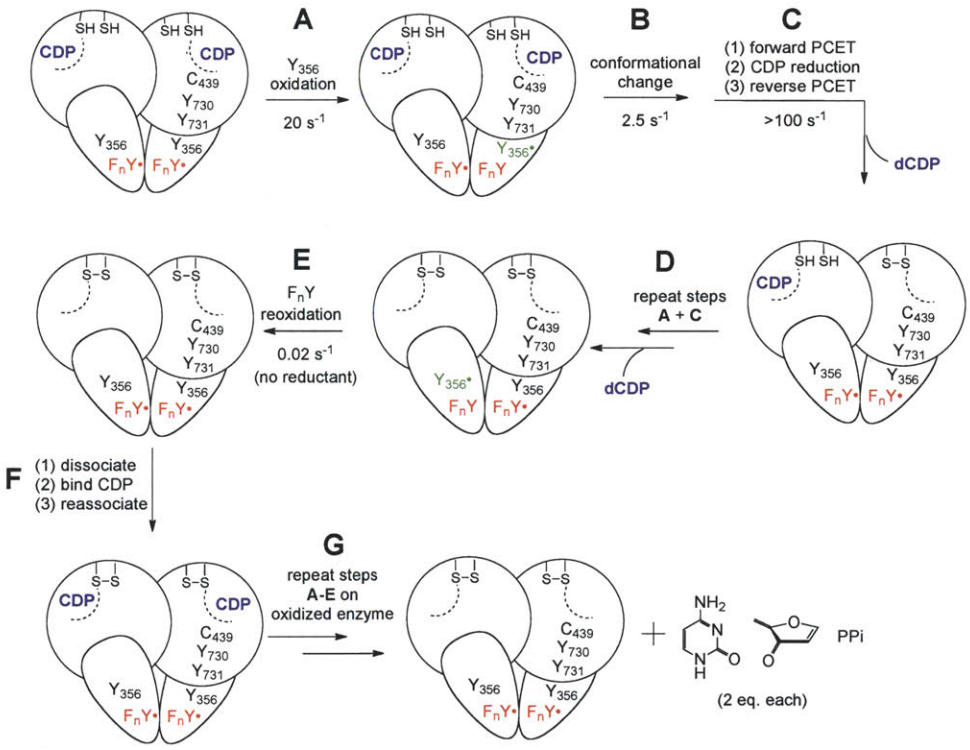

Figure 7.21 Kinetic model for product formation in the reaction of $Y_{122}(2,3,5)F_3Y$-β2 with wt-α2, CDP, and ATP in the absence of reductant.

7.4.4 Fluorotyrosines as generally useful probes for biochemical research. Finally, the results in this chapter highlight a few of the ways in which site-specifically engineering proteins to contain F_nYs may prove generally useful for enzymology and biochemistry. The utility of F_nY•s as spectroscopic handles is apparent when examining the F_nY• X-band EPR spectra. The width of spectrum and the presence of distinct fluorine hyperfine couplings, which give rise to features in the low and high field spectral regions, allow accurate subtraction of F_nY•s from other g ~2 radicals.[2,6] F_nY•s afford the first opportunity to identify low concentrations of radical species that would otherwise go undetected in complicated reaction mixtures.[3] F_nY•s may prove similarly useful in HF EPR and ENDOR studies. For proteins that do not use radicals, F_nYs may be incorporated as probes of structure and/or local environment for ^{19}F-NMR studies.[43] Thus, application of F_nYs as spectroscopic probes may be extended to the broader research community.

7.5 REFERENCES

1. Ge, J., Yu, G., Ator, M.A. & Stubbe, J. Pre-steady-state and steady-state kinetic analysis of *E. coli* class I ribonucleotide reductase. *Biochemistry* **42**, 10071-83 (2003).
2. Yokoyama, K., Uhlin, U. & Stubbe, J. A hot oxidant, 3-NO2Y_{122} radical, unmasks conformational gating in ribonucleotide reductase. *J. Am. Chem. Soc.* **132**, 15368-79 (2010).
3. Yokoyama, K., Smith, A.A., Corzilius, B., Griffin, R.G. & Stubbe, J. Equilibration of tyrosyl radicals (Y356•, Y731•, Y730•) in the radical propagation pathway of the *Escherichia coli* class Ia ribonucleotide reductase. *J. Am. Chem. Soc.* **133**, 18420-32 (2011).
4. Yokoyama, K., Uhlin, U. & Stubbe, J. Site-specific incorporation of 3-nitrotyrosine as a probe of p*K*a perturbation of redox-active tyrosines in ribonucleotide reductase. *J. Am. Chem. Soc.* **132**, 8385-97 (2010).
5. Seyedsayamdost, M.R., Reece, S.Y., Nocera, D.G. & Stubbe, J. Mono-, di-, tri-, and tetra-substituted fluorotyrosines: new probes for enzymes that use tyrosyl radicals in catalysis. *J. Am. Chem. Soc.* **128**, 1569-79 (2006).
6. Seyedsayamdost, M.R., Xie, J., Chan, C.T., Schultz, P.G. & Stubbe, J. Site-specific insertion of 3-aminotyrosine into subunit α2 of *E. coli* ribonucleotide reductase: direct evidence for involvement of Y730 and Y731 in radical propagation. *J. Am. Chem. Soc.* **129**, 15060-71 (2007).
7. Bollinger, J.M., Tong, W. H., Ravi, N., Huynh, B. H., Edmondson, D. E. & Stubbe, J. Mechanism of assembly of the tyrosyl radical-diiron(II) cofactor of *Escherichia coli* ribonucleotide reductase 3. Kinetics of the limiting Fe^{2+} Reaction by optical, EPR, and Mössbauer spectroscopies. *J. Am. Chem. Soc.* **116**, 8024-32 (1994).
8. Uhlin, U. & Eklund, H. Structure of ribonucleotide reductase protein R1. *Nature* **370**, 533-539 (1994).
9. Stubbe, J., Nocera, D.G., Yee, C.S. & Chang, M.C.Y. Radical initiation in the class I ribonucleotide reductase: long-range proton-coupled electron transfer? *Chem. Rev.* **103**, 2167-201 (2003).
10. Chen, H., Gollnick, P. & Phillips, R.S. Site-directed mutagenesis of His343-->Ala in *Citrobacter freundii* tyrosine phenol-lyase. Effects on the kinetic mechanism and rate-determining step. *Eur. J. Biochem.* **229**, 540-9 (1995).
11. Minnihan, E.C., Young, D.D., Schultz, P.G. & Stubbe, J. Incorporation of fluorotyrosines into ribonucleotide reductase using an evolved, polyspecific aminoacyl-tRNA synthetase. *J. Am. Chem. Soc.* **133**, 15942-5 (2011).
12. Minnihan, E.C., Seyedsayamdost, M.R., Uhlin, U. & Stubbe, J. Kinetics of radical intermediate formation and deoxynucleotide production in 3-aminotyrosine-substituted *Escherichia coli* ribonucleotide reductases. *J. Am. Chem. Soc.* **133**, 9430-40 (2011).

13. Chivers, P.T. et al. Microscopic pK_a values of *Escherichia coli* thioredoxin. *Biochemistry* **36**, 14985-91 (1997).

14. Russel, M. & Model, P. Direct cloning of the *trxB* gene that encodes thioredoxin reductase. *J. Bacteriol.* **163**, 238-42 (1985).

15. Palmer, G. Electron paramagnetic resonance. *Methods Enzymol.* **10**, 595-610 (1967).

16. Stoll, S. & Schweiger, A. EasySpin, a comprehensive software package for spectral simulation and analysis in EPR. *J. Magn. Reson.* **178**, 42-55 (2006).

17. Yee, C.S., Seyedsayamdost, M.R., Chang, M.C.Y., Nocera, D.G. & Stubbe, J. Generation of the R2 subunit of ribonucleotide reductase by intein chemistry: insertion of 3-nitrotyrosine at residue 356 as a probe of the radical initiation process. *Biochemistry* **42**, 14541-52 (2003).

18. Seyedsayamdost, M.R., Yee, C.S., Reece, S.Y., Nocera, D.G. & Stubbe, J. pH rate profiles of F_nY_{356}-R2s (n = 2, 3, 4) in *Escherichia coli* ribonucleotide reductase: evidence that Y_{356} is a redox-active amino acid along the radical propagation pathway. *J. Am. Chem. Soc.* **128**, 1562-8 (2006).

19. Steeper, J.R. & Steuart, C.D. A rapid assay for CDP reductase activity in mammalian cell extracts. *Anal. Biochem.* **34**, 123-30 (1970).

20. Ballou, D.P. Freeze-quench and chemical-quench techniques. *Methods Enzymol.* **54**, 85-93 (1978).

21. Sahlin, M., Graslund, A., Petersson, L., Ehrenberg, A. & Sjöberg, B.M. Reduced forms of the iron-containing small subunit of ribonucleotide reductase from *Escherichia coli*. *Biochemistry* **28**, 2618-25 (1989).

22. Seyedsayamdost, M.R. & Stubbe, J. Forward and reverse electron transfer with the Y356DOPA-β2 heterodimer of *E. coli* ribonucleotide reductase. *J. Am. Chem. Soc.* **129**, 2226-7 (2007).

23. Atkin, C.L., Thelander, L., Reichard, P. & Lang, G. Iron and free radical in ribonucleotide reductase. Exchange of iron and Mössbauer spectroscopy of the protein B2 subunit of the *Escherichia coli* enzyme. *J. Biol. Chem.* **248**, 7464-72 (1973).

24. Seyedsayamdost, M.R. & Stubbe, J. Site-specific replacement of Y_{356} with 3,4-dihydroxyphenylalanine in the β2 subunit of *E. coli* ribonucleotide reductase. *J. Am. Chem. Soc.* **128**, 2522-3 (2006).

25. Ormo, M., Regnstrom, K., Wang, Z., Que, L., Jr., Sahlin, M. & Sjöberg, B. M. Residues important for radical stability in ribonucleotide reductase from *Escherichia coli*. *J Biol Chem* **270**, 6570-6576 (1995).

26. Yee, C.S. (2003).

27. Hristova, D., Wu, C.H., Jiang, W., Krebs, C. & Stubbe, J. Importance of the maintenance pathway in the regulation of the activity of *Escherichia coli* ribonucleotide reductase. *Biochemistry* **47**, 3989-99 (2008).

28. Zhou, P., Zou, J., Tian, F. & Shang, Z. Fluorine bonding--how does it work in protein-ligand interactions? *J. Chem. Inf. Model.* **49**, 2344-55 (2009).

29. Muller, K., Faeh, C. & Diederich, F. Fluorine in pharmaceuticals: looking beyond intuition. *Science* **317**, 1881-6 (2007).

30. Tommos, C., Skalicky, J.J., Pilloud, D.L., Wand, A.J. & Dutton, P.L. De novo proteins as models of radical enzymes. *Biochemistry* **38**, 9495-507 (1999).

31. Danyal, K., Mayweather, D., Dean, D.R., Seefeldt, L.C. & Hoffman, B.M. Conformational gating of electron transfer from the nitrogenase Fe protein to MoFe protein. *J. Am. Chem. Soc.* **132**, 6894-5 (2010).

32. Ator, M.A. & Stubbe, J. Mechanism of inactivation of *Escherichia coli* ribonucleotide reductase by 2'-chloro-2'-deoxyuridine 5'-diphosphate: evidence for generation of a 2'-deoxy-3'-ketonucleotide via a net 1,2 hydrogen shift. *Biochemistry* **24**, 7214-21 (1985).

33. Mao, S.S. et al. Interaction of C225SR1 mutant subunit of ribonucleotide reductase with R2 and nucleoside diphosphates: tales of a suicidal enzyme. *Biochemistry* **31**, 9744-51 (1992).

34. van der Donk, W.A., Yu, G. X., Perez, L., Sanchez, R. J., Stubbe, J., Samano, V. & Robins, M. J. Detection of a new substrate-derived radical during inactivation of ribonucleotide reductase from *Escherichia coli* by gemcitabine 5'-diphosphate. *Biochemistry* **37**, 6419-26 (1998).

35. Artin, E. et al. Insight into the mechanism of inactivation of ribonucleotide reductase by gemcitabine 5'-diphosphate in the presence or absence of reductant. *Biochemistry* **48**, 11622-9 (2009).

36. Stubbe, J. & van der Donk, W.A. Ribonucleotide reductases: Radical enzymes with suicidal tendencies. *Chemistry & Biology* **2**, 793-801 (1995).

37. Sjöberg, B.M., Reichard, P., Gräslund, A. & Ehrenberg, A. Tyrosine free-radical in ribonucleotide reductase from *Escherichia coli*. *J. Biol. Chem.* **253**, 6863-5 (1978).

38. Svistunenko, D.A. & Cooper, C.E. A new method of identifying the site of tyrosyl radicals in proteins. *Biophys. J.* **87**, 582-95 (2004).

39. Seyedsayamdost, M.R., Chan, C.T., Mugnaini, V., Stubbe, J. & Bennati, M. PELDOR spectroscopy with DOPA-β2 and NH_2Y-α2s: distance measurements between residues involved in the radical propagation pathway of *E. coli* ribonucleotide reductase. *J. Am. Chem. Soc.* **129**, 15748-9 (2007).

40. Holder, P.G., Pizano, A.A., Anderson, B.L., Stubbe, J. & Nocera, D.G. Deciphering radical transport in the large subunit of class I ribonucleotide reductase. *J. Am. Chem. Soc.* **134**, 1172-80 (2012).

41. Madej, E. & Wardman, P. The oxidizing power of the glutathione thiyl radical as measured by its electrode potential at physiological pH. *Arch. Biochem. Biophys.* **462**, 94-102 (2007).

42. Stubbe, J. & van der Donk, W.A. Protein radicals in enzyme catalysis. *Chem. Rev.* **98**, 705-62 (1998).

43. Li, C. et al. Protein (19)F NMR in *Escherichia coli*. *J. Am. Chem. Soc.* **132**, 321-7 (2010).

Chapter 8

Miscellany: investigating the role of E_{350} in the PCET mechanism & studying the reactivity of $Y_{356}NH_2Y$-ββ′

8.1 INTRODUCTION

8.1.1 Overview. This chapter briefly summarizes experiments that are of general interest to those studying the mechanism of long-range PCET in *E. coli* class Ia RNR, but that were either inconclusive or not sufficiently substantial to constitute their own chapter. Specifically, the chapter will focus on studies intended to investigate the role of E_{350} in the mechanism of long-range PCET, and on experiments exploring the chemistry and reactivity of the heterodimeric mutant $Y_{356}NH_2Y$-$\beta\beta'$.

8.1.2 Investigating the role of E_{350} in the PCET mechanism: a possible proton acceptor? The residue E_{350} is conserved among all class Ia RNRs, and resides in the structurally disordered C-terminal tail of the β subunit.[1] Climent et al. have previously reported that a non-conservative mutation of this residue ($E_{350}A$) renders the enzyme inactive (<0.5% wt activity).[2] However, this mutant maintains its ability to bind wt-α2 (K_d of 0.5 μM compared to 0.2 μM for the wt under identical conditions) and to form a diferric-Y_{122}• cofactor (1.1 Y•/β2, 2.8 Fe/β2), suggesting that the residue does not play an essential structural role in subunit interactions or cofactor assembly. Instead, it was proposed that the essentiality of E_{350} for RNR activity stems from its participation in the long-range radical propagation pathway. More specifically, we have proposed that E_{350} acts as the proton acceptor for orthogonal PCET through Y_{356} (Figure 8.1). With the ability to site-specifically incorporate unnatural Y analogues with perturbed pK_as at position 356, we can design experiments to test directly this hypothesis.

The first experiment involves the double-mutant enzyme $E_{350}A/Y_{356}NH_2Y$-β2. The NH_2Y incorporation provides a direct spectroscopic readout of radical propagation to position 356, while introducing minimal perturbation to the phenolic pK_a relative to the native Y. If, indeed, E_{350} is the proton acceptor for 356, then one would expect no NH_2Y_{356}• formation in the

reaction of $E_{350}A/Y_{356}NH_2Y$-β2 with wt-α2, CDP, and ATP. Unfortunately, the results of this experiment are not conclusive, as a negative result (i.e., absence of NH_2Y_{356}• formation) does not directly implicate E_{350} as a proton acceptor, only as a key residue in mediating radical propagation through position 356.

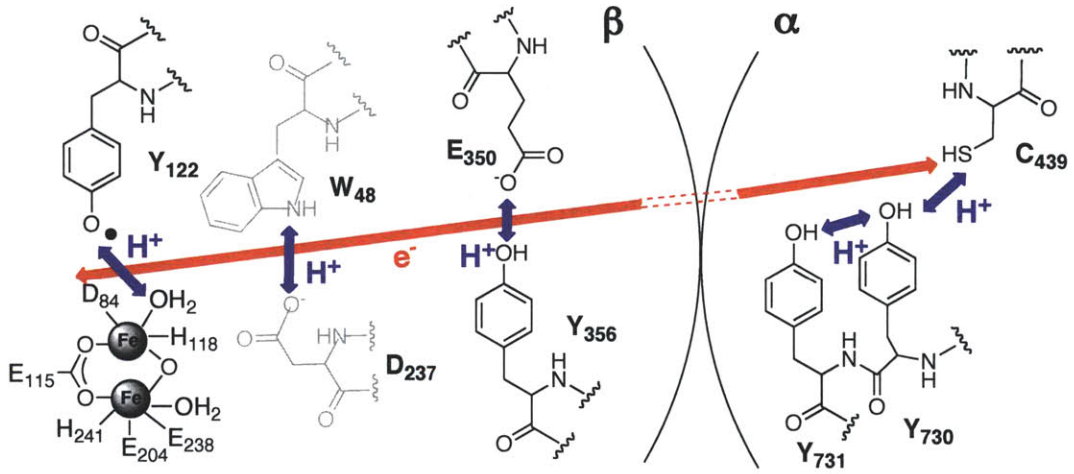

Figure 8.1 Working mechanism for long-range PCET in *E. coli* class Ia RNR. The current hypothesis holds that protons (blue arrows) move orthogonally to the electron (red arrow) in β2 and co-linearly with the electron in α2. The mechanism across the α/β interface is unknown. Y_{356} and its proposed proton acceptor, E_{350}, are located in the thermally labile C-terminal tail of β2, and thus their location within the structure is unknown.[1] The purpose of experiments in the first half of this chapter is to test this proposed role for E_{350}.

The recent development of technology for the *in vivo* site-specific incorporation of a series of fluorinated tyrosines (F_nYs, n = 1-4) to all positions on the pathway[3] has allowed a second set of experiments to more directly investigate the role of E_{350}. We have proposed previously that orthogonal PCET is functional in β2 (Figure 8.1). Initial experimental support for this hypothesis came from a pH rate profile of EPL-generated $Y_{356}(2,3)F_2Y$-β2, which demonstrated no correlation between enzyme activity and the protonation state of the fluorophenol.[4] This led to the conclusion that a shift in mechanism from orthogonal PCET to ET was operative at pHs above the pK_a of 2,3-F_2Y. Additional studies examining the pH

dependence of enzyme activity in a series of $Y_{356}F_nY$-β2s supported the claim that F_nY protonation state and activity are not linked.[5] With the new technology available, the double mutant $E_{350}X/Y_{356}(3,5)F_2Y$-β2 (X = A, D, Q) can be easily prepared and the pH dependence of its activity studied between pH 6-9. If E_{350} serves as the obligate proton acceptor during oxidation at 356, we would predict a dramatic loss of activity in the pH regime in which 3,5-F_2Y (pK_a ~7.2) is protonated, and a recovery of activity correlating with increasing pH and corresponding deprotonation of the phenol. Previous pK_a titrations of $Y_{356}NO_2Y$-β2 indicate that there is minimal pK_a perturbation by the protein environment at this position relative to the phenolic pK_a in solution.[6] The first half of Chapter 8 describes the results of these experiments.

8.1.3 Investigating the reactivity of $Y_{356}NH_2Y$-ββ′. The docking model proposes a symmetrical α2β2 complex as the active form of class Ia RNR.[7] However, substantial biochemical evidence has amassed in favor of an asymmetric α2β2 complex which gives rise to the unique half-sites reactivity of RNR.[8-12] While the structural basis for this asymmetry is unknown, the phenotype it gives rise to has been well documented, namely that upon binding of α2, β2, substrate (S), and effector (E), radical propagation and nucleotide reduction chemistry are initiated on a single α/β pair. The experimental data support a model in which C_{439} oxidation and nucleotide reduction chemistry occurs on the second α/β pair only after successful dCDP formation and reverse PCET in the first. This model has been substantiated by studies with a number of mechanism-based inhibitors and unnatural amino acid-containing RNRs. Reaction of wt-α2, wt-β2, and ATP with the inhibitor 2′-azido-2′-deoxycytidine (N_3CDP) results in the conversion of 50% of the starting Y_{122}• to a new nitrogen-centered active site radical (N•) with >90% loss of activity.[13,14] In the same vein, reaction of Y_{356}DOPA-β2 (0.3 Y_{122}•/β2) with wt-α2, CDP, and ATP results in the trapping of half the initial radical as $DOPA_{356}$•,[11] whereas the

reaction of $Y_{122}NO_2Y$-β2 (1.2 NO_2Y_{122}•/β2) with wt-α2, CDP, and ATP gives rise to 0.6 eq dCDP and traps 50% of the initial NO_2Y_{122}• as a pathway radical (primarily Y_{356}•) during reverse hole migration.[15]

The basis of the asymmetry that gives rise to the observed half-sites reactivity has been investigated previously by comparing the reactivity of Y_{356}DOPA-β2 to that of Y_{356}DOPA-ββ′, a heterodimer of one full-length monomer and one 353-truncated monomer that is formed due to complexities inherent to EPL ligation.[12,16] Reaction of Y_{356}DOPA-ββ (0.3 Y_{122}•/ββ′) with wt-α2, CDP, and ATP results in a 25% loss of initial Y_{122}• concomitant with $DOPA_{356}$• formation. An unexpected result of these studies was the first observation of reverse radical propagation in the reaction of Y_{356}DOPA-ββ′, wt-α2, CDP, and ATP. This reaction was very slow and was observed specifically with the CDP/ATP S/E pair. Given these interesting yet confusing results, we sought to examine study the reactivity of $Y_{356}NH_2Y$-ββ′, isolated as a byproduct during $Y_{356}NH_2Y$-β2 purification (section 2.3.2), in a series of experiments mimicking those conducted on the corresponding full-length homodimer.

8.2 MATERIALS AND METHODS

8.2.1 Materials. Fluorotyrosines (F_nYs, n=2-4) were synthesized enzymatically from pyruvate, ammonia, and the appropriate fluorinated phenol, with tyrosine phenol lyase (TPL) as the catalyst as described previously[17,18] and in Chapter 6. The desired products were isolated in 60-85% yield and characterized by ^1H NMR, ^{19}F NMR, and UV-vis absorption spectroscopy. TPL was expressed, purified, and assayed following a modification of the literature protocol,[17] as described in Chapter 6. $E_{350}X$-β2s (X = A, D, Q) were expressed and purified previously by Matt Winston (Stubbe lab) and their diferric-Y•s reconstituted by Dr. Rick Kelley (Nocera lab, MIT). $Y_{356}NH_2Y$-ββ′ was isolated as a major side product in the purification of $Y_{356}NH_2Y$-β2 (section 2.2.3).[19] N-Strep-5-$Y_{356}NH_2Y$-ββ′ was isolated as a major side product in the purification of N-Strep-5-$Y_{356}NH_2Y$-β2 (section 2.2.8).[19] Wt-α2 (2500 nmol/min/mg), His_6-α2(wt) (2200 nmol/min/mg), and wt-β2 (1.2 Y_{122}•/β2, 7600 nmol/min/mg) were expressed and purified as previously described.[19] *E. coli* thioredoxin (TR, 40 U/mg) and thioredoxin reductase (TRR, 1400 U/mg) were isolated as described.[20,21] [5-^{3}H]-CDP was purchased from ViTrax (Placentia, CA). Assay buffer consists of 50 mM Hepes, 1 mM EDTA, and 15 mM $MgSO_4$, pH 7.6. Plasmids pAC-NH_2Y and pEVOL-F_nY-RS were described previously.[3,22]

8.2.2 Expression and purification of $E_{350}A/Y_{356}NH_2Y$-β2. The Quikchange Kit (Stratagene) with *Pfu* Ultra II polymerase was used according to manufacturer's instructions to generate the double mutant plasmid pTrc-*nrdB*-$GCA_{350}TAG_{356}$ from the template, pTrc-*nrdB*-TAG_{356}, the forward primer 5′-GGTTGCTCCGCAGGCAGTGGAAGTCAGTTC-3′, and its reverse complement. The mutation was confirmed by sequencing at the MIT Biopolymers Laboratory. The protein $E_{350}A/Y_{356}NH_2Y$-β2 was expressed following the procedure reported for $Y_{356}NH_2Y$-β2 in section 2.2.3 to give 1.7 g/L.[19] Purification by the method reported in

section 2.2.3 afforded $E_{350}A/Y_{356}NH_2Y$-ββ′ (0.56 Y•/β2, 1.35 mg/g) and $E_{350}A/Y_{356}NH_2Y$-β2 (0.44 Y•/β2, 0.85 mg/g).

8.2.3 Reaction of $E_{350}A/Y_{356}NH_2Y$-β2 (or $E_{350}A/Y_{356}NH_2Y$-ββ′) with wt-α2, CDP, and ATP monitored by EPR spectroscopy. Pre-reduced His_6-α2(wt) and ATP were mixed rapidly with $E_{350}A/Y_{356}NH_2Y$-β2 (or $E_{350}A/Y_{356}NH_2Y$-ββ′) and CDP in assay buffer to give final concentrations of 25 μM, 3 mM, 25 μM, and 1 mM, respectively. Total initial Y• was 10-12.5 μM. The reaction was hand-quenched at 30 s in liquid N_2 and its EPR spectrum recorded. EPR spectra were recorded as described in section 2.2.6. Spin quantitation and analysis of composite reaction spectra were carried out as described in the same section.

8.2.4 Reaction of $E_{350}A/Y_{356}NH_2Y$-β2 (or $E_{350}A/Y_{356}NH_2Y$-ββ′) with wt-α2, CDP, and ATP monitored by SF UV-vis spectroscopy. SF kinetics were performed on an Applied Photophysics DX 17.MV instrument equipped with the Pro-Data upgrade. All reactions were carried out in assay buffer at 25 °C. Pre-reduced His_6-α2(wt) and ATP in one syringe were mixed rapidly with $E_{350}A/Y_{356}NH_2Y$-β2 (or $E_{350}A/Y_{356}NH_2Y$-ββ′) and CDP in a second syringe to yield a final concentration of 12.5 μM protein (5-6.25 μM Y•), 1 mM CDP, and 3 mM ATP. The reactions were monitored at 410 nm for Y_{122}• (ε ~3,700 $M^{-1}cm^{-1}$) and 324 nm for NH_2Y_{356}• (ε ~10,500 $M^{-1}cm^{-1}$) using PMT detection. In each experiment, the most reproducible traces (5-10 shots) were averaged and kinetic parameters obtained by curve fitting using KaleidaGraph.

8.2.5 Expression and purification of $E_{350}X/Y_{356}(3,5)F_2Y$-β2s (X = A, D). $E_{350}A/Y_{356}(3,5)F_2Y$-β2 was expressed from the plasmids pEVOL-F_nY-RS and pTrc-*nrdB*-$GCA_{350}TAG_{356}$; $E_{350}D/Y_{356}(3,5)F_2Y$-β2 was expressed from the plasmids pEVOL-F_nY-RS and pBAD-*nrdB*-$GAC_{350}TAG_{356}$, as described in section 6.2.6. The proteins were purified according

to the protocol used for $Y_{356}F_nY$-β2s, as described in section 6.2.6, in yields of 3 (pTrc) to 16 (pBAD) mg/g (homodimer) with as-isolated radical content of 0.7-1.1 Y•/β2.

8.2.6 pH rate profiles of $E_{350}X/Y_{356}(3,5)F_2Y$-β2s (X = A, D). pH rate profiles were determined by the radioactive assay as described in section 6.2.7.

8.2.7 Activity assays of $Y_{356}NH_2Y$-ββ′. The activities of $Y_{356}NH_2Y$- ββ′ (~80-85% pure, 0.9 Y•/dimer) and N-Strep-5-$Y_{356}NH_2Y$-ββ′ (>95% pure, 0.1 Y•/dimer) were determined by the radioactive RNR assay as described previously[5] with ββ′ between 0.2 – 2.0 μM, and wt-α2 in a five-fold excess. [^{3}H]-CDP had a specific activity of 7300 cpm/nmol.

8.2.8 SF UV-vis kinetics of NH_2Y• formation in $Y_{356}NH_2Y$-ββ′. Instrument setup was identical to that described in section 8.2.4. Reactions were conducted at 25 °C. In all cases, pre-reduced α2 and E in one syringe were rapidly combined with $Y_{356}NH_2Y$-ββ′ and S from a second syringe to yield a final concentration of 25 μM for each protein subunit. The following S and/or E combinations (final concentrations) were studied: CDP/ATP (1 mM, 3 mM) and GDP/TTP (1 mM, 0.2 mM). The reactions were monitored at 324 nm for NH_2Y_{356}• and 410 nm for Y_{122}• using PMT detection. In each experiment, the most reproducible traces (5-10 shots) were averaged and kinetic parameters obtained by curve fitting using KaleidaGraph.

8.3 RESULTS

8.3.1 Confirming low activities of $E_{350}X$-β2s. The activity of E_{350}A-β2 has been reported previously by Climent et al. as 17 nmol/min/mg. While a fraction of the activity was attributed to co-purifying chromosomal β2, experiments looking at Y_{122}• loss in the presence of E_{350}A-β2, wt-α2, N_3CDP, and TTP suggested the mutant was capable of radical propagation to the active site, albeit at a very slow rate.[2] To reevaluate the activity of E_{350} mutants, the proteins E_{350}X-β2s (X = A, D, Q) were expressed, purified, and their diferric-Y•s reconstituted. The K_ds of these mutants (0.5-1.4 μM) to wt-α2 had been measured previously and found to be 2.5- to 7-fold higher than that of the wt-β2:wt-α2 interaction, suggesting only a small structural perturbation upon mutation of this conserved residue.[23] This is consistent with what has been reported previously for E_{350}A-β2.[2] Given these K_ds, the specific activities of the purified, reconstituted mutants were determined by the radioactive assays under conditions in which >80% of the limiting subunit is in complex. The results are summarized in Table 8.1 and demonstrate that all three mutants appear to have very low levels of catalytic activity. It is difficult to discern, however, whether these activities are inherent to the mutants or whether they arise from contaminating, endogenous *E. coli* wt β2. The latter possibility seems likely.

Table 8.1 Specific activities of E_{350}X-β2s as determined by the radioactive assay.

Sample	**SA, Measured** nmol•min^{-1}•mg^{-1}	**Y•/β2**	**SA, Scaled** nmol•min^{-1}•mg^{-1}	**% Wild Type**
E_{350}A-β2[a]	3	0.7	5	0.07
E_{350}D-β2[a]	18	1.1	20	0.29
E_{350}Q-β2[a]	6	1.1	7	0.10
wt-β2	7000	1.2	na	na

a. Mutant proteins expressed and purified by Matthew Winston as described previously[23] and their diferric-Y• cofactors reconstituted by Dr. Rick Kelley.

8.3.2 Reactions of $E_{350}A/Y_{356}NH_2Y$-β2 (or $E_{350}A/Y_{356}NH_2Y$-ββ′) with wt-α2, CDP, and ATP monitored by EPR and SF UV-vis spectroscopies. The protein $E_{350}A/Y_{356}NH_2Y$-β2 was expressed and purified following the procedure reported for $Y_{356}NH_2Y$-β2.[19] This protocol allowed isolation of two species, $E_{350}A/Y_{356}NH_2Y$-β2 and $E_{350}A/Y_{356}NH_2Y$-ββ′, in yields of 0.8 mg/g and 1.35 mg/g, respectively. As-isolated homodimer had 0.44 Y•/β2 and heterodimer had 0.5 Y•/β2, as determined by the UV-vis dropline correction and EPR spectroscopy. As described in Chapter 2, formation and characterization of NH_2Y_{356}• in the reaction of $Y_{356}NH_2Y$-β2, wt-α2, S, and E has been studied extensively by EPR and SF UV-vis spectroscopies.[19] The reaction of $E_{350}A/Y_{356}NH_2Y$-β2 (or $E_{350}A/Y_{356}NH_2Y$-ββ′) with wt-α2, CDP, and ATP was investigated under identical single-turnover conditions using the same spectroscopic methods. If the hypothesis put forth in Figure 8.1 concerning E_{350} is correct, one would expect that mutation of this residue to A would prevent formation of NH_2Y_{356}•.

Indeed, the reaction of $E_{350}A/Y_{356}NH_2Y$-β2 with wt-α2, CDP, and ATP hand quenched at 30 s and analyzed by X-band EPR (Figure 8.2) shows no evidence of of NH_2Y_{356}• formation in the reaction mixture. Upon subtraction of the Y_{122}• contribution, the only visible features in the difference spectra are subtle spectral changes to Y_{122}• that occur upon α2/β2 complex formation. Furthermore, spin quantitation revealed no spin loss over the 30 s reaction course, suggesting that other short-lived radical species were not overlooked by hand-quenching. An identical result was obtained for the reaction of $E_{350}A/Y_{356}NH_2Y$-ββ′ with wt-α2, CDP, and ATP (data not shown). The results of these experiments may be compared to those obtained in the identical reaction with $Y_{356}NH_2Y$-β2, in which 20% of the total spin is lost over 30 s, and the remaining spin is distributed between NH_2Y_{356}• (41%) and Y_{122}•(59%).[19]

To examine whether there are any observable changes on the ms timescale, the reactions with both the homo- and heterodimer were repeated on the SF UV-vis spectrometer. For the single mutant homodimer, $Y_{356}NH_2Y$-β2, NH_2Y• formation occurs with a fast phase of 36 s^{-1} (25% conversion) and a slow phase of 2.1 s^{-1} (5%). NH_2Y_{356}• formation is monophasic for the heterodimer (*vide infra*), with a rate constant of 0.4 s^{-1} (17%). Under the same conditions, the double mutants $E_{350}A/Y_{356}NH_2Y$-β2 and $E_{350}A/Y_{356}NH_2Y$-ββ′showed no evidence of Y_{122}• loss (410 nm) or NH_2Y_{356}• formation (325 nm) upon rapid mixing with wt-α2, CDP, and ATP (Figure 8.3). Thus, these data suggest that neither $E_{350}A/Y_{356}NH_2Y$-β2 nor $E_{350}A/Y_{356}NH_2Y$-ββ′ can generate NH_2Y_{356}•, consistent with our working hypothesis that E_{350} is the proton acceptor for Y_{356}• formation.

The results of reactions with $E_{350}A/Y_{356}NH_2Y$-β2 and $E_{350}A/Y_{356}NH_2Y$-ββ′ are consistent with previous studies on the reaction of $E_{350}X$-β2 (X= A, D, Q) with $Y_{731}NH_2Y$-α2, CDP, and ATP, which were examined by SF UV-vis spectroscopy (Kelley, Nocera, and Stubbe, unpublished results). The results of these experiments indicated that the E_{350} mutation in β2 prevents NH_2Y• formation at position 731 of α2, consistent with a mechanism in which Y_{356} cannot be oxidized in the E_{350} mutant and thus is not available to propagate the radical to position 731.

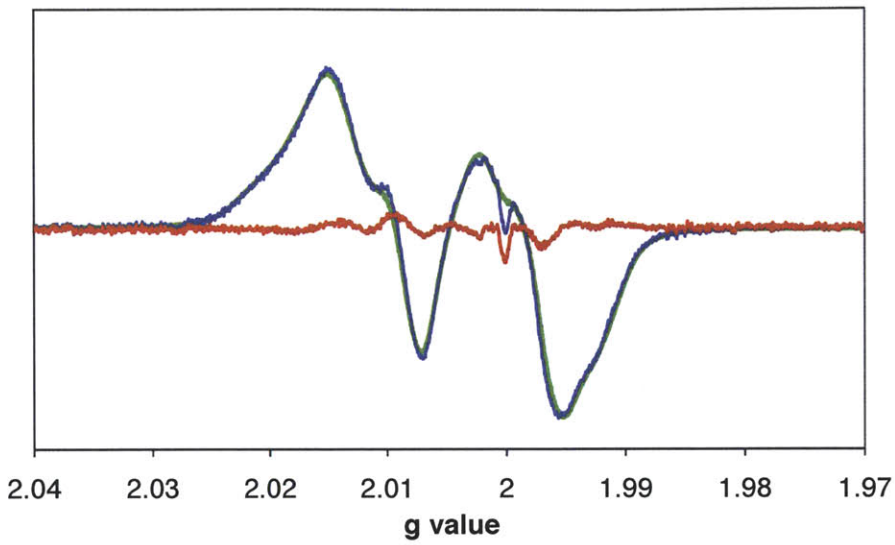

Figure 8.2 EPR spectrum of the reaction of wt-α2, CDP, and ATP with $E_{350}A/Y_{356}NH_2Y$-β2 hand quenched in N_2 (l) after 30 s at 25 °C. Reaction spectrum is in blue, residual Y_{122}• is in green, and net subtracted spectrum is in red.

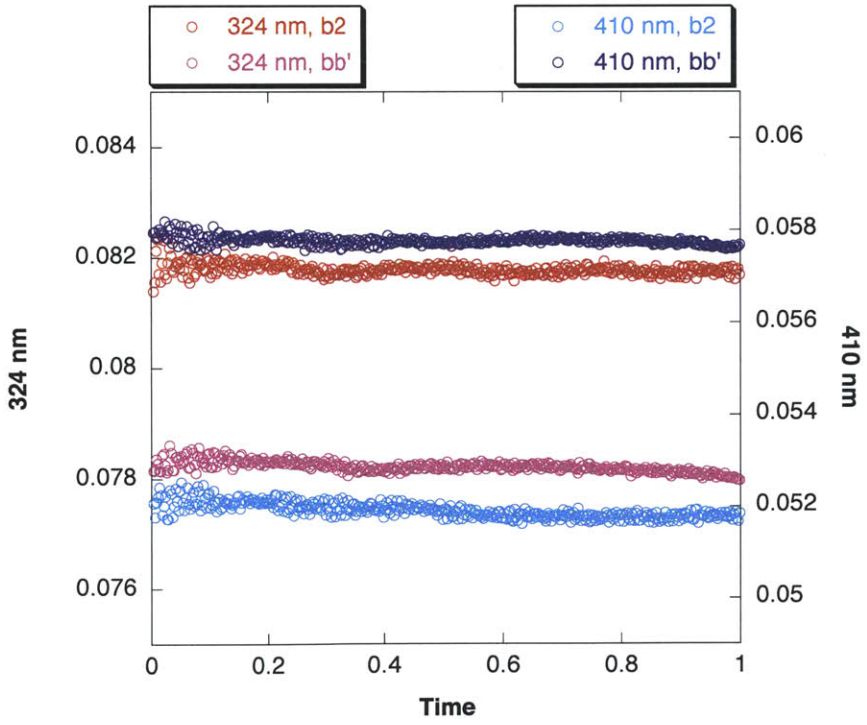

Figure 8.3 SF UV-vis spectroscopy of the reaction of $E_{350}A/Y_{356}NH_2Y$-β2 (or $E_{350}A/Y_{356}NH_2Y$-ββ′) with wt-α2, CDP, and ATP under single-turnover conditions at 25 °C. The kinetics were followed at 324 nm to look for NH_2Y_{356}• formation (red trace for β2, pink for ββ′) and 410 nm to look for Y_{122}• loss (cyan for β2, blue for ββ′).

8.3.3 pH rate profiles of $E_{350}X/Y_{356}(3,5)F_2Y$-β2s (X = A, D). Given the suggestive but not conclusive results with the NH_2Y-containing mutants, we designed an experiment to specifically test whether E_{350}'s role is to serve as a proton acceptor for orthogonal PCET through position 356. In this experiment, the activity of the double mutant $E_{350}X/Y_{356}(3,5)F_2Y$-β2 (X = A or D) is monitored as a function of pH. It has been demonstrated previously that $Y_{356}(3,5)F_2Y$-β2 generated by EPL showed ~100% of wt activity over the pH 6.5-9 regime and that the activity did not vary as a function of the protonation state of the phenol.[5] The pH rate profile of $Y_{356}(3,5)F_2Y$-β2 generated by the *in vivo* suppression method is distinct from that of the EPL-generated analogue (Chapter 6), likely due to two additional point mutations in the immediate vicinity of position 356 in the EPL protein. Despite these differences, the same result was expected from the experiment with the $E_{350}X/Y_{356}(3,5)F_2Y$-β2 double mutant, namely that the protein would be inactive at pHs below the pK_a of the F_2Y (~7.2) and active at higher pHs.

The proteins $E_{350}A/Y_{356}(3,5)F_2Y$-β2 and $E_{350}D/Y_{356}(3,5)F_2Y$-β2 were expressed and purified following the protocol optimized for $Y_{356}F_nY$-β2s (section 6.3.7). The double mutant $E_{350}A/Y_{356}(3,5)F_2Y$-β2 was examined first. A rough pH rate profile of the double mutant protein was constructed, examining the activity from pH 6.2-9.0 in 0.4 pH unit increments. Surprisingly, the maximum activity observed was only 40 nmol/min/mg (at pH 8.2), or 0.5% the activity of wt-β2. This result strongly suggests that the isolated double mutant is completely inactive (over the entire pH regime), and that the detected activity originates from contaminating wt β2. This hypothesis was substantiated by comparison of the pH rate profile of $E_{350}A/Y_{356}(3,5)F_2Y$-β2 with those of wt-α2 and wt-β2 (Figure 8.4), all three of which demonstrate nearly identical pH dependence. The results of these assays were very surprising, and suggest that the role(s) of E_{350} in radical propagation is(are) more complicated than merely accepting a proton from 356. Such

roles could be related to structure, or to maintaining extended H-bonding networks, or to mediating radical propagation between Y_{356} and Y_{731}.

To begin to address these questions, we turned to the more conservative mutant, $E_{350}D/Y_{356}(3,5)F_2Y$-β2. Recall that the $E_{350}D$ single mutation allowed β2 to maintain a small amount (~0.3%) the wt activity. Thus, a pH rate profile was constructed from radioactive assays over the same pH range. The maximum activity observed for $E_{350}D/Y_{356}(3,5)F_2Y$-β2 was only 10 nmol/min/mg, or 0.2% the activity of wt-β2, indicating that the isolated double mutant is likely inactive over the entire pH regime (Figure 8.5), as we suspect the discernable activity arises from contaminating wt-β2. The lower activity in this mutant (0.2% wt) may be compared to that observed for $E_{350}A/Y_{356}(3,5)F_2Y$-β2 (0.5% wt), and the difference between the two may be attributed to differences in expression systems. The latter was expressed from pTrc and constituted a much lower percentage of the total cellular protein compared to the former, which was expressed from the optimized pBAD system. One would expect to see a higher contaminating wt contribution in lower-yielding mutant, in agreement with what is observed here. The results of the pH rate profiles are consistent with what was previously observed $E_{350}A/Y_{356}(3,5)F_2Y$-β2 and suggest that the 350 mutation disrupts radical propagation in a fashion that is more complicated than elimination of a single proton acceptor.

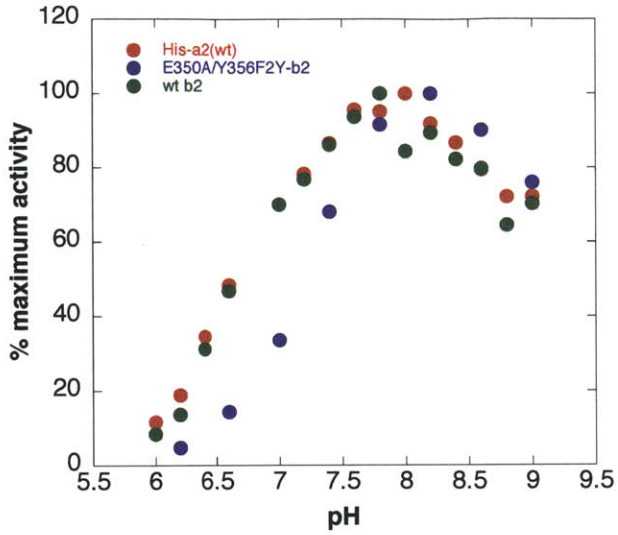

Figure 8.4 The percent maximum activity of $E_{350}A/Y_{356}(3,5)F_2Y$-β2 as a function of pH. This plot is derived from the specific activities (Figure 8.5), but is intended to normalize the data on a single Y axis. Results are compared to existing data for wt-α2 and wt-β2. Data points are colored follows: His-α2(wt) (red), wt-β2 (green), and $E_{350}A/Y_{356}(3,5)F_2Y$-β2 (blue).

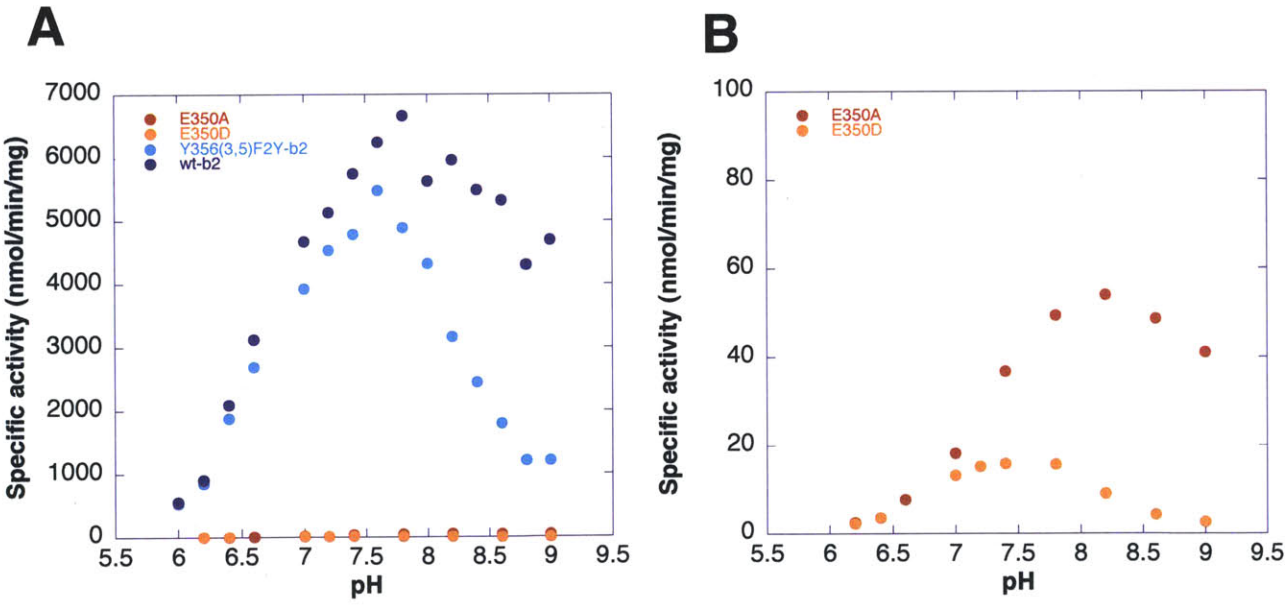

Figure 8.5 (A) pH rate profiles of wt-β2 (blue), $Y_{356}(3,5)F_2Y$-β2 (cyan), $E_{350}A/Y_{356}(3,5)F_2Y$-β2 (red), and $E_{350}D/Y_{356}(3,5)F_2Y$-β2 (orange). (B) Scaling the Y axis from panel (A) highlights the low activities of the E_{350} double mutants.

8.3.4 Determining the catalytic activity of $Y_{356}NH_2Y$-ββ′. We now shift our attention to the study of the $Y_{356}NH_2Y$-ββ′ heterodimer. Many lines of evidence now support the proposed half-sites reactivity of RNR.[8-12] In light of this hypothesis, we explored the reactivity of the $Y_{356}NH_2Y$-ββ′ heterodimer with respect to NH_2Y_{356}• formation and dCDP production. $Y_{356}NH_2Y$-ββ′ is isolated as a major side product when purifying the corresponding homodimer. The $Y_{356}NH_2Y$-β2 homodimer has been determined to contain 4-5% the activity of wt-β2, or 8-10% when scaled for radical content. Previous studies indicated that the wt-ββ′ heterodimer has 25% of the activity of EPL-generated wt-β2 (~100 nmol/min/mg).[6] These observations prompted us to examine whether $Y_{356}NH_2Y$-ββ′ is active in deoxynucleotide formation.

The activity of $Y_{356}NH_2Y$-ββ′ (~80-85% pure, 0.9 Y•/β2) was determined by the radioactive RNR assay using final ββ′ concentrations of 0.3-2.0 μM and a five-fold excess of wt-α2. The results are summarized in Table 8.2 and indicate that $Y_{356}NH_2Y$-ββ′ has 0.1% the activity of wt-β2 regardless of subunit concentration. In all cases, the radioactive scintillation counts observed were >3-fold over the zero timepoint, suggesting that the activity measurements are discernable over background. This low activity cannot be attributed to the elevated K_d of the ββ′ heterodimer for wt-α2 (relative to β2),[2,12] as there is no correlated increase in activity with increasing protein concentration. As mentioned above, EPL-generated wt-ββ′ has 25% the activity of wt-β2 generated by the same method. Thus, the activity of $Y_{356}NH_2Y$-ββ′ is significantly lower than the 2-2.5% wt activity one would predict on the basis of the previously determined activity of $Y_{356}NH_2Y$-β2 (8-10% wt). However, it is worth noting that "wt"-β2 generated by EPL has a maximum specific activity of 450 nmol/min/mg associated with low radical content (~0.3 Y•/β2) and two additional mutations ($V_{353}G$ and $S_{354}C$) necessary for peptide ligation. Thus, the percent activity of its heterodimer may not be comparable to a

heterodimer generated by the *in vivo* suppression technology. A different heterodimer of wt-β2 (ββ′, where β′ is truncated due to specific proteolysis after residue 345 of 375 total amino acids) has been reported by Sjöberg et al. to have 1-2% the activity of the corresponding wt subunit. This activity quantitation is more consistent with what we observe with $Y_{356}NH_2Y$-ββ′ relative to $Y_{356}NH_2Y$-β2. However, given the incredibly low activity measured (Table 8.2), it is entirely possible that this activity is associated with co-purifying contaminating wt, rather than inherent to the $Y_{356}NH_2Y$-ββ′ heterodimer. Thus, we cannot state conclusively whether $Y_{356}NH_2Y$-ββ′ is active with 1% the activity of its corresponding homodimer, or whether it is completely inactive.

Table 8.2 Specific activity of $Y_{356}NH_2Y$-ββ′ determined by the radioactive assay with various protein concentrations.

$Y_{356}NH_2Y$-ββ′ (μM)	**α2** (μM)	**Spec Act** (nmol/min/mg)	**% wt activity** (scaled for Y•)
0.3 μM	1.5	5.6	0.1
1.0 μM	5.0	7.8	0.1
2.0 μM	10.0	6.0	0.1

8.3.5 Measuring the kinetics of NH_2Y_{356}• formation in $Y_{356}NH_2Y$-ββ′ by SF UV-vis spectroscopy. It was previously demonstrated that the heterodimer Y_{356}DOPA-ββ′ formed $DOPA_{356}$• with all S/E pairs, albeit with slower rate constants and lower amplitudes than the intact homodimer Y_{356}DOPA-β2.[12] For the CDP/ATP pair, a total of 25% the initial Y_{122}• was converted to $DOPA_{356}$• with a rate constant of 1 s^{-1}. For the analogous reaction with the homodimer, a 47% conversion was observed over three phases with rate constants of 38 s^{-1}, 6.8 s^{-1}, and 0.7 s^{-1}. Similar changes in rate constants and amplitudes were observed for the other S/E pairs.

We sought to examine by SF UV-vis spectroscopy whether $Y_{356}NH_2Y$-ββ′ was capable of generating NH_2Y• and, if so, how the rate constants and amplitudes of NH_2Y_{356}• formation

compare to those of the homodimer. The S/E pairs CDP/ATP (1 mM, 3 mM) and GDP/TTP (1 mM, 0.2 mM) were examined, and the kinetics measured at 324 nm (NH_2Y_{356}•) and 410 nm (Y_{122}•). For CDP/ATP, Y_{122}• loss and NH_2Y• formation occurred with a rate constant of 0.4 s^{-1} and a 30% total conversion of initial Y_{122}• to NH_2Y_{356}• (Table 8.3 and Figure 8.6 A). This rate constant is 100-fold slower than the fast phase for NH_2Y_{356}• formation in $Y_{356}NH_2Y$-β2, and 5-fold slower than the slow phase (section 2.3.3 and 2.3.10). Interestingly, it is on par with k_{cat} measured for the homodimer, and the total overall amplitude of radical formation is the same between the two mutants. With the GDP/TTP pair, $Y_{356}NH_2Y$-ββ′ and wt-α2 generate NH_2Y_{356}• with biphasic kinetics of 2.6 s^{-1} (10% conversion) and 0.2 s^{-1} (20% conversion, Table 8.3 and Figure 8.6 C). This may be compared to rate constants of 38 s^{-1} (25%) and 1.8 s^{-1} (7%) in the analogous reaction with the homodimer. Thus, we observe a ~10-fold reduction in rate constants and a redistribution of amplitudes between the two phases when moving from the β2 to ββ′.

Arguably the most exciting result obtained in studies of Y_{356}DOPA-ββ′ was the observation of reverse ET from Y_{122} to $DOPA_{356}$•. This was the first direct observation of reverse ET in any RNR, mutant or wild-type. Interestingly, reoxidation of Y_{122} was observed exclusively in the presence of the CDP/ATP pair. The basis for observing the phenomenon under these specific conditions is not understood. We sought to examine if reverse ET was detectable in the reactions of $Y_{356}NH_2Y$-ββ′. Indeed, when the reaction of $Y_{356}NH_2Y$-ββ′, wt-α2, CDP, and ATP is monitored over a longer time, a slow loss of NH_2Y_{356}• is observed concomitant with reformation of Y_{122}• with a rate constant of 0.015 s^{-1} (Figure 8.6 B). Approximately 40% of the total NH_2Y_{356}• formed is converted to Y_{122}•, or 12% of the total initial Y_{122}•. The "reverse" ET phases at 325 nm and 410 nm are in good agreement with one another, suggesting that the two events are strictly correlated. This may be compared with the reaction of

Y_{356}DOPA-ββ′, wt-α2, CDP, and ATP, in which 36% of the initial DOPA• formed is competent in Y_{122} re-oxdiation. Similar to what was observed in the DOPA system, no evidence of reverse ET from NH_2Y_{356}• to Y_{122} is apparent with the GDP/TTP pair, even monitoring over very long time frames (Figure 8.6 D). However, NH_2Y_{356}• appears to decay slowly with a rate constant of 0.004 s^{-1}. This decay rate is identical to that which was determined previously by EPR for NH_2Y_{730}• spin loss in the reaction of $Y_{730}NH_2Y$-α2, wt-β2, CDP, and ATP (Chapter 2), consistent with some non-specific degradation pathway for NH_2Y• intermediates.

Table 8.3 Kinetic parameters for NH_2Y_{356}• formation in $Y_{356}NH_2Y$-ββ′

S/E	λ (nm)	$k_{fast,\ for}$ (s^{-1})	Amplitude (% initial Y_{122}•)	$k_{slow,\ for}$ (s^{-1})	Amplitude (% initial Y_{122}•)	$k_{ET,\ rev}$ (s^{-1})	Amplitude (% initial Y_{122}•)
CDP/ATP	325	0.4	30	-[a]	-	0.015	12
	410	0.4	30	-[a]	-	0.015	11
GDP/TTP	325	2.6	10	0.2	20	-[b]	-
	410	2.1	10	0.1	20	-[b]	-

a. A second phase is not observed; *b.* Reverse ET is not observed.

Figure 8.6 SF UV-vis spectroscopy was used to determine the kinetics of NH_2Y_{356}• formation (324 nm, red) and Y_{122}• loss (410 nm, blue) in the reaction of $Y_{356}NH_2Y$-ββ′, wt-α2, S, and E under single-turnover conditions at 25 °C. (A) The CDP/ATP reaction showing NH_2Y_{356}• formation at early time points; (B) The CDP/ATP reaction showing NH_2Y_{356}• loss concomitant with Y_{122}• reformation at longer time points; (C) The GDP/TTP reaction showing NH_2Y_{356}• at early time points; (D) The GDP/TTP reaction showing NH_2Y_{356}• decay but *no* Y_{122}• reformation at longer time points. Fits to the data at early time points (A and C) are indicated by black lines.

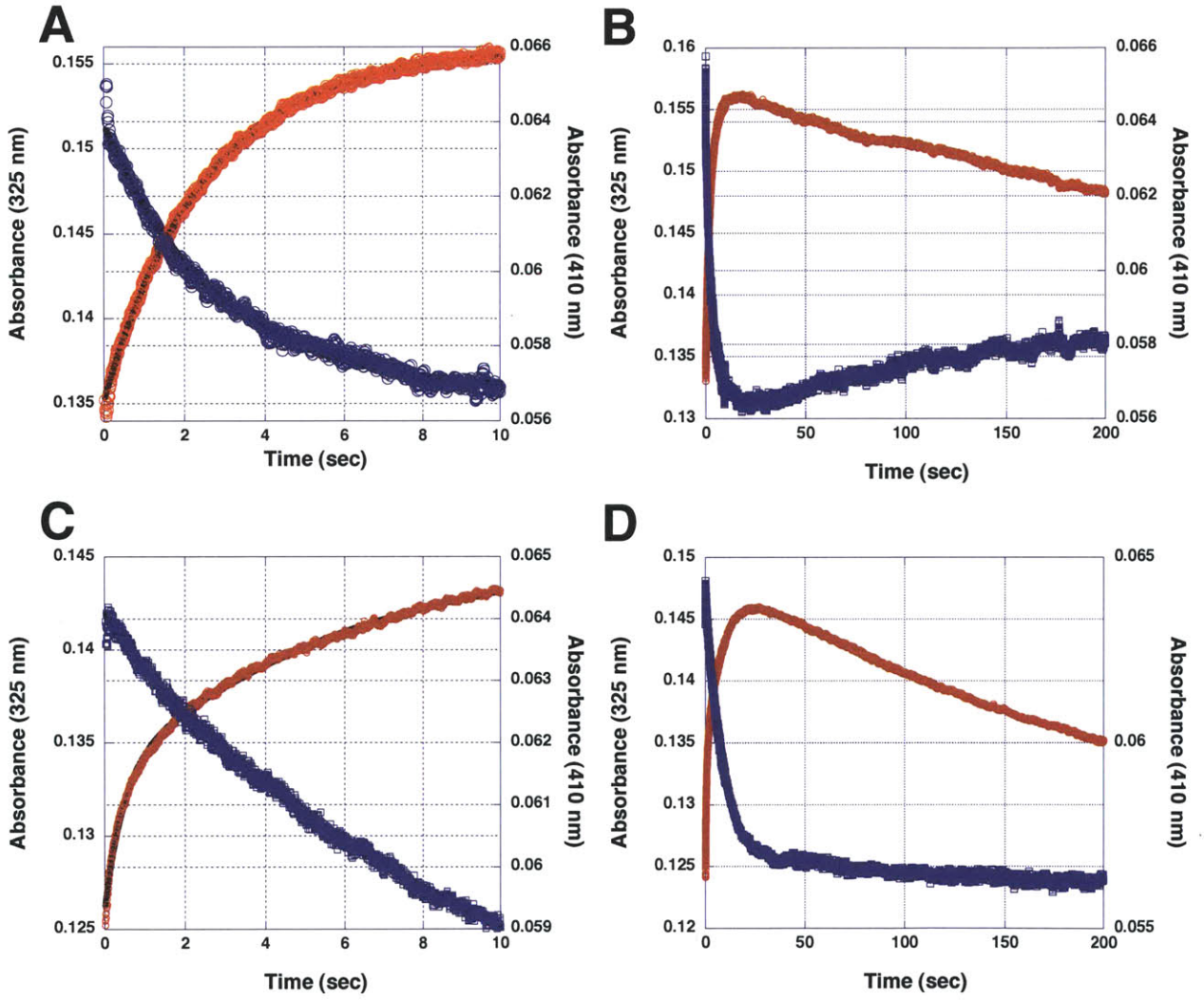

8.4 DISCUSSION AND FUTURE DIRECTIONS

8.4.1 Re-evaluating the role of E_{350} in radical propagation. The critical role of E_{350} in catalysis was first demonstrated over two decades ago by insertion of a single point mutation at this position.[2] With advances in protein engineering technology, we have sought to design more sophisticated experiments to examine the role of E_{350} in radical propagation. Namely, we have demonstrated that insertion of an $E_{350}X$ (X = A, D, Q) mutation prevents formation of $NH_2Y\bullet$ at either position 356 of β2 or 731 of α2. However, attempts to directly implicate E_{350} as the proton acceptor upon Y_{356} oxidation proved unsuccessful, as both $E_{350}A/Y_{356}(3,5)F_2Y$-β2 and $E_{350}D/Y_{356}(3,5)F_2Y$-β2 were shown to be inactive at all pHs. While this result does not discount the existing hypothesis, it suggests that the role of E_{350} in radical propagation may be more complicated than originally predicted. Future experiments include the isolation of the structurally homologous mutant $E_{350}Q/Y_{356}(3,5)F_2Y$-β2 and investigation of the pH dependence of its catalytic activity (if measurable). Furthermore, the pH dependence of activity between $E_{350}X$-β2 mutants and $Y_{731}(3,5)F_2Y$-α2 may be examined. Currently there is no strong hypothesis for the mechanism of radical propagation across the subunit interface, and the proton acceptor for Y_{731} has not been identified. Thus, it is possible that E_{350} may play a role in this process. Unfortunately, without any high-resolution structural information about the protein complex, or any structural information about E_{350} or Y_{356} in the independent β2 subunit, it is difficult to predict the full extent to which E_{350} participates in radical propagation.

It is also important to note that the recently measured pH rate profiles of F_nY-RNRs generated by the *in vivo* nonsense suppression method indicate that, for these mutants, the pH dependence likely reports on rate-limiting conformational changes rather than the chemistry of radical propagation (Chapter 6). Thus, even if conditions were found under which an E_{350} mutant

demonstrated significant activity, interpretation of the pH dependence may be more complicated than was anticipated at the outset of these experiments.

Interestingly, a primary sequence alignment of nrdBs with nrdFs (class Ib β subunit) reveals that E_{350} aligns with a serine (S_{298}, *E. coli* nrdF numbering) that is conserved among all class Ibs. However, the C-terminal tails of nrdFs are rich in acidic residues, with at least one conserved aspartate (D_{316}) that could function as a proton acceptor upon oxidation of Y_{304} (equivalent to the class Ia Y_{356}) during long-range PCET.

8.4.2 $Y_{356}NH_2Y$-ββ′ rendered inactive due to slow kinetics of conformational changes and/or reverse ET. $Y_{356}NH_2Y$-ββ′ is generated from the *in vivo* dimerization of an intact, full-length $Y_{356}NH_2Y$-β monomer and a 355-truncated β monomer, and is isolated as a major side product in the purification of the full-length $Y_{356}NH_2Y$-β2 homodimer. Given the ease of its isolation and prior interesting data obtained on the analogous heterodimer Y_{356}DOPA-ββ′, we sought to conduct a few preliminary experiments to study its reactivity. With previous knowledge of the activities of $Y_{356}NH_2Y$-β2 (8-10% wt) and EPL-generated wt-ββ′ (25% wt), we predicted that the NH_2Y-heterodimer would be active with ~2% the wt activity. In practice, a steady-state activity of 0.1% that of wt-β2 was observed (or ~1% the activity of $Y_{356}NH_2Y$-β2) under multiple conditions (Table 8.3). At present, we cannot conclude whether that activity is inherent to $Y_{356}NH_2Y$-ββ′ or is the result of contaminating wt-β2 that could arise from the sources described in Chapter 2. Evidence against contaminating wt-β2 as the source of the activity lies in the very different migration properties of ββ′ and β2 during anion exchange chromatography. The highly-charged C-terminal tail of β gives rise to a characteristic elution profile in which β′2, ββ′, and β2 elute first, second, and third, respectively, with increasing salt concentration. Thus, one might suspect that $Y_{356}NH_2Y$-ββ′ would separate from wt-β2 during

protein purification. However, as described in Chapter 2, isolation of $Y_{356}NH_2Y$-β2 in >90% yield is a complicated process involving three anion-exchange columns to fully separate the hetero- and homodimers, so we cannot rule out the possibility of some co-elution of the two species.

It is interesting to note that the as-isolated radical content of $Y_{356}NH_2Y$-ββ′ (0.6-0.9 Y•/β2) is routinely higher than that of $Y_{356}NH_2Y$-β2 (0.3-0.5 Y•/β2). We have hypothesized previously (Chapter 2) that the low radical content of $Y_{356}NH_2Y$-β2 may be due to the presence of a low-potential radical "sink" at position 356 that interferes with the thermodynamics of *in vitro* cluster assembly.[19] A similar hypothesis has been put forth with respect to Y_{356}DOPA-β2.[12,16] In the EPL-assembled mutant, radical content was significantly increased if reconstitution of the diferric-Y• cluster occurred before ligation of the C-terminal peptide containing $DOPA_{356}$. For the purpose of this thesis, we have worked under the assumption that radical loading is symmetrical for these *in vitro* reconstituted mutants (i.e., an even distribution of Y_{122}• between the two β monomers). The heterodimer of $Y_{356}NH_2Y$-ββ′ could thus prove unique if its truncated protomer contains increased radical with respect to the full-length $Y_{356}NH_2Y$-β protomer.

Returning to the question of whether $Y_{356}NH_2Y$-ββ′ is inherently active, it would interesting to examine the activity of $Y_{356}NH_2Y$-ββ′ under single-turnover conditions in an experiment akin to those experiments described in Chapter 2 on the intact NH_2Y-RNRs. Provided the amount of product formed is sufficiently high compared to the radiochemical background, the results form this experiment could help distinguish the source of the activity in the steady-state assay – mutant heterodimer or contaminating wt – and, if the latter, could indicate whether $Y_{356}NH_2Y$-ββ′ is active in only a single turnover (i.e., generates a single dCDP

on the $Y_{356}NH_2Y$-β/α pair and then stops when it is unable to do chemistry on the β′/α pair). It is also possible that the stoichiometry of product formation in a single turnover could provide insight to the distribution of Y_{122}• in the heterodimer, though we know that product quantitation in NH_2Y-RNRs is complicated (section 2.3.7). At this time, we cannot speculate on the likely outcome of a $Y_{356}NH_2Y$-ββ′ single-turnover assay, but the potential to glean useful information from this experiment makes it worthwhile.

One possible explanation for a loss of Y_{356} NH_2Y-ββ′ activity could be disruption of the conformational changes that gate radical propagation and likely optimize the pathway for efficiency and fidelity. These sensitive conformational changes are triggered by the assembly of a complex of α2β2, S, and E; assembly of the α2β2 complex is governed primarily by interactions of the C-terminal tail of β, one of which is completely absent in $Y_{356}NH_2Y$-ββ′. We have previously interpreted the rate constants of NH_2Y• formation to be reporting on the conformational changes that trigger radical propagation (section 2.3.10), and indeed SF UV-vis experiments of the reaction of $Y_{356}NH_2Y$-ββ′ with wt-α2, S, and E indicate that the rate constants of NH_2Y_{356}• formation are decreased 5- to 100-fold relative to the analogous reaction with $Y_{356}NH_2Y$-β2. Alternatively, it is possible that $Y_{356}NH_2Y$-ββ′ forms a complex with wt-α2, S, and E, generates a single dCDP on the $Y_{356}NH_2Y$-β/α pair, and, unable to initiate radical propagation on the β′/α pair, accumulates radical at position 356. This would necessitate formation of a moderately stable $Y_{356}NH_2Y$-ββ′•wt-α2 complex, similar to that proposed for wt-β2•$Y_{730}NH_2Y$-α2 in Chapter 5 but lacking the second C-terminal tail. Depending on conformational subtleties imparted by the S/E pair (i.e., CDP/ATP versus GDP/TTP), NH_2Y_{356}• could either re-oxidize Y_{122} on the minute time scale (Figure 8.6 B) or could be slowly reduced through a non-specific pathway (Figure 8.6 D).

8.5 REFERENCES

1. Nordlund, P., Sjöberg, B.M. & Eklund, H. Three-dimensional structure of the free radical protein of ribonucleotide reductase. *Nature* **345**, 593-8 (1990).
2. Climent, I., Sjöberg, B.M. & Huang, C.Y. Site-directed mutagenesis and deletion of the carboxyl terminus of *Escherichia coli* ribonucleotide reductase protein R2 - effects on catalytic activity and subunit interaction. *Biochemistry* **31**, 4801-4807 (1992).
3. Minnihan, E.C., Young, D.D., Schultz, P.G. & Stubbe, J. Incorporation of fluorotyrosines into ribonucleotide reductase using an evolved, polyspecific aminoacyl-tRNA synthetase. *J. Am. Chem. Soc.* **133**, 15942-5 (2011).
4. Yee, C.S., Chang, M.C.Y., Ge, J., Nocera, D.G. & Stubbe, J. 2,3-difluorotyrosine at position 356 of ribonucleotide reductase R2: A probe of long-range proton-coupled electron transfer. *J. Am. Chem. Soc.* **125**, 10506-7 (2003).
5. Seyedsayamdost, M.R., Yee, C.S., Reece, S.Y., Nocera, D.G. & Stubbe, J. pH rate profiles of F_nY_{356}-R2s (n = 2, 3, 4) in *Escherichia coli* ribonucleotide reductase: evidence that Y_{356} is a redox-active amino acid along the radical propagation pathway. *J. Am. Chem. Soc.* **128**, 1562-8 (2006).
6. Yee, C.S., Seyedsayamdost, M.R., Chang, M.C.Y., Nocera, D.G. & Stubbe, J. Generation of the R2 subunit of ribonucleotide reductase by intein chemistry: insertion of 3-nitrotyrosine at residue 356 as a probe of the radical initiation process. *Biochemistry* **42**, 14541-52 (2003).
7. Uhlin, U. & Eklund, H. Structure of ribonucleotide reductase protein R1. *Nature* **370**, 533-539 (1994).
8. Sjöberg, B.M., Karlsson, M. & Jornvall, H. Half-site reactivity of the tyrosyl radical of ribonucleotide reductase from Escherichia coli. *J. Biol. Chem.* **262**, 9736-43 (1987).
9. van der Donk, W.A., Yu, G. X., Perez, L., Sanchez, R. J., Stubbe, J., Samano, V. & Robins, M. J. Detection of a new substrate-derived radical during inactivation of ribonucleotide reductase from *Escherichia coli* by gemcitabine 5'-diphosphate. *Biochemistry* **37**, 6419-26 (1998).
10. Ge, J., Yu, G., Ator, M.A. & Stubbe, J. Pre-steady-state and steady-state kinetic analysis of *E. coli* class I ribonucleotide reductase. *Biochemistry* **42**, 10071-83 (2003).
11. Seyedsayamdost, M.R. & Stubbe, J. Site-specific replacement of Y_{356} with 3,4-dihydroxyphenylalanine in the β2 subunit of *E. coli* ribonucleotide reductase. *J. Am. Chem. Soc.* **128**, 2522-3 (2006).
12. Seyedsayamdost, M.R. & Stubbe, J. Forward and reverse electron transfer with the Y356DOPA-β2 heterodimer of *E. coli* ribonucleotide reductase. *J. Am. Chem. Soc.* **129**, 2226-7 (2007).
13. Salowe, S. et al. Alternative model for mechanism-based inhibition of *Escherichia coli* ribonucleotide reductase by 2'-azido-2'-deoxyuridine 5'-diphosphate. *Biochemistry* **32**, 12749-60 (1993).

14. Fritscher, J. et al. Structure of the nitrogen-centered radical formed during inactivation of *E. coli* ribonucleotide reductase by 2'-azido-2'-deoxyuridine-5'-diphosphate: trapping of the 3'-ketonucleotide. *J. Am. Chem. Soc.* **127**, 7729-38 (2005).

15. Yokoyama, K., Uhlin, U. & Stubbe, J. A hot oxidant, 3-NO2Y_{122} radical, unmasks conformational gating in ribonucleotide reductase. *J. Am. Chem. Soc.* **132**, 15368-79 (2010).

16. Seyedsayamdost, M.R. Ph.D. Thesis, Massachusetts Institute of Technology (2007).

17. Chen, H., Gollnick, P. & Phillips, R.S. Site-directed mutagenesis of His343-->Ala in Citrobacter freundii tyrosine phenol-lyase. Effects on the kinetic mechanism and rate-determining step. *Eur. J. Biochem.* **229**, 540-9 (1995).

18. Seyedsayamdost, M.R., Reece, S.Y., Nocera, D.G. & Stubbe, J. Mono-, di-, tri-, and tetra-substituted fluorotyrosines: new probes for enzymes that use tyrosyl radicals in catalysis. *J. Am. Chem. Soc.* **128**, 1569-79 (2006).

19. Minnihan, E.C., Seyedsayamdost, M.R., Uhlin, U. & Stubbe, J. Kinetics of radical intermediate formation and deoxynucleotide production in 3-aminotyrosine-substituted *Escherichia coli* ribonucleotide reductases. *J. Am. Chem. Soc.* **133**, 9430-40 (2011).

20. Chivers, P.T. et al. Microscopic pK_a values of *Escherichia coli* thioredoxin. *Biochemistry* **36**, 14985-91 (1997).

21. Russel, M. & Model, P. Direct cloning of the *trxB* gene that encodes thioredoxin reductase. *J. Bacteriol.* **163**, 238-42 (1985).

22. Seyedsayamdost, M.R., Xie, J., Chan, C.T., Schultz, P.G. & Stubbe, J. Site-specific insertion of 3-aminotyrosine into subunit α2 of *E. coli* ribonucleotide reductase: direct evidence for involvement of Y730 and Y731 in radical propagation. *J. Am. Chem. Soc.* **129**, 15060-71 (2007).

23. Winston, M. Final report on undergraduate research in the Stubbe lab. (2007).